EFFECTS OF MULTIPLE DAMAGE-HEAT STRAIGHTENING REPAIRS ON THE STRUCTURAL PROPERTIES OF BRIDGE STEELS

FINAL REPORT

By,

Amit H. Varma, Principal Investigator, MSU
Keith Kowalkowski, Graduate Research Assistant, MSU

Michigan State University
Department of Civil and Environmental Engineering
3546 Engineering Building
East Lansing, MI 48823
Phone No. (517) 355 5107
Fax No. (517) 432 1827

Report No. RC-1456
Sponsored by Michigan Department of Transportation

November 14, 2004

Technical Report Documentation Page

1. Report No. RC-1456	2. Government Accession No.	3. MDOT Project Manager Roger Till
4. Title and Subtitle Effects of Multiple Damage-Heat Straightening Repair on the Fundamental Properties of Bridge Steels		5. Report Date November 14, 2004
7. Authors Amit H. Varma Keith J. Kowalkowski		6. Performing Organization Code
9. Performing Organization Name and Address Michigan State University Department of Civil and Environmental Engineering 3546 Engineering Building East Lansing MI, 48823		8. Performing Org Report No.
12. Sponsoring Agency Name and Address Michigan Department of Transportation Construction and Technology Division P.O. Box 30049 Lansing, MI 48909		10. Work Unit No. (TRAIS) 11. Contract Number: 1994-1699 11(a). Authorization Number: 27
15. Supplementary Notes		13. Type of Report & Period Covered Final Report, Mar. 2002-Sept. 2004 14. Sponsoring Agency Code

16. Abstract

The effects of multiple damage-heat straightening repair events on the structural properties and fracture toughness of A36, A588, and A7 bridge steels were investigated experimentally. The damage and repair parameters included in the project are: (i) the damage strain ε_d, (ii) the restraining stress σ_r, (iii) the number of damage-repair cycles N_r, and (iv) the maximum heating temperature T_{max}. Extensive laboratory-scale and large-scale tests were conducted to evaluate the effects of these parameters on the structural properties including: (a) elastic modulus E, (b) yield stress σ_y, (c) ultimate stress σ_u, (d) % elongation, (e) surface hardness, (f) fracture toughness, and (g) microstructure.

Ninety-one laboratory-scale specimens, and six large-scale beam specimens made from A36, A588, and A7 steel were tested. The experimental results indicate that multiple damage-repair cycles do no have a significant influence on E, σ_y, σ_u, and surface hardness. However, they have a significant influence on the % elongation and fracture toughness. Based on the experimental results and findings, it is recommended that: (1) A7 and A36 steel beams should be replaced after three damage-repair cycles, (2) A588 steel beams can be subjected to five damage-repair cycles. And, (3) additional research is needed further validate the conclusions regarding overheating A36 and other types of steel above the recommended limit of 1200°F.

17. Key Words Steel Bridges, Heat Straightening, Structural Properties, Fracture Toughness, Surface Hardness, Microstructure	18. Distribution Statement No restrictions. This document is available to the public through the Michigan Department of Transportation.		
19. Security Classification (report) Unclassified	20. Security Classification (Page) Unclassified	21. No of Pages 418	22. Price

[Intentionally Blank Page]

ACKNOWLEDGMENTS

This research project was sponsored by the Michigan Department of Transportation (Roger Till – cognizant program official). It was conducted at Michigan State University by the principal investigator (Dr. Amit H. Varma) and his Ph.D. student (Keith Kowalkowski). Significant help was provided by Siavosh Ravanbaksh, Jason Shingledecker, and Sig of Langenberg Machine Products.

The authors would like to acknowledge:

(a) The foresight of the MDOT, Construction and Technology Division, Testing and Research Section for funding this important and timely research project.
(b) Roger Till for his unique insight, intelligence, and guidance on several topics relevant to this research.
(c) The MDOT maintenance division (Christopher Idusuyi and Corey Rogers) for helping with practical matters and setting up the site visits.
(d) Peter Jansson for his help with various issues including the decommissioned A7 steel bridge.
(e) The engineers who served on the project research advisory panel including Steve Cook and Steve Beck for their interest and enthusiasm regarding the findings

DISCLAIMER

EFFECTS OF MULTIPLE DAMAGE-HEAT STRAIGHTENING REPAIRS ON THE FUNDAMENTAL PROPERTIES OF BRIDGE STEELS

TABLE OF CONTENTS

EFFECTS OF MULTIPLE DAMAGE-HEAT STRAIGHTENING REPAIRS ON THE FUNDAMENTAL PROPERTIES OF BRIDGE STEELS

LIST OF TABLES

EFFECTS OF MULTIPLE DAMAGE-HEAT STRAIGHTENING REPAIRS ON THE FUNDAMENTAL PROPERTIES OF BRIDGE STEELS

LIST OF FIGURES

EXECUTIVE SUMMARY

The research project focuses on the multiple damage-heat straightening repair of steel bridges. The objectives were to: (a) evaluate the effects of multiple cycles of damage-heat straightening repair on the structural properties of bridge steels, and (d) to develop guidelines for replacing steel beams subjected to multiple damage-repair cycles. The research project was conducted in four research tasks.

The first task involved: (i) detailed literature review of heat straightening repair and its effects on the structural properties of bridge steels, (ii) survey of state DOTs to determine existing heat straightening procedures and guidelines, and (iii) analysis of the 1976-2001 Michigan high load hits database to identify the steel types most frequently subjected to damage-heat straightening repair. The results from this task indicate that there is a significant lack of knowledge and guidelines for evaluating the effects of multiple damage-heat straightening repair cycles on steel structural properties. The most frequently damaged-repaired steel types in Michigan are A7, A373, A588, A36, and A572 Gr.-50 in descending order.

The second task involved three field visits to heat straightening repair sites in Michigan. Details of the MDOT heat straightening repair procedures and guidelines are presented in the report. In some cases, overheating of the steel to temperatures greater than the recommended limit of 1200^{o}F was noted.

The third task conducted detailed experimental investigations on laboratory scale specimens to evaluate the effects of multiple damage-heat straightening repair cycles on the structural properties of A36, A588, and A7 steels. The damage and repair parameters included were: (i) the damage strain ε_d, (ii) the restraining stress σ_r, (iii) the number of damage-repair cycles N_r, and (iv) the maximum heating temperature T_{max}. The effects of these parameters were evaluated on the structural properties including: (a) elastic modulus E, (b) yield stress σ_y, (c) ultimate stress σ_u, (d) % elongation, (e) surface hardness, (f) fracture toughness, and (g) microstructure. Ninety-one laboratory scale specimens were tested: twenty-eight A36, thirty A588, and seventeen A7 steel specimens were subjected to multiple damage-repair cycles with heating temperatures were less than the recommended limit of 1200^{o}F; sixteen A36 specimens were subjected to multiple damage-repair cycles with heating temperatures approaching 1400 - 1600^{o}F. The experimental results indicate that multiple damage-repair cycles do no have a significant influence ±15% on E, σ_y, σ_u, and surface hardness. However, they have a significant influence on the % elongation and fracture toughness. The experimental results indicate that: (1) A36 and A7 steel beams should be replaced after three damage-repair cycles, (2) A588 steel beams can be subjected to five damage-repair cycles. Overheating the A36 steel to temperatures > 1200^{o}F has improves the fracture toughness of the damage-repaired steel significantly.

The fourth task conducted experimental investigations on large-scale beam specimens to validate the conclusions from the Task III laboratory-scale specimen tests. Six A36, A588, and A7 steel beam specimens were subjected to three damage-repair cycles. The results from task IV validate the conclusions and recommendations from Task III noted above.

Based on the laboratory-scale and large-scale specimen tests, it is recommended that: (1) A7 and A36 steel beams should be replaced after three damage-repair cycles. (2) A588 steel beams can be subjected to five damage-repair cycles. And, (3) additional research is needed further validate the conclusions regarding overheating A36 and other types of steel above 1200^{o}F.

[Intentionally Blank Page]

1 INTRODUCTION, OBJECTIVES, AND RESEARCH PLAN

1.1 RESEARCH PROBLEM STATEMENT

Heat straightening is a cost-effective and efficient technique for repairing steel beam bridges damaged by collisions with overheight loads. It involves heating the damaged (inelastic) portions of the steel member in specific patterns to temperatures up to 1200 °F (for mild carbon steels) while maintaining an external restraining force, which results in thermo-plastic deformations in the heated region and straightening of the member. Heat straightening affects the structural properties of steel. It increases the yield stress and reduces the ductility in the heated region. The influence of heat straightening on the fracture toughness of damaged steel is not known accurately.

Significant research on the behavior of heat straightened steel members has been conducted. However, most of the research has focused on: (a) the development of empirical equations and guidelines to facilitate heat straightening in the field; (b) the influence of heat straightening on the structural properties of undamaged steel; and (c) experimental investigations of the deformations and residual stresses caused by heat straightening. Prior to this research project, there is a significant lack of knowledge of the influence of multiple damage-heat straightening repair cycles on the structural properties, namely, the yield stress, the ultimate stress, the strain ductility, the notch toughness, and the surface hardness of steel.

Owing to this lack of knowledge, most state departments of transportation replace steel members after the second or third damage event. Heat straightening can be very cost effective as compared to replacing portions of the steel bridge [*1*]. Therefore, there is significant research interest in the development of recommendations and guidelines for evaluating and replacing steel members subjected to multiple damage-heat straightening repair events.

The Michigan Department of Transportation (MDOT) funded a research project to answer the questions relating the effects of multiple heat straightening repairs

1.2 INTRODUCTION TO HEAT STRAIGHTENING

1.2.1 Structural Damage due to a Collision

The collision of an overheight truck with a steel beam bridge can cause significant structural damage to the steel beams. The structural damage is usually quite complicated. It causes significant plastic strains in localized regions of the steel beams. The complicated structural damage is a combination of four fundamental damage categories shown in Figure 1.1, which are identified as strong axis damage (Category S), weak axis damage (Category W), torsional damage (Category T), and local buckling damage (Category L) [*2*]. For bridges with composite steel beams, the structural damage is usually a combination of Categories T and L damage. The collisions may cause significant out-of-plane movement of the bottom flange as in Category W damage. For bridges with non-composite steel beams, the structural damage is usually a combination of Categories W and L damage.

1.2.2 Basic Heat Straightening Patterns

Figure 1.2 shows the four fundamental heat straightening patterns for plate elements [*1*], [*3*], [*4*], which are identified as (a) the Vee heat, (b) the strip heat, (c) the line heat, and (d) the spot heat. The Vee heat pattern is most effective in bending a plate element about its strong axis, the strip heat is most effective in shortening a plate element, the line heat is most effective in bending a plate element about its minor axis, and the spot heat is most effective in causing local bulging in the plate element.

The heat straightening patterns used to repair damaged steel beam bridges are combinations of the four fundamental heat straightening patterns shown in Figure 1.2. They are developed based on the structural damage caused by the collision and the need to keep portions of the bridge open to traffic while the repair is being conducted.

1.2.3 Heat Straightening Mechanics

Heat straightening relies on two fundamental aspects of steel material behavior, which are: (1) the effects of elevated temperature on the yield stress; and (2) the post-yield inelastic behavior of the material. For example, Equations (1.1) and (1.2) summarize the effects of elevated temperature (T) on the yield stress of mild carbon steel [1].

$$\frac{\sigma_{yT}}{\sigma_y} = 1.0 - \frac{T - 100}{5822} \qquad (100\ °F \geq T \geq 800\ °F) \qquad (1.1)$$

$$\frac{\sigma_{yT}}{\sigma_y} = (4200T - 2.75T^2 - 720{,}000)x10^{-6} \qquad (800\ °F \geq T \geq 1200\ °F) \qquad (1.2)$$

In Equations 1.1 and 1.2, σ_y and σ_{yT} are the yield stress at ambient and elevated temperatures, respectively. Equation 2 indicates that at 1200 °F, σ_{yT} is approximately 36 percent of σ_y.

Figure 1.3 shows a simple schematic to illustrate the mechanics of heat straightening. Consider a steel bar of length (L) placed snug in a tight vice as shown in Figure 1.3(a). As the bar is heated over a small region close to mid-length, it tries to expand longitudinally. The longitudinal expansion is restrained by the vice, which results in the development of straining compressive stresses (σ_r) and strains in the bar as shown in Figure 1.3(b). However, the steel yield stress at elevated temperatures is much lower than the ambient steel yield stress. As a result, the heated region of the steel bar yields in compression and plastic compressive strains develop. Lateral expansion (upsetting) also occurs in the heated region following plastic flow rules. The steel bar contracts as it cools from the heated temperature. Since the vice restrains the contraction of the steel bar, the final length is shorter than the original length (L) as shown in Figure 1.3(c). The plastic compressive strains that develop in the bar due to the restraint of thermal expansion (σ_r) cause the shortening of the bar. These thermo-plastic deformations form the basis of the heat straightening method.

1.2.4 Cautions during Heat Straightening

Some important issues that must be paid careful attention to during the heat straightening operation are as follows:

The Heating Temperature: Steel undergoes a phase transition from a body centered cubic (BCC) structure to a face centered cubic (FCC) structure at a temperature of around 1340 °F. As a result, rapid cooling from temperatures greater than 1340 °F can result in the formation of maternsite, which is a more brittle form of steel. Phase transition of steel is discussed more in Section 4.3.4. Additionally, quenched and tempered steels must not be heated to temperatures greater than the tempering temperature (1100 °F to 1150 °F). Table 1.1 summarizes the maximum heating temperatures for various steels (Avent et al. 2001).

The Restraining Force: The restraining force has a significant influence on the heat straightening operation. However, very large restraining forces are not advisable because of the reduced yield stress of steel at elevated temperatures. Avent et al. [*2*] have recommended a maximum restraining force that would cause 50% of the plastic moment (M_p) of the damaged section.

The Cooling Method: Avent et al. [*2*] recommended that the ambient air is the safest for cooling heated steel members. Rapid cooling can be dangerous if the steel is overheated. However, rapid cooling of the steel when heated to temperatures below the phase transformation temperature of 1340 °F is not harmful. The steel surfaces should be allowed to cool below 600 °F before rapid cooling. Accelerated cooling with compressed air or water mist can be used. Research conducted by Till [*5*] at MDOT indicated different toughness values for steels cooled by different methods. The highest notch toughness values were for steels cooled by compressed air.

Mechanical Hot Working: Sometimes a large restraining force combined with a heating temperature much lower than 1200 °F is used to mechanically straighten damaged steel members. This process called mechanical hot-working, and is not the same as heat straightening. It is not recommended for repairing damaged steel bridges because of possible degradation of the steel material properties.

1.3 OBJECTIVES AND SIGNIFICANCE

The objectives of the research project are summarized as follows:

- To review the current MDOT heat straightening procedures and to conduct a survey of heat straightening procedures and guidelines used by other state departments of transportation.
- To experimentally investigate the effects of multiple heat straightening on the structural properties, namely, the yield stress, ultimate stress, strain ductility, modulus of elasticity, notch toughness, and surface hardness, and the microstructure of steel.
- To develop simple recommendations and guidelines for evaluating and replacing steel members subjected to multiple damage - heat straightening repair events.

MDOT does not specify a maximum limit on the number of multiple heat straightening repairs of the same steel member. The decision to replace steel members depends on the magnitude of the damage and type of structure. This information was provided as part of a state DOT survey discussed in Section 2.2.1. MDOT does not have any specific provisions regarding multiple heat straightening of the same steel member. As mentioned previously, heat straightening is much more economical than replacing damaged steel beams. Therefore, MDOT has identified this problem as one of the research focus areas. Development of recommendations and guidelines for evaluating and replacing steel members subjected to multiple damage-heat straightening repair cycles has significant cost benefits and added confidence in heat straightening operations conducted in the field.

1.4 RESEARCH PLAN

The objectives were achieved by dividing the research project into four major tasks. The four major task groups with brief descriptions are summarized as follows.

Task I. Literature Review, Survey, and High Load Hits Database

- Develop a state-of-the-art report reviewing and summarizing the current state-of-knowledge on heat straightening repair of damaged steel members, the effects of single and multiple heat straightening on steel material properties, and the current guidelines for conducting effective heat straightening in the field.
- Survey different state departments of transportation to review their heat straightening procedures and guidelines, and their criteria and limitations for multiple heat straightening.
- Summarize a database of all high load damage-repair events that have occurred at bridges in the State of Michigan. This database should investigate the amount of damage repairs on different steel types and structure types.

Task II. Review MDOT Heat Straightening Procedures

- Monitor the heating temperatures and patterns, and the restraining forces used in the field by MDOT for repairing steel beam bridges.
- Determine the influence of heat straightening on the structural properties or microstructure of in-situ steel.
- Review and comment on the heat straightening policies and procedures used by MDOT.

Task III. Effects of Multiple Heat Straightening on the Structural Properties of Steel

- Experimentally investigate the effects of multiple damage - heat straightening repair on the structural properties of steel using several laboratory scale specimens.
  - Parameters included in the study are the steel type, the initial damage strain, the restraining force, and the number of damage-repair cycles.
  - Structural properties included in the study are: elastic modulus, yield stress, ultimate stress, strain ductility, fracture toughness, hardness, and microstructure of steel.
- Develop empirical models for predicting the effects of multiple damage – heat straightening repair on the structural properties of steel.
- Develop simple recommendations and non-destructive techniques for evaluating steels subjected to multiple damage - heat straightening repair.

Task IV. Effects of Multiple Heat Straightening on Large-Scale Steel Beams

- Evaluate the conclusions and recommendations made in Task III by conducting experimental investigations on large-scale steel beams.
- Experimentally investigate the effects of multiple damage-heat straightening repair cycles on the structural properties using large-scale steel beams.

1.5 REPORT LAYOUT

This section addresses the layout of this report. The research project was separated into four task groups.

Chapter 2 of this report focuses on Task I, Literature Review, Survey, and High Load Hits Database. Task I included: (1) a literature review of all prior experimental and analytical investigations conducted on heat straightening, (2) a survey on heat-straightening practices has provided by a number of state DOTS; and (3) a high-load hits database which summarizes all of the heat straightening repair work conducted on steel bridge members in the state of Michigan from 1976-2001.

Chapter 3 of this report focuses on Task II, Review of MDOT Heat Straightening Procedures. The MSU research team visited three heat-straightening repair sites in the state of Michigan and spent time with the Statewide Bride Crew (SBC). Descriptions of the heat straightening repair procedures used by the SBC are summarized in Chapter 3. Chapter 3 also includes a summary of the MDOT heat straightening specifications and provides comments of the MSU researchers in regards to these specifications.

Most of the work conducted in this research project involved the experimental investigations as part of Task III, Effects of Multiple Heat Straightening on the Structural Properties of Steel. Due to the length of the description, the write up of Task III has been divided into three chapters. Chapter 4 provides a full description of Task III including an introduction, testing methodologies, the test matrix, the test setup, the experimental procedure, etc. Chapter 5 provides a summary of all the experimental results. The

experimental results include the damage and heat-straightening repairs, as well as the results fro material testing of damage-repaired steel. Chapter 6 summarizes the material testing results and presents the conclusions regarding the effects of heat straightening on the structural properties of steel.

Task IV, Effects of Multiple Heat Straightening on Large-Scale Steel Beams, has been separated into two chapters. Chapter 7 provides a full description of Task IV including an introduction, the test matrix, the test setup and specimen design, and the experimental procedure. Chapter 7 also includes an analytical fiber analysis used to predict the damage-repair stress-strain history within the beam specimens. Chapter 8 presents the summary and conclusions from the experimental results of Task IV. The experimental results include the damage-repair history of each beam specimen as well as the results of material testing on damage-repaired steel are also included in Chapter 8. This chapter also compares the material testing results of Task IV with those from Task III.

Chapter 9 provides a summary of the entire research project. The most significant conclusions, recommendations for examining and replacing steel beam bridges, and recommendations for further heat straightening investigations are provided in Chapter 9.

Tables, figures, and equations are labeled in the order, which they were mentioned in the text. For instance, the first figure in Chapter 1 is labeled Figure 1-1. References, Tables, and Figures are provided at the end of each corresponding chapter.

1.6 REFERENCES

1. Roeder, C. W., *Journal of Structural Engineering*, ASCE, Vol. 112, No. 10, Oct. 1986, pp. 2247-2262.
2. Avent, R. R., Mukai, D.J., and Robinson, P.F, *Journal of Structural Engineering*, ASCE, Vol.126, No. 7, July 2000, pp. 755-763.
3. Avent, R. R., Mukai, D.J., Robinson, P.F., and Boudreaux, R.J., *Journal of Structural Engineering*, ASCE, Vol. 126, No. 7, July 2000, pp. 747-754.
4. FHWA, "Heat-Straightening Repairs of Damaged Steel Bridges – A Technical Guide and Manual of Practice," Report NO. FHWA-IF-99-004, Federal Highway Administration, Washington, D.C., 1998
5. Till, R. D., "Effect of Elevated Temperature on Fracture Critical Steel Members," MDOT Research Report No. R-1344, Materials and Technology Division, Michigan Department of Transportation, 1996, pp. 1-17.

Table 1.1
Maximum heating temperatures for steels

Steel type	Max. heating temperatures
Mild carbon steel (A36, A572 Gr. 50)	1200°F
Quenched and tempered steel A514, A709 Gr. 100	1100°F
Quenched and tempered steel A709 Gr. 70W	1050°F

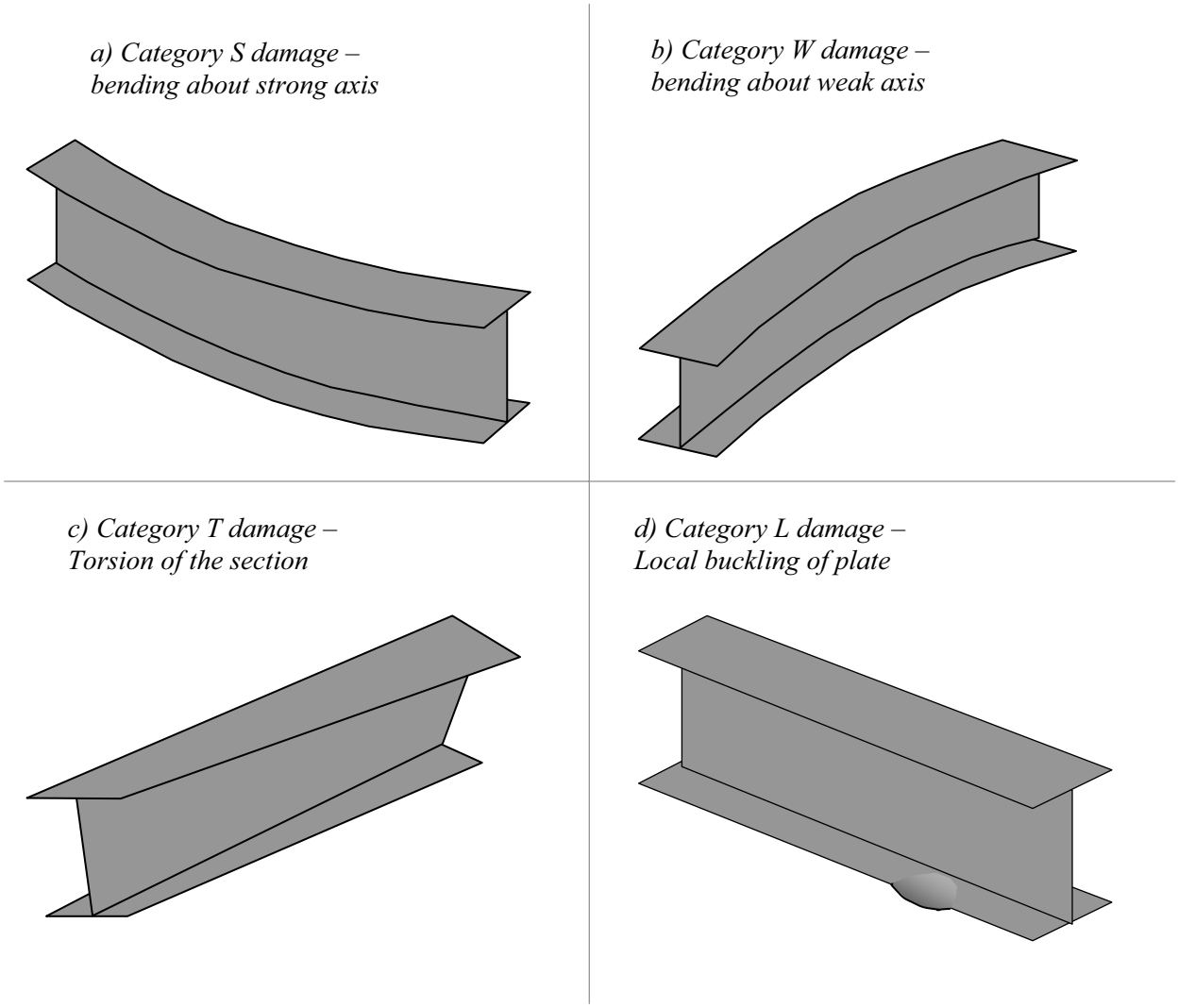

Figure 1.1
Fundamental damage categories for steel beams: Categories (a) S; (b) W; (c) T; and (d) L

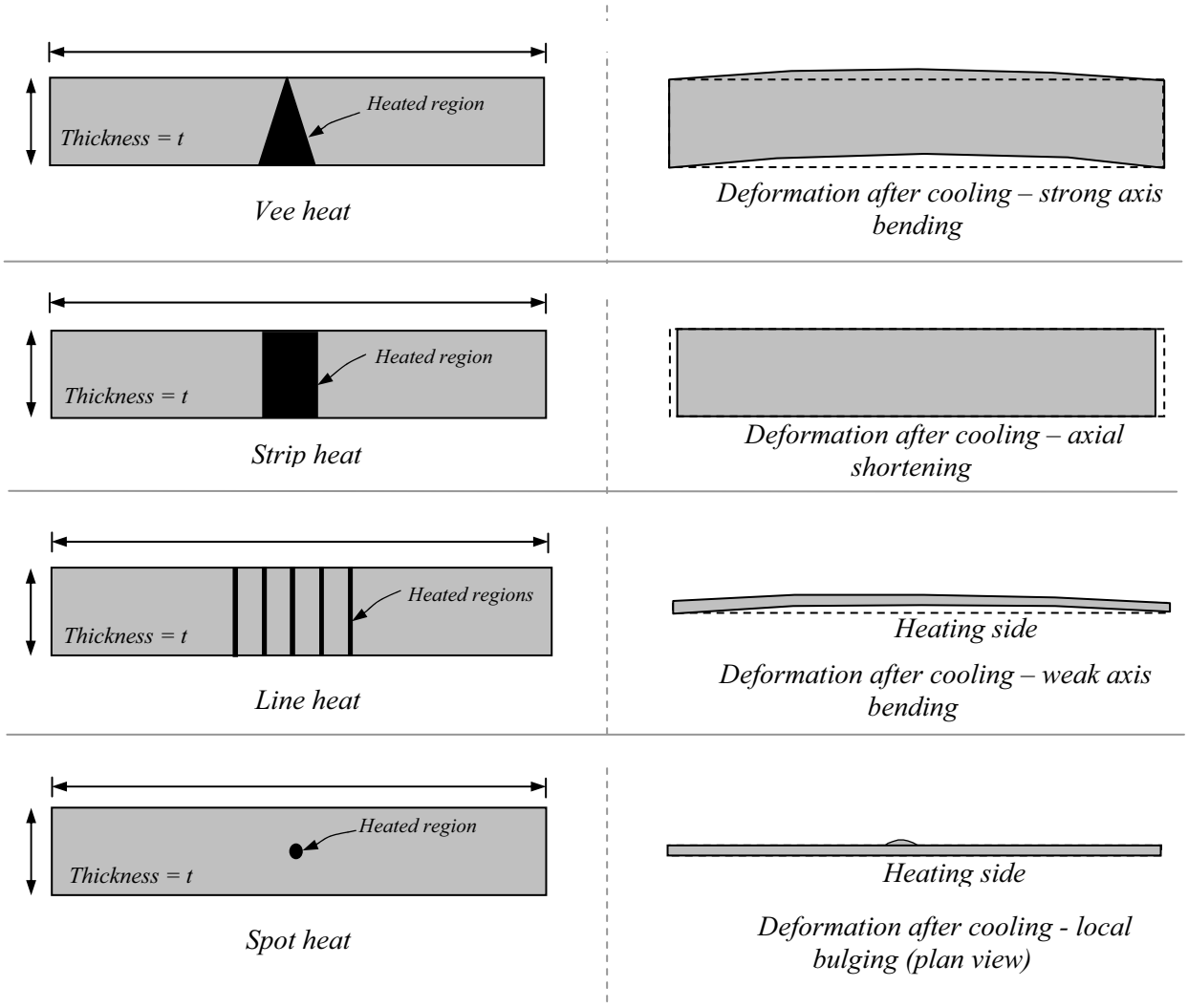

Figure 1.2
Four fundamental heat straightening patterns; (a) Vee, (b) Strip, (c) Line, and (d) Spot; heats

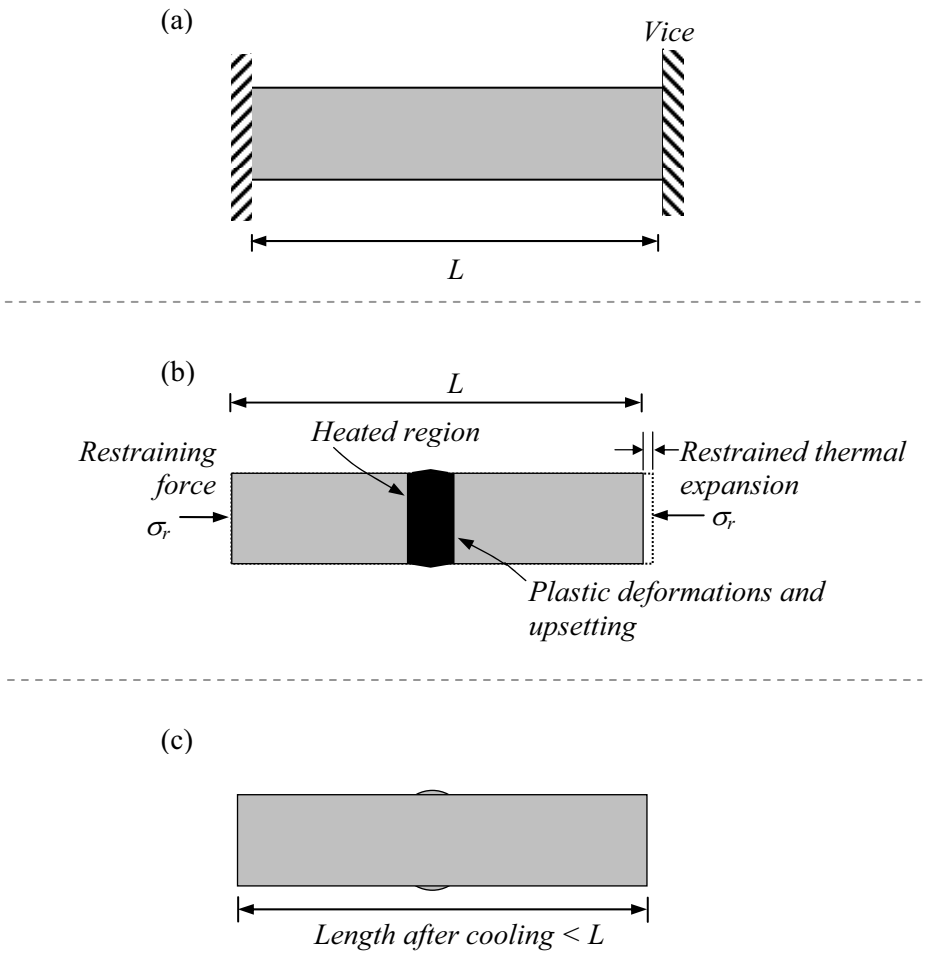

Figure 1.3
Conceptual example of heat straightening: (a) Initial specimen; (b) Heated specimen; (c) Specimen after cooling

[Intentionally Blank Page]

2 LITERATURE REVIEW, SURVEY, AND DATABASE ANALYSIS

2.1 LITERATURE REVIEW

2.1.1 Introduction

An extensive literature review of prior heat straightening experimental and analytical investigations as well as current provisions for heat straightening repair are provided in this section. Previous research on heat straightening damaged steel bridges has addressed the following issues in some detail:

- Heat straightening repair techniques for damaged steel members by Weerth [*1*], Horton [*2*], Roeder [*3*], Avent and Fadous [*4*] and Avent et al. [*5*] among others.
- Effects of heat straightening on the structural properties of steel by Pattee et al. [*6*], Nicholls and Weerth [*7*], Avent et al. [*5*], and Till [*8*] among others
- Development of design guidelines and recommendations for heat straightening by Shanafelt and Horn [*9*], Avent [*10*], Avent and Mukai [*11*], and FHWA [*12*]

Section 2.2 of this report provides a summary review of the previous research conducted on heat straightening. Section 2.2.1 presents some of earliest (historical) research on heat straightening in the United States. Section 2.2.2 focuses on experimental research on heat straightening steel plates and beams in the laboratory. Section 2.2.3 presents some of the analytical research on heat straightening. Section 2.2.4 presents a summary and review of the large-scale field studies on heat straightening damaged steel bridges. Section 2.3 presents some of the current heat straightening provisions and guidelines recommended by FHWA [*12*] and various state departments of transportation (DOTs). Section 2.4 summarizes the major findings and conclusions from the literature review and identifies gaps in the knowledge of the effects of heat straightening on the structural properties of steel beam bridges.

2.1.2 Previous Research

A summary review of previous heat straightening research is presented in this section. In general, prior heat straightening research has addressed the following objectives:

- Understanding the thermo-plastic deformation process
- Determining the heating parameters that have the greatest impact on and benefit plastic deformations
- Calculating the residual stress magnitudes and distributions induced by heat straightening
- Developing analytical models for plastic rotation and residual stress patterns aided with experimental data
- Determining the detrimental effects of heat straightening on the structural properties of steel
- Investigating the effects of multiple damage-heat straightening repairs on steel members
- Developing practical guidelines for implementation of heat straightening in the field

Three comprehensive studies have been conducted to summarize prior experimental data and knowledge and to provide guidelines for practitioners [*9*], [*4*], [*5*]. The two latter studies have provided substantial scientific data from experimental and analytical studies to support recommendations for damage assessment, optimization of heat straightening techniques, and development of heat straightening repair procedures.

2.1.2.1 Historical Research

This section presents a summary of some of the earliest research involving heat straightening damaged steel members. These initial studies focused on developing a better understanding of the thermal stresses, plastic deformations, and practical applications of heat straightening.

Fabricators have employed thermal stresses for dimensional modifications since the 1930's [*13*]. These stresses have typically been used to camber and sweep steel bridge beams, but more recently to repair damaged bridge beams. Bridge beams are usually damaged as a result of over-height trucks, fire, wind, earthquake, blast, mishandling, out-of-control vehicles, and over-loading. Early heat straightening repairs were performed with insufficient scientific rationale. Hence, early research studies were focused on understanding the thermal expansion and contraction properties of the steel [*14*], [*15*], [*16*] and general procedures for applications [*17*].

In 1938, J. Holt wrote one of the first technical papers on heat straightening. Holt [*18*] addressed the power of thermal contraction and its effectiveness in dimensional modification of structural steel members and procedures for heat straightening steel members damaged to various configurations. This paper was revised and published in 1955 [*14*]. Additions to the revised paper include various applications for heat straightening repairs, detailed examples for implementing heat straightening, and the role and effect that restraining forces have on plastic rotations during the heat straightening process.

R. Holt published three papers on the subject of heat straightening that provided practitioners with heat straightening guidelines. In his first paper, R. Holt [*17*] addresses procedures for applying a Vee heat pattern and the importance of not retracing the serpentine path of the Vee heat pattern as the prior heated material is providing the necessary confinement. R. Holt [*17*] also addresses how the steel can be monitored by visual inspection. At about 1200 °F, the steel appears a dull red. The steel color appears satin silver with a shade four welding lens.

In his second paper, R. Holt [*19*] addresses the effects of external restraints as well as the application of different heating patterns such as the line heat, the spot heat, the strip heat, and the Vee heat (See Figure 1.2). R. Holt [*19*] emphasizes that external restraints are a combination of applied jacking forces and dead loads resulting from members such as diaphragms. Attached members can restrain plastic rotation of the heated steel member under certain conditions. External jacking forces should always be applied before heating the member. In his third paper, R. Holt [*20*] addresses the local buckling of steel members and relates local buckling to the width of the heating pattern.

2.1.2.2 Experimental Studies

Five major experimental studies have been conducted on the heat-straightening repair of steel bridges. These studies have focused on the deformations of heat straightened specimens (plastic rotations), residual stresses induced from heat straightening, and structural properties of heat straightened steel.

2.1.2.2.1 Plastic Rotations

Plastic rotation is defined as the angular change of the intersection of the tangents extended from opposite sides of the damaged area as illustrated in Figure 2.1. Initial experimental studies focused on evaluating the plastic rotations associated with heat curving undamaged steel plates and wide flange sections utilizing an edge-heating pattern [*21*], [*22*], [*2*]. This heating pattern is typically used to introduce a smooth curvature (sweep) in bridge girders. The resulting plastic deformation occurs primarily within the heated area of the specimen [*7*]. The fundamental heating pattern for heat straightening is the Vee heat that produces a small but sharp curvature at the location of the heat. Vee heats are used to induce both strong and weak axis bending in beams. Researchers have investigated this heating pattern with variations of different heating parameters. The following parameters have been considered by previous

experimental studies; (a) initial yield stress, (b) heating temperature, (c) heating time, (d) heating sequence and pattern, (e) Vee angle (d) Vee depth, (e) geometric shape and size, (f) external restraining forces, (g) internal restraining forces, and (h) quenching.

Weerth [*1*] performed the earliest experimental research on the application of Vee heats to initially straight (undamaged) steel plates. The objective of the experimental research was to evaluate the behavior of steel plates subjected to the Vee heat pattern with variations in the Vee angle and the depth of the Vee. Three A36 grade steel plates 6 in. wide by 3/8 in. thick were subjected to a total of 21 Vee heats. The Vees were applied to only one side of the plate and the Vee depth ratios were held constant for each plate. The temperature of the specimens was monitored using thermal sticks. The experimental program consisted of variations of the Vee angle (24^o, 30^o, 36^o, 42^o, 48^o, 54^o, and 60^o), and the depth of the Vee in respect to the base width of the flange (1/2, 3/4, and 1). A maximum heating temperature of 1200 °F was enforced. Restraining forces of 490 lb. were applied prior to the application of the Vee heat. The results from this study revealed that plastic rotation is directly proportional to the angle of the Vee heat and full-depth Vee heats and restraining forces positively influence the plastic rotation of the heated specimen.

Horton [*2*] performed the earliest experimental research on the application of Vee heats to initially straight (undamaged) steel wide flange sections. The objective of this experimental research was similar to Weerth's [*1*] study except that it was conducted on wide flange sections. The objective was to evaluate the behavior of the wide-flange sections subjected to Vee heating patterns with variations in the Vee angle and the Vee depth. Sixty individual Vee heats were conducted on ten W6 x 15.5, four W8 x 10, and four W10 x 33 sections made from hot rolled A36 steel. Five heating sequences were used to produce full and partial sweep and cambering movements in the specimens. All sections were supported as cantilevers with a dead load attached at the end of the beam prior to Vee heating. This load produced a bending stress of 9.0 ksi at the extreme fibers of the heated zone for all specimens. The temperature of the specimens was monitored using thermal indicator sticks. The experimental program consisted of variations of the Vee angles (30^o, 40^o, and 50^o) and depth ratios of full-depth or half-depth in respect to the base width. A maximum heating temperature of 1200 °F was enforced. The specimens were cooled using one of three methods; (1) convection, (2) immediate atomized water spray, or (3) delayed atomized water spray. Results from this study revealed the following conclusions:

- Significant increases in the plastic rotation occur when a full-depth Vee heat is applied in comparison to half-depth Vee heat.
- The study indicates that the relationship between plastic rotation and Vee angle is fairly linear.
- Effective heating sequences and patterns for wide flange sections were revealed in this study.
- Water mist cooling was insignificant in increasing the plastic rotation in the heated specimens. It merely hastened the application of subsequent heats.

Roeder [*3*], [*13*] experimental investigated the application of Vee and strip heats to initially straight (undamaged) steel plates and wide flange sections. The objective of this study was to improve the understanding of the thermal or heat straightening process for seismic damage-repair. The experimental study consisted of three series of individually heated test specimens. Series A consisted of sixty-eight plate specimens subjected to Vee heating patterns. Series B1 consisted of eight axially loaded wide flange sections subjected to Vee heating patterns. Series B2 consisted of two simply supported wide flange sections subjected to strip heating patterns. The following heating parameters were varied throughout the study; (a) heating temperature, (b) heating time, (c) geometric size, (d) geometric shape, (e) geometry of heating pattern, (f) initial yield strength, (g) external restraining forces, (h) internal restraining forces, and (i) quenching. Emphasis was placed on obtaining the exact temperature of the heated specimens. Therefore, temperature monitoring devices such as an Omega non-contact pyrometer, thermocouples, and temperature indicating crayons were used throughout the experiments. Deflections were measured using linear voltage displacement transducers (LVDTs). Strain gauges provided a measure of the time and

temperature dependent forces and moments in the column specimens. A 10 in. Whittemore Gage was used to measure the strains at specified locations in the beam specimens. The experimental program consisted of the following details and variations of the heating parameters:

- Series A consisted of fifty-nine plates made of A36 (36 ksi) grade steel and nine plates made of A514 (100 ksi) grade steel. Sixty of the plates were 3/8 in. by 6 in., four of the plates were 1/4 in. by 8 in., and four of the plates were 3/4 in. by 6 in. Thirteen plates were quenched prior to the experiments. The Vee angles were 45°, 60°, or 82°. The depth ratio was either 3/4 or 1 times the width of the plate. In some cases, restraining forces were applied at midspan causing a restraining moment equal to 25% of the plastic moment capacity (M_p) at midspan where the Vee heat was applied. Maximum heating temperatures varied from 800 °F to 1600 °F.
- Series B1 consisted of eight wide flange sections (W6x25) sections made from A36 grade steel. Vee heats were applied to a single flange at a depth of 2/3 times the base width and at Vee angles of 45^o, 60^o, and 82^o. All sections were simply supported for weak axis buckling. Compressive loads were applied on six specimens from 40% to 80% of AISC design service load. The other two specimens were not subjected to compressive loads. Kl/r ratios ranged from 60 to 120. A maximum heating temperature of 1200 °F was applied to all columns.
- Series B2 consisted of two wide flange sections (W12x14) sections made from A36 grade steel. The beam specimens were simply supported at 7ft. and subjected to continuous strip heating patterns along the top flange. External restraining forces were not applied. A maximum heating temperature of 1200 °F was applied to all beams.

This experimental study considered a wide range of heating parameters and was by far the most extensive experimental study on heat straightening when it was published. Additionally, sophisticated monitoring equipment was implemented to capture as much scientific data throughout the experiments as possible. Roeder [*3*], [*13*] suggested that future experiments should utilize more complex heat patterns, restraint conditions, structural shapes, and configurations. Future experiments should also perform extensive evaluations of the interaction between buckling and thermal stress. Results from this study are summarized as follows:

- Thermo-plastic deformation is dependent upon the temperature.
- Temperatures higher than 1330 ^{o}F are likely to produce (1) out-of-plane distortions, (2) plate buckling, and (3) pitting and surface damage to the steel.
- Increasing the Vee angle increases the occurrence of local buckling.
- Quenching may increase plastic rotation by 20% to 80%.
- Quenching may reduce tendency towards local buckling.
- Plastic deformation is developed by the Vee heat and occurs primarily within the heated area.
- Increasing the applied bending moment increases the plastic rotation

One disadvantage of this study was the multitude of heating parameters compared to the relatively limited number of experimental tests. This causes difficulty in accurately interpreting the effects that individual heating parameters have on the behavior of the test specimens.

Avent and Fadous [*4*] conducted an extensive experimental program targeted on studying heat straightening repair for damaged steel bridge girders. The experimental tests were presented as part of Boudreaux's [*23*] Master's thesis. The objective of the study was to optimize the development of engineered heat straightening repairs. The experimental study consisted of the application of 255, 18, 37, and 133 individual Vee heats to initially straight (undamaged) A36 grade steel plates, angles, channels, and wide flange sections, respectively. Prior research provided a limited number of data points with large

variations [*1*], [*2*], [*4*]. Therefore, the study focused on obtaining supplemental experimental data for undamaged plates and rolled shapes. The most effective heating sequences and patterns from Horton's [*2*] study were used on the rolled shape tests. In all cases, the test specimens were allowed to cool in air. The experimental program consisted of heating temperature from 700 ^{o}F to 1500 ^{o}F, depth ratios of 1/2, 3/4, and 1 times the width of the plate, Vee angles of 20 ^{o}, 30 ^{o}, 45^{o}, 60^{o}, and 82^{o}, and restraining moments (load ratios) of 0.0, 0.16, 0.25, 0.37, 0.50 and 0.56 times the plastic moment capacity (M_p).

This experimental study provided additional data related to the behavior of Vee heated undamaged plates and rolled shapes subjected to various heating parameters. The authors commented that additional experiments on plates and rolled shapes, analysis of the residual stress distributions of Vee heated plates and rolled shapes, and single and multiple damage-heat straightening repair comparisons of plates and rolled shapes are future research needs. The results of this experimental study revealed the following conclusions:

- A linear relationship between the Vee angle and plastic rotation was verified for plates and rolled shapes.
- Vee depth ratios of 3/4 and 1 produce slightly larger plastic rotations than a Vee depth ratio of 1/2. However, the influence of the Vee depth on the plastic rotation requires further evaluation.
- Plate thickness and geometry have an insignificant effect on the plastic rotations.
- A maximum temperature of 1200 ^{o}F allows for some temperature variation during heating.
- More data points are needed to define relationship between restraining forces and plastic rotation.

Avent et. al [*5*] completed a comprehensive experimental investigation of heat straightening repair of steel as part of Robinson's [*24*] Master's thesis. The objectives of the study were to quantify the various factors that affect the behavior of plates and rolled shapes subjected to single and multiple heat straightening repairs. The experimental study consisted of the application of 18, 18, and 32 individual Vee heats to undamaged angles, channels, and wide flanges, respectively, as well as 336, 29, 14, and 283 individual Vee heats to damaged plates, angles, channels, and wide flanges, respectively. All specimens were made from hot rolled A36 steel. The study incorporated both strong and weak axis bending. The experimental program consisted of heating temperatures of approximately 1200 ^{o}F, Vee depth ratios of 3/4, and 1 times the width the plate, Vee angles of 20^{o}, 30^{o}, 45^{o}, and 60^{o}, and restraining moments 0.0, 0.25, 0.33, 0.50 times the plastic moment capacity (M_p). Damage strains of $0\varepsilon_y$, $30\varepsilon_y$, $80\varepsilon_y$, $90\varepsilon_y$, and $100\varepsilon_y$ were considered and were computed using the radius of curvature method [*4*]. Multiple damage- heat straightening repairs of 2, 4, and 8 were applied to wide flange beams.

This experimental study was the first known to investigate the effects that heating parameters have on the behavior of initially deformed (damaged) test specimens. Additionally, it is the first study to perform multiple damage- heat straightening repairs. The study also indicated that damage strains of $100\varepsilon_y$ can be successfully heat straightened. The authors, however, indicated that additional laboratory testing of rolled shapes and built up members typically found in bridges needs to be conducted and research on heat straightening repair of localized damage and fatigue characteristics of heat-straightened members is still lacking. Application of this research to actual repair situations and procedures for assessing the degree of damage are needed. The results of this study indicated that plastic rotations of undamaged and damaged plates, angles, and channel sections were found to be similar. Full-depth Vee heats did not cause more shortening of the member compared to three-quarter depth Vee heats.

De Bejar [*25*], [*26*] presented two experimental studies focused on assessing the behavior of Vee heated damaged plates and rolled shapes. The objective of these studies was to obtain the data for use in analytical studies, which were part of the project. The experimental program was designed to provide additional experimental data and not to investigate novel heating parameters. Only the Vee depth ratio (0.75 and 1.00 of the plate width) and the load ratio (0.25, 0.33, and 0.50 of the plastic moment capacity

(M_p)) were varied. All test specimens were made from hot rolled A36 steel, heated to approximately 1200 ^{o}F and were subjected to 45^{o} Vee heats. The authors did not present any conclusions related to the behavior of the Vee heated test specimens.

2.1.2.2.2 Residual Stresses

Residual stresses are defined as stresses that remain in structural members after fabrication and rolling. The plastic deformations from the damage-heat straightening repair cycle also produce residual stresses. Several researchers have experimentally investigated the residual stresses resulting from heat straightening undamaged specimens [*3*], [*4*], [*5*]. Only one study was found in the literature to address the residual stresses resulting from heat straightening damaged plates and rolled shapes [*5*].

Brockenbrough and Ives [*21*] measured the residual stresses resulting from heat curving a plate girder using line heats. Residual stresses were measured in the girder using the "sectioning method" before and after the heat curving operation. In this method, two gage marks are punctured on the steel and measured. A narrow strip containing the two marks is milled out providing a stress relief within the strip. The gage marks are then remeasured and the change in length reflects the magnitude of residual stresses in the strip. The plate girders used by Brockenbrough and Ives [*21*] were made from A36 steel. Results of this study indicate that the residual stresses in all parts of the plate girder were reduced except at mid-width of the flange. Tensile residual stresses approximately equal to the yield stress were found at the heated edges of the flange and compressive residual stresses were found in the web [*21*]. This study was the first found in the literature involving residual stresses resulting from the use of an oxy-acetylene torch. However, the applicability of these residual stress results to heat straightening research is limited.

Roeder [*3*] evaluated the effects of residual stresses on heat straightening by comparing the plastic rotations of *re-heated* test specimens. He challenged the frequently suggested statement that residual stresses have a major impact on the plastic rotation of heat straightened specimens. Roeder [*3*] stated, "If this is correct, different plastic rotations must be expected for virgin specimens that have been damaged due to prior loading and specimens which were deformed during earlier heating, since the residual stress will be quite different for each of these conditions". The experimental program consisted of comparing three test specimens that had been heat curved one time to three test specimens that were subjected to similar heating parameters and heat curved twice. Roeder [*3*] found an insignificant difference in the plastic rotation between the test specimens and concluded that residual stresses insignificantly affect the plastic rotation. These experimental investigations were conducted in the context of heat curving initially straight (undamaged) specimens and the heating parameters for the control and test specimens were "comparable" but not identical.

Avent and Fadous [*4*] studied the residual stresses produced in heat-straightened specimens. The experimental program consisted of eight undamaged A36 plates (4" x 1/4" x 24") subjected to Vee heating. The Vee heated plates were subjected to four heating cycles using a depth ratio of 1 and a Vee angle of 45º. External restraining forces were not applied and the plates were heated to approximately 1200 ºF. Longitudinal residual stresses in each member were determined using the "sectioning method". The results indicated that the edges of the Vee heated plates were found to be in tension and the centers were in compression. These stresses were significant in comparisons to an unheated control specimen. The authors suggested that additional experimental research of residual stresses is needed to study the magnitudes, distributions, and strain-aging effects of residual stresses on heat-straightened specimens.

Most recently, Avent et al. [*5*] conducted experimental investigations of the residual stress patterns in heat-straightened specimens. The experimental program consisted of testing undamaged and damaged plates, angles, channels and wide flange beams subjected to Vee heating. The beam specimens were damaged in both weak axis bending (Category W) and strong axis bending (Category S). Undamaged specimens were subjected to four heating cycles while the damaged specimens were subjected to the amount of heating cycles required for full repair. Several beam specimens were subjected to multiple

damage-heat straightening repairs and then the residual stresses were determined. Longitudinal residual stresses in each member were determined using the "sectioning method". All test specimens were made of A36 grade steel and were heated to approximately 1200 ºF. Residual stresses were calculated using both the assumed and the measured modulus of elasticity for some specimens. The magnitude and distribution of residual stresses in the unheated and Vee heated test specimens were analyzed and conclusions were presented. Presented below are the distinguished experimental investigations and results for each geometric shape that was considered.

Residual stress distributions were determined in eight undamaged and five damaged plate specimens [*5*]. Heating parameters for the undamaged plates included Vee angles of 20°, 45°, 60°, and 82°, load ratios of 0.00 and 0.50, and depth ratios of 3/4 and 1. Heating parameters for the damaged plates included Vee angles of 20°, 45°, and 60° degrees, load ratios of 0.25 and 0.50, and depth ratios of 1/4, 1/3, and 1/2. Average residual stresses were determined using the "sectioning method" for three different regions. The results from this study indicated that both the undamaged and damaged plates exhibited similar residual stress distributions as Roeder's [*3*] theoretical distribution. The plates had a significantly larger plastic rotation during the first few heating cycles as apposed to further heating cycles. Residual stresses were determined to contribute to this selective behavior [*27*].

Residual stress distributions were determined in two undamaged angles, two damaged angles, and one undamaged channel [*5*]. A Vee depth ratio of 1 was used for all test specimens. The two undamaged angles were heated with Vee angles of 20° and 45° and without external forces. The two damaged angles were heated with Vee angles of 45° and with load ratios of 0.50 and 0.33. The undamaged channel was heated with a Vee angle of 45° and with a load ratio of 0.50. Eight strips were tested from both the Vee heated leg and the strip heated leg of the angles. The results from this study indicate that similar residual stress patterns develop in damaged and undamaged angles. Further tests on the residual stress patterns of damaged-repaired channels and angles are needed.

Residual stress distributions were determined in four undamaged Category W and five undamaged Category S beam specimens. The Category S beam specimens were heated using either small (20^o and 30^o) or large (45^o) Vee angles. The results from this study indicate that the effects of the Vee angle and the load ratio on the residual stress patterns are small. Residual stresses were greater in the Vee heated beam specimens as compared to the unheated control specimen. The compressive residual stress in flanges typically increased with respect to the unheated control specimen, which is unfavorable for columns.

Finally, residual stress distributions were determined in four-damaged Category W and one damaged Category S beam specimens. The Category W beams were repaired using depth ratios of 3/4, Vee angles of 45^o, and load ratios of 0.5. The Category S beams were repaired using depth ratios of 1, Vee angles of 45^o, and load ratios of 0.5. The four Category W beams were subjected to 1, 2, 4 and 8 multiple damage-heat straightening repairs before testing for residual stresses. The results from this study indicate that residual stress patterns are consistent for beams subjected to one and two damage-repairs and for beams subjected to four and eight damage-repairs. The residual stress patterns in the Category W damaged beams were opposite that of the undamaged beams (i.e. tension in the flanges and compression in the web), which is favorable for column repairs. The residual stress pattern in the Category S damaged beam was similar to that of the Category S undamaged beams but with greater compressive stresses.

2.1.2.3 Thermal and Structural Properties

Several researchers have studied the effects of heat straightening on the structural properties of damaged-heat straightening repaired steel. These structural properties include the; modulus of elasticity, yield stress, tensile stress, ductility, fracture toughness, surface hardness, and fatigue strength. The majority of prior research has been conducted on undamaged steel specimens subjected to four or less heating cycles. One comprehensive study has performed structural property tests on initially damaged

steel specimens and full-scale simulated girders that were completely heat straightened [*5*]. The effects of heat straightening on the thermal and structural properties of steel are presented below:

Thermal Expansion

Thermal expansion is the most fundamental aspect of heat straightening steel. This property enables the steel member to expand and experience a net contraction in the direction of desired rotation. The coefficient of thermal expansion is the measure of rate of strain per degree of temperature. Figure 2.2 depicts the variation of the coefficient of thermal expansion for low carbon steel vs. temperature [*3*]. Roeder [*3*] has shown that for Vee heats, the coefficient of thermal expansion increases in a predictable manner up to 1600 °F for carbon steels. The coefficient of thermal expansion has shown to be linear and directly related to the temperature from approximately 250-1200 ºF [*15*], [7], [*28*], [13]. Other research has shown that the coefficient varies in an unpredictable manner [*16*]. It is also noted that surface damage (pitting) to steel and out-of-plane distortion becomes likely at temperatures over 1400ºF.

Modulus of Elasticity

The modulus of elasticity of steel varies inversely with temperature, i.e., as the temperature increases the modulus of elasticity decreases as shown in Figure 2.3. The equations used for in Figure 2.3 for the modulus of elasticity, assuming E_o = 30000 ksi are provided in Equations 2.1-2.3 [*3*].

$$\frac{E_t}{E_o} = 1.0 \qquad 0\ °F \le T \le 100\ °F \qquad (2.1)$$

$$\frac{E_t}{E_o} = 1.02 - 0.0002T \qquad 100\ °F \le T \le 700\ °F \qquad (2.2)$$

$$\frac{E_t}{E_o} = (500000 - 1333T + 1.111T^2) * 10^{-6} \qquad T > 700\ °F \qquad (2.3)$$

At 1200 ºF, the modulus of elasticity of steel is approximately half of its typical value [*12*]. Only three heat straightening studies have mentioned the calculation of the modulus of elasticity [*1*], [*7*], [*2*]. These studies implied that no appreciable difference could be measured between the heat-straightened specimen and the unheated specimen on mild steel specimens subjected to single Vee heat applications. However, these three studies were conducted on initially straight specimens that were typically subjected to four or less Vee heats. Recent research on damaged specimens indicates that a change in the modulus of elasticity is more apparent [*29*]. The research indicated average reductions, as compared to the original modulus of elasticity, of 11-77% for damaged plates and 8-23% for damaged wide flange beams.

Yield Stress

Yield stress is the largest stress that steel can withstand before enduring plastic deformations. Research has revealed that the yield stress of steel is affected in two different ways due to heat straightening. First, there is a variation in the yield stress of steel as it is heated (FHWA, 1998) as shown in Figure 2.4. The equations used for in Figure 2.4 for the normalized relationship of the yield stress are provided in Equations 2.4-2.6 [*3*].

$$\frac{\sigma_{yt}}{\sigma_{yo}} = 1.0 \qquad 0\ °F \le T \le 100\ °F \qquad (2.4)$$

$$\frac{\sigma_{yt}}{\sigma_{yo}} = 1.0 - (T - 100)/5833 \qquad 100\ °F \le T \le 800\ °F \qquad (2.5)$$

$$\frac{\sigma_{yt}}{\sigma_{yo}} = -(720000 - 4200T + 2.75T^2) * 10^{-6} \qquad T > 800\ °F \qquad (2.6)$$

Second, heat straightening has a permanent effect on the yield stress of steel after it has cooled to room temperature. Researchers are interested in the long-term effects that heat straightening has on the yield stress of steel and ultimately on the integrity of the structure. Previous material property studies [*7*], [*30*], [*31*] have compared the results of undamaged heated specimens to unheated specimens. The results indicate that the yield stress of most heated structural steels increases. Only the quenched and tempered steels undergo reductions in yield stress after heat straightening. Table 2.1 displays the typical average percent changes in the yield stress from heat straightening initially straight specimens (undamaged). The specimens were subjected to four or less heating cycles with variations in heating parameters.

Tensile tests have been performed on damaged plates and damaged wide flange beams [*5*]. Results of the tests vary considerably. All of the tests on coupons removed from the heated regions show increases in the yield stress compared to the coupons taken from the unheated regions. In one instance, a coupon taken from the apex portion of a Vee heated specimen resulted in an 88% increase in yield stress as compared to the unheated coupon. The majority of coupons taken from the apex of the Vee heating pattern exhibited the largest increases in yield and tensile stress.

Table 2.2 displays the material properties of heat straightened damaged plates and damaged wide flange beams as a percentage of the values of the unheated control specimens. It can be seen that the yield stress increases at a greater rate than the tensile stress. Therefore, it appears that a net effect of heat straightening narrows the gap between the yield stress and the tensile stress in heated specimens, which may also indicate that the steel at specific sections may have not been fully repaired.

Ductility

Ductility is the mechanical property of steel, which allows it to plastically deform when subjected to large tensile stresses. It is usually calculated as the percent elongation over a two-inch gage length. Previous research [*5*] indicates a 10-20% reduction in the ductility of heat straightened undamaged steel plates. This decrease in the test specimens is significant but the ductility of the specimens is still within an acceptable range. Table 2.3 displays the average percent reduction in ductility for several steel types that have been previously studied.

Avent et al. [*5*] conducted ductility tests on damaged-repaired plates and wide flange beams. Test specimens were made of hot-rolled A36 steel. Results from these studies indicate that the reduction in ductility is significantly higher for single and multiple damage-heat straightening repairs than previously assumed from undamaged plate studies. Ductility test results on unheated strips revealed an initial percent elongation from 41-46%. Results from the damage-heat straighten repaired plates revealed a final percent elongation from 32-37% [*12*]. This results in a 10-30% reduction in elongation after the repair process. Results from the ductility tests were similar for all of the plates despite variations in the heating parameters, which include the degree of damage, jacking ratio, Vee depth, and the number of heats applied to heat-straighten the member. Heat straightened damaged wide flange beams exhibited ductility losses similar to that of the damaged plates. Strip tests from the heated regions resulted in percent elongations from 15-36%. Unheated strips had percent elongations from 42-45%. This resulted in an average ductility reduction of 15-66%.

Putherickal [*32*] conducted a field case study that involved testing the mechanical properties of the heat-straightened girder. It is the only such study found in the literature. The Iowa Department of Transportation (IDOT) removed the W30 x 108 girder from service for unknown reasons. The unheated

portions of the web and flange were 34% and 36% elongation, respectively. The percent elongation of heated strips from the web and flange were 22.5% and 26% elongation, respectively. This constitutes a reduction of the ductility in the web and flange of 34% and 28%, respectively.

Fracture Toughness

A Charpy V-notch test is a standard American Society of Testing Materials (ASTM) [*33*] test that determines the fracture toughness of steel coupons at specified temperatures. The Drop Weight Tear test is another test used to measure the fracture toughness of steel coupons. Fracture toughness of steel can be measured in three ways; (1) fracture energy using the Charpy V-notch test, (2) T_{50} of upper shelf energy using Charpy V-notch test, and (3) fracture transition temperature using Drop Weight Tear test.

Several researchers have tested the notch toughness of steel subjected to heat straightening [*34*], [*35*], [*6*], [*40*], [*8*]. Results from tests, using various grades of steel plates, have indicated that there is an insignificant change in the upper shelf energy absorption before and after application of heat straightening [*12*]. Considerable variations have been found within a steel grade when comparing the T_{50} of the upper shelf energy using the Charpy V-notch test. Average values indicate that only the quenched and tempered low alloy steels have a significant positive shift. One researcher used the Drop Weight Tear test to evaluate the notch toughness of several grades of steel [*35*]. This study showed that only the A517-A steel grade exhibited a positive shift, which indicates an increase in fracture sensitivity. Till [*8*] performed 54 Charpy v-notch tests on A36 steel. This research was directed at assessing the effect of elevated temperatures on fracture critical steel members. He obtained an ASTM A36 steel plate (16" x 8" x 1") taken from the web of a relatively undamaged W36 x 300 fracture critical uplift bridge member. The plate had sustained limited damage and was cut into nine specimens. The specimens were heated to a specified temperature for one-minute and then cooled using one of the following methods: under room conditions, compressed air, or water mist. The charpy specimens, removed from the heated specimens, were cooled for 24 hours at negative 15 ºF and then tested. Results from the tests indicate that most heated Charpy specimens show an increase in notch toughness as compared to the control specimen. Microscopic investigations revealed recrystallization of the grains had occurred in heated specimens.

Rockwell Hardness

The Rockwell Hardness test is a standard ASTM test used to measure the surface hardness of a material. Several researchers have conducted Rockwell hardness tests on initially straight (undamaged) heat straightened specimens [*35*], [*6*], [*34*], [*8*]. The results of both Pattee [*35*] and Harrison [*34*] indicate that heat straightening did not significantly change the hardness values of the steel. These conclusions are based on laboratory testing of undamaged steel specimens subjected to a few heating cycles. Till [*8*] performed Rockwell Hardness tests on the heated steel specimens. Results of the Rockwell Hardness tests indicate that heating the steel specimens had an effect on the hardness of the steel. Heating to 1100 ^{o}F - 1500 ^{o}F decreased the average hardness of the steel. Metallurgical inspection verified that recrystallization of the grains had occurred, making the material less hard but more ductile. The author mentions that variations in the hardness were likely due to the cooling rate of the specimens [*8*]. Hardness tests performed on damaged-heat straightened steel plates were not found in the literature.

Fatigue Life

Fatigue life is defined as the total number of alternating cycles at a specified stress level (fatigue limit) to cause the initiation of cracks of an appreciable critical size to appear. The fatigue endurance limit is the stress in which a theoretically infinite amount of cycles can be applied without the effects of fatigue. If pressed beyond this limit, the material with the presence of notches, holes, etc. is limited to a finite number of cycles before fatigue failure. The fatigue-crack-initiation threshold in various steels has been shown in studies to be associated with the yield and tensile strength of steel [*36*].

One study on fatigue tests of heat-straightened members was found in the literature [*37*]. Three eye bars made of A-7 steel were fatigue cycled at 500,000 and 1,000,000 cycles. Significant difference in fatigue life was not indicated between the heat-shortened members and similar unheated members. Shanafelt and Horn [*9*] suggested that non-redundant tension members should not be subjected to heat straightening repairs. They offered no scientific research or evidence in their report to back up such a recommendation. To date, there is a lack of scientific research or evidence that suggests that heat straightening reduces the fatigue life of steel members.

2.1.2.4 Analytical Studies

Review of analytical studies in the literature yielded research in the development of two theoretical models used to predict residual stress magnitudes/patterns and member behavior resulting from heat straightening. Numerous researchers [*22*], [*1*], [*2*], [*5*] have performed experimental studies to provide the necessary data to develop and calibrate residual stress models, while others have concentrated their efforts on analyzing the behavior of heat straightened plates and rolled shapes. Simplistic [*17*], [*19*], [*38*], [*4*] and comprehensive computer models [*22*], [*2*], [*3*], [*13*], [*1*] have been developed for predicting the behavior of heat straightened plates and rolled shapes. The usefulness of these models resides in their ability to accurately predict the number of heating cycles required to completely heat straighten a damaged girder. Therefore, this serves as a powerful tool for assisting structural engineers in designing heat straightening repair jobs. Theoretical studies that have been found in the literature are presented in this report.

Currently, analytical studies in the following areas are either inadequate or incomplete and need to be addressed by future researchers:

- Analytical formulations used for predicting member behavior for design
- Procedures for assessing the degree of damage in terms of the reduced capacity of the structure
- Developing patterns and methodology for designing localized damage repairs
- Analytical formulations for predicting member behavior

Researchers have attempted to model the behavior of heat straightened steel plates and rolled shapes with theoretical models. In general, these models are developed and then compared to existing experimental data for accuracy. Both simple and complex theoretical models have been developed. Simple models, generally known as the Holt formula, are merely algebraic equations based on simplifying assumptions requiring minimal computational time. Complex models are aided with computer processing and are based on thermal and finite strip stress analysis. These models required significant computation time when published. Studies utilizing both models are summarized and presented below.

Holt [*17*], [*19*] developed one of the first analytical models for predicting plastic behavior. This approach considers only the global action of the Vee heat. Holt [*17*], [*19*] understood that the plastic flow resulting from the heating would result in a net contraction in the direction of confinement. The plastic strain for a specimen is computed by subtracting the elastic strain from the total free expansion for a given temperature. The formula is based on the following assumptions; uniformly distributed heating temperature of 1200 ºF, ideal single axis confinement, and linear strain variation across the width of the plate. This equation is very basic and provides approximate values. The model neglects strain compatibility conditions for the Vee heat and assumes an unrealistic temperature distribution as well as the conductivity of steel [*3*]. Additionally, the model neglects an estimate of the effect of restraint and the Vee depth. Moberg [*38*] modified the Holt [*17*], [*19*] formula to include the Vee angle, depth of the Vee, and the plate width.

Weerth [*11*] and Horton [*2*] developed analytical models for predicting residual stresses, strains, and curvature in steel plates and rolled shapes. Their models were based on the Duhamel strip analogy. The Vee heating pattern was divided into eight longitudinal strips and subjected to temperature distribution

steps. Each strip (time step) is allowed to freely expand and then compress back to the initial length. This enforces compatibility between adjacent strips. A strain pattern is initially assumed and a trial and error method is used for determining the stress distribution that satisfies equilibrium. The resulting stress distribution becomes a load in the next step. Residual strains from the last step are used to calculate the theoretical camber induced in the plate from the Vee heat [*39*]. This approach resulted in a good correlation between the analytical and experimental data. However, the trial and error solution required a large amount of computer time for the analysis. Horton [*2*] did not have time to complete his analytical models for comparison with his experimental data. Some simplifying assumptions for the formulation that were considered include; initial distribution of residual stresses ($0.3\sigma_y$ in tension at plate ends, $0.3\sigma_y$ in compression at the middle of the plate), linear strain distribution for any static temperature distribution, elastic-perfectly plastic stress-strain relationship for A36 steel, accuracy in temperature gradient in the plate during heating, control of the effective heating area, and lateral strains have an insignificant effect on the longitudinal stresses.

The initial residual stress distribution is common and widely accepted in the industry. Some of the above assumptions are sources for large errors. However, the resulting theoretical camber values compared well to the experimental camber values from the initially straight plates for both studies. Weerth [*1*] concludes that full-depth Vee heats result in more desirable residual stress magnitudes and distribution compared to that of 3/4 depth Vee heats [*7*]. Horton [*2*] concludes that the residual stress distribution in the test specimens reversed as compared to the initial stress distribution. Tensile yielding occurred at the apex of the Vee heats (flanges) and at several strip-heat locations in the web, while compressive stresses were found in the base of the Vee heats.

Roeder [*3*] suggested a different approach that would capture both the local and global behavior of the Vee heating pattern. This theoretical model was developed to separately analyze the heat flow and elastic deformation problems. A finite difference model was employed to generate time independent temperature distributions. These profiles became steps for a non-linear finite element analysis. His results compared favorably well with the experimental data. However, the solution required large computational time.

De Bejar et al. [*25*], [*26*] conducted analytical studies on estimating the number of heats required to completely straighten a specimen. The theory of reliability and spectral analyses was employed to develop several equations based on minor axis bending. These equations are based on using the following heating parameters; 45^o Vee angle, 0.75 Vee depth ratio, 0.50 load ratio, and 1200 ºF heating temperature. Results from the equations for damaged plates and wide flange shapes have provided excellent agreement with experimental studies. A model for predicting the number of heats based on the linearized theory of reliability was developed for when a sample experiment is known and when the damage angle and the heating conditions are provided.

Avent and Fadous [*4*] developed a simple analytical formula for predicting the behavior of Vee heated plate specimens. The global formula was based on the Holt [*17*], [*19*] formula but incorporated recent research [*3*] in regards to some of the assumptions used in the development of the formula. For instance, the perfect single axis confinement assumption has been proven to be inadequate. Therefore, the formula was improved using the experimental data from a research program [*4*]. A preliminary analytical model for rolled shapes was developed. The authors report that the analytical and experimental results compared well, though further research on rolled shapes is necessary to refine the model. The assumptions that the analytical formula is based upon are:

- Longitudinal plastic strain occurs only in the Vee heated zone.
- Longitudinal strains are constant in throughout the width of the Vee heat.
- Planes defined by the Vee remain plane after heating and rotate about the apex of the Vee.

- Externally applied forces provide linear constraint with a load ratio of 0.323 providing perfect confinement.
- The internal constraint provides 45% of the external confinement.

Most recently, Avent et al. [*5*] expanded and refined the analytical formulations developed by Avent and Fadous [*4*]. A simple formula for predicting the plastic rotation from a single Vee heat was developed. The formula was developed as a function of the heating parameters used in the experimental program of the study. The researchers addressed the role of external restraining forces on composite girders. The theoretical model attempts to simplify the behavior of a heat straightened composite girder to that of a Vee heated plate. Multiplication factors for rolled shapes were developed based on the damage type and primary stiffening elements in the section. These factors were then calibrated for predicting the plastic rotation of rolled shapes using the simple plate equation. In addition, analytical studies were performed on full-size steel bridge components. For indeterminate structures, the members are subjected to a restraining moment that is induced in the bottom flange. Therefore, an additional multiplication factor was determined for the formula. All of the analytical formulas are merely algebraic equations and can be easily calculated. It is noted that all of the formulas were verified using experimental data from the same study.

2.1.2.5 Full-Scale Studies

Review of full-scale testing of heat straightened beams and columns in the literature resulted in field studies and prototype bridge tests. Field studies have been conducted on the following damaged bridges throughout the United States; Bothell Bridge, IA 130 Bridge, Lake Charles Bridge, and Crowley Bridge. These studies have addressed topics such as damage assessment, traffic control, application of heat straightening procedures, and plastic rotation data. The heat facility at Louisiana State University (LSU) has been a prime site for prototype bridge beam tests. This facility consists of a testing frame that was created to provide a controlled environment for testing full-scale bridge beams and axially loaded compression members and is capable of testing composite and non-composite beams spanning 20-feet. Studies performed at the facility have been used to investigate many issues including damage assessment, heating patterns and sequences, and plastic rotation. Summaries of the field studies and prototype bridge tests are presented below.

2.1.2.5.1 Field Studies

Bothell Bridge

Moberg [*38*] presented a masters thesis on damage assessment and contraction (heat) straightening of the Bothell Bridge in the State of Washington. The first part of his thesis outlines the general principles, tasks and procedures for damage assessment and the proper application of heat straightening necessary to repair the bridge. Moberg [*38*] defined the damage assessment operation to incorporate public safety and protecting public property near the damaged structure, visually verifying the structural integrity of the structure, and obtaining the necessary data for engineering the repair.

The damage assessment analysis concluded that the following components of the Bothell Bridge needed repair; two beams (W33x118), the diaphragm frame, the deck, and the sidewalk bracket. The two wide flange beams were damaged about their weak-axis and repaired using Vee heats applied to the bottom flange. A web indentation was repaired using circumferential line heats. Only one heating sequence and load ratio was used during the heat straightening repair of the bridge. The beams were displaced in the direction of impact 4.01 in. and 0.75 in. The displacements from the damage and heating operations were measured using the taut line method. In this method, a taut line is strung from the ends of the member and offsets are measured between the string and the damaged member at specified

distances. Spacing between offset measurements was not specified in the report. The author indicates that an accuracy of ± 0.01 in. is possible with this method. Due to time constraints, Moberg [*38*] was only able to record heat straightening (plastic rotation) data at the end of each workday.

IA 130

The Iowa Bridge repair project was collaboration between Dr. Richard R. Avent of Louisiana State University and the Iowa Department of Transportation (IDOT) maintenance personnel. An over-height vehicle damaged the IA 130 overpass over I-80 as it was leaving the underpass. The bridge featured W36 x 170 continuous girders over supports with 190 ft. spans. The damage assessment revealed that the lower flange, which had apparently been damaged prior, was displaced approximately 7 in. out-of-plane. Local bulging had occurred in the web when the bolts from a diaphragm failed and three plastic hinges formed in the girder. The objectives of this project were to conduct a training program to teach IDOT personnel the correct heat straightening repair procedures, have the recently trained IDOT personnel successfully repair the damaged bridge, and measure and document the response of the heat-straightened girder during the repair.

The training program consisted of two days of presentations. IDOT personnel proceeded to repair the bridge under the supervision of Dr. Avent [*40*]. The heat straightening crew successfully repaired the bridge in a 4-day period. A structural analysis of the girder system was performed to determine the proper placement of heating patterns and placement of the restraining forces. The restraining forces were limited such that the internal moment would not exceed 0.33 of the yield moment (M_y) for the section [*41*]. A maximum heating temperature of 1200 °F was regulated to the yield zones. The heating sequence utilized to straighten the girder was a Vee heat applied to the bottom flange combined with strip heats to the web. Twenty-two heating cycles, where the first eight were within the diaphragm in place, were required to completely straighten the girder. After this was accomplished, the local bulge in the web was repaired using a star Vee pattern.

This study provided an excellent opportunity to obtain experimental data relating to the effects of various restraining forces applied to the lower flange of the girder. It was found that the use of the jacking forces expedited the plastic rotation per heating cycle until the diaphragm offered increasing restraint to the heat straightening process. The author also noted, “If the jacking/restraining forces are too high, a fracture might occur during straightening” [*40*]. Results from this field study revealed the following conclusions:

- DOT personnel can successfully heat-straighten damage steel beams after a two-day training session.
- Future heat straightening repairs of beams with similar damage will result in a savings of $11,000 using IDOT personnel versus a specialty contractor.
- The theoretical modeling of the damaged beam over predicted the plastic rotation per heat cycle.
- Additional modifications to the theoretical formula may be necessary for more predictions that are accurate.

Crowley Bridge

Avent et al. [*5*] conducted a field repair as part of a heat straightening research program. The repair was conducted on the Crowley Bridge in Louisiana. Research objectives for the case study were to successfully repair the damaged bridge using the state-of-the-art heat straightening bridge repair procedures and to measure and document the response of the heat-straightened girder during the repair.

Crowley Bridge featured four simply supported primary supporting girders, which spanned 75 ft. Initial damage assessment determined that an over-height vehicle struck the bottom flange of the girder, inducing an out-of-plane displacement of 2.95 in. The nearest diaphragm had been severely damaged and

created a large local bulge in the web. A traffic control plan was designed to ensure the safety of the commuters and workers during the repair project. The project consisted of ten heating cycles that utilized Vee heats on the bottom flange with strip-heats on the web. After the fifth heating cycle, the heating pattern was redesigned since the bottom flange indicated no movement. It was determined that the lateral bracing was imposing a negative constraint on the thermal contraction effect [*5*]. The heating patterns were revised in order to re-obtain plastic rotation. Restraining forces were applied to the damaged girder using a hydraulic jack. The jack was positioned 2 ft. away from the impact point and created a restraining force of 12,900 lbs resulting in a restraining moment of 0.25 M_p. The lateral displacement of the girder resulting from each heating cycle was measured and recorded. The bottom flange remained deflected 1.83 in. after the last heating cycle. The average lateral displacement per heating cycle was 0.11 in.

Lake Charles Bridge

A project implementing the latest heat straightening technology was performed on the Lake Charles Bridge in Louisiana [*42*]. The project was a joint effort between Louisiana State University, the Louisiana Bridge Maintenance Division, and District 7. The Lake Charles Bridge features a simply supported noncomposite steel stringer (A-440) spanning 75 ft. Objectives of the repair project were to inspect the damaged bridge and assess the damage type and degree, design a heat straightening repair scheme, and implement the repair with Department of Transportation personnel.

The bridge was initially inspected to assess public safety and structural stability issues related to its usage. The inspection revealed that the bridge was stable and that the lower flange had displaced approximately 17 in. out-of-plane from the impact of an over-height vehicle. Diaphragms on both sides of the impact point had been partially crushed but most of the bolts were still in place. A decision was made to replace the diaphragms rather than repair them [*11*]. The damage to the bridge was assessed using the taut line method. The lateral offsets were measured every 3 ft. except in areas of web bulges. These areas were measured on a six-inch-by-six-inch grid in order to capture the entire damage picture. A contour gauge was employed to obtain a continuous measure of curvature in areas of high localized yielding. This information was used to design a heat straightening repair plan.

The repair plan consisted of the selection of heating patterns for each damaged region, determining the length and location of line heats, determination of Vee angles, location and magnitudes of restraints, and an estimate of the number of heats required. Since the repair would require heat-straightening procedures to be implemented over the entire span of the beam, closure of the eastbound lanes was eminent. Therefore, the repair plan was construed such that the lanes would be alternately closed and the heat straightening operations would still be effective. Strong backs were employed to prevent the beam from falling if a crack initiated since all of the diaphragms were eventually removed.

Heat straightening of the beam was successful with the exception of two aspects. First, the dimple at the impact point on the lower flange of the beam had strain values that exceeded the recommended heat straightening guidelines [*10*]. It was decided not to repair the dimple but rather to grind and prevent stress concentrations. Second, the top flange of the beam had been displaced several inches from the impact and the heat straightening operation did not return the flange back into the deck slot. It was decided to have the bridge maintenance crew fill the gap with grout. This field study provides a step-by-step example of the repair procedure for heat straightening beams subjected to complex damage patterns. An interactive CD-ROM featuring the repair of this bridge is also available. A list of recommendations is also provided in the report for assisting DOT agencies in the implementation of heat straightening as a viable repair alternative.

2.1.2.5.2 Prototype Bridge Studies

A Heat Straightening Evaluation and Testing (HEAT) facility was constructed on the campus of Louisiana State University [*43*]. This facility allows full-scale bridge girders to be studied without the

need for traffic control or other safety issues associated with actual field studies. Two four-year studies have been conducted at the facility to date. The first study (1985-1988) involved composite girders, while the second study (1989-1992) included composite, non-composite girders and axially loaded truss members. These two extensive studies have documented the actual damage and repair behavior of full-scale bridge girders and axially loaded truss members.

The first study [*23*], [*44*] included two different 20-ft. long composite wide flange beams that were subjected to two damage-repair cycles each (Cases SB-1 to SB-4). Case SB-1 and SB-2 involved the repair of a W10x39 girder damaged by static lateral loads. Case SB-3 and SB-4 involved the repair of W24x76 girders damaged by dynamic and static loads respectively. The prototype girders were simply supported with a concrete deck bolted to simulate composite action. Two diaphragms, one at each end, connected the test girder to the test setup. Damage was induced at mid-span with either a static or a dynamic lateral load. The dynamic lateral load was applied using a swinging pendulum.

The second study [*24*] extended the testing and analytical developments from the first study [*4*]. The W24x76 girder from the first study [*4*] was subjected to two additional cycles of damage followed by heat straightening repair. It fractured during the fourth damage-repair cycle. In addition, a non-composite W24x76 beam was subjected to three damage-repair cycles.

2.1.3 Heat straightening Guidelines

Two major reports have been published to provide general guidelines for conducting heat straightening repair in the field. They are the NCHRP [*9*] and the FHWA [*12*].

The first comprehensive report on heat straightening addressed the general damage assessment of structures. In general, this report provides a rational approach to using heat straightening as a repair method [*9*]. The report provides a set of guidelines for the damage assessment and heat straightening repairs of damaged steel bridge members. Shanafelt and Horn [*9*] also presented a method for quantifying the damage of the steel member in terms of strain by using three offset measurements. The radius of curvature (RC) along the edge of the damaged member is calculated by these three offset measurements along with their respective distances relative to each other. The authors suggest that measuring points be placed at one-foot intervals throughout the curved regions. In some cases, this interval could be too large and is incapable to capture the complete profile of the damaged area. Thus, the damage assessment could be significantly underestimated.

The calculated RC is compared to the RC of a typical cross-section when the extreme tension fiber has begun to undergo yielding. The calculated RC can then be expressed in terms of a multiple of the yield strain. Recommendations were made concerning upper strain limits for which heat straightening repairs should be made on primary tension members. Members having greater than five percent (approximately 42 times the yield strain ($42\varepsilon_y$) value for A36 steel) should not be straightened unless additional splice material is added to the straightened areas. Additionally, repairs to primary tension members in severe fatigue critical areas (AASHTO stress categories lower than C) were limited to 15 ε_y (approximately the strain hardening state) even if the nominal strain was less than 5 percent.

If the severe critical details were present, the guidelines suggest that the damaged member could be straightened but would need to be strengthened with a minimum of 50 percent additional material. This suggestion is based on the premise that the member was probably designed for an allowable working stress of $0.50\sigma_y$. Therefore, in reality, the heat straightened element could be neglected entirely and the recommended additional material would support the entire load.

The above guidelines suggest that primary tension members in severe fatigue critical areas with less than or equal to $15\varepsilon_y$ can be straightened with the addition of more material. These strain limitations apply for tensile areas of damaged members. No limitations have been placed on compression members. It is crucial to keep in mind that no scientific studies have been conducted to establish the above limits. They

are merely suggestions from the authors regarding the applicability of heat straightening based on strain limits.

The second comprehensive report that contributed to the development of heat straightening guidelines contains an engineering guide on the implementation of heat straightening for repairing damaged steel members [*4*]. The guide addresses engineering issues related to the analysis and design of heat straightening repairs for damaged structural steel. The purpose of the guide is to provide the structural engineer with some analysis and design tools on heat straightening in a similar fashion that they are accustomed. The guide incorporates damage assessment, material assessment, and design of heat straightening repair sequence as well as tips for supervising field repairs.

Damage assessment is the first step in implementing heat straightening repairs in practice. The authors point out that the cause and damage type is influential on the design considerations for the repair [*4*]. Evaluation and damage assessment methods are presented for primary and secondary damage. These damage assessment methods include the offset method, optical measurements, and image processing. A classification system for characteristic patterns of primary damage in rolled shapes is also defined. The system defines Mode I, Mode II, and Mode III, which correspond to weak axis bending, strong axis bending, and twisting about the longitudinal axis, respectively [*46*]. Further sub-divisions of Modes I, II, and III are based on where the stiffening element is located [*4*]. Classification of the structural configuration and a structural analysis is also important during the damage assessment stage.

The authors provide material assessment guidelines for damaged members. The assessment includes investigating the resulting; yield stress, hairline fracture, yield lines, plastic hinges, radius of curvature, calculation of damage as a multiple of yield strain, local buckling or bulges, and evaluation of residual stresses affecting heat straightening. Guidance for designing a repair sequence includes; development of the restraint conditions, development of heating patterns, and temperature limitations. Guidelines for the field supervisor include; field safety, reviewing heating patterns, and monitoring heating temperature and the restraining forces being applied to the damaged member. It is recommended that the heating temperature be monitored by either temperature sensing crayons, contact pyrometers, or visual observation of steel color [*4*].

The third comprehensive report contributing to the development of heat straightening guidelines featured extensive experimental and analytical tests that were used to develop a companion report, "Design Procedures for Heat straightening Repairs: An Engineering Guide" [*41*]. This companion report is a prototype-engineering guide for implementing heat straightening repairs. It supplements the previous engineering guide [*4*] with the addition of research obtained from the third comprehensive report [*5*]. The following results were quantified and included in the new engineering guide:

- Formulas for calculating plastic rotations for plates, angles, channels and wide flange sections were developed.
- Residual stress patterns in damaged-heat straighten repaired members were quantified.
- Material properties in heated zones may vary significantly. Ductility in the heated zones may be greatly reduced.
- Damaged steel should not be repaired more than twice at the same location.
- Member shortening from Vee-heats (full and 3/4 depth) can be calculated.
- Restraining forces must be calculated based on both external and internal redundancy. Methods are used to analyze the restraining forces.
- Composite girders, non-composite girders and axially loaded members have been studied and analytical models (plastic rotation) have been developed.
- Experimental results of successfully repaired specimens damaged up to 100 ε_y were documented.

Experimental studies have shown that the yield strength of heated steel is greatly reduced when heated [*22*], [*1*], [*3*]. Therefore, it is recommended that jacking forces should be gauged and limited to causing a moment in the heated zone to be less than 0.33 of the yield moment (M_y) plus the residual stresses in the unheated section [*10*]. It is implicit in this recommendation that a structural analysis is performed and the moment capacity of the beam is readily available. It was also discovered that defining the degree of damage using "angle of damage" provided more consistent definitions of the damage as compared to using the radius of curvature (RC). Four offset measurements are used to define the "angle of rotation (degree of damage) between non-yielded portions on both sides of the plastic hinge yield zone" [*10*].

Current DOT and FHWA heat straightening guidelines have been developed from the three major studies that were discussed above. The Federal Highway Administration (FHWA) sponsored a project, which complimented the Lake Charles Bridge repair [*11*], [*47*], [*42*]. The objectives of the FHWA study were to develop training materials based on the results of the application of the latest heat straightening research on the Lake Charles Bridge repair. Deliverables from the study included a Technical Guide and Manual of Practice [*12*], as well as a video and multimedia CD-ROM computer program. The manual offers the latest guidelines to structural engineers for implementing heat straightening repairs for damaged steel bridge members. The CD-ROM computer program offers an interactive interface that offers a built-in calculator for designing heat straightening repairs.

2.1.4 Conclusions from Literature Review

To date, great strides have been made in understanding the behavior and effect that heat straightening has on the structural properties of steel. Based on the above literature review, the following research areas are found to be sufficiently investigated:

- Development of heat straightening repair techniques for damaged steel members
- Development of guidelines and recommendations for heat straightening repair
- Estimating plastic rotations achieved during each Vee heat
- Predicting residual stresses caused by heat straightening in initially straight (undamaged) plates and rolled shapes
- Effects of heat straightening on the structural properties of initially straight (undamaged) plates and rolled shapes

Based on the above literature review, the following research areas are either inadequate or have yet to be addressed by researchers:

- Investigation of fatigue characteristics of heat straightened members
- Effects of heat straightening on the structural properties of initially damaged plates and rolled shapes (surface hardness and microstructure investigations are clearly lacking).
- Effects of heat straightening on the structural properties of different steel grades (most of the research work was conducted on A36)
- Effects of multiple damage and heat straightening repairs on the structural properties of steel
- Laboratory experiments on a greater variety of rolled shapes and built-up members commonly used in bridge design

2.2 SURVEY ANALYSIS

A survey form was sent to each state Department of Transportation (DOT). Twenty-two state DOTs responded to the questions of the survey form. Some state DOTs also provided the MSU research team with their respective heat straightening provisions. The results of the survey are provided in Section 2.2.1. Comparisons between the available state provisions are discussed in Section 2.2.2.

2.2.1 Survey of various DOTs

A survey questionnaire was developed for distribution to different state departments of transportation (DOTs). This survey included seven questions with multiple-choice type answers to facilitate answering it. The questions and the corresponding multiple-choice answers are given in Figure 2.5.

As shown in Figure 2.5, the questions focused on identifying the heat straightening provisions and guidelines, and the multiple damage – heat straightening repair criteria being used by various state DOTs. This survey questionnaire was approved and distributed to all state DOTs in the U.S. by the MDOT program manager, Roger Till. Twenty-two state DOTs responded to the survey. These include the DOTs from Alaska, Arkansas, California, Connecticut, Delaware, Georgia, Hawaii, Iowa, Kansas, Maine, Massachusetts, Michigan, Missouri, Minnesota, Nebraska, New Hampshire, North Carolina, New Jersey, New Mexico, Tennessee, Texas, Virginia, Washington, and Wyoming. The results from the survey are shown in graphical form in Figure 2.6(a-g).

- As shown in Figures 2.6(a), only 35% of the surveyed state DOTs have heat straightening provisions and guidelines. The remaining 65% of the surveyed state DOTs do not have heat straightening provisions or guidelines.
- As shown in Figure 2.6(b), the FHWA research report IF-99-004 [*47*] forms the basis of the heat straightening provisions for 24% of the surveyed DOTs, while the NCHRP Report 271 [*9*] forms the basis for 9% of the surveyed DOTs. 7% of the surveyed DOTs use their own research, and 22% of the surveyed DOTs combine these and other sources for developing heat straightening provisions and guidelines.
- As shown in Figure 2.6(c), 4% of the state DOT heats straightening provisions are available from the Internet. The only state that has the provisions available from the internet is Michigan.
- As shown in Figure 2.6(d), none of the surveyed DOTs have specific provisions for multiple heat straightening repair of the same steel beam.
- As shown in Figure 2.6(e), all the surveyed state DOTs are interested in the results of this research project.
- As shown in Figure 2.6(f), 9% of the surveyed state DOTs believe that the number of repairs governs the maximum number of multiple heat straightening repairs. 4% of the surveyed DOTs believe that the damage magnitude governs, and 52% of the surveyed state DOTs believe that the combination of the damage magnitude and the number of repairs governs the maximum number of multiple heat straightening repairs.
- As shown in Figure 2.6(g), 4% of the surveyed DOTs limit the number of multiple heat straightening repairs to one, 9% of the surveyed DOTs limit the number to two, 4% of the surveyed DOTs limit the number to three, and 57% of the surveyed DOTs have other criteria for limiting the number of multiple heat straightening repairs.

2.2.2 Specific DOT Provisions

A few state DOTs, i.e., Massachusetts, Iowa, Kansas, and New Hampshire sent their special heat straightening provisions by mail or email. This section compares the heat straightening provisions for these states as well as that for the Michigan Department of Transportation (MDOT). The MDOT provisions are further discussed in Section 3.2. The comparisons addressed are limited to the interest of this research project. Critical provisions in relation to this research project are organized in Table 2.3 such that comparisons can be made. These provisions include: (1) the maximum heating temperature; (2) the cooling temperature before successive heats; (3) the maximum torch diameter; (4) the maximum Vee angle; and (5) the maximum base width of the Vee heat. "Not provided" in Table 2.3 indicates that a limit is not provided by the specifications of the respected DOT.

For all five state DOTs, the maximum heating temperature allowed ranges from 1100-1200 °F. The cooling temperature before successive heats was specified by Kansas and Michigan to be approximately 250 °F. Avent et al (2001a) suggests that the steel should be cooled to 200 °F. All states with the exception of Kansas specify that the maximum torch tip diameter should be 1 in. For the states which provided the parameter, the maximum Vee angle is 20°. Avent et al (2001a) suggests a maximum Vee angle of 20° as well. Massachusetts allows their base width to be as high as 45° if applicable. The maximum base width specified varies from 6-10 in. Other important provisions as specified by the different state DOTs are provided below. These provisions include information regarding the external restraining stress as well as guidelines for cooling between successive heats which are areas significant to the research project.

Michigan:

- Apply a minimum external restraining force.
- No forced cooling allowed.
- Restraining force cannot resist contraction or produce local buckling.

Kansas:

- Only use jacking forces to restrain the members or elements against undesired movement associated with expansion during the cycles of applying heat.
- Assume that existing steel has a yield stress of 34.8 ksi.
- Simultaneous Vee heats are permitted provided the clear spacing is greater than the width of the plate element.
- Water cooling is not allowed.

New Hampshire:

- Compressive stress shall not exceed 24 ksi for A373 and A7 steels, 27 ksi for A36, and 37 ksi for grade 50 steels.
- Do not reheat untilled cooled completely.

Massachusetts:

- Jacks should be applied before heating and not increased by external means during heating or cooling.
- Jacks should not impede contraction during the cooling phase and they should not produce local buckling of the compression elements.

- The stresses in the member prior to heating should not exceed 27 ksi.

Iowa:

- Jacking forces shall be limited to 25 tons (50 kips).
- The jacking force shall not be adjusted during heating or before the temperature in the beam has cooled to 600 ºF.
- Cooling with compressed air may be done only after the steel has cooled naturally to less than 600 ºF.

A significant amount of variability exists between the different state provisions. The discrepancies are most significant in the application of the external restraining stress. New Hampshire appears to take the most caution by specifying a maximum restraining stress of approximately 0.75 σ_y for various steel types. These maximum restraining stresses seems valid if residual stresses induced by damage are being considered in the computation.

2.3 HIGH LOAD HITS DATABASE ANALYSIS

The Michigan high-load hits database from 1976 to 2001 was obtained from MDOT and analyzed to determine the steel types and the structure types that are damaged and heat straightened most frequently and thus most relevant to this research project. The high-load hits database included a total number of 280 damage-heat straightening repair cases corresponding to 183 steel bridges. Some of damage-repair cases were multiple damage-heat straightening repair of the same steel bridge. The results from the database analysis are shown in Figure 2.7(a-f).

- Figure 2.7(a) shows the annual distribution of the total (280) damage-heat straightening repair cases from 1976 to 2001. As shown in Figure 2.7(a), the number of high-load hits and corresponding heat straightening repairs has decreased over the past few years.
- Figure 2.7(b) shows the frequency distribution of the total number (280) of damage-heat straightening repair cases as a function of the steel type. In developing Figure 2.7(b), the steel type corresponding to a bridge subjected to multiple damage-repair cycles is counted multiple times. Thus, if a bridge made from A7 steel occurs twice in the high load hits database, then the corresponding A7 steel is counted twice.
- Figure 2.7(c) shows the frequency distribution of the total number (183) of steel bridges occurring in the high-load hits database as a function of the steel type. In developing Figure 2.7(c), the steel type corresponding to a bridge subjected to multiple damage-repair cycles is counted only once.
- Figures 2.7(b) and 2.7(c) clearly indicate that A7 and A373 are the steel types that are most frequently damaged and heat straightened in Michigan. Figures 2.7(b) and 2.7(c) indicate that the steel types that are most relevant to this research project in their order of relative importance are A7, A373, A588, A36, and A572.
- Figure 2.7(d) shows the frequency distribution of the total number (280) of damage-heat straightening repair cases in the database as a function of the structure type. In Figure 2.7(d), structure type 332 is a simply supported composite wide-flange steel beam, structure type 382 is a simply supported composite steel plate girder, and structure type 432 is a continuous composite wide-flange steel beams. Other structure types (302, 303, 325 etc.) in Figure 2.7(d) are not identified because they are not relevant to the present discussion.
- Structure types 332, 382, and 432 compromise 82.1 percent of all repair cases. In developing Figure 2.7(d), the structure type corresponding to a bridge subjected to multiple damage-repair cycles is counted multiple times.

- Figure 2.7(e) shows the frequency distribution of the total number (183) of steel bridges occurring in the high-load hits database as a function of the structure type. In developing Figure 2.7(e), the structure type corresponding to a bridge subjected multiple damage-repair cycles is counted only once.
- Figures 2.7(d) and 2.7(e) clearly indicate that structure type 332 (simply supported composite wide-flange steel beams) is most frequently damaged and heat straightened in Michigan, and thus most relevant to this research.
- Figure 2.7(f) shows the frequency distribution of bridges subjected to multiple damage-heat straightening repair events as a function of the number of damage-repair events and the steel type. For example, as shown in Figure 2.7(f), twelve A7 steel bridges and thirteen A373 steel bridges were subjected to two damage-heat straightening repair events. Steel bridges made from A7 steel and A373 are most frequently subjected to multiple damage-heat straightening repair events, and thus most relevant to this research.

2.4 HEAT TREATMENTS AND METALLURGY OF STEEL

2.4.1 Introduction

Heat treatments are useful to cause desired changes in the metallurgical structure of steel. These metallurgical changes inherently change the properties of steel including structural, electivity, magnetic, and surface texture [*49*]. Different heat treatments have different effects on the resulting structural properties of steel. The structural properties that typically interest heat treaters are the resulting hardness and strength of the material [*49*]. Heat treatments also have an influence on the resulting toughness and ductility. Heat treatments are often applied to cold-work deformed steels to revert the material properties back to the pre cold-worked state.

Previous experimental investigations [5], [*6*], [*7*], and [*8*] have investigated the effects of heat straightening on the structural properties of steel. However, there is a lack of investigations on the effects of heat straightening on the resulting microstructure of steel and how microstructural changes relate to the structural properties. The most significant difference between heat straightening and common annealing procedures is the time for which the temperatures are held to produce the desired effects. Most annealing procedures are also not aided by an external restraining force.

The purpose of this section is to review the microstructural aspects of steel and attempt to relate different heat treatments to heat straightening. Most of the information summarized in this section is adapted from numerous textbooks on steel heat treatments and material science. The influence of various temperature ranges, microstructural aspects, prior deformation, and alloys on the transition temperatures, recrystallization temperatures, and resulting structural properties are discussed. Section 2.4.2 discusses the microstructure of low-carbon and high-strength low-alloys steels at ambient and elevated temperatures. Section 2.4.3 discusses the effects of cooling rate of steel heated to temperatures exceeding the phase transformation eutectoid temperature and the possible microconstituents that may result. These microconstituents include ferrite, pearlite, martensite, and bainite. Section 2.4.4 summarizes the effects of grain size on the structural properties of steel. Section 2.4.5 summarizes the effects on engineering alloys on the phase transformation temperatures and the resulting physical and structural properties of steel. Section 2.4.6 summarizes the cold-worked (damaged) structure of steel. Section 2.4.7 discusses recovery, recrystallization, and grain growth, which are changes that occur in the microstructure of damaged steel at elevated temperatures.

Prior to further discussion, it must be noted that the maximum temperature enforced for heat straightening is typically 1200 °F (650 °C). Most of the experimental investigations conducted in this research project included small-scale specimens and beam specimens that were damaged and repaired

with a maximum heating temperature of 1200 °F (650 °C) (refer to Chapters 4 and 7). In addition, sixteen A36 small-scale specimens and one A36 beam specimen was damaged and repaired with a maximum temperature of either 1400 °F (760 °C) or 1600 °F (870 °C). Therefore, the maximum temperature ranges considered in this section are as high as 1600 °F (870 °C).

2.4.2 Grain Structure of Low-Carbon Steel and High-Strength Low-Alloy steels

This research project included studies of low-carbon (LC) steels and high-strength low-alloy (HSLA) steels. LC steels contain up to 0.25% carbon [*50*] along with various other elements such as manganese (up to 1.65%), sulfur (up to 0.05%), phosphorous (up to 0.04%), silicon (up to 0.60%), and copper (up to 0.60%) [*49*]. HSLA steels provide better mechanical properties and/or greater resistance to atmospheric corrosion than conventional carbon steels. These HSLA steels have lower carbon contents (0.05-0.25% C) to produce adequate formability and weldability. HSLA steels also have manganese contents up to 2.0%. Small quantities of chromium, nickel, molybdenum, copper, nitrogen, vanadium, niobium, titanium and zirconium are also added in various combinations [*49*].

LC and HSLA contain less than 0.8% carbon, which classifies them as *hypoeutectoid* steels. A schematic of the transformation of a hypoeutectoid plain carbon steel at elevated temperatures is shown in Figure 2.8 [*51*]. An actual photograph of A36 steel at ambient temperatures is also shown in Figure 2.8 (480X). It should be clarified that this schematic is only valid for steels that are cooled relatively slowly. For faster cooling rates, refer to information in Section 2.4.3.

At high temperatures exceeding the stable austenite temperature (Ac3), the hypoeutectoid structure is in a stable γ-austenite phase. As the steel cools below the Ac3 temperature, proeutectoid ferrite will nucleate and grow at the austenite grain boundaries. As the steel continues to cool from the Ac3 temperature to the eutectoid temperature (Ac1), the amount of proeutectoid ferrite formed will continue to grow and the austenite will increase in percent carbon content. At the Ac1 temperature (approximately 1340 °F), the remaining austenite will transform into pearlite with consists of both ferrite and cementite (Fe_3C) layers [*51*]. The ferrite that is present within the pearlite is referred as eutectoid ferrite to distinguish from proeutectoid ferrite. Thus, at ambient temperatures, a LC or HSLA microstructure consists of proeutectoid ferrite and pearlite. If the initial carbon content is higher than 0.4%, then more pearlite exists in the microstructure. The physical and structural characteristics of pearlite and other microconstituents such as bainite and martensite are described later.

2.4.3 Isothermal and Continuous Cooling Transformation Diagrams

Formation of Different Microconstituents

Two types of temperature dependent transformation diagrams are used to predict formations of different microconstituents. Note that these diagrams are only applicable if the steel is heated to values exceeding the Ac1 temperature of approximately 1370 °F. An isothermal transformation diagram (TTT) is a plot of temperature vs. logarithm of time for steel alloys of definite composition [*52*]. This type is used to determine when transformation begins and ends for an isothermal heat treatment (constant temperature) of a previously austenized alloy. A continuous cooling transformation diagram (CCT) is also a plot of temperature vs. logarithm of time for a steel alloy of definite composition. However, this type of diagram is used to determine when transformations begin and end when a previously austenized alloy is continuously cooled at a specified rate. During heat straightening, the cooling time-temperature profile represents a continuous cooling period. Continuous cooling transformation diagrams have longer times and lower temperatures in forming the different microconstituents as apposed to isothermal transformation diagrams. A number of TTT diagrams for various steels were found in the literature [*53*], [*54*]. However, not as much research has been performed for the development of CCT diagrams.

Derivation of a CCT diagram is a rather tedious task, and for many purposes not essential because of the fundamental relationship between TTT and CCT diagrams [*53*].

Figure 2.9 shows a continuous cooling transformation diagram for AISI 1010 steel, which is a low carbon steel with similar chemical composition to A36 [*54*]. As shown in Figure 2.9, this steel contained 0.12%C, 0.50% Mn, and 0.16% Si, which is similar to the A36 material used in this research project (0.15%C, 0.66%Mn, and 0.24%Si). This figure was superimposed on Microsoft Excel for use in this research project as shown in Figure 2.10. Critical cooling rates for the formation of bainite and the formation of martensite are also shown in Figure 2.10. The Ac3 and Ac1 temperatures in Figure 2.10 were calculated from the chemical composition of the A36 steel using Equations 2.7 and 2.8 [*55*]. Equation 2.9 was also found in the literature for computing Ac1 [*49*]. The effects of engineering alloys such as manganese (Mn) or nickel (Ni) in Equations 2.1-2.3 are discussed in more detail in Section 2.4.6.

$$A_{c1}(°C) = 723 - 10.7(\%Mn) - 16.9(\%Ni) + 29.1(\%Si) + 16.9\%Cr + 290(\%As) + 6.38(\%W) \quad (2.1)$$

$$A_{c3}(°C) = 910 - 203\sqrt{\%C} - 15.2(\%Ni) + 44.7(\%Si) + 104(\%V) + 31.5(\%Mo) + 13.1(\%W) \quad (2.2)$$

$$A_{c1}(°C) = 739 - 22(\%C) + 2(\%Si) - 7(\%Mn) + 14(\%Cr) + 13(\%Mo) + 13(\%Ni) + 20(\%V) \quad (2.3)$$

The time axis on continuous cooling diagrams begins when the steel temperature falls below the Ac3 temperature. The microstructure is initially in the γ-austenite phase and can form various microconstituents dependent on the cooling rate. The cooling rates as shown in Figure 2.10 represent the lower and upper rates for which different microstructures may form for the AISI 1010 steel. If the steel cools in between two rates specified in Figure 2.10, the microconstituent combination indicated on the bottom will form.

Pearlite

Pearlite consists of layers of α−ferrite and cementite (Fe_3C) layers. Cementite is much harder and more brittle than ferrite [*52*]. Thus, an increased amount of pearlite increases the hardness, yield strength, and ultimate strength of steel. However, both the ductility and the toughness of the material will decrease. Dependent on the cooling period, the resulting pearlite may be fine or coarse grained. A more coarse-grained pearlite microstructure will form upon longer cooling periods. Slower cooling periods produced relatively thick layers of both the α-ferrite and Fe_3C. Fine pearlite is harder and stronger, yet more brittle than course pearlite.

Although a change in the percent pearlite during a damage-repair cycle is unlikely, it is measured as a microstructure parameter in this research project (see Chapters 3, 5, and 8 later). The percentage of pearlite is dependent on the spot used for the photograph of the microstructure. An example of this is shown for undamaged A36 steel in Figure 2.11. Although, the two pictures were taken within 1 in. of the same piece of steel, more pearlite grains are clearly indicated in the Figure 2.11(b). The grain size and percent pearlite grains were computed using the general line intercept procedures discussed later in Section 4.9.4. The grain size and percent pearlite grains of the microstructure in Figure 2.11(a) are 0.0298 mm. and 25.0%, respectively. The grain size and percent pearlite grains of the microstructure in Figure 2.11(b) are 0.0290 mm. and 35.0%, respectively. Therefore, the MSU researchers were more interested to see if significant trends existed in the resulting percentage of pearlite grains.

Bainite

Bainite is an austenitic transformation product found in some steels. It forms at temperatures between which pearlite and martensite forms [*52*]. The production of bainite on the continuous cooling transformation diagram is shown in Figure 2.10. A bainite microstructure consists of both α-ferrite and a fine dispersion of cementite. A microstructure consisting of bainite does not necessarily consist of proeutectoid ferrite. Since bainite has a finer structure, it is generally stronger, harder, and consequently

more brittle than pearlite. Bainite microstructures exhibit a desirable combination of strength and ductility for a number of engineering applications [*52*].

Martensite

Martensite is formed from austenized iron-carbon alloys that are rapidly cooled or quenched to a relatively low temperature [*52*]. In other words, martensite is a nonequilibrium single-phase structure that results from the diffusionless transformation of austenite. For alloys containing less than 0.6 wt% C (LC and HSLA), the martensite grains form as long and thin plates which are aligned side by side and parallel to each other. The formation of martensite can be predicted using a continuous cooling transformation diagram as shown in Figure 2.10. If the steel cools faster than the indicated curve on the far left in Figure 2.10, the iron-carbon alloy will completely transform to martensite. Figure 2.10 indicates that martensite is a direct transformation of austenite and may be accompanied by ferrite, bainite, and to some extent pearlite [*51*].

Martensite is the hardest, strongest, and the most brittle form of microconstituent for an iron-carbon alloy. The hardness and strength of martensite increase with an increase in carbon content. Martensite has negligible ductility [*52*]. Therefore, the formation of martensite during heat straightening of a steel bridge needs to be strictly avoided. Section 5.4.2.2 further discusses the possible formation of martensite and bainite from experimental data in this research project.

2.4.4 Heat Treatments of Steel

A variety of steel heat treatments is used by heat treaters in order to enhance the material properties of steel. The purpose of this section is to discuss the most common heat treatments and relate them to heat straightening. The heat processes summarized in this section include; soft or spheroidizing annealing, process annealing, isothermal annealing, normalizing, tempering, and thermomechanical treatments. Such heat treatments change the microstrucutural aspects of steel and therefore enhance or deteriorate structural properties.

Process Annealing

Process Annealing is usually applied to hypoeutectoid steels with up to 0.3% C. The steel is heated to temperatures of typically 550-650 °C (932-1202 °F), which are below the Ac1 temperature. The steel is held at these temperatures for the necessary time and then cooled at a desired rate. Process annealing is frequently referred to as a “stress-relief” or “recovery” treatment since it partially softens cold-worked steels by relieving internal stresses (residual stresses) from cold working [*51*]. This process will not cause any phase changes but recrystallization may occur [*49*].

Process annealing is fairly related to heat straightening as both relieve the damage induced after cold working and similar temperature ranges are used. The maximum temperature limit for heat straightening is typically 1200 °F (650 °C). The intent of the two processes are somewhat different as heat straightening is used to straighten the cold worked members and does not consider the removal of internal residual stresses. Ref. [*49*] indicates that the soaking time required for process annealing is a much longer period than could be considered when heat straightening. The soaking times for process annealing are typically measured in hours.

Soft or Spheroidzing Annealing

Soft or spheroidizing annealing is an annealing process at temperatures slightly above or below the Ac1 temperature, with subsequent cooling [*49*]. The steel considered for soft annealing typically has a carbon content of at least 0.60 %, which would not include LC or HSLA steels. The process is generally considered for hypereutectoid steels (%C >0.80%). The aim of soft annealing is to produce a soft

structure by changing all hard constituents such as pearlite, bainite, and martensite into a structure of spheriodized carbides (spheroidite) in a ferritic matrix. The holding time at the selected temperature is approximately 1 min per millimeter of work piece cross section. For alloyed steels, the soft annealing temperature may be calculated according to the empirical formula given in Equation 2.10 [*49*].

$$T(°C) = 705 + 20(\%Si - \%Mn + \%Cr - \%Mo - \%Ni + \%W) + 100(\%V) \qquad (2.10)$$

Soft annealing is not related to heat straightening due to the required period for developing the spheroidite microstructure. The required period is typically between 18-24 hours [*52*]. The kinetics of spheroidite is not included on isothermal or continuous cooling transformation diagrams. Therefore, spheroidite was not distinguished in Section 2.4.3.

Isothermal Annealing

Hypoeutectoid steels that are used for carburizing as well as medium-carbon structural steels that are used for hardening and tempering are often isothermally annealed for better machinability [*49*]. An isothermally annealed structure should have; a high proportion of ferrite, uniformly distributed pearlite, fine lamellar pearlite grains, short pearlite lamellae, and coarse ferrite grains. Isothermal annealing includes austenitizing, followed by fast cooling to the temperature range of pearlite formation (about 1200 °F (650 °C)), holding at this temperature range until the complete transformation of pearlite, and cooling to room temperature at a arbitrary cooling rate. Isothermal annealing is clearly unrelated to heat straightening since heat straightening is characterized by continuous cooling rates.

Normalizing

LC and HSLA steels that have been plastically deformed consist of pearlite grains that are irregularly shaped and relatively large, but vary substantially in size. Normalizing is a heat treatment process consisting of austenitizing (heating to temperatures in the range to cause an austenite microstructure) at temperatures 30-80 °C (86-176 °F) above the Ac3 temperature (for hypoeutectoid steels) followed by slow cooling [*49*]. This annealing process is used to refine the grains and produce a more uniform and desirable grain size distribution [*52*]. Normalizing is typically performed on steels that have been coarse-grained as a result of being heated to high temperatures due to forging or welding, needlelike ferrite resulting in steel castings, or when the steel grains are oriented in the rolling direction [*49*]. The normalizing parameters include the heating rate, the austenitizing temperature, the holding time, and the cooling rate.

From this description, and from the experimental results presented in Section 5.4.3.4, it appears as A36 steel damaged and repaired using a maximum temperature of 1600 °F is being normalized as a much finer and more uniform grain distribution is found in the resulting microstructure. However, the literature indicates that the holding time at austenitizing temperature may be calculated using the empirical equation below [*49*].

$$t = 60 + D \qquad (2.11)$$

In Equation 2.11, t is holding time in *minutes* and D is the maximum diameter of the work piece. In heat straightening, the maximum temperature of 1600 °F is only held for only a few seconds. Therefore, the two heating processes become rather unrelated. Normalizing is even more unrelated to heat straightening when maximum heating temperatures of either 1200 °F or 1400 °F are used for the repair because the Ac3 temperature is not exceeded.

Tempering

Martensite is formed when austenized steel is quenched at a fast rate (see Figure 2.10). Tempering is the process of heating martensitic steel to a temperature below the eutectoid temperature for a specified

time period. This tempering heat treatment produces tempered martensite [*52*]. Tempered martensite may be nearly as hard and strong as martensite but with enhanced ductility and toughness.

Tempering is substantially unrelated to heat straightening. The austenized steel is not being cooled fast enough for the production of martensite. Martensite is the only microconstituent that can be enhanced by this type of heat treatment.

Thermomechanical Treatments

Thermomechanical treatments are processing treatments very similar to tempering or soft annealing, with the exception that they combine plastic deformation with the treatments. The purpose of thermomechanical treatments is to enhance structural properties such as strength with ductility and/or toughness [*55*]. For example, hot rolling is an example of a thermomechanical treatment. Three forms of thermomechanical treatments are: (1) low temperature thermomechanical treatment (LTMT); (2) high temperature thermomechanical treatment (HTMT); and (3) isoforming [*57*]. Figure 2.12 shows these three treatments schematically on an isothermal transformation diagram [*57*]. The LTMT process (also known as ausforming) consists of lowering the temperature of the steel quickly below the Ac1 temperature so that no other microconstituents form leaving the steel in a *metasable* austenite (MSA) phase. The steel in the MSA phase is deformed and then quenched rapidly to form martensite. This is followed by tempering to achieve the appropriate balance of structural properties.

The ausforming treatment can be contrasted with a high temperature thermomechanical treatment (HTMT), where the steel is deformed in the *stable* austenite phase above the Ac3 temperature. The steel is again quenched to martensite and tempered at appropriate temperatures. In a third process, isoforming, the steel is deformed in the austenite phase at a temperature below the Ac1 temperature. However, in contrast to ausforming, the deformation continues until the phase transformation to ferrite/pearlite has completed. The steel is then slowly cooled to room temperature.

All three thermomechanical treatments involve plastic deformations at elevated temperatures, which occur in heat straightening. LTMT and HTMT are both relatively different from heat straightening. Both processes require a holding temperature, followed by quenching and tempering which are not characteristics of heat straightening. Isoforming is similar to heat straightening at elevated temperatures with the exception of the holding time required for isoforming. The desired spheroidite microstructure was not seen in the microstructure investigations of damaged-repaired overheated A36 steel, which are presented in Section 5.4.3.4.

2.4.5 Effect of Grain Size on the Structural Properties of Steel

This section discusses the effects of the microstructural grain size on the resulting structural properties of steel. It also includes the effects of grain size and the ability to form new grains during a heat treatment process. In general, a coarse-grain structure (large) is not as desirable as a fine-grain structure (small) for most steels as it leads to lower strengths and only moderately decreased ductility. The tendency to fracture also increases in a more coarse-grained structure [*50*]. Finer-grained steels have more grain boundaries that act as barriers to dislocations. Therefore, a higher density of grain boundaries will produce higher yield and tensile stresses [*Smith, 1993*]. Plane strain fracture toughness normally increases with a reduction in grain size when composition and other microstructural variables are maintained constant [*52*]. Decreasing the grain size significantly decreases the transition temperature, which is the temperature that governs the ductile to brittle fracture [*49*]. Hence, refining the grain size increases both the strength and the fracture toughness of steels.

Cold-worked, fine-grained steel also requires less time at annealing temperatures before nucleation begins [*57*]. Nucleation is discussed in more detail in Section 2.4.8.2. Therefore, more nucleation sites are available and the formation of new grains is more likely to occur. During the transformation of austenite to pearlite, pearlite nucleates preferentially at austenitic grain boundaries. Thus, the more grain boundary

surface available for pearlitic nucleation, the easier it is to form pearlite. When pearlite is more *easily* formed, the hardenability decreases as well. Therefore, the smaller the grain size, the lower the hardenability of the steel when all other factors are remained constant [*Smith, 1993*].

2.4.6 Effects of Alloying Elements on Phase Transformations

The addition of several alloying elements affects the physical and structural properties of steel in a variety of ways. Alloying elements also affect the eutectoid temperature (Ac1) and the temperature that defines stable austenite (Ac3). As mentioned in Section 2.4.3, the following equations can be used to predict the Ac1 and Ac3 temperatures as a function of the different alloying elements [*55*], [*49*]:

$$A_{c1} = 723 - 10.7(\%Mn) - 16.9(\%Ni) + 29.1(\%Si) + 16.9\%Cr + 290(\%As) + 6.38(\%W) \quad (2.7)$$

$$A_{c3} = 910 - 203\sqrt{\%C} - 15.2(\%Ni) + 44.7(\%Si) + 104(\%V) + 31.5(\%Mo) + 13.1(\%W) \quad (2.8)$$

$$A_{c1}(°C) = 739 - 22(\%C) + 2(\%Si) - 7(\%Mn) + 14(\%Cr) + 13(\%Mo) + 13(\%Ni) + 20(\%V) \quad (2.9)$$

Table 2.4 shows the chemical compositions of A36 and A588 steels used for the small-scale (A588 only) and large-scale specimens of this research project (see Chapters 4 and 7 later). Table 2.4 also shows the computed values of Ac1 and Ac3 from Equations 2.7-2.9. These equations are derived empirically from charts that have been developed to relate the effects of alloying elements on the critical transformation points. Figure 2.13 shows the effects of the most significant alloying elements on the Ac1 temperature [*51*]. Manganese (Mn) and nickel (Ni) are distinguished as austenite-stabilizing elements that lower the eutectoid temperature, and thereby expand the temperature range over which austenite is stable [*55*]. Other alloying elements such as silicone (Si), chromium (Cr), molybdenum (Mo), arsenic (As), niobium (Nb), and tungsten (W) are distinguished as ferrite stabilizing elements (also called carbide-forming elements), which raise the eutectoid temperature of the steel and reduce the temperature range over which austenite is stable [*51*], [*55*]. Vanadium (V) is an alloying element that delays the transformation of α-ferrite to austenite and therefore raises the Ac3 temperature.

The bainite transformation takes place in carbon steels under precipitation curve of under cooled austenite in the interval of approximately 500-250 ºC (930-480 ºF). This is called the intermediate transformation range as it occurs between the pearlite and martensite transformations as shown in Figure 2.10 [*49*]. Alloying elements effect this intermediate transformation, although to an insignificant extent than in the case of the pearlite transformation.

The transformation of austenite into martensite is most significantly effected by the amount of carbon (C). Experiments concerned with the influence of other alloying elements on the position of the martensite point show that cobalt (Co) and aluminum (Al) elevate the martensite point slightly, Si has a little if any effect, and all other elements decrease the martensite point [*49*]. However, for a wider range of carbon content, the quantitative influence of other elements can be different. The martensite transformation temperature of medium-carbon alloy steels can be estimated using the empirical equation shown below, which is only valid for 0.2-0.8% carbon steel.

$$M_H(ºC) = 520 - 320(\%C) - 50(\%Mn) - 30(\%Cr) - 20[\%(Ni + Mo)] - 5[\%(Cu + Si)] \quad (2.12)$$

2.4.7 Effects of Alloying Elements on the Material Properties

This section summarizes the effects of various alloying elements on the physical and structural properties of steel. This section is summarized from Chapter 15 in Ref. [*49*].

- Carbon (C) is essential to the formation of pearlite, spheroidite, bainite, and iron-carbon martensite. Therefore, the hardness and strength of the steel increases as the ductility and toughness of the steel decreases when more carbon is added [*51*].

- Aluminum (Al) is widely used as a deoxidizer and a grain refiner. Al does not significantly affect the material properties of steel.
- Boron (B) can significantly increase the hardenability of steel without decreasing ductility. Its effectiveness is most noticeable at lower carbon levels. Large amounts of B result in brittle, unworkable steel.
- Cobalt (Co) inhibits grain growth at high temperatures and significantly improves the retention of temper and high-temperature strengths, resulting in an increase in tool life.
- Copper (Cu) has a moderate tendency to segregate and therefore enhances hardenability. Cu is detrimental to the surface quality but improves the corrosion resistance and the tensile properties in alloy and low-alloy steels.
- Chromium (Cr) is a strong carbide former, which increases hardenability and corrosion resistance. Cr is the most efficient of the common hardening elements and is frequently used with a toughening element such as nickel (Ni) to produce superior mechanical properties.
- Lead (Pb) is sometimes added to carbon and alloy steels to improve machinability. Pb does not have a significant effect on the material properties of steel.
- Manganese (Mn) is present in virtually all steels. It is essentially a deoxidizer and desulfurizer. Mn increases the strength, hardness, also favorably effects forgeablity, and weldability.
- Molybdenum (Mo) is a strong carbide former. The addition of Mo produces fine-grained steels, increases the depth of hardness, and improves the fatigue strength. Mo also increases corrosion resistance and is thus used with high-alloy Cr steels and with austenic Cr-Ni steels.
- Nickel (Ni) is a ferrite strengthener and toughener that improves the ductility, toughness, and the strength of the steel.
- Niobium (Nb) is a ferrite former that reduces the austenite phase. Small amounts of Nb increase the yield strength and the tensile strength of steel. The increased strength may be accompanied by considerably reduced notch toughness unless special measures are employed to refine grain size during hot rolling.
- Phosphorous (P) slightly increases the strength and hardness of the steel. A large quantity decreases ductility and fracture toughness. A higher P content is specified in low carbon free-machining steels to improve machinability.
- Silicon (Si) is one of the principal deoxidizers used in steel making. It has a determinable effect on the surface quality of low-carbon steels. With Si content is steel is below 0.30%, it dissolves completely in ferrite, increasing the strength without greatly decreasing ductility.
- Sulfur (S) has a detrimental effect on transverse ductility, fracture toughness, weldability, and surface quality, but only has a slight effect on longitudinal mechanical properties.
- Tin (Sn) in relatively small amounts is harmful to steels for deep drawing. The effects of Sn in the amounts usually presented are negligible.
- Titanium (Ti) is used widely in stainless steels as a carbide former for stabilization against intergranular corrosion. Ti increases creep rupture strength.
- Tungsten (W) is a very important carbide former. It improves toughness and prevents grain growth.
- Vanadium (V) is an excellent deoxidizer, carbide former, and grain refiner. It dissolves in ferrite, imparting strength and toughness. V increases fracture strength on one hand and improves notch

sensitivity on the other. V steels exhibit a much finer structure than steels of similar composition without V. It provides other important alloying effects such as increases hardenability, secondary hardening effects on tempering, and increased elevated temperature hardness.

- Zirconium (Zr) is added to killed high-strength low-alloy steels to obtain improvements in inclusion characteristics that improve ductility in transverse bending.

2.4.8 Effects of Plastic Deformation on Microstructure

Plastic deformation of metals is commonly classified as cold-work or hot-work. In a cold-worked deformation, there is no accompanying recrystallization, which is discussed in Section 2.4.8.2. Hot-work has spontaneous recrystallization occurring simultaneously. Plastic deformation is the product of movement of individual crystal defects called dislocations [*57*]. A very large number of dislocations exist in deformed metal. Dislocation density can be uniform or highly variable from point to point. The variety of dislocations gives rise to a variety of large-scale deformations, including slip and twinning.

Deformation and slip in a polycrystalline material (one composed of more than one single crystal such as steel) is somewhat complex [*52*]. Due to random crystallographic orientations of the numerous grains, the direction of slip varies from one grain to another. For each, dislocation motion occurs along the slip system that has the most favorable orientation.

The fundamental dislocation motion of an individual grain is by nature a localized event [*57*]. The metallographic features of deformation that are large in comparison with the grains of the martial include mechanical fibering, flow lines, strain markings, shear bands, and Luder's lines. The features that are on the size comparable to that of the grains of the material include curly grain structure, orange pearl, slip lines, deformation bands, deformation twins, and kink bands.

Slip lines are visible traces of slip planes, which can be seen on the surface of the steel [*57*]. A slip line represents a transfer of the material on opposite sides of the slip plane. Planer slip refers to slip lines that are straight, whereas wavy slip refers to slip lines that are irregularly shaped. Wavy slip lines indicate a series of microscopic shears in two or more intersecting slip planes such as that caused by the departed cross slip of a screw dislocation. A comparison between planer slip lines and wavy slip lines is show in Figure 2.14. Figure 2.15 shows two photographs of the A36 steel microstructure used for the experimental investigations of this research project at 1200X. Figure 2.15(a) shows the undamaged steel and Figure 2.15(b) shows the steel at a damage strain of 60 ε_y. Slip lines are clearly indicated on the surface of the A36 steel in Figure 2.15(b). Further discussions of the damaged state of the steel used in this research project are interpreted in Section 5.5.

2.4.9 Recovery, Recrystallization, and Grain Growth

A plastically deformed polycrystalline material exhibits possible changes in grain shape, strain hardening, and an increase in dislocation density [*52*]. Some fraction of the internal energy is stored in the metal as strain energy, which is associated with tensile, compressive, and shear zones around the newly created dislocations. These properties may be reverted to the prior cold-worked states by heat treatments such as annealing. Such restoration results from two different processes that occur at elevated temperatures identified as recovery and recrystallization, which may be followed by grain growth.

Recovery

Recovery is the relief of some of the stored internal strain energy of a previously cold-worked metal by heat treatment. During recovery, the physical and mechanical properties of the cold worked steel begin to revert to the properties that existed prior to cold-working [*57*]. The rate of recovery is a thermally activated process and it decreases with increasing time and decreasing temperature [*58*].

Early in the recovery process, some internal stresses are relieved and a number of dislocations slightly reduce. As recovery proceeds, dislocation interaction results in an increase of dislocation density as dislocation arrays are formed. These arrays constitute the walls of new cells (subgrains) of recovered steel and have lower energy configurations than the dislocation tangles, which made up the in the cold-worked metal [*49*], [*52*]. The internal strain energy is therefore relieved by a virtue of dislocation energy due to enhanced atomic diffusion at elevated temperatures. Recovery constructs the dislocations in a more stable arrangement forming small angle grain boundaries. This process is known as polygonization and often is a structural change that precedes recrystallization [*51*].

Stabilizing polygonization is the process of redistribution of dislocations on heating of a deformed material with a homogeneous dislocation structure formed through operation of a few number of slips systems. This process results in annihilation of unlike dislocations and the formation of new stable sub boundaries of low curvature and low disorientation angles. This process is completed with the process of recrystallization. Prerecrystallization polygonization is a process of redistribution of dislocations on heating deformed material with a cell structure resulting in partial annihilation of dislocations in dislocation pile-ups that form cell walls. The process is essentially an initial stage to recrystallization and thus does not compete with recrystallization. Polygonization is generally effective on relatively light cold deformations. In cases of hot deformation, this is also valid for higher degrees of deformation, especially at lower deformation rates [*59*].

The temperature of grain recovery T_{GR} correlates with the recrystallization temperature T_R and the melting temperature T_M of the same material according to Equation 2.13 [*49*]. Assuming a melting temperature of 1400 °C (2550 °F), the temperature of grain recovery and the recrystallization temperature is computed as 260 °C (500 °F) and 560 °C (1040 °F), respectively, using Equation 2.13 [*49*].

$$T_{GR} = T_R - 300 = 0.4T_M - 300 \text{ [°C]} \quad (2.13)$$

During heat treatment, it is difficult to draw a clear division between recovery and recrystallization as the two processes typically overlap. Typically, only a slight decrease in the strength and hardness can be detected during recovery. Usually, the restoration of mechanical properties to annealed values is one-fifth achieved during recovery [*58*].

Grain recovery is likely to govern the microstructural changes during heat straightening although the appropriate holding time for the grain recovery of steel was not found in the literature. The annealing of a cold-worked state produced by plastic deformation is quite complicated, since many types of point defects as well as dislocations can be present simultaneously and may interact during annealing. Probably the main problem in studying the annealing of plastically deformed steel is the differentiation between effects due to dislocations and those due to point defections. Research has shown that some dislocations are rearranged during recovery, as indicated by slight increases in average particle size prior to the temperature at which recrystallization produces a sharp hardness drop [*58*].

Recrystallization

Recrystallization refers to the formation of a new set of strain-free grains within a previously cold worked material [*52*]. In primary recrystallization, formation and growth occur in a deformed matrix of new grains, which are distortion-free, and appreciably more prefect than the matrix after polygonization [*59*]. An annealing heat treatment such as process annealing is necessary for this recrystallization to occur. During recrystallization, the restoration of mechanical and physical properties is completed, and there is a change in the preferred orientation before grain growth. There is a significant drop in tensile strength and hardness and a large increase in the ductility of steel. Dynamic recrystallization is a process that combines elevated temperatures and plastic deformation. The process is therefore a form of hot working with subsequent recrystallization of deformed metal occurring. In contrast, the process of recrystallization that takes place after deformation is termed static recrystallization. In the course of hot deformation of a metal, strain hardening and softening are occurring in parallel [*59*].

The most important factors that affect recrystallization in metals and alloys are; (1) amount of prior deformation, (2) temperature, (3) time, (4) initial grain size, and (5) composition of the metal or alloy [*51*]. The recrystallized volume in the material increases during annealing owing to two processes: the nucleation rate and the growth of the nuclei where the rate is described by two parameters know as the rate of nucleation, N, and the rate of growth, G. Both primarily depend on the amount of prior cold deformation. In hot deformation, they depend on both the amount and rate of deformation [*59*].

Amount of deformation ε: Beginning from a critical deformation, an increase in plastic strain causes N and G to increase and therefore the rate of recrystallization to grow. The size of the grains at the end of primary recrystallization is smaller after greater deformations. Coarse-grained structures can result after moderate or heavy deformations. However, this behavior is usually associated with secondary recrystallization. Secondary recrystallization requires long holding times and therefore is less likely to occur during heat straightening. In deformations below the critical strain ε_{cr} value, only polygonization takes place during heating [*59*]. The values for the critical strain ε_{cr} for steels are lacking in the literature. Elevated temperatures and slower heating shifts ε_{cr} towards greater values.

Heat temperature: The kinetics of primary recrystallization is clearly temperature dependent. The recrystallization behavior of a particular metal alloy is sometimes specified in terms of a recrystallization temperature T_M defined as the temperature at which recrystallization just reaches *completion* in 1 hour [*49*]. As mentioned in Section 2.4.8.2, the recrystallization temperature of low carbon steel is approximately 1000 °F. A greater prior deformation and an increase in annealing time decrease the temperature for the start of recrystallization. The grains that form at the end of primary recrystallization at conventional heating rates become noticeably coarser with a further increase in temperature [*49*].

Time of annealing. According to most researchers, the average rate of growth G, in contrast to N, is *independent* of annealing time until the growing recrystallization nuclei begin to collide. On the other hand, it has been established by direct observations that the rate of growth does vary with time. When deformations slightly exceed the critical value, the two processes of growth of initial grains and growth of recrystallization nuclei can occur in parallel. Therefore, the results of recrystallization and average grain size, based on annealing time at various strains are rather complicated [*59*].

Initial grain size. A finer grain size increases the area of grain boundaries, which increases the probability of nucleation sites to form. Therefore, a finer original grain size accelerates the process of primary recrystallization [*59*].

Solute impurities. Solute impurities and alloying additions strongly influence the rate of primary recrystallization. For instance, a zone-refined iron deformed 10% undergoes polygonization at 250 °C and does not recrystallize. For an iron with 0.03% C, polygonization has no time to end and gives way to recrystallization. An addition of a few percent of manganese, phosphorous, and sulfur to steel raises the temperature of recrystallization from 660 °F (350 °C) to 930 °F (500 °C) [*59*].

Rate of Heating. Rapid heating to the recrystallization temperature prevents full recovery prior to recrystallization and hence causes a large driving force for recrystallization to remain. In addition, with rapid heating, higher temperatures are reached before recrystallization has time to begin, which facilitates nucleation of new grains [*59*]. Therefore, the higher the heating rate, the higher the recrystallization temperature [49].

Grain Growth

After recrystallization is complete, the strain free grains will continue to grow if the steel specimen is left at elevated temperatures. Grain growth is referred to as the increase in average grain size of a polycrystalline material. Grain growth generally follows recovery and recrystallization. It occurs by the migration of grain boundaries. Not all grains can enlarge. Therefore, large grains grow at the expense of small grains [*52*]. Extended annealing at a high temperature can cause a few grains to grow to a very large

size, which is known as secondary recrystallization or abnormal grain growth [*57*]. After reviewing the literature on recrystallization, it appears that long holding periods would be required for the full process of recrystallization. Therefore, it is likely that grain growth is a negligible process during the application of heat straightening.

2.4.10 Summary and Conclusions from the Review of Steel Heat Treatments

This section presented and overview of the most accepted heat treatments of steel and the metallurgy of low carbon and high-strength low-alloy steels. The experimental investigations conducted as part of this research project include maximum temperatures of 1200 °F for A36, A588, and A7 steels, as well as 1400 °F and 1600 °F for A36 steel. Therefore, the temperatures ranges considered in this section were as high as 1600 °F. The microconstituents that exist in the microstructure at elevated (exceeding 1340 °F) and ambient temperatures when moderately slow cooling rates are applied was summarized and shown schematically. The possible formation of other microconstituents due to rapid cooling was also discussed. These alternate microconstituents include martensite and bainite, which are harder, stronger, and more brittle than pearlite. The literature revealed that an extremely fast cooling period would be required for the formation of martensite or bainite.

A summary of the relative steel heat treatments currently used to enhance the physical and structural properties was discussed. The review of these heat treatments indicated that process annealing is relatively similar to heat straightening even when applying a maximum temperature of 1200 °F. Process annealing is applied to *recover* the internal strain energy and may be accompanied by recrystallization. The problematic comparison with process annealing is the holding time required to achieve the desired affect. The literature indicated holding times from one to forty-eight hours. However, the literature does not discuss the effects of shorter holding times with the exception of the statement that “annealing temperature decreases with longer holding times”. Normalizing annealing uses higher temperatures followed by moderate cooling in air. The heat treatment is similar to heat straightening when overheated temperatures are used. Again, the problematic comparison between normalizing annealing and heat straightening is the holding time required for the two processes. When heat straightening, temperatures exceeding the eutectoid temperature will only exist for a matter of seconds as apposed to hours, which is generally required for normalizing. Other heat treatments do not appear to correlate to heat straightening.

This section also discussed the influence of grain size on the resulting structural properties. A more fine-grained structure with the same chemical composition as a more coarse-grained structure has higher strength and toughness with a moderate decrease in ductility. The effects of engineering alloys on the structural properties of steel were summarized. The most important engineering alloys for low carbon steels indicated from the literature include carbon, molybdenum, nickel, manganese, silicon, and vanadium. For the particular high-strength low-alloy steel investigated in this research project (A588), chromium is a significant alloy for corrosion resistance.

This section then discussed the structure of plastically deformed steel. The only defect seen in the damaged steel microstructure presented later in Section 5.5 is the formation of slip lines within the grains. Processes were discussed that occur in heated steels that revert the material properties to the pre cold-worked state. These processes included recovery, recrystallization, and grain growth. Relatively low temperatures and holding times are required for recovery. Therefore, it is very likely that this process is occurring upon heat straightening. The resulting microstructures shown in Chapter 5 of this report indicate that recrystallization also occurs when heat straightening. The issue again arises as to whether a heat-straightened member has the required holding time for recrystallization to *complete*. The literature revealed that the temperature required for recrystallization in low carbon and high-strength low alloy steels is approximately 1000 °F and should be held for 1 hour to *complete*. However, recovery and recrystallization begins immediately as the steel is heated. The recrystallization temperature decreases with increasing strain and longer holding periods. The influence of shorter heating periods and the aid of

an external restraining stress could not be fully interpreted from the literature. An important finding from this review is that recrystallization is greatly dependent on the amount of prior deformation. A higher dislocation density increases the amount of area available for nucleation to proceed and decreases the recrystallization temperature. A specimen damaged to a higher strain has more area for nucleation sites to grow and is also subjected to more heating cycles. If elevated temperatures are held for a long enough period, the phenomenon known as grain growth proceeds recrystallization. It appears that the holding time of heat straightening is not long enough for grain growth to occur. It is also very difficult to review the resulting microstructure pictures and detect grain growth.

2.5 REFERENCES

1. Weerth, D. E., "Theoretical and Experimental Analysis of Heat Curved Mild Steel," MS Thesis, University of Washington, 1971.
2. Horton, D. L., "Heat Curved Mild Steel Wide Flange Sections: An Experimental and Theoretical Analysis," MS Thesis, University of Washington, 1973.
3. Roeder, C. W., "Use of Thermal Stress for Seismic Damage Repair," Final Report on NSF Grant CEE-82-05260, University of Washington, Seattle, Oct. 1985.
4. Avent, R. R. and Fadous, G. M., "Heat straightening Techniques for Repair of Damaged Structural Steel in Bridges," Final Report, Louisiana Transportation Research Center, Louisiana State University, Baton Rouge, 1988.
5. Avent, R. R., Robinson, P.F., Madan, A., and Shenoy, S., "Development of Engineering Design Procedures for Heat straightening Repair of Damaged Structural Steel in Bridges," LTRC 251, Louisiana Transportation Research Center, Baton Rouge, LA, 1992.
6. Pattee, H. E., Evans, R. M. and Monroe, R. E., "Effect of Flame and Mechanical Straightening on Material Properties of Weldments," Summary Report on Ship Structure Committee on Project SR-185, Straightening Distorted Weldments, 1970.
7. Nichols, J. I. and Weerth, D. E., *Engineering Journal*, AISC, Oct. 1972, pp. 137-141.
8. Till, R. D., "Effect of Elevated Temperature on Fracture Critical Steel Members," MDOT Research Report No. R-1344, Materials and Technology Division, Michigan Department of Transportation, 1996, pp. 1-17.
9. Shanafelt, G. O. and Horn, W. G., "Guidelines for Evaluation and Repair of Damaged Steel Bridge Members," NCHRP Report No. 271, Transportation Research Board, National Research Council, Washington, DC, June 1984.
10. Avent, R. R., "Design Procedures for Heat straightening Repairs: An Engineering Guide," FHWA/LA-92/252, Louisiana Transportation Research Center, Louisiana State University, Baton Rouge, 1992.
11. Avent, R.R. and Mukai, D.J., "Implementation of Heat straightening Repairs for Louisiana Bridges", State Project Number 736-99-0680, Louisiana Transportation Research Center, Louisiana State University, Baton Rouge, 1998.
12. FHWA, "Heat straightening Repairs of Damaged Steel Bridges – A Technical Guide and Manual of Practice," Report NO. FHWA-IF-99-004, Federal Highway Administration, Washington, D.C, 1998.
13. Roeder, C. W., "Experimental Study of Heat Induced Deformation," *Journal of Structural Engineering*, ASCE, Vol. 112, No. 10, Oct. 1986, pp. 2247-2262.
14. Holt, J. E., *Welding Engineer*, Vol. 40, No. 10, October, pp. 44-46, No. 12, Dec. 1955, pp. 30-31.
15. Ditman, O., "Determination of Thermal Shrinkage in Structural Steel," MS Thesis, University of Washington, 1961.
16. For Chin, W., "Linear Shrinkage of Steel," MS Thesis, University of Washington, 1962.
17. Holt, R. E., *Welding Engineer*, Vol. 50, No. 9, Sept. 1965, pp. 49-53.
18. Holt, J. E., "Contraction a Friend in Need," Typed and Copyrighted, 1938.
19. Holt, R. E., *Welding Engineer*, Vol. 56, No. 6, June 1971, pp. 416-424.

20. Holt, R. E., *Welding Design and Fabrication*, June 1977, pp. 98-102.

21. Brockenbrough, R.L. and Ives, K.D., *Journal of the Structural Division*, ASCE, Vol. 96, No. ST7, Proc. Paper 7400, July 1970, pp. 1305-1331.

22. Brockenbrough, R.L., *Journal of the Structural Division*, ASCE, Vol. 96, No. ST7, Proc. Paper 7410, July 1970, pp. 1421-1444.

23. Boudreaux, R.J., "Heat straightening of Steel: Identifying the Important Parameters and Predicting Member Response," MS Thesis, Louisiana State University, Baton Rouge, 1987.

24. Robinson, P.F. (1991). "Behavioral characteristics of damaged steel repaired by heat straightening," MS thesis, Louisiana State Univ., Baton Rouge, La.

25. deBejar, L. A., Robinson, P.F. and Avent, R.R., *Journal of Structural Engineering*, ASCE, 118(12), 1992, pp. 3394-3409.

26. deBejar, L. A., Robinson, P.F. and Avent, R.R., *Journal of Structural Engineering*, ASCE, 118(12), 1992, pp. 3440-3426.

27. Avent, R. R., Mukai, D.J., Robinson, P.F. and Boudreaux, R.J., *Journal of Structural Engineering*, ASCE, Vol. 126, No. 7, July 2000, pp. 747-754.

28. Blodgett, O.W., *Welding Engineer*, Feb. 1972, pp. 40-46.

29. Avent, R. R., Mukai, D.J. and Robinson, P.F., Journal of Materials in Civil Engineering, ASCE, Vol. 13, No. 1, Jan./Feb. 2001, pp. 18-25.

30. Rothman, R. L., "Flame Straightening Quenched and Tempered Steels in Ship Construction," Ship Structures Committee, Report No. 235, 1973.

31. Avent, R. R., Mukai, D.J. and Robinson, P.F., *Journal of Materials in Civil Engineering*, ASCE, Vol. 12, No. 3, Aug. 2000, pp. 188-195.

32. Putherickal, J., "Effects of Heat Straightening Structural Steel", Final Report for MLR-91-3, Iowa Dept. of Transportation, Ames, Iowa, 1992.

33. ASTM, "Standard Test Methods and Definitions for Mechanical Testing of Steel Products," A370-97a, West Conshohocken, PA, 1999.

34. Harrison, H. L., *Welding Journal*, Vol. 31, No. 5, May 1952, Research Supplement, pp. 257s-262s.

35. Pattee, H. E., Evans, R. M. and Monroe, R. E., "Flame Straightening and its Effect on Base Metal Properties," Summary Report to Ship Structure Committee concerning the first phase of Project SR-185, Straightening Distorted Weldments, Battelle Memorial Institute, Columbus, Ohio, Aug. 1969.

36. Barsom J. M. and Rolfe, S. T., *Fracture & Fatigue Control in Structures-Applications of Fracture Mechanics*, 2nd Edition, Prentice-Hall, Englewood Cliffs, New Jersey, 1987.

37. American Railway Engineering Association, "Flame Shortening Eyebars to Equalize the Stress," Bulletin No. 460, 1946.

38. Moberg, K. L., "Damage Assessment and Contraction Straightening of Steel Structures," MS Thesis, University of Washington, 1979.

39. Avent, R. R. and Boudreaux, R. J., "Heat straightening Effects on the Behavior of Plates and Rolled Shapes," Second Interim Report of Phase I, Louisiana Transportation Research Center, Louisiana State University, Baton Rouge, 1987.

40. Avent, R. R. and Brakke, B.L., *Transportation Research Record*, No. 1561, TRB, National Research Council, Washington, D.C., 1996, pp. 26-36.

41. Avent, R. R., *Proceedings, National Steel Construction Conference*, AISC, Las Vegas, Nev., June 1992, pp. 21-23.

42. Avent, R. R. and Mukai, D.J., *Journal of Bridge Engineering*, Mar. /Apr. 2001, pp. 95-102.

43. Avent, R. R. and Fadous, G. M., "Heat straightening Effects on the Behavior of Full-Scale Simulated Bridge Girders," First Interim Report of Phase 2, Louisiana Transportation Research Center, Louisiana State University, Baton Rouge, 1987.

44. Fadous, G. M., "Heat straightening Effects on the Behavior of a Full-Scale Simulated Bridge Girder," MS Thesis, Louisiana State University, Baton Rouge, 1987.

45. Avent, R. R. and Fadous, G. M., *Journal of Structural Engineering*, ASCE, Vol. 115, No. 7, July 1989.

46. Avent, R. R., Fadous, G.M., and Boudreaux, R. J., *Transportation Research Board*, No. 1319 TRB, National Research Council, Washington, DC., 1991, pp. 86-93.

47. Avent, R. R., and Mukai D.J., "Heat Straightening Repairs of Damaged Steel for Bridges", FHWA Report, U.S. Dept. of Transportation, Federal Highway Administration, Washington, D.C, 1998.

48. Avent, R. R. and Mukai, D.J., *Engineering Journal*, First Quarter, 38(1), 2001, pp. 27-49.

49. Totten, G.E. and Howes, M.A., *Steel Heat Treatment Handbook*, Marcel Dekker, Inc., New York, New York, 1997.

50. Smith, W.F., *Structure and Properties of Engineering Alloys*, Second Edition, McGraw-Hill Inc., New York, New York, 1993.

51. Smith, W.F., Foundations of Material Science and Engineering, Third Edition, McGraw-Hill Inc., New York, New York, 2004.

52. Callister, W.D., *Material Science and Engineering, an Introduction*, Fourth Edition, John Wiley & Sons Inc., New York, New York, 1997.

53. United States Steel Company, *Atlas of Isothermal Transformation Diagrams*, United States Steel, Pittsburg, Pennsylvania, 1943.

54. American Society of Metals, *Atlas of Isothermal Transformation and Continuous Cooling Diagrams*, American Society for Metals, Metals Park, Ohio, 1977.

55. Krauss, G., *Principals of Heat Treatment of Steel*, American Society for Metals, Metals Park, Ohio, 1980.

56. Key to Metals Task Force & INI International, *Low and High Temperature Thermomechanical Treatments*, <http://www.key-to-steel.com/Articles/Art108.htm>, (October 3, 2004).

57. American Society for Metals, *Metals Handbook*, American Society of Metals, Volume 8, Metals Park, Ohio, pp 211-218.

58. Byrne, J.G., *Recovery, Recrystallization, and Grain Growth*, The Macmillan Company, New York, New York, 1965.

59. Gorelik, S.S., *Recrystallization in Metals and Alloys*, Translated from Russian by Afanasyev, V., Mir Publishers, Moscow, 1981.

Table 2.1
Steel types and respective average percent change in yield stress after heat straightening [*12*]

Steel Type	Percent Yield Change
Carbon Steel	10%
High-Strength, Low Alloy Steel	2%
Heat-Treated, High Strength Carbon Steel	7%
Quenched and Tempered Steel	-6%

Table 2.2
Steel types and respective percent reduction in ductility after heat straightening [*12*]

Steel Type	Percent Ductility Reduction
Carbon Steel	8%
High Strength, Low-Alloy Steel	18%
Quenched & Tempered Steel	14%
Quenched & Tempered Constructional-Alloy Steels	11%

Table 2.3
Comparisons of various DOTs heat-straightening provisions

Parameter	Iowa	Kansas	Michigan	New Hampshire	Massachusetts
Maximum Temperature (F)	1200	1103	1200	1150	1200
Cooling Temperature prior to subsequent heating cycle (F)	Not Provided	248	250	Not Provided	Not Provided
Maximum Torch Diameter (in)	1	Not Provided	1	1	1
Maximum Vee Angle (deg)	Not Provided	Not Provided	20	20	20-45
Base Width (in)	Not Provided	6.35	6	10	10

Table 2.4
Chemical compositions of A36 and A588 steel

Designation %	A36 (Large)	A588 (Small)	A588 (Large)
C	0.150	0.160	0.150
Si	0.240	0.420	0.330
Mn	0.660	0.980	1.140
Mo	0.021	0.043	0.020
Cu	0.240	0.290	0.280
Cr	0.120	0.550	0.530
V		0.043	0.035
Ni	0.080	0.140	0.200
Nb		0.002	0.001
B			0.006
S	0.013	0.013	0.010
Al		0.006	0.030
Ti		0.002	0.009
N		0.010	0.009
Ca			0.001
P	0.010	0.012	0.009
Sn	0.012	0.019	0.014
Ac1 °*C* (Eqn. 2.1)	724	732	726
Ac1 °*F* (Eqn. 2.1)	1334	1349	1339
Ac3 °*C* (Eqn. 2.2)	833	842	838
Ac3 °*F* (Eqn. 2.2)	1531	1548	1541
Ac1 °*C* (Eqn. 2.3)	734	738	736
Ac1 °*F* (Eqn. 2.3)	1352	1360	1357

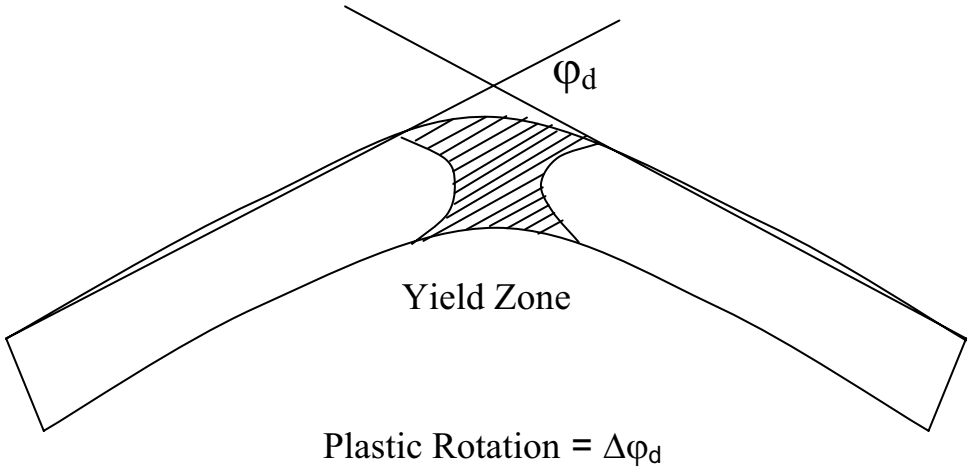

Figure 2.1
Illustration of the measurement of plastic rotation

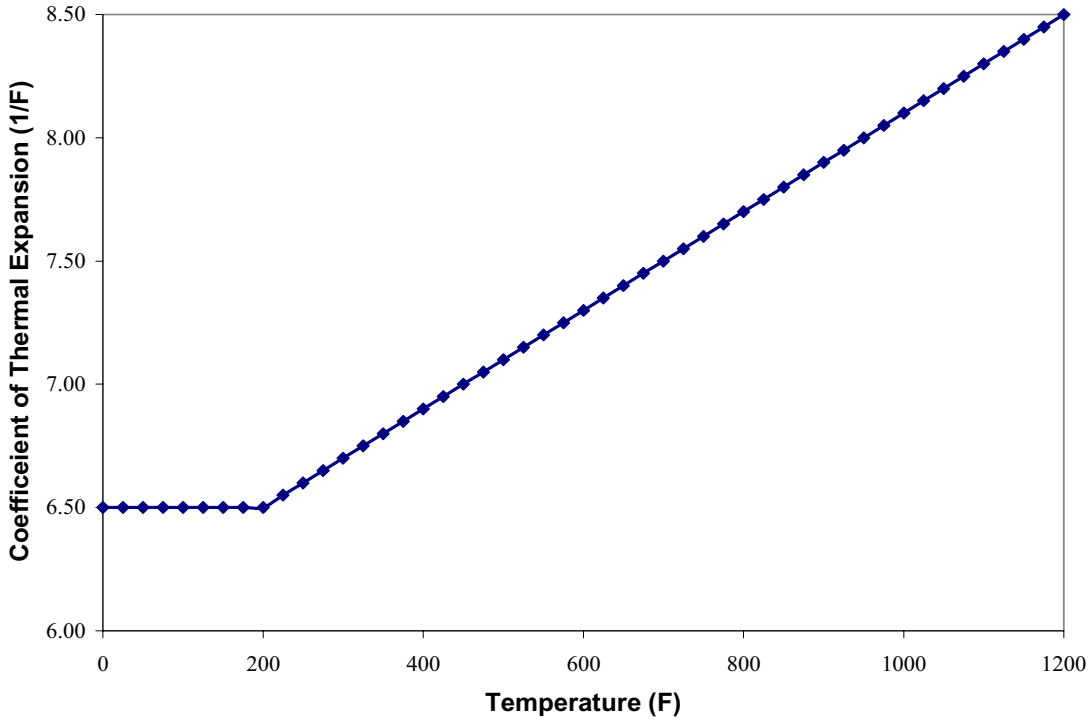

Figure 2.2
Variation of the coefficient of thermal expansion versus temperature [*3*]

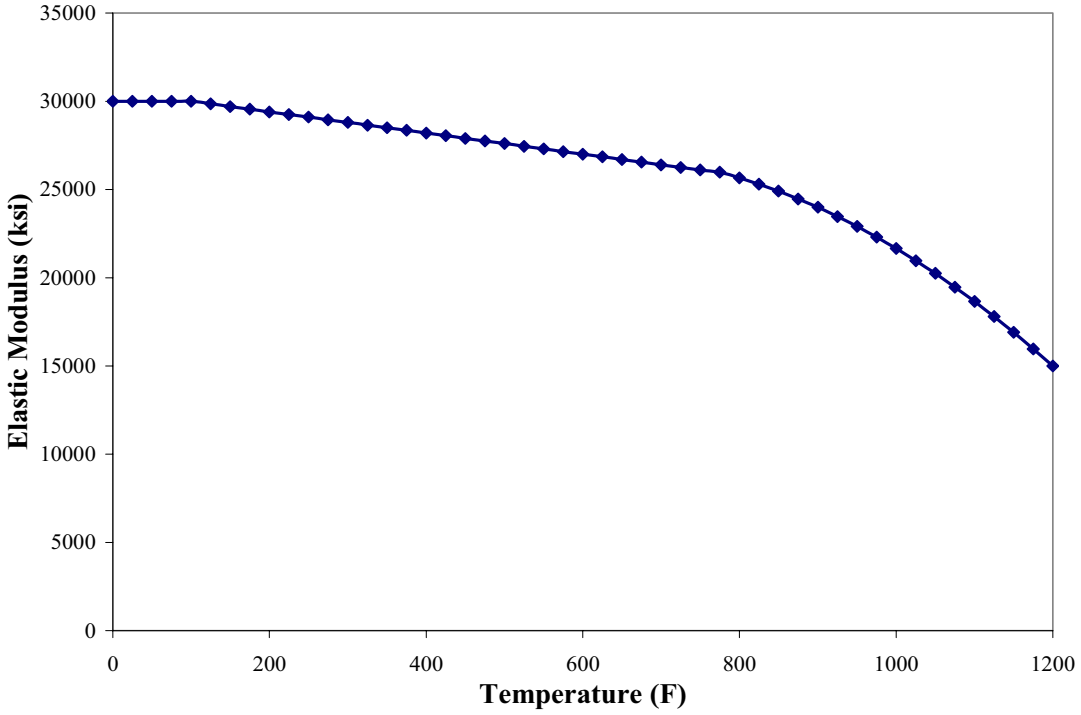

Figure 2.3
Variation of the modulus of elasticity vs. temperature [*3*]

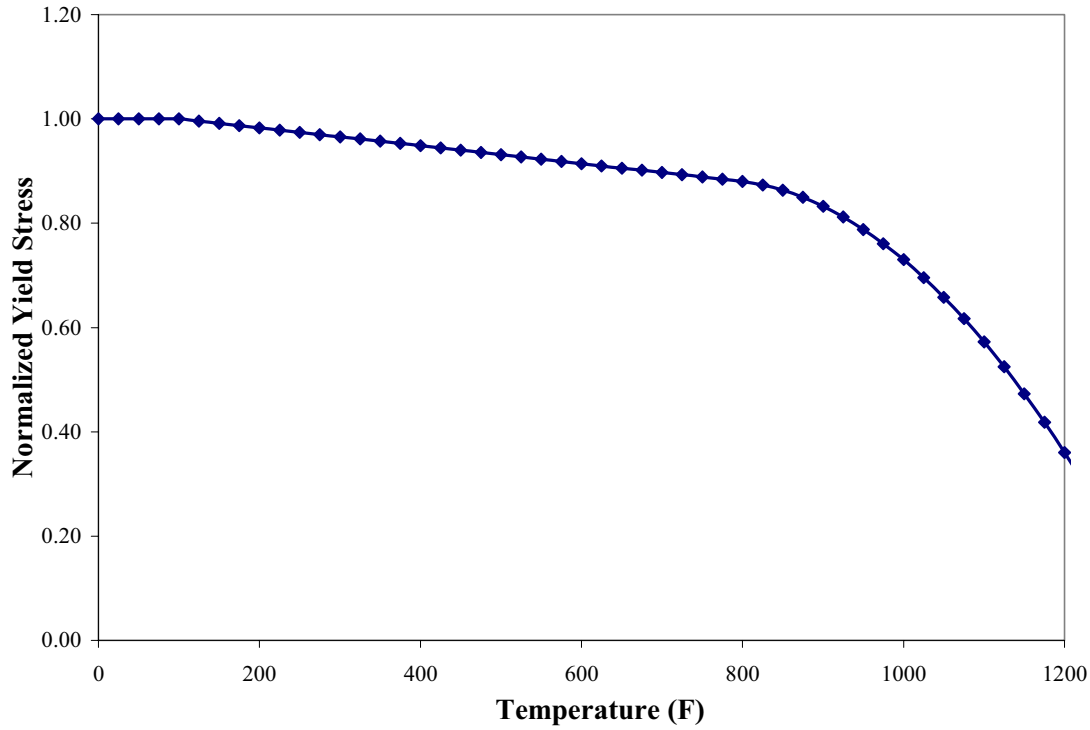

Figure 2.4
Variation of the normalized yield stress vs. temperature [*3*]

1) Does your DOT have special provisions and guidelines for heat straightening? ___ *Yes (Please provide)* ___ *No*
2) What is the basis for these heat straightening provisions? ___ *DOT Research* ___ *FHWA Research* ___ *Other (Please provide info)*
3) Are these provisions available from the Internet? ___ *Yes (Please provide link_____)* ___ *No*
4) Does your DOT have special provisions for *multiple* heat straightening of the same beam? ___ *Yes (Please provide)* ___*No*
5) Which parameter governs the maximum number of *multiple* heat straightening repairs of the same beam? ___ *No. of repairs* ___ *Structure type* ___ *Damage magnitude* ___ *Combination of above parameters*
6) How many times does your DOT allow *multiple* heat straightening of the same beam? ___ *One* ___ *Two* ___ *Three* ___ *Four* ___*Other (Please provide number)*
7) Would you be interested in the results of our research project? ___ *Yes* ___ *No*

Figure 2.5
Survey form distributed to various state departments of transportation (DOTs)

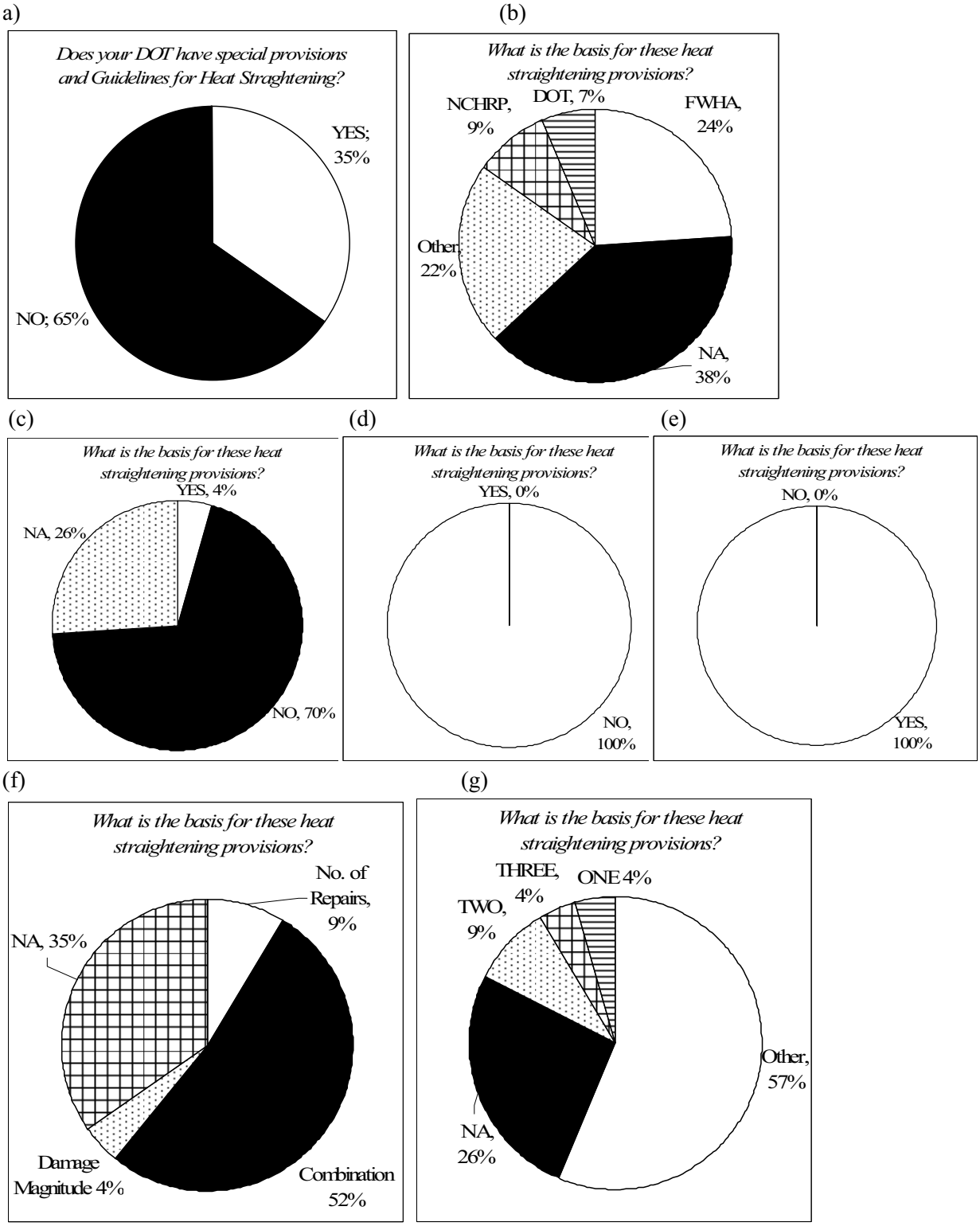

Figure 2.6
Results from survey of state DOTs

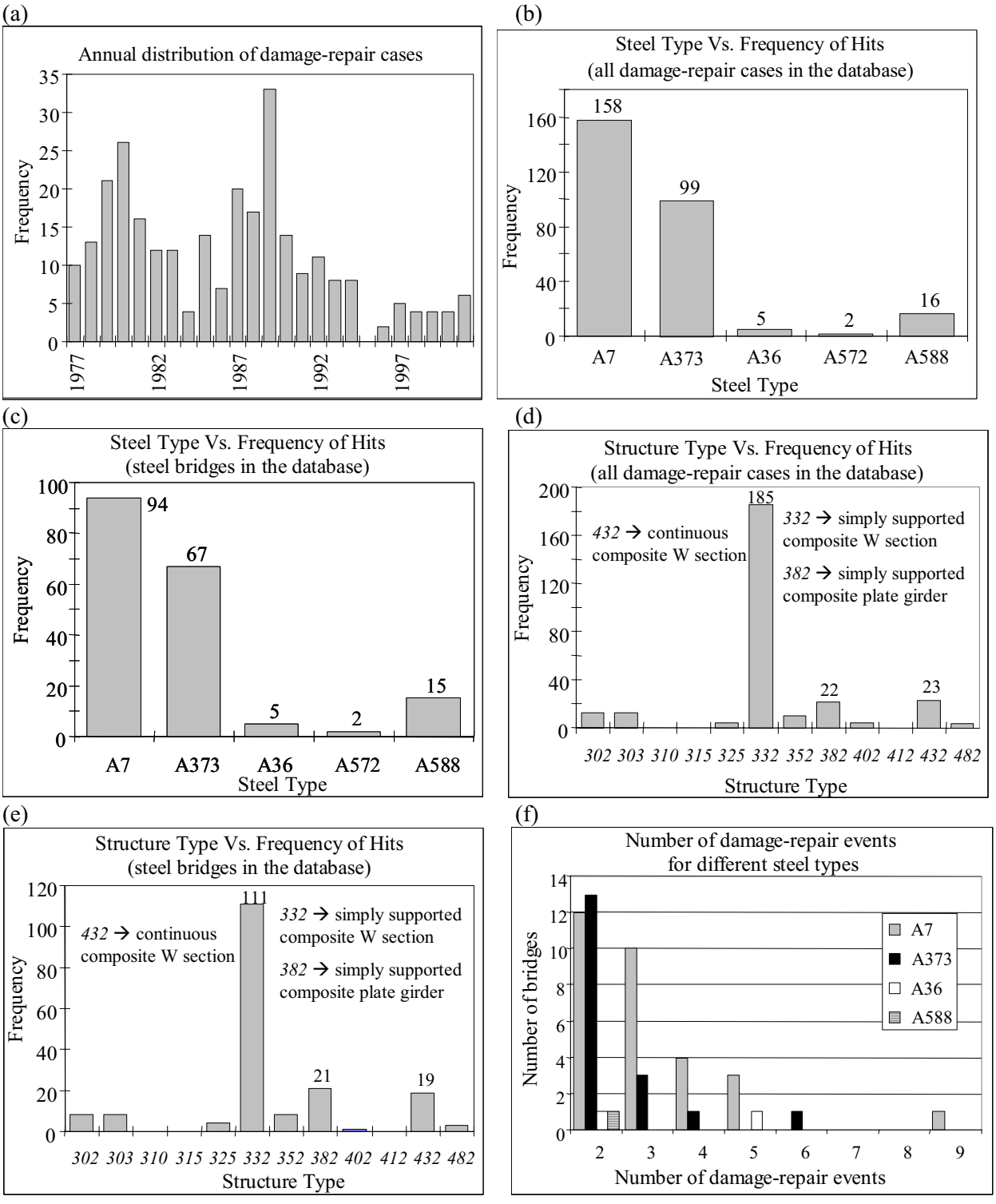

Figure 2.7
Results from 1976-2001 Michigan high-load hits database analysis

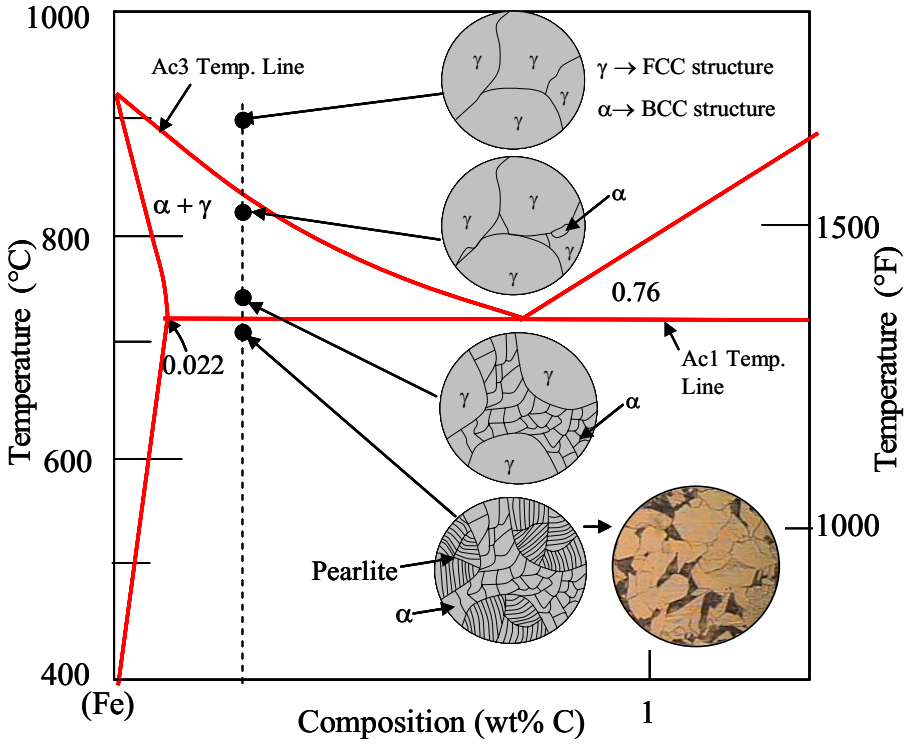

Figure 2.8
Transformation of hypoeutectoid plain-carbon steel with slow cooling [*51*]

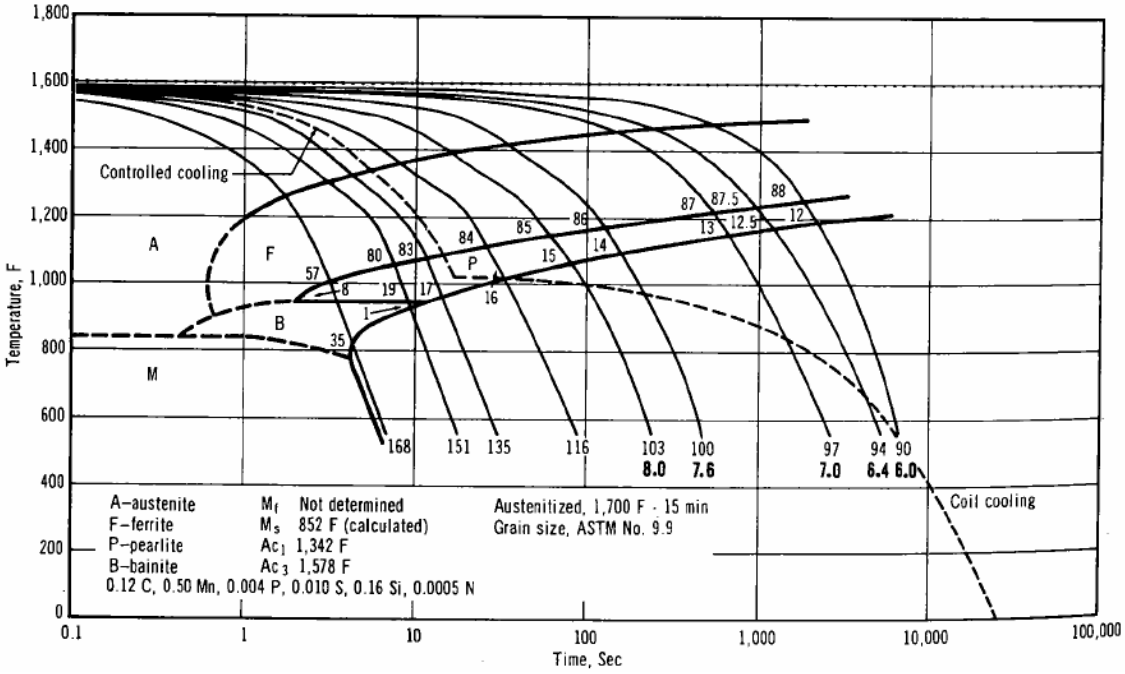

Figure 2.9
Continuous cooling diagram of a AISI (0.12%C) steel [*54*]

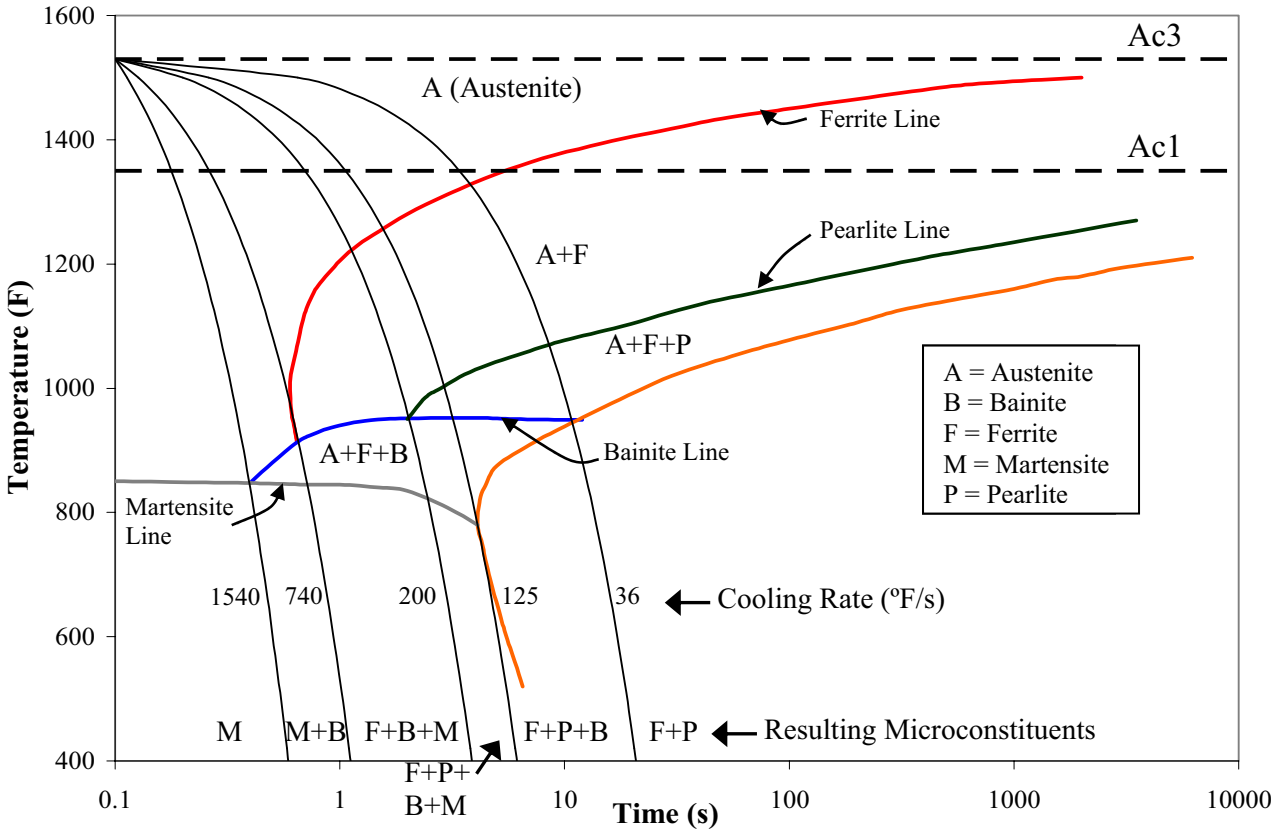

Figure 2.10
Superimposed continuous cooling diagram of a AISI (0.12%C) steel

(a) Less Pearlite (25%)

(b) More Pearlite (35%)

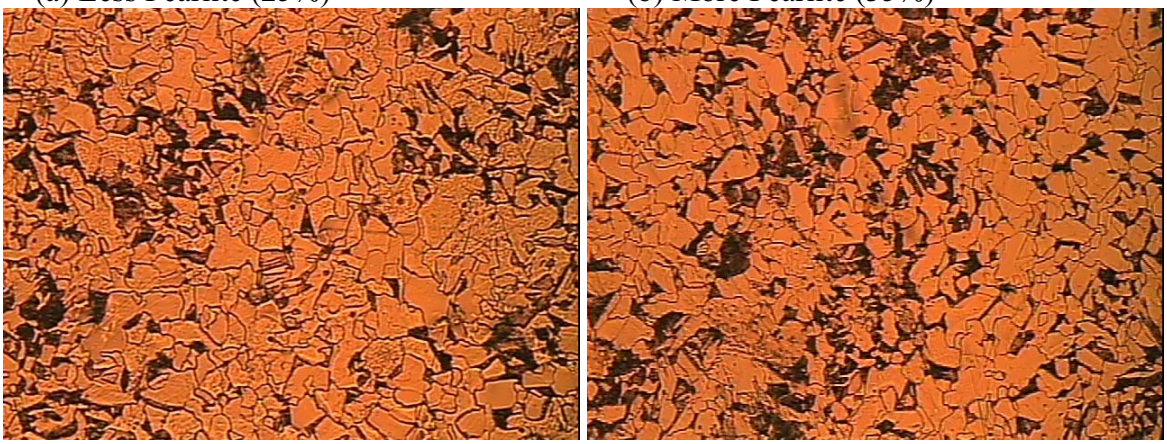

Figure 2.11
Variation in the percent pearlite in the same steel specimen

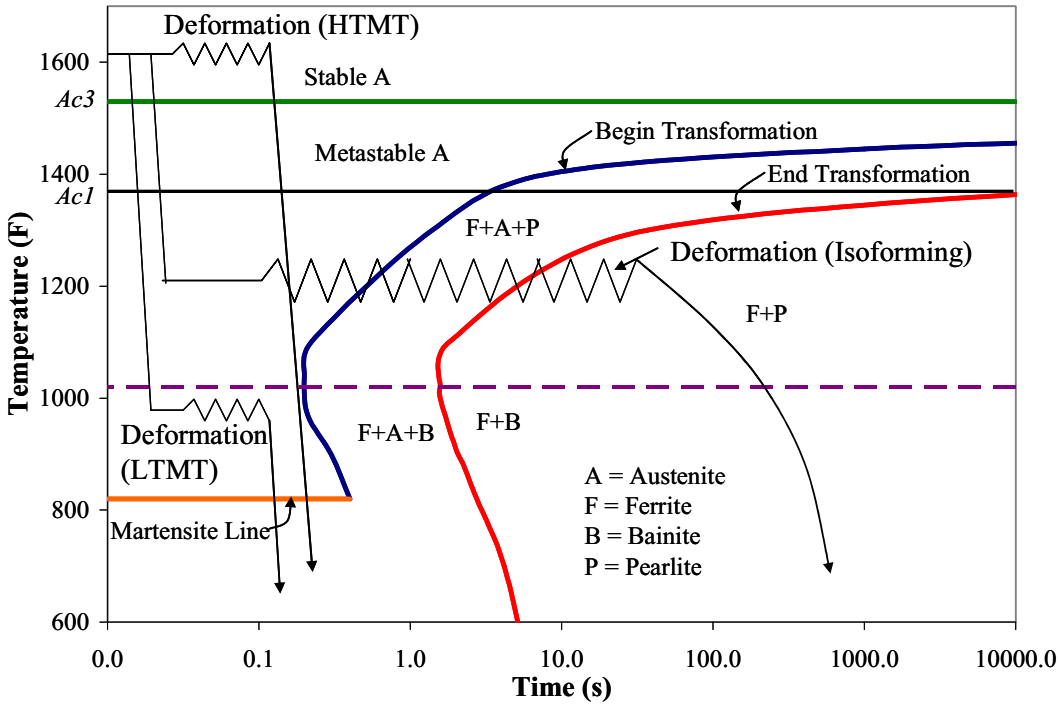

Figure 2.12
Thermomechanical treatments on an isothermal transformation diagram [*56*]

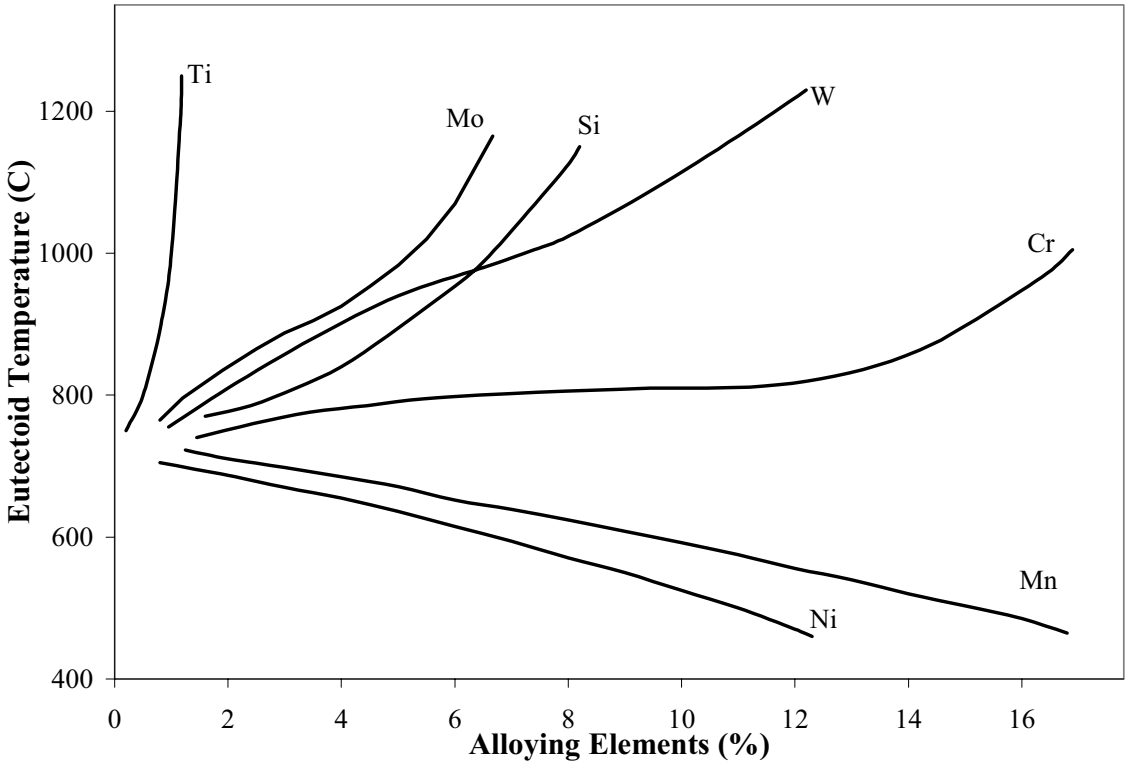

Figure 2.13
Effect of alloying elements on the eutectoid transformation temperature *Ac1* [*49*]

a) Planer slip lines (Co-8Fe alloy)

b) Wavy slip lines (Single Crystal of Al)

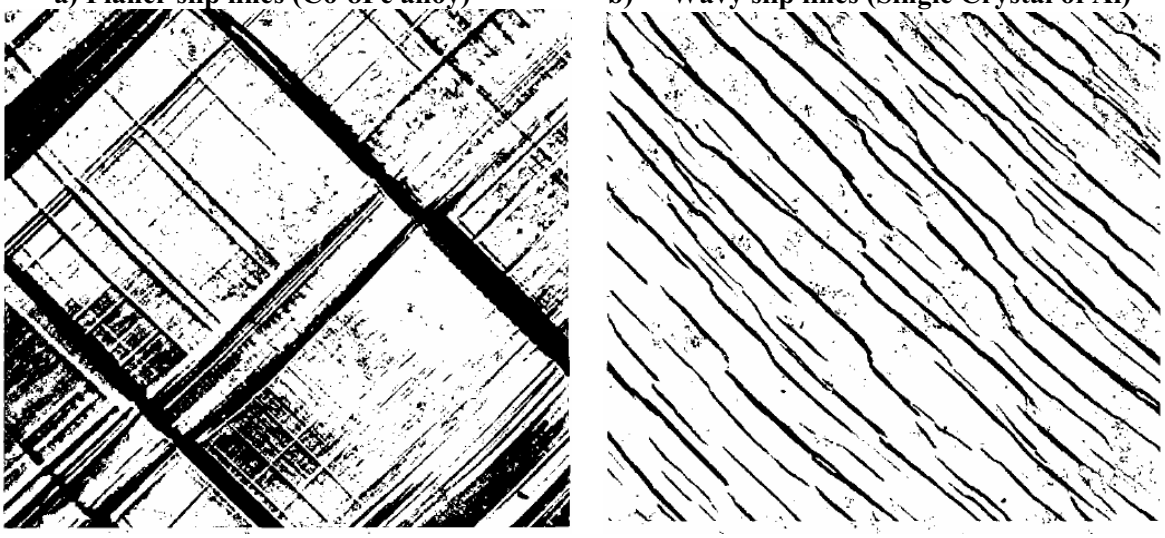

Figure 2.14
Comparison of (a) planer slip lines and (b) wavy slip lines at 250X [*57*]

(a) Undamaged Steel

(b) Damaged to 60 ε_y

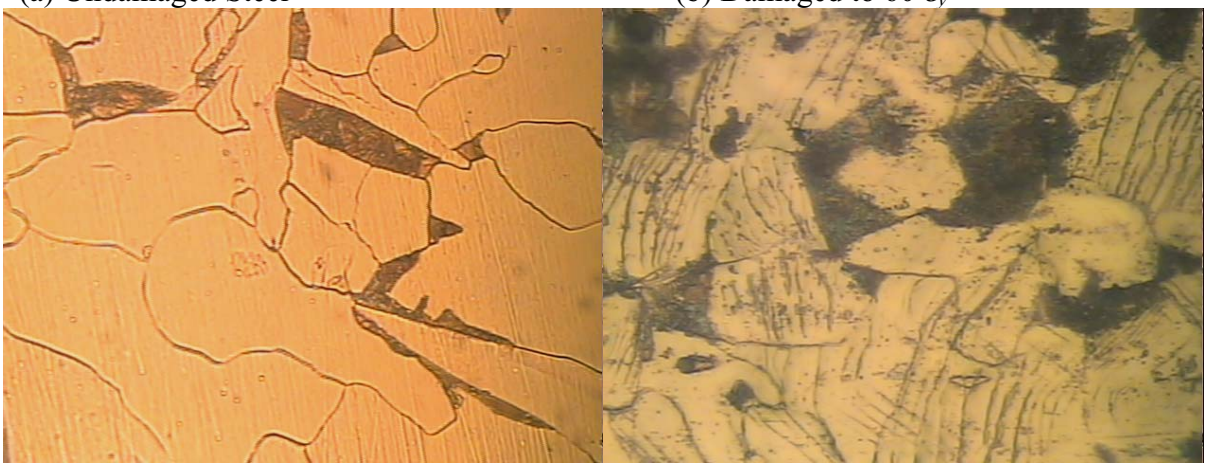

Figure 2.15
Slip lines in plastically deformed A36 steel (1200X)

3 REVIEW OF MDOT HEAT STRAIGTHENING PROCEUDRES

3.1 FIELD VISITS TO HEAT STRAIGHTENING REPAIR SITES

The MSU research team visited three heat-straightening bridge repair sites in Michigan to review the MDOT heat-straightening procedure. The first site was located at the Lake Lansing Road bridge crossing over US - 127 South (S01- 33172: US- 127 SB) which was visited on October 23, 2002. The second and third sites were located along Interstate I-94 at the overpasses of Lansing Road (S07- 38101: I-94 WB) and Elm Road (S09- 38101: I-94 WB), respectively. These sites were visited during the week of October 10-16, 2003. All three beams were damaged by collision with over-height trucks. The MDOT Statewide Bridge Crew (SBC) repaired the damaged steel beam bridges by heat-straightening. The research team from MSU visited the repair sites and spent some time with the SBC to understand the heat straightening repairs being conducted. Additionally, the MSU research team took two 0.5 in. diameter cores from the web of each beam; one core was removed from the damaged and heated portion of the web and the second core was removed from the undamaged and unheated portion of the web. These 0.5 in. diameter steel cores were used to investigate the effects of heat straightening on the microstructure and the hardness of steel. Any other material specimens could not be obtained because the repaired bridges remained in service.

Section 3.1.1 describes the damage (Section 3.1.1.1) and the repair (Section 3.1.1.2) of the Lake Lansing Road Bridge and the locations of the steel cores in the web (Section 3.1.1.3). This was a preliminary field visit for the MSU research team to become familiar with the SBC members, techniques, and equipment used.

Section 3.1.2 describes the damage (Section 3.1.2.1) and the repair (Section 3.1.2.2) of the Lansing Road Bridge and the locations from where the two steel cores were taken (Section 3.1.2.3). The MSU research team spent a significant amount of time with the SBC at this site and several significant observations are reported in Section 3.1.2.

Section 3.1.3 describes the damage (Section 3.1.3.1) and the repair (Section 3.1.3.2) of the Elm Road Bridge and the locations from where the two steel cores were taken (Section 3.1.3.3). The damage and repair procedure of the Elm Road Bridge was very similar to the repair of the Lansing Road Bridge. Therefore, similar observations are reported in Section 3.1.3.

The results of the metallographic inspection and hardness tests on the 0.5 in. diameter steel cores for all three bridges are shown in Section 3.1.4 and 3.1.5, respectively.

3.1.1 Lake Lansing Road Bridge Site (S01- 33172)

The MSU research team visited a heat straightening project along US-127 at the overpass of Lake Lansing Rd. in East Lansing, Michigan. The Statewide Bridge Crew (SBC) was there to repair the damage induced on the south fascia beam above the southbound lanes. The steel beam was a 54 in. deep plate girder with a composite concrete deck-slab.

3.1.1.1 Description of Damage

MDOT engineers provided the following description of the damage to the Lake Lansing road bridge crossing over US - 127 South (S01- 33172: US- 127 SB): “The subject bridge was damaged by a high load and up close inspection of the beam shows that the bottom flange is cracked. The crack is transverse to the beam's length and ex tends 6 in. from flange edge width propagating to the web. The crack is located at the point of impact, approximately 57 ft. from the beam's end at the west abutment. At the

location of several of the intermediate stiffeners, stiffeners 12-W to 20-W from the beam end at the west abutment, the web has "smiley face" hair-line cracks and torn at about 1 in. from the bottom flange. The beam was struck by an over-height truck causing about 4 in. out-of-plane deformation of the bottom flange as shown in Figure 3.1.

3.1.1.2 Description of Repair

The MDOT engineers provided the following description of the repair for the damaged beam: "The flange crack was drilled at the end to prevent propagation and then cut out in a Vee shape. The Vee cut out of the bottom flange was then filled with weld and ground smooth. The other 'smiley face' cracks at the stiffeners on the web were drilled at the end also. The beam was heat straightened and an angle 'L' plate was bolted to connect the top of the bottom flange to the web.

3.1.1.3 Locations of Steel Cores

Two 0.5 in. diameter steel cores were taken from the web of the repaired steel beam. One core was taken from the damaged and heated region of the web, and the second core was taken from the undamaged portion of the web. One-inch diameter holes were drilled in the web to obtain the 0.5 in. diameter steel cores. As per MDOT requirements, both cores were taken from the web as close to the neutral axis (NA) as possible and the one-inch holes were sealed with fully-tensioned 7/8 in. diameter galvanized bolts.

The steel beam was a 54 in. deep plate girder with a 7 in. composite concrete deck-slab. The neutral axis (NA) of the composite section was estimated to be about 44.4 in. from the bottom of the bottom flange. Therefore, the core from the undamaged region of the web was taken at a distance of 44.3 in. from the bottom of the bottom flange and 22.8 in. east of stiffener number 13 from the west abutment. In the region of damage, the statewide bridge crew had applied heating to the beam web about 6-7 in. below the top flange because it was about 2 in. out-of-alignment. Therefore, the core from the heated region of the web was taken at a distance of 46.0 in. from the bottom of the bottom flange and 24.25 in. east of stiffener number 12 from west abutment. The longitudinal spacing between the two cores was approximately equal to 60 in. Metallographic inspections and Rockwell Hardness tests on these steel cores are summarized in Sections 3.1.4 and 3.1.5, respectively.

3.1.2 Lansing Road Overpass (S07-38101)

The MSU research team visited a heat straightening project along Interstate I-94 at the overpass of Lansing Rd. in Jackson, Michigan. The Statewide Bridge Crew (SBC) was there to repair the damage induced on the west fascia beam above the westbound lanes. The steel beam is a W30x99 composite sections with a 7 in. concrete deck and a 0.5 in. cover plate. The steel girder was grade A373.

3.1.2.1 Description of Damage

The composite beam was hit by an over-height truck causing out-of-plane deformation of the bottom flange, which extended approximately 25 ft. of the beam. The maximum out-of-plane displacement was approximately 8 in. The impact location was approximately 17 ft. south of the north pier over the right lane. The beam-to-diaphragm connections close to the damage location were also damaged. Three bolts had fractured in the beam-to-diaphragm connection north of the damage location and closer to the pin-hanger detail. Four bolts fractured in the beam-to-diaphragm connection south of the damage location. Figure 3.2 shows a photograph of the damaged beam. Maximum out-of-plane deformation of the bottom flange occurred at the end of the cover plate, which is seen more clearly in Figure 3.3 (close-up photograph of damaged region).

3.1.2.2 Description of Repair

The SBC used a 30-ton (60 kips) jack corresponding to a hydraulic pressure of 10,000 psi to apply the restraining forces. Figure 3.4 shows the equipment and setup for applying the pulling restraining force. Considering the flange deformations shown in Figure 3.3, the restraining force was applied to pull the bottom flange towards the interior beam represented by P_R.

In the first heating cycle, the crew applied a strip heat to the web, which extended from the point of damage to the pin-hanger detail. The strip heat was applied in a 5 in. band slightly below (1-2 in.) the concrete deck slab. While heating the web, the pressure in the jack was approximately equal to 1000 psi, which corresponds to a restraining force of 6 kips. The pressure in the jack decreased gradually as the web was heated. However, the crew maintained the pressure around 1000-1200 psi (6-7.5 kips). According to the SBC, this strip heating of the web makes the steel at the slab-to-beam connection softer. This reduces the forces induced at the shear connection when the flange Vee heats are applied. The strip heat also rotates the web plate about its weak axis. Figure 3.5 shows a photograph of a crew member applying the web strip heat.

The SBC increased the jack hydraulic pressure to 2500 psi, corresponding to a restraining force of 15 kips, and applied a partial (half) depth Vee heat to the bottom flange with cover plate as shown in Figure 3.6. The width of the Vee heat at the open end of the Vee was approximately equal to 5 in., which is the width the SBC uses on all Vee heat applications of this damage type. The Vee angle was computed to be approximately 55^o. The Vee heat temperatures were monitored by the MSU research team using a handheld infrared-temperature indicating instrument. The Vee heat temperatures were close to 1200 °F, but sometimes increased to about 1350 °F. Figure 3.7 shows a photograph of a Vee heat being applied to the bottom flange with cover plate using two torches simultaneously. The SBC allowed the steel to cool to 250 °F before relieving the heated steel by heating the portion of the flange at the opposite end of the partial depth Vee heat.

The second heating cycle was applied in the same fashion as that of the first heating cycle. Heating temperatures remained close to about 1200 °F. Figure 3.8 shows a photograph of the beam after two heat straightening repair cycles.

Before conducting the third heating cycle, the SBC inserted three structural bolts at the web-to-diaphragm connection close to the pin-hanger detail, forcing them in using a hammer. The web strip heat was applied closer to the flange-web junction, while maintaining a pressure of 1000 psi (6 kips) in the jack. The heating temperatures were monitored and found to be close to 1000 °F. At this stage, the SBC began heating the diaphragm-to-web connection plate (angle section). The researchers believe the connection plate was heated to temperatures exceeding 1400 °F.

During the fourth heating cycle, a strip heat was applied to the web directly underneath the concrete slab with a slightly higher pressure close to 1500 psi corresponding to 9 kips. The pressure was then increased to 2500 psi (corresponding to 15 kips) and a partial (half) depth Vee heat was applied to the bottom flange. The heating temperatures were close to 1350 °F.

The bridge repair was continued the following day starting with the fifth heating repair cycle. During the fifth repair cycle, the SBC extended the web strip heat from the web diaphragm north of the damage location to the pin-hanger detail south of the damage location. The hydraulic pressure was maintained at 1000 psi (6 kips). The width of the strip heat was more than used for the previous four heating cycles. The SBC also heated the diaphragm connection plate. The web strip heat temperatures were below 1200 °F. However, the connection plate was so severely overheated that it became red hot.

Three Vee-heats were applied to the bottom flange with cover plate. The hydraulic pressure in the jack was close to 2500 psi, corresponding to a restraining force of 15 kips. One Vee-heat was applied to the bottom flange at the end of the cover plate. The bottom flange without the cover plate was overheated

quickly, due to a sudden reduced thickness. The actual temperature of the steel could not be measured accurately but the color of the heated steel appeared to indicate a temperature of about 1350 °F. The SBC continued to let the steel cool to 250 °F before relieving the steel by heating the flange at the opposite end of the partial depth Vee heat.

For the six and final full heating cycle, the restraining force location was moved much closer to the pin-hanger detail. The web strip heat extended from the diaphragm north of the damage location to the pin-hanger detail only. Two Vee heats were applied to the bottom flange. The crew applied a strip heat in between the diaphragm connection and the pin-hanger detail starting close to the concrete slab and moving down in a serpentine motion towards the bottom flange. The SBC attempted to hammer the diaphragm connection together while the beam was still warm. Figure 3.9 shows a photograph of the strip heat being applied close to the pin- hanger detail. Figure 3.10 shows the condition of the pin-hanger detail after the sixth heating cycle.

After cooling, it was found that the sixth heating cycle produced significant movement and the beam was almost straight. A further heating cycle was conducted to make small improvements but its impact was quite insignificant. A photograph of the repaired beam is shown in Figure 3.11.

3.1.2.3 Locations of Steel cores

Two 0.5 in. diameter cores were taken from the web of the repaired beam. One core was taken from the damage and heat straightened region of the web, and the second core was taken from the unheated portion of the web. One-inch diameter holes were drilled in the web to obtain the 0.5 in. diameter steel cores. As per MDOT requirements, both cores were taken from the web as close to the neutral axis (NA) as possible and the one-inch holes were filled with fully-tensioned 7/8 in. diameter galvanized bolts as shown in Figure 3.12. Both cores were removed approximately 27.4 in. from the bottom of the cover plate, which corresponds to the location of the neutral axis for the composite section.

3.1.3 Elm Road Overpass (S09-38101)

The MSU research team visited a heat straightening project along Interstate I-94 at the overpass of Elm Road in Jackson, Michigan. The Statewide Bridge Crew (SBC) was there to repair the damage induced on the west fascia beam above the westbound lanes. The steel beam is a W36x170 composite section with a 7 in. concrete deck. The steel was grade A7. The damage and repair procedure induced to the Elm Road bridge girder was very similar to that of the Lansing Road bridge girder.

3.1.3.1 Description of Damage

The composite beam was hit by an over-height truck causing out-of-plane deformation of the bottom flange, which extended approximately 20 ft. of the beam. The maximum out-of-plane displacement was approximately 3 in. The impact location was approximately 20 ft. south of the north pier over the right lane. The impact also fractured the diaphragm-to-beam connection. Figure 3.13 shows the out-of-plane movement of the bottom flange and Figure 3.14 shows the fractured diaphragm-to-beam connection.

3.1.3.2 Description of Repair

Two heating cycles were conducted in the presence of the MSU research team. These two heating cycles produced most of the deformations (approximately 80%) required to repair the beam. The methods used to repair this beam were very similar to those used to repair the Lansing Road Bridge. The restraining forces were applied using the same 30-ton as which was shown in Figure 3.4.

During the first heating cycles, a 5 in. strip heat was applied just underneath the top flange while maintaining a pressure of 1000 psi corresponding to a restraining force of 6 kips. The temperature of the

steel in the web strip heat region was approximately 900 °F. The strip heat extended about 7 ft. to the south of the fractured diaphragm and about 2 ft. to the north of the diaphragm. The pressure in the hydraulic jack was raised to 2500 psi, corresponding to 15 kips, and three partial depth (half) Vee-heats were applied to the bottom flange. The temperature of the steel appeared to remain under 1200 °F. The width of the Vee heat at the open end of the Vee was equal to 5 in. The Vee angle was thus approximately equal to 50^{o}. The crew let the Vee heated steel cool to 250 °F before relieving the steel by heating the flange at the opposite end of the partial depth Vee heats.

The second heating cycle was similar to the first heating cycle with the exception that four partial depth Vee heats were applied to the bottom flange. Temperatures appeared to remain below 1200 °F. The location and separation of the four Vee-heats is shown in Figure 3.15. The portion of the flange heated to relieve the steel is also indicated in Figure 3.15. To repair the diaphragm-to-beam bolted connection, the SBC temporarily supported the connection by welding. The SBC was about to drill new bolt holes in the connection plate, when the repair was halted due to contractor activities in the lane below the damage location.

3.1.3.3 Locations of Steel cores

Two 0.5 in. diameter cores were taken from the web of the repaired beam. These cores were taken with only 80% of the damage repaired. One core was taken from the damage and heat straightened region of the web, and the second core was taken from the unheated portion of the web. One-inch diameter holes were drilled in the web to obtain the 0.5 in. diameter steel cores. As per MDOT requirements, both cores were taken from the web as close to the neutral axis (NA) as possible and the one-inch holes were filled with fully-tensioned 7/8 in. diameter galvanized bolts. Both cores were removed approximately 24.5 in. from the bottom of the bottom flange, which corresponds to the location of the neutral axis of the composite section.

3.1.4 Metallographic inspections

The surfaces of the steel cores were mirror-polished and etched with a 2% nitol solution composed of 2 - 2.5 mL nitric acid (HNO_3) and 100 mL ethanol to prepare them for metallographic inspection. The procedures used for preparing the surfaces for metallographic inspections are provided later in Section 4.9.4. Figure 3.16 shows the microstructure of the unheated (a) and heated (b) cores from the Lake Lansing Road Bridge at a magnification of 480X. Figure 3.17 shows the microstructure of the unheated (a) and heated (b) cores from the Lansing Road Bridge at a magnification of 480X. Figure 3.18 shows the microstructure of the unheated (a) and heated (b) cores from the Elm Road Bridge at a magnification of 240X. Figures 3.16 to 3.18 demonstrate typical microstructures for low carbon ferrite-pearlite steel. The white grains are ferrite and the black-grey portions between the grains are pearlite. Ferrite is much softer than pearlite, which is brittle and hard.

A comparison of Figure 3.16, (a) and (b), indicates slight (almost insignificant) ferrite grain-growth and reduction of pearlite (black grey portions) in the steel core from the heated region. A comparison of Figure 3.17 (a) and (b) indicates that the microstructures of the heated and unheated portions of the Lansing Road Bridge appear very similar. A comparison of Figure 3.18 (a) and (b) indicates that microstructure of the heated and unheated portions of the Elm Rd. Bridge appear to be slightly different. In all cases, heating does not seem to have a significant influence on the microstructure (grain size) of the steel, which is relevant for some structural properties like fracture toughness and hardness.

The grain size of each steel core sample was determined using the general line intercept procedure outlined in ASTM E112. The general line intercept procedure is also described in detail later in Section 4.9.4. In addition, each pearlite and ferrite grain was distinguished separately and the percentage of pearlite grains within each steel core was determined. The results of the microstructure investigations on

the steel core samples are given in Table 3.1. There appears to be no direct trend in the effects of damage and heating the resulting grain sizes or percent pearlite. As later described in Section 4.9.4, a more fine-grained microstructure is generally stronger and tougher than a more coarse-grained microstructure. There is a slight increase on the surface hardness and a slight decrease on the ductility. A microstructure that is more pearlitic is harder, stronger, and more brittle. However, only significant and consistent changes in the percent pearlite would be further analyzed as the amount is related to the location taken for the picture as discussed in Section 2.4.3. The results are provided in Table 3.1 for completeness. The discrepancies are likely due to inherent variations of microstructure within the steel girders before damage.

3.1.5 Hardness testing

Hardness tests were conducted on both the steel cores removed from the unheated and heated region of the webs. These tests were conducted using an automated Rockwell hardness testing machine. The specimens were found to be too soft for the Rockwell - C scale. Therefore, the hardness tests were conducted on the Rockwell - B scale using a hardened steel pin and 100 kg-force as per ASTM standards. The calibration of the testing machine was verified each day of testing using a standard calibration plate with hardness equal to 80.3 ± 1.0. The average hardness values from four measurements taken on each sample are provided with the standard deviations in Table 3.2. Table 3.2 also provides approximate tensile strengths as reported by ASTM standards. With the knowledge gained after performing the investigations of Task III, the results of the approximate tensile values appear to be overestimated for the Lansing Road Bridge and the heated region of the Lake Lansing Road Bridge.

With the exception of the Lansing Road Bridge, the steel cores from the damaged and heated regions have slightly greater hardness and tensile strength than the steel cores from the unheated region of the web. The results of the microstructure investigations on the Lansing Road Bridge were also very similar. These results relate well to conclusions made on the hardness results on the undamaged and damage-repaired specimens as part of Task III (see Chapter 5).

3.2 REVIEW OF MDOT CODES AND GUIDELINES

This section reviews the MDOT codes and guidelines as specified by Subsection 713.03 G (Heat Straightening Damaged Structural Steel) of the "MDOT – 2003 Standard Specifications for Construction" [*1*]. These guidelines are somewhat brief and some additional information may be applicable.

The code provides the following requirements for the contractor:

- Approved by MDOT
- Min. 3 years of continuous work on steel
- Must submit details to engineer at least 48 hours before work begins

The MSU researchers agree that contractors need to be well experienced. Three years seems to be good criteria for at least one member of the crew. It would be beneficial if each crew member passes a training session such that they understand a general knowledge of the heat straightening mechanics and harms of avoiding the specifications.

The code provides the following general requirements of the heat straightening application:

- Heating shall be applied to a maximum temperature of 1200 °F.
  - Monitored w/ contact thermometer, pyrometric stick, or other approved device (supplied by contractor)
- Torch tip diameter between 0.75 in. and 1 in.

- All and only plastic yield zones heated
- Line, strip, spot, or Vee heats permitted
- No forced cooling
- Must cool to < 250° F before next heating cycle

As mentioned in Section 3.1.2.2, the SBC sometimes exceeded the maximum temperature requirement. This maximum temperature appears to be enough safe guard to avoid raising the temperature beyond the steel transition temperature. As specified, the steel must cool to 250 °F prior to further heating cycles and no forced cooling should be allowed. These specifications are important to allow proper recrystallization of the grains.The MSU research team used 5/8 in. diameter torches for experimental investigations and suggests that this size should be allowed and perhaps should be used for plate members ≤ 3/4 in. to avoid overheating.

The specification provides the following requirements for the Vee heat: (a) Vee angle ≤ 20°; (b) Base width ≤ 6 in.; and (c) Heat applied from apex. The SBC did not follow all of these requirements as Vee angles were calculated to be approximately 50-55°. The SBC uses a consistent approach that idealizes a partial (half) depth Vee with a base width of 5 in. Avent et al. [*2*] conducted experimental investigations to investigate the effects of the Vee angle on induced residual stresses of heat-straightened plates. The experimental results indicated that larger Vee angles produced slightly higher residual stresses in the cross-section. However, the discrepancies were somewhat insignificant for up to a maximum Vee angle of 60° in both investigations. Therefore, perhaps the angles used by the SBC should be allowed.

The specification provides the following requirements for the external restraining force: (a) Minimum mechanical force should be applied; (b) Cannont resist contraction during cooling; and (c) cannot produce local buckling during heating. Additional guidelines are suggested concerning the external restraining force. The maximum mechanical force should be set such that yielding will not occur prior to heating (cold-working). Avent and Mukai [*3*] have recommended that stresses in the heated zone should not exceed 0.5 the nominal yield stress at ambient temperatures. This computation should be made by the engineer, considering the external restraining force, and may not consider the initial residual stresses in the steel section.

The specification provides the following requirements for the tolerances in the repaired member:

- All bends, creases, folds, and dents eliminated in:
  - Web plates
  - Flange plates
  - Angles
  - Stiffeners
  - Channels
  - Gusset plates
  - Torn areas
- Flange plates and angles:
  - Within ¼” of tilt rotation at edges from web
  - Within ½” sweep in 20 ft. (3/4” at pt. of impact)
- Web:
  - Less than ½” out of plumb
  - Localized deflections less than ½” (measured w/ straight edge held both vertically and horizontally)
  - Burrs, nicks, gouges, scrapes, etc:
  - Ground to surface finish of 125 micro inches per inch rms

- Tapered using 1 to 10 slope

These tolerances may be difficult to address and the SBC crew used visual inspection without actual measurements to check the tolerances of the repaired beam. The specification then briefly addresses the environmental considerations of when not to perform heat straightening. Heat-straightening should not be permitted in freezing or winter conditions because the fracture toughness of cold steel is very low. Additional requirements and limits on multiple damage heat-straightening repair cycles must be included based on the results presented in this report later.

3.3 REFERENCES

1. MDOT – 2003 Standard Specifications for Construction, Subsection 713.03 G, http://www.mdot.state.mi.us/specbook/, Last accessed August 13, 2004.
2. Avent, R. R., Mukai, D. J, and Robinson, P. F., *Journal of Materials in Civil Engineering*, ASCE, Vol. 13, No. 1, Jan/Feb. 2001, pp. 18-25
3. Avent, R. R. and Mukai, D.J., *Engineering Journal*, First Quarter, 38(1), 2001, pp. 27-49.

CHAPTER 3: TABLES

Table 3.1
Microstructure results of core samples taken from heat-straightening bridge sites

Bridge Site	Core Location	Grain Size (mm)	Percent Pearlite
Lake Lansing	Unheated	0.0309	36.03
	Heated	0.0391	25.13
Lansing	Unheated	0.0273	16.49
	Heated	0.0303	17.46
Elm	Unheated	0.0342	21.97
	Heated	0.0303	27.38

Table 3.2
Rockwell hardness results of core samples taken from heat-straightening bridge sites

Bridge Site	Core Location	Average Rockwell B Hardness	Std. Dev	ASTM Approx. Tensile Str. (ksi)
Elm Road	Unheated	62.0	0.73	62
	Heated	71.0	1.76	53
Lansing Road	Unheated	85.4	1.07	81
	Heated	85.7	2.09	81
Lake Lansing Road	Unheated	74.1	0.35	65
	Heated	80.8	0.6	73

Figure 3.1
Out-of-plane movement of the Lake Lansing Road Bridge north fascia beam

Figure 3.2
Damage on the south side of the Lansing Road Bridge west fascia beam

Figure 3.3
Out-of-plane movement of the Lansing Road Bridge west fascia beam

Figure 3.4
Restraining force apparatus

Figure 3.5
Photograph of the strip heat applied to the web

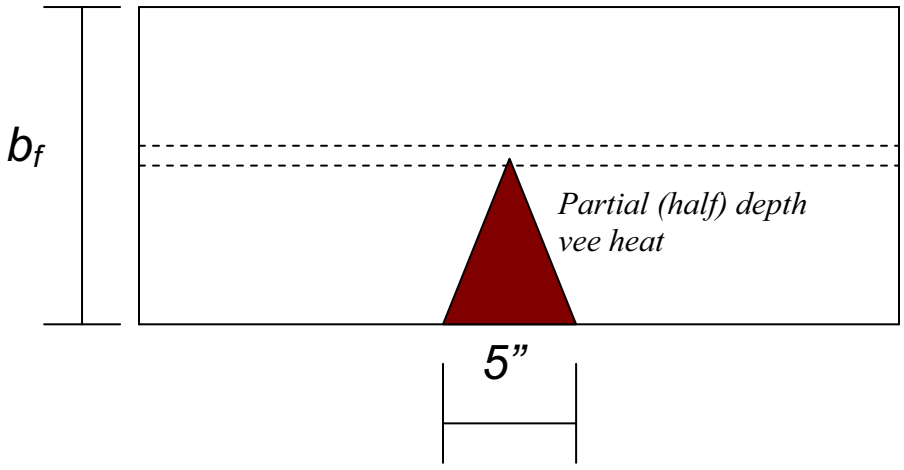

Figure 3.6
Dimensions of the Vee heats applied by the SBC to the bottom flange

Figure 3.7
Vee-heat of the bottom flange and cover plate using two torches

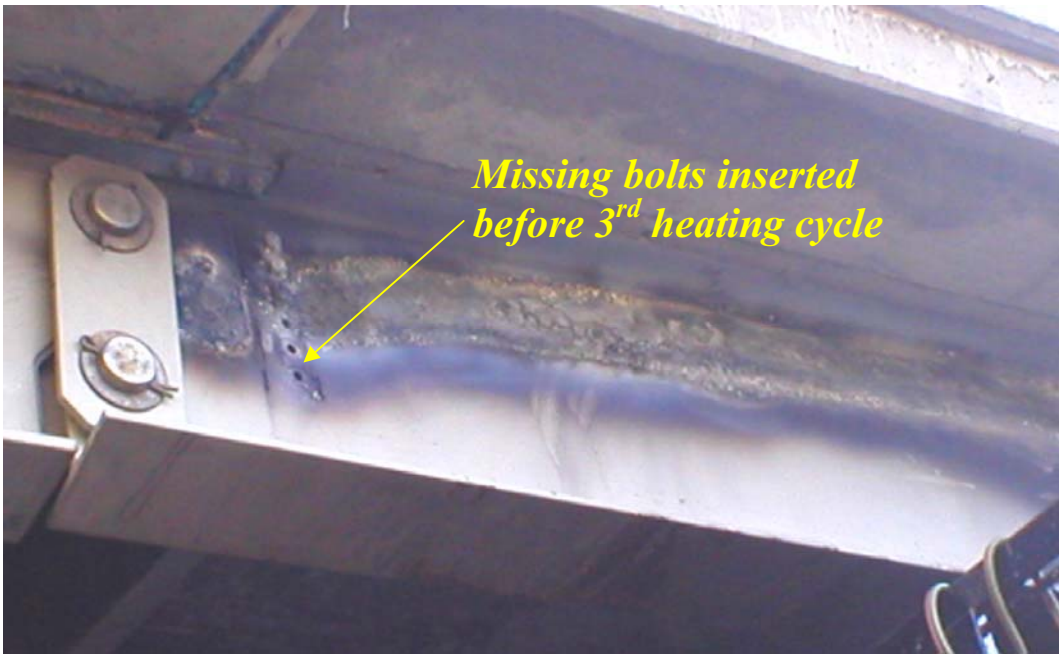

Figure 3.8
Appearance of the Lansing Road bridge girder after two heating cycles

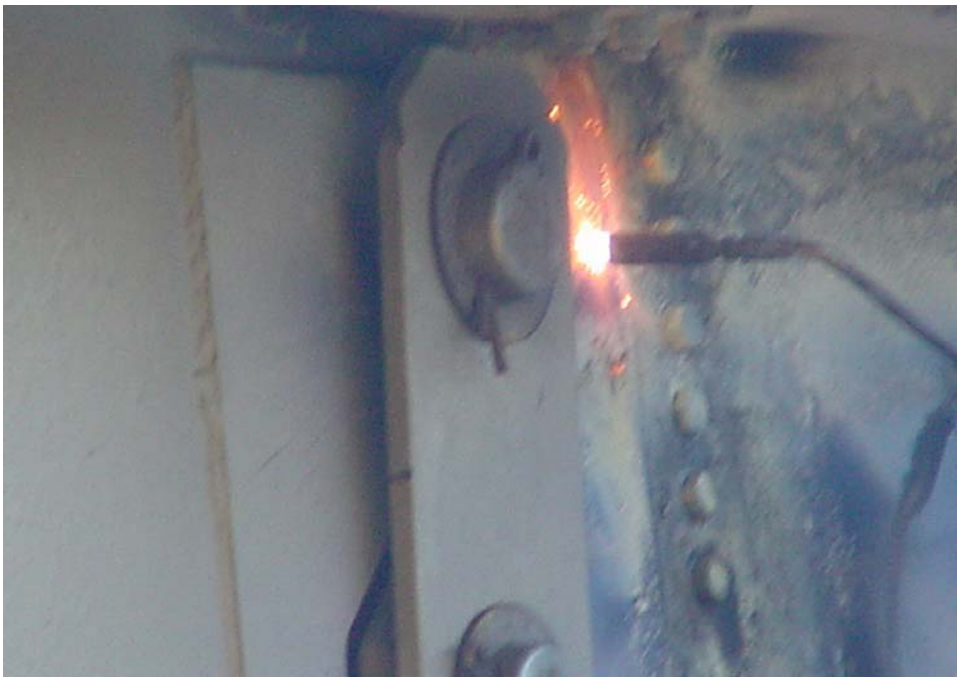

Figure 3.9
Strip heat applied close to the pin-hanger detail

Figure 3.10
Condition of bridge girder after applying strip heat close to pin-hanger detail

Figure 3.11
Condition of bridge girder after heat straightening repair procedure

Figure 3.12
Replacement of the removed steel cores using galvanized steel bolts

Figure 3.13
Out-of-plane movement of the Elm Road Bridge west fascia beam

Figure 3.14
Fractured diaphragm-to-beam connection

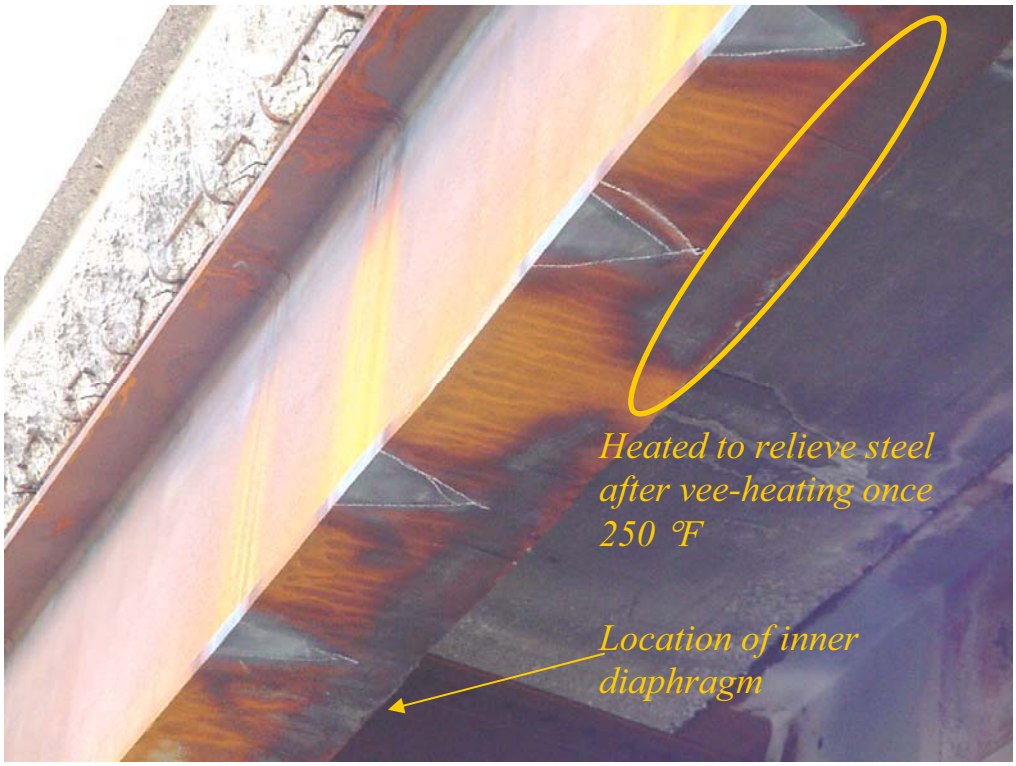

Figure 3.15
Multiple Vee heats applied to the bottom flange

a) Unheated 480X

b) Heated 480X

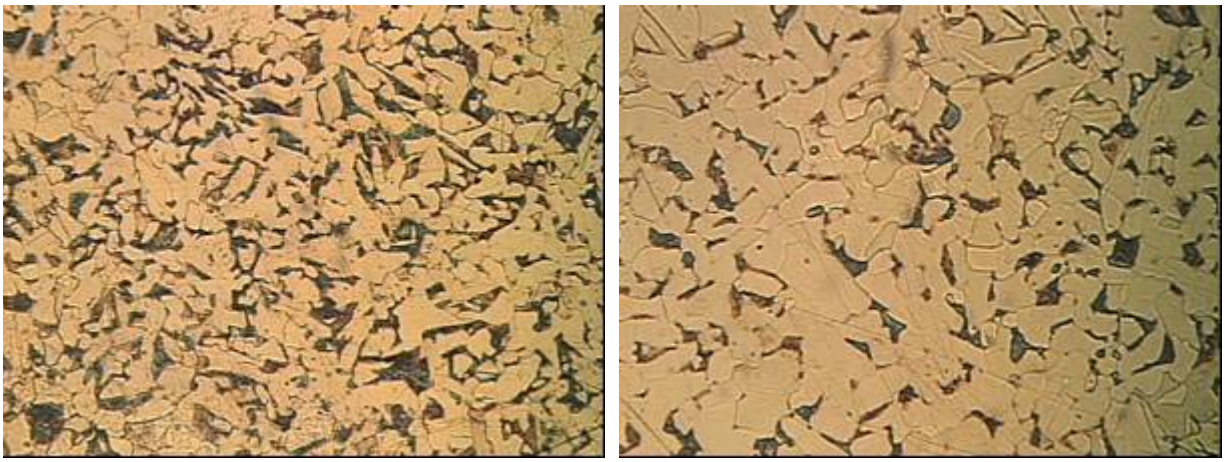

Figure 3.16
Microstructure of heated and unheated sections of the Lake Lansing Road Bridge

a) Unheated 480X b) Heated 480X

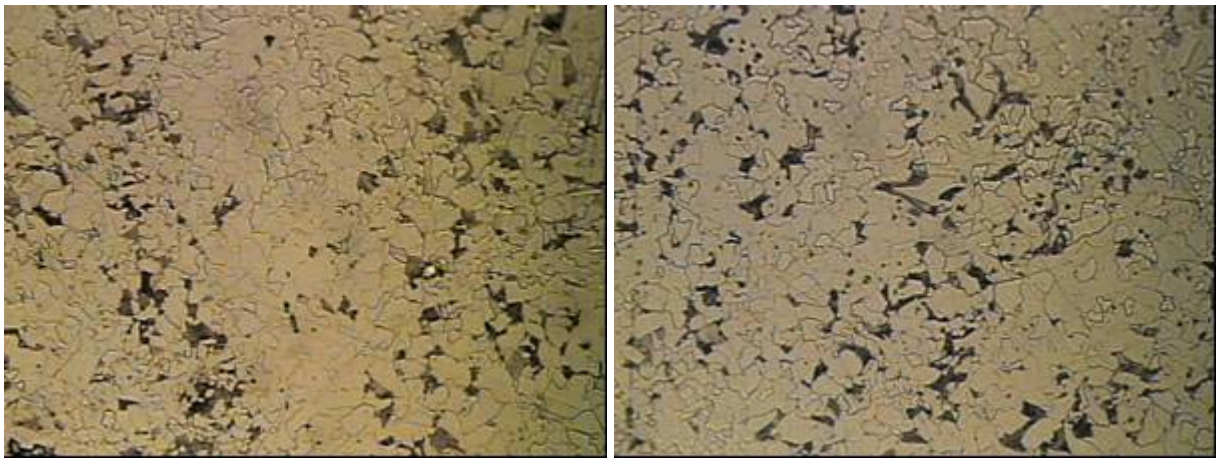

Figure 3.17
Microstructure of heated and unheated portions of the Lansing Road Bridge

a) Unheated 240X b) Heated 240X

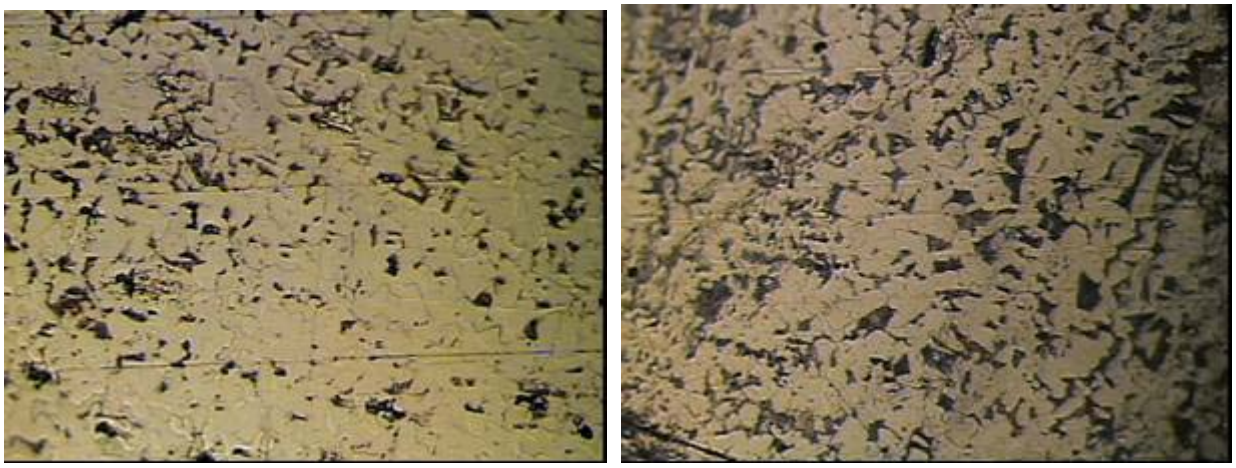

Figure 3.18
Microstructure of heated and unheated portions of the Elm Road Bridge

4 EXPERIMENTAL INVESTIGATIONS OF LABORATORY-SCALE SPECIMENS

4.1 INTRODUCTION AND OBJECTIVES

Task III of this research focused on experimentally investigating the effects of multiple damage-heat straightening repairs on the structural properties of steel, namely, the yield stress, ultimate stress, strain ductility, modulus of elasticity, fracture toughness, and surface hardness, and the microstructure of steel. Laboratory-scale specimens were damaged and repaired by heat straightening. The damage and repair were limited to a controlled test area, which was designed to accommodate the required number of material specimens to measure the structural properties with statistical significance. The objectives of Task III were given as follows:

- Experimentally investigate the effects of multiple damage-heat straightening repairs on the structural properties of steel
  - Parameters included in the study are the steel type, the damage strain, the restraining stress, the maximum heating temperature, and the number of damage-repairs.
  - Structural properties included in the study are the elastic modulus, yield stress, ultimate stress, strain ductility, fracture toughness, surface hardness, and microstructure of steel.
- Develop empirical models for predicting the effects of multiple damage-heat straightening repairs on the structural properties of steel.
- Develop simple recommendations and non-destructive techniques for evaluating steels subjected to multiple damage-heat straightening repairs.

This chapter provides a full description of Task III. Section 4.2 summarizes the high load hits database analysis results and identifies the steel types for the research. Section 4.3 presents the test matrix identifying the various damage and repair parameters for each steel type. The testing methodology is discussed philosophically in Section 4.4. Section 4.5 presents the design of the laboratory-scale test specimens. The design and fabrication of the test setup for subjecting the specimens to damage-repair cycles are discussed in Section 4.6. The testing procedures are summarized in Section 4.7. Section 4.8 summarizes tests conducted on a trial specimen that were used to validate the test setup and testing procedure. Section 4.9 summarizes the standard procedures for testing material specimens from undamaged and damaged-repaired steels.

4.2 SUMMARY OF DATABASE ANALYSIS AND STEEL TYPES

The Michigan high-load hits database from 1976 to 2001 was analyzed to determine the steel types and structure types that are damaged and heat-straightened most frequently in Michigan and thus most relevant to this research project. The high-load hits database was discussed more extensively in Section 2.3. The database included 280 heat straightening repair cases corresponding to 183 damaged steel bridges. Thus, several damage-repair cases were *multiple* damage-heat straightening repairs of the same steel bridge. Figure 4.1(a) shows the frequency distribution of the total number (280) of damage-heat straightening repair cases as a function of the steel type. Figure 4.1(b) shows the frequency distribution of the total number (183) of steel bridges subjected to damage-repair cycles as a function of the steel type. Figures 4.1(a) and 4.1(b) indicate that A7 and A373 are the steel types that are most frequently damaged and heat straightened in Michigan. These figures indicate that the steel types most relevant to this research project in their order of relative importance are A7, A373, A588, A36, and A572. However, the availability of the steel was a major issue in choosing the appropriate steel types to be used for the laboratory-scale specimens of Task III. The older steel types A7 and A373 are no longer available

commercially. Hence, the laboratory-scale specimens were fabricated from A36 steel, which is available commercially and similar in chemical composition to A7 and A373 steel. Additionally, laboratory-scale specimens were made from A588 steel. Finally, a limited number of laboratory-scale specimens were fabricated from the A7 steel webs of a decommissioned W24x76 steel beam.

4.3 EXPERIMENTAL TEST MATRIX

Three steel types A36, A588, and A7 steel were considered and the following sub-sections present the corresponding test matrices. The following sub-sections present the planned test matrix, which was modified slightly later due to unavoidable logistic problems, as explained in the next chapter, which includes the actual test matrix. The test matrix identifies the parameters included in this study, which are the: (a) steel type; (b) damage strain; (c) restraining stress; (d) number of damage-repair cycles; and (e) heating temperature.

4.3.1 A36 Experimental Test Matrix

Thirty laboratory-scale specimens and one undamaged specimen were made from the same 1.0 in. thick A36 steel plate. The test matrix for these specimens is summarized in Table 4.1. As shown in Table 4.1, three damage strain levels (ε_d), two restraining stresses (σ_r) for each ε_d, and five damage-repair cycles (N_r) for each ε_d-σ_r combination were considered for A36 specimens. The specimens were repaired by heating to a maximum temperature of 1200 ºF.

4.3.2 A588 Experimental Test Matrix

Thirty laboratory-scale specimens and one undamaged specimen were made from the same 1.0 in. thick A588 steel plate. The test matrix for these specimens is summarized in Table 4.2. As shown in Table 4.2, three damage strain levels (ε_d), two restraining stresses (σ_r) for each ε_d, and five damage-repair cycles (N_r) for each ε_d-σ_r combination were considered for A588 specimens. The test matrix was similar to the test matrix for A36 steel specimens. The specimens were repaired by heating to a maximum temperature of 1200 ºF.

4.3.3 A7 Experimental Test Matrix

Eighteen laboratory-scale specimens were fabricated from the web of a decommissioned W24x76 steel beam made from A7 steel. The test matrix for these specimens is summarized in Table 4.3. As shown in Table 4.3, three damage strain levels (ε_d), two restraining stresses (σ_r) for each ε_d, and three damage-repair cycles (N_r) for each ε_d-σ_r combination were considered for A7 steel specimens. The specimens were repaired by heating to a maximum temperature of 1200 ºF.

4.3.4 Overheated A36 Experimental Test Matrix

Sixteen laboratory-scale specimens and one undamaged specimen were made from the same 1.0 in. thick A36 steel plate. The overheating temperatures were selected as follows. Figure 4.2 shows the complete iron-iron carbide (Fe-Fe_3C) phase diagram [*1*]. A36 steel has a carbon content of 0.3%, which will place it at the extreme left region of Figure 4.2. This region is shown more clearly in Figure 4.3. As shown in Figure 4.3, A36 steel is composed of ferrite (α-Iron) and pearlite (Fe-Fe_3C) phases at ambient temperature. As the temperature increases beyond the eutectoid temperature (1340 ºF or 727 ºC), the pearlite begins to transform to ferrite-austenite phase, i.e., α-Iron and γ-Iron phase. More and more pearlite transforms to α+γ Iron as the temperature increases until the temperature reaches about 1550 ºF or 825 ºC when all pearlite has completely transformed to α+γ Iron. As this temperature is exceeded, all the α-Iron transforms to γ-Iron giving a pure austenite phase at temperatures greater than 1550 ºF. Based

on this discussion, the two overheating temperatures chosen were 1400 ºF and 1600 ºF. At 1400 ºF, the ferrite-pearlite phase has transformed significantly to α+γ Iron phase and at 1600 ºF, the austenite (γ-Iron) phase alone exists [*1*].

The test matrix is summarized in Table 4.4. As shown in Table 4.4, two damage strain levels (ε_d), two restraining stresses (σ_r) for each ε_d, two damage-repair cycles (N_r) for each ε_d-σ_r combination, and two maximum heating temperatures (T_{max}) for each ε_d-σ_r-N_r combination were considered for the overheated A36 specimens.

4.4 TESTING METHODOLOGY

The high-load hits database analysis presented in Section 2.3 indicated that the structure type most frequently subjected to heat straightening repair is the composite steel beam bridge. The composite steel beam is damaged by collision with an overheight truck as shown in Figure 4.4, where P_T represents the load induced by a moving truck at Section A-A. This type of impact causes significant out-of-plane movement of the bottom flange. The maximum out-of-plane movement results at the contact point with geometry similar to that shown in Figure 4.5. Figure 4.6 shows the out-of-plane movement of the bottom flange along the length of a beam.

The damaged force (P_T) causes yielding and plastification along the length of the bottom flange as shown in Figure 4.7. The damaged beam is repaired by heat straightening, where several Vee heats are applied along the length of the bottom flange as shown in Figure 4.8. The MDOT-SBC uses partial and full depth Vee heats as shown in Figure 4.8 and Figure 3.15. The Vee heat is applied using an oxy-acetylene torch following a serpentine motion as shown in Figure 4.9.

At elevated temperatures, the coefficient of thermal expansion of the steel increases and the elastic modulus and yield strength of the steel decreases. During heating, longitudinal expansion is repressed by a combination of internal and external forces [*2*]. The Vee area thus thickens. The Vee heat may be aided with an external restraining force that induces an initial compressive stress on the elongated (heated) side and a tensile stress on the shortened (non-heated) side. The fundamental mechanics of how the Vee heat works is shown in Figure 4.10. When applying the Vee heat to the plate element, the material tries to expand as shown in Figure 4.10(a). The dashed line represents the expansion of the Vee assuming no internal forces resist. The expansion is restricted by the unheated material, which puts an additional compressive force on the Vee-heated region as shown in Figure 4.10(b). At higher temperatures, the material yields and shortens upon cooling as shown in Figure 4.10(c). Thus, a net contraction of the steel occurs, producing a closure of the Vee [*2*]. Since the shortened side never gets heat treated, compressive strains are still present and the length of the plate becomes shorter than it was before damage.

There were two possible approaches for conducting the experimental investigations. The first approach involves fabricating steel plate specimens, damaging them in bending about the major axis, and repairing them using Vee heat straightening patterns and restraining moments. In this approach, the specimen cross-section and length are subjected to different magnitudes of damage strain, restraining stress, and heat straightening repair. This hinders obtaining several material specimens subjected to consistent damage-repair magnitudes and testing them to obtain statistically significant structural properties. The second approach involves fabricating (dog-bone type) steel plate specimens with reduced test-areas, damaging the test-areas in uniaxial tension, and repairing them using strip heat straightening patterns and restraining compressive forces. The specimen test-areas are subjected to consistent damage strains, restraining stresses, and heat straightening repair. This facilitates obtaining several material specimens from the test-areas and testing them to obtain statistically significant structural properties. The second approach can be used more effectively to evaluate the effects of multiple damage-repair cycles on the structural properties of steels. Hence, it was preferred and used for this research.

When applying the Vee heat to a damaged steel plate, the fiber, which is subjected to the most damage-repair, is located at the extreme tension side during damage as shown in Figure 4.7. Therefore, the test setup was designed to compare to the damage-repair history of the extreme tension fiber to that of the laboratory-scale specimens.

Strips heats, also called rectangular heats, are applied similar to the Vee heat and are accomplished in a similar manner [*2*]. For this heating pattern, an oxy-acetylene torch is moved from one edge to the opposite using the serpentine motion and covering a rectangular area as shown in Figure 4.11. Unheated regions restrict the expansion of the material. An external restraining stress (q) will also cause yielding in the heated region. The test specimen design is discussed next in Section 4.5.

4.5 TEST SPECIMEN DESIGN

4.5.1 A36 and A588 Small Scale Test Specimens

Laboratory-scale test specimens were fabricated from A36 and A588 steel plates. Details of the A588 and A36 test specimens are given in Figure 4.12. The test specimens were made from 1.0 in. thick steel plates and were 8.0 in. wide and 46.25 in. long. The specimen thickness was designed to prevent local or global buckling at ambient and elevated temperatures. The test area is the reduced section that is 3.25 in. wide and 5.0 in. long and located at the center of the specimen as shown in Figure 4.12. The specimen test area is subjected to damage-heat straightening repair. The test area dimensions were designed to accommodate two uniaxial tension specimens and six charpy v-notch that will be fabricated after subjecting the test area to multiple damage-heat straightening repair cycles.

An 8 in. width was chosen to prevent yielding of the bolted connection. The bolt holes have a diameter of 1.1875 in., which are used for 1.125 in. diameter bolts. The bolts transfer the forces from the planar frame to the test specimen. The planar frame is described in Section 4.6. Spacing of the bolts and edge distances were designed as specified by AISC for bolted connections.

After completing the multiple damage-heat straightening repair experiments, structural property tests were conducted on material specimens fabricated from the test area of the specimens. The locations of these material specimens in the test area are shown in Figure 4.13(a-c). As shown in Figures 4.13(a-c), two 2-in. gage length tension specimens and six charpy specimens (3 at the quarter-thickness and 3 at the half-thickness) were machined from the test area. These material specimens were used to determine the influence of multiple damage-heat straightening repairs on the: yield strength, elastic modulus, ultimate strength, strain ductility, fracture toughness, surface hardness, and microstructure of steel. Descriptions of the material testing procedures are provided in Section 4.9.

4.5.2 A7 Test Specimen Dimensions

Two W24 x76 A7 steel beams were obtained from a decommissioned steel bridge in Michigan. These beams were approximately 26 ft. long, with welded end supports, and painted with lead-based paint. Both beams had some flange distortions or dents. The webs however appeared to be in satisfactory condition. Laboratory-scale specimens were fabricated from the web of one A7 beam, and the second beam was used for the full-scale testing as part of Task IV. The beam chosen for laboratory-scale specimens was selected as the beam with poorer flange conditions as only the web was used to fabricate the laboratory-scale specimens. The beams as received by the MSU researchers are shown in Figure 4.14. Figure 4.14(a) shows the end conditions, Figure 4.14(b) shows some dents in the flange of one of the beams, and Figure 4.14(c) shows the full beam span used for fabricating laboratory-scale specimens. The beams were sandblasted in order to remove the lead-based paint. The final lengths of the cut and sandblasted beams delivered by the contractor were as follows; (a) one beam was 23 ft. 3 in. long, and (b) the second beam

was cut into three segments that are 93 in. (7ft. 9 in.). The conditions of the three 93 in. beams after sandblasting are shown in Figure 4.15.

Eighteen laboratory-scale specimens made from A7 steel were fabricated. Some requirements on the fabrication of A7 specimens were as follows:

- All eighteen specimens should be made from the same steel beam to maintain uniformity in the material.
- At least two tension and six charpy specimens should be fabricated from the web of the same steel beam to establish undamaged steel material properties. The uniaxial tension specimens and the charpy specimens should correspond to the mid-thickness of the 0.45 in. thick web.
- The specimen dimensions, namely, the specimen width (b_s) and the test area width (b_t) must be designed to prevent fracture or excessive yielding of the net section when the test area is subjected to significant inelastic strains.

Six specimens were fabricated from each 93 in. beam as shown in Figure 4.16. Figure 4.16 also shows the area from where the undamaged material specimens were obtained. The dimensions of the A7 test specimen are shown in Figure 4.17.

The removal of two 8 in. *flat* tensile specimens and six charpy specimens from the test area is shown in Figure 4.18. As shown in Figure 4.18(a), the grip areas of the tensile specimens extend outside of the boundaries of the test area. As shown in Figure 4.18(b), all six charpy specimens are taken out of the mid-thickness and the uniaxial tension specimens are taken as the same width as the plate. Details involved in the material testing procedures are provided in Section 4.9.

4.6 TEST SETUP DESIGN, FABRICATION, AND CONSTRUCTION

4.6.1 Purpose and General Description

Figure 4.19 shows a schematic of the test-setup that subjects the specimens to multiple damage-heat straightening repair cycles. Figure 4.20 shows a photograph of the test setup identifying the primary components. The instrumentation used during testing is not shown for clarity. As shown in Figure 4.20, the test-setup includes a bottom steel beam that is post-tensioned to the laboratory strong floor. The specimen is bolted to the bottom beam using 1.125 in. diameter high strength steel bolts. Two hollow-core hydraulic actuators are also bolted to the bottom steel beams as shown in Figure 4.20. The specimen is bolted to the top steel beam in the same way it is bolted to the bottom beam. The hollow core actuators are connected to the top beam using 2.5 in. diameter threaded rods and several bearing plates and nuts (see Figure 4.20). The actuators use hydraulic pressure generated by the electric pump to push up or pull down the top steel beam, thus subjecting the specimen to tensile or compressive axial forces. The hydraulic pressure in both actuators is equalized and maintained using special split-flow and needle valves.

Four concrete blocks were casted and post-tensioned to provide out-of-plane buckling restraint to the planar frame of the test-setup. The concrete blocks serve as safety restraints to the researchers involved the experimental tests. The plan view of the test setup is shown in Figure 4.21. A picture of the test setup being constructed is shown in Figure 4.22.

4.6.2 Test setup stability

The four concrete blocks and the bottom beam are post-tensioned to the Civil Infrastructure Lab (CIL) strong floor. To provide a stable and flat surface for conducting the post-tensioning application, hydrostone was casted on the CIL strong floor. Hydrostone is stone-like cement that is especially suitable where high strength and resistance to wear are necessary. The hydrostone was left to set 48 hours before the post-tensioning of the concrete blocks and bottom beam. Dywidag anchor bars with 1.375 in. diameters are fastened into the bottom of the CIL strong floor. The bottom beam is post-tensioned to the laboratory floor with a force of 50 kips at each tie down point. The concrete blocks are post-tensioned to the floor with a force of 150 kips each.

4.6.3 Description of Test Setup Planar Frame

The design details of the top and bottom beams of the planar test frame are shown in Figure 4.23(a-b). Both the top and bottom beams are built-up cross-sections made from AISI 1018 cold-drawn steel with a yield stress equal to 54 ksi. The 7/16 in. fillet welds were made using E80XX electrodes. The only difference between the top and bottom beams is that 2.75 in. holes were fabricated in the top beam for the passage of 2.5 in. high strength threaded rods and 1.75 in holes were fabricated in the bottom beam for the passage of 1.375 in. dywidag anchor bars.

Two base plates were set on the top flange of the bottom beam to act as supports for the hydraulic actuators. Holes were drilled through the top flange of the bottom beam to allow the passing of 0.625 in. threaded rods through the flange and base plate. The threaded rods are made of grade B7 material and rotated 0.75 in. into the bottom of the hydraulic actuators.

Threaded rods with a diameter of 2.5 in. and made from B7 (100 ksi) material are threaded approximately 5 in. into the top of the hydraulic actuators. Structural nuts (3 in. long) are threaded onto the rod before placing the top beam. Bearing plates (2 in. thick) are positioned between the top beam and the structural nuts to provide flat supports for the stability of the top beam. Bearing plates (2 in. thick) are also placed on the top of the beam and the connection is tightened with structural nuts (3 in. long). The bearing plates that support the top beam and the cylinder base plates are shown with dimensioning in Figure 4.24.

The test specimen is attached to the top and bottom beam by using 12 or 8 structural bolts, which are 6 in. long by 1.125 in. diameter. The structural bolts are made of Grade A490 material. The thickness of the test specimens is 1 in. and the gaps in the top and bottom beams are 1.5 in. To remove the gaps, 0.1875 in. thick shim plates are placed on either side of the specimen within the top and bottom beams. 0.0625 in. thick shim plates were also fabricated to achieve the tightest possible connection between the test specimens and the beams. Figure 4.25 shows the dimensions of the shim plates.

4.6.4 Adjustments to Test Setup for A7 Steel Specimens

Adjustments to the test setup were required while testing the A7 specimens to reduce their effective length. The A7 specimens had a thickness of 0.45 in. and developed significant curvature during heating. The effective length is considered the distance from lateral stiffness points. For example, in the A36 and A588 experimental tests, the effective length is the distance from the bottom of the top beam to the top of the bottom beam.

The researchers fabricated small angle sections that were clamped to the bottom beam on both sides of the test specimen. The angle sections were bolted together only when repairing the specimen. This adjustment reduced the effective length by 8 in. The positioning of the angle sections in respect to the bottom beam and the test specimen is given in Figure 4.26.

This adjustment reduced the effective length of the A7 test specimen as shown in Figure 4.27. Longer shim plates were also fabricated such that they provide more contact with the specimen below the top beam. The test setup as used for experimental investigations on A36 and A588 steel is shown for comparisons in Figure 4.28.

4.7 EXPERIMENTAL PROCEDURE

4.7.1 Damage Cycle

To subject the specimen test area to the respected damage level, the hydraulic actuators are set to advance mode, which lifts the top beam and subjects the test specimen to tensile stresses. Hydraulic oil is pumped out of a 20-series electric pump into the bottom of the hydraulic core actuators. The pressure in the advanced region is monitored using calibrated pressure transducers that are attached into the hydraulic network. The area of the bottom piston within the hydraulic actuator is 20.63 in^2. With the pressure known, the force in each actuator and the average stress in the cross-section of the test area are computed as follows:

$$P_i \text{ (kips)} = \text{pressure (psi)} * 20.63 \text{ (in}^2\text{)} / 1000 \quad (4.1)$$

$$\sigma(\text{ksi}) = \frac{\text{TotalLoad(kips)}}{\text{A(in}^2\text{)}} = \frac{P_1 + P_2}{A} \quad (4.2)$$

The stress subjected to the test area of the specimen is monitored on a computer screen while testing. The loading rates of each hydraulic actuator are equalized early for each damage of the test specimens.

The damage strain during the first damage cycle of each test specimen was monitored most particularly using strain gages. Multiple damage cycles were monitored using displacement transducers, which measure the displacement of the test area. For the first three specimens tested, four strain gages were attached to all sides of the specimen. Looking from the center of the laboratory at the test setup, these strain gages are identified as “Strain_Front”, “Strain_Back”, “Strain_Left”, and “Strain_Right”. The strain gages were attached longitudinally at the center of the face of the test area.

Starting with the fourth specimen, the two strain gages on the sides of the specimen were removed and only the two on the front and back were monitored for damaging the specimen. Analysis of the first three specimens tested indicated that less plastic strain was being induced along the sides of the specimen. This phenomenon was further aided with a finite element model and discussed in more detail in Section 4.8.

The average strain of the test area needs to be held constant for equal amounts of damage. For this purpose, two punch marks are punctured on both sides of the specimens at the test area edges. The distance between them is measured before and after each damage and repair event using high precision vernier calipers. The process of using high precision vernier calipers is the most accurate way to ensure the correct amount of damage has been subjected to the test area and validates the full repair of the specimen.

To record and monitor the total displacement of the test area using the data acquisition system during loading, steel brackets were attached to the specimen at the ends of the test area. The top and bottoms are lined up with the punch marks. The sides were connected together with wing nuts. Two aluminum supports were C-clamped to the top bracket with 1.0 in. displacement transducers attached to the ends. Flat aluminum angles were clamped to the bottom bracket to give bottom supports for the displacement transducers. As strain is introduced to the test area, the top and bottom brackets begin to separate, causing the displacement transducers to elongate. Figure 4.29 gives an side view illustration of the displacement transducer setup in relation to the test area of the specimen. Figure 4.30 shows a photograph of the slider

setup on a test specimen. The amount of damage subjected to the test specimen for multiple damage cycles was monitored using these instruments and comparisons of these readings to that of the strain gages from the first damage cycle.

The average strain over the test area can be computed from the LVDT's or from the caliper readings. The average strain is computed using Equation 4.3:

$$\varepsilon_A = \Delta L/L \tag{4.3}$$

An illustration of the stress-strain relationships monitored using the instruments measured in this section is shown in Figure 4.31.

4.7.2 Repair Cycles

Heat straightening repair cycles were conducted by applying an external restraining stress of typically 0.25 σ_y or 0.5 σ_y. These restraining stress levels were altered for some A36 and A7 specimens as discussed in Sections 5.1.2, and 5.3.2. When applying an external restraining force, hydraulic oil is pumped out of a 20-series electric pump into the top of the hydraulic actuators. This pulls the top beam down and induces compressive stresses to the specimen. The hydraulic system has been designed to maintain equal pressures within each actuator.

To monitor the restraining stress level, the pressure transducers were attached to measure pressure within the retract region of the hydraulic network. The load in each actuator is computed by multiplying the top cylinder area of 13.54 in^2. The monitored stress was estimated as:

$$\sigma(\text{ksi}) = \frac{(P_1 + P_2) * 13.54(\text{in}^2)}{1000 * 3.25(\text{in}^2)} \tag{4.4}$$

Heating cycles were performed using 5/8 in. diameter oxy-acetylene heating torches. Two researchers used two oxy-acetylene torches and applied heat to both sides of the test specimens. The temperature at the surface of the steel was monitored using an ST80 infrared temperature gun. Heat straightening practice was conducted monitoring the temperature of the surface of application between 1100 ºF and 1200 ºF. MDOT among other DOTs limit heat straightening practices to 1200 ºF and this upper limit was enforced in the research project with the exception of the overheated A36 steel specimens. Heat straightening was conducted using a strip pattern moving from side to side over the rectangular test area as described in Section 4.4. The bottom is generally heated first to allow the heat to rise within the test region. Figure 4.32 shows a heat straightening repair cycle being conducted. Figure 4.33 shows how temperature is monitored using the infrared temperature gun. The bright red is the infrared ray pointed on the steel.

Two 1.5 in. displacement transducers were used to measure the displacements between the top and the bottom beam close to the hydraulic actuators. Aluminum bars are tied together and allowed to slide up and down with respect to each other. The displacement transducers were attached to aluminum brackets glued to the top beam and flat supports were attached to the aluminum bracket glued to the bottom beam. The transducers were used to estimate the expansion and shortening of the test area vs. temperature and pressure over time. A 1.5 in. displacement transducer is shown in Figure 4.34. The locations with respect to the test setup are highlighted in Figure 4.35.

An infrared thermometer was chosen to record the time-temperature profile of the test specimen during the heat straightening repair cycles. A picture of the infrared thermometer is shown in Figure 4.36. The thermometer was chosen to record accurate temperature readings up to 2500 °F. The thermometer was set up to record temperatures at midheight on either side along the thickness or at the front or back of the specimen test area.

The data being recorded was monitored and graphed for each experimental repair cycle. Figure 4.37 provides an example of such a chart. “Pressure Left and Right” represents the pressures in the left and right hydraulic actuators in ksi, “Infrared Thermometer” represents the temperature of the steel as indicated by the infrared thermometer in degrees Fahrenheit, and “Displacement Transducer Right” and “Displacement Transducer Left” represent the two 1.5 in. displacement transducers that give a displacement between the top and bottom beam in inches. These values are multiplied by -10000 so they can be distinguished with the other values being monitored.

The heat straightening repair was considered complete when the length of the test area was within 0.01 in. of the length measure by the same digital caliper before damage.

4.8 TRIAL TESTS FOR VALIDATION OF TEST SETUP

One A36 steel specimen was used to conduct trial tests and validate the test setup and the testing procedure prior to conducting tests on the actual test specimens. This specimen was also used to validate the heating techniques and repair procedures. This section provides details regarding the changes made to the testing procedures and the test matrix based on the trial test results. The trial specimen was damaged and repaired multiple times. Adjustments had to be made to limit the leaks found in the hydraulic network.

4.8.1 Restraining Stress Issues

The trial specimen was damaged to 30 ε_y. It was subjected to a restraining stress of 0.25 σ_y and repaired by heating one side with an oxy-acetylene torch. The amount of movement for each heating cycle was found to be somewhat negligible. It would have taken a few days to complete one repair cycle of a specimen damaged to only 30 ε_y. The displacements of the test area as estimated by the 1.5 in. displacement transducers for one heating cycle performed with one torch at 0.25 σ_y is shown in Figure 4.38. This figure indicates that very little movement was achieved. The pressure did decrease by approximately 2%, which indicates that some shortening of the steel did occur. Figure 4.39 shows two heating cycles also conducted on the dummy specimen at a restraining stress level of 0.50 σ_y. Figure 4.41 shows that much more significant yielding was occurring at the higher restraining stress level. Hence, the restraining stresses applied to repair A36 steel were modified from 0.25 σ_y and 0.50 σ_y to 0.40 σ_y and 0.70 σ_y, respectively. However, during the third damage-repair cycle of Specimen A36-30-70-3, it was determined that the higher restraining stress of 0.70 σ_y was too high and produced significant curvature in the specimen. The researchers decided another adjustment was needed to the test matrix. The trial specimen was placed back into the test setup to do some analysis on the amount of movement generated using two heating torches, applying heat simultaneously to both sides of the specimen. Using two torches generated more heat through the thickness of the specimen, which produced more movement. To avoid the addition of another parameter, the researchers decided not use two torches until after the first series of experiments were concluded on all ten A36 specimens damaged to 30 ε_y. Since two torches generated enough movement to reduce the time of each repair cycle and the specimen was undergoing too much curvature at 0.70 σ_y, the restraining stresses were modified back to the original values of 0.25 σ_y and 0.5 σ_y for A36 steel damaged to 60 ε_y and 90 ε_y.

4.8.2 Instrumentation Issues

The trial specimen was also used to investigate the use of the different instrumentation. The trial specimen as well as the first few actual experimental specimens had four longitudinal strain gages attached to the center of all four sides of the test area. The experimental results indicated that less longitudinal strain was being induced on the sides (right and left) than that directly at the center. An example of the experimental strain results, which are for Specimen A36-30-40-2, is shown in Figure 4.40.

In Figure 4.40, “Average Strain Right” and “Average Strain Left” represent the strains as indicated by the 1 in. displacement transducers attached along the specimen test area. “StrainBack” and “StrainFront” represent the strains on the front and back face of the test area. “StrainRight” and “StrainLeft” represent the strain gages on the right and left faces, which are along the thickness of the specimen. A finite element model developed using ABAQUS Version 6.3 [*3*] was used to validate the strain results. The results of the finite element model are shown in Figure 4.41. The finite element model validated the results observed from experimental data. Since the first damage of further test specimens was damaged using the front and back strain gages only, the side strain gages were not used for further experiments.

The original trial specimen, as well as the first couple of actual experimental specimens, had Type K contact thermocouples attached to the opposite side of heating. Several difficulties occurred when using these types of thermocouples: (1) the thermocouples had problems reacting to rapid increases in temperature, as the values never reached the high temperatures the specimens were subjected to; (2) the ceramic bond used to attach the thermocouples to the specimen could not hold large strains; (3) the process of attaching the thermocouples was cumbersome and the ceramic material took time to set; and (4) the thermocouples were also found to be inconsistent as their accuracy depends on the quality of bond to the steel. Regardless of the other issues in using these thermocouples, they had to be removed as soon the researchers began heating both sides of the specimen simultaneously. Thermocouple data is provided from a heating cycle conducted on the trial specimen in Figure 4.42.

4.8.3 Heating Practice

Finally, prior to subjecting specimens to maximum heating temperatures greater than 1200 °F, the trial specimen was used once again to practice and see the color of the steel at the higher temperatures. The researchers practiced numerous times on the trial specimen reaching maximum temperatures of 1400 °F and 1600 °F before proceeding with the experimental investigations. The infrared temperature gun only reaches 1450 °F. Therefore, monitoring 1600 °F was based on the researchers’ view of the steel and referring to the readings as indicated by the infrared thermometer.

4.9 MATERIAL TESTING PROCEDURES

Material testing was conducted on the specimens fabricated from the undamaged and damaged-repaired steels according to the applicable ASTM standards [*4*]. The structural properties being considered in this research include the: yield stress, ultimate stress, strain ductility, percent elongation, modulus of elasticity, fracture toughness, surface hardness, and the microstructure of steel. Therefore, the material testing included: (1) uniaxial tension tests, (2) charpy impact fracture toughness tests, (3) Rockwell hardness tests, and (4) microstructure investigations. Descriptions of each of these tests are provided in the preceding sub-sections.

4.9.1 Uniaxial Tension Tests

Uniaxial tension tests were performed according to ASTM E8 to determine the: (a) elastic modulus, (b) yield stress, (c) ultimate stress, (d) percent elongation, (e) strain ductility, and (f) percent reduction. Two tension specimens were removed from each damaged-repaired specimen. The locations of the uniaxial tension specimens in the test areas were given in Figure 4.13 for A36 and A588 steel specimens and Figure 4.18 for A7 specimens.

The A36 and A588 specimens were *round* tension specimens with a grip diameter of 0.75 in. and a reduced diameter of 0.50 in. Details for the dimensioning of the tensile specimens are shown in Figure 4.43. The same type of specimen could not be fabricated from the A7 specimens since the thickness of the material is only 0.45 in. Therefore, the A7 tensile specimens were *flat* sheet-type specimens. The

thickness of the A7 tensile specimens was taken as the thickness of the plate. The dimensions of the A7 tensile specimens are given in Figure 4.44.

As indicated in Figure 4.43 and 4.44, the reduced section has a length of 2.25 in. The percent elongation was determined by marking a gage length along the reduced section 2 in. long as indicated in Figure 4.45. The percent elongation was computed with the original gage length and the gage length of the same marks after fracture using Equation 4.5. Measurements were taken after marking the gage lengths to ensure the accuracy. According to ASTM E8, gage lengths should be recorded to the nearest 0.002 in. High precision vernier calipers were used to measure the gage lengths and diameters of the reduced section before and after the tests. For the A588 specimens, overheated A36 specimens, and A7 specimens, two gage lengths were marked and measured on each specimen.

$$\text{percent elongation} = \frac{(L - L_o)}{L_o} * 100\% \tag{4.5}$$

The percent reduction of the cross-sectional area was computed using the original average diameter and the final major and minor axis diameters as the specimens fracture in an elliptical shape. The reduced area was computed with the guidance of ASTM E8, using Equation 4.6. The percent reduction of area was computed using Equation 4.7.

$$A_r = \frac{\pi * d_1 * d_2}{4} \tag{4.6}$$

$$\text{percent reduction} = \frac{(A_r - A_o)}{A_o} * 100\% \tag{4.7}$$

Other structural properties, such as the upper, lower, and plateau yield stresses (σ_y), the elastic modulus (E), the ultimate stress (σ_u), and the strain at ultimate stress (ε_u), were carefully estimated from the uniaxial tension stress-strain relationships as shown in Figure 4.45. The elastic modulus (E) corresponds to the elastic slope of the stress-strain relationship. The yield strain (ε_y) was computed as a ratio of σ_y to E. The strain ductility was computed as $\varepsilon_u/\varepsilon_y$.

4.9.2 Fracture Toughness Tests and Statistical Evaluation

Charpy impact tests were conducted according to ASTM E23. The locations of the charpy specimens in relation to the test areas were given in Figure 4.13 for the A36 and A588 steel specimens and Figure 4.20 for the A7 steel specimens. The dimensions of the charpy specimens are shown in Figure 4.46. According to AASHTO specifications, charpy specimens are to be cooled to 40 °F and tested within 5 seconds of taking out of this temperature. The researchers found it difficult to obtain this temperature and test more than one specimen at a time. A suggestion was given by MDOT to place the specimens in a liquid silicone bath. The temperature of the liquid silicone bath rose very slowly, which allowed the testing of more than one specimen at one time. The liquid silicone bath was set inside a convenient refrigerator. Prior to testing, the bath was removed from the refrigerator and allowed to rise to 40 °F. The temperature of the bath was monitored using a high precision temperature probe with an guaranteed accuracy of ± 0.5 °F. Specimens were allowed to cool in the liquid silicone bath in the refrigerator at least three hours prior to testing to induce uniform temperatures in the thickness. A maximum of six charpy specimens were tested in one sequence.

The fracture toughness results of damaged-repaired steel were compared to the results of undamaged steel. One of the comparisons that were conducted was the Student's t-test, which dominantly compares the mean values of two samples and thus determines a statistical difference between the data sets. Student's t-tests were conducted directly between the damaged-repaired specimens and the undamaged

specimens using Equation 4.8 [*5*]. In Equation 4.8, μ_i, n_i, and σ_i, represent the means, number of samples, and standard deviations of the undamaged (subscript u) or the damaged-repaired (subscript dr) fracture toughness results.

$$t = \frac{\left|\mu_u - \mu_{dr}\right|}{\sqrt{\left(\frac{n_u + n_{dr}}{n_u * n_{dr}}\right)\left(\frac{\sigma_u^2}{n_u - 1} + \frac{\sigma_u^2}{n_u - 1}\right)}} \qquad (4.8)$$

Student's *t*-test deals with the problems associated with inference based on "small" samples. The t-tests assume two normally distributed data sets and the inquiry reduces to whether the likely ranges of the data sets overlap or if they do not overlap. The t-test formulas assume that each data point is independent of the other measurements and that the two data sets are independent or unpaired of each other. Numerous tables have been published in statistical textbooks that measure the probability distribution that two data sets will overlap in a comparable method as the more customary z-test, which is used for larger data sets. The probability of the null hypothesis represents the probability that the means of two samples are statistically similar and is a function of the *t*-result and the degrees of freedom *ν*. The degrees of freedom are computed using Equation 4.9.

$$\nu = n_u + n_{dr} - 2 \qquad (4.9)$$

Numerous books have published statistical tables for predicting the probability of the null hypothesis as a function of the *t*-result and the degrees of freedom. However, the values in these tables are limited to critical values for the probability such as 0.25, 0.1, 0.05, and 0.025 [*5*]. Hence, statistical software available from a website of the physics department at the College of Saint Benedict and Saint John's University was used to compute the probability of null hypothesis [*6*]. To verify this software, some values were compared to a table in Ref. [*5*]. An example compares the undamaged fracture toughness results of A36 steel and the results of Specimen A36-60-25-2 where the statistical software yielded a probability of null hypothesis of 0.050. The value in Ref. [5] is equal to 0.025 and is multiplied by 2 to consider both ends of a probability distribution. Therefore, the statistical software is verified.

4.9.3 Rockwell hardness tests

Rockwell hardness tests were conducted on the multiple damage-heat straightening repair specimens according to ASTM E18 using the type B-scale with a steel ball indenter. The Rockwell apparatus was calibrated each day of testing using standardized test blocks with a known hardness value of either 60.4 (± 1.0) or 80.3 (± 1.0). The tests were conducted to determine how heat straightening affects the hardness of the material and to investigate relationships between the resulting hardness and ultimate strengths. One charpy v-notch specimen was required for conducting the Rockwell hardness tests and preparation for microstructure analysis. The charpy specimen identified as Specimen 2 in Figures 4.13 and 4.19 was used. This specimen is located in the center of the upper half of the test area with its center located at the quarter thickness. Four Rockwell hardness tests were conducted on each charpy specimens at the estimated locations shown in Figure 4.47.

4.9.4 Microstructure Investigations

Investigations were conducted to discover how multiple damage-heat straightening repairs affect the microstructure of steel. The charpy specimens used to conduct Rockwell hardness tests were also used for the microstructure investigations. The specimens were prepared in accordance to ASTM E3. These

procedures gave guidelines on grinding and polishing the specimens. Fine grinding was conducted by rubbing the specimen on a sequence of 240, 320, 400, and 600-grit abrasive papers. Aqueous suspensions of 600-grit, 5.0-μm, 0.3-μm, and 0.05-μm aluminum oxide or alumina powder were utilized to provide a well-polished finish. From ASTM E407-93, a proper etchant solution was chosen. The specimens were etched with a solution composed of 2-2.5 mL nitric acid (HNO_3) and 100 mL ethanol.

The etched specimens were placed under a metallurgical microscope with a photo micrographic camera attached. The camera was calibrated using high precision vernier calipers to a magnification of 24X. The actual magnification viewed as a digital file was computed by multiplying the lens magnification by 24, which limited the possible magnifications for analysis to 120X, 240X, 480X, and 1200X. Dependent on the steel type, magnifications of either 240X or 480X were chosen for determining the grain sizes.

The process of preparing the specimens for microstructure was tedious and sometimes difficult. Extra preparation was conducted when necessary to obtain improved pictures. Some pictures appear better than others do. All of the final pictures were sure to display grain boundaries and the capability to distinguish between pearlite and proeutectoid ferrite grains.

The grain size of each specimen was determined using the general line intercept procedure outlined in ASTM E112. This method involves drawing a number of random lines with a known length and counting the number of grains that intercept each line. The process is illustrated using the A36 undamaged specimen in Figure 4.48. Twelve 6-inch lines were drawn on each image using PowerPoint with the pattern shown in Figure 4.48. Each line actually represents 0.025 in. (obtained from 6/240) of the specimen. The total number of grains intercepting all lines was divided by twelve to find the average number of grains per line. The grain size diameter was computed by dividing the length of one line (0.025 in.) by the average number of grains per line.

Section 2.4.5 discussed the effects of grain size on the structural properties of steel when alloying elements and other variables are constant. A finer-grained microstructure has a higher strength and fracture toughness than a coarse-grained microstructure. The hardness of the steel increases slightly and the ductility of the steel decreases. In general, a finer grained structure may be more desirable in damage-repaired steel as its impact may balance the dislocation defects that still exist in the microstructure.

Section 2.4.3 discussed the possible microstructural constituents of steel and their effects on the material properties. After reviewing photographs of the microstructure, the formation of bainite and martensite do not result from heat straightening. The resulting microstructures consist of ferrite and pearlite, as they did prior to damage. Pearlite consists of cementite, which is a harder, stronger, yet more brittle structure than ferrite. Therefore, the resulting amount of pearlite in the microstructure was a concern in this research project. The problem is that the amount of pearlite is a function of the spot chosen for the photograph of the microstructure as illustrated in Figure 2.9. Therefore, the researchers were interested in significant trends in the data. All values are provided in tables in Chapters 5, 7, and 8 for completeness. The percentage of pearlite grains was established by dividing the number of pearlite grains intercepting all lines by the total number of grains intercepting all lines.

The microstructure investigations may not be as accurate as other material property tests performed. The variation of the material itself may vary substantially throughout the original plates.

4.10 REFERENCES

1. Callister, W.D., *Material Science and Engineering, an Introduction*, Fourth Edition, John Wiley & Sons Inc., New York, New York, 1997.
2. Avent, R. R., Mukai, D.J. and Robinson, P.F., *Journal of Structural Engineering*, ASCE, Vol.126, No. 7, July 2000, pp. 755-763.
3. ABAQUS, *ABAQUS/Standard User's Manuals*, Volumes I-III Hibbitt, Karlsson, and Sorenson, Inc., Pawtucket, Rhode Island, 1998.
4. ASTM, "Standard Test Methods and Definitions for Mechanical Testing of Steel Products," A370-97a, West Conshohocken, PA, 1999.
5. Ayyub, B.M. and McCuen, R. H., Probability, Statistics, and Reliability for Engineers and Scientists, Chapman and Hall/CRC, Washington, D.C., 2003.
6. Physics Department of Saint Benedict and Saint John's University, *Student's T-Test*, <http://www.physics.csbsju.edu/stats/t-test.html>, (October 1, 2004).

CHAPTER 4: TABLES

Table 4.1
Planned test matrix for A36 laboratory-scale specimens

Damage Strain (ε_d)	*Restraining Stress (σ_r)*	*Number of Repair Cycles (N_r)*	*Specimen Name*
30 ε_y	0.25 σ_y	1	A36-30-25-1
		2	A36-30-25-2
		3	A36-30-25-3
		4	A36-30-25-4
		5	A36-30-25-5
	0.50 σ_y	1	A36-30-50-1
		2	A36-30-50-2
		3	A36-30-50-3
		4	A36-30-50-4
		5	A36-30-50-5
60 ε_y	0.25 σ_y	1	A36-60-25-1
		2	A36-60-25-2
		3	A36-60-25-3
		4	A36-60-25-4
		5	A36-60-25-5
	0.50 σ_y	1	A36-60-50-1
		2	A36-60-50-2
		3	A36-60-50-3
		4	A36-60-50-4
		5	A36-60-50-5
90 ε_y	0.25 σ_y	1	A36-90-25-1
		2	A36-90-25-2
		3	A36-90-25-3
		4	A36-90-25-4
		5	A36-90-25-5
	0.50 σ_y	1	A36-90-50-1
		2	A36-90-50-2
		3	A36-90-50-3
		4	A36-90-50-4
		5	A36-90-50-5

Table 4.2
Planned test matrix for A588 laboratory-scale specimens

Damage Strain (ε_d)	*Restraining Stress (σ_r)*	*Number of Repair Cycles (N_r)*	*Specimen Name*
30 ε_y	0.25 σ_y	1	A588-30-25-1
		2	A588-30-25-2
		3	A588-30-25-3
		4	A588-30-25-4
		5	A588-30-25-5
	0.50 σ_y	1	A588-30-50-1
		2	A588-30-50-2
		3	A588-30-50-3
		4	A588-30-50-4
		5	A588-30-50-5
60 ε_y	0.25 σ_y	1	A588-60-25-1
		2	A588-60-25-2
		3	A588-60-25-3
		4	A588-60-25-4
		5	A588-60-25-5
	0.50 σ_y	1	A588-60-50-1
		2	A588-60-50-2
		3	A588-60-50-3
		4	A588-60-50-4
		5	A588-60-50-5
90 ε_y	0.25 σ_y	1	A588-90-25-1
		2	A588-90-25-2
		3	A588-90-25-3
		4	A588-90-25-4
		5	A588-90-25-5
	0.50 σ_y	1	A588-90-50-1
		2	A588-90-50-2
		3	A588-90-50-3
		4	A588-90-50-4
		5	A588-90-50-5

Table 4.3
Planned test matrix for A7 laboratory-scale specimens

Damage Strain (ε_d)	*Restraining Stress (σ_r)*	*Number of Repair Cycles (N_r)*	*Specimen Name*
30 ε_y	0.25 σ_y	1	A7-30-25-1
		3	A7-30-25-3
		5	A7-30-25-5
	0.50 σ_y	1	A7-30-50-1
		3	A7-30-50-3
		5	A7-30-50-5
60 ε_y	0.25 σ_y	1	A7-60-25-1
		3	A7-60-25-3
		5	A7-60-25-5
	0.50 σ_y	1	A7-60-50-1
		3	A7-60-50-3
		5	A7-60-50-5
90 ε_y	0.25 σ_y	1	A7-90-25-1
		3	A7-90-25-3
		5	A7-90-25-5
	0.50 σ_y	1	A7-90-50-1
		3	A7-90-50-3
		5	A7-90-50-5

Table 4.4
Test matrix for overheated A36 laboratory-scale specimens

Damage Strain (ε_d)	*Restraining Stress (σ_r)*	*Number of Repair Cycles (N_r)*	*Maximum Temperature (T_{max})*	*Specimen Name*
60 ε_y	0.25 σ_y	1	1400 ºF	A36-60-25-1-1400
		1	1600 ºF	A36-60-25-1-1600
		3	1400 ºF	A36-60-25-3-1400
		3	1600 ºF	A36-60-25-3-1600
	0.50 σ_y	1	1400 ºF	A36-60-50-1-1400
		1	1600 ºF	A36-60-50-1-1600
		3	1400 ºF	A36-60-50-3-1400
		3	1600 ºF	A36-60-50-3-1600
90 ε_y	0.25 σ_y	1	1400 ºF	A36-90-25-1-1400
		1	1600 ºF	A36-90-25-1-1600
		3	1400 ºF	A36-90-25-3-1400
		3	1600 ºF	A36-90-25-3-1600
	0.50 σ_y	1	1400 ºF	A36-90-50-1-1400
		1	1600 ºF	A36-90-50-1-1600
		3	1400 ºF	A36-90-50-3-1400
		3	1600 ºF	A36-90-50-3-1600

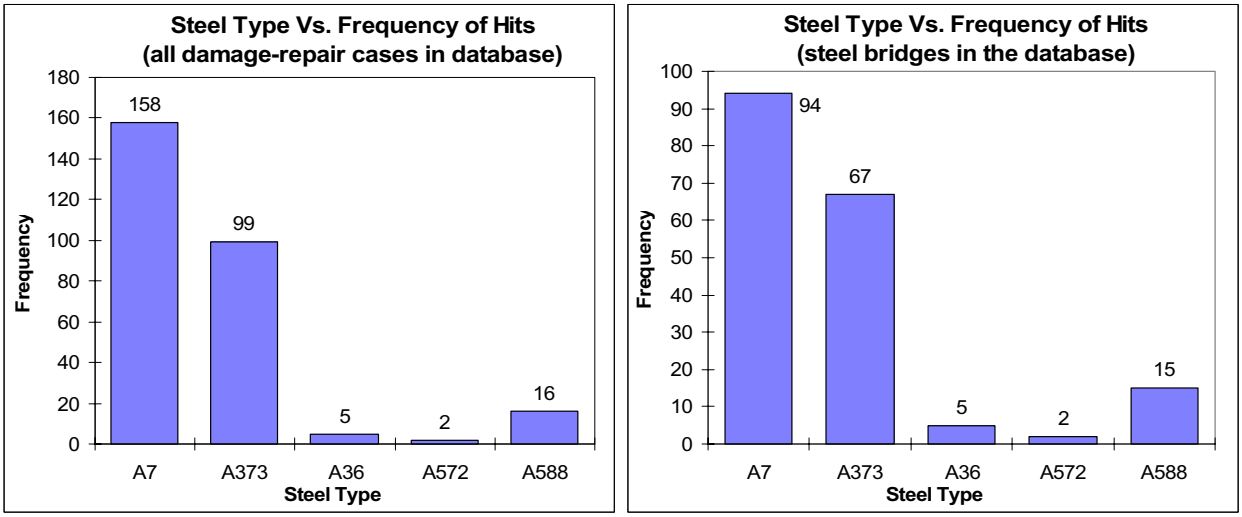

Figure 4.1
Results from high-load hits database analysis emphasizing relevant steel types

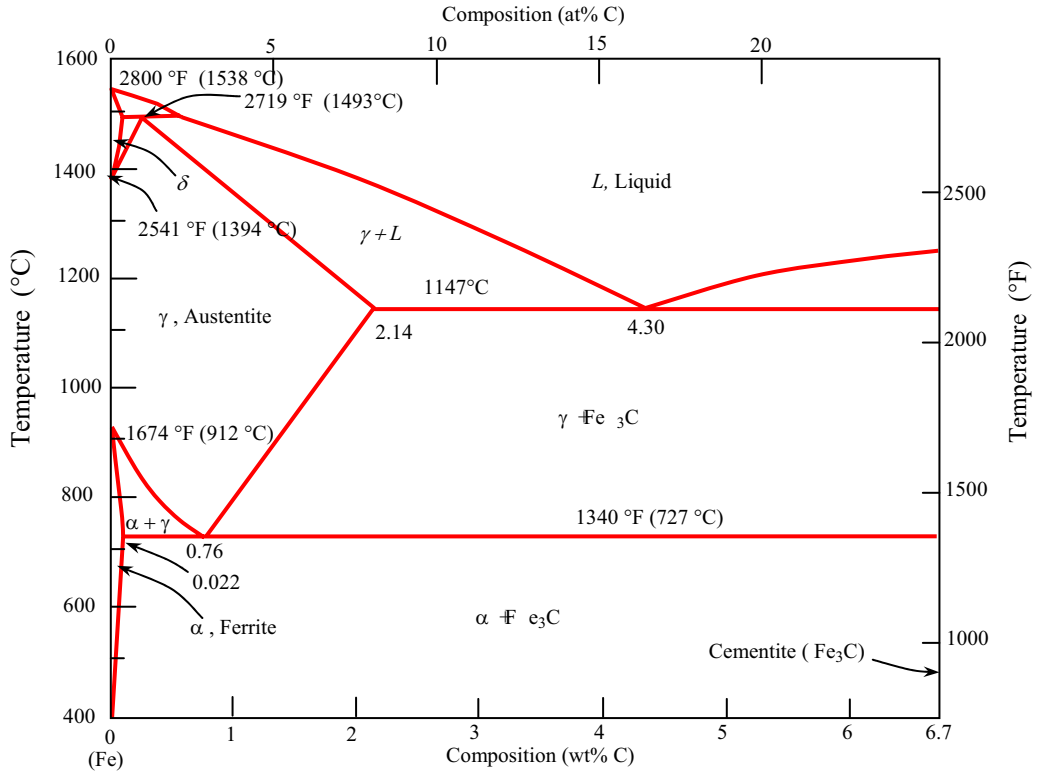

Figure 4.2
Iron-iron carbide phase diagram [*1*]

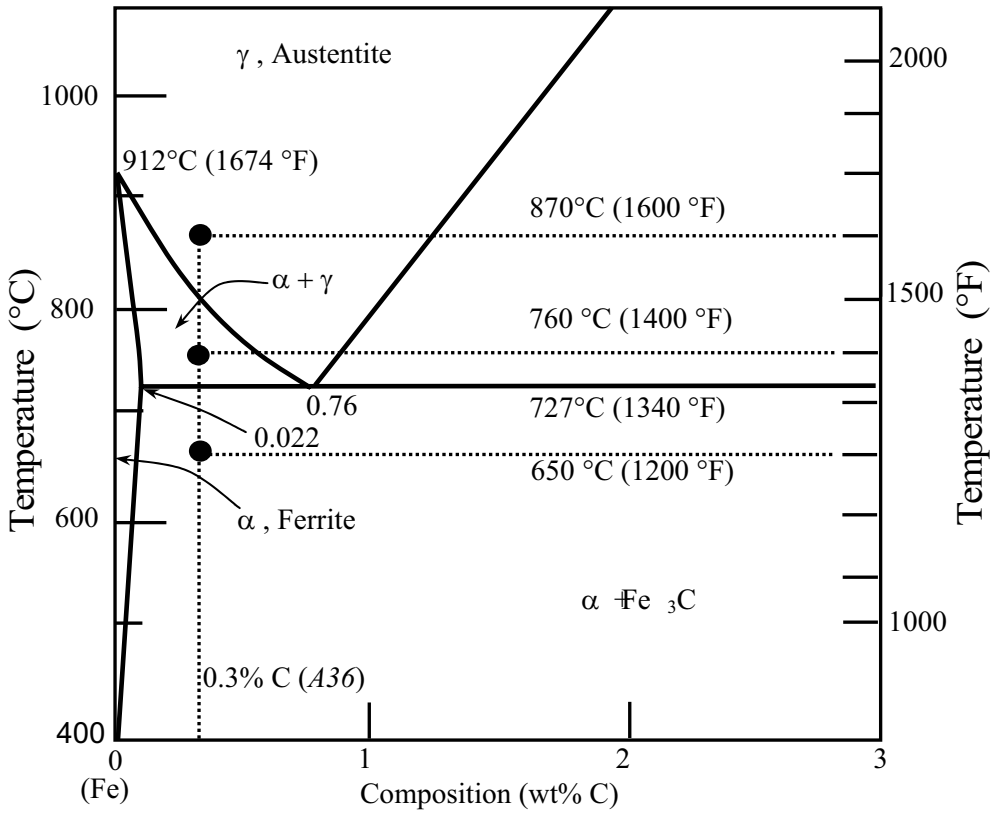

Figure 4.3
Temperatures located on the iron-iron carbide phase diagram for 0.3% carbon steel

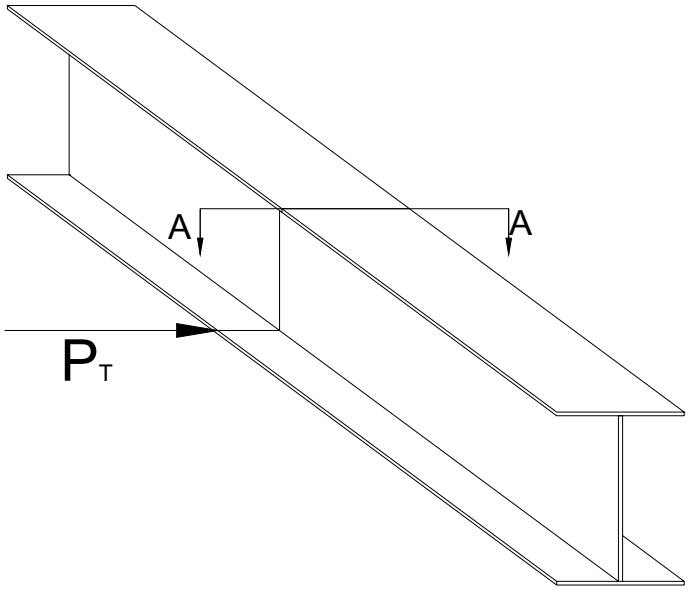

Figure 4.4
Illustration of a beam subjected to a lateral truck load P_T

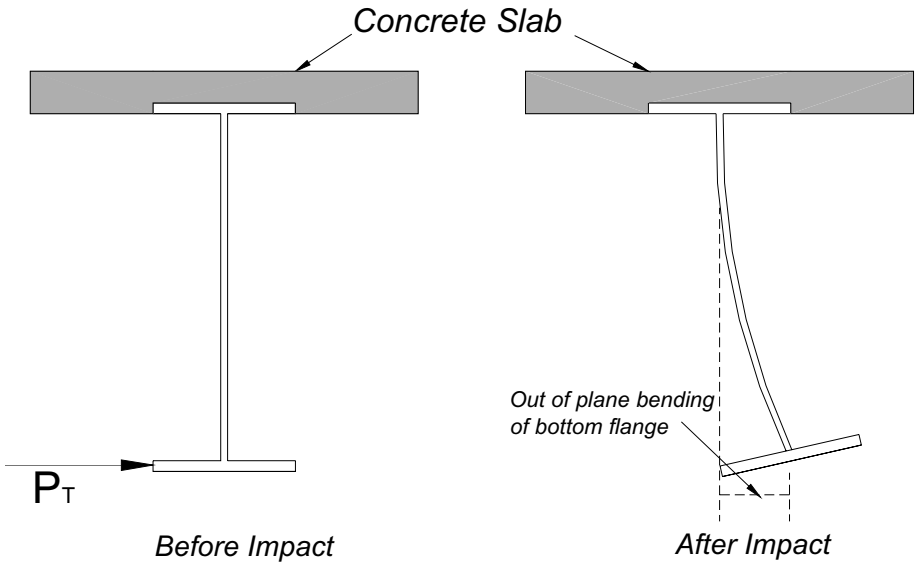

Figure 4.5
Composite beam subjected to out-of-plane movement due to truck load P_T (Section A-A)

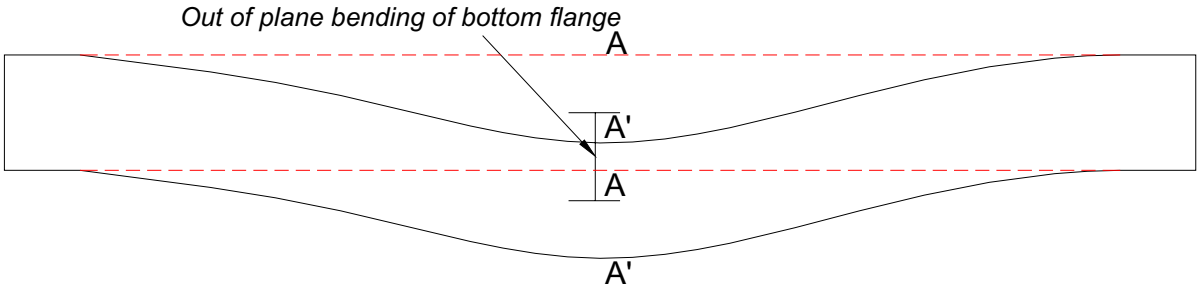

Figure 4.6
Out-of-plane movement of the bottom flange due to truck load P_T

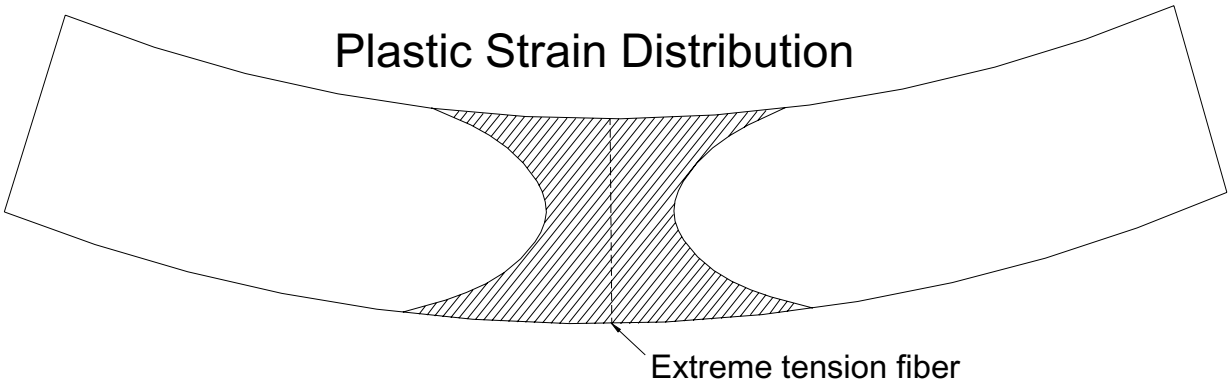

Figure 4.7
Plastic strain distribution of a damaged steel plate

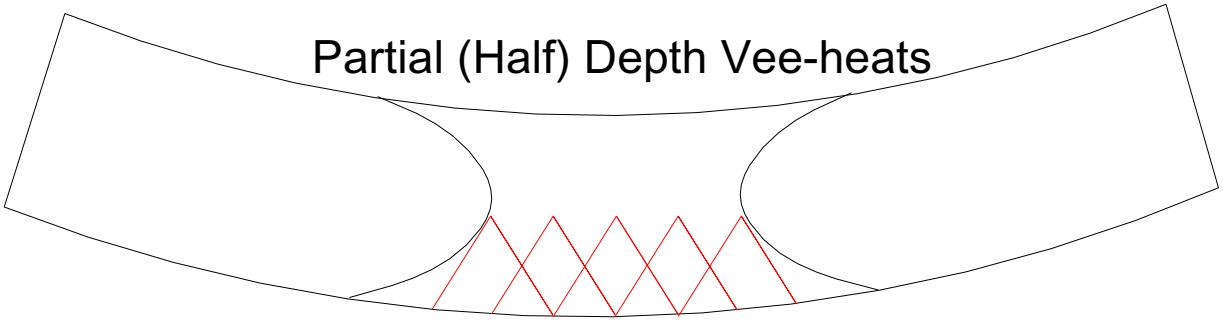

Figure 4.8
Partial depth Vee heats applied to the elongated side of a damaged steel plate

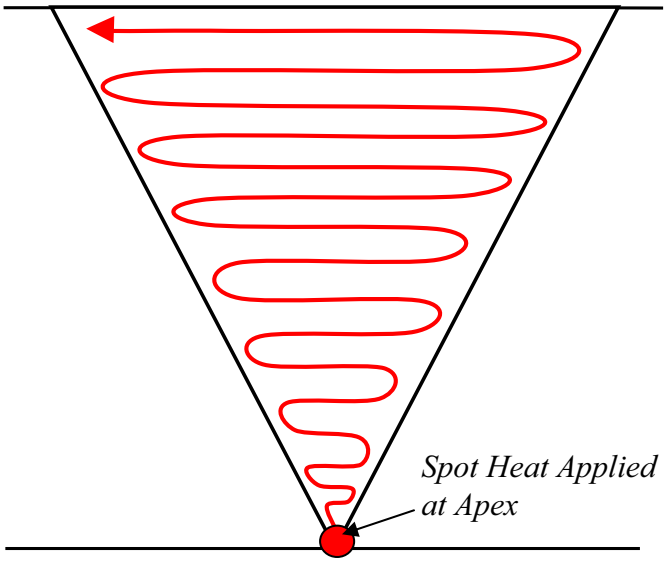

Figure 4.9
Serpentine movement of a Vee heat applied to a damage steel plate

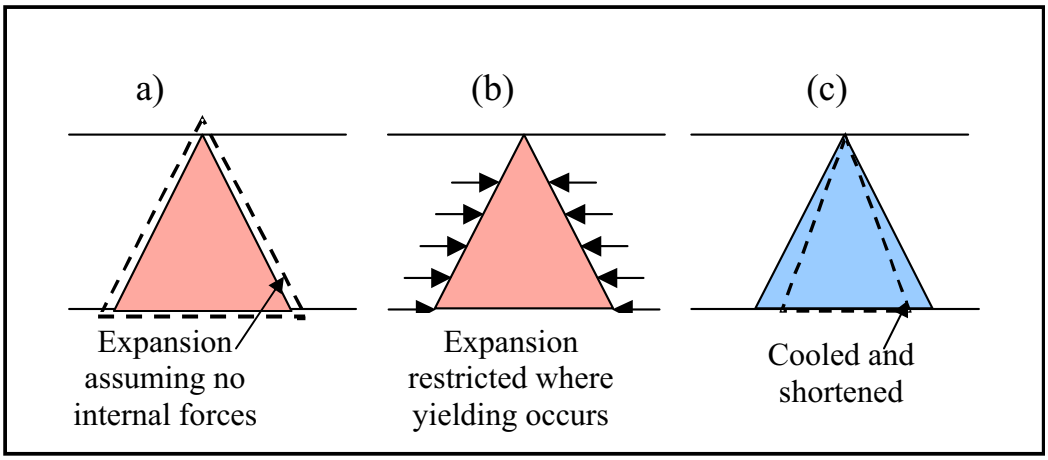

Figure 4.10
Fundamental mechanics of Vee heated steel

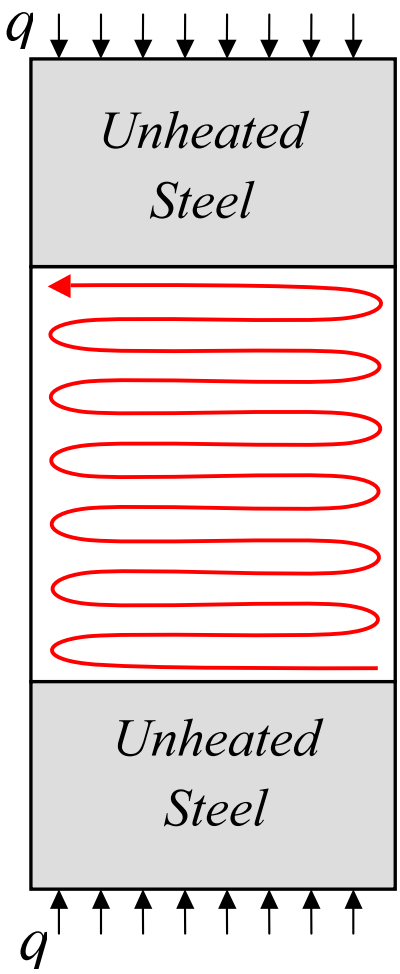

Figure 4.11
Fundamental mechanics of the strip heat that will be used for the repair in Task III

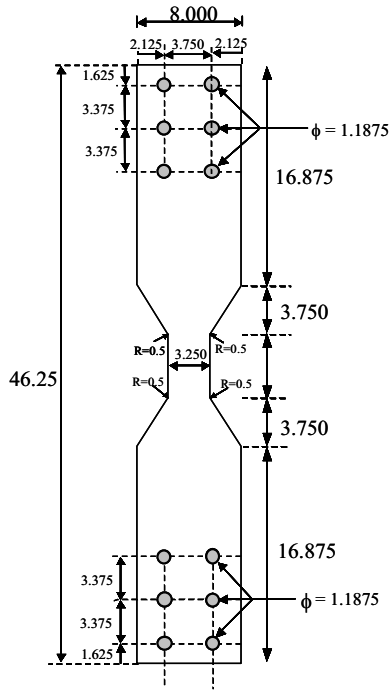

Test specimen thickness = 1.000 in.

Material = A36 or A588 steel

Figure 4.12
A588 and A36 small-scale test specimen design

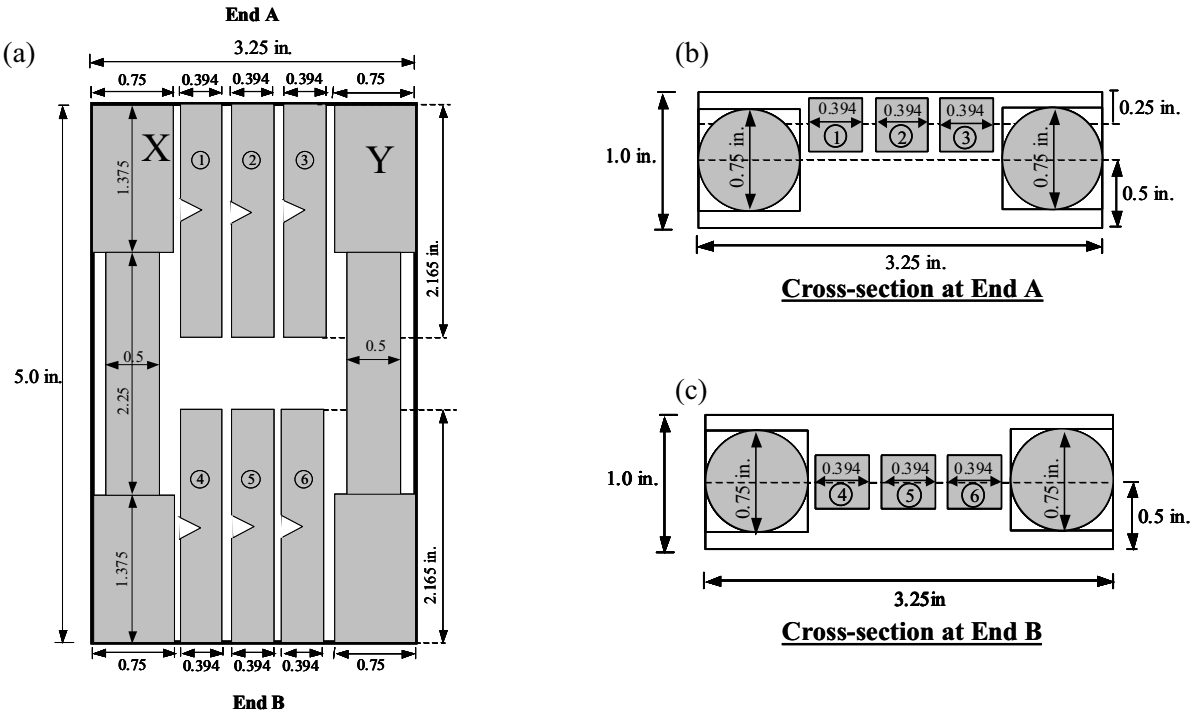

Figure 4.13
Removal of material testing coupons from the A36 and A588 test area

a) End conditions

b) Dents in the flange.

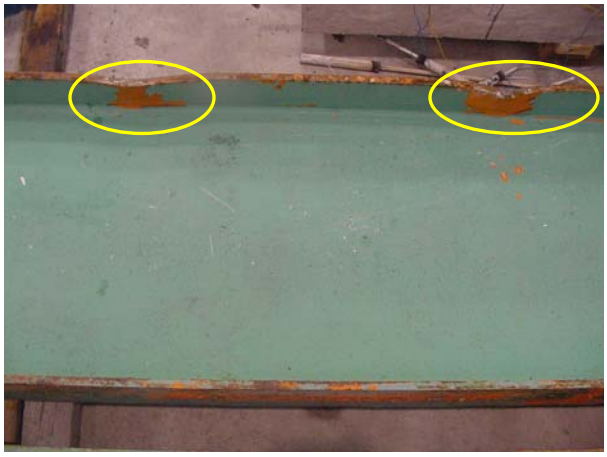

c) Beam used for the fabrication of small scale experimental tests.

Figure 4.14
Condition of W24 x76 A7 steel beams as received by the MSU researchers

a) Beam 1

b) Beam 2

c) Beam 3

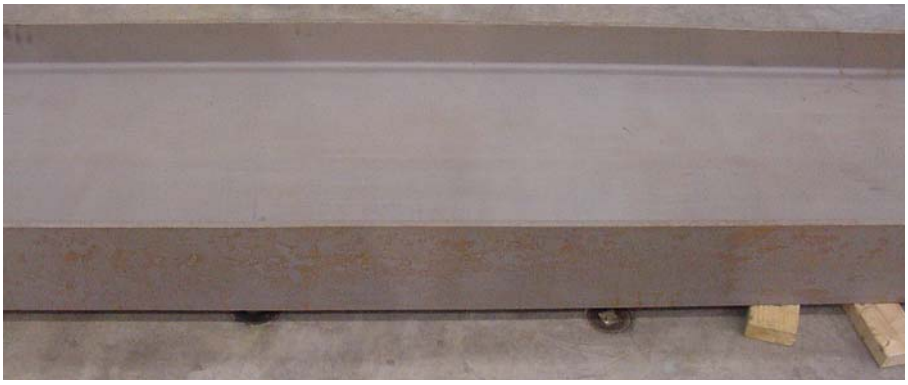

Figure 4.15
Three 93 in. A7 steel beams used for the fabrication of small-scale specimens

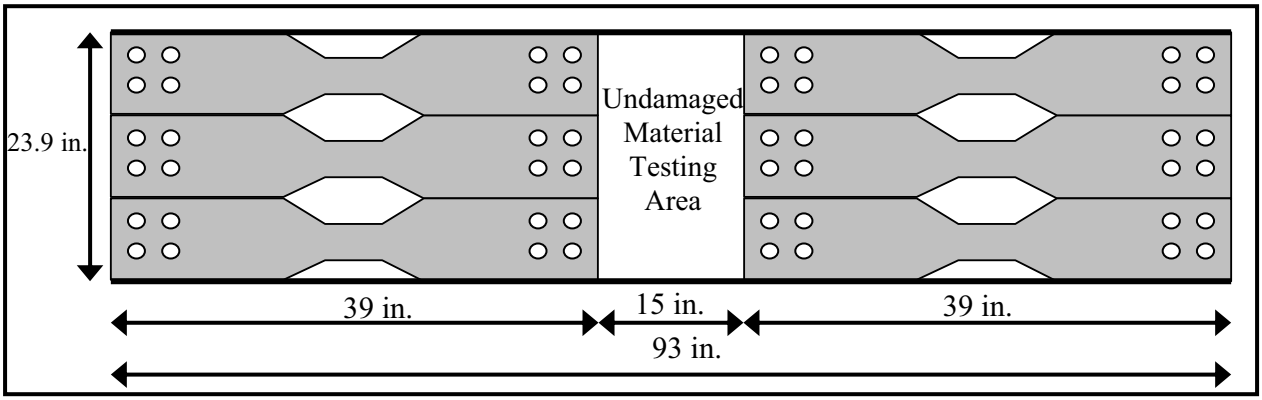

Figure 4.16
Location of six A7 steel specimens from W24x76 beam segment

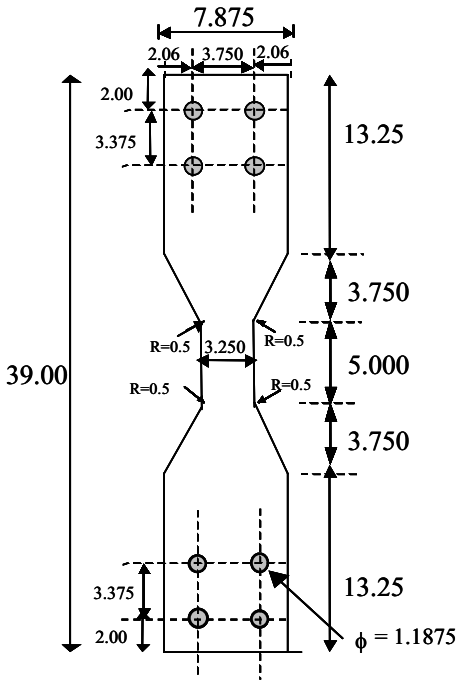

Test specimen thickness = 0.45 in.

Material = A7 steel

Figure 4.17
A7 small-scale test specimen design

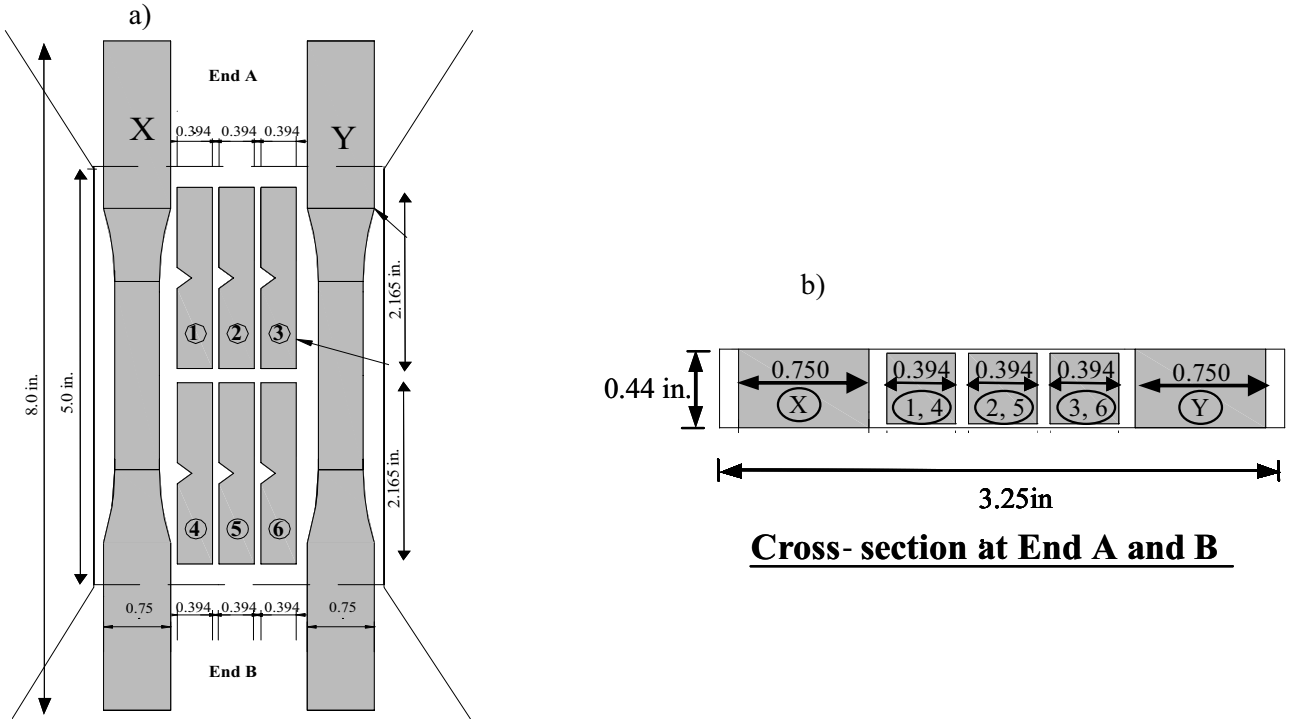

Figure 4.18
Removal of material testing coupons from A7 the test area

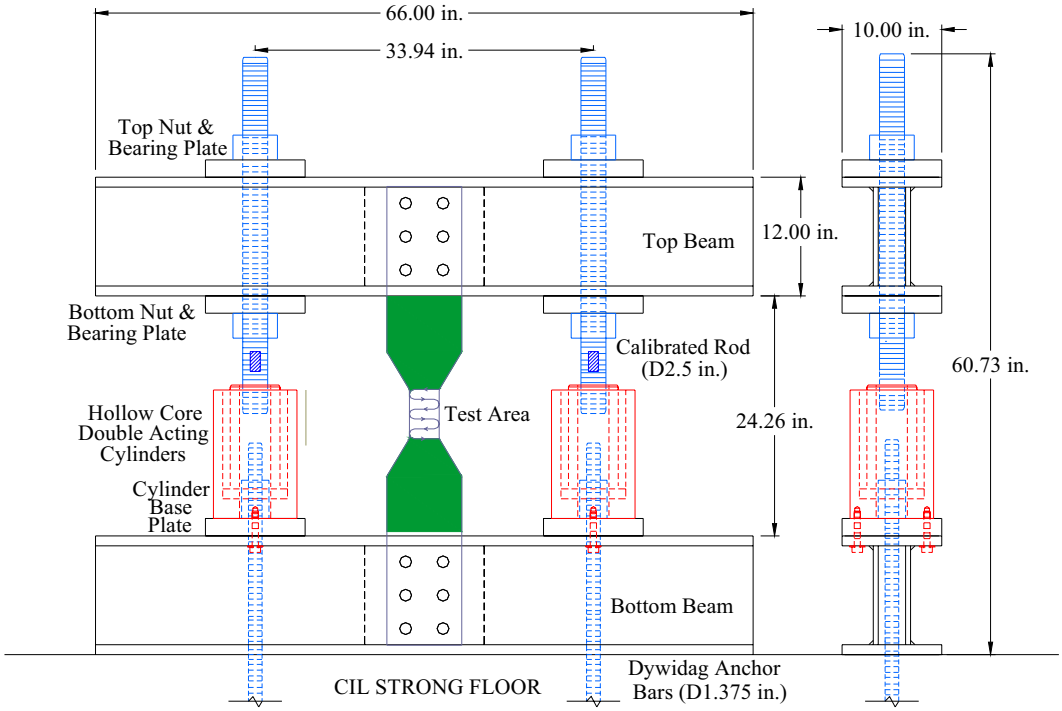

Figure 4.19
Planer test frame elevation and side views

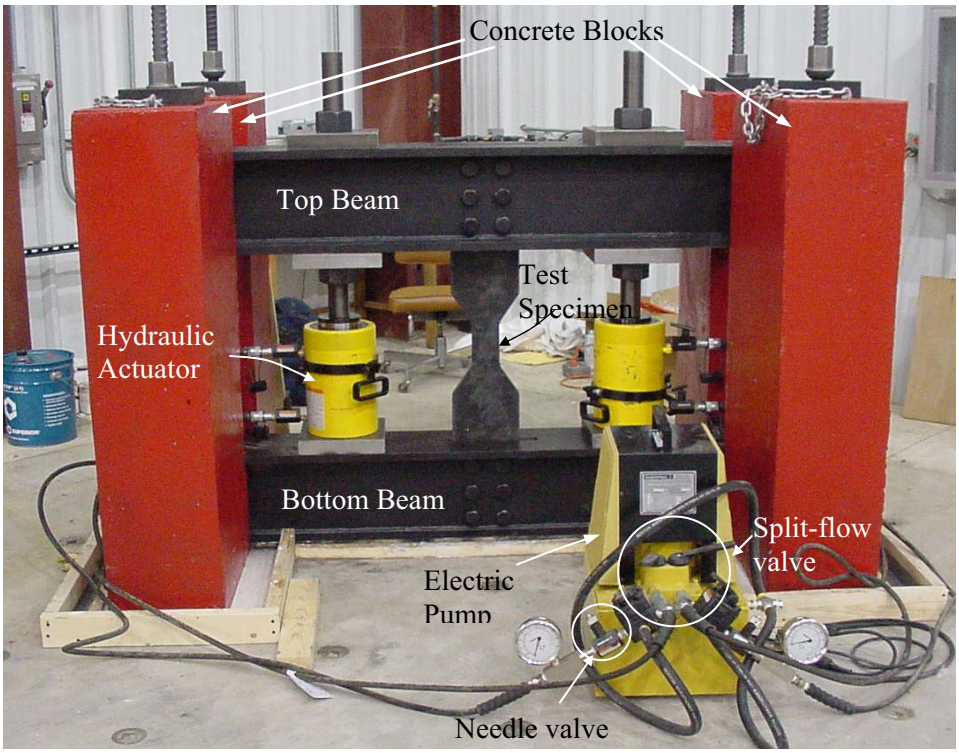

Figure 4.20
Photograph of test setup

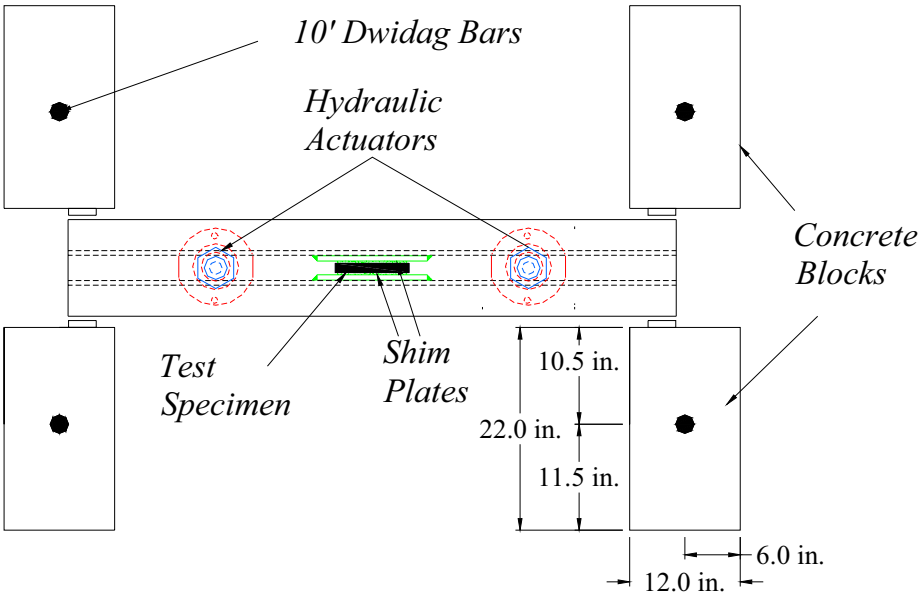

Figure 4.21
Plan view of planer test frame and out-of-plane restraints

Figure 4.22
Photograph of test setup being assembled

(a) Top Beam

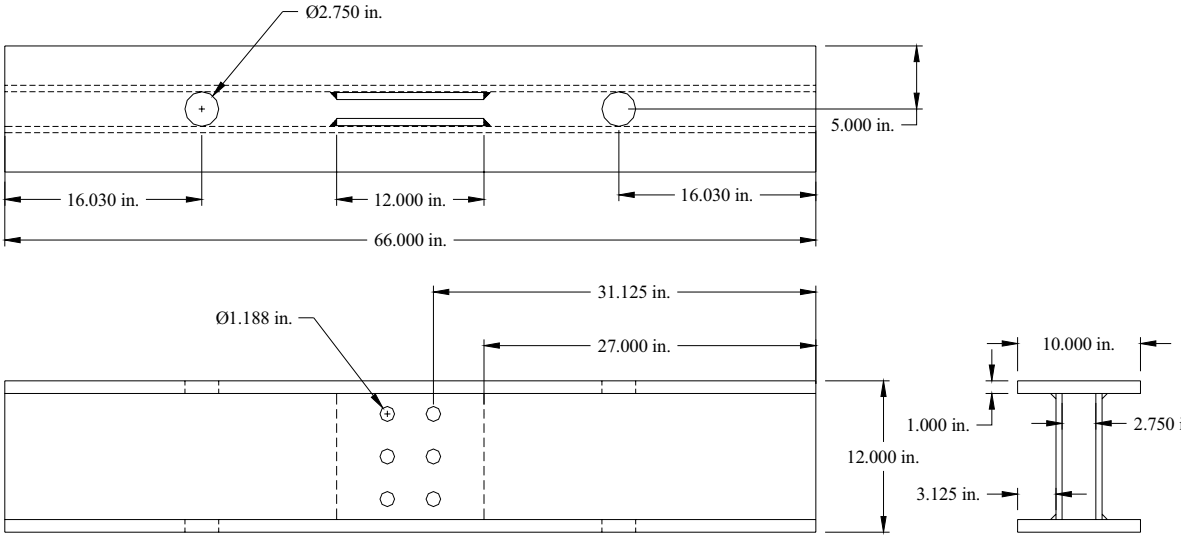

(b) Bottom Beam

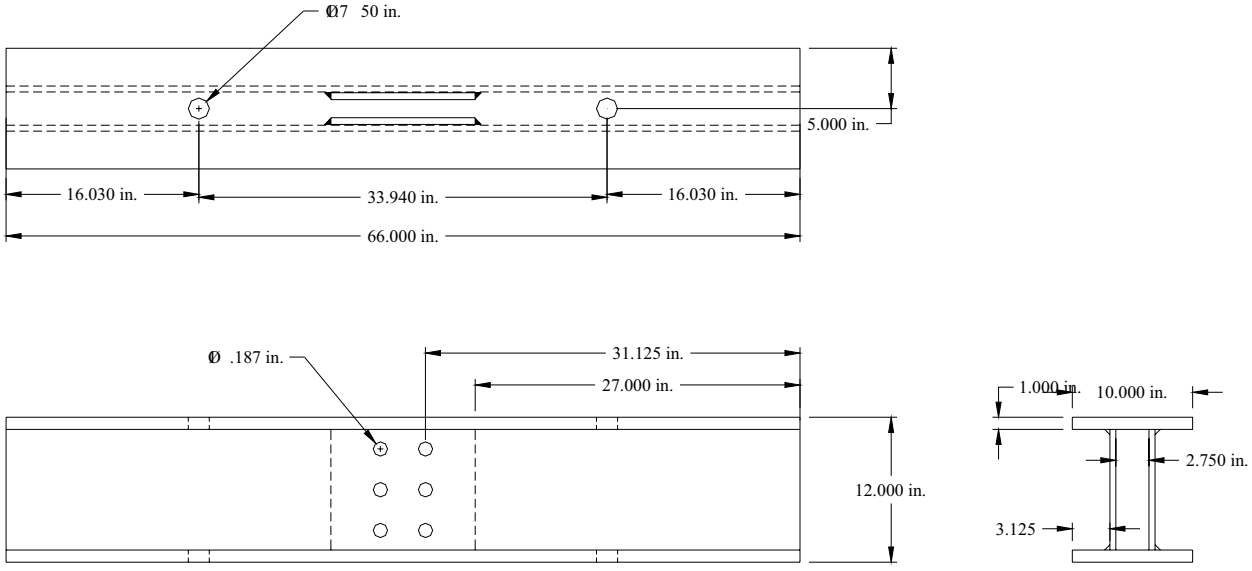

Figure 4.23
Design details of (a) top beam and (b) bottom beam

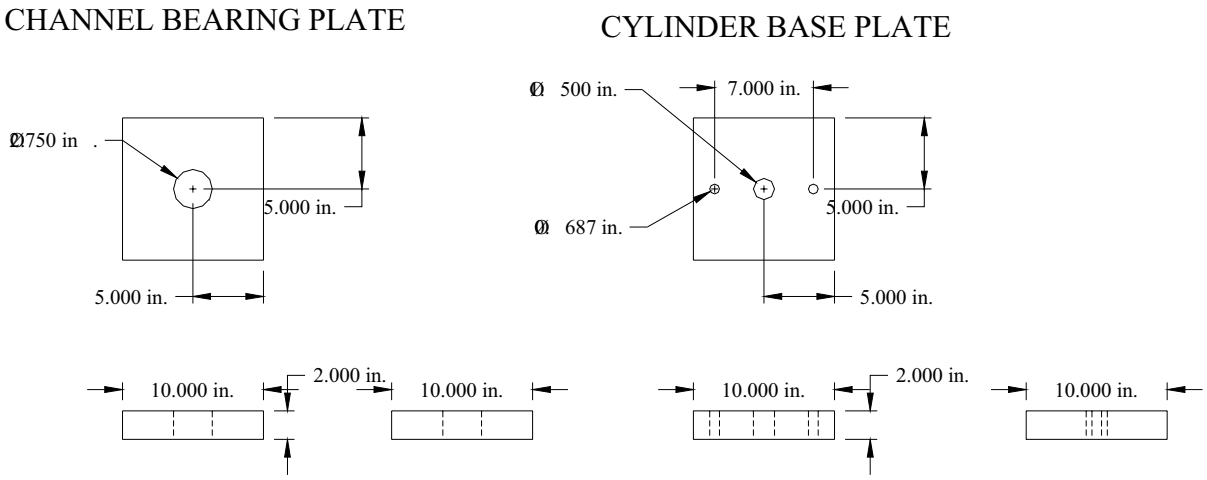

Figure 4.24
Design details of channel bearing and cylinder base plates

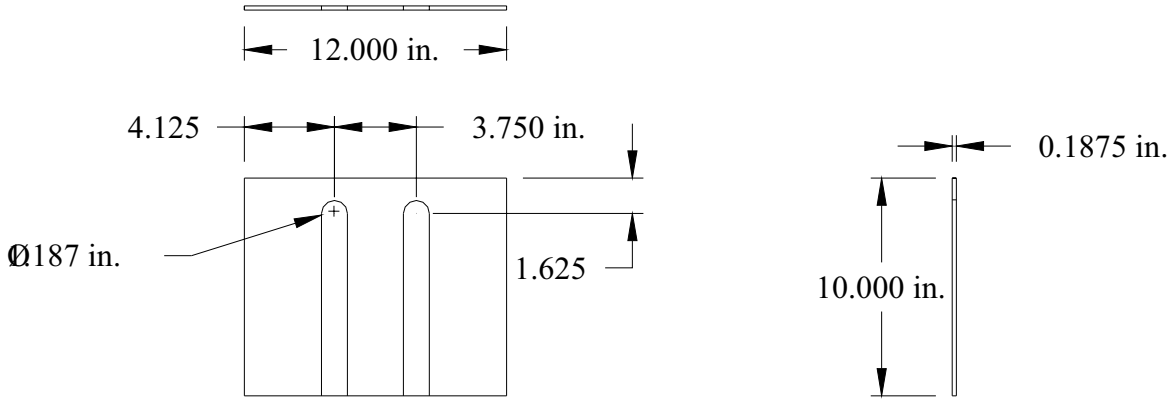

Figure 4.25
Design details of the shim plates

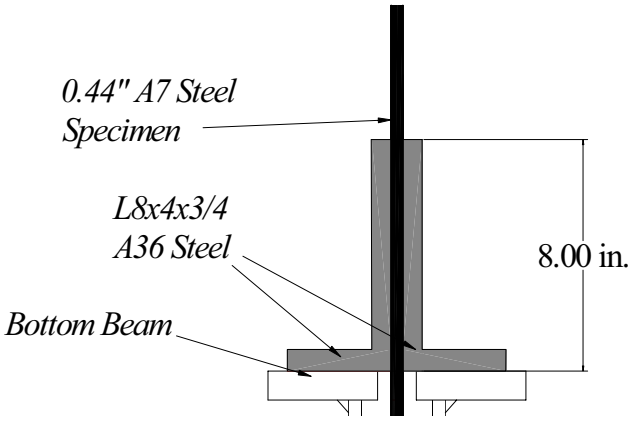

Figure 4.26
Schematic of angle sections used to reduce effective length of the A7 test specimen

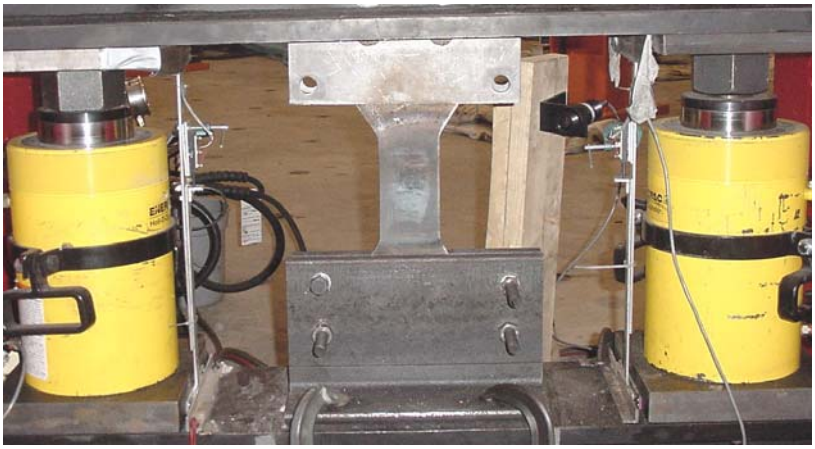

Figure 4.27
Adjustments to test setup to reduce the effective length for the A7 test specimen

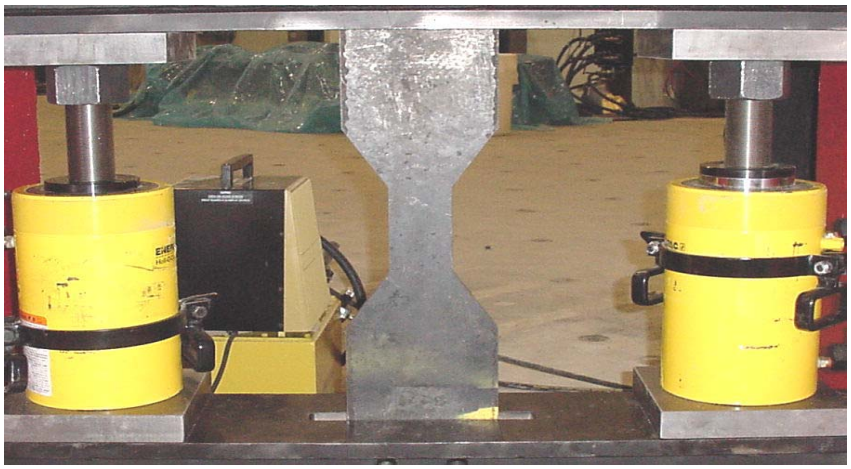

Figure 4.28
Test setup for the A36 and A588 specimens

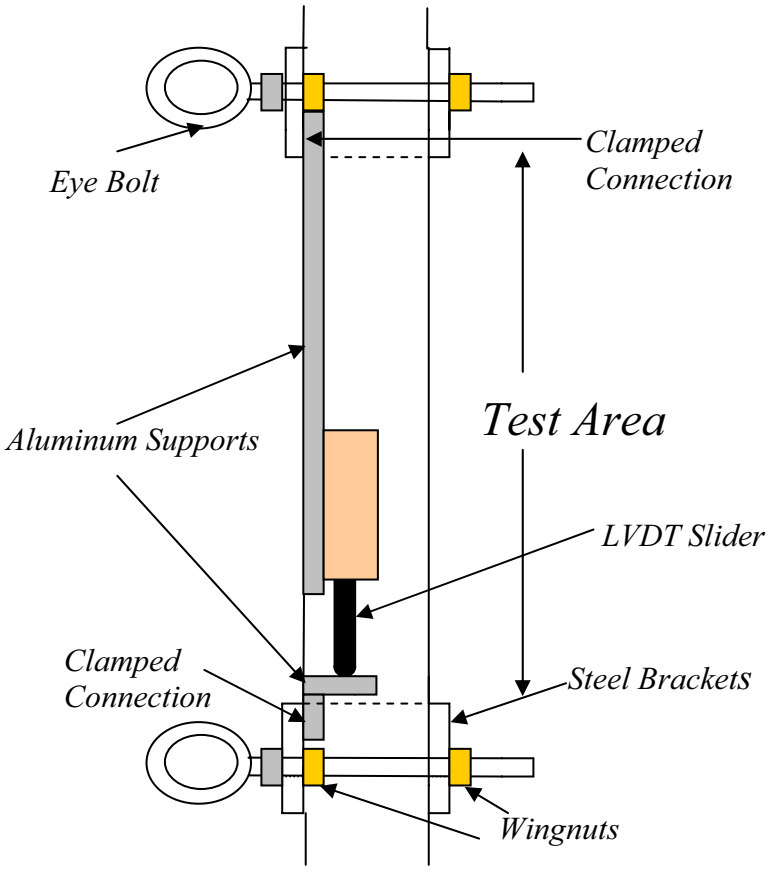

Figure 4.29
Schematic of displacement transducer setup measuring elongation of test area

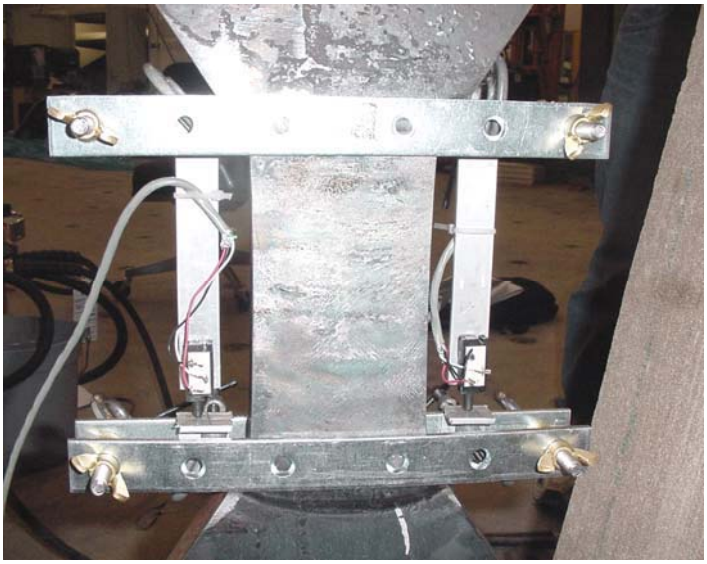

Figure 4.30
Photograph of displacement transducers attached to specimen test area

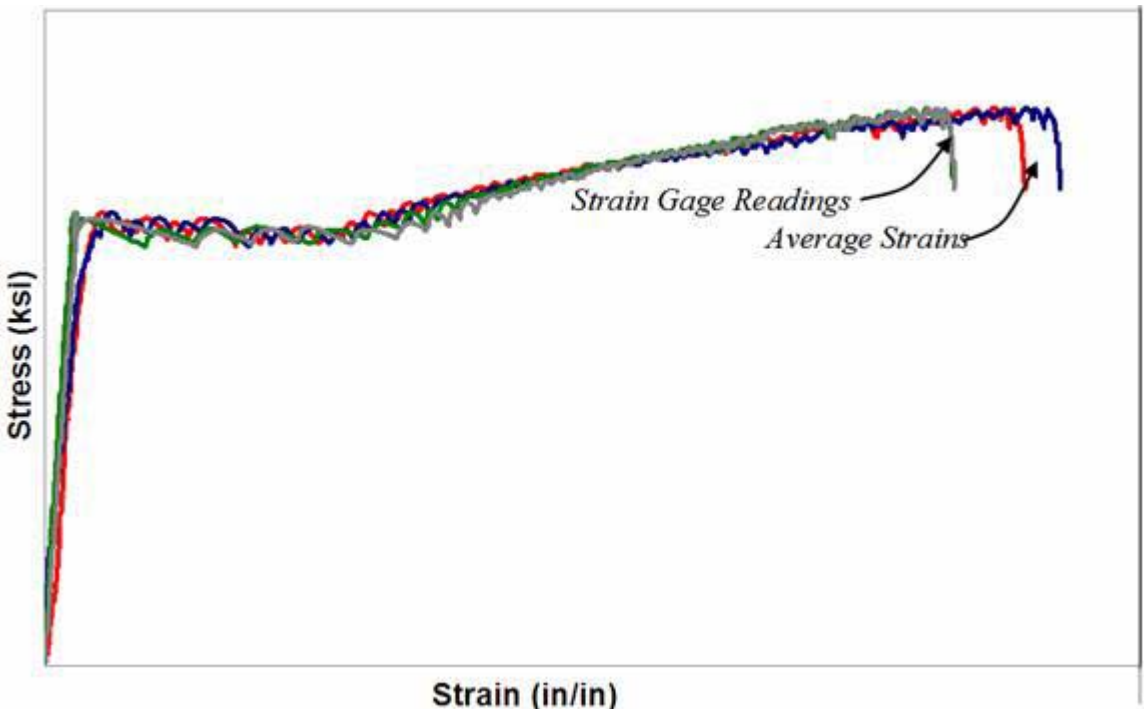

Figure 4.31
Example of stress-strain relationships measured during damage cycles

Figure 4.32
Application of the strip heat to the test area

Figure 4.33
Photograph of how the temperature at the surface of the steel was monitored

Figure 4.34
1.5 in. displacement transducer measuring the movement between the top and bottom beams

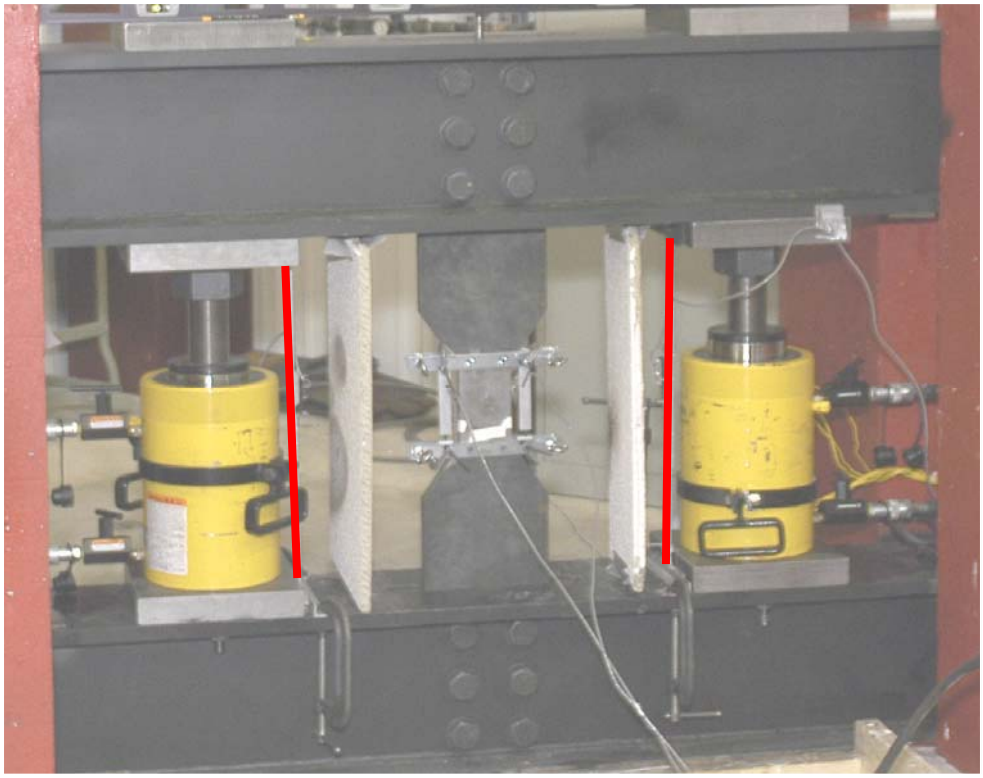

Figure 4.35
1.5 in. displacement transducer locations in respect to the test setup

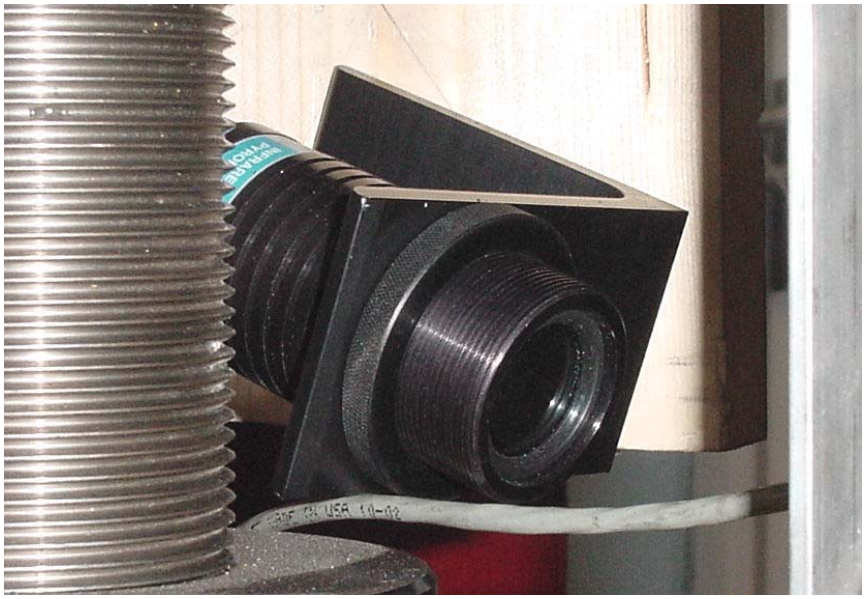

Figure 4.36
Infrared thermometer measuring temperature at the surface of the steel

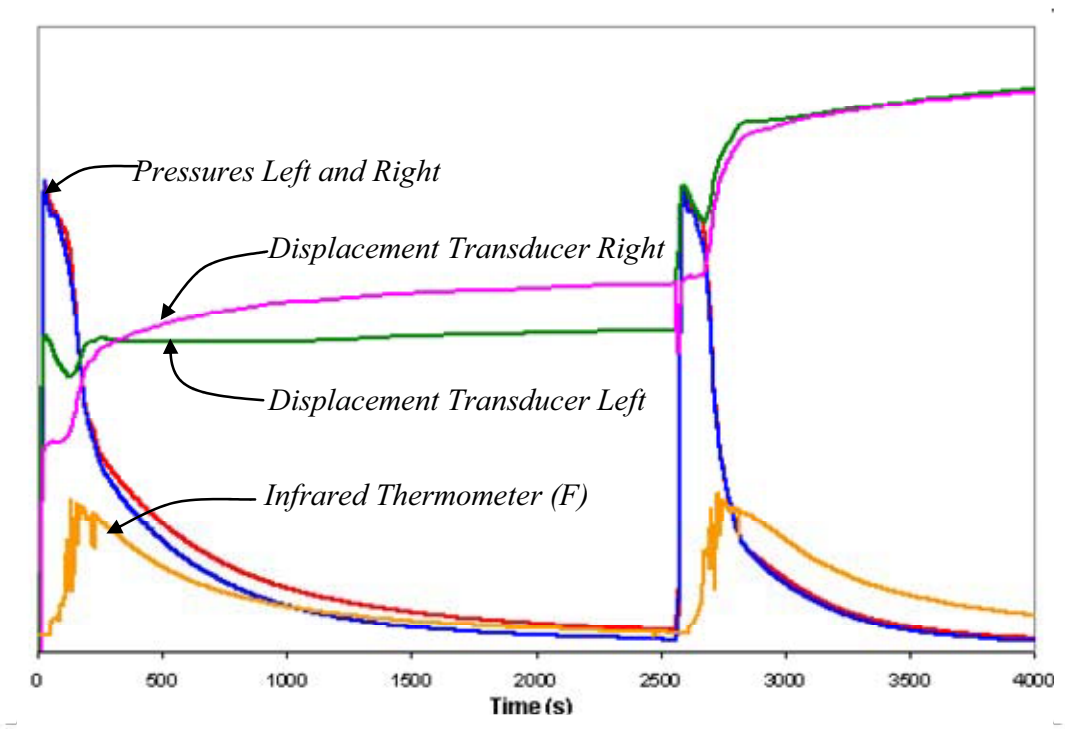

Figure 4.37
Instrumentation data being recorded during the experimental repair cycles

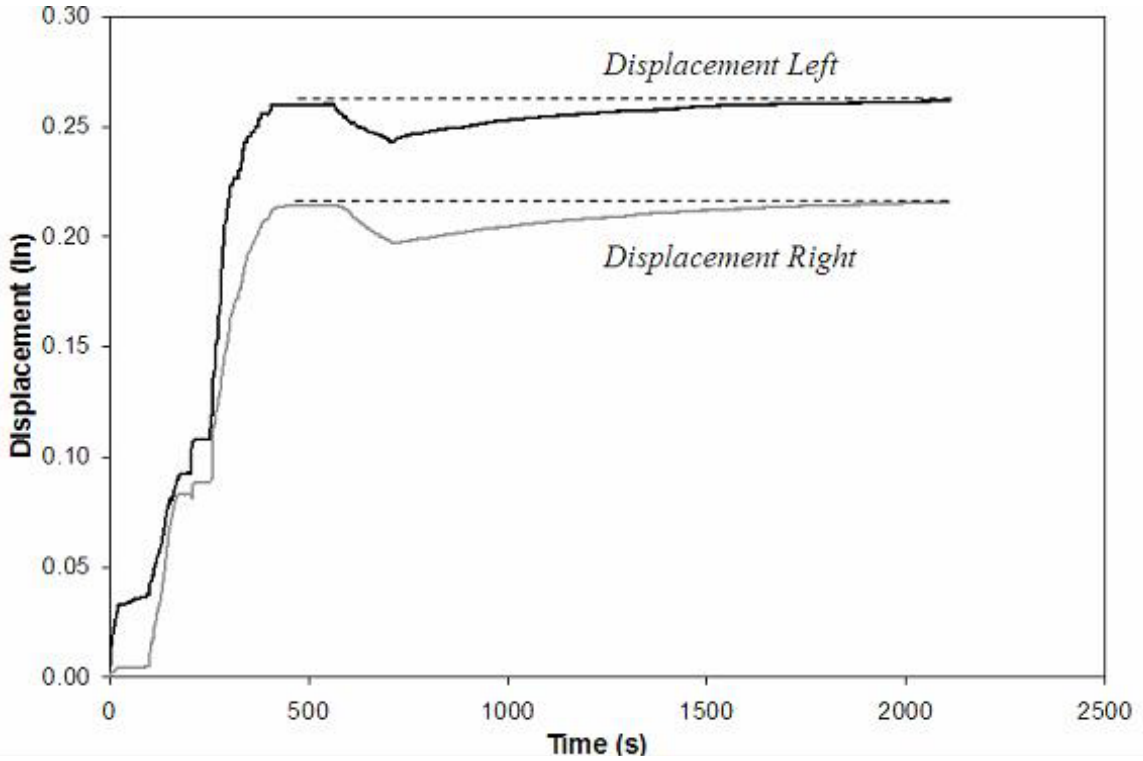

Figure 4.38
Displacements of trial specimen with an applied restraining stress of 0.25 σ_y

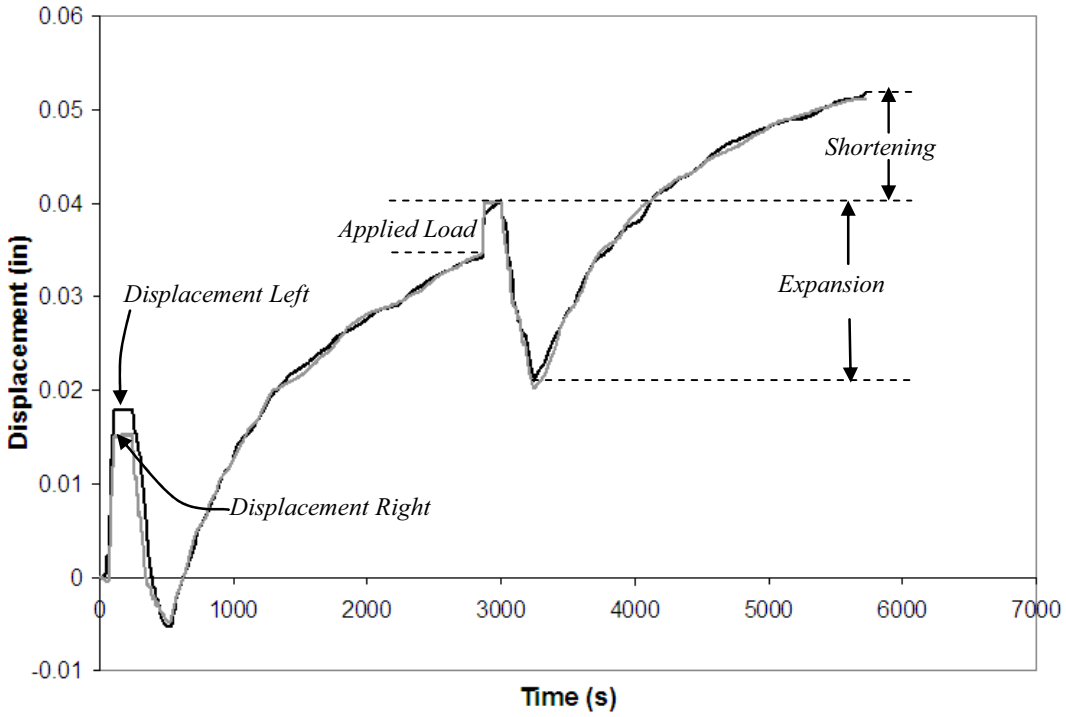

Figure 4.39
Displacements of trial specimen with an applied restraining stress of 0.50 σ_y

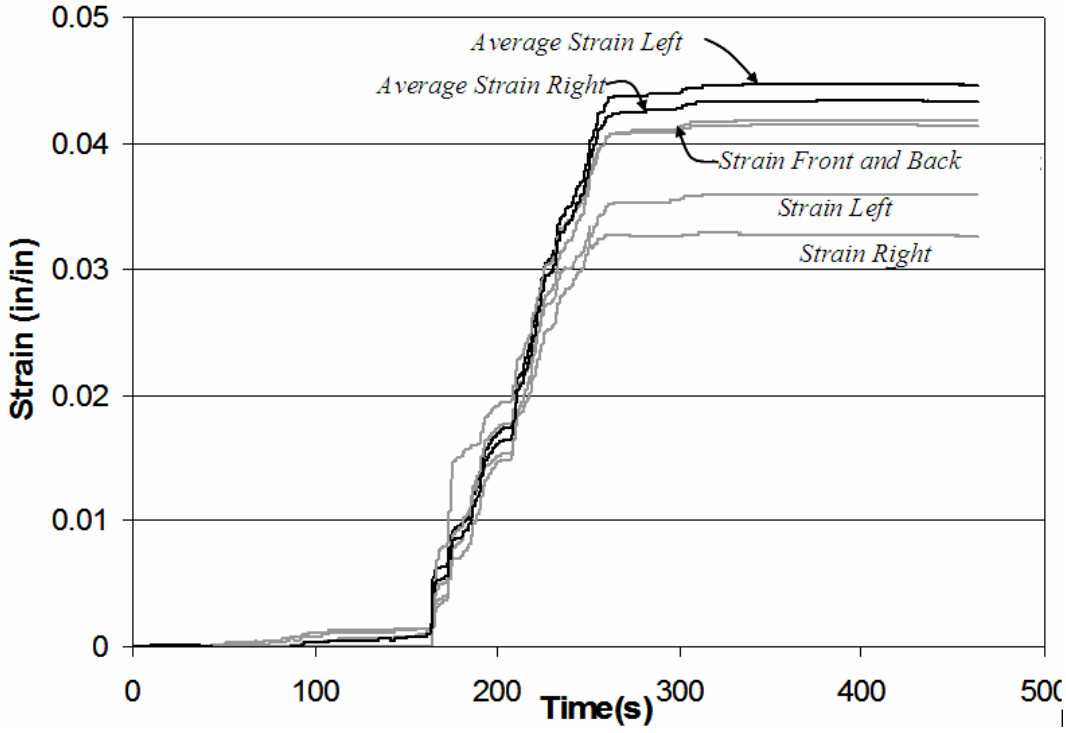

Figure 4.40
Strain gage readings for the first damage cycle of Specimen A36-30-40-2

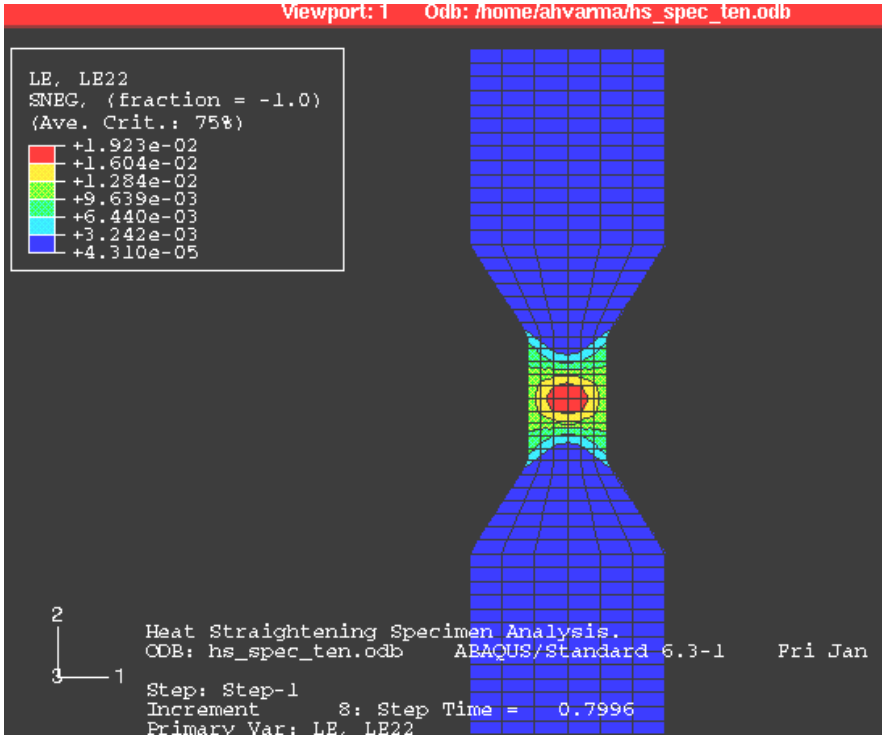

Figure 4.41
Finite element model of the A36 specimen subjected to tensile damage

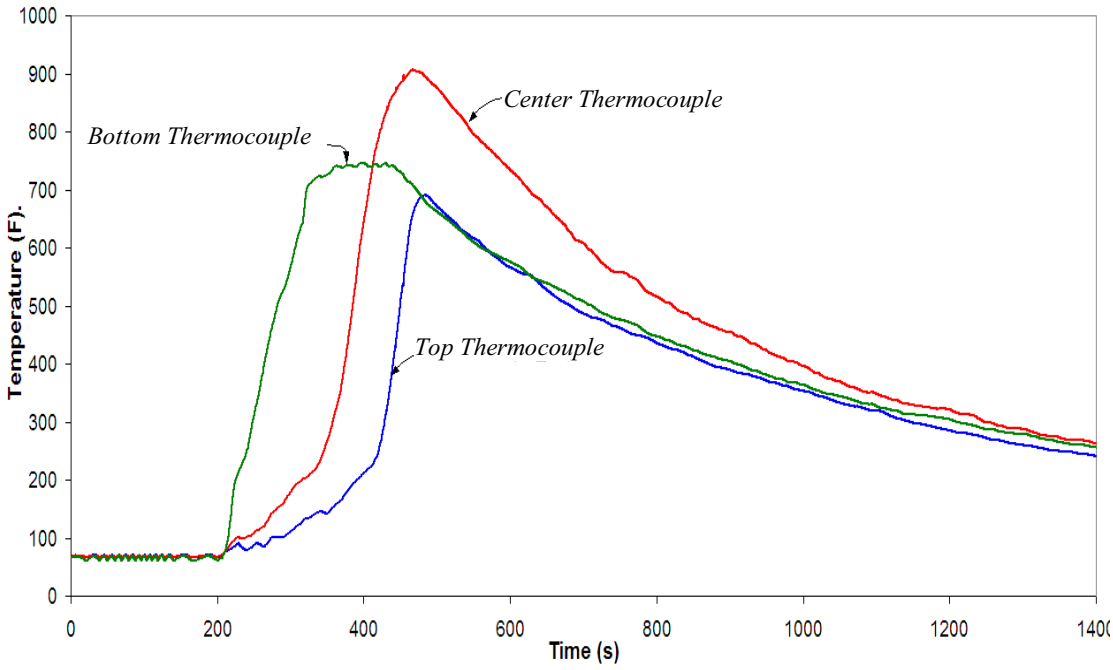

Figure 4.42
Type K contact thermocouple data during heat straightening of the trial specimen

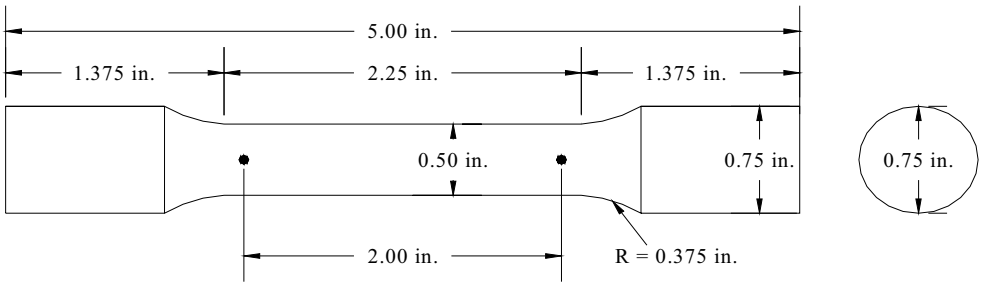

Figure 4.43
A36 and A588 *round* tension specimen dimensions [*4*]

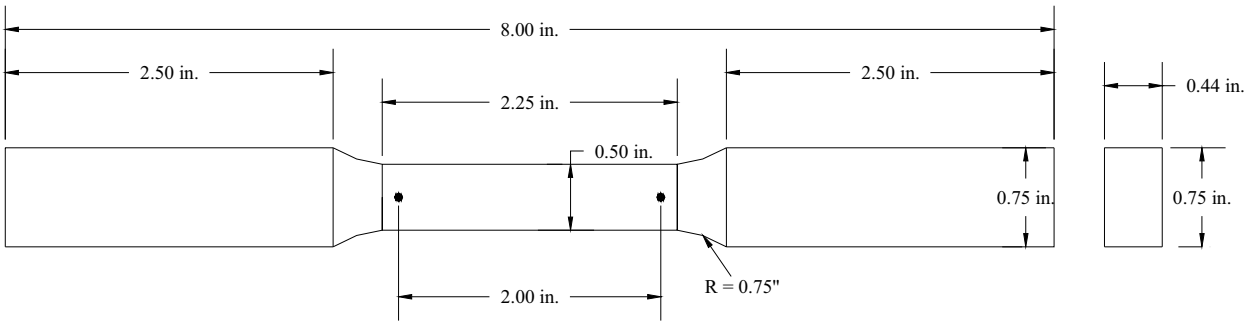

Figure 4.44
A7 *flat* tension specimen dimensions [*4*]

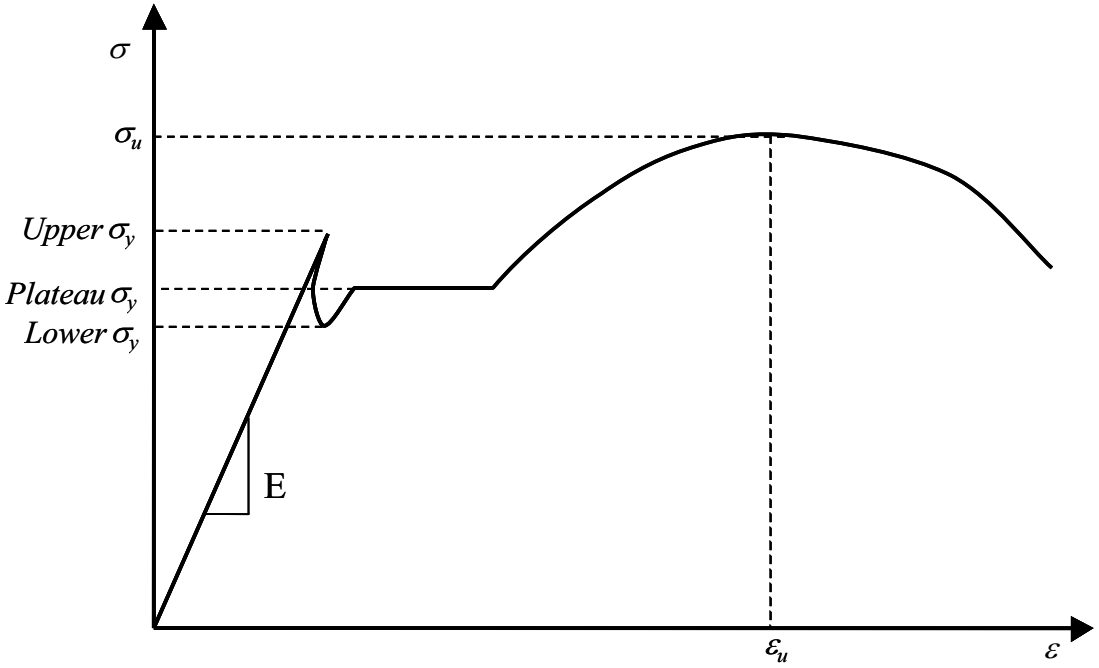

Figure 4.45
Structural properties determined from a uniaxial tension stress-strain curve [*4*]

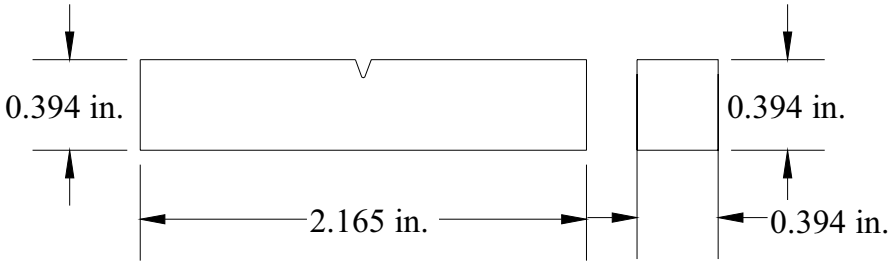

Figure 4.46
Dimensions of a charpy v-notch fracture toughness specimen [*4*]

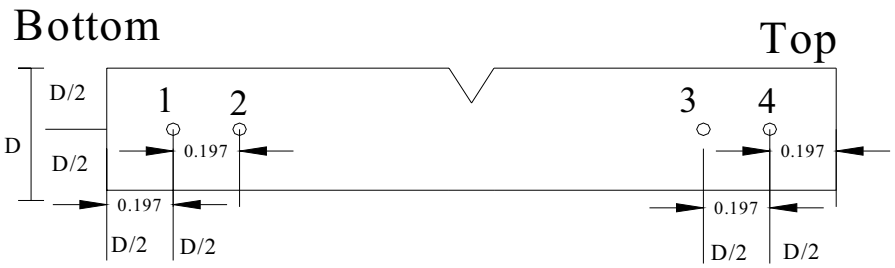

Figure 4.47
Rockwell hardness points on Charpy v-notch specimen

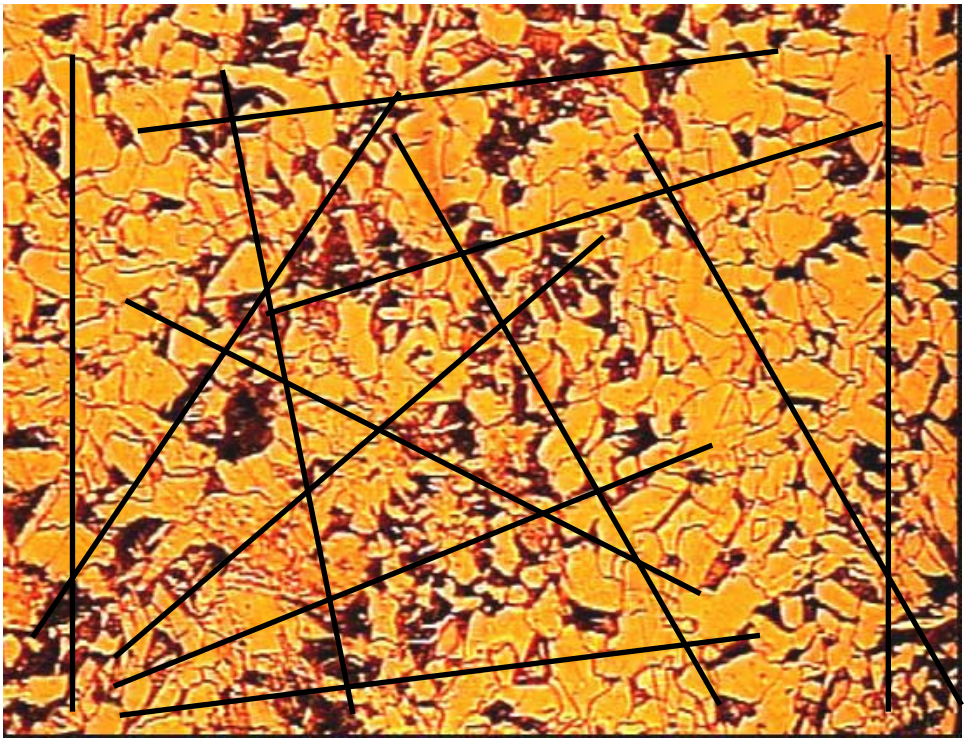

Figure 4.48
Illustration of how the grain size was determined for the each microstructure

5 EXPERIMENTAL BEHAVIOR AND RESULTS FROM LABORATORY SCALE SPECIMENS

5.1 A36 STEEL LABORATORY-SCALE SPECIMENS

This section discusses all of the experimental investigations and presents the results of material tests on A36 steel. As mentioned previously, thirty specimens were subjected to multiple damage-heat straightening repair cycles, and one specimen remained undamaged. All thirty-one specimens were fabricated from the same 1.0 in. thick plate. Material specimens were obtained from the undamaged and damaged-repaired specimens as explained earlier. Section 5.1.1 presents the results of testing the material specimens made from undamaged A36 steel. Section 5.1.2 presents the final test matrix of the damaged-repaired A36 steel specimens and reasons for derivations from the planned test matrix (see Section 4.3.1). Section 5.1.3 presents the details of the damage and heat straightening repair of the A36 steel specimens. The results of the material tests on specimens fabricated from the damaged-repaired specimens are presented in Section 5.1.4.

5.1.1 Undamaged A36 Material Properties

Uniaxial tension coupons and charpy v-notch fracture toughness specimens were fabricated from the undamaged A36 steel specimen. Uniaxial tension tests, charpy v-notch fracture toughness tests, Rockwell hardness tests, and microstructure investigations were conducted on the material specimens according to the applicable standards presented in Section 4.9. This sub-section presents the results of the uniaxial tension tests and the charpy v-notch fracture toughness tests. The results of Rockwell hardness tests and microstructure investigations on undamaged A36 steel are presented later along with the corresponding material tests for damaged-repaired steels in Sections 5.1.4.3 and 5.1.4.4.

Tension Tests

Uniaxial tension tests were conducted on tension coupons manufactured from the undamaged steel specimen. Figure 5.1 shows the stress-strain behavior of the three uniaxial test specimens, which are identified as A36-Undamaged_1, A36-Undamaged_2, and A36-Undamaged_3. The yielding of the specimens is shown in Figure 5.2. The corresponding structural properties: (a) yield stress, (b) elastic modulus, (c) yield strain, (d) ultimate stress, (e) ultimate strain, (f) strain ductility, (g) percent elongation, and (h) percent reduction, are given in Table 5.1. These properties were determined as explained in Section 4.9.1. The structural properties of all three undamaged material coupons are very comparable with the exception of the yield stress of A36-Undamged_2. The hydraulic actuators of the testing machine adjusted abruptly while this specimen was yielding. With the exception of the yield stress and strain from this specimen, the average material properties of undamaged A36 steel was the average of the material properties from all three tests.

Fracture Toughness Tests

Several standard charpy v-notch specimens were tested according to ASTM E23 to determine the fracture toughness of undamaged A36 steel. The MSU researchers put considerable effort to verify their fracture toughness machine, specimen fabrications, and testing procedures as explained below. The testing machine was serviced and verified by the manufacturer (Tinius Olsen) first. The specimen testing procedure was verified by testing nine specimens using the MSU verified testing machine and six specimens using the MDOT NIST certified testing machine. The fracture toughness values from these tests using the MSU and MDOT certified testing machines are given in Table 5.2 and 5.3, respectively. The fracture toughness values are comparable with some discrepancies due to variation in material fracture toughness.

The specimen fabrication technique was verified by comparing the notches of six specimens made by the MSU machinist and seven companion specimens made by the MDOT machinist. All thirteen specimens were tested using the MDOT NIST certified machine. Table 5.4 presents the fracture toughness values of specimens fabricated by the MSU machinist and Table 5.5 presents the fracture toughness values of specimens fabricated by the MDOT machinist. As shown in Tables 5.4 and 5.5, the fracture toughness of charpy specimens fabricated by the MSU machinist was significantly lower. This is attributed to the poor condition (notch radius) of the notches machined by the MSU machinist. Figures 5.3 and 5.4 compare the notches of the specimens made by the MSU and MDOT machinists, respectively. These pictures were taken using an optical comparator. The MSU machinist was using a cutting tool to machine the notches, while the MDOT machinist was using a broaching tool. The MSU machinist's cutting tool was wearing down too quickly and producing the poor quality notch radius seen in Figure 5.3.

The MSU machinist completely changed his machining technique and obtained a broaching tool to machine the charpy specimens. However, by this time, he had already machined the charpy specimens from all the A36 damaged-repaired steels. All these charpy specimens had poor notch radius. Hence, the MSU machinist re-touched the specimens to cleanup the notch radius using the broaching tool. This process reduced the break depth of the charpy specimens fabricated from the damaged-repaired A36 steel to 0.304 in. from the standard 0.315 in. Hence, the charpy specimens from the undamaged A36 steel were also fabricated with a reduced break depth of 0.304 in. Additionally, some charpy specimens were also machined with the standard break depth of 0.315 in. to evaluate the effects of the reduced depth. The MSU machinist was able to fabricate specimens with good notch radius using the broaching tool. He also purchased an optical comparator, which was used by the MSU researchers to exercise quality on the machined fracture toughness specimens. Figure 5.5 shows a picture of a typical charpy specimen notch machined by the MSU machinist using the broaching tool.

Table 5.6 summarizes the fracture toughness values of undamaged A36 steel with the standard break depth of 0.315 in. This table includes all valid results of 'good' charpy specimens tested by MSU and MDOT. Table 5.7 summarizes the fracture toughness values of the undamaged A36 steel with the reduced break depth of 0.304 in. All these specimens were made by the MSU machinist and tested by the MSU researchers. Both Tables 5.6 and 5.7 include the results of statistical analysis of the fracture toughness values. The statistical analysis results include the: (a) mean (average), (b) 95% confidence interval (high and low values) for the actual mean, (c) standard deviation, (d) median, and (e) average absolute deviation from the median.

Student's t-test analyses were conducted to evaluate the statistical differences between the: (a) the quarter and mid-thickness fracture toughness values for a break depth of 0.315 in.; (b) the quarter and mid thickness fracture toughness values for a break depth of 0.304 in.; (c) the quarter thickness fracture toughness values for specimens with break depths of 0.315 and 0.304 in.; and (d) the mid thickness fracture toughness values for specimens with break depths of 0.315 and 0.304 in. As mentioned previously in Section 4.9.2, the t-test evaluates the statistical difference between two data sets using their respective means, standard deviations, and sample set sizes. The results from the t-test include the t-value and the corresponding probability of null hypothesis, where the null hypothesis implies that the data sets are statistically similar. Tables 5.8, 5.9, and 5.10 summarize the results of the t-test analyses. These tables indicate that the probability that the data sets are statistically similar for cases (a), (b), (c), and (d) mentioned above are 68%, 90%, 80% and 79%, respectively.

Reducing the break depth to 0.304 in. has a small (but not negligible) influence on the fracture toughness values as evidenced by the 80% and 79% probabilities of the data sets being similar. The quarter and mid-thickness fracture toughness values for charpy specimens with break depths of 0.304 in. are statistically similar (90% probability). Hence, they were combined into one set without distinction. Table 5.11 shows the statistical analysis of the combined set of fracture toughness data for charpy specimens with break depth of 0.304 in. Similarly, the 0.304 in. break depth charpy specimens were also combined without distinction between the quarter and mid-thickness toughness values. Further

comparisons between the undamaged and damaged-repaired fracture toughness do not distinguish between the quarter and mid-thickness values.

5.1.2 Final Experimental Test Matrix of A36 Laboratory-Scale Specimens

The planned test matrix for the laboratory-scale A36 steel specimens was provided earlier in Table 4.1. The planned test matrix was developed to effectively evaluate the effects of each parameter (damage strain, restraining stress, and number of damage-repair cycles) while other parameters were kept constant. The planned test matrix included thirty A36 steel specimens with restraining stresses of 0.25 σ_y and 0.50 σ_y. As mentioned in Section 4.8, one A36 specimen was used as a trial specimen to validate the test setup and various heating procedures. The MSU researchers were only using only one torch to heat the damaged specimens first. As presented in Section 4.8.1, this procedure was not efficient for a restraining stress of 0.25 σ_y. Hence, the matrix was modified for restraining stresses of 0.40 σ_y and 0.70 σ_y. However, 0.70 σ_y was found to be too high of a compressive stress causing significant curvature in the repaired specimens. One specimen (A36-30-70-3) developed too much curvature and could not be repaired at all. The MSU researchers experimented with the use of two torches heating both sides of the specimens simultaneously. This process worked efficiently for σ_r = 0.25 σ_y and 0.50 σ_y. Hence, after the first ten tests at ε_d = 30 ε_y, the test matrix was reverted to the planned test matrix with σ_r = 0.25 σ_y and 0.50 σ_y. Two specimens (one trial and one curved beyond repair) could not be included in the final test matrix and it was modified to include only twenty-eight specimens. As shown in Table 5.12, the final test matrix included only twenty-eight specimens. Two specimens (A36-90-25-2 and A36-90-25-4) were eliminated from the planned test matrix.

5.1.3 Experimental Investigations on A36 steel

This section provides a summary of the experimental investigations conducted on A36 steel indicating how damage and heat-straightening repairs proceeded and discusses the resulting conditions of the specimens.

5.1.3.1 Damage Cycles

The first damage cycle of each specimen was the easiest procedure in the experimental investigations. The pressures in the hydraulic actuators were equalized and the specimens were subjected to damage until the two longitudinal strain gage readings averaged 0.040 in/in, 0.080 in/in, and 0.120 in/in, for 30 ε_y, 60 ε_y, and 90 ε_y, respectfully.

To determine if the displacement transducers were accurate instruments for monitoring the strain levels for multiple damage cycles, their accuracy and consistency during the first damage cycle was extremely important. The strains as indicated by the displacement transducers were approximately 0.044 in/in after the first damage cycle of a specimen subjected to 30 ε_y. Therefore, multiple damage cycles were considered completed when the two displacement transducers averaged approximately this value. The damage strains were validated using the digital caliper punch marks, which were found consistently higher after multiple damage events.

As discussed in Section 4.8, the first few specimens had four longitudinal strain gages attached to all four sides of the specimen during the first damage cycle. The side strain gages were removed after Specimen A36-30-40-3. Stress-strain relationships were developed for each experimental damage cycle with the procedures outlined in Section 4.7.1. For specimens damaged to 30 ε_y, the amount of stress increase after the first damage-repair cycle was substantial. This trend did not necessarily continue after further damage cycles. An example of the stress-strain behavior for specimens subjected to 30 ε_y is shown for Specimen A36-30-40-3 in Figure 5.6. In Figure 5.6, “Strain Front”, “Strain Back”, “Strain Right”, and

"Strain Left", represent the strains during the first damage cycle measured with strain gages. The rest of the nomenclatures used for the stress-strain relationships represent the damage cycle number and the positioning of the displacement transducer. For Example, "Cycle-1_Avg Right" represents the strain during the first damage cycle as indicated by the right displacement transducer.

For multiple damages of 60 ε_y, the average value of the average strains was brought to 0.080 in/in to complete the test. For multiple damages of 90 ε_y, the higher value of strain was brought to 0.120 in/in to complete the test. All damage levels were validated using digital caliper punch marks. Figure 5.7 shows the four damage cycles of Specimen A36-60-50-4. Figure 5.7 indicates how each multiple damage cycle was considered complete by averaging the strains for a damage level of 60 ε_y. Figure 5.8 shows the four damage cycles of Specimen A36-90-50-4. Figure 5.8 indicates how each damage cycle to 90 ε_y was consistently completed when one of the displacement transducers indicated a strain level of 0.120 in/in.

5.1.3.2 Repair Cycles

Heat-straightening repair cycles focused on shortening the test area to the original length before damage. The length of the test area was monitored using a digital caliper and punch marks. The researchers tried to maintain uniform cross-section along the test area while heating. The length, width, and thickness of the test area were monitored with digital calipers in between heating cycles to check uniformity. The first heating cycle was typically conducted from the bottom of the specimen to the top. The second was typically conducted from the top of the specimen to the bottom. Further heating cycles were conducted by heating thin areas first and moving up or down as needed. The area heated first always yielded at high temperatures. This decreased the load before the rest of the test area was heated and thus creating non-uniformity in the amount of restraining stress applied while the entire test area was heated.

When repairing Specimen A36-30-40-1, heat was applied using one oxy-acetylene torch. Each heating cycle was performed on the front side of the specimen. For other A36 specimens damaged to 30 ε_y, one torch was used while applying heats to alternate sides of the specimen. For specimens damaged to either 60 ε_y or 90 ε_y, heating cycles were conducted using two oxy-acetylene torches applying heat to both sides of the specimen.

The temperature of the steel while heating was monitored using the infrared temperature gun as shown in Figure 4.35. When reaching elevated temperatures of 1100 °F and 1200 °F, a reddish glow would appear on the surface of the steel. This reddish glow is shown for 1100 °F and 1200 °F in Figure 5.9 (a-b). These photographs were taken while repairing Specimen A36-90-50-4.

The level of restraining stress significantly influenced the amount of time required to complete a repair cycle. Typically, a specimen subjected to a damage level of 30 ε_y took 9-11 heating cycles to repair at 0.40 σ_y and 2-3 heating cycles to repair at 0.70 σ_y. A specimen subjected to a damage level of 60 ε_y took 7-9 heating cycles to repair at 0.25 σ_y and 2-3 heating cycles to repair at 0.5 σ_y. A specimen subjected to a damage level of 90 ε_y took 8-9 heating cycles at 0.25 σ_y and 4-5 heating cycles at 0.50 σ_y.

Figure 5.10 shows the repair cycle of a specimen subjected to a damage strain level of 60 ε_y and a restraining stress of 0.25 σ_y while heat straightening. In Figure 5.10, "Pressure Right" represents the pressure the right hydraulic actuator in ksi, "Thermometer" represents the temperature of the steel indicated by an infrared thermometer in degrees Fahrenheit, and "Displacement Transducer Right" and "Displacement Transducer Left" represent the two 1.5 in. displacement transducers that give a displacement between the top and bottom beam in inches. These values are multiplied by -10^3 so they can be distinguished from other measurements being monitored. The instrumentation used while repairing the specimens was discussed in Section 4.7.2.

As indicated in Figure 5.10, the left hydraulic actuator was not moving in tandem with the right actuator during each heating cycle. The beam level was regulated by lowering the left and raising the right

slightly between each heating cycle. This procedure was idealized to obtain equal shortening of both sides of the test area (measured using digital calipers) during and after completion of the heat-straightening repair of the specimen.

Figure 5.11 shows the repair cycle of a specimen subjected to damage level of 60 ε_y and a restraining stress of 0.50 σ_y while heat straightening. The increased amount of shortening of the specimen and the equal displacements between the two hydraulic actuators at this restraining stress level can clearly be seen in Figure 5.11. The pressure starts decreasing even before the point where the infrared thermometer is monitoring reaches the maximum elevated temperatures.

Although the amount of movement is extensively increased when using higher restraining stresses, it is more difficult to control uniformity in the cross-sectional area, equivalent caliper readings, and out-of-plane curvature of the test area. The final caliper readings were within 0.005 in. of the original values after testing, which corresponds to a strain of 0.001 in. /in.

An infrared thermometer was used to record the time-temperature curve of points in the test area of the specimen during the heating. The infrared thermometer was shown in Figure 4.38. The thermometer was set up to record temperatures at midheight on either side along the thickness of the specimen test area or at the front or back of the test specimen. The thermometer readings at the front and the back of the test area are a little sloppy as hands and torches get in the way of the infrared ray.

Figure 5.12 shows four time-temperature profiles with the infrared thermometer pointed on all four sides of the test specimen. Also shown in Figure 5.12 is Type K thermocouple data when heating the specimen with only one oxy-acetylene torch. When using two oxy-acetylene torches, the specimens remained colored for periods of less than a minute. This was not a behavior that occurred while heating the specimens with one torch. Therefore, a comparison was made between using one or two torches, which is shown in Figure 5.13. Figure 5.13 shows the cooling rates for the four locations of the test area specified in Figure 5.12 using two torches as well as three cooling rates of a specimen heated with one torch. For the cooling rates of the one-torch application, one was monitored using a Type K thermocouple and two were monitored using the infrared thermometer. The infrared thermometer was pointed on the left side of the specimen during the tests. The specimen cools more rapidly at elevated temperatures when heated with one torch. Then similar cooling rates between one and two torches begin around 700 °F.

5.1.3.3 Condition of A36 Steel Specimens after Experimental Investigations

Some A36 specimens had some significant curvature in the test area after the damage-repair cycles. The MSU researchers attempted to prevent the curvature by various techniques such as heating the opposite sides of curvature to shorten only the desired side, etc. Most of these procedures did not sufficiently improve the conditions of most specimens.

Specimens A36-30-40-1, A36-30-70-3, A36-30-70-4, A36-30-70-5, A36-60-25-2, and A36-90-25-5 exhibited significant curvature in the test area after testing. Only Specimens A36-30-40-1 exhibited single curvature in the test area while other specimens exhibited double curvature in the test areas. Specimen A36-30-40-1 was the only specimen that was repaired by applying heat to only one side. Figure 5.14 shows the resulting curvature of the test area of Specimen A36-30-40-1. Figure 5.15 shows the resulting curvature of the test area of Specimen A36-90-25-5.

Figure 5.16 shows a group of specimens that have been subjected to multiple damage-repair cycles. The group consists of the A36-60-50 series of five specimens as well as specimens A36-90-25-1 and A36-90-25-3. All of these specimens were considered to be in satisfactory condition. Other specimens with significant curvature in the test area will be noted when the material testing results are discussed.

5.1.4 Results of Material Testing on A36 Steel

This section presents the results of material tests conducted on specimens fabricated from the test areas of A36 laboratory-scale specimens subjected to multiple damage-repair cycles. The material tests were conducted according to the applicable ASTM standards [*1*] as discussed in Section 4.9. The comparisons and conclusions using the material test results are discussed later in Section 6.2.

5.1.4.1 Uniaxial Tension Tests

The dimensions of the material coupons, descriptions of testing procedures, and definitions of the structural properties determined from the stress-strain relationships were discussed in Section 4.9.1. From each damaged-repaired specimen, two tension coupons were removed, one from the left side and one from the right as shown in Figure 4.13. The material coupons were labeled as X and Y where X was removed from the left side of the test area and Y was removed from the right side of the test area (Note that for the first 8 specimens in the test matrix of Table 5.12, the side which the specimens came from was unknown). The results of tension coupons from A36-30-40 specimens are given in Table 5.13. The results of tension coupons from A36-30-70 specimens are given in Table 5.14. The results of tension coupons from A36-60-25 specimens are given in Table 5.15. The results of tension coupons from A36-60-50 specimens are given in Table 5.16. The results of tension coupons from A36-90-25 specimens are given in Table 5.17. The results of tension coupons from A36-90-50 specimens are given in Table 5.18. These results are discussed and compared in more detail later in Section 6.2.1.

5.1.4.2 Charpy Impact Fracture Toughness Results

Fracture toughness tests were conducted according to ASTM E23 on charpy v-notch specimens from the damaged-heat straightening repaired A36 specimens. The techniques used for conducting the charpy impact fracture toughness tests were presented in Section 4.9.2. The results of the tests on undamaged A36 steel were presented in Section 5.1.1. A reduced break depth of 0.304 in. had to be used for all charpy specimens fabricated for reasons presented in Section 5.1.1. All tests were conducted by removing the specimens from a liquid silicone bath at a temperature of 40 °F. The results are given in Table 5.19. In Table 5.19, “QA” represents an average of the quarter thickness results (Specimens 1, 2, and 3) and “MA” represents an average of the mid thickness results (Specimens 4, 5, and 6). The results of the charpy impact fracture toughness tests are further interpreted and compared in Section 6.2.2.

5.1.4.3 Rockwell Hardness Tests

Rockwell hardness tests were conducted to determine the surface hardness of damaged-repaired A36 steel. These tests were conducted according to ASTM E18 using the type B-scale with a steel ball indenter. The procedures were outlined in Section 4.9.3. The charpy specimen identified as “*2*” in Figure 4.13 was used for determining the surface hardness of the damaged-repaired steel. Table 5.20 shows the average surface hardness, standard deviation, and the estimated ultimate strength for all the damaged-repaired A36 steels. The results are further discussed and compared in Section 6.2.3.

5.1.4.4 Microstructure investigations

Investigations were conducted to determine the effects of multiple damage-heat straightening repairs on the microstructure of A36 steel. The charpy specimens used to conduct Rockwell hardness tests were also used for the microstructure investigations. The specimens were prepared in accordance to ASTM E3 as discussed in Section 4.9.4. The etched specimens were placed under a metallurgical microscope with a photo micrographic camera attached. The magnification of 240X was chosen since grain boundaries could not be seen at 120X and the grain size could not be computed according to ASTM E112 at 480X. Figure 5.17 (a-f) shows the microstructure of undamaged A36 steel and some of the multiple damage-heat

straightening repaired steel at 240X. The resulting grains sizes and percentage of pearlite grains are given for all specimens in Table 5.20. As discussed in Section 4.9.4, a more fine-grained microstructure is generally stronger and tougher than a more coarse-grained microstructure. There is a slight increase on the surface hardness and a slight decrease on the ductility. A microstructure that is more pearlitic is harder, stronger, and more brittle. However, only significant and consistent changes in the percent pearlite would be further analyzed as the amount is related to the location taken for the picture as discussed in Section 2.4.3. The results are provided in Table 5.20 for completeness. The results are further discussed and compared in Section 6.2.3.

5.2 A588 STEEL LABORATORY-SCALE SPECIMENS

This section discusses all of the experimental investigations and presents the results of material tests on A588 steel. This section is organized very similar to Section 5.1 for A36 steel. Undamaged A588 material properties are discussed in Section 5.2.1. A summary of the adjusted test matrix is presented in Section 5.2.2. The damage and heat-straightening repair cycles are discussed in Section 5.2.3. The experimental results are provided in Section 5.2.4.

5.2.1 Undamaged A588 Material Properties

This section provides the results of the uniaxial tension tests and fracture toughness tests on undamaged A588 steel. The results of Rockwell hardness tests and microstructure investigations on undamaged A588 steel are presented in Sections 5.2.4.3 and 5.2.4.4.

Tension Tests

Three uniaxial tensile tests were conducted on undamaged A588 to determine the material properties of the steel before heat straightening. Figure 5.18 shows the stress-strain behavior of the undamaged specimens identified as A588-Undamaged_1, A588-Undamaged_2, and A588-Undamaged_3. The specimens are numbered in the order by which they were tested. The yielding of the steel is shown in Figure 5.19. The corresponding structural properties (defined in Section 4.9.1) are given in Table 5.21. The structural properties of all three tensile coupons related well to each other. Therefore, average material properties of undamaged A588 steel were taken as an average of all three results.

Fracture Toughness Tests

Fracture toughness tests were conducted on charpy specimens made from undamaged A588 steel using the procedures discussed in Section 4.9.2. As discussed in Section 5.1.1, the MSU machinist's first cutting too was wearing down rapidly. He changed the machining procedure completely to use a broaching tool, but that was after the charpy specimens from the first ten A588 damaged-repaired specimens had been fabricated. The broaching tool was used to clean up the notch radius of these charpy specimens. This procedure reduced the break depth to 0.300 in. for these ten specimens. The charpy specimens from the remaining twenty damaged-repaired A588 specimens were fabricated with a full break depth of 0.315 in.

Charpy specimens from undamaged A588 steel were fabricated with break depths of 0.300 in. and 0.315 in. Table 5.22 presents the fracture toughness values for quarter and mid thickness charpy specimens with a break depth of 0.300 in. Table 5.22 includes the results of the statistical analysis of the data, i.e., the mean (average), 95% confidence interval (CI) for actual mean, standard deviation, median, and average absolute deviation from the median. Table 5.23 presents the fracture toughness values for quarter and mid thickness charpy specimens with a break depth of 0.315 in. from undamaged A36 steel. Table 5.23 also includes the results of the statistical analysis of the data.

Student's t-test analyses were conducted to evaluate the statistical differences between: (a) the quarter and mid-thickness fracture toughness values for a break depth of 0.300 in.; (b) the quarter and mid

thickness fracture toughness values for a break depth of 0.315 in.; (c) the quarter thickness fracture toughness values for specimens with break depths of 0.300 and 0.315 in.; and (d) the mid thickness fracture toughness values for specimens with break depths of 0.300 and 0.315 in. As mentioned previously in Section 4.9.2, the t-test evaluates the statistical difference between two data sets using their respective means, standard deviations, and sample set sizes. The results from the t-test include the t-value and the corresponding probability of null hypothesis, where the null hypothesis implies that the data sets are statistically similar. Tables 5.24, 5.25, and 5.26 summarize the results of the t-test analyses. These tables indicate that the probability of the data sets being statistically similar for cases (a), (b), and (c) mentioned above is less than 0.01%, and the probability of null hypothesis for case (d) is 13%.

Thus, the quarter and mid-thickness toughness values are statistically different for charpy specimens with break depths of 0.300 and 0.315 in. Additionally, the toughness values for charpy specimens with break depths of 0.300 and 0.315 in. are also statistically different. Hence, the fracture toughness of the first ten damage-repaired (A588-20) specimens will be compared with the undamaged toughness values for a break depth of 0.300 in. The fracture toughness values for the remaining damage-repaired (A588-40 and A588-60) specimens will be compared with the undamaged toughness values for a break depth of 0.315 in. The quarter and mid-thickness toughness values will be considered separately for both cases.

5.2.2 Final A588 Test Matrix

The planned A588 test matrix was given in Table 4.2. This planned matrix was modified as follows. Strain ductility ($\varepsilon_u/\varepsilon_y$) of undamaged A588 steel was found to be low (approximately 78). An A588 specimen damaged to 90 ε_y (as planned in Table 4.2) would be past the ultimate strain and undergo necking on a path to failure. This was unacceptable, and therefore, an adjustment was made to limit the damage strain for A588 specimens. The damage strains were altered from the planned values of 30 ε_y, 60 ε_y, and 90 ε_y to the actual values of 20 ε_y, 40 ε_y, and 60 ε_y. These damage strains corresponded to the A36 damage strains of 30 ε_y, 60 ε_y, and 90 ε_y. The A36 and A588 stress-strain relationships are compared in Figure 5.20. The three damage strains levels for each steel type are indicated in Figure 5.20. The resulting adjusted test matrix is provided in Table 5.27.

5.2.3 Experimental investigations on A588 steel

This section provides a summary of the experimental investigations conducted on A588 laboratory-scale specimens. It includes details regarding the damage and heat-straightening repairs of the A588 steel specimens and final conditions of the damaged-repaired specimens.

5.2.3.1 Damage Cycles

The experimental damage cycles of A588 steel progressed well. There were no significant problems with the instrumentation or the equipment used. The procedures and instrumentation used during the experimental damage cycles were presented in Section 4.7.1.

The first damage cycle of each specimen was monitored using the longitudinal strain gages attached to the center of the front and back faces of the test area. Multiple damage cycles were controlled using the displacement transducers, which were attached to the specimen such that they measure displacement of the test area only. The longitudinal strain gages always indicated good relationships with each other. The displacement transducers were slightly, yet consistently different in relationship to each other. The strain as indicated by the right displacement transducer was always slightly higher in magnitude that the strain indicated by the left displacement transducer. Consistent comparisons between the readings of the displacement transducers and that of the digital caliper punch marks were noticed. Consistency was enforced for the completion of each damage strain level.

For a damage strain level of 20 ε_y, the loading continued until the strains indicated by the two displacement transducers averaged 0.040 in/in. For damage levels of 40 ε_y, the loading continued until the strains averaged 0.080 in/in. For damage levels of 60 ε_y, the loading continued until the strain as indicated by the right displacement transducers reached 0.120 in/in. Examples of the multiple damage behavior of A588 steel are provided in Figures 5.21 and 5.22. Figure 5.21 shows the stress-strain relationships of all four damage cycles of Specimen A588-20-25-4. Figure 5.22 shows the stress-strain relationships of all five damage cycles of Specimen A588-60-25-5. From the experimental data, it appeared that heat straightening slightly reduced the strength of A588 steel.

5.2.3.2 Repair Cycles

Heat-straightening repairs conducted on damaged A588 steel were very similar to that conducted on damaged A36. Compressive restraining stresses of either 0.25 σ_y or 0.50 σ_y were applied to the specimen test area prior to heating. The amount of displacement of each hydraulic actuator was monitored using two displacement transducers. These displacement transducers were attached to the beams close to the hydraulic actuators and gave an indication of the specimen shortening. Two researchers used two oxy-acetylene torches and applied heat simultaneously to both sides of the specimens. The temperature at the surface of the steel was monitored using an infrared temperature gun. In addition, the infrared thermometer was used to record the time-temperature profile during the experiments on all four sides of the specimen.

The heat-straightening repairs of the A588 specimens went much smoother than that of the A36 specimens. For specimens damaged to 20 ε_y, it took 2-3 heating cycles at a restraining stress of 0.25 σ_y and 1-2 heating cycles at a restraining stress of 0.50 σ_y. For specimens damaged to 40 ε_y, it took 4-5 heating cycles at a restraining stress of 0.25 σ_y and 2-3 heating cycles at a restraining stress of 0.50 σ_y. For specimens damaged to 60 ε_y, it took 5-7 heating cycles at a restraining stress of 0.25 σ_y and 4-5 heating cycles at a restraining stress of 0.50 σ_y.

The left hydraulic actuator was often lowered before the right hydraulic actuator prior to the heating cycles to maintain equal shortening of both sides of the test area. The pressures in the hydraulic actuators remained relatively equivalent. However, the amount of displacement of the right hydraulic actuator was always higher than the displacement of the left hydraulic actuator as the specimen shortened. The typical behavior of a repair with a restraining stress level of 0.25 σ_y is represented in Figure 5.23, which shows the fourth repair cycle of Specimen A588-60-25-5. The typical behavior at a restraining stress of 0.50 σ_y is given in Figure 5.24, which shows the repair cycle of specimen A588-60-50-1. Figures 5.23 and 5.24 indicated the temperature at the front surface of the steel as indicated by the infrared thermometer.

5.2.3.3 Condition of A588 Steel Specimens after Experimental Investigations

The A588 steel specimens were found to be in better conditions after experimental investigations as opposed to the A36 steel specimens. The frontal and side views of the specimen series A588-40-25 are shown in Figures 5.25 and 5.26.

The specimens showing significant curvature in the test area were A588-40-25-5, A588-60-25-1 and A588-60-25-4. Close-ups of the test areas are shown in Figures 5.27, 5.28, and 5.29**,** respectively. Specimen A588-60-25-1 exhibited the most severe curvature in the test area.

5.2.4 Results of Material Testing of A588 Steel

This section presents the results of material tests conducted on specimens from all the A588 damaged-repaired specimens. The material tests were conducted according to the applicable ASTM standards [*1*] as discussed in Section 4.9. The comparisons and conclusions using the material test results are discussed later in Section 6.3.

5.2.4.1 Uniaxial Tension Tests

Uniaxial tension tests were conducted on the tension coupons from damaged-repaired A588 specimens according to ASTM E8. The dimensions of the coupons, descriptions of testing procedures, and definitions of the structural properties determined from the stress-strain relationships were discussed in Section 4.9.1. From each damage-repaired specimen, two tension coupons were removed, one from the left side labeled "X" and one from the right labeled "Y" as shown in Figure 4.13. The results of A588-20-25 specimens are given in Table 5.28. The results of A588-20-50 specimens are given in Table 5.29. The results of A36-588-25 specimens are given in Table 5.30. The results of A588-40-50 specimens are given in Table 5.31. The results of A588-60-25 specimens are given in Table 5.32. The results of A588-60-50 specimens are given in Table 5.33. The results are further discussed and compared in Section 6.3.1.

5.2.4.2 Charpy Impact Fracture Toughness Results

The procedures for conducting charpy impact fracture toughness tests were presented in Section 4.9.2. The results of the charpy tests on undamaged A588 steel were presented in Section 5.2.1. As also discussed in Section 5.2.1, a reduced break depth of 0.300 in. had to be used for coupons fabricated from the first ten specimens. These specimens were all damaged to 20 ε_y. All tests were conducted directly after removing the specimens from a liquid silicone bath at a temperature of 40 °F. The results of the charpy impact fracture toughness tests of specimens with a reduced break depth are provided in Table 5.34. The results of the charpy impact fracture toughness tests of specimens with a full break depth are provided in Table 5.35. In Tables 5.34 and 5.35, "QA" represents an average of the quarter thickness results (Specimens 1, 2, and 3) and "MA" represents an average of the mid thickness results (Specimens 4, 5, and 6). The results of the charpy impact fracture toughness tests are further interpreted and compared in Section 6.3.2.

5.2.4.3 Rockwell Hardness Results

Rockwell hardness tests were conducted to determine the surface hardness of damaged-repaired A588 steel. These tests were conducted according to ASTM E18 using the type B-scale with a steel ball indenter. The procedures were outlined in Section 4.9.3. The charpy specimen identified as "2" in Figure 4.13 was used for determining the surface hardness of the damaged-repaired steel. Table 5.36 shows the average surface hardness, standard deviation, and the estimated ultimate strength for all the damaged-repaired A588 steels. The results are further discussed and compared in Section 6.3.3.

5.2.4.4 Microstructure investigations

Investigations were conducted to determine the effects of multiple damage-heat straightening repairs on the microstructure of A588 steel. The charpy specimens used to conduct Rockwell hardness tests were also used for the microstructure investigations. The specimens were prepared in accordance to ASTM E3 as discussed in Section 4.9.4. The etched specimens were placed under a metallurgical microscope with a photo micrographic camera attached. The magnification of 480X was chosen to compute the grain sizes of A588 steel. Figure 5.30 (a-f) shows the microstructure of undamaged A588 steel and some of the multiple damage-heat straightening repaired specimens at 480X. The resulting grains sizes and percentage of pearlite grains are given for all A588 specimens in Table 5.36. As discussed in Section 4.9.4, a more

fine-grained microstructure is generally stronger and tougher than a more coarse-grained microstructure. There is a slight increase on the surface hardness and a slight decrease on the ductility. A microstructure that is more pearlitic is harder, stronger, and more brittle. However, only significant and consistent changes in the percent pearlite would be further analyzed as the amount is related to the location taken for the picture as discussed in Section 2.4.3. The results are provided in Table 5.36 for completeness. The results are further discussed and compared in Section 6.3.3.

5.2.5 Comparison of Chemical Compositions of Old and New A588 Material

A concern was addressed by the Research Advisory Panel (RAP) on the conclusions and recommendations made in Task III and Task IV for A588 steel (refer to Sections 6.3 and 8.2.3) and their applications for older A588 material currently being heat-straightened in Michigan. The results of the Michigan high-load hits database (refer to Section 2.3) indicated that fourteen of fifteen A588 heat-straightened bridges were constructed in the 1970's and one bridge was constructed in 1964. The steel plate used for the fabrication of small-scale specimens from Task III was prepared in 2003. A technical report was provided by the RAP to the MSU researchers, which summarized an evaluation of weathering steel [*3*]. The eight-year program began in 1976 and included A588 steel. The chemical composition of the A588 steel was provided in the report for this program. The chemical composition was compared to the chemical composition of the plates used for the fabrication of small-scale and large-scale A588 specimens and is shown in Table 5.37.

More additives, such as Nitrogen, Titanium, and Tin were indicated from a heat analysis of the new A588 material. If all components could be measured at the time of the heat analysis of the older A588 steel is unknown. The results indicate that more nickel and slightly less silicon was found in the old A588 material. All three steels meet the requirements of ASTM A588 [*1*]. The comparison generally indicates negligible differences between the chemical compositions of the old and new A588 material.

5.3 A7 STEEL LABORATORY-SCALE SPECIMENS

This section discusses all of the experimental investigations and presents the results of material tests on A7 steel. This section is organized very similar to Section 5.1 for A36 steel and Section 5.2 for A588 steel. Undamaged A7 steel material properties are discussed in Section 5.3.1. The test matrix is presented in Section 5.3.2. The experimental damage-heat straightening repair cycles are discussed in Section 5.3.3 along with the conditions of the damaged-repaired specimens. The material testing results are provided in Section 5.3.4.

5.3.1 Undamaged Material Properties

Uniaxial tension coupons and charpy v-notch fracture toughness specimens were fabricated from the undamaged A7 steel plate, which was fabricated from the center of the 93 in. W24x76 steel beams (see Figure 4.16). Uniaxial tension tests, charpy v-notch fracture toughness tests, Rockwell hardness tests, and microstructure investigations were performed using ASTM standards [*1*] as summarized in Section 4.1.9. This section provides the results of the uniaxial tension and fracture toughness tests on undamaged A7 steel. The results of Rockwell hardness tests and microstructure investigations on undamaged A7 are presented in Sections 5.3.3.3 and 5.3.3.4.

Tension Tests

Three uniaxial tensile tests were conducted on undamaged A7 steel to determine the material properties before the experimental investigations. Figure 5.31 shows the stress-strain behavior of the undamaged specimens identified as A7-Undamaged_1, A7-Undamaged_2, and A7-Undamaged_3. The yielding of the steel is shown in Figure 5.32. The corresponding structural properties obtained from the stress-strain relationships (defined in Section 4.9.1) are given in Table 5.38. The structural properties of

all three specimens were found to be very similar in respect to each other. Therefore, the average value of each structural property was used to define the average undamaged A7 steel material properties.

Fracture Toughness Tests

Fracture toughness tests were conducted on undamaged A7 steel according to ASTM E23. Sixteen charpy specimens were fabricated from the undamaged A7 plate. All charpy specimens were taken from the mid thickness. The results of these tests are provided in Table 5.39. There appears to be only slight variation in the fracture toughness results as opposed to A36 steel. The standard deviation was found to be 7.58 lb-ft as opposed to the approximate values of 30-40 lb-ft for undamaged A36 steel.

5.3.2 Final A7 Test Matrix

This section summarizes adjustments made to the A7 experimental test matrix. Finite element models were made of the A7 steel specimens using ABAQUS version 6.3 [*2*]. The thickness of the plates was 0.45 in. The material properties were specified in the finite element model as a function of the temperature of the steel. These material properties included the stress-strain relationships, the elastic modulus, and the coefficient of thermal expansion. The finite element analysis in this section includes a buckling analysis, a heat transfer analysis, and a compressive stress analysis. For the compressive stress analysis, loads are applied to the specimen subjected to elevated temperatures. The buckled shape of the specimen was determined using an eigenvalue analysis in ABAQUS. The buckled shape that permits lateral translation of the top of the specimen is shown in Figure 5.33. This buckling mode was similar to that observed in damaged-repaired A36 and A588 specimens. Prior to running a compressive stress analysis, a heat transfer analysis was conducted giving the nodes a thermal degree of freedom and allowing heat to migrate through the plate. The nodes within the test area were given a time-temperature profile that was recorded during actual heat-straightening experiments using an infrared thermometer.

To apply an external restraining force, a spring element was connected to the top of the specimen. The specimen was loaded specifying the far node of the spring a displacement in the direction of loading. As the specimen continues to expand at higher temperatures, the spring shortens which increases the stress on the specimen. As the specimen gets further heated, it will yield reducing the force in the spring. The finite element model aided the design of the A7 laboratory-scale specimen.

Once the dimensions of the A7 specimens were finalized, the finite element model was subjected to external restraining stresses of 0.25 σ_y, 0.40 σ_y, or 0.50 σ_y. The specimen exhibited severe buckling in the test area at a restraining stress level of 0.50 σ_y as shown in Figure 5.34. The contours in Figure 5.34 represent the plastic strains, which indicate the magnitude and locations of yielding. Figure 5.34 indicates that 0.50 σ_y is too high of a restraining stress level for the 0.45 in. plate. Figure 5.35 represents the results of a 1 in. plate subjected to an external restraining stress of 0.50 σ_y, which was the thickness of the A36 and A588 laboratory-scale specimens. The 1 in. plate does not buckle. Some double curvature was noticed in the test area very similar to the resulting condition of some A36 and A588 experimental test specimens. Therefore, the finite element analysis conducted on the 0.45 in. plate was proposed to be valid.

A finite element analysis was conducted on the 0.45 in. steel plate with subjecting an external restraining stress of 0.40 σ_y. The results are shown in Figure 5.36. The specimen showed negligible indications of curvature and no signs of buckling at a restraining stress of 0.40 σ_y. The only out-of-plane movement was due to the initial implemented imperfection. Aided with the propositions given by MDOT Research Advisory Panel, the restraining stress levels were modified from 0.25 σ_y and 0.50 σ_y to 0.25 σ_y and 0.40 σ_y.

Adjustments were made to the test setup in order to reduce the effective length of the A7 specimen as discussed in Section 4.6.4. The adjustments were made specifically because problems occurred during the

experimental investigations when repairing specimens damaged to 60 ε_y. Each heating cycle created a small imperfection of the test area in the lateral direction. The imperfections increased which eventually led to failure of a specimen. During the 2nd repair cycle of the original Specimen A36-60-25-3, buckling occurred at an elevated temperature. The specimen had to be discarded, as it could not be repaired back to its original length. Therefore, the amount of specimens in the test matrix was reduced to 17.

The researchers had troubles repairing each specimen that was damaged to 90 ε_y. The amount of out-of-plane curvature continued to increase during each heating cycle regardless of the adjustments made to the test setup. Specimens, who were damaged and repaired three times, exhibited significant curvature, which will be further discussed in Section 5.3.3.3. The repair of specimens damaged as high as five times would exhibit more curvature to the point that the experimental results could not be validated. Therefore, Specimens A7-90-25-5 and A7-90-40-5 were removed from the test matrix.

The MSU researchers found it beneficial to have one replicate specimen for comparisons in their data. For a replicate, Specimen A7-60-25-3 was chosen as its level of damage and number of damage-repairs was considered average. The final A7 experimental test matrix is shown in Table 5.40. For specimens labeled A7-60-25-3-1 or A7-60-25-3-2, the last number represents the order by which they were tested.

5.3.3 Experimental Investigations on A7 Test Specimens

This section summarizes the experimental investigations conducted on the seventeen A7 laboratory-scale specimens. A summary of the experimental behavior during the damage cycles is discussed in Section 5.3.3.1. A summary of the experimental behavior during the heat straightening repair cycles is discussed in Section 5.3.3.2. The condition of the completed test specimens is discussed in Section 5.3.3.3.

5.3.3.1 Damage Cycles

This section discusses the experimental damage cycles conducted on the A7 steel specimens.

Much lower forces were required to damage the A7 specimens because of the significant decrease in thickness of the material. Therefore, the experiments were conducted much more quickly than on other steel types. Damage cycles were monitored using the front and back strain gages during the first damage cycle. The strain gage readings always related well to each other. During the first damage cycles, it was noticed that the right displacement transducer related favorably well to the strain gage readings and the left displacement transducer had a tendency to fall behind. Therefore, consistency was enforced and each multiple damage cycle was completed when the right displacement transducer reached the required strain level. Examples of the behavior of instrumentation for multiple damage cycles are provided in Figures 5.37 and 5.38. Figure 5.37 shows the three damage cycles of Specimens A7-30-40-3. Figure 5.38 shows the first four damage cycles of Specimen A7-60-25-5. Figures 5.37 and 5.38 indicate the consistency, which was enforced to end each damage cycle.

For multiple damage cycles of specimens damaged to 90 ε_y, the damage levels were monitored using the right displacement transducer. However, due to the significant curvatures developed after the previous repair, the damage levels were somewhat questionable. The damage strains were validated using the digital caliper punch marks, which also measure the displacements of the test area. The digital caliper punch marks related well the strains indicated by the right displacement transducer. The MSU researchers used their best judgment for the completion of each multiple damage cycle for all A7 experimental test specimens. Figure 5.39 shows all three experimental damage cycles conducted on Specimen A7-90-25-3. The nonlinear elastic stiffness observed in Figure 5.39 indicates that the specimen has some initial curvature after one damage-repair event.

5.3.3.2 Repair Cycles

Heat-straightening repair cycles were conducted by heating up the specimens to a maximum temperature of 1200 °F. Since the specimens were significantly thinner, they heated up much quicker than the A36 and A588 specimens did. Heating the specimens to the maximum temperature seemed almost instantaneous and efforts not to overheat became important. The specimens also cooled much faster which increased the amount of heating cycles conducted within a given time period. Therefore, the time required to complete the experiments was significantly reduced. A comparison between the cooling rates of A36 steel, A588 steel, and A7 steel for a temperature range of 1100 °F to 250 °F is provided in Figure 5.40.

The displacements measured between the two hydraulic actuators were much more even when conducting the repairs on A7 steel as opposed to A36 and A588. Since the A7 specimens were much thinner, there was a significant reduction in the amount of pressure required in the hydraulic actuators. The 1st repair cycle of specimen A7-60-25-3 is shown in Figure 5.41. The 1st repair cycle of specimen A7-60-40-5 is shown in Figure 5.42.

Experimental investigations were found to be difficult in regards to A7 specimens damaged to 90 ε_y. These four specimens were all shortened to their original length as indicated by the digital caliper readings but significant curvature existed at the end of testing. Specimen A7-90-25-1 was aided in straightening by subjecting it to tensile stresses three times in an attempt to reduce the amount of curvature.

Specimens A7-90-25-3 and A7-90-40-3 were subjected to tensile stresses three times as well. However, a strip heat was applied on the compressive side of the curved test area to try and elongate only the desired side. These procedures were conducted only during the third repair cycle of both specimens.

5.3.3.3 Condition of Test Specimens after Experimental Investigations

The condition of A7 experimental test specimens after testing were worse than the final conditions of A36 and A588 test specimens. Specimens which were damaged and repaired to damage strains of 30 ε_y and 60 ε_y were in satisfactory condition as shown in Figures 5.43 to 5.45. Figure 5.43 shows a frontal view of specimens subjected to a damage strain of 30 ε_y. Figure 5.44 shows the side view of specimens subjected to a damage strain of 30 ε_y. Figure 5.45 shows the side view of specimens subjected to a damage strain of 60 ε_y. As shown in Figure 5.45, specimens A7-60-40-3 and A7-60-40-5 exhibited some signs of curvature after testing.

Specimens subjected to damage strains of 90 ε_y were found to be in very poor condition after repair. The curvatures in the test area of all four specimens are shown in Figures 5.46 to 5.49. The specimens, which indicated curvature in the test area, are identified in discussions of the experimental results.

5.3.4 Results of Material Testing on A7 Steel

This section presents the results of material tests conducted on specimens fabricated from the test areas of A7 laboratory-scale specimens subjected to multiple damage-repair cycles. The material tests were conducted according to the applicable ASTM standards [*1*] as discussed in Section 4.9. The comparisons and conclusions using the material test results are discussed later in Section 6.4.

5.3.4.1 Uniaxial Tension Tests

Uniaxial tension tests were conducted on coupons from the damaged-repaired A7 specimens. The dimensions of the coupons, descriptions of testing procedures, and definitions of the structural properties determined from the stress-strain relationships were discussed in Section 4.9.1.

From each damage-repaired specimen, two tension coupons were removed, one from the left side and one from the right side as shown in Figure 4.19. Since the tensile coupons were fabricated from the same thickness of the resulting experimental specimens, some of the tensile coupons exhibited significant curvature after the respected number of damage-repairs as shown in Figure 5.50. The yield strength, elastic modulus, and yield strain of the material could not be defined from the stress-strain relationships for a number of specimens due to initial curvature. The nonlinear elastic behavior of uniaxial tension coupons fabricated from Specimens A7-90-40-1 is compared to the behavior of coupons fabricated from Specimen A7-30-40-1 and also from undamaged A7 steel in Figure 5.51.

The results of the structural properties of A7-30-25 specimens are provided in Table 5.41. The results of A7-30-40 specimens are provided in Table 5.41. The results of A7-60-25 specimens are provided in Table 5.43. The results of A7-60-40 specimens are provided in Table 5.44. The results of A7-90 specimens are provided in Table 5.45. The results are further discussed and compared in Section 6.4.1.

5.3.4.2 Charpy Impact Fracture Toughness Results

Fracture toughness tests were conducted according to ASTM E23 on charpy specimens from all the damaged-repaired A7 specimens. The process for conducting the tests was presented in Section 4.9.2. The results of the tests conducted on undamaged A7 steel were presented in Section 5.3.1. All tests were conducted by removing the specimens from a liquid silicone bath at a temperature of 40 °F. The results of the charpy impact fracture toughness tests are provided in Table 5.46. The break depth of all specimens was 0.315 in. (± 0.001 in.). The results of the charpy impact fracture toughness tests are further interpreted and compared in Section 6.4.2.

5.3.4.3 Rockwell Hardness Results

Rockwell hardness tests were conducted to determine the surface hardness of damaged-repaired A7 steel. These tests were conducted according to ASTM E18 using the type B-scale with a steel ball indenter. The procedures were outlined in Section 4.9.3. The charpy specimen identified as "*2*" in Figure 4.18 was used for determining the surface hardness of the damaged-repaired steel. Table 5.47 shows the average surface hardness, standard deviation, and the estimated ultimate strength for all the damaged-repaired A7 steels. The results are further discussed and compared in Section 6.4.3.

5.3.4.4 Microstructure investigations

Investigations were conducted to determine the effects of multiple damage-heat straightening repairs on the microstructure of A7 steel. The charpy specimens used to conduct Rockwell hardness tests were also used for the microstructure investigations. The specimens were prepared in accordance to ASTM E3 as discussed in Section 4.9.4. The etched specimens were placed under a metallurgical microscope with a photo micrographic camera attached. The magnification of 480X was chosen to compute the grain sizes of A7 steel. Figure 5.52 (a-f) shows the microstructure of undamaged A7 steel and some of the multiple damaged-heat straightening repaired specimens at 480X. The resulting grains sizes and percentage of pearlite grains are given for all A7 specimens in Table 5.47. As discussed in Section 4.9.4, a more fine-grained microstructure is generally stronger and tougher than a more coarse-grained microstructure. There is a slight increase on the surface hardness and a slight decrease on the ductility. A microstructure that is more pearlitic is harder, stronger, and more brittle. However, only significant and consistent changes in the percent pearlite would be further analyzed as the amount is related to the location taken for the picture as discussed in Section 2.4.3. The results are provided in Table 5.47 for completeness. The results are further discussed and compared in Section 6.4.3.

5.4 OVERHEATED A36 STEEL LABORATORY-SCALE SPECIMENS

This section presents the experimental investigations of A36 steel laboratory-scale specimens subjected to multiple damage-overheated repair cycles. The undamaged A36 steel material properties are presented in Section 5.4.1. The multiple damage-overheated repair cycles and final conditions of the repaired test specimens are discussed in Section 5.4.2. The results of material tests on specimens made from the damaged-repaired A36 steel are presented in Section 5.4.3. The test matrix of overheated A36 steel specimens was not changed from the planned matrix shown in Table 4.4.

5.4.1 Undamaged A36 Steel Material Properties

Uniaxial tension coupons and charpy v-notch specimens were fabricated from the undamaged A36 steel specimen. This A36 steel will be referred as A36-Plate 2 to distinguish it from the other A36 plate. Note that earlier A36 specimens, which were repaired with a maximum heating temperature of 1200 °F, were not fabricated from the same plate as the overheated specimens. The results of Rockwell hardness tests and microstructure investigations are presented later in Sections 5.4.3.3 and 5.4.3.4.

Tension Tests

Two uniaxial tensile tests were conducted to determine the undamaged A36 steel material properties. Figure 5.53 shows the stress-strain behavior of the undamaged A36 steel tension coupons which are identified as A36-Undamaged_1-Plate_2 and A36-Undamaged_2-Plate_2. Uniaxial tension coupons from A36-Plate 1 are also shown in Figure 5.15 for comparison. The yielding of the steel is shown in Figure 5.54. The corresponding structural properties (defined in Section 4.9.1) are given in Table 5.48. The structural properties of both tensile coupons related favorably with each other.

Fracture Toughness Tests

Charpy specimens made from undamaged A36-Plate 2 were tested according to ASTM E23. The fracture toughness values are given in Table 5.49. This table also includes the results of statistical analysis of the fracture toughness data, namely, the statistical mean (average), the 95% confidence interval (CI) for the actual mean, the standard deviation, the median, and the average absolute deviation from the median.

Student's t-test analysis was conducted to evaluate the statistical differences between the quarter and mid-thickness fracture toughness values. As mentioned previously in Section 4.9.2, the t-test evaluates the statistical difference between two data sets using their respective means, standard deviations, and sample set sizes. The results from the t-test include the t-value and the corresponding probability of null hypothesis, where the null hypothesis implies that the data sets are statistically similar. Table 5.50 summarizes the results of the t-test analysis and indicates that the probability of the data sets being statistically similar is only 24%. Considering the fracture toughness data in Table 5.49, the outliers (i.e. 30 lb-ft from the quarter thickness and 76 lb-ft and 82 lb-lb from the mid thickness) were removed and the t-test was performed again, which indicated a 72% probability of that the data sets are statistically similar. Hence, the quarter and mid-thickness toughness values are combined into one set for the A36 steel and considered without differentiation in this report. Table 5.51 presents the statistical analysis of all the quarter and mid-thickness charpy specimens combined into one set. The outliers are included in this statistical analysis.

5.4.2 Experimental Investigations on Overheated A36 Steel

This section discusses all the experimental investigations conducted on overheated A36 steel. The behavior of the specimens while damaging is summarized in Section 5.4.2.1. The behavior of the specimens while repairing by overheating is summarized in Section 5.4.2.2. The conditions of the final repaired specimens are summarized in Section 5.4.2.3.

5.4.2.1 Damage Cycles

The overheated A36 specimens were subjected to damage strains of 60 ε_y and 90 ε_y corresponding to either 0.77 in/in or 0.116 in/in. The experimental procedure and instrumentation used were similar to other tests discussed in Section 4.7.1. The experimental damage cycles progressed well for this group of specimens. The left and right displacement transducers, which measured the average strains of the test area, related well to each other. The right displacement transducer typically indicated a slightly higher strain than the strain gages. The multiple damage cycles were all completed when the right displacement transducer reached the desired level of displacement. For example, Figure 5.55 shows all three damage cycles of Specimen A36-60-25-3-1600 and Figure 5.56 shows all three damage cycles of Specimen A36-90-25-3-1600. In Figures 5.55 and 5.56, "Uniaxial Tension Test" indicates the stress-strain curve of an undamaged A36 steel specimen. Usually, the A36 steel material strength increases after one damage-repair event.

5.4.2.2 Repair Cycles

The experiments of A36 steel specimens repaired with a maximum heating temperature of 1400 °F progressed well. At 1400 °F, a red glow would appear on the heated surface. The heating temperatures were verified using the infrared temperature gun. After removing the torch, the specimen remained red as shown in Figure 5.57(a). A specimen heated to a maximum heating temperature of 1200 °F is shown for comparison in Figure 5.57(b). When repairing the specimens at a maximum temperature of 1600 °F, the surface of the steel shined a bright orange color and was hot enough to give the appearance of becoming fluid on the surface. A view of Specimen A36-60-25-1-1600 at 1600 °F is shown in Figure 5.58(a) and a view of Specimen A36-90-25-3-1600 while cooling but still at elevated temperatures (approximately 1100°F) is shown in Figure 5.58(b). Figure 5.58(b) shows surface pealing of Specimen A36-90-25-3-1600. This specimen was subjected to the most heating cycles for specimens heated to 1600 °F.

The overheated specimens repaired faster than other specimens repaired with maximum heating temperatures of 1200 °F. The experimental behavior of specimens subjected to 90 ε_y and 0.25 σ_y while heating to maximum temperatures of 1200 °F, 1400 °F, and 1600 °F are compared in Figures 5.59, 5.60, and 5.61, respectively. It took approximately 4 heating cycles to repair a specimen while using overheated temperatures (1400 °F or 1600 °F) and 6-8 heating cycles to repair while using a maximum temperature of 1200 °F. For specimens subjected to a restraining stress of 0.50 σ_y, it typically took 3 heating cycles to repair a specimen while overheating (1400 °F or 1600 °F) as opposed to 4-5 heating cycles when heating it to 1200 °F.

A phase transformation diagram for an iron-iron carbide material was provided in Figure 4.2. At a temperature of 1341 °F, the steel begins a polymorphic transformation from the ferrite-pearlite phase to the α–γ Iron phase. At a temperature of 1470 °F, the α–γ Iron state transforms completely to γ-Iron or austenite. If the steel then cools too rapidly, the production of martensite or bainite, which is much more brittle than pearlite, may be possible. An isothermal transformation diagram for AISI 1010 steel, which has similar chemical composition of A36 steel, is shown in Figure 5.62. If the steel cools faster than the cooling period indicated on the far left, 100% martensite will form. If the steel cools at a rate that lies between the far left and far right cooling periods, a combination of ferrite, martensite, bainite, or pearlite will form. If the steel cools slower than the cooling period on the right, ferrite and pearlite will form. The cooling time-temperature curves measured with the infrared thermometer for specimens repaired using a maximum temperature of 1600 °F are shown in Figure 5.62 to the right. Time zero represents the moment when the temperature at the surface drops under 1470 °F. From the experimental data observed in Figure 5.62, the steel is cooling gradually enough that the production of martensite and bainite should not be an issue.

Since the weather conditions in the lab setting do not necessarily relate to conditions when heat straightening repairs are conducted, the researchers as suggested by MDOT found it necessary to heat the steel to temperatures of at least 1600 °F outdoors on a cooler day. A discarded A7 steel specimen and a discarded A36 steel specimen were used to conduct the outdoor investigations. Three time-temperature profiles were recorded for each steel type between 8:30-10:00 A.M. on April 27, 2004 for both steel types. The specimens were allowed to cool to 250 °F in between heating cycles. The temperature in the East Lansing area was approximately 34 °F. The outdoor conditions were also quite windy. The outdoor cooling rates of two time-temperature profiles of each steel type are compared in Figure 5.63. Figure 5.63 also shows two cooling rates of an overheated A36 steel specimen tested in the lab for comparison purposes. The temperature range used in Figure 5.63 is from 1470 °F to 250 °F. The time-temperature profiles were plotted on the continuous cooling diagram shown in Figure 5.64. From Figure 5.64, it appears that cooling outside on a cold day will not significantly change the time-temperature curve, and will not lead to the possible formation of unwanted martensite or bainite microstructures. The cooling periods in Figure 5.64 are not measured from the Ac3 temperature of 1530 °F. However, plotting from this higher temperature would further indicate these formations are not an issue.

5.4.2.3 Condition of Overheated A36 Steel Specimens after Experimental Investigations

Significant curvature was not seen in any of the overheated A36 steel specimens after the experimental investigations. All of the possible causes of curvature in the test setup were accounted for while testing the original A36 and A588 steel specimens. Photographs were taken from the front and side views of all overheated specimens. A front view of specimens damaged to 60 ε_y is shown in Figure 5.65. Figures 5.66 and 5.67 show side views of the resulting specimens.

The surface conditions of Specimens A36-90-50-3-1600 and A36-90-25-3-1600 are shown in Figure 5.68(a, b). The condition of the steel as shown in Figure 5.68 is similar for all specimens heated to maximum temperatures of 1600 °F.

5.4.3 Results of Material Testing on Overheated A36 Steel

This section presents the results of material tests conducted on specimens fabricated from the test areas of overheated A36 laboratory-scale specimens subjected to multiple damage-repair cycles. The material tests were conducted according to the applicable ASTM standards [*1*] as discussed in Section 4.9. The comparisons and conclusions using the material test results are discussed later in Section 6.5.

5.4.3.1 Uniaxial Tension Tests

Uniaxial tension tests were conducted on coupons from the damaged-repaired overheated A36 specimens. The dimensions of the coupons, descriptions of testing procedures, and definitions of the structural properties determined from the stress-strain relationships were discussed in Section 4.9.1.

From each damage-repaired specimen, two tension coupons were removed, one from the left side and one from the right as shown in Figure 4.13. The results from the two coupons typically related well to each other. The average value of the two coupons for each damage-repaired specimen will be used for further comparisons. The results of the uniaxial tension stress-strain relationships for specimens subjected to a damage strain of 60 ε_y and a maximum temperature of 1400 °F are shown in Table 5.52. The results for specimens subjected to a damage strain of 60 ε_y and a maximum temperature of 1600 °F are shown in Table 5.53. The results for specimens subjected to a damage strain of 90 ε_y and a maximum temperature of 1400 °F are shown in Table 5.54. The results for specimens subjected to a damage strain of 90 ε_y and a maximum temperature of 1600 °F are shown in Table 5.55. The results are further discussed and compared in Section 6.5.1.

5.4.3.2 Charpy Impact Fracture Toughness Results

Fracture toughness tests were conducted according to ASTM E23 on charpy specimens from all the damaged-repaired overheated A36 specimens. The process for conducting the tests was presented in Section 4.9.2.The results of the charpy tests on undamaged A36 steel from A36-Plate 2 were presented in Section 5.4.1. All tests were conducted by removing the specimens from a liquid silicone bath at a temperature of 40 °F. The results of the charpy impact fracture toughness tests are provided in Table 5.56. In Table 5.56, "QA" represents an average of the quarter thickness results (Specimens 1, 2, and 3) and "MA" represents an average of the mid thickness results (Specimens 4, 5, and 6). The results of the charpy impact fracture toughness tests are further interpreted and compared in Section 6.5.2.

5.4.3.3 Rockwell Hardness Results

Rockwell hardness tests were conducted to determine the surface hardness of damaged-repaired overheated A36 steel. These tests were conducted according to ASTM E18 using the type B-scale with a steel ball indenter. The procedures were outlined in Section 4.9.3. The charpy specimen identified as "*2*" in Figure 4.13 was used for determining the surface hardness of the damaged-repaired steel. Table 5.57 shows the average surface hardness, standard deviation, and the estimated ultimate strength for all the damaged-repaired overheated A36 steels. The results are further discussed and compared in Section 6.5.3.

5.4.3.4 Microstructure investigations

Investigations were conducted to determine the effects of multiple damage-heat straightening repairs on the microstructure of overheated A36 steel. The charpy specimens used to conduct Rockwell hardness tests were also used for the microstructure investigations. The specimens were prepared in accordance to ASTM E3 as discussed in Section 4.9.4. The etched specimens were placed under a metallurgical microscope with a photo micrographic camera attached. The magnification of 480X was chosen to compute the grain sizes of overheated A36 steel. Figure 5.69 (a-f) shows the microstructure of undamaged A36 steel and some of the multiple damaged-heat straightening repaired specimens at 480X. The resulting grains sizes and percentage of pearlite grains are given for all overheated A36 specimens in Table 5.57. As discussed in Section 4.9.4, a more fine-grained microstructure is generally stronger and tougher than a more coarse-grained microstructure. There is a slight increase on the surface hardness and a slight decrease on the ductility. A microstructure that is more pearlitic is harder, stronger, and more brittle. However, only significant and consistent changes in the percent pearlite would be further analyzed as the amount is related to the location taken for the picture as discussed in Section 2.4.3. The results are provided in Table 5.57 for completeness. The results are further discussed and compared in Section 6.5.3.

5.5 MICROSTRUCTURE OF STEEL AFTER DAMAGE

One flat sheet-type tensile coupon (see Figure 4.46, thickness = 0.5 in) was fabricated from each undamaged plate (A36-Plate 1, A588, A7, and A36-Plate 2). The coupons were prepared for microscopic investigations according to ASTM E3 as discussed in Section 4.9.4. Each coupon was subjected to the three damage strains considered in Task III, which were 30 ε_y, 60 ε_y, and 90 ε_y for A36 and A7 and 20 ε_y, 40 ε_y, and 60 ε_y for A588. Microstructure pictures were taken of the tensile coupon before and after each damage level.

Steel is classified as a polycrystalline material which refers to a material composed of more than one crystal or grain. Gross plastic deformation of a polycrystalline specimen corresponds to the comparable distortion of the individual grains by means of slip. During deformation, mechanical integrity and coherency are maintained along the grain boundaries; that is, the grain boundaries usually do not come apart or open up. Each grain is constrained by the neighboring grains. According to Callister [*4*], plastic deformations should result in the production of slip planes and grain elongation along the direction in

which the specimen was extended. A dislocation is a linear or one-dimensional defect around by which some of the atoms are misaligned [*4*]. The process by which plastic deformation is produced by dislocation motion is termed slip. The crystallographic plane along which the dislocation line transverses is the slip plane.

The microstructure of undamaged and after all three damage strain levels is shown in Figures 5.70(a-d), 5.71(a-d), 5.72(a-d) and 5.73(a-d) for A36-Plate 1, A588, A7, and A36-Plate 2, respectively. The microstructures of the repaired specimens are also shown in Figures 5.70-5.73 (e-f) for further comparisons. Figure 5.70 is taken at a magnification of 240X and Figures 5.71-5.73 are taken at a magnification of 480X. A36-Plate 1 corresponds to comparisons between the first twenty-eight A36 specimens and A36-Plate 2 corresponds to comparisons between the sixteen overheated specimens.

The microstructures of plastically deformed steel shown in Figures 5.70-5.73 do not necessary relate well to the predictions as discussed by Callister [*4*]. The linear lines shown are the formation of slip planes and suggested by Callister [*4*], the directions of the slip planes vary from one grain to another. In difference to the theories introduced by Callister [*4*], the grains did not appear to elongate in any particular direction. The grain size at different damage strains does not alter for A7 and A36 steel. However, the grain size of A588 steel decreased after damage.

As shown in Figures 5.70-5.3 (e-f), slip planes are not present after the heat straightening applications. Also noticed, is that the grain sizes are becoming smaller after repair for A7 and A36 steels.

5.6 REFERENCES

1. ASTM, “Standard Test Methods and Definitions for Mechanical Testing of Steel Products,” A370-97a, West Conshohocken, PA, 1999.
2. ABAQUS, *ABAQUS/Standard User’s Manuals*, Volumes I-III Hibbitt, Karlsson, and Sorenson, Inc., Pawtucket, Rhode Island, 1998.
3. Tinklenberg, G.L., “Evaluation of Weathering Steel in a Detroit Freeway Environment, Second Eight-Year Study”, Michigan Department of Transportation, Materials and Technology Division. R-1277, 1986.
4. Callister, W.D., *Material Science and Engineering, an Introduction*, Fourth Edition, John Wiley & Sons Inc., New York, New York, 1997.

Table 5.1
Structural properties of undamaged A36 steel

Property	1	2	3	Average
Upper Yield Stress (σ_y)	45.0	39.3	46.0	43.4
Lower Yield Stress (σ_y)	38.8	37.76	38.7	38.4
Plateau Yield Stress (σ_y)	39.5	37.8	39.1	39.3
Elastic Modulus (E)	30287	30409.1	30874.9	30523.7
Yield Strain (ε_y)	0.00130	0.00124	0.00127	0.00129
Ultimate Stress (σ_u)	64.4	64.4	64.8	64.5
Ultimate Strain (ε_u)	0.19	0.19	0.20	0.20
ε_u / ε_y	145.68	155.37	157.93	153.0
% Elongation	-	39.00	39.33	39.16
% Reduction	-	72.66	74.03	73.34

Table 5.2
Fracture toughness results of A36 steel using MSU verified testing machine

Number	Temperature (F)	Location	FT (lb-ft)
1	39.8	Quarter	226
2	39.9	Quarter	210
3	39.9	Quarter	209
4	39.9	Quarter	206
5	40.0	Quarter	199.5
6	40.3	Quarter	194
7	39.5	Quarter	153
8	39.6	Quarter	115
9	39.7	Quarter	100

Table 5.3
Fracture toughness steel of A36 steel using MDOT NIST certified machine

Number	Temperature (F)	Location	FT (lb-ft)
1	40	Quarter	144
2	40	Quarter	141
3	40	Quarter	141
4	40	Quarter	136
5	40	Quarter	125
6	40	Quarter	86

Table 5.5
Fracture toughness results of A36 steel fabricated by MSU machinist

Number	Temperature (F)	Location	FT (lb-ft)
1	40	Quarter	92
2	40	Quarter	142
3	40	Quarter	33
4	40	Quarter	29
5	40	Quarter	29
6	40	Quarter	35

Table 5.4
Fracture toughness results of A36 steel fabricated by MDOT machinist

Number	Temperature (F)	Location	FT (lb-ft)
1T	40	Quarter	74
2T	40	Quarter	138
3T	40	Quarter	118
4T	40	Quarter	156
5T	40	Quarter	159
6T	40	Quarter	122
7T	40	Quarter	202

Table 5.6
Fracture toughness results of undamaged A36 steel (Break depth = 0.315 in.)

Specimen	Quarter (lb-ft)	Mid (lb-ft)
1	74	85
2	86	91
3	92	94
4	108	97
5	118	102
6	120	104
7	122	105
8	124	113
9	125	136
10	136	150
11	138	154
12	138	154
13	141	167
14	141	182
15	144	200
16	151.5	
17	156	
18	159	
19	160	
20	169.5	
21	202	
Mean	134	129
95% confidence interval for mean	120.2 – 147	108.6 – 149.3
Std. Deviation	29.4	36.7
Median	138	113
Average absolute deviation from median	21.8	31.0

Table 5.7
Fracture toughness results of undamaged A36 steel (Break depth = 0.304 in.)

Specimen	Quarter (lb-ft)	Mid (lb-ft)
1	105	88
2	113	100
3	122	106
4	145	150
5	148	151
6	190	210
Mean	137	134
95% confidence interval for actual mean	104.6 – 169.8	86.35 – 182.0
Std. Deviation	31.0	45.6
Median	134	128
Average absolute deviation from median	23.8	36.2

Table 5.8
Student's t-test comparing the means of data sets in Table 5.6

t-test to establish the statistical difference between quarter and mid thickness fracture toughness for A36 charpy specimens with break depth = 0.315 in.
Results of unpaired t-test (see Section 4.9.2):
t=0.421
Std. deviation=32.6
Degrees of freedom=34
Probability of null hypothesis (the data sets are statistically similar) = 0.68

Table 5.9
Student's t-test comparing the means of data sets in Table 5.7

t-test to establish the statistical difference between quarter and mid thickness fracture toughness for A36 charpy specimens with break depth = 0.304 in.
Results of unpaired t-test (see Section 4.9.2):
t=0.133
Std. deviation=39.0
Degrees of freedom=10
Probability of null hypothesis (the data sets are statistically similar) = 0.90

Table 5.10
Student's t-test comparing the means of data sets in Tables 5.6 and 5.7

t-test to establish the statistical difference between quarter thickness fracture toughness for A36 charpy specimens with break depth = 0.315 and 0.304 in.
Results of unpaired t-test (see Section 4.9.2):
t=0.261
Std. deviation=29.8
Degrees of freedom=25
Probability of null hypothesis (the data sets are statistically similar) = 0.80

t-test to establish the statistical difference between mid thickness fracture toughness for A36 charpy specimens with break depth = 0.315 and 0.304 in.
Results of unpaired t-test (see Section 4.9.2):
t=0.276
Std. deviation=39.2
Degrees of freedom=19
Probability of null hypothesis (the data sets are statistically similar) = 0.79

Table 5.11
Statistical values of the combined quarter and mid thickness charpy specimens (break depth=0.304 in.)

Property	Value
Mean	136
95% Confidence Interval for actual mean	112-159.3
Std. Deviation	37.2
Median	134
Average absolute deviation from median	30

Table 5.12
Final test matrix of A36 small-scale specimens

Damage Strain (ε_d)	*Restraining Stress (σ_r)*	*Number of Repair Cycles (N_r)*	*Specimen Name*
30 ε_y	0.40 σ_y	1	A36-30-40-1
		2	A36-30-40-2
		3	A36-30-40-3
		4	A36-30-40-4
		5	A36-30-40-5
	0.70 σ_y	1	A36-30-70-1
		2	A36-30-70-2
		3	A36-30-70-3
		4	A36-30-70-4
		5	A36-30-70-5
60 ε_y	0.25 σ_y	1	A36-60-25-1
		2	A36-60-25-2
		3	A36-60-25-3
		4	A36-60-25-4
		5	A36-60-25-5
	0.50 σ_y	1	A36-60-50-1
		2	A36-60-50-2
		3	A36-60-50-3
		4	A36-60-50-4
		5	A36-60-50-5
90 ε_y	0.25 σ_y	1	A36-90-25-1
		3	A36-90-25-3
		5	A36-90-25-5
	0.50 σ_y	1	A36-90-50-1
		2	A36-90-50-2
		3	A36-90-50-3
		4	A36-90-50-4
		5	A36-90-50-5

Table 5.13
Structural properties of damaged-repaired A36-30-40 specimens

	A36-30-40-1		A36-30-40-2		A36-30-40-3		A36-30-40-4		A36-30-40-5	
	X	**Y**	**X**	**Y**	**X**	**Y**	**X**	**Y**	**X**	**Y**
Upp. σ_y (ksi)	44.8	44.3	46.6	48.0	48.7	48.0	45.7	43.8	47.1	45.3
Low. σ_y (ksi)	43.5	41.7	45.4	45.3	48.7	46.5	45.7	43.8	43.3	42.6
Pla. σ_y (ksi)	44.3	42.8	45.9	45.9	48.5	46.5	45.7	44.1	43.5	43.8
E (ksi)	31766	31352	32274	32314	32229	33440	30770	32911	33168	32327
ε_y	0.00137	0.00133	0.00141	0.00140	0.00151	0.00139	0.00148	0.00133	0.00131	0.00132
σ_t	68.66	67.73	68.69	68.78	71.87	70.37	68.1	68	65.11	64.72
ε_u	0.14	0.14	0.16	0.14	0.10	0.15	0.14	0.14	0.16	0.13
ε_u / ε_y	99.8	102.3	110.9	102.7	69.3	105.7	91.0	101.4	122.6	97.9
% Elongation	30.47	28.35	31.38	30.38	27.55	30.85	30.95	29.84	32.35	31.89
% Reduction	66.35	66.88	66.41	68.24	67.88	67.99	68.81	69.24	63.69	62.85

Table 5.14
Structural properties of damaged-repaired A36-30-70 specimens

	A36-30-70-1		A36-30-70-2		A36-30-70-3		A36-30-70-4		A36-30-70-5	
	X	**Y**	**X**	**Y**	**X**	**Y**	**X**	**Y**	**X**	**Y**
Upp. σ_y (ksi)	44.7	46.1	44.0	44.8	46.4	46.1	47.0	48.6	45.1	47.1
Low. σ_y (ksi)	41.5	42.2	42.7	43.9	46.4	45.6	45.8	45.7	45.1	47.1
Pla. σ_y (ksi)	41.9	44.2	43.2	44.7	46.5	46.0	45.9	46.7	45.1	47.1
E (ksi)	31453	32110	30596	30555	31051	30321	30243	30255	30053	30053
ε_y	0.00132	0.00131	0.0014	0.00144	0.00149	0.0015	0.00151	0.00151	0.0015	0.00157
σ_t	66.6	68.4	68.6	69.5	69.8	69.2	67.8	70	68.8	71.5
ε_u	0.15	0.17	0.16	0.15	0.13	0.16	0.14	0.16	0.12	0.09
ε_u / ε_y	116	129	114	105	86	107	92	104	78	59
% Elongation	32.93	34.45	28.22	26.99	29.21	31.43	30.1	32.58	26.6	25.6
% Reduction	70.85	70.95	60.76	68.01	69.49	60.3	69.04	66.78	66.23	69.58

Table 5.15
Structural properties of damaged-repaired A36-60-25 specimens

	A36-60-25-1	A36-60-25-2		A36-60-25-3		A36-60-25-4		A36-60-25-5	
	X	X	Y	X	Y	X	Y	X	Y
Upp. σ_y (ksi)	40.6	46.3	44.3	48.5	45.6	46.1	45.0	45.5	45.6
Low. σ_y (ksi)	40.0	42.8	40.8	43.7	42.2	42.1	41.3	41.0	39.7
Pla. σ_y (ksi)	40.6	43.1	42.1	42.9	42.1	41.6	44.0	40.1	42.5
E (ksi)	32184	31564	29763	29815	30273	31144	30393	31052	31492
ε_y	0.00124	0.00136	0.00137	0.00147	0.00139	0.00135	0.00136	0.00132	0.00126
σ_t (ksi)	63.6	65.4	65.4	65.4	65.7	63.9	63.5	63.2	62.8
ε_u	0.17	0.16	0.16	0.16	0.15	0.17	0.18	0.176	0.186
ε_u / ε_y	136.8	118	116.7	109.2	107.6	125.8	132.5	133.3	147.5
% Elongation	34.4	30.5	34.2	33.53	30.55	33.8	35.02	34.7	36.36
% Reduction	69.57	69.38	70.18	70.03	71.26	70.67	70.42	69.44	72.79

Table 5.16
Structural properties of damaged-repaired A36-60-50 specimens

	A36-60-50-1		A36-60-50-2		A36-60-50-3	A36-60-50-4		A36-60-50-5	
	X	Y	X	Y	X	X	Y	X	Y
Upp. σ_y (ksi)	47.7	43.2	41.0	44.6	43.8	44.1	43.7	44.0	44.5
Low. σ_y (ksi)	41.2	41.0	41.0	43.7	40.7	39.7	40.8	41.0	42.4
Pla. σ_y (ksi)	41.4	41.1	41.2	44.4	41.0	40.0	41.1	42.3	44.3
E (ksi)	32574	31408	28521	31070	31598	30911	31130	30688	30513
ε_y	0.00127	0.00131	0.00144	0.00143	0.00130	0.00129	0.00132	0.00138	0.00145
σ_t (ksi)	65.6	65.2	67.6	67.5	65.0	64.2	64.8	64.1	65.6
ε_u	0.18	0.19	0.136	0.16	0.167	0.176	0.184	0.144	0.149
ε_u / ε_y	142.3	145.5	94.6	113.8	129.7	137	140.4	107.8	107.2
% Elongation	34.34	35.04	30.74	35.14	33.5	35.38	31.58	33.87	30.94
% Reduction	70.61	69.7	68.68	70.87	70.95	64.65	63.37	71.27	71.43

Table 5.17
Structural properties of damaged-repaired A36-90-25 specimens

	A36-90-25-1		A36-90-25-3		A36-90-25-5	
	X	**Y**	**X**	**Y**	**X**	**Y**
Upper σ_y (ksi)	43.8	43.5	41.3	42.5	42.5	41.7
Lower σ_y (ksi)	39	39.9	38.8	39.7	40.4	41.4
Plateau σ_y (ksi)	39.6	40.3	39.6	39.8	40.4	41.4
E (ksi)	29881	30152	31076	30222	28756	30140
ε_y	0.00131	0.00132	0.00125	0.00131	0.0014	0.00137
σ_t (ksi)	64.3	64.6	61.4	61.9	60.8	61.6
ε_u	0.179	0.167	0.19	0.184	0.19	0.184
ε_u / ε_y	137.1	126.2	152.2	140.1	135.2	134
% Elongation	32.03	31.22	37.54	35.55	37.27	37.88
% Reduction	71.15	70.83	76.31	73.84	76.18	74.42

Table 5.18
Structural properties of damaged-repaired A36-90-50 specimens

	A36-90-50-1		A36-90-50-2		A36-90-50-3		A36-90-50-4		A36-90-50-5	
	X	**Y**	**X**	**Y**	**X**	**Y**	**X**	**Y**	**X**	**Y**
Upp. σ_y (ksi)	318.5	317.2	284.1	303.4	309.6	286.1	299.2	310.3	327.5	331.0
Low. σ_y (ksi)	283.4	277.9	270.3	291.7	280.6	279.9	284.8	286.1	289.6	294.4
Pla. σ_y (ksi)	283.4	278.6	279.2	300.6	285.5	285.5	288.2	292.3	291.0	293.7
E (ksi)	199.4	209.7	201.9	207.2	214.4	210.4	204.4	213.4	212.6	214.5
ε_y	0.00142	0.00132	0.00134	0.00141	0.00131	0.00133	0.00139	0.00134	0.00136	0.00137
σ_t (ksi)	437.8	437.8	437.1	445.4	434.4	435.8	429.6	441.3	435.8	437.1
ε_u	0.19	0.19	0.17	0.17	0.18	0.18	0.17	0.18	0.19	0.18
ε_u / ε_y	133	142.6	127.7	117.2	137.5	138.3	124.2	132.8	137.3	128.9
% Elongation	31.4	33.86	32.53	32.57	37.76	36.04	36.36	35.71	36.67	35.08
% Reduction	65.8	64.68	73.82	72.12	75.29	74.7	76.41	72.78	74.19	74.71

Table 5.19
Fracture toughness of damaged-repaired A36 specimens (Break depth = 0.304 in.)

	Quarter Thickness			Mid Thickness				
Specimen	**1**	**2**	**3**	**4**	**5**	**6**	**QA**	**MA**
***A36-30-40-1*	72.5	70	43	81	95	27.5	62	68
A36-30-40-2	72	-	68	32	17.5	22.5	70	24
A36-30-40-3	66	55	93	54	81	40	71	58
A36-30-40-4	95	66	96	77	93	87	86	86
A36-30-40-5	43	36	46	28.5	35	27	42	30
A36-30-70-1	89	115	69	77	99	107	91	94
A36-30-70-2	27	43	26	24	28	24	32	25
***A36-30-70-3*	70	25	46	17	61	64	47	47
***A36-30-70-4*	91	63	79	66	82	72	78	73
***A36-30-70-5*	8.5	49	57	40	50	62	38	51
A36-60-25-1	213	175	214	88	98	48	201	78
A36-60-25-2	173	110	120	51	64	16	134	44
A36-60-25-3	36	31	75	70	97	20	47	62
A36-60-25-4	21	212	32	63	22.5	16	88	34
A36-60-25-5	19.5	19.5	20	10	15	14	20	13
A36-60-50-1	148	143	157	23.5	50	39	149	38
A36-60-50-2	200	157	219	28	26	95	192	50
A36-60-50-3	110	37	18	78	95	67	55	80
A36-60-50-4	32	28	33	30	45	18	31	31
***A36-60-50-5*	89	61	77	19	17	78	76	38
A36-90-25-1	236	115	239	78	143	112	197	111
A36-90-25-3	15	169	68	242	-	242	84	242
***A36-90-25-5*	242	220	238	21.5	13.5	20.5	233	19
A36-90-50-1	28	23	29.5	12	32	28	27	24
A36-90-50-2	24	97	21.5	89	240	105	48	145
A36-90-50-3	19	21.5	25	30	88	17	22	45
A36-90-50-4	95	92	109	240	230	232	99	234
A36-90-50-5	67	95	74	232	94	110	79	145

*Refers to specimens with significant curvature after heat straightening. Data is not entirely reliable. "QA" refers to the average of the quarter thickness charpy specimens and "MA" refers to the average of the mid thickness charpy specimens.

Table 5.20
Rockwell hardness and microstructure results of damaged-repaired A36 steel

Specimen	Hardness Average	Hardness Std. Dev.	Tensile strength for comparison σ_t (ksi)	Grain Size (mm)	Percent Pearlite
Virgin	64.5	0.346	64.5	0.0303	34.9
***A36-30-40-1*	68.2	0.361	68.2	0.0277	28.4
A36-30-40-2	68.7	0.404	68.7	0.0345	16.3
A36-30-40-3	71.1	0.896	71.1	0.0253	26.6
A36-30-40-4	68.1	1.217	68.1	0.0252	23.1
A36-30-40-5	64.9	3.236	64.9	0.0286	24.3
A36-30-70-1	67.5	1.159	67.5	0.0293	32.7
A36-30-70-2	69.1	0.361	69.1	0.0270	28.4
***A36-30-70-3*	69.5	1.332	69.5	0.0269	24.7
***A36-30-70-4*	68.9	0.737	68.9	0.0310	22.8
***A36-30-70-5*	70.2	0.603	70.2	0.0316	21.6
A36-60-25-1	63.6	3.037	63.6	0.0339	26.2
A36-60-25-2	65.4	0.3	65.4	0.0291	21
A36-60-25-3	65.6	0.058	65.6	0.0263	29
A36-60-25-4	63.7	1.97	63.7	0.0291	21.4
A36-60-25-5	63	0.611	63	0.0251	25.3
A36-60-50-1	65.4	0.814	65.4	0.0277	26.2
A36-60-50-2	67.6	1.286	67.6	0.0297	23.7
A36-60-50-3	65	0.611	65	0.0274	23.7
A36-60-50-4	64.5	5.082	64.5	0.027	19.1
***A36-60-50-5*	64.9	0.764	64.9	0.0299	18.4
A36-90-25-1	64.5	1.343	64.5	0.0246	18.7
A36-90-25-3	61.7	0.889	61.7	0.023	26.5
***A36-90-25-5*	61.2	1.258	61.2	0.027	23.4
A36-90-50-1	63.5	0.737	63.5	0.0305	17.6
A36-90-50-2	64	0.611	64	0.0292	16.5
A36-90-50-3	63.1	2.443	63.1	0.0292	22.6
A36-90-50-4	63.2	0.346	63.2	0.0286	14.6
A36-90-50-5	63.3	0.611	63.3	0.0251	17.4

*Refers to speci mens with significant curvature after heat straightening. Data is not entirely reliable.

Table 5.21
Structural properties of undamaged A588 steel

	1	2	3	Average
Upper Yield Stress (σ_y)	63.4	63.3	57.8	61.5
Lower Yield Stress (σ_y)	57.0	57.3	55.6	56.6
Plateau Yield Stress (σ_y)	57.3	57.1	57.7	57.4
Elastic Modulus (E)	28333	29187	27336	28285
Yield Strain (ε_y)	0.00202	0.00196	0.00211	0.00203
Ultimate Stress (σ_u)	82.8	83.4	83.2	83.1
Ultimate Strain (ε_u)	0.153	0.160	0.160	0.158
ε_u / ε_y	75.65	81.78	75.80	77.75
% Elongation	-	33.94	33.27	33.60
% Reduction	-	71.85	71.03	71.44

Table 5.22
Fracture toughness results of undamaged A588 steel (Break depth = 0.300 in.)

Specimen	Quarter (lb-ft)	Mid (lb-ft)
1	83	70
2	83	70
3	86	71
4	89	72
5	90	78
6	92	78
7		79
Mean	87.2	74.0
95% confidence interval for actual mean	83.22 – 91.12	70.19 – 77.81
Std. Deviation	3.76	4.12
Median	87.5	72.0
Average absolute deviation from median	3.17	3.43

Table 5.23
Fracture toughness results of undamaged A588 steel (Break depth = 0.315 in.)

Specimen	Quarter (lb-ft)	Mid (lb-ft)
1	88	70
2	96	70
3	98	70
4	98	71
5	99	80
6	102	80
7	104	81
8	105	81
9	107	89
10	108	90
11	109	90
12	112	
13	113	
14	119	
Mean	104	79.3
95% confidence interval for mean	99.50 – 108.8	73.82 – 84.72
Std. Deviation	8.05	8.11
Median	105	80
Average absolute deviation from median	6.29	6.36

Table 5.24
Student's t-test comparing the means of data sets in Table 5.22

t-test to establish the statistical difference between quarter and mid - fracture toughness for A588 charpy specimens with break depth = 0.300 in.
Results of unpaired t-test (see Section 4.9.2):
t=5.97
std. deviation=3.96
degrees of freedom=11
Probability of null hypothesis (the data sets are statistically similar) < 0.0001

Table 5.25
Student's t-test comparing the means of data sets in Table 5.23

t-test to establish the statistical difference between quarter and mid thickness fracture toughness for A588 charpy specimens with break depth = 0.315 in.
Results of unpaired t-test (see Section 4.9.2):
t=7.64
Std. deviation=8.08
Degrees of freedom=23
Probability of null hypothesis (the data sets are statistically similar) < 0.0001

Table 5.26
Student's t-test results comparing the means of data sets in Tables 5.22 and 5.23

t-test to establish the statistical difference between quarter thickness fracture toughness for A588 charpy specimens with break depth = 0.315 and 0.300 in.
Results of unpaired t-test (see Section 4.9.2):
t=4.89
Std. deviation=7.12
Degrees of freedom=18
Probability of null hypothesis (the data sets are statistically similar) < 0.0001
t-test to establish the statistical difference between mid thickness fracture toughness for A588 charpy specimens with break depth = 0.315 and 0.300 in.
Results of unpaired t-test (see Section 4.9.2):
t=1.58
Std. deviation=6.89
Degrees of freedom=16
Probability of null hypothesis (the data sets are statistically similar) = 0.13

Table 5.27
Final test matrix of A588 small-scale specimens

Damage	*Restraining*	*Number of Repair*	*Specimen*
Strain (ε_d)	*Stress (σ_r)*	*Cycles (N_r)*	*Name*
20 ε_y	0.25 σ_y	1	A588-20-25-1
		2	A588-20-25-2
		3	A588-20-25-3
		4	A588-20-25-4
		5	A588-20-25-5
	0.50 σ_y	1	A588-20-50-1
		2	A588-20-50-2
		3	A588-20-50-3
		4	A588-20-50-4
		5	A588-20-50-5
40 ε_y	0.25 σ_y	1	A588-40-25-1
		2	A588-40-25-2
		3	A588-40-25-3
		4	A588-40-25-4
		5	A588-40-25-5
	0.50 σ_y	1	A588-40-50-1
		2	A588-40-50-2
		3	A588-40-50-3
		4	A588-40-50-4
		5	A588-40-50-5
60 ε_y	0.25 σ_y	1	A588-60-25-1
		2	A588-60-25-2
		3	A588-60-25-3
		4	A588-60-25-4
		5	A588-60-25-5
	0.50 σ_y	1	A588-60-50-1
		2	A588-60-50-2
		3	A588-60-50-3
		4	A588-60-50-4
		5	A588-60-50-5

Table 5.28
Structural properties of damaged-repaired A588-20-25 specimens

	A588-20-25-1		A588-20-25-2		A588-20-25-3		A588-20-25-4		A588-20-25-5	
	X	**Y**	**X**	**Y**	**X**	**Y**	**X**	**Y**	**X**	**Y**
Upp. σ_y (ksi)	65.4	65.1	61.5	62.2	62.1	60	61.6	60.8	63.1	62.4
Low. σ_y (ksi)	59.3	59.3	57.1	57.8	57.9	57.9	57.1	56.4	57.7	58.7
Pla. σ_y (ksi)	59.7	59.6	58.4	58	58.6	58.7	57.6	56.9	58.3	59.6
E (ksi)	29580	-	29888	30980	30592	29688	29670	30033	28898	30798
ε_y	0.00202	-	0.00195	0.00187	0.00192	0.00198	0.00194	0.00189	0.00202	0.00194
σ_t (ksi)	84.0	84.1	83.0	83.0	82.0	83.4	80.9	80.6	81.2	-
ε_u	0.15	-	0.15	0.15	0.14	0.13	0.13	0.15	0.13	-
ε_u / ε_y	76.3	-	74.21	77.45	73.09	66.25	66.45	78.12	64.44	-
% Elongation	28.79	30.64	30.71	29.77	28.03	28.43	26.83	29.75	29.09	26.77
% Reduction	69.12	69.15	68.09	67.22	69.86	66.52	70.04	72.35	69.59	69.1

Table 5.29
Structural properties of damaged-repaired A588-20-50 specimens

	A588-20-50-1		A588-20-50-2		A588-20-50-3		A588-20-50-4		A588-20-50-5	
	X	**Y**	**X**	**Y**	**X**	**Y**	**X**	**Y**	**X**	**Y**
Upp. σ_y (ksi)	67.1	66.9	64.4	62.9	66.8	64.8	61.5	64.4	62.0	64.9
Low. σ_y (ksi)	61.2	60.9	60.9	61.1	58.8	61.0	57.1	60.5	60.7	63.4
Pla. σ_y (ksi)	61.9	61.3	61.9	62.4	59.6	63.0	58.1	60.9	62.0	64.9
E (ksi)	30537	30552	29021	29468	30275	30154	30027	29518	30218	30047
ε_y	0.00203	0.00201	0.00213	0.00212	0.00197	0.00209	0.00193	0.00206	0.00205	0.00216
σ_t (ksi)	86.8	86.3	85.0	86.4	83.0	85.4	82.6	84.9	83.5	86.2
ε_u	0.14	0.14	0.11	0.12	0.13	0.11	0.15	0.13	0.12	0.11
ε_u / ε_y	66.60	67.28	52.98	55.25	66.55	51.21	76.49	62.53	57.51	49.54
% Elongation	27.58	28.34	25.88	27.03	27.23	25.78	31.36	26.83	27.45	26.79
% Reduction	68.09	69.30	68.19	67.86	69.88	67.15	70.89	69.27	66.78	67.09

Table 5.30
Structural properties of damaged-repaired A588-40-25 specimens

	A588-40-25-1		A588-40-25-2		A588-40-25-3		A588-40-25-4		A588-40-25-5	
	X	**Y**	**X**	**Y**	**X**	**Y**	**X**	**Y**	**X**	**Y**
Upp. σ_y (ksi)	60.7	59.1	62.3	63.2	65.6	63.7	62.3	66.5	64.3	67.0
Low. σ_y (ksi)	55.2	55.1	57.0	57.4	56.0	58.7	57.8	61.2	58.4	62.1
Pla. σ_y (ksi)	57.6	55.7	57.0	59.0	56.1	58.7	58.2	61.2	58.7	62.1
E (ksi)	30281	31056	31195	30209	30802	30862	30113	31108	30809	30422
ε_y	0.00190	0.00179	0.00183	0.00195	0.00182	0.00190	0.00193	0.00197	0.00191	0.00204
σ_t (ksi)	81.8	81.7	80.5	81.7	78.9	82.2	80.8	82.9	80.5	83.0
ε_u	0.14	0.12	0.16	0.13	0.16	0.15	0.15	0.14	0.14	0.14
ε_u / ε_y	73.07	64.12	84.83	64.51	87.85	77.29	75.54	71.16	71.90	68.58
% Elongation	29.04	26.05	30.02	26.00	32.78	28.96	30.54	26.36	28.32	27.90
% Reduction	71.12	71.91	71.26	67.76	71.57	69.60	71.53	66.85	68.36	66.75

Table 5.31
Structural properties of damaged-repaired A588-40-50 specimens

	A588-40-50-1		A588-40-50-2		A588-40-50-3		A588-40-50-4		A588-40-50-5	
	X	**Y**	**X**	**Y**	**X**	**Y**	**X**	**Y**	**X**	**Y**
Upp. σ_y (ksi)	63.8	64.8	62.9	64.4	61.6	63.8	59.1	63.2	62.1	63.8
Low. σ_y (ksi)	60.3	58.5	59.0	61.2	56.1	56.8	56.0	61.0	55.5	59.9
Pla. σ_y (ksi)	62.3	61.3	59.6	61.8	56.3	58.2	54.4	59.8	56.4	60.7
E (ksi)	30792	29527	29987	29596	30927	30741	29969	31028	30019	30142
ε_y	0.00202	0.00208	0.00199	0.00209	0.00193	0.00189	0.00182	0.00193	0.00188	0.00201
σ_t (ksi)	84.4	83.9	83.3	85.8	80.7	81.9	79.8	83.1	79.5	82.3
ε_u	0.11	0.11	0.14	0.14	0.15	0.12	0.14	0.11	0.15	0.14
ε_u / ε_y	51.90	52.02	70.94	67.53	78.35	65.50	77.68	58.11	78.77	71.01
% Elongation	24.76	25.24	28.35	28.34	29.92	26.46	28.90	24.81	31.72	28.62
% Reduction	67.09	69.03	67.57	67.10	73.27	71.02	72.56	69.69	72.50	68.27

Table 5.32
Structural properties of damaged-repaired A588-60-25 specimens

	A588-60-25-1		A588-60-25-2		A588-60-25-3		A588-60-25-4		A588-60-25-5	
	X	**Y**	**X**	**Y**	**X**	**Y**	**X**	**Y**	**X**	**Y**
Upp. σ_y (ksi)	58.9	62.1	61.3	63.8	58.3	60.2	65.1	65.7	63.3	64.6
Low. σ_y (ksi)	55.3	58.9	56.1	57.8	53.3	55.1	59.8	58.8	56.9	57.5
Pla. σ_y (ksi)	56.1	59.1	56.6	58.3	53.5	56.2	59.9	59.9	57.5	57.7
E (ksi)	30786	30285.3	30440	29528	30446	30058	30364	30674	30732	30555
ε_y	0.00182	0.00195	0.00186	0.00197	0.00176	0.00194	0.00190	0.00195	0.00187	0.00196
σ_t (ksi)	81.0	83.1	78.8	80.4	77.0	78.3	80.5	79.8	77.8	79.3
ε_u	0.14	0.15	0.16	0.15	0.17	0.16	0.14	0.14	0.15	0.14
ε_u / ε_y	77.92	75.33	83.36	76.48	95.04	80.95	72.10	69.64	79.10	71.92
% Elongation	26.68	30.18	32.14	28.79	31.28	30.03	27.00	29.17	31.18	28.36
% Reduction	72.01	69.44	72.02	70.64	74.06	71.69	66.64	66.47	73.56	70.70

Table 5.33
Structural properties of damaged-repaired A588-60-50 specimens

	A588-60-50-1		A588-60-50-2		A588-60-50-3		A588-60-50-4		A588-60-50-5	
	X	**Y**	**X**	**Y**	**X**	**Y**	**X**	**Y**	**X**	**Y**
Upp. σ_y (ksi)	62.4	62.4	59.9	62.7	59.4	65.6	60.9	64.1	66.2	66.9
Low. σ_y (ksi)	58.9	60.0	54.7	60.7	55.1	60.5	59.1	60.9	59.9	62.6
Pla. σ_y (ksi)	60.0	60.4	55.5	60.8	57.3	61.0	60.9	64.1	60.9	62.7
E (ksi)	30294	30672	30238	30646	30010	29944	30933	31158	30430	31132
ε_y	0.00198	0.00197	0.00184	0.00198	0.00191	0.00204	0.00197	0.00206	0.00200	0.00201
σ_t (ksi)	84.3	85.6	80.8	84.6	79.3	81.8	82.0	82.7	80.7	82.6
ε_u	0.14	0.14	0.16	0.14	0.15	0.14	0.12	0.12	0.15	0.14
ε_u / ε_y	71.69	70.08	86.63	72.08	77.51	67.25	58.92	56.39	72.95	71.00
% Elongation	28.94	27.73	31.47	28.43	29.42	27.71	25.96	25.27	28.84	28.56
% Reduction	70.26	68.11	72.24	68.63	70.27	67.98	69.12	67.98	70.98	67.33

Table 5.34
Fracture toughness of damaged-repaired A588 specimens (Break depth = 0.300 in.)

	Quarter			Mid				
Specimen	**1**	**2**	**3**	**4**	**5**	**6**	**QA**	**MA**
A588-20-25-1	77	67	78	52	31	48	74	44
A588-20-25-2	113	108	145	54	56	42	122	51
A588-20-25-3	158	148	124	47	77	52	143	59
A588-20-25-4	156	157	124	84	110	77	146	90
A588-20-25-5	92	82	89	78	107	77	88	87
A588-20-50-1	65	77	78	34	29.5	38	73	34
A588-20-50-2	58	59	60	32	47	31	59	37
A588-20-50-3	77	93	62	48	41	55	77	48
A588-20-50-4	60	59	62	42	45	32	60	40
A588-20-50-5	95	96	115	61	73	48	102	61

Table 5.35
Fracture toughness of damaged-repaired A588 specimens (Break depth = 0.315 in.)

	Quarter			Mid				
Specimen	**1**	**2**	**3**	**4**	**5**	**6**	**QA**	**MA**
A588-40-25-1	148	151	154	86	98	114	151	99
A588-40-25-2	230	160	228	88	74	93	206	85
A588-40-25-3	232	178	160	80	126	95	190	100
A588-40-25-4	256	157	133	93	112	115	182	107
***A588-40-25-5*	-	139	143	26.5	91	49	141	56
A588-40-50-1	114	124	150	54	75	67	129	65
A588-40-50-2	82	69	61	79	65	76	71	73
A588-40-50-3	142	146	161	82	104	89	150	92
A588-40-50-4	132	141	150	58	49	69	141	59
A588-40-50-5	137	130	129	74	96	82	132	84
***A588-60-25-1*	145	130	126	40	51	52	134	48
A588-60-25-2	233	192	194	112	124	78	206	105
A588-60-25-3	125	190	96	120	115	119	137	118
***A588-60-25-4*	79	66	43	40	93	53	63	62
A588-60-25-5	117	93	101	-	105	93	104	99
A588-60-50-1	119	109	135	72	72	95	121	80
A588-60-50-2	-	110	108	60	32	52	109	48
A588-60-50-3	91	72	103	-	48	51	89	50
A588-60-50-4	81	119	108	127	138	69	103	111
A588-60-50-5	112	175	131	47	25	66	139	46

*Refers to speci mens with significant curvature after heat straightening. Data is not entirely reliable.

Table 5.36
Rockwell hardness and microstructure results of damaged-repaired A588 steel

Specimen	Hardness		Tensile strength for comparisons σ_t (ksi)	Grain Size (mm)	% Pearlite
	Average	Std. Dev.			
Virgin	87.2	1.632	83.1	0.0132	25
A588-20-25-1	87.6	1.333	84.1	0.0145	23.2
A588-20-25-2	87.9	1.012	83	0.0159	15.4
A588-20-25-3	87.6	0.359	82.7	0.0147	17.4
A588-20-25-4	86.4	2.137	80.8	0.0164	12.1
A588-20-25-5	88.7	0.163	81.2	0.0187	12.8
A588-20-50-1	90	0.51	86.6	0.0151	22.6
A588-20-50-2	89.1	0.544	85.7	0.0179	21.1
A588-20-50-3	87.8	0.707	84.2	0.0187	18.1
A588-20-50-4	86.4	1.103	83.8	0.0166	22.3
A588-20-50-5	89.5	0.789	84.9	0.0169	16.4
A588-40-25-1	91.3	1.121	81.8	0.0147	9.3
A588-40-25-2	91	1.987	81.1	0.0182	6.7
A588-40-25-3	90.8	3.738	80.6	0.016	18.1
A588-40-25-4	87	0.733	81.9	0.0163	16.2
***A588-40-25-5*	91.7	1.501	80.5	0.015	11.8
A588-40-50-1	91.4	1.466	84.2	0.0164	14.2
A588-40-50-2	92	0.806	84.6	0.0134	14.1
A588-40-50-3	91.4	2.335	81.3	0.0157	16.5
A588-40-50-4	89.9	1.097	81.5	0.0153	16.5
A588-40-50-5	89.8	2.118	80.9	0.0143	8.6
***A588-60-25-1*	90.8	0.48	82.1	0.0165	28.1
A588-60-25-2	90.7	1.832	79.6	0.0169	23
A588-60-25-3	90.8	3.045	77.7	0.0151	11.9
***A588-60-25-4*	91.2	1.646	80.2	0.0159	20.1
A588-60-25-5	91.4	0.387	77.8	0.0144	7.6
A588-60-50-1	92.4	1.49	85	0.0176	18.4
A588-60-50-2	92.7	1.873	82.7	0.0149	15.7
A588-60-50-3	91.4	2.175	80.6	0.0153	24.9
A588-60-50-4	93.8	1.676	82.4	0.0145	23.6
A588-60-50-5	93.4	1.615	81.7	0.015	23.2

*Refers to speci mens with significant curvature after heat straightening. Data is not entirely reliable.

Table 5.37
Chemical composition of new and old A588

Component	A588 (Small Scale)	A588 (Large scale)	A588 (Old)
C	0.160	0.150	0.140
Si	0.420	0.330	0.280
Mn	0.980	1.140	1.070
Mo	0.043	0.020	0.020
Cu	0.290	0.280	0.280
Cr	0.550	0.530	0.550
V	0.043	0.035	0.023
Ni	0.140	0.200	0.320
B	-	0.006	-
S	0.013	0.010	0.022
Al	0.006	0.030	0.026
Ti	0.002	0.009	-
N	0.010	0.009	-
Ca	-	0.001	
P	0.012	0.009	0.011
Sn	0.019	0.014	-

Table 5.38
Structural properties of undamaged A7 steel

	1	2	3	Average
Upper σ_y (ksi)	38.8	39.3	40.2	39.4
Lower σ_y (ksi)	38.0	38.1	39.1	38.4
Plateau σ_y (ksi)	38.3	38.3	39.5	38.7
E (ksi)	31020	31581	31082	31228
ε_y	0.00123	0.00121	0.00127	0.00124
σ_t (ksi)	62.0	61.7	62.5	62.1
ε_u	0.223	0.224	0.224	0.224
ε_u / ε_y	180.62	184.71	176.26	180.53
% Elongation	45.75	42.97	43.68	44.14
% Reduction	62.74	58.89	63.28	61.63

Table 5.39
Fracture toughness results of undamaged A7 steel

Specimen	FT (lb-ft)
1	24
2	27.5
3	29
4	31
5	32
6	39
7	40
8	40
9	42
10	42
11	42
12	45
13	45
14	47
15	47
16	47
Mean	38.7
95% confidence interval for actual mean	34.68 – 42.76
Std. Deviation	7.58
Median	41.0
Average absolute deviation from median	5.91

Table 5.40
Final test matrix for A7 small-scale specimens

Damage	*Restraining*	*Number of Repair*	*Specimen*
Strain (ε_d)	*Stress (σ_r)*	*Cycles (N_r)*	*Name*
30 εy	0.25 σ_y	1	A7-30-25-1
		3	A7-30-25-3
		5	A7-30-25-5
	0.40 σy	1	A7-30-40-1
		3	A7-30-40-3
		5	A7-30-40-5
60 εy	0.25 σy	1	A7-60-25-1
		3	A7-60-25-3-1
		3	A7-60-25-3-2
		5	A7-60-25-5
	0.40 σy	1	A7-60-40-1
		3	A7-60-40-3
		5	A7-60-40-5
90 εy	0.25 σy	1	A7-90-25-1
		3	A7-90-25-3
	0.40 σy	1	A7-90-40-1
		3	A7-90-40-3

Table 5.41
Structural properties of damaged-repaired A7-30-25 specimens

	A7-30-25-1		**A7-30-25-3**		**A7-30-25-5**	
	X	**Y**	**X**	**Y**	**X**	**Y**
Upper σ_y (ksi)	38.1	37.3	37.0	37.2	41.8	41.0
Lower σ_y (ksi)	38.1	36.9	36.0	35.5	41.8	41.0
Plateau σ_y (ksi)	38.1	37.0	36.2	36.7	41.5	41.0
E (ksi)	29346	28598	31483	31429	26462	26849
ε_y	0.0013	0.00129	0.00115	0.00117	0.00157	0.00153
σ_t (ksi)	61.5	60.9	60.5	60.0	60.0	60.6
ε_u	0.22	0.23	0.15	0.21	0.14	0.14
ε_u / ε_y	170.99	176.22	133.06	178.12	90.54	89.72
% Elongation	38.47	40.24	31.92	39.66	27.01	29.14
% Reduction	61.91	62.55	64.03	66.10	54.71	62.50

Table 5.42
Structural properties of damaged-repaired A7-30-40 specimens

	A7-30-40-1		A7-30-40-3		A7-30-40-5	
	X	**Y**	**X**	**Y**	**X**	**Y**
Upper σ_y (ksi)	40.0	38.2	41.3	42.2	43.8	40.7
Lower σ_y (ksi)	39.2	38.1	40.3	40.6	42.2	40.7
Plateau σ_y (ksi)	39.2	38.1	40.8	41.3	42.4	40.7
E (ksi)	31797	26453	27584	28601	27126	25986
ε_y	0.00123	0.00144	0.00148	0.00144	0.00156	0.00157
σ_t (ksi)	62.9	61.5	62.3	62.0	64.4	63.7
ε_u	0.19	0.23	0.22	0.22	0.20	0.15
ε_u / ε_y	153.30	158.30	150.09	148.89	127.95	97.05
% Elongation	33.60	36.29	34.48	35.83	34.23	31.93
% Reduction	61.86	60.96	62.10	64.56	59.15	58.89

Table 5.43
Structural properties of damaged-repaired A7-60-25 specimens

	A7-60-25-1		A7-60-25-3-1		A7-60-25-3-2		A7-60-25-5	
	X	**Y**	**X**	**Y**	**X**	**Y**	**X**	**Y**
Upper σ_y (ksi)	39.6	37.2	37.8	37.6	38.1	36.8	40.0	39.6
Lower σ_y (ksi)	37.5	31.1	37.8	34.3	27.2	36.8	40.0	38.8
Plateau σ_y (ksi)	39.6	37.2	37.8	37.6	34.2	36.8	40.0	37.2
E (ksi)	25492	28247	31510	-	26376	28027	27577	26677
ε_y	0.00155	0.00132	0.0012	-	0.0013	0.00131	0.00145	0.00139
σ_t (ksi)	60.7	60.3	61.8	61.0	58.9	58.8	61.0	61.5
ε_u	0.20	0.20	0.23	0.17	0.21	0.19	0.21	0.18
ε_u / ε_y	131.32	154.14	191.73	-	160.41	146.99	141.33	129.80
% Elongation	34.36	33.88	34.56	31.64	28.81	37.92	24.61	29.99
% Reduction	61.52	64.83	58.87	58.00	61.26	61.75	56.17	63.19

Table 5.44
Structural properties of damaged-repaired A7-60-40 specimens

	A7-60-40-1		A7-60-40-3		A7-60-40-5	
	X	**Y**	**X**	**Y**	**X**	**Y**
Upper σ_y (ksi)	43.2	42.8	38.1	38.3	49.8	44.1
Lower σ_y (ksi)	39.2	39.4	37.0	37.7	48.7	44.1
Plateau σ_y (ksi)	39.6	40.0	37.1	37.7	49.2	44.1
E (ksi)	27781	27099	-	-	-	15134
ε_y	0.00143	0.00148	-	-	-	0.00291
σ_t (ksi)	61.0	61.5	58.8	59.5	63.1	62.3
ε_u	0.18	0.21	0.22	0.19	0.08	0.17
ε_u / ε_y	126.98	138.88	-	-	-	56.97
% Elongation	32.57	35.06	38.08	33.48	24.72	25.87
% Reduction	65.02	60.00	63.29	66.47	60.74	60.18

Table 5.45
Structural properties of damaged-repaired A7-90 specimens

	A7-90-25-1		A7-90-25-3		A7-90-40-1		A7-90-40-3	
	X	**Y**	**X**	**Y**	**X**	**Y**	**X**	**Y**
Upper σ_y (ksi)	41.7	44.6	40.8	34.5	34.8	38.7	42.4	37.7
Lower σ_y (ksi)	40.6	42.7	39.8	34.5	32.8	24.6	42.4	29.7
Plateau σ_y (ksi)	41.6	43.7	39.8	34.5	34.8	31.7	42.4	34.5
E (ksi)	34945	25668	24126	24126	-	-	-	-
ε_y	0.00125	0.0017	0.00165	0.00143	-	-	-	-
σ_t (ksi)	60.5	60.8	60.0	60.5	59.1	60.0	60.4	59.0
ε_u	0.21	0.20	0.21	0.20	0.24	0.23	0.17	0.25
ε_u / ε_y	163.93	117.47	126.69	139.16	-	-	-	-
% Elongation	38.01	38.01	33.60	31.10	33.75	33.97	34.98	31.85
% Reduction	65.76	63.77	61.21	61.50	66.12	65.94	62.27	64.43

Table 5.46
Fracture toughness of damaged-repaired A7 specimens

	1	2	3	4	5	6	Average
A7-30-25-1	34	40	38	30	26.5	39	34.6
A7-30-25-3	30	30	24	17.5	15	16	22.1
A7-30-25-5	15	19	14.5	18	10.5	18	15.8
A7-30-40-1	25.5	26	26.5	33	13	32	26.0
A7-30-40-3	38	36	24	23	13.5	13	24.6
A7-30-40-5	97	92	53	8	5.5	6.5	43.7
A7-60-25-1	25	28.5	23	24.5	21.5	26	24.8
A7-60-25-3-1	31	15.5	13.5	90	102	97	58.2
A7-60-25-3-2	79	32	13	92	90	60	61.0
A7-60-25-5	76	62	74	67	78	96	75.5
A7-60-40-1	22	30	23	32	29	12	24.7
A7-60-40-3	30	33	11.5	27	9.5	8.5	19.9
***A7-60-40-5*	13	21.5	10	8.5	9	7.5	11.6
***A7-90-25-1*	32	29	33	50.5	59	38	40.3
***A7-90-25-3*	62	51	50	41	24	23.5	41.9
***A7-90-40-1*	53	51	46	32	54	25	43.5
***A7-90-40-3*	56	32	34	44	30	10	34.3

*Refers to specimens with significant curvature after heat straightening. Data is not entirely reliable.

Table 5.47
Rockwell hardness and microstructure results of damaged-repaired A7 steel

Specimen	Hardness Average	Hardness Std. Dev.	Tensile strength for comparison σ_t (ksi)	Grain Size (mm)	Percent Pearlite
Virgin	69.7	0.61	62.1	0.0340	24.8
A7-30-25-1	71.4	3.79	61.2	0.0333	20.5
A7-30-25-3	73.1	1.65	60.3	0.0376	21.2
A7-30-25-5	77.7	1.34	60.3	0.0387	34.0
A7-30-40-1	77.2	1.97	62.2	0.0303	27.8
A7-30-40-3	77.1	1.21	62.2	0.0329	26.3
A7-30-40-5	79.6	1.93	64.1	0.0244	27.9
A7-60-25-1	74.4	3.00	60.5	0.0360	27.8
A7-60-25-3-1	78.3	2.55	61.4	0.0329	21.6
A7-60-25-3-2	71.0	1.42	58.9	0.0276	21.0
A7-60-25-5	75.5	0.85	61.3	0.0256	27.9
A7-60-40-1	75.3	2.35	61.3	0.0291	30.9
A7-60-40-3	73.6	2.41	59.2	0.0290	29.7
***A7-60-40-5*	74.1	0.90	62.7	0.0319	17.2
***A7-90-25-1*	77.1	0.33	60.7	0.0265	17.4
***A7-90-25-3*	77.4	2.47	60.3	0.0239	20.4
***A7-90-40-1*	72.2	1.19	59.6	0.0256	20.8
***A7-90-40-3*	74.8	2.81	59.7	0.0290	13.3

*Refers to specimens with significant curvature after heat straightening. Data is not entirely reliable.

Table 5.48
Structural properties of undamaged A36 steel from Plate 2

	1	2	Average
Upper σ_y (ksi)	40.5	45.8	43.2
Lower σ_y (ksi)	37.8	38.9	38.4
Plateau σ_y (ksi)	38.8	39.4	39.1
E (ksi)	30037	30554	30296
ε_y	0.00129	0.00129	0.00129
σ_t (ksi)	66.3	67.1	66.7
ε_u	0.195	0.202	0.199
ε_u / ε_y	150.96	156.65	153.81
% Elongation	38.88	38.96	38.92
% Reduction	67.35	67.23	67.29

Table 5.49
Fracture toughness of undamaged A36 steel from Plate 2

Specimen	Quarter (lb-ft)	Mid (lb-ft)
1	43	30
2	49	45
3	56	47
4	56	54
5	57	55
6	60	56
7	61	60
8	62	61
9	76	66
10	82	67
Mean	60.2	54.1
95% confidence interval for mean	52.68 - 67.72	46.58 - 61.62
Std. Deviation	11.5	11.1
Median	58.5	55.5
Average absolute deviation from median	8.00	7.90

Table 5.50
Student's t-test results comparing the means of data sets in Table 5.49

t-test to establish the statistical difference between quarter and mid thickness fracture toughness for A36 charpy specimens fabricated from Plate 2
Results of unpaired t-test (see Section 4.9.2):
t=1.21
Std. deviation=11.3
Degrees of freedom=18
Probability of null hypothesis (the data sets are statistically similar)= 0.24

Table 5.51
Statistical values of the combined quarter and mid thickness charpy specimens

Property	Value
Mean	57.1
95% confidence Interval for mean	51.79-62.51
Std. Deviation	11.4
Median	56.5
Average Absolute deviation from median	8.05

Table 5.52
Structural properties of damaged-repaired overheated A36 steel subjected to damage strains of 60 ε_y and maximum temperatures of 1400 °F

	A36-60-25-1-1400		A36-60-50-1-1400		A36-60-25-3-1400		A36-60-50-3-1400	
	X	Y	X	Y	X	Y	X	Y
Upper σ_y (ksi)	52.4	50.7	51.3	47.6	49.3	48.4	50.0	49.0
Lower σ_y (ksi)	47.1	47.8	46.2	45.2	46.6	44.1	46.6	45.8
Plateau σ_y (ksi)	48.3	47.6	47.8	46.3	47.9	45.1	47.2	47.9
E (ksi)	30122	29520	31466	31674	29292	28995	29855	31483
ε_y	0.0016	0.00161	0.00152	0.00146	0.00164	0.00156	0.00158	0.00152
σ_t (ksi)	71.6	70.9	69.7	69.9	70.1	64.4	70.0	69.8
ε_u	0.20	0.17	0.17	0.20	0.16	0.16	0.17	0.15
ε_u / ε_y	122.86	103.57	112.57	136.82	99.68	102.22	106.26	99.90
% Elongation	34.67	31.30	33.84	31.64	31.83	32.83	33.77	30.74
% Reduction	69.69	71.45	73.07	72.33	73.46	72.30	75.31	71.66

Table 5.53
Structural properties of damaged-repaired overheated A36 steel subjected to damage strains of 60 ε_y and maximum temperatures of 1600 °F

	A36-60-25-1-1600		A36-60-50-1-1600		A36-60-25-3-1600		A36-60-50-3-1600	
	X	Y	X	Y	X	Y	X	Y
Upper σ_y (ksi)	54.8	54.9	50.8	48.8	51.8	47.7	50.0	48.3
Lower σ_y (ksi)	47.7	47.2	47.3	47.6	45.8	49.4	44.3	43.5
Plateau σ_y (ksi)	48.9	48.2	47.9	47.9	47.6	49.1	44.9	44.0
E (ksi)	30531	30554	29462	29355	29634	30213	31433	30099
ε_y	0.0016	0.00158	0.00163	0.00163	0.00161	0.00163	0.00143	0.00146
σ_t (ksi)	70.9	72.0	72.3	72.3	70.6	70.7	69.9	69.6
ε_u	0.20	0.18	0.19	0.20	0.17	0.12	0.19	0.17
ε_u / ε_y	126.74	116.01	118.71	119.50	102.72	75.69	132.31	119.03
% Elongation	37.69	33.90	32.80	38.48	30.17	26.59	30.37	28.63
% Reduction	72.89	71.04	71.67	70.88	71.42	72.06	72.87	73.31

Table 5.54
Structural properties of damaged-repaired overheated A36 steel subjected to damage strains of 90 ε_y and maximum temperatures of 1400 °F

	A36-90-25-1-1400		A36-90-50-1-1400		A36-90-25-3-1400		A36-90-50-3-1400	
	X	Y	X	Y	X	Y	X	Y
Upper σ_y (ksi)	49.4	57.2	52.2	50.2	47.6	49.4	53.0	52.6
Lower σ_y (ksi)	47.7	47.9	49.0	49.0	44.1	45.7	47.3	46.1
Plateau σ_y (ksi)	48.7	48.7	49.8	49.2	45.3	46.0	48.6	48.8
E (ksi)	31045	29882	30796	31447	29298	31545	29568	30173
ε_y	0.00157	0.00163	0.00162	0.00156	0.00155	0.00146	0.00164	0.00162
σ_t (ksi)	71.8	72.6	71.8	72.0	69.4	70.1	71.2	72.4
ε_u	0.16	0.20	0.20	0.18	0.18	0.20	0.18	0.17
ε_u / ε_y	102.63	120.26	123.06	115.05	116.42	137.84	107.08	105.73
% Elongation	31.22	35.85	37.45	35.20	34.39	35.81	35.30	33.53
% Reduction	68.49	66.80	73.37	73.21	74.61	72.63	74.77	70.50

Table 5.55
Structural properties of damaged-repaired overheated A36 steel subjected to damage strains of 90 ε_y and maximum temperatures of 1600 °F

	A36-90-25-1-1600		A36-90-50-1-1600		A36-90-25-3-1600		A36-90-50-3-1600	
	X	Y	X	Y	X	Y	X	Y
Upper σ_y (ksi)	50.7	51.0	49.1	52.5	48.5	49.9	50.7	50.8
Lower σ_y (ksi)	46.1	46.8	45.2	45.9	46.9	45.9	44.5	45.4
Plateau σ_y (ksi)	47.2	47.9	47.3	46.8	47.5	46.2	48.0	47.6
E (ksi)	-	30680	30969	29640	31618	31395	30031	30458
ε_y	-	0.00156	0.00153	0.00158	0.0015	0.00147	0.0016	0.00156
σ_t (ksi)	71.4	71.0	71.8	70.0	71.6	70.0	70.8	70.4
ε_u	-	0.16	0.19	0.20	0.18	0.19	0.12	0.14
ε_u / ε_y	-	104.40	125.05	129.20	120.48	129.11	77.58	87.02
% Elongation	28.20	31.30	35.11	36.40	36.49	39.11	27.72	28.40
% Reduction	71.54	74.17	73.10	73.10	70.90	70.47	72.47	73.78

Table 5.56
Fracture toughness of damaged-repaired overheated A36 steel

Specimen	1	2	3	4	5	6	QA	MA
A36-60-25-1-1400	208	189	185	222	241	252	194	238
A36-60-25-3-1400	225	175	250	133	111	237	217	160
A36-60-50-1-1400	187	179	175	145	131	216	180	164
A36-60-50-3-1400	216	185	234	216	180	204	212	200
A36-90-25-1-1400	185	159	203	77	126	75	182	93
A36-90-25-3-1400	239	211	216	machined	263	244	222	254
A36-90-50-1-1400	223	206	216	183	238	175	215	199
A36-90-50-3-1400	243	228	251	machined	109	126	241	118
A36-60-25-1-1600	128	125	122	230	221	223	125	225
A36-60-25-3-1600	210	170	209	254	251	248	196	251
A36-60-50-1-1600	216	162	198	75	128	125	192	109
A36-60-50-3-1600	170	185	199	66	124	228	185	139
A36-90-25-1-1600	240	223	217	112	90	102	227	101
A36-90-25-3-1600	185	200	219	177	135	212	201	175
A36-90-50-1-1600	251	215	228	113	126	125	231	121
A36-90-50-3-1600	234	200	231	58	92	30	222	60

Table 5.57
Rockwell hardness and microstructure results of damaged-repaired overheated A36 steel

Specimen	Hardness Average	Hardness Std. Dev	Tensile strength for comparison $\sigma_{t\ (ksi)}$	Grain Size (mm)	Percent Pearlite
Virgin	78.4	0.576	66.7	0.0393	33
A36-60-25-1-1400	77.3	0.217	71.3	0.0336	29.5
A36-60-50-1-1400	79.2	0.683	67.3	0.0259	22.4
A36-60-25-3-1400	76.3	0.421	69.8	0.0294	9.3
A36-60-50-3-1400	77.4	1.26	69.9	0.0266	24.4
A36-90-25-1-1400	76.6	0.923	72.2	0.0269	19.1
A36-90-50-1-1400	79.8	1.244	69.8	0.0258	22.3
A36-90-25-3-1400	77.9	0.776	71.9	0.0274	19.2
A36-90-50-3-1400	77.1	2.137	71.8	0.0247	23.3
A36-60-25-1-1600	74	2.273	71.5	0.0286	17.6
A36-60-50-1-1600	76.3	2.379	70.7	0.0309	32.4
A36-60-25-3-1600	76.1	2.744	72.3	0.0269	19.8
A36-60-50-3-1600	76.8	1.411	69.8	0.031	28
A36-90-25-1-1600	79.3	2.038	71.2	0.0305	27.2
A36-90-50-1-1600	77.3	1.218	70.8	0.0336	22.9
A36-90-25-3-1600	76.3	1.69	70.9	0.034	28.1
A36-90-50-3-1600	76.6	1.875	70.6	0.0279	29.6

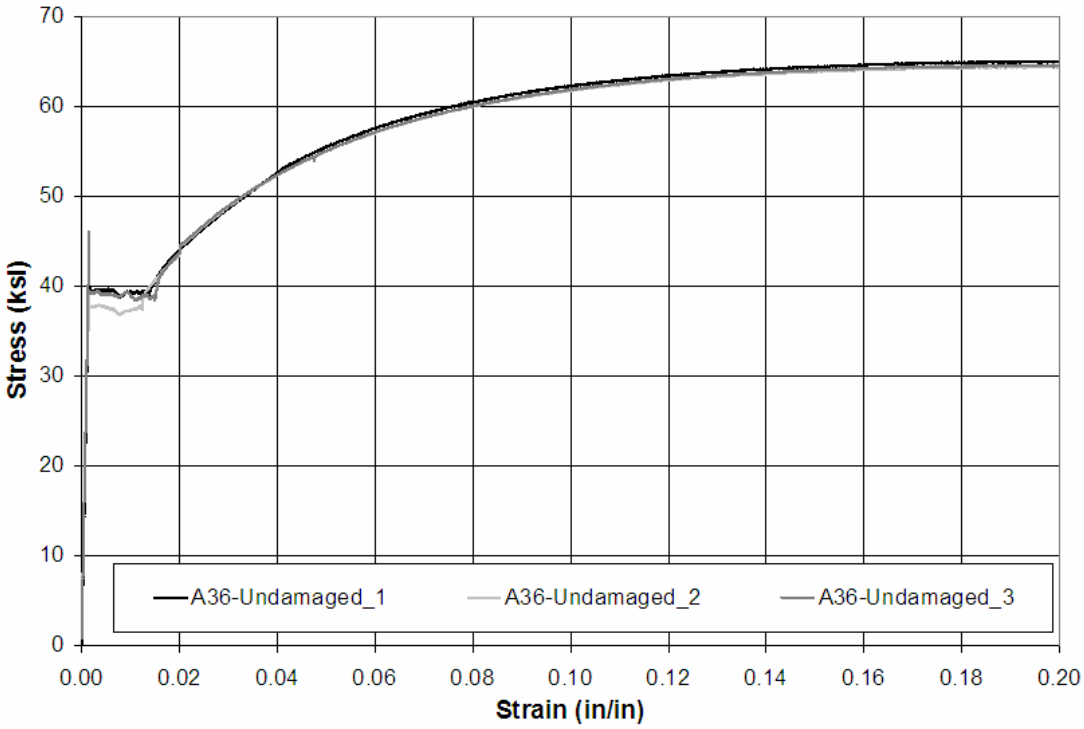

Figure 5.1
Stress-strain relationships of undamaged A36 steel

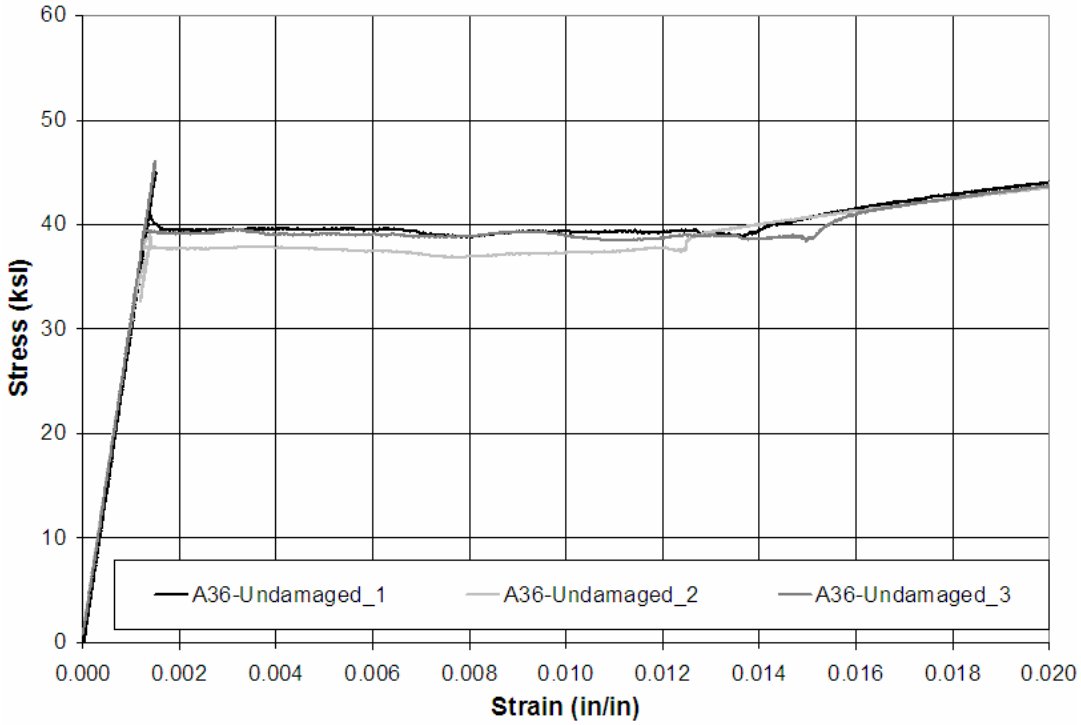

Figure 5.2
Initial stress-strain relationships of undamaged A36 steel

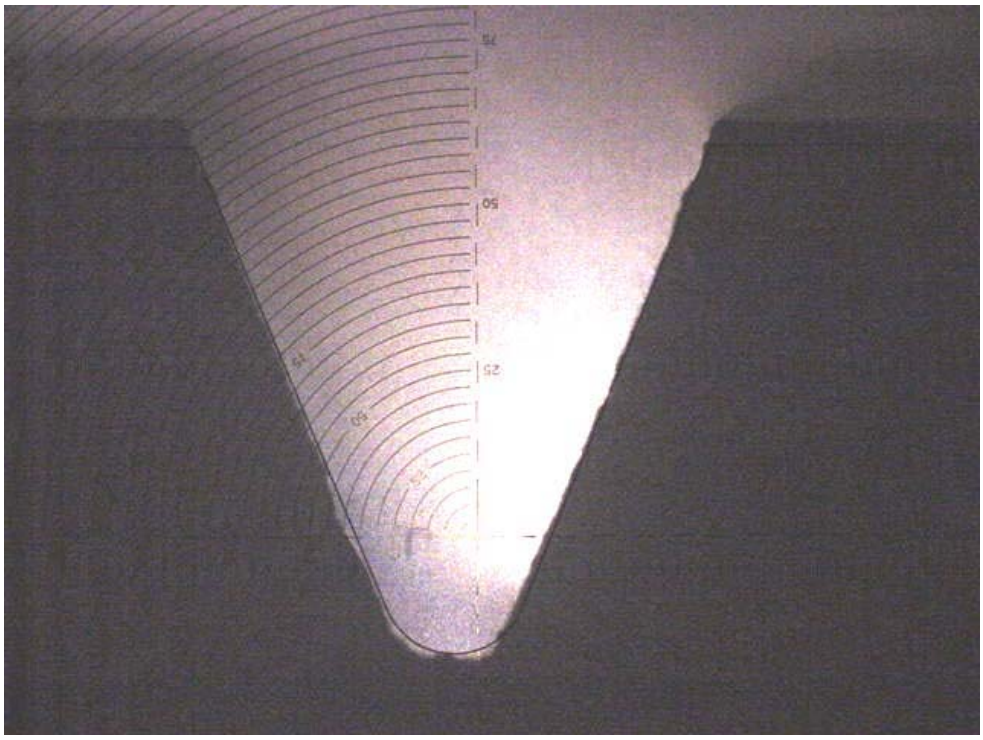

Figure 5.3
Notch of charpy specimen fabricated by MSU machinist

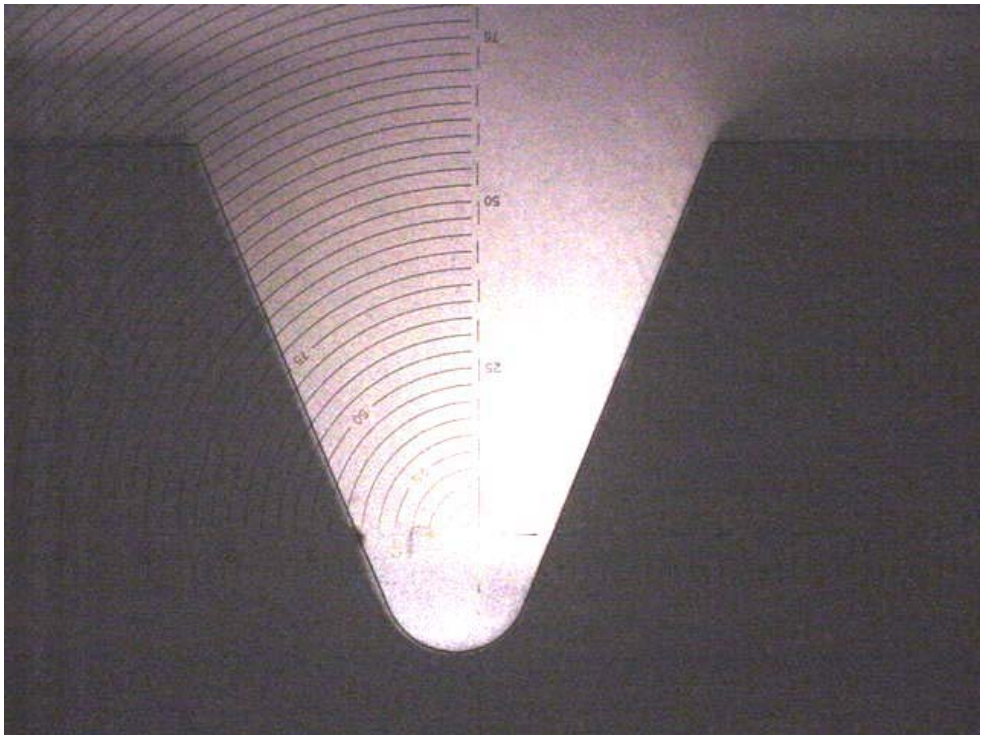

Figure 5.4
Notch of charpy specimen fabricated by MDOT machinist

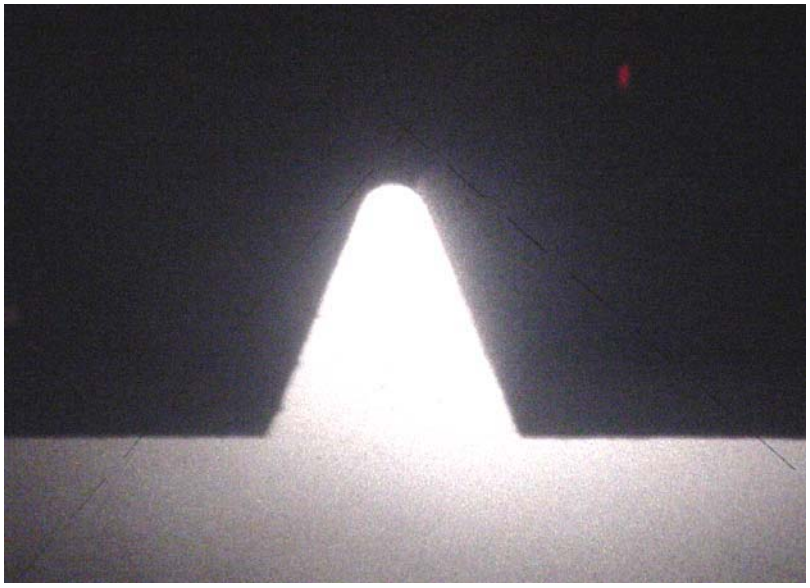

Figure 5.5
Typical v-notch of charpy specimen fabricated by MSU machinist using broach

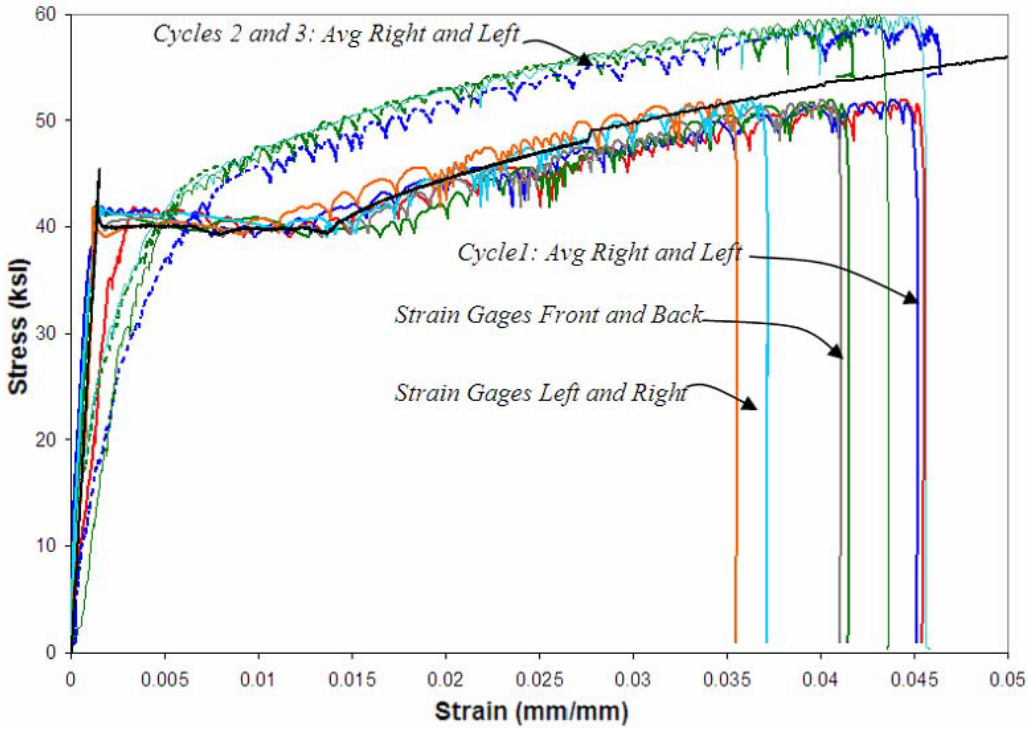

Figure 5.6
Stress-strain behaviors of all three damage cycles of Specimen A36-30-40-3

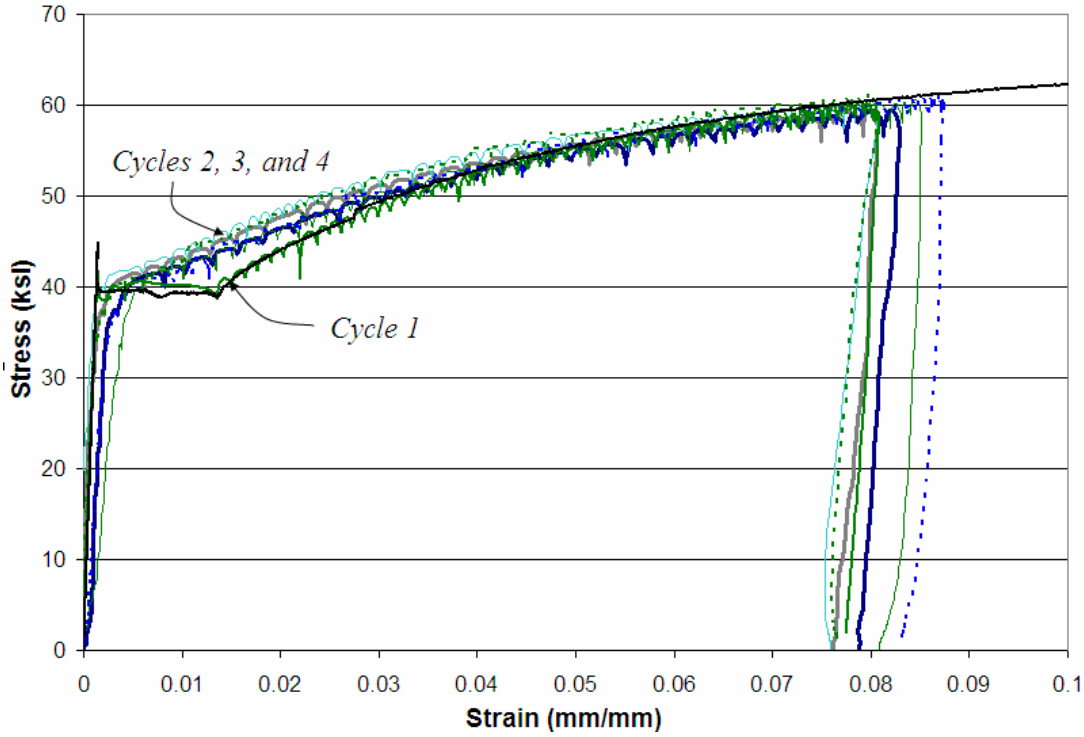

Figure 5.7
Stress-strain behaviors of all three damage cycles of Specimen A36-60-50-4

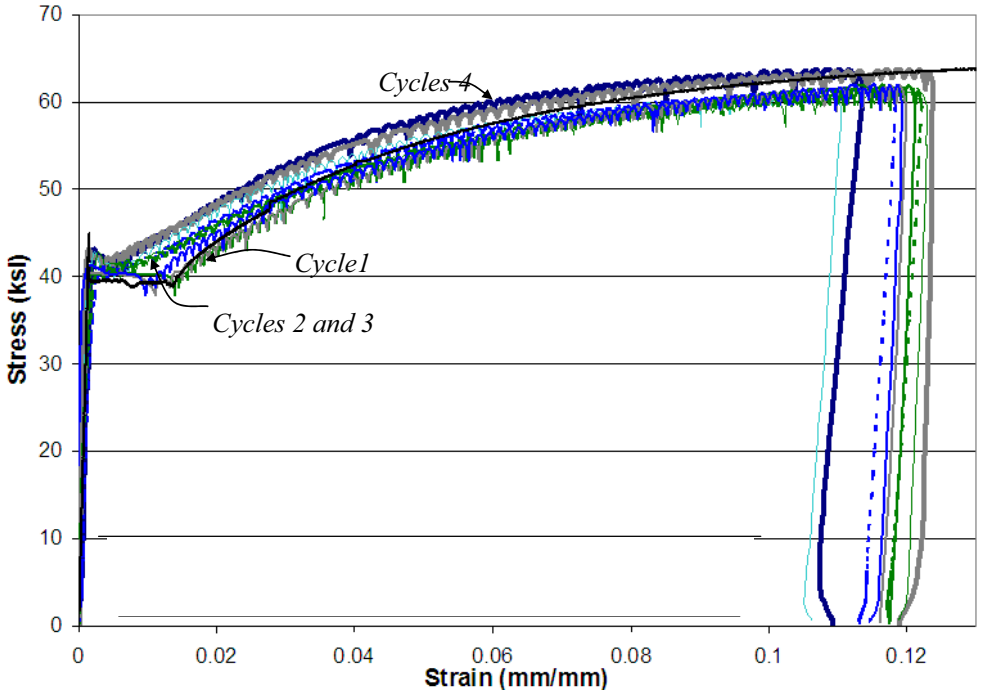

Figure 5.8
Stress-strain behaviors of all three damage cycles of Specimen A36-90-50-4

a) 1200 °F b) 1100 °F

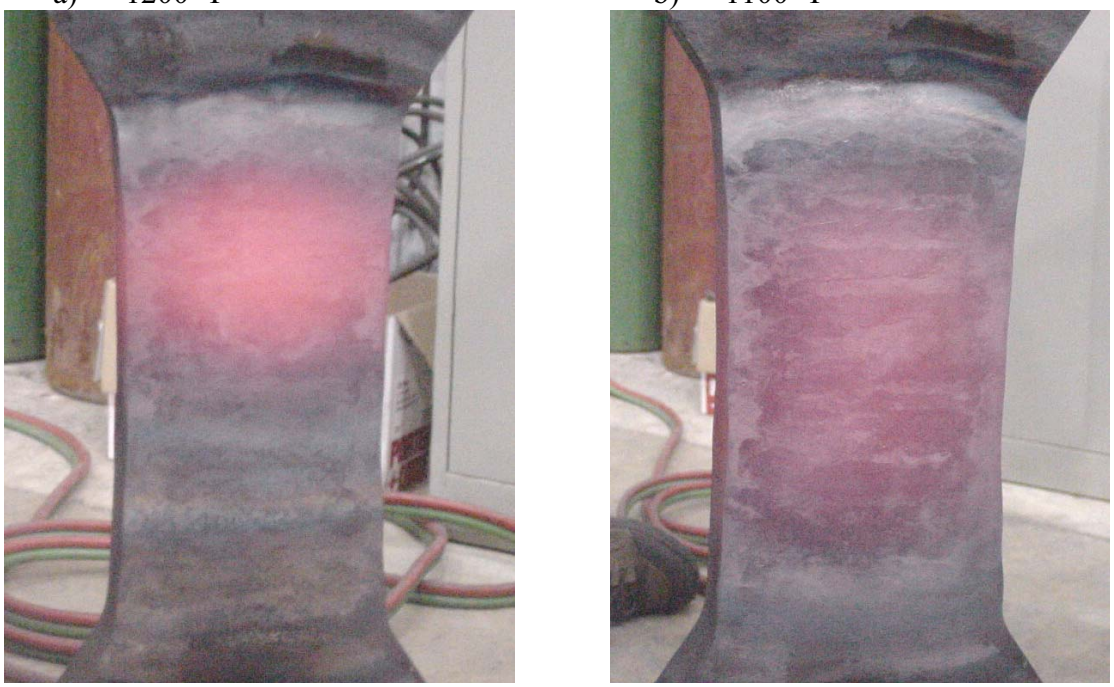

Figure 5.9
Color of A36 steel at elevated temperatures

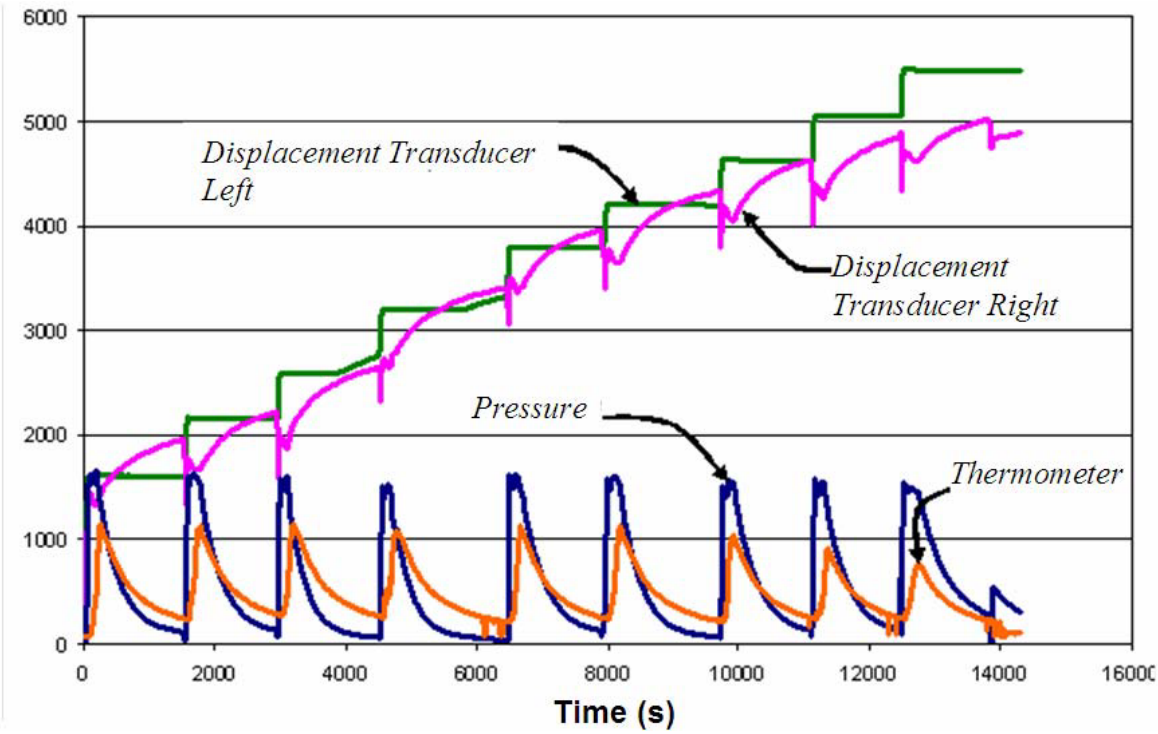

Figure 5.10
Instrument data during the second repair cycle of Specimen A36-60-25-4

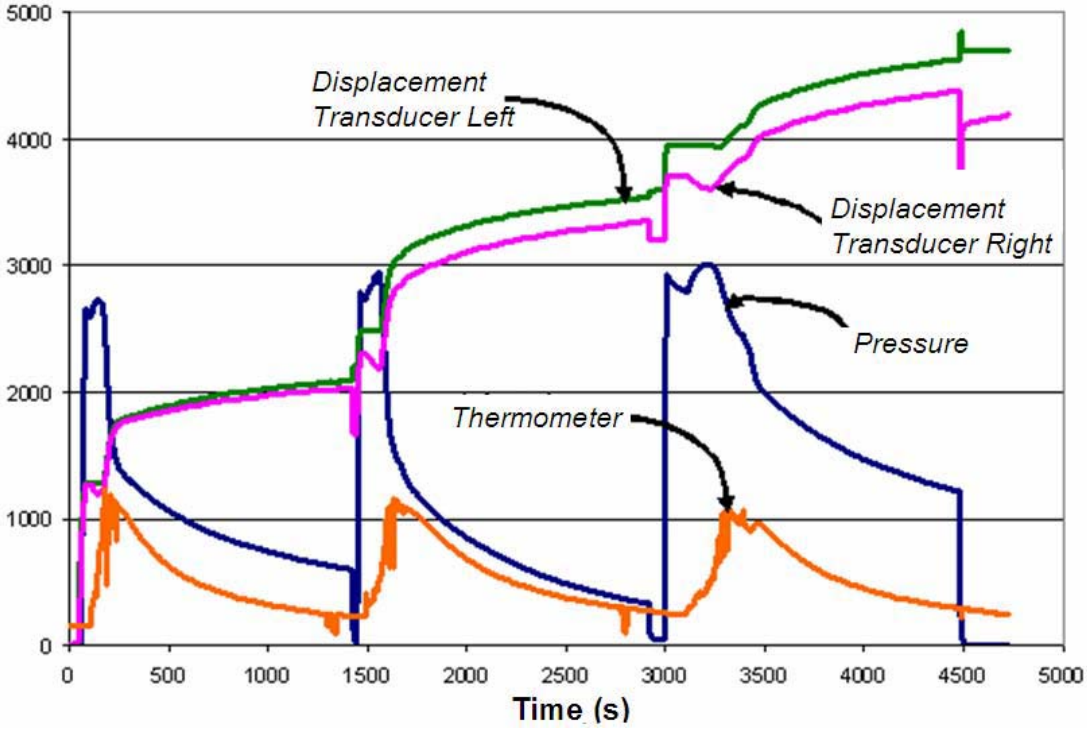

Figure 5.11
Instrument data during the second repair cycle of A36-60-50-3

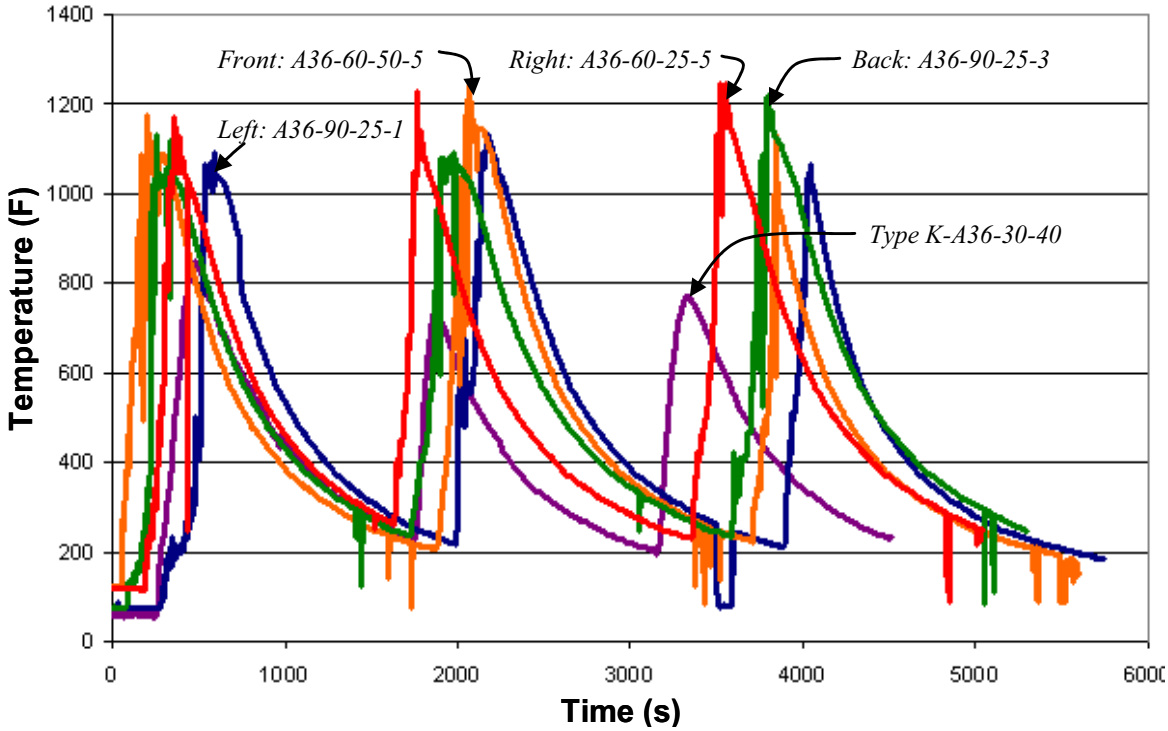

Figure 5.12
Temperature-time profiles for all faces of the A36 test areas

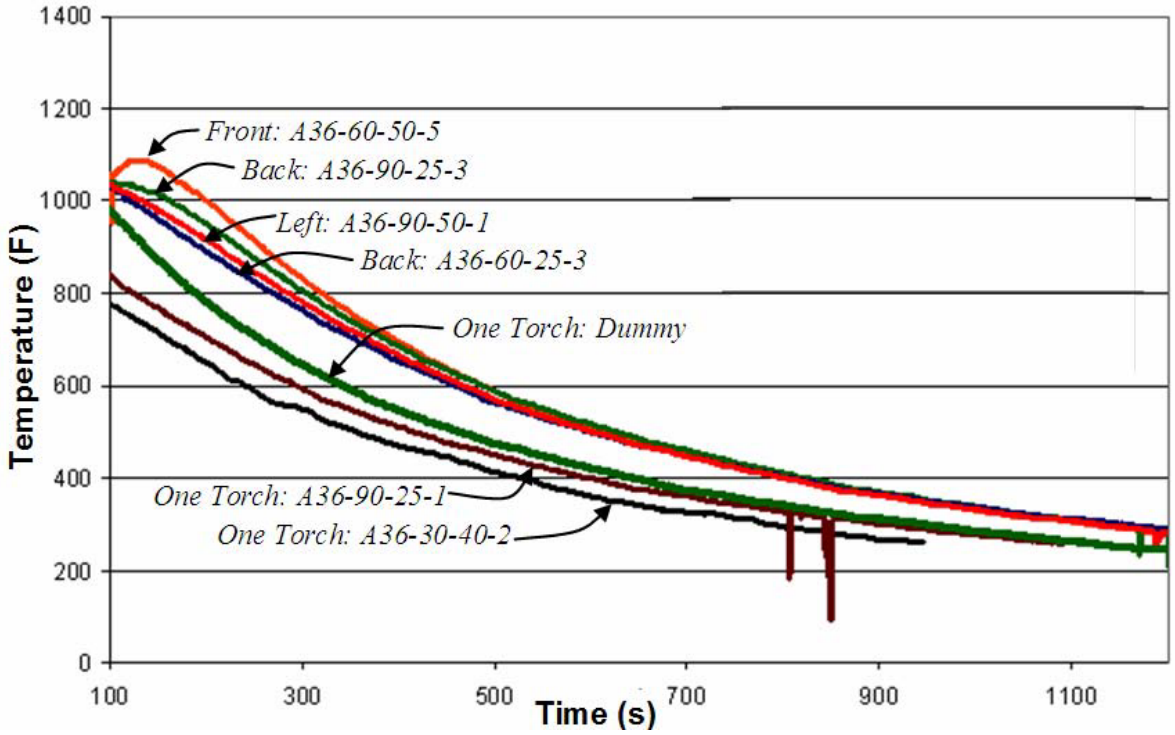

Figure 5.13
Cooling period of different specimens using one torch or two

Figure 5.14
Single curvature in the test area of Specimen A36-30-40-1 when complete

Figure 5.15
Double curvature in the test area of Specimen A36-90-25-5 when complete

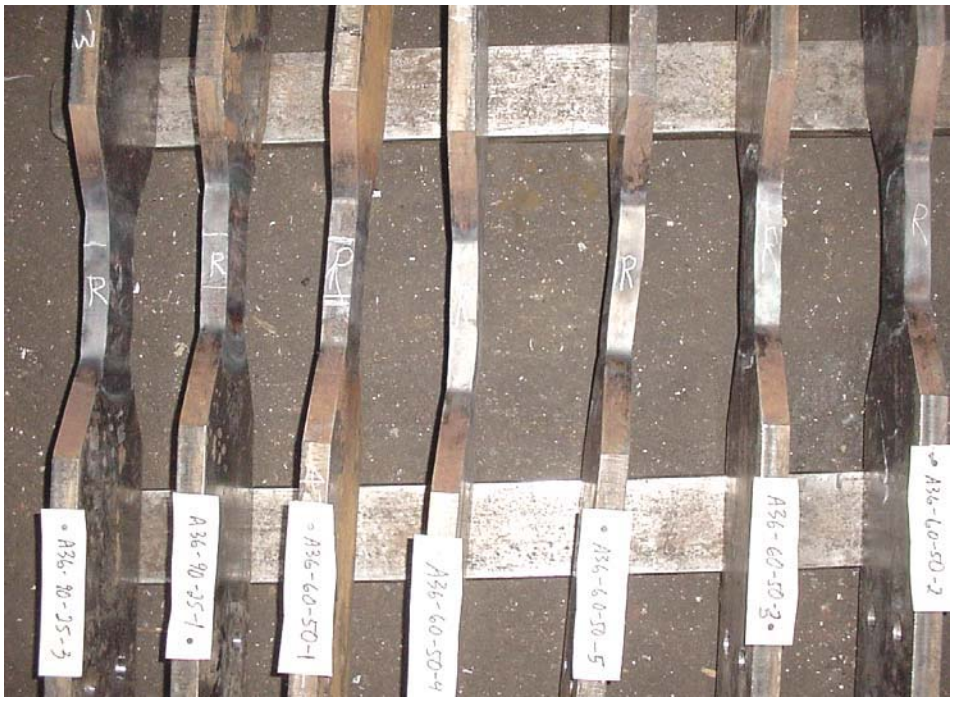

Figure 5.16
A36 test specimens after experimental investigations

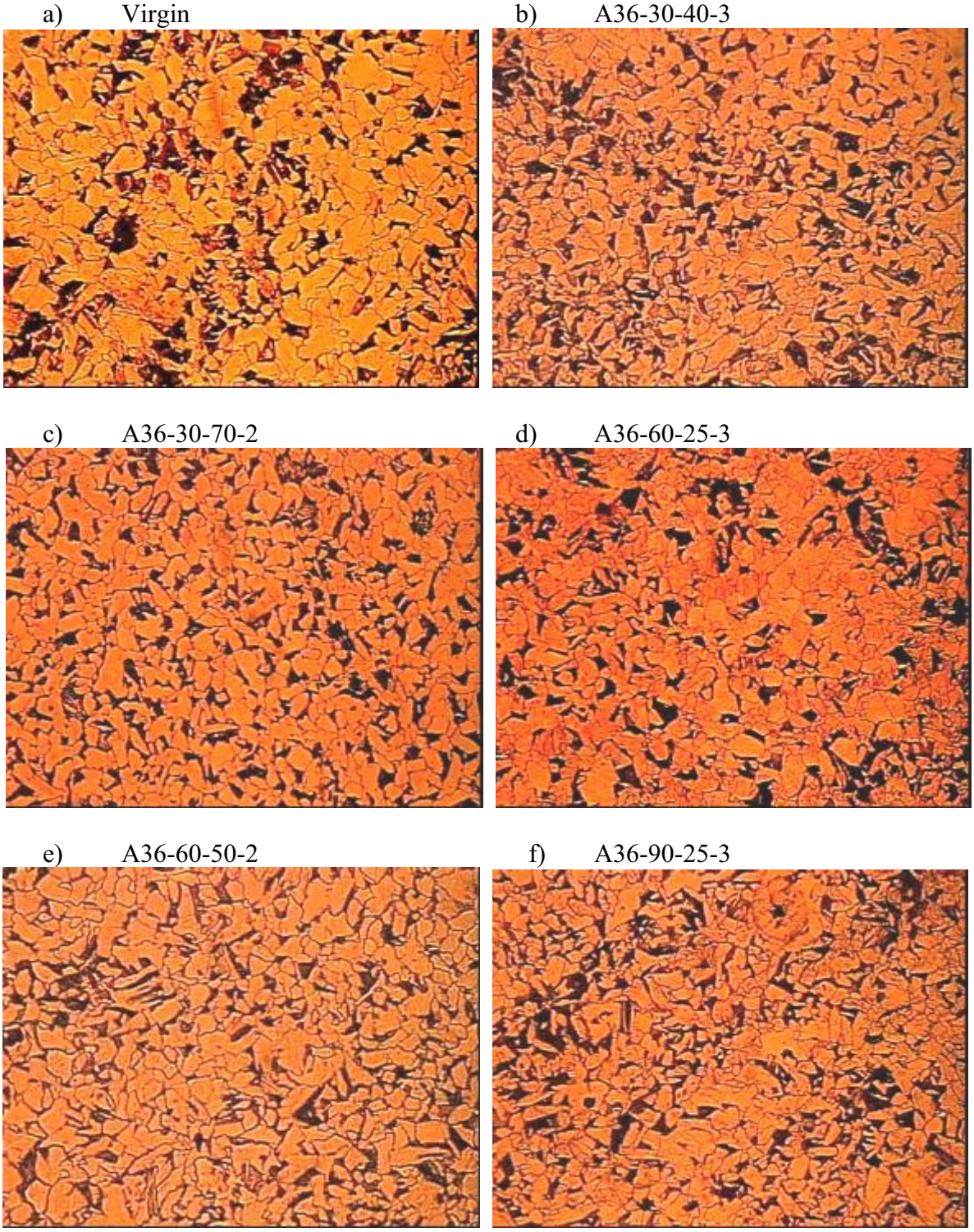

Figure 5.17
Microstructures of undamaged A36 steel and various A36 damaged-repaired steel

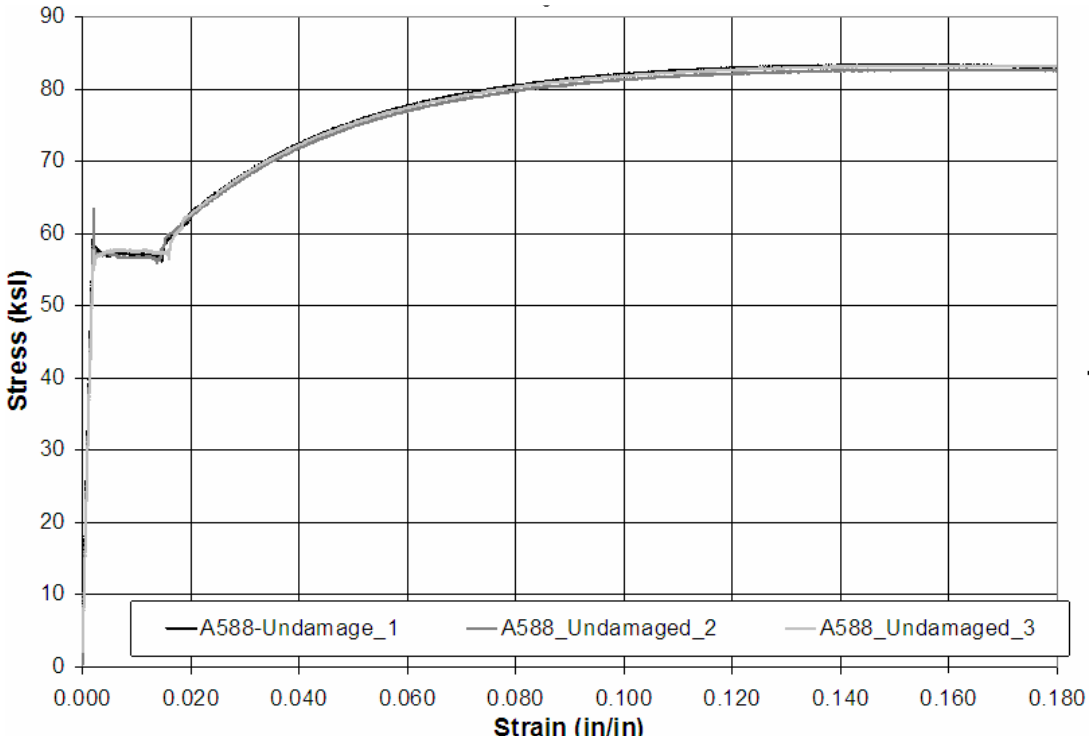

Figure 5.18
Stress-strain relationships of undamaged A588 steel

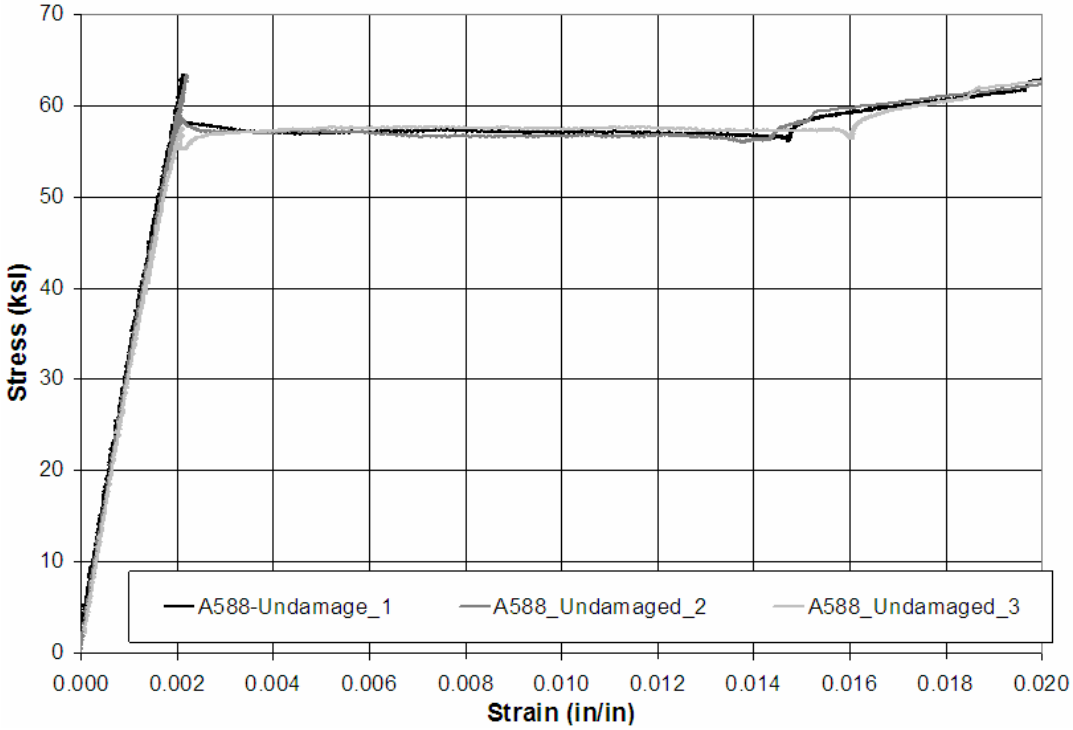

Figure 5.19
Initial stress-strain relationships of undamaged A588 steel

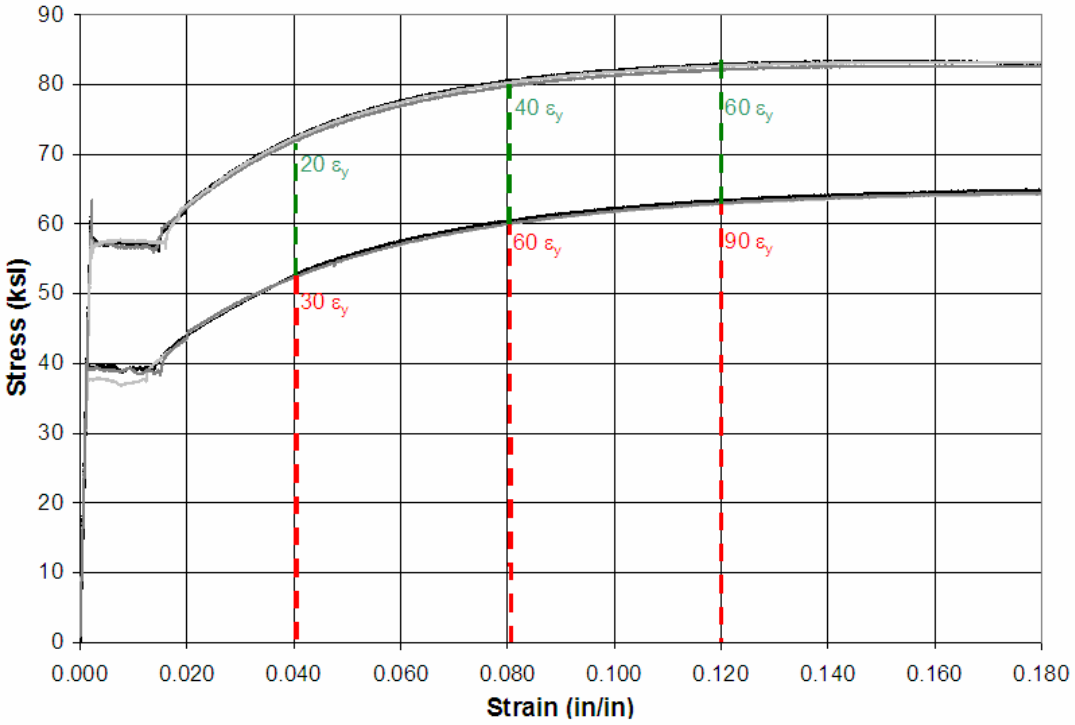

Figure 5.20
Comparisons of stress-strain relationships for undamaged A36 and A588 steel

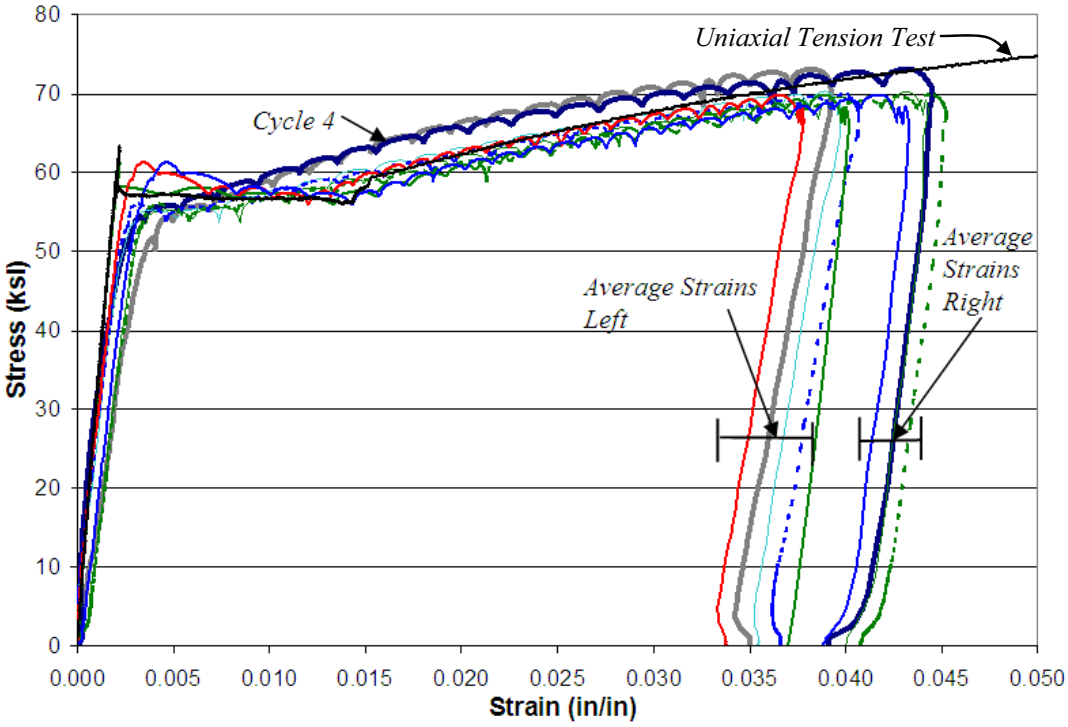

Figure 5.21
Stress-strain behaviors of all four damage cycles of Specimen A588-20-25-4

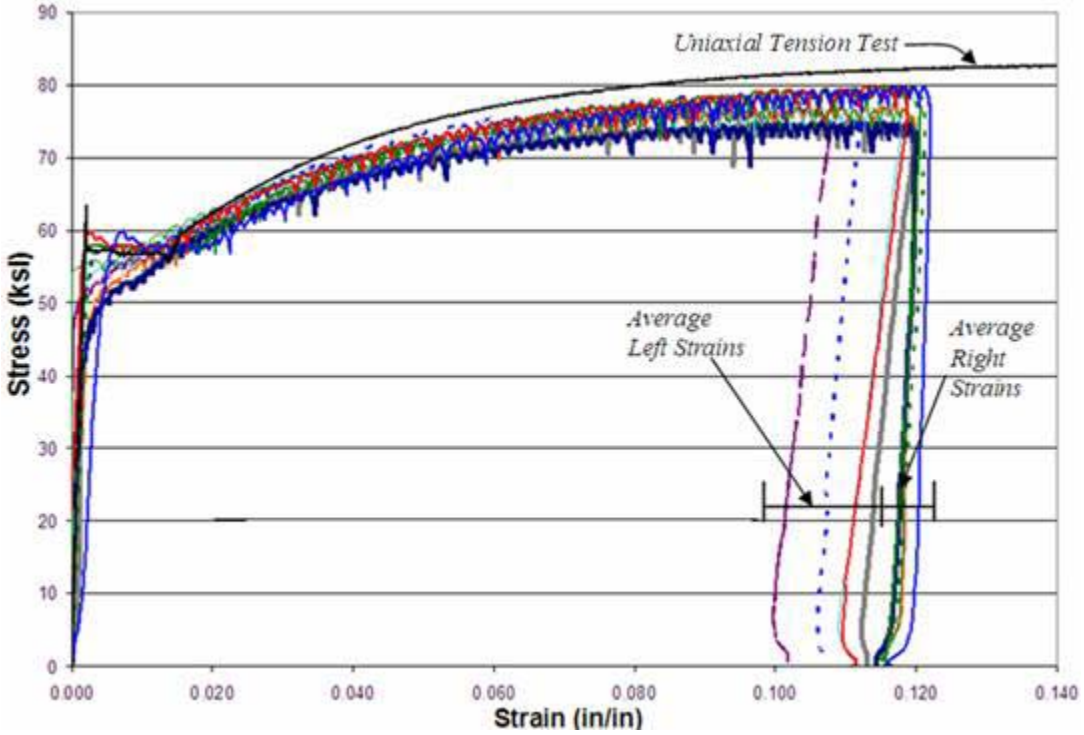

Figure 5.22
Stress-strain behaviors of all five damage cycles of Specimen A588-60-25-5

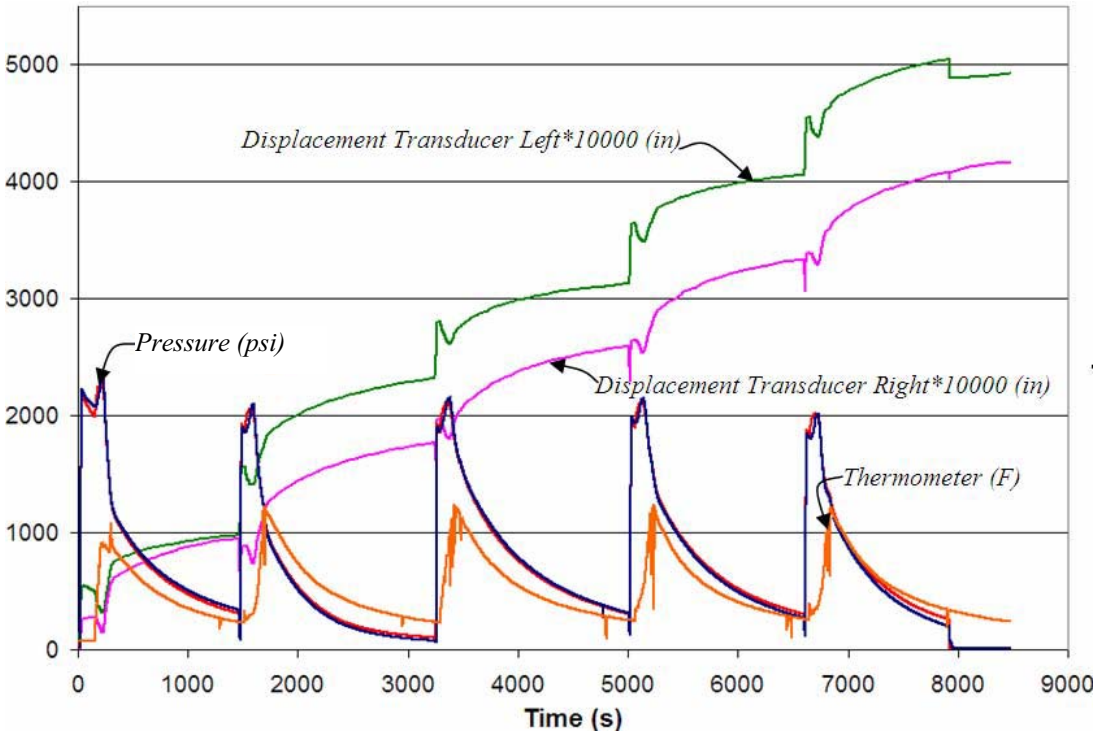

Figure 5.23
Instrument data during the fourth repair cycle of Specimen A588-60-25-5

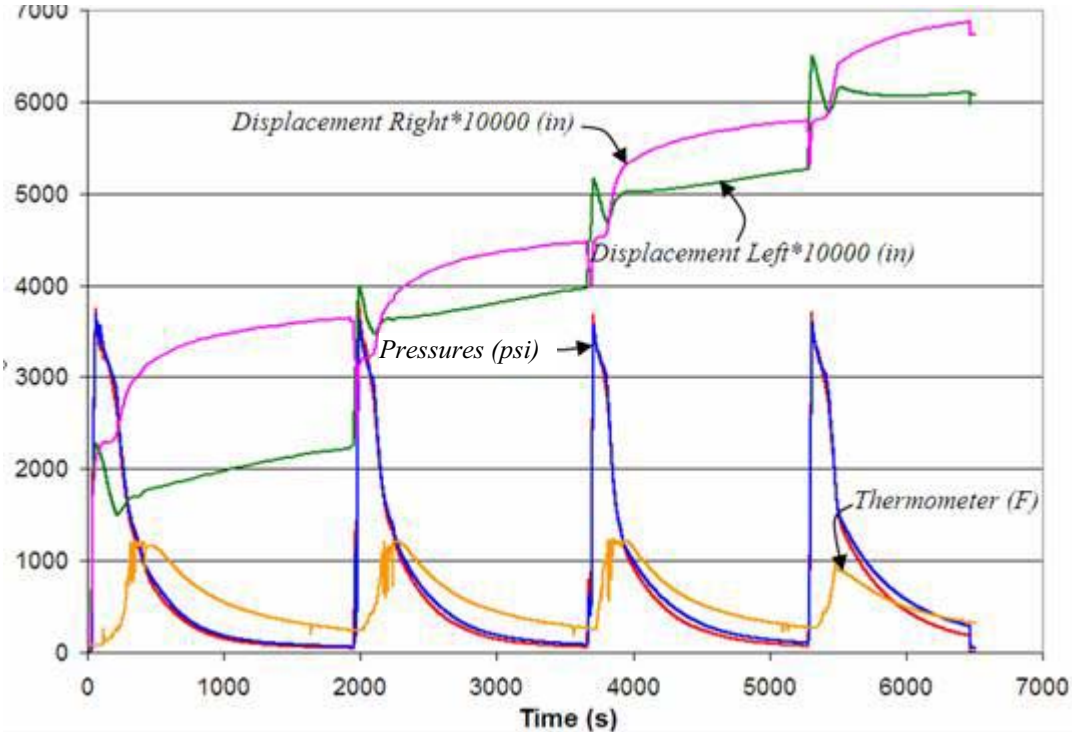

Figure 5.24
Instrument data during the first repair cycle of Specimen A588-60-50-1

Figure 5.25
Frontal view of A588-40-25 specimens after experimental investigations

Figure 5.26
Side view of A588-40-25 specimens after experimental investigations

Figure 5.27
Test area of Specimen A588-40-25-5 after experimental investigations

Figure 5.28
Test area of Specimen A588-60-25-1 after experimental investigations

Figure 5.29
Test area of Specimen A588-60-25-4 after experimental investigations

a) Undamaged A588

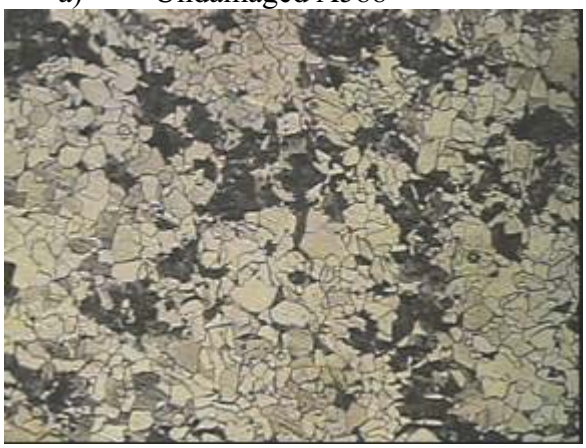

b) A588-20-50-1

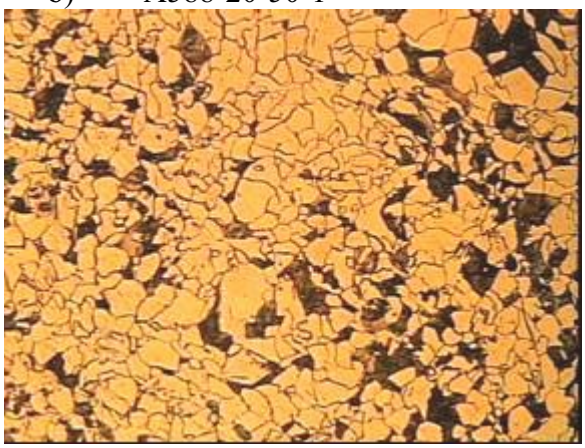

c) A588-40-25-3

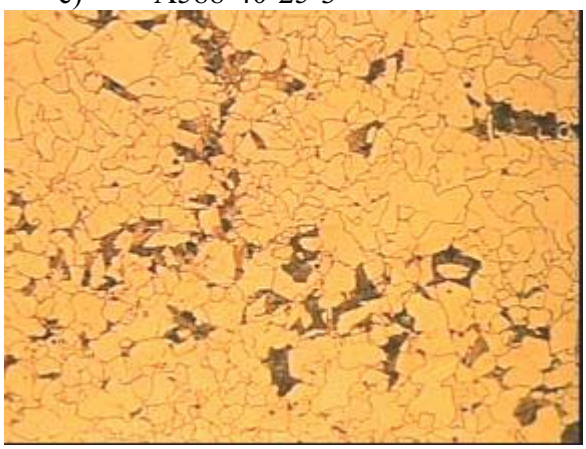

d) A588-40-50-3

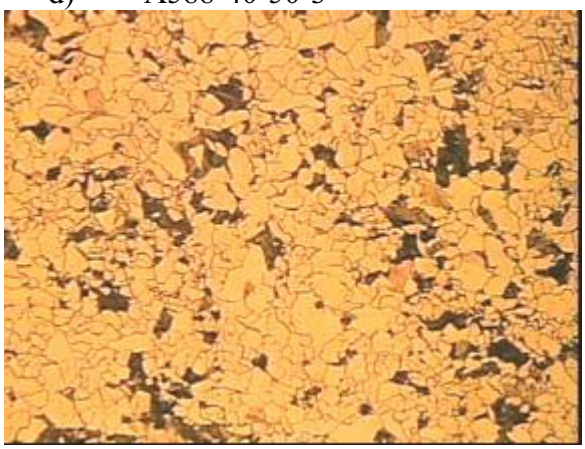

e) A588-60-25-1

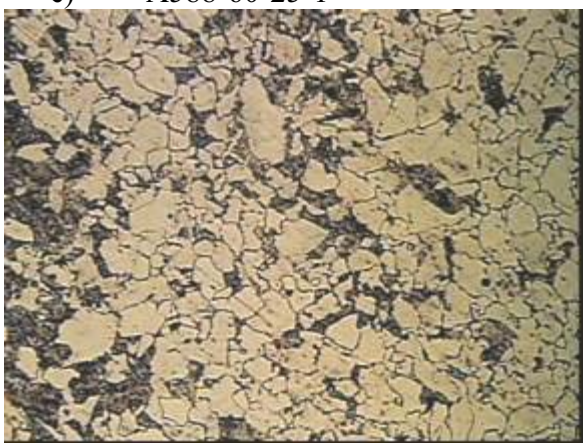

f) A588-60-50-4

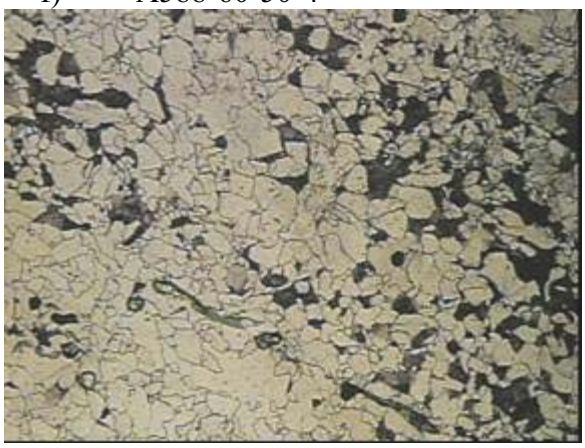

Figure 5.30
Microstructures of undamaged A588 steel and various A588 damaged-repaired steel

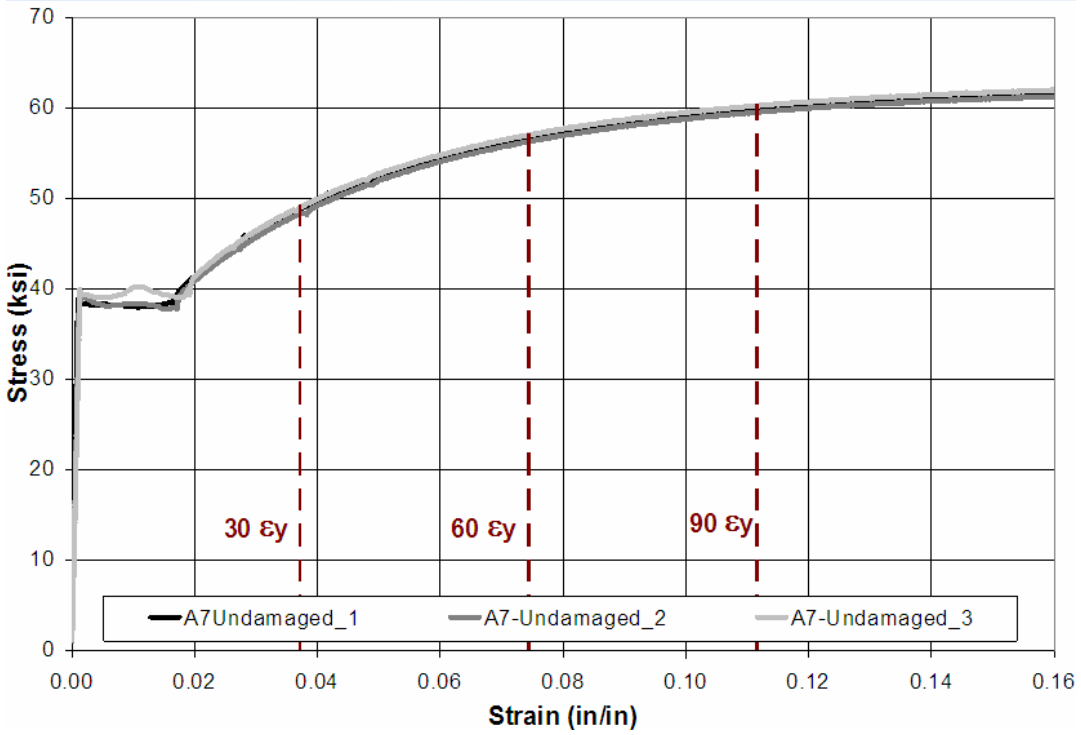

Figure 5.31
Stress-strain relationships of undamaged A7 steel

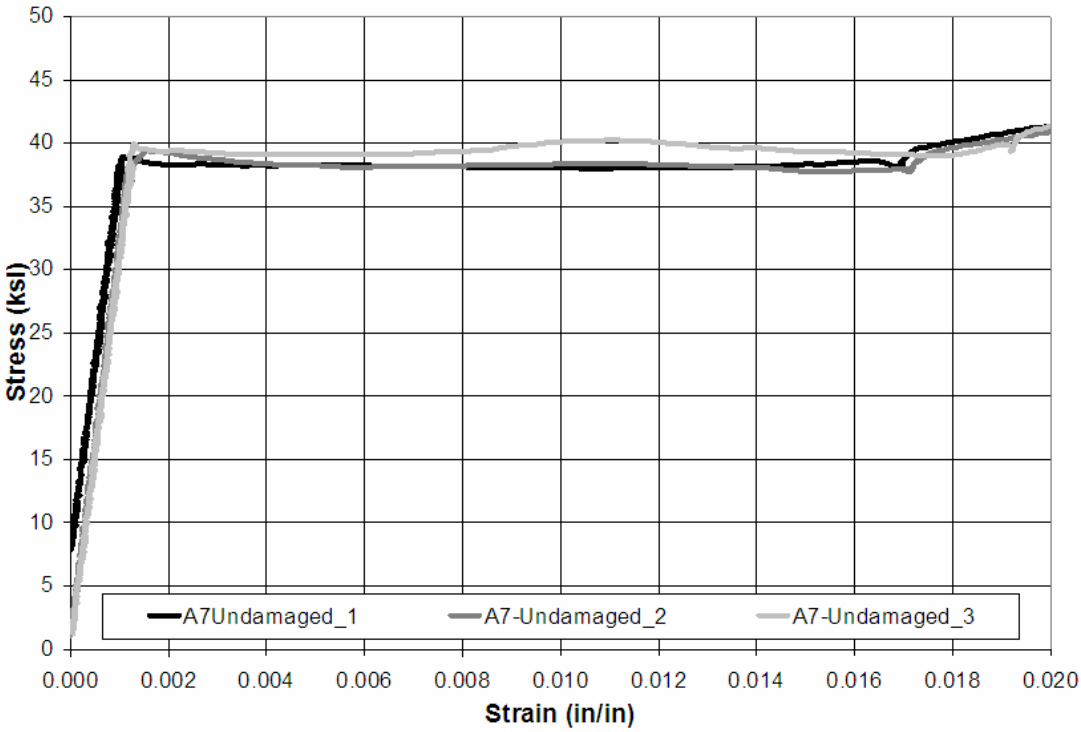

Figure 5.32
Initial stress-strain relationships of undamaged A7 steel

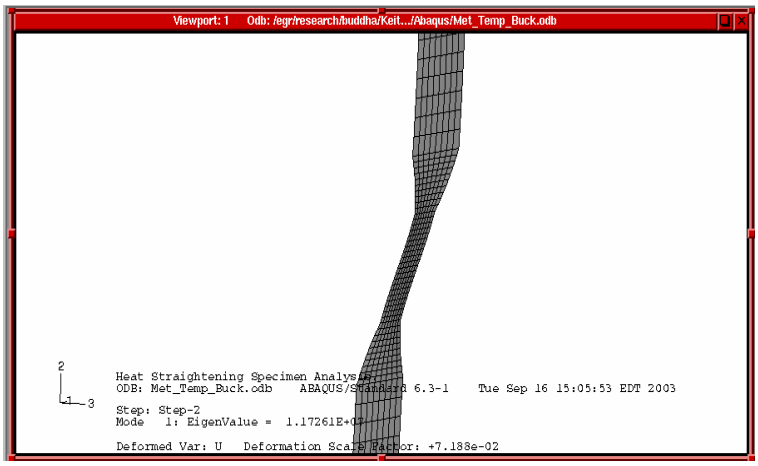

Figure 5.33
Finite element model showing the buckled shape of the A7 small-scale specimens

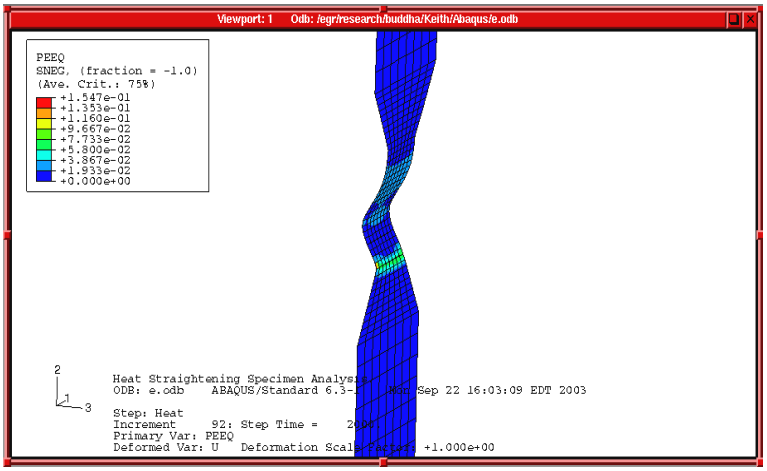

Figure 5.34
Buckling of the A36 specimen test area while heating, σ_r = 0.50 σ_y (t = 0.44 in)

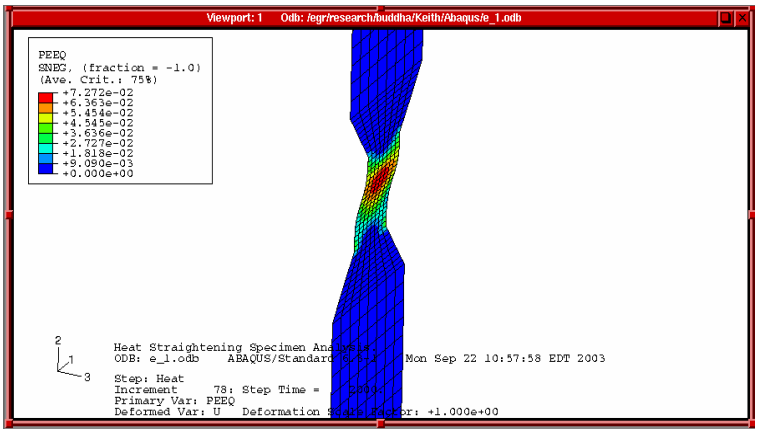

Figure 5.35
Condition of the A36 specimen test area while heating, σ_r = 0.50 σ_y (t = 1.0 in)

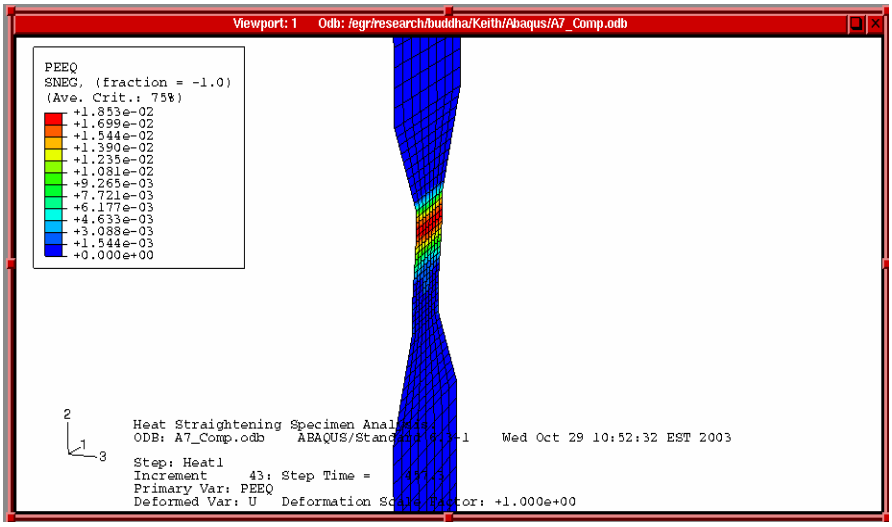

Figure 5.36
Condition of the A36 specimen test area while heating, $\sigma_r = 0.40\ \sigma_y$ (t = 0.44 in)

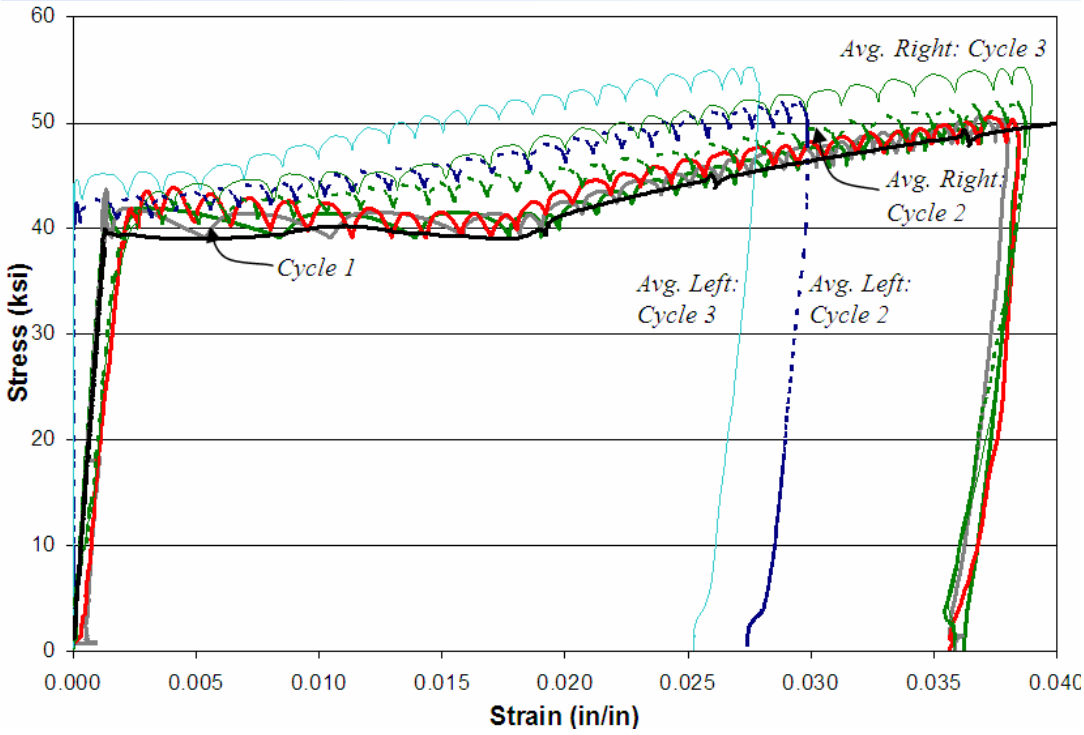

Figure 5.37
Stress-strain behaviors of all three damage cycles of Specimen A7-30-40-3

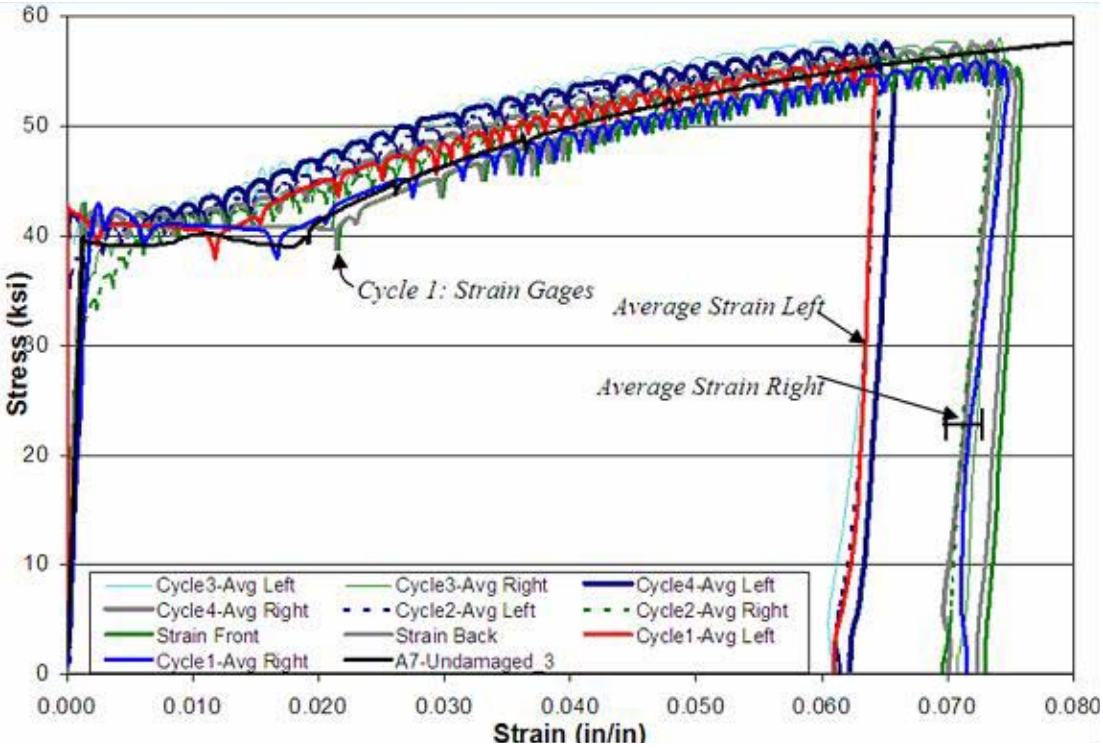

Figure 5.38
Stress-strain behaviors of the first four damage cycles of Specimen A7-60-25-5

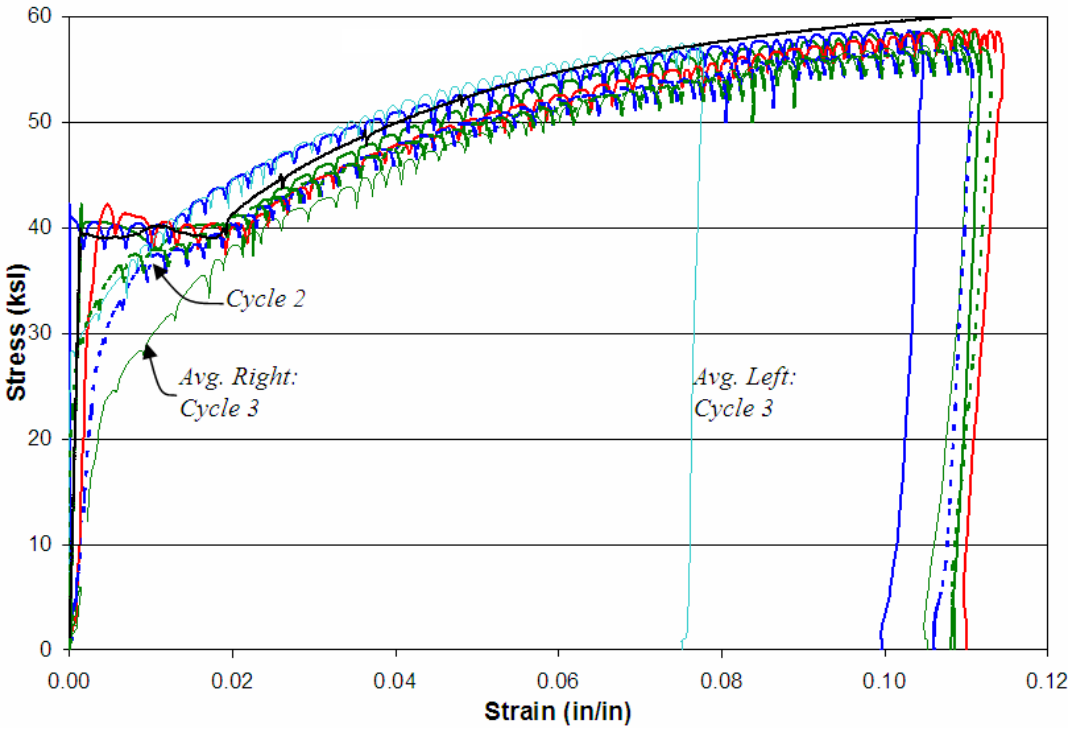

Figure 5.39
Stress-strain behaviors of the three damage cycles of Specimen A7-90-25-3

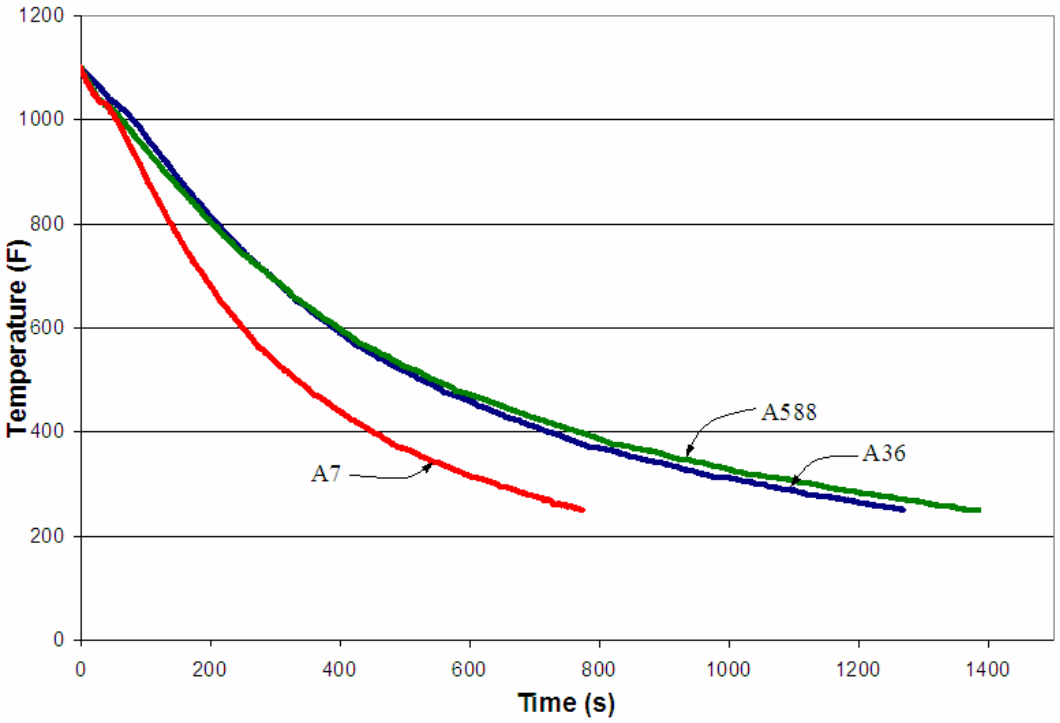

Figure 5.40
Cooling periods of A36, A588, and A7 steel (1100-250 °F)

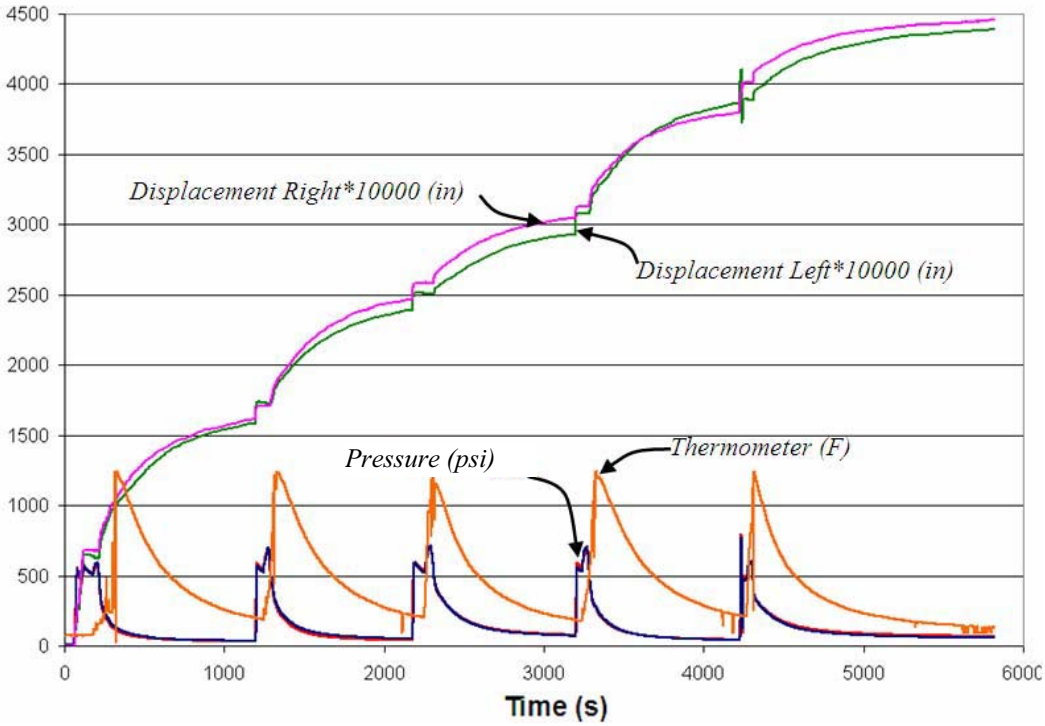

Figure 5.41
Instrument data during the first repair cycle of Specimen A7-60-25-3

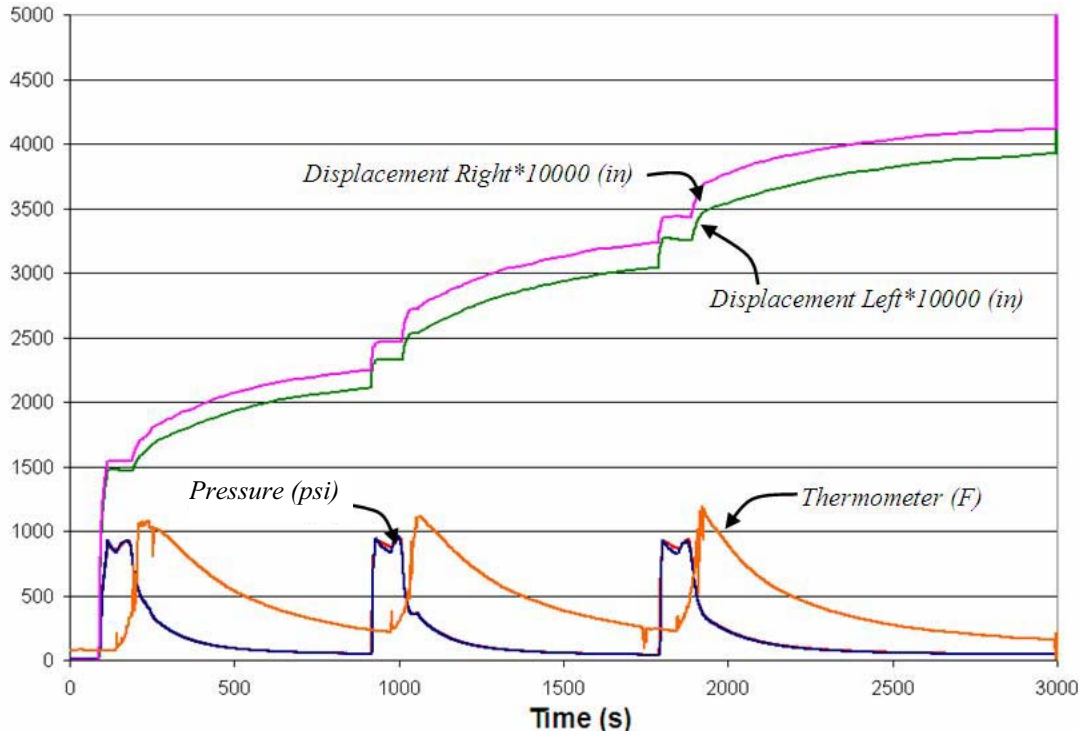

Figure 5.42
Instrument data during the first repair cycle of Specimen A7-60-40-5

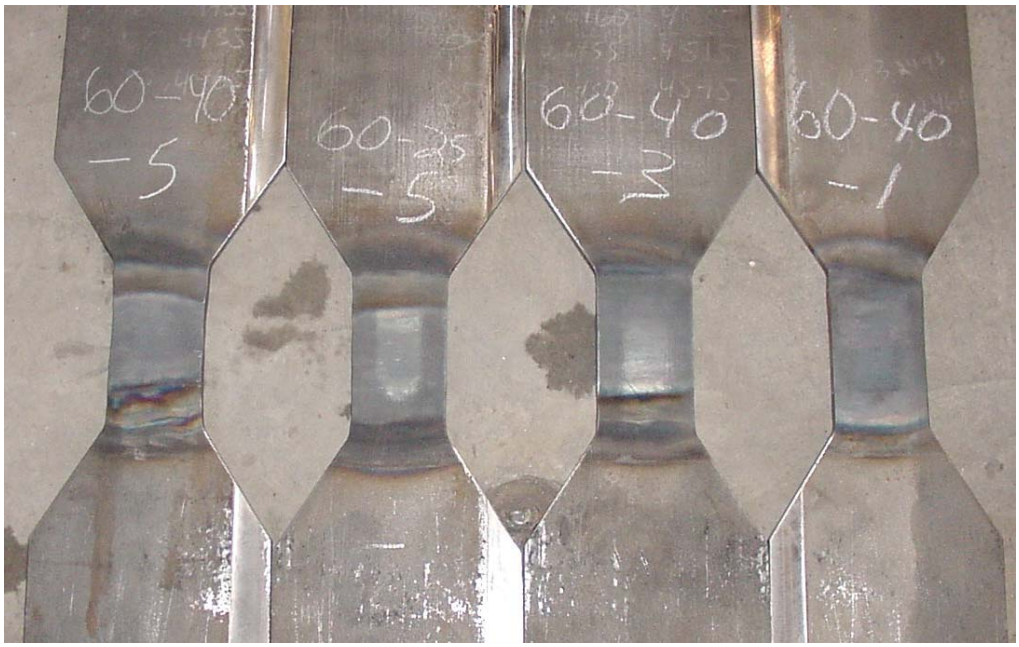

Figure 5.43
Frontal view of A7 steel specimens after experimental investigations

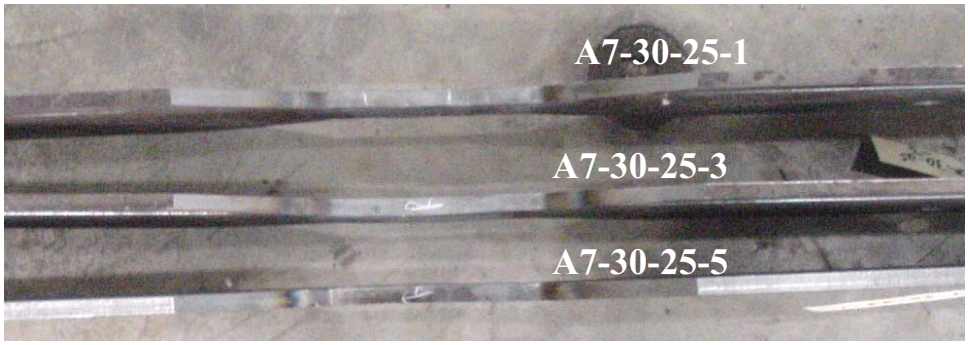

Figure 5.44
Side view of A7-30-25 specimens after experimental investigations

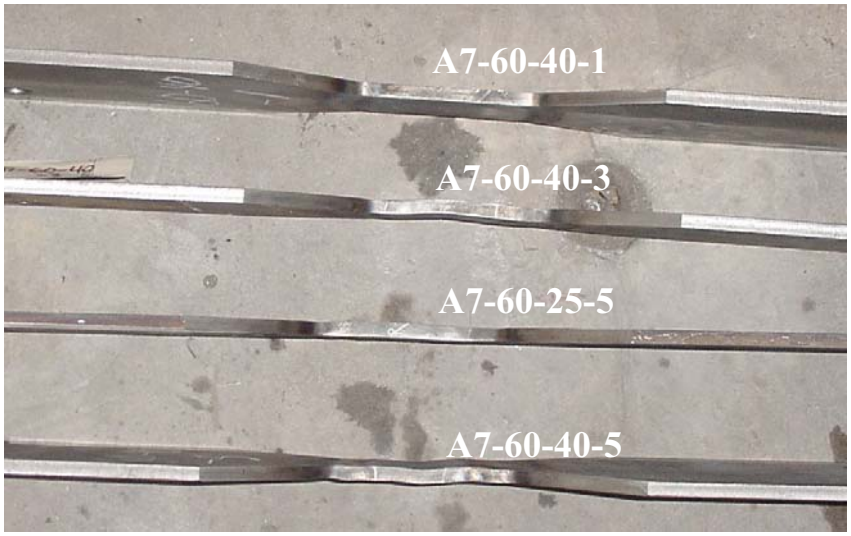

Figure 5.45
Side view of A7 steel specimens after experimental investigations

Figure 5.46
Induced curvature in the test area of Specimen A7-90-25-1

Figure 5.47
Induced curvature in the test area of Specimen A7-90-25-3

Figure 5.48
Induced curvature in the test area of Specimen A7-90-40-1

Figure 5.49
Induced curvature in the test area of Specimen A7-90-40-3

a) A7-60 b) A7-90

Figure 5.50
Indication of curvature of the A7 uniaxial tensile coupons

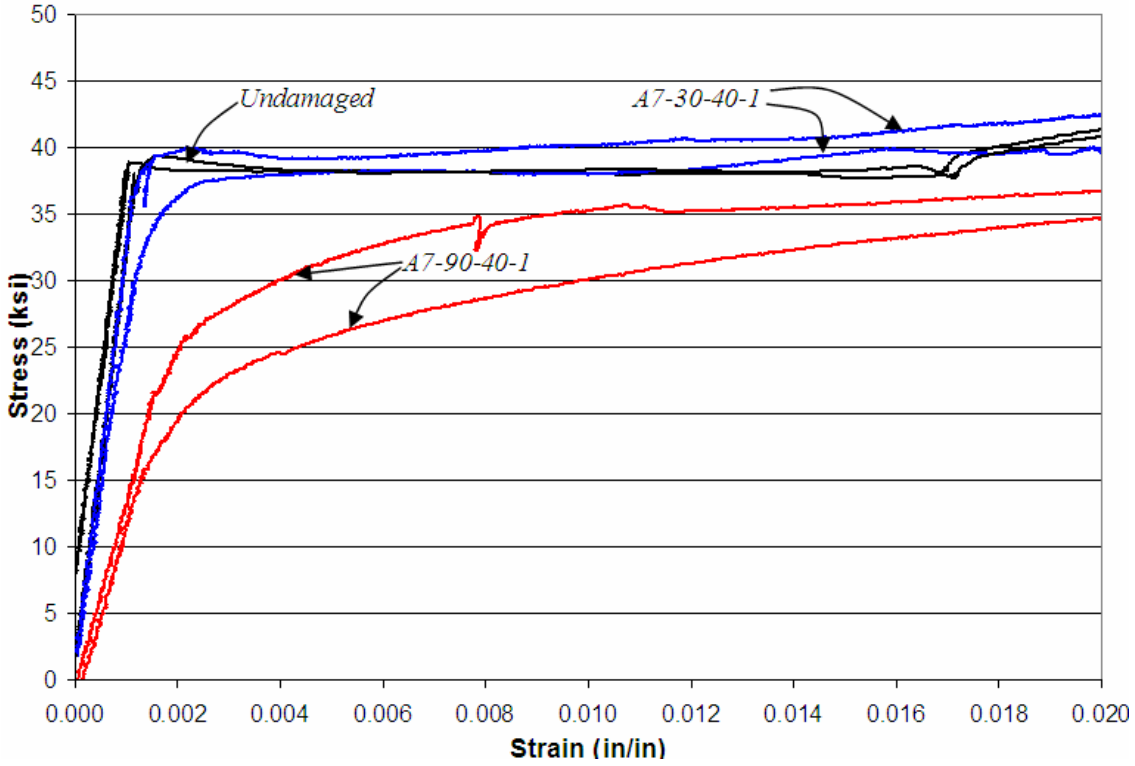

Figure 5.51
Comparisons of initial stress-strain relationships of A7 uniaxial tension coupons

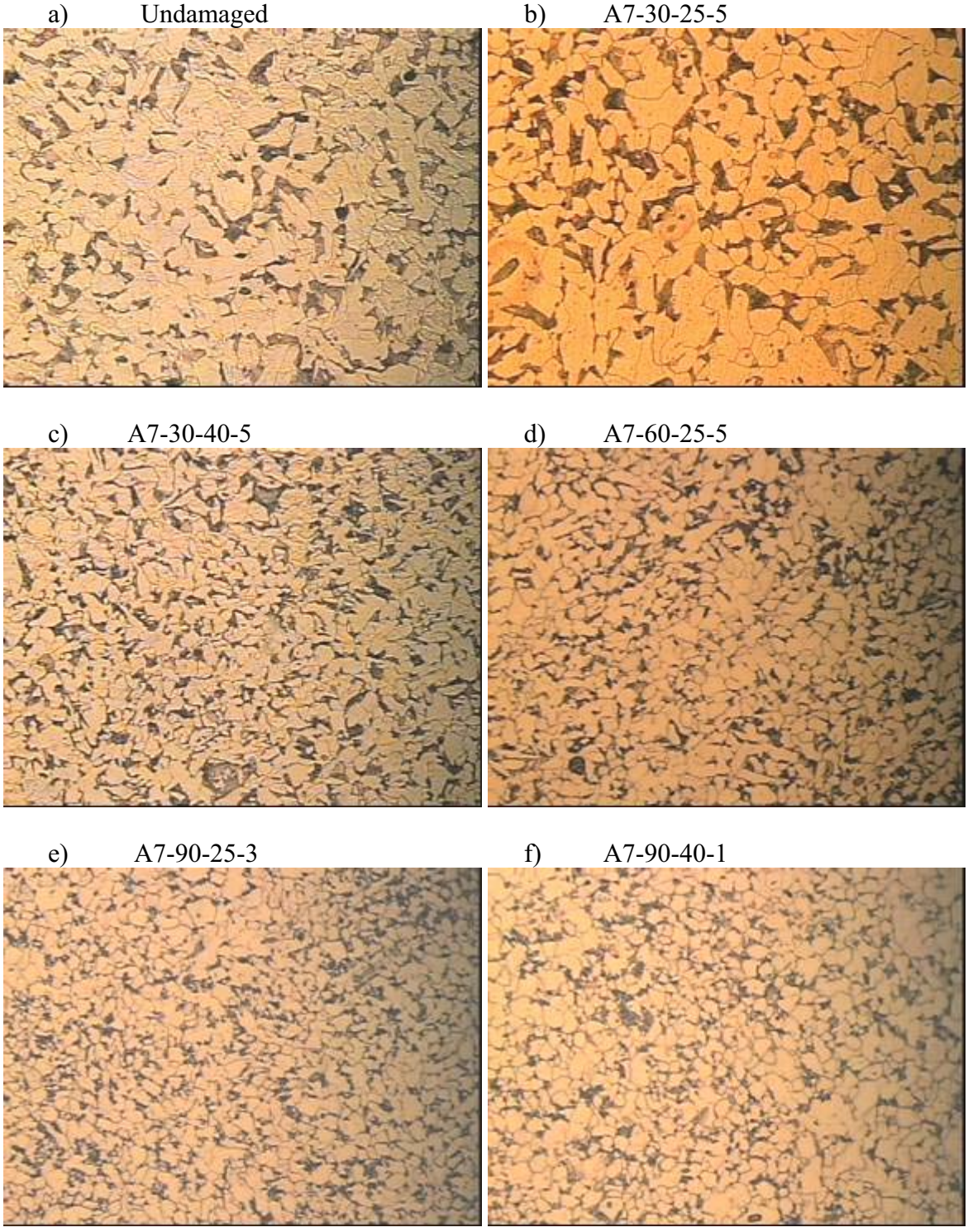

Figure 5.52
Microstructures of undamaged A7 steel and various A7 damage-repaired specimens

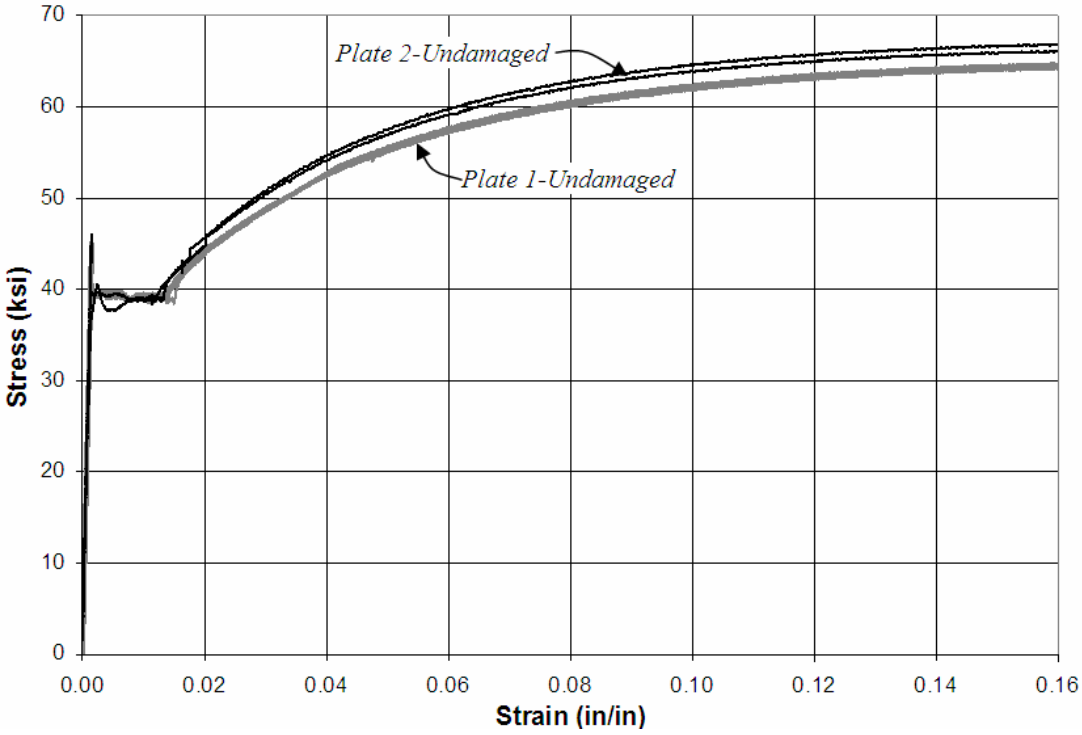

Figure 5.53
Stress-strain relationships of undamaged A36 steel from both steel plates

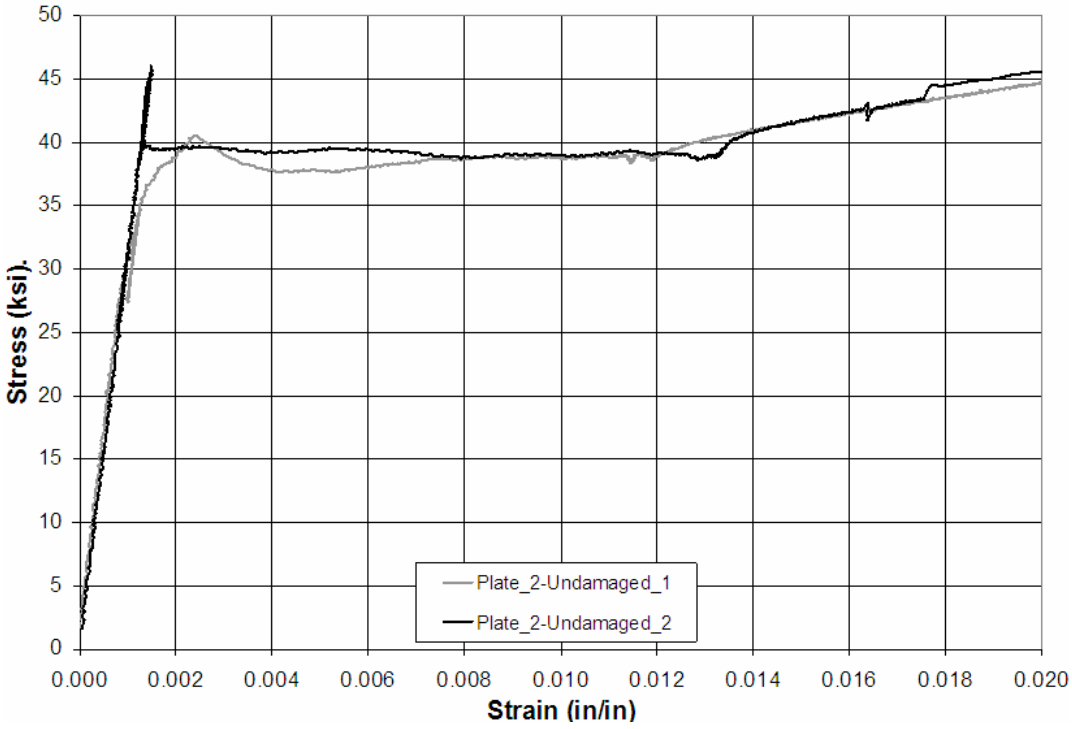

Figure 5.54
Initial stress-strain relationships of A36 steel from Plate 2

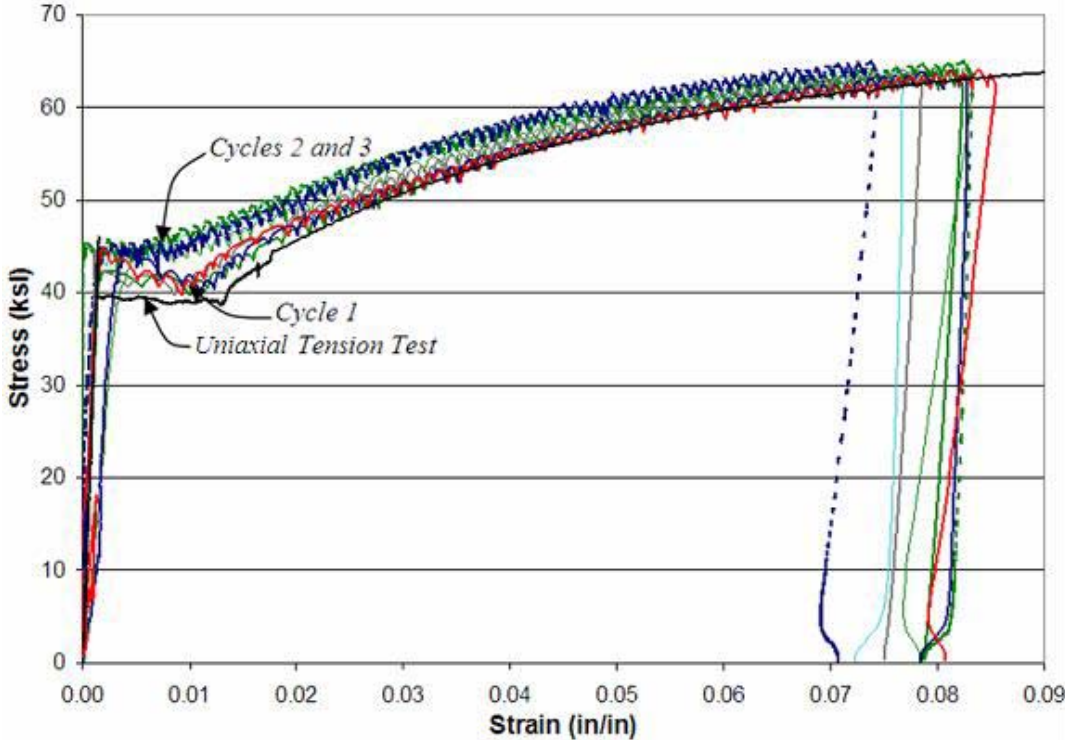

Figure 5.55
Stress-strain behaviors of all three damage cycles of Specimen A36-90-25-3-1600

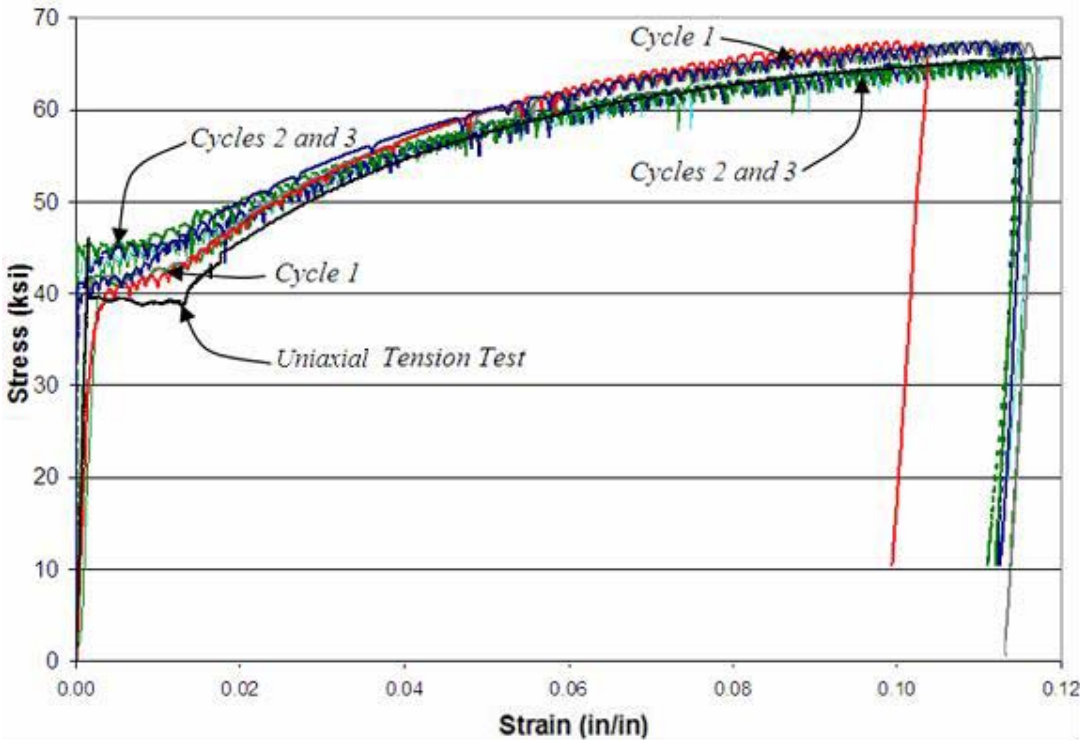

Figure 5.56
Stress-strain behaviors of all three damage cycles of Specimen A36-60-25-3-1600

a) 1400 °F

b) 1200 °F

Figure 5.57
Color of A36 steel at maximum heating temperatures of 1400 °F (a) and 1200 °F (b)

a) Maximum Temperature
(A36-60-25-1-1600)

b) High Temperature
(A36-90-25-3-1600)

Figure 5.58
Color and condition of A36 steel at elevated temperatures (T_{max} = 1600 °F)

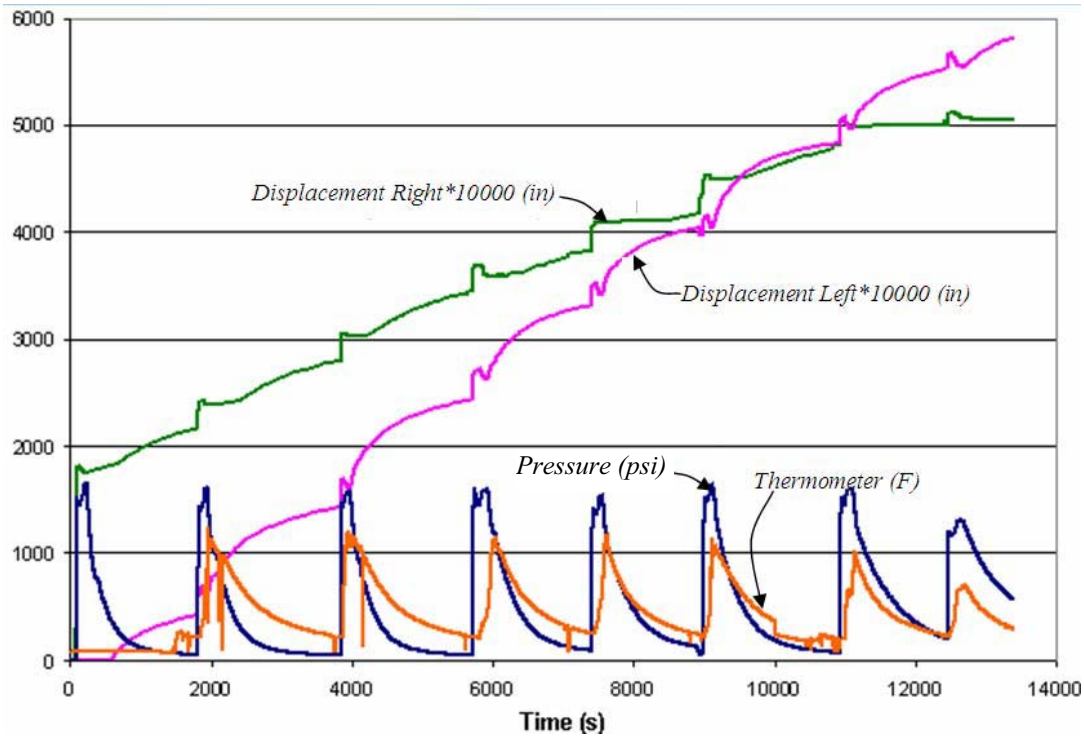

Figure 5.59
Instrument data during the first repair cycle of Specimen A36-90-25-3

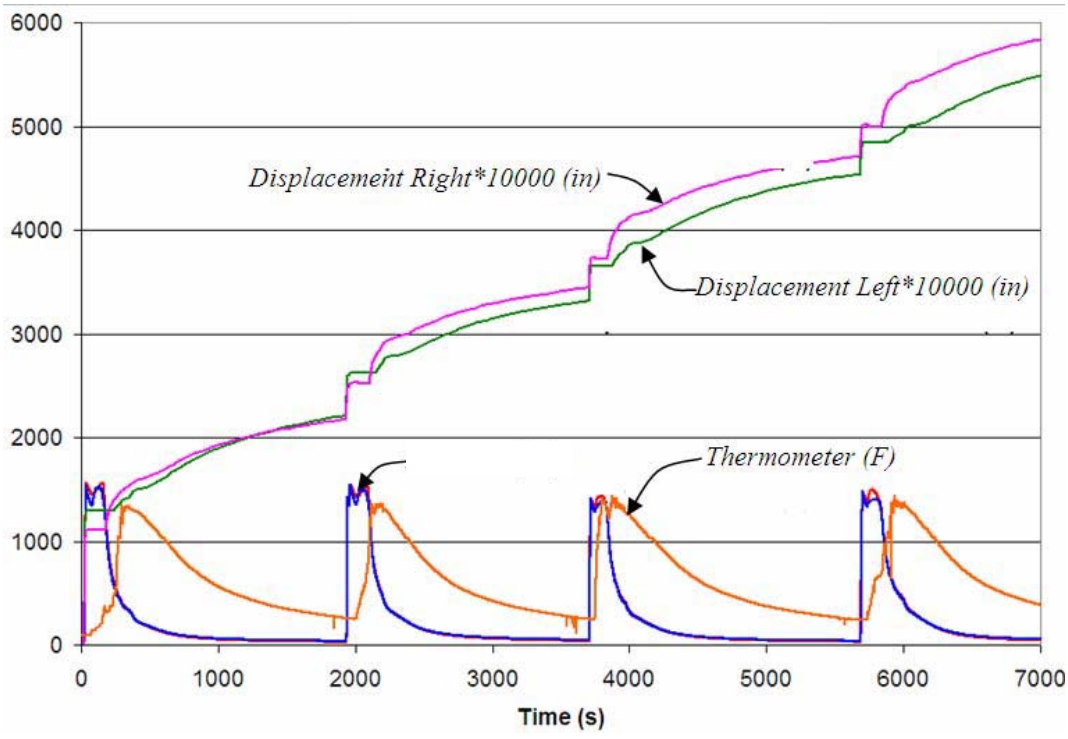

Figure 5.60
Instrument data during the third repair cycle Specimen A36-90-23-3-1400

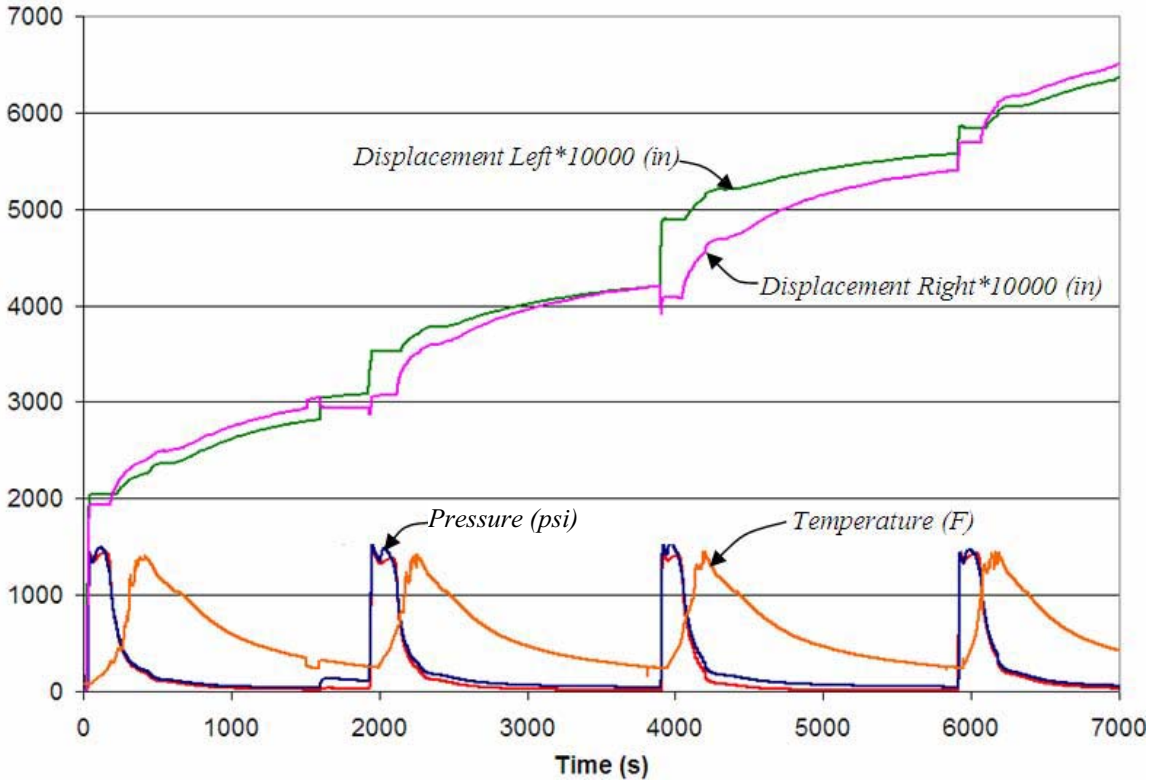

Figure 5.61
Instrument data during the first repair cycle Specimen A36-90-25-1-1600

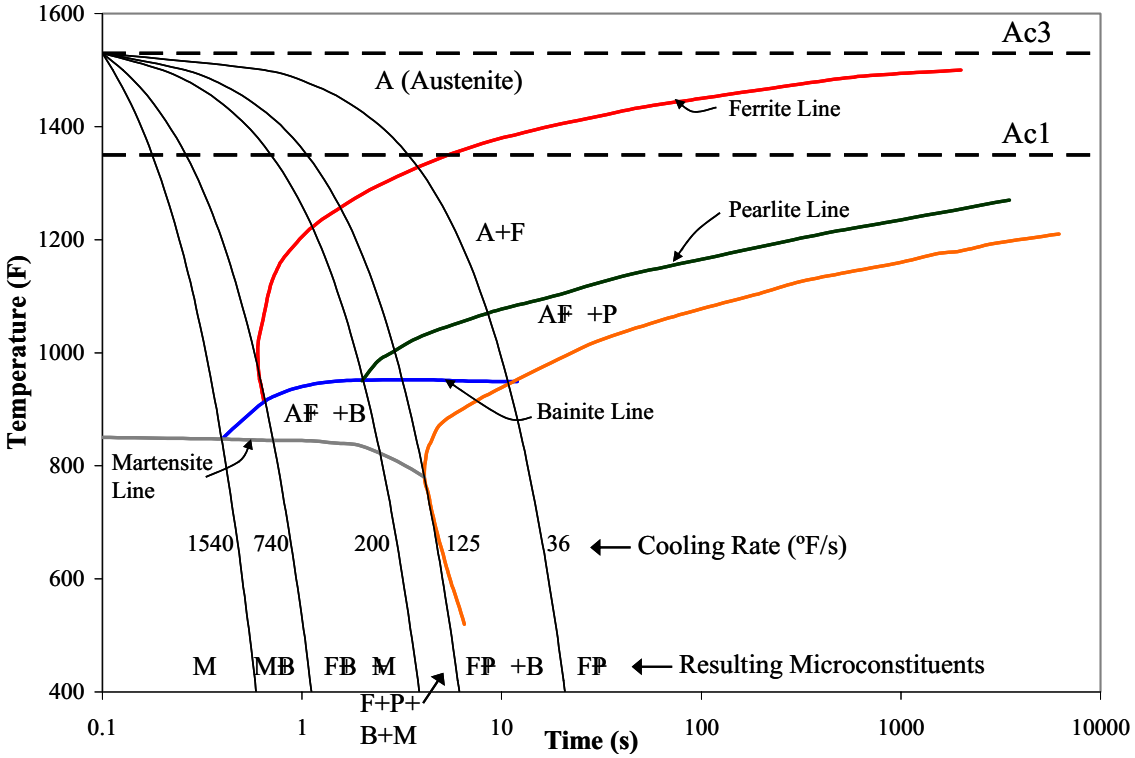

Figure 5.62
Continuous cooling diagram for 0.12% carbon steel

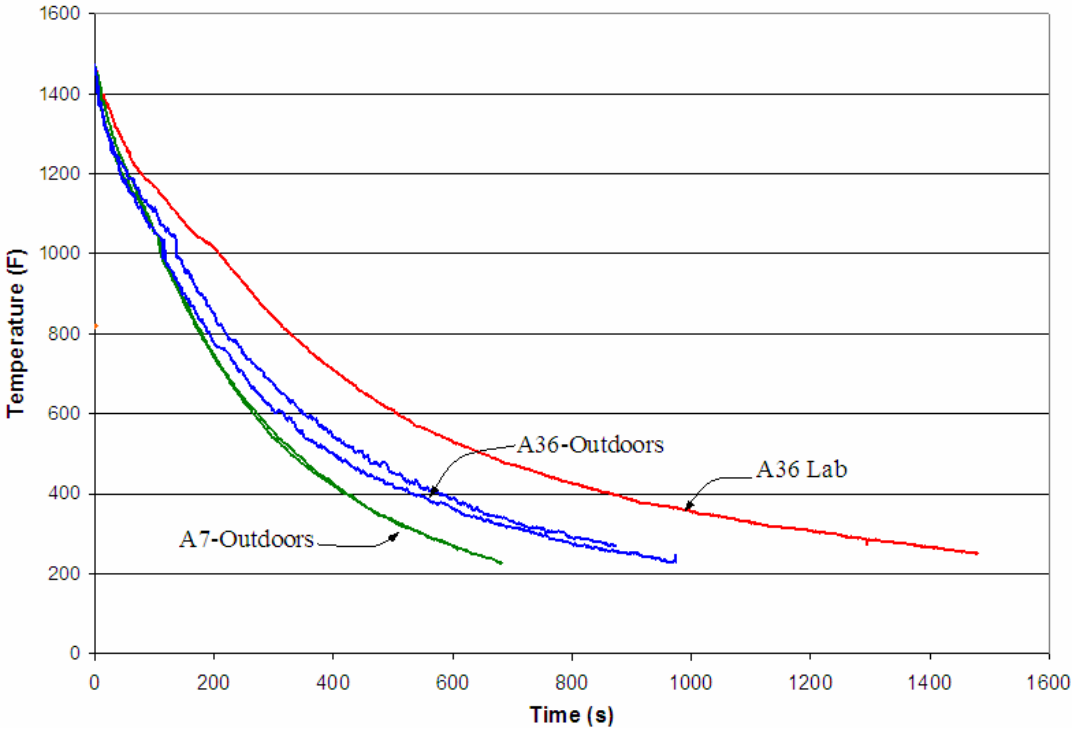

Figure 5.63
Cooling periods of overheated steel in different temperature conditions

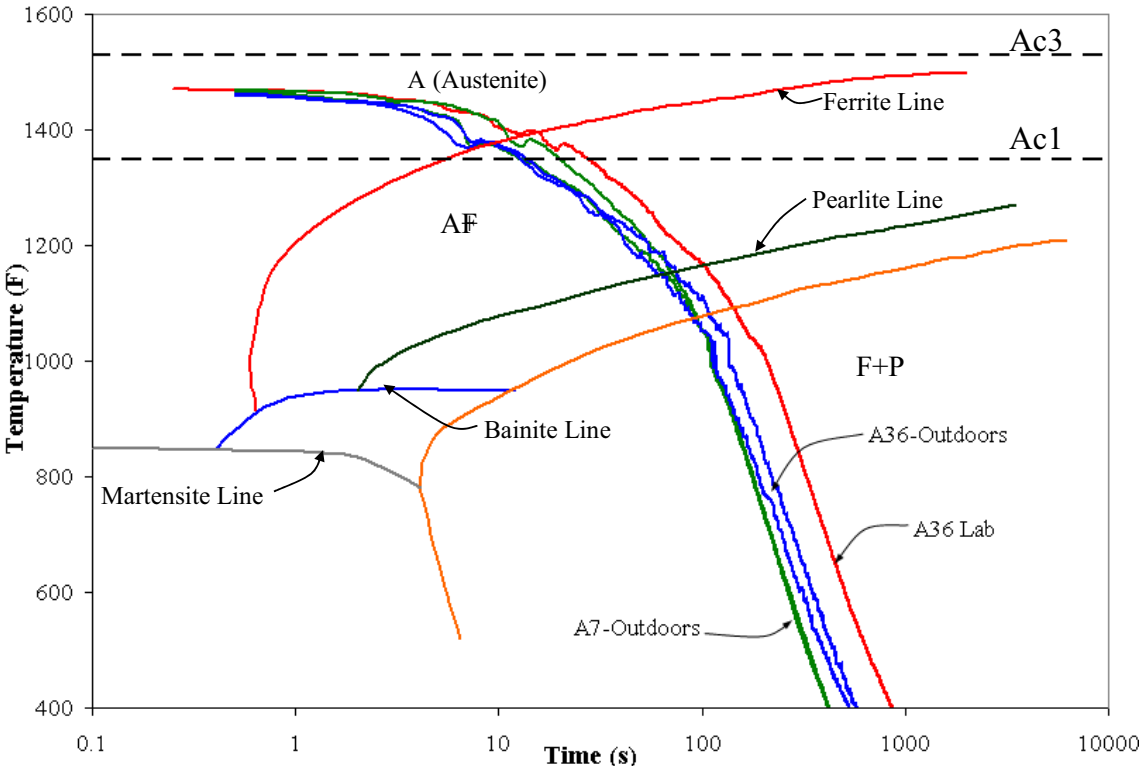

Figure 5.64
Cooling periods plotted on the continuous cooling diagram for 0.12% carbon steel

Figure 5.65
Frontal view of overheated A36 specimens after experimental investigations

Figure 5.66
Side view of overheated A36 specimens after experimental investigations

Figure 5.67
Side view of overheated A36 specimens after experimental investigations

a) A36-90-50-3-1600 b) A36-90-25-3-1600

Figure 5.68
Surface conditions of A36 steel after being repaired with T_{max} = 1600 °F

a) Undamaged A36

b) A36-60-25-1-1400

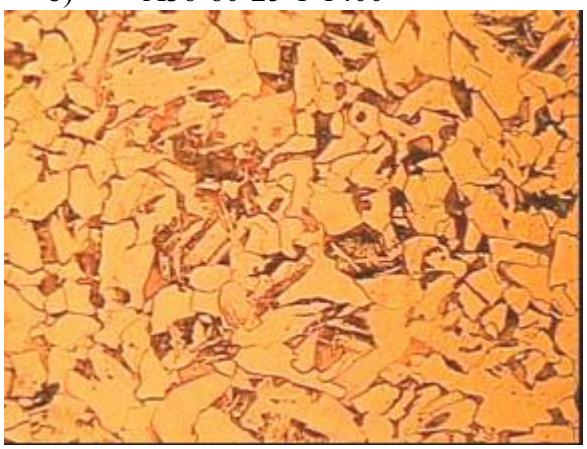

c) A36-60-50-3-1400

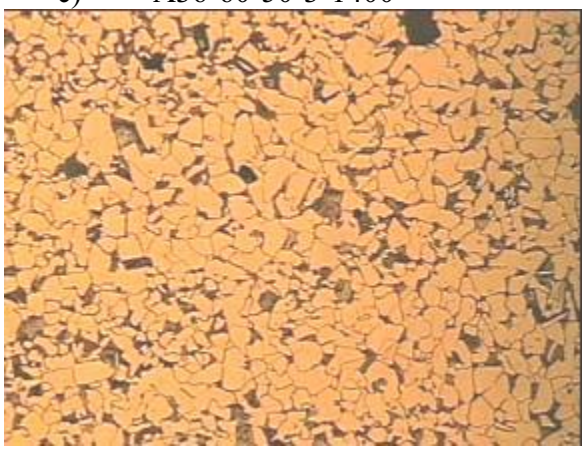

d) A36-60-50-3-1600

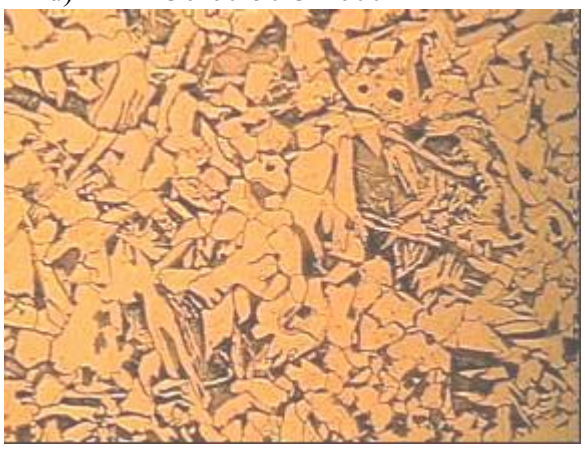

e) A36-90-25-1-1400

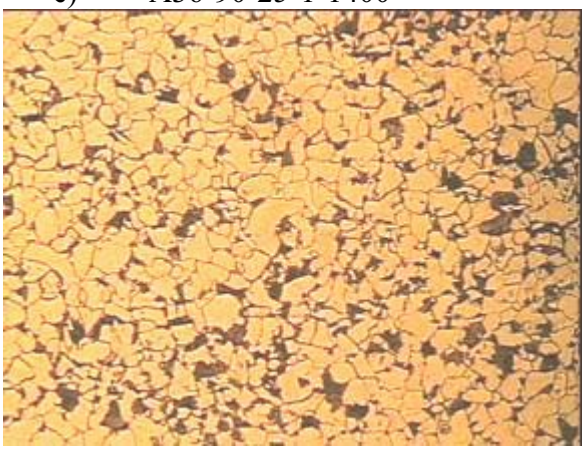

f) A36-90-25-1-1600

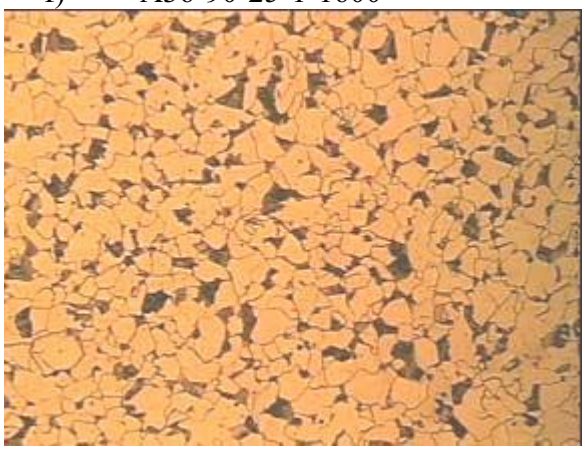

Figure 5.69
Microstructures of undamaged A36 steel and overheated A36 damaged-repaired specimens

a) Undamaged A36 Steel (Plate 1)

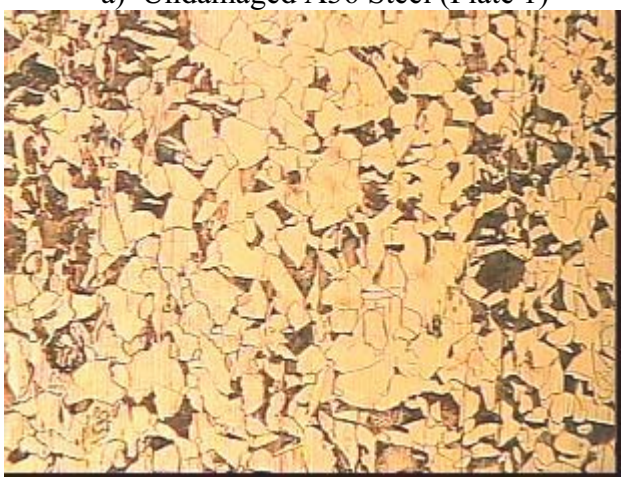

b) After Damage of 30 ε_y

c) After Damage of 60 ε_y

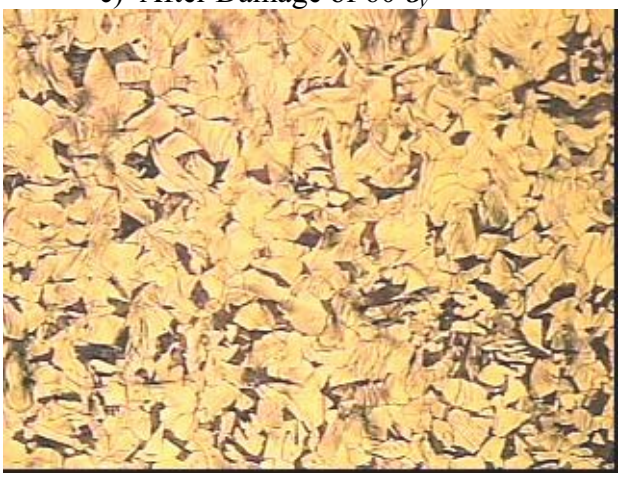

d) After Damage of 90 ε_y

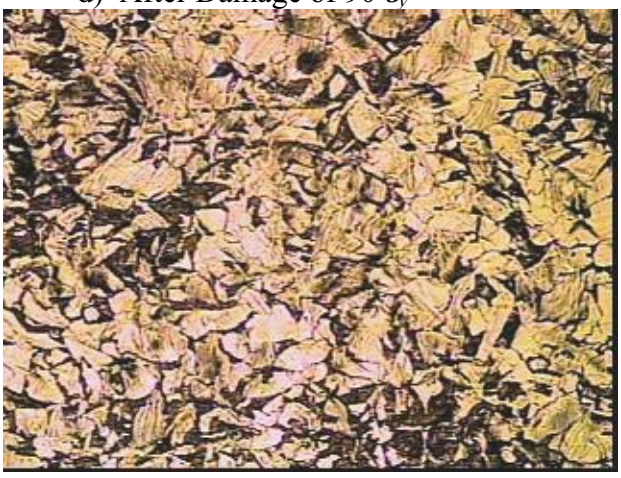

e) After Repair (A36-60-50-1)

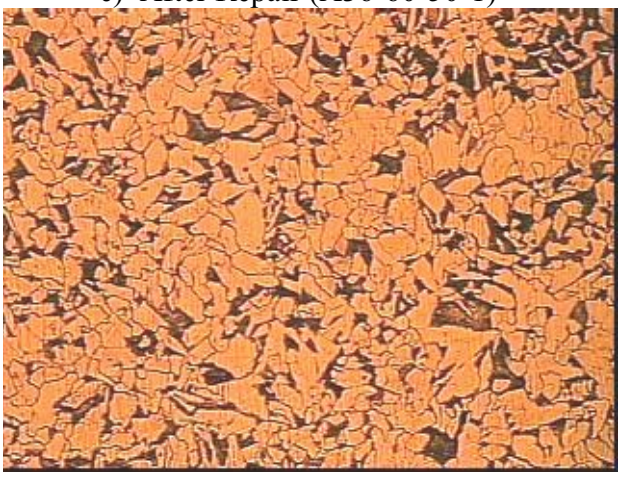

f) After Repair (A36-90-25-1)

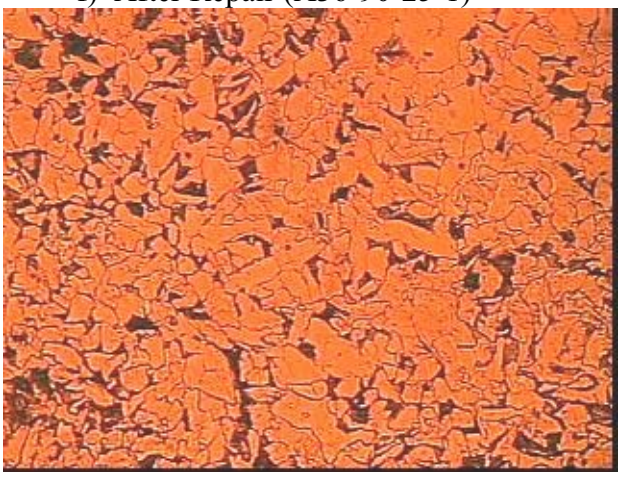

Figure 5.70
Microstructure of undamaged, damaged, and repaired A36 steel (Plate 1)

a) Undamaged A588 Steel

b) After Damage of 20 ε_y

c) After Damage of 40 ε_y

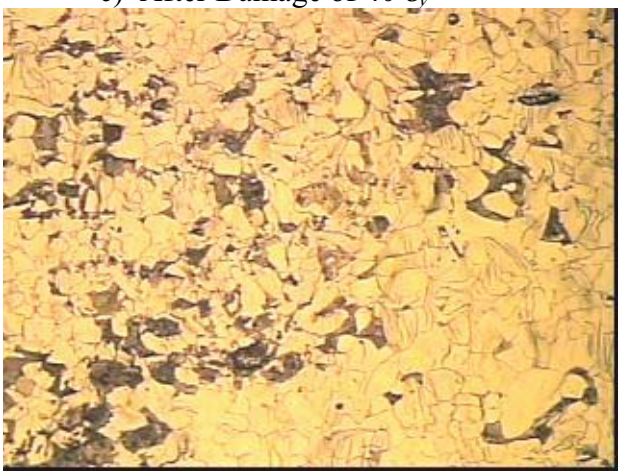

d) After Damage of 60 ε_y

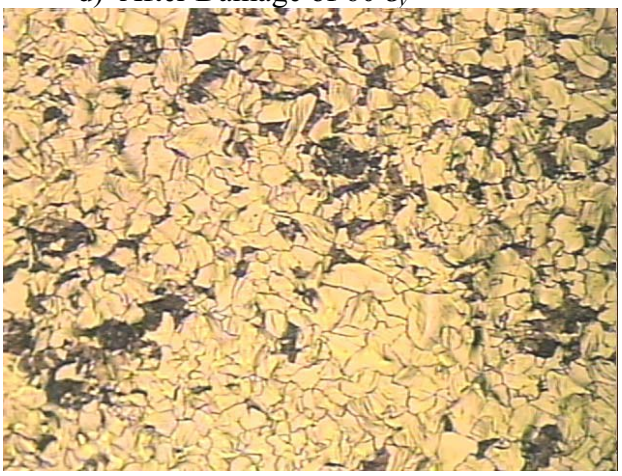

e) After Repair (A588-20-50-1)

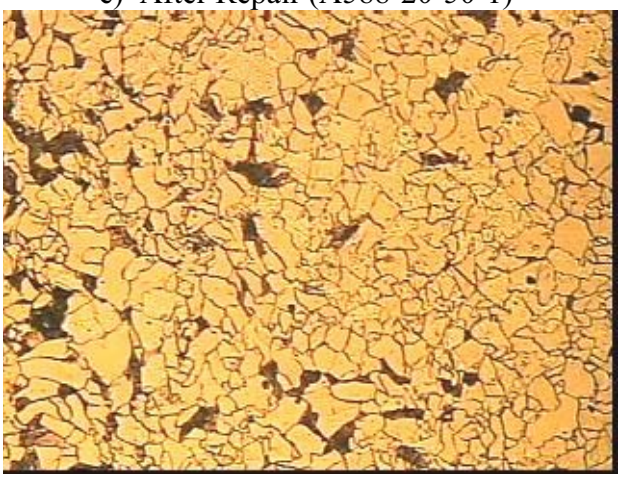

f) After Repair (A588-40-50-1)

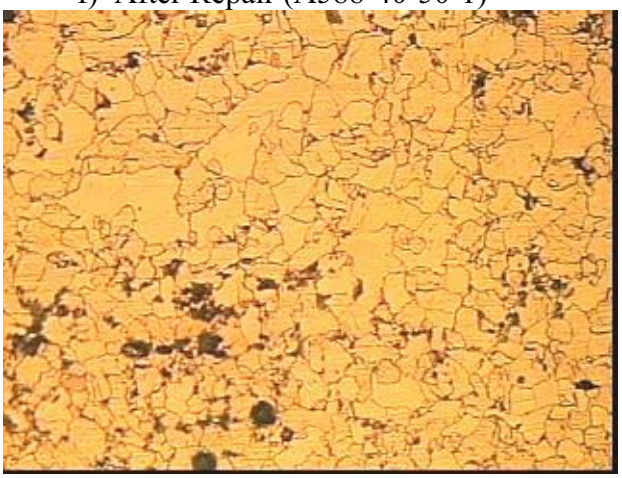

Figure 5.71
Microstructure of undamaged, damaged, and repaired A588 steel

a) Undamaged A7 Steel

b) After Damage of 30 ε_y

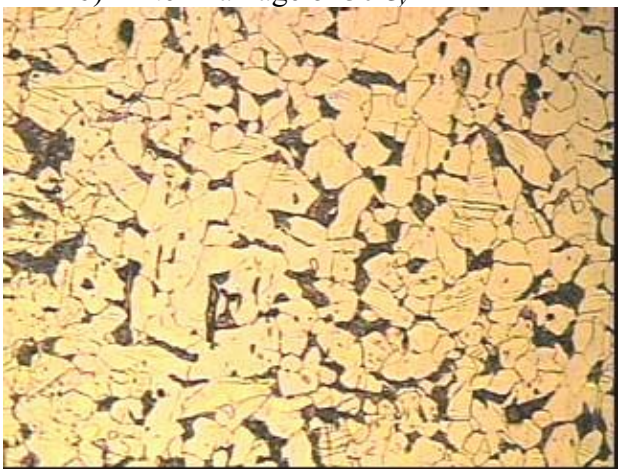

c) After Damage of 60 ε_y

d) After Damage of 90 ε_y

e) After Repair (A7-60-40-1)

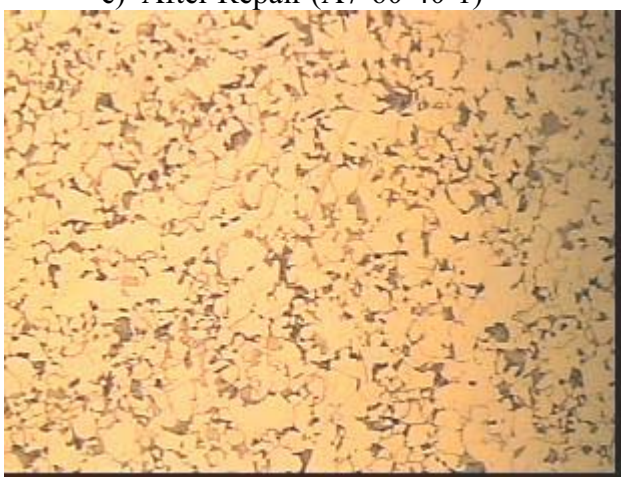

f) After Repair (A7-90-40-1)

Figure 5.72
Microstructure of undamaged, damaged, and repaired A7 steel

a) Undamaged A36 Steel (Plate 2)

b) After Damage of 30 ε_y

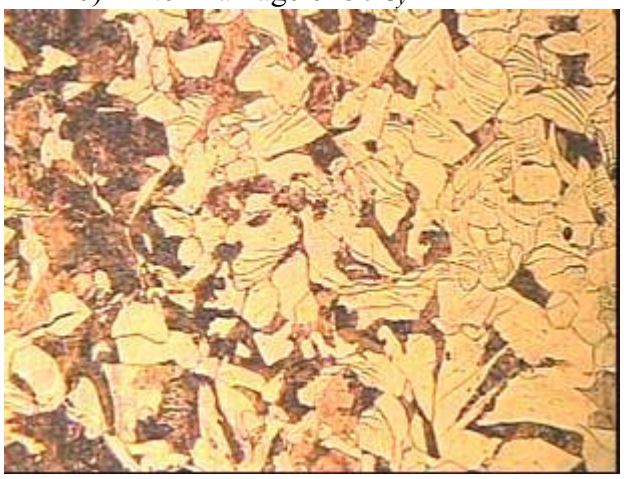

c) After Damage of 60 ε_y

d) After Damage of 90 ε_y

e) After Repair (A36-60-25-1-1400)

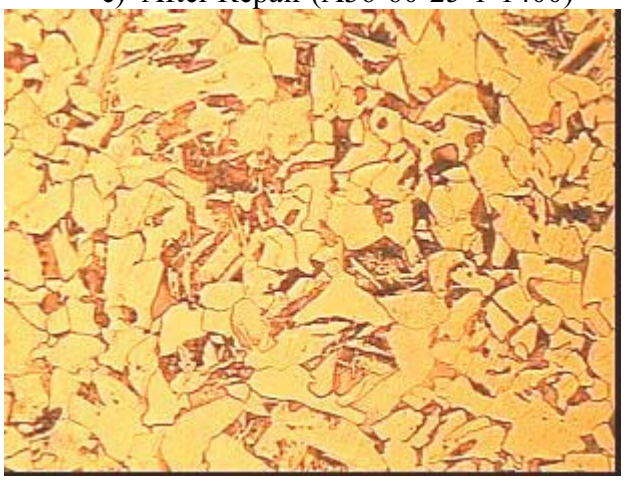

f) After Repair (A36-90-25-1-1600)

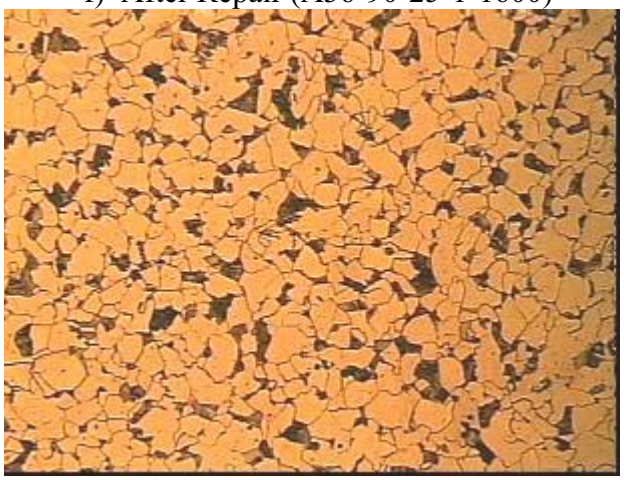

Figure 5.73
Microstructure of undamaged, damaged, and repaired A36 steel (Plate 2)

[Intentionally Blank Page]

6 EVALUATION OF EXPERIMENTAL RESULTS FROM LABORATORY-SCALE TESTS

6.1 OUTLINE OF RESULTS SUMMARY AND CONCLUSIONS

This chapter summarizes the results of material tests conducted on standard specimens fabricated from the damaged-repaired A36, A588, and A7 steel. The damaged-repaired steel material properties are compared with the corresponding undamaged steel material properties. These comparisons evaluate the effects of damage and repair parameters on the material properties of bridge steel. The damage and repair parameters included in the study were: (1) the damage strain ε_d, (2) the restraining stress σ_r, (3) the number of damage-repair cycles N_r, and (4) the maximum heating temperature T_{max} used for repair. The material properties considered include the: (a) elastic modulus E, (b) yield stress σ_y, (c) ultimate stress σ_u, (d) percent elongation, (e) surface hardness, (f) fracture toughness, and (g) microstructure (grain size). Sections 6.2-6.5 present the summary results and conclusions for A36, A588, and A7, and overheated A36 steel, respectively.

Uniaxial Tension Tests

Uniaxial tension tests were conducted according to ASTM E8. The results from these tests include the uniaxial tension stress-strain (σ–ε) response of the material that is used to estimate the: (a) elastic modulus E, (b) yield stress σ_y, and (c) ultimate stress σ_u. See Figure 4.47 for the definitions of E, σ_y, and σ_u from the σ–ε response. Two uniaxial tests were conducted on coupons taken from the test area of each damaged-repaired laboratory-scale specimen. Figures 4.13 and 4.18 show the original locations of these coupons (designated X and Y) within the test area. The results for these coupons were averaged to obtain the average material properties (E, σ_y, σ_u, and percent elongation) for the damaged-repaired specimens as shown in tables and illustrations as part of this chapter.

Additionally, three uniaxial tests were conducted on coupons from the undamaged laboratory-scale specimen of each steel type. These coupons were taken in the same grain direction as the coupons from the damaged-repaired specimens. These results were averaged to obtain the average undamaged steel material properties (E, σ_y, σ_u, and percent elongation). The damaged-repaired steel material properties are normalized with respect to the corresponding undamaged steel material properties. The normalized material properties are used to evaluate the effects of the damage and repair parameters ε_d, σ_r, and N_r on the material properties of steel. This chapter includes figures and tables summarizing these comparisons for each steel type.

Fracture Toughness Tests

Fracture toughness tests were conducted according to ASTM E23. The charpy specimens were cooled to 40 ºF, and tested using a verified impact-testing machine. Six charpy specimens were fabricated from the test area of each damaged-repaired specimen. Figure 4.13 shows the original locations of these charpy specimens (three from quarter thickness and three from mid thickness) within the test area.

The fracture toughness values for the damaged-repaired specimens were compared with the fracture toughness values for undamaged steel as follows:

- Student's t-tests were conducted first to establish the statistical difference between the undamaged quarter and mid-thickness fracture toughness values for each steel type. As mentioned previously in Section 4.9.2, the t-test evaluates the statistical difference between two data sets using their respective means, standard deviations, and sample set sizes. The results from the t-test include the t-value and the corresponding probability of null hypothesis, where the null hypothesis implies that the data sets are statistically similar. This procedure was discussed in Sections 5.1.1, 5.2.1, and 5.4.1 for A36,

A588, and overheated A36 steel, respectively. Student's t-tests were not conducted on undamaged A7 material because the plate thickness was only 0.45 in. and the specimens were removed from the mid thickness. When the data sets are statistically similar (e.g. A36 steel, see Section 5.1.1), the quarter and mid thickness fracture toughness values are combined into one set, and further comparisons do not differentiate between them. When the data sets are not statistically significant (e.g. A588 steel, see Section 5.2.1), further comparisons consider quarter and mid thickness fracture toughness values separately.

- Student's t-tests were also conducted to establish the statistical difference between the undamaged fracture toughness values and the damaged-repaired fracture toughness values for A36, A7, and overheated A36 steel. Student's t-tests were not conducted to establish the statistical difference between the undamaged fracture toughness to the damage-repaired fracture toughness of A588 steel. The undamaged data indicated that significant statistical difference existed between the undamaged quarter and mid thickness values. Therefore, only three damaged-repaired values from each specimen could be used in one t-test.
- The fracture toughness values for each undamaged steel type were analyzed statistically to determine the: (a) mean (average), (b) 95% confidence interval (CI) for actual mean (high and low), (c) standard deviation, (d) median, and (e) average absolute deviation from median for each steel type. The fracture toughness values for the damaged-repaired steels were also analyzed statistically to determine the values (a–e) mentioned here.
- The mean fracture toughness and the 95% CI high and low values for the damaged-repaired steels were normalized with respect to the corresponding values for the corresponding undamaged steel type. These normalized values are plotted in line graphs presented later in Sections 6.2.2–6.5.2. They provide a comprehensive evaluation of the effects of damage and repair parameters (ε_d, σ_r, and N_r) on the fracture toughness of steel.

Rockwell Hardness Tests and Metallographic Inspection

Rockwell hardness tests were conducted using a calibrated Rockwell hardness-testing machine according the ASTM E18 standard. The hardness values were measured on the polished inside surface of a quarter-thickness charpy specimen. Four hardness values were measured for each damaged-repaired specimen and for the undamaged specimen of each steel type. The average hardness of the damaged-repaired specimens is normalized with respect to the average hardness of the corresponding undamaged steel type. The normalized average hardness values are used to evaluate the effects of damage and repair parameters.

Metallographic inspections were conducted on the surfaces of undamaged and damaged-repaired specimens using the procedures outlined in Section 4.9.4. The specimens were polished according to ASTM E3 standard. Microstructure pictures were taken at magnifications of 240X and 480X. Grain sizes for undamaged and damaged-repaired specimens were computed using the standard ASTM E112 line intercept method. The normalized grain sizes are used to evaluate the effects of damage and repair parameters.

Special Notes

Some specimens developed significant curvature after the multiple damage-repair cycles. These specimens are identified with a * before their name in the tables and figures presented in Sections 6.2 – 6.4. Development of curvature is identified like this because it is a significant issue that influences some of the measured material properties, for example, σ_y and E.

6.2 DAMAGED-REPAIRED A36 STEEL

Twenty-eight laboratory scale specimens made from A36 steel were tested by subjecting them to multiple damage-repair cycles. The damage and repair parameters for these specimens were summarized in Table 4.1. Standard material tests were conducted on samples taken from the test area of the damaged-repaired specimens and an undamaged specimen. The results and comparisons of these material tests are presented in Sections 6.2.1 to 6.2.4. Section 6.2.1 summarizes the results form the tension tests. Section 6.2.2 summarizes the fracture toughness results. Section 6.2.3 focuses on the Rockwell hardness and metallographic inspection results. Finally, Section 6.2.4 presents the conclusions and recommendations for damaged-repaired A36 steel.

6.2.1 Uniaxial Tension Test Results

The uniaxial tension test results for coupons from undamaged and damaged-repaired specimens are averaged and summarized in Table 6.1. The values in Table 6.1 include the yield stress (σ_y), the elastic modulus (E), the yield strain (ε_y), the ultimate stress (σ_u), the ultimate strain (ε_u), the strain ductility ($\varepsilon_u/\varepsilon_y$), the percent elongation, and the percent reduction (area). The damaged-repaired steel material properties (E, σ_y, σ_u, and percent elongation) are normalized with respect to the corresponding undamaged steel material properties and plotted in Figures 6.1 to 6.4. Figure 6.1 shows the normalized yield stress for all damaged-repaired specimens. Figure 6.2 shows the normalized elastic modulus. Figure 6.3 shows the normalized ultimate stress, and Figure 6.4 shows the normalized percent elongation.

The yield stress data in Table 6.1 and Figure 6.1 indicate that:

- Damage-heat straightening repair usually increases the yield stress of A36 steel. However, this increase in the yield stress is not significant: it varies between 4 –24% with most values between 5 – 12% of the undamaged yield stress.
- The increase in yield stress is higher for damaged-repaired specimens subjected to smaller damage strains. Thus, the increase in yield stress for A36-30 specimens ($\varepsilon_d = 30\varepsilon_y$) is greater than the increase for A36-60 specimens ($\varepsilon_d = 60\varepsilon_y$), which is greater than the increase for A36-90 specimens ($\varepsilon_d = 90\varepsilon_y$).
- The increase in yield stress does not have a clear trend with the number of damage-repair cycles (N_r) or the restraining stress (σ_r).

The elastic modulus data in Table 6.1 and Figure 6.2 indicate that:

- Damage-repair cycles do not have a significant influence on the elastic modulus of A36 steel. The elastic modulus of damaged-repaired specimen usually varies between 95-110% of the undamaged elastic modulus.
- The change in elastic modulus does not have a clear or direct trend with the damage and repair parameters (ε_d, σ_r, or N_r).

The ultimate stress data in Table 6.1 and Figure 6.3 indicate that:

- Damage-repair cycles do not have a significant influence on the ultimate stress of A36 steel. The ultimate stress of damaged-repaired specimens usually varies between 95-110% of the undamaged ultimate stress.
- The increase in ultimate stress is higher for damaged-repaired specimens subjected to smaller damage strains. Thus, the increase in ultimate stress for A36-30 specimens ($\varepsilon_d = 30\varepsilon_y$) is greater than the increase for A36-60 specimens ($\varepsilon_d = 60\varepsilon_y$), which is greater than the increase for A36-90 specimens ($\varepsilon_d = 90\varepsilon_y$).

- In fact, the ultimate stress for A36-60 ($\varepsilon_d = 60\varepsilon_y$) specimens is approximately equal to the ultimate stress of undamaged steel, and the ultimate stress for A36-90 specimens ($\varepsilon_d = 90\varepsilon_y$) is less than the ultimate stress for undamaged steel.
- The change in ultimate stress does not have a clear or direct trend with the restraining stress (σ_r) or the number of damage-repair cycles (N_r).

The percent elongation data in Table 6.1 and Figure 6.4 indicate that:

- Damage-heat straightening repair reduces the percent elongation (ductility) of A36 steel. This reduction in ductility is reasonably significant with percent elongation values for damaged-repaired steel ranging from 66 - 95% of the percent elongation value for of undamaged A36 steel.
- The reduction in ductility is higher for damaged-repaired specimens subjected to smaller damage strains. That is, the reduction in ductility for A36-30 specimens ($\varepsilon_d = 30\varepsilon_y$) is greater than the reduction for A36-60 ($\varepsilon_d = 60\varepsilon_y$) or A36-90 ($\varepsilon_d = 90\varepsilon_y$) specimens.
- The reduction in ductility does not have a clear or direct trend with the restraining stress (σ_r) or the number of damage-repair cycles (N_r).
- Damaged-repaired specimens with greater increase in ultimate stress (Figure 6.3) have a greater reduction in ductility. This is an expected trend because higher strength steel has less ductility.

6.2.2 Fracture Toughness Results

Fracture toughness tests were conducted on charpy v-notch specimens fabricated from undamaged and damaged-repaired specimens. The toughness tests were conducted at 40 ºF according to the ASTM E23 standard. However, due to some problems with the machining procedure (presented in Section 5.1.1), the charpy specimens from the damaged-repaired A36 specimens were fabricated with a break depth of 0.304 in. This break depth is smaller than the ASTM E23 standard break depth of 0.315 ± 0.003 in. Therefore, two sets of charpy specimens with break depths = 0.315 in. and 0.304 in. were fabricated and tested from the undamaged specimen. The results were given in Tables 5.6 and 5.7. The normalized relationships in this section compare with the results of charpy specimens with undamaged break depth of 0.304 in.

Comparisons of undamaged and damaged-repaired fracture toughness

Tables 6.2 to 6.7 present the fracture toughness values for the damaged-repaired A36 specimens. Six fracture toughness values are reported for each damaged-repaired specimen. The toughness values for each specimen are arranged in ascending order, and the statistical mean, 95% confidence interval, standard deviation, median, and average absolute deviation from median for each specimen are reported.

Figures 6.5 to 6.7 compare (numerically) the fracture toughness values for the damaged-repaired specimens with the toughness values for the undamaged specimens. These figures provide a visual comparison of the effects of damage-repair parameters on the range of fracture toughness values. These figures clearly indicate that the fracture toughness of damaged-repaired specimens is much lower (for almost all cases) than the fracture toughness of undamaged specimens. In several cases, the fracture toughness of damaged-repaired specimens falls below the AASHTO limit of 21 ft-lbs. Figure 6.5 to 6.7 are not very easy to read or interpret because they present numerical values without normalization.

Therefore, the 95% confidence interval (high), mean, and 95% CI low fracture toughness values for each damaged-repaired specimen were normalized with respect to the corresponding undamaged A36 steel mean value. The normalized mean fracture toughness and the 95% confidence interval (CI) bounds are shown in Figure 6.8. Figure 6.8 provides excellent visual and numerical comparisons of the effects of damage and repair parameters on the fracture toughness. In Figure 6.8, when the 95% CI high and low

bounds have a large range about the mean, it implies large variation in the measured toughness values for the corresponding damaged-repaired specimen.

Evaluation of toughness results

As shown in Figure 6.8, the normalized fracture toughness of damaged-repaired A36-30 specimens ($\varepsilon_d = 30\varepsilon_y$) is much lower than the toughness of undamaged specimens. The mean fracture toughness after two damage-repair cycles is approximately 25% of the undamaged toughness. The mean toughness increases slightly after two cycles and reaches approximately 50% of the undamaged toughness after four cycles. After five cycles, the mean toughness again reduces to 25% of the undamaged toughness. The restraining stress (σ_r) parameter does not seem to have a significant influence on the toughness.

The normalized fracture toughness of A36-60 specimens ($\varepsilon_d = 60\varepsilon_y$) is usually lower than the toughness of undamaged steel. After one damage-repair cycle, the mean fracture toughness is still close to the undamaged toughness. The mean toughness decreases almost continuously with further damage-repair cycles. After three cycles, the mean toughness is approximately 50% of the undamaged toughness. After four cycles, the mean toughness is approximately 25% of the undamaged toughness, and after five cycles, the toughness is very low. The lower bound of the 95% confidence interval reduces to approximately 25% of the undamaged toughness after one or two damage-repair cycles depending on the restraining stress (σ_r). Besides this, the restraining stress parameter does not have a significant influence on the fracture toughness.

The normalized fracture toughness of A36-90 ($\varepsilon_d = 90\varepsilon_y$) has significant scatter. The mean fracture toughness of specimens repaired with a lower restraining stress ($\sigma_r = 0.25\sigma_y$) are close to the undamaged toughness. However, the lower bound of the 95% confidence interval reduces below 25% of the undamaged toughness after three cycles. The mean fracture toughness of specimens repaired with higher restraining stress ($\sigma_r = 0.50\sigma_y$) reduces below 25% of the undamaged toughness after one cycle. The mean toughness increases to 75% of the undamaged toughness after two cycles, and it reduces again to 25% after three cycles. The mean toughness is close to the undamaged toughness after four & five cycles, however the lower bound of the 95% confidence interval is much lower. For the A36-90 specimens, the higher restraining stress results in greater reduction in the fracture toughness.

6.2.3 Rockwell Hardness and Microstructure investigation Results

Table 5.20 summarized the averaged results of the Rockwell hardness tests and the microstructure investigations. Figure 6.9 shows the normalized hardness of the damaged-repaired specimens to that of the undamaged steel. This figure indicates:

- Heat straightening generally increases the hardness of A36 steel. The increase in hardness is greater for the specimens subjected to smaller damage strains.
- Good correlation exists between the trends in the hardness data and the ultimate stress of damaged-repaired steel (compare Figures 6.9 and 6.3).
- The hardness of damaged-repaired specimens is within a range of 98-116% of the undamaged steel.
- Other damage-repair parameters (σ_r and N_r) do not have a significant influence on the hardness.

The average grain size of the damaged-repaired specimens is normalized with respect to the undamaged steel grain size. Figure 6.10 shows the normalized grain size of the damaged-repaired specimens. This figure indicates:

- The impact of damage-repair cycles on the grain size of A36 steel does have any clear trend.

- The grain size of damaged-repaired steel is approximately 75-114% of the undamaged steel grain size. In most damage-repair cases (23 of 28), the grain size decreases which relates to the results of other steel types.

As a note, the grain size of the undamaged A36 steel was computed twice since the results after the first case did not relate well to what was concluded from A588, A7, and overheated A36. The results of both measurements were very similar.

6.2.4 Conclusions and Recommendations for Damaged-Repaired A36 Steel

- Damage-heat straightening repair cycles do not have a significant influence on the yield stress, elastic modulus, ultimate stress, surface hardness, or grain size of A36 steel. Most of the damaged-repaired are within ± 15% of the undamaged values, and are acceptable according to AASHTO requirements.
- However, the percent elongation (ductility) of damaged-repaired A36 steel is quite low, approximately 66-95% of the undamaged percent elongation. The reduction in percent elongation is greater for specimens subjected to smaller damage strains.
- Overall, it seems that the smaller damage strain of $\varepsilon_d=30\varepsilon_y$ had more adverse effects on the strength and ductility of A36 steel.
- The fracture toughness of damaged-repaired A36 steel is quite poor with respect to the undamaged toughness.
    - The mean fracture toughness of specimens damaged to 30 ε_y becomes less than 50% of the undamaged toughness after two damage-repair cycles.
    - The fracture toughness of specimens damaged to 60 ε_y becomes less than 50% of the undamaged toughness after three damage-repair cycles.
    - The mean fracture toughness of specimens damaged to $90\varepsilon_y$ was found to have significant scatter. The lower bound of the 95% confidence interval reduces below 25% generally after three damage-repair cycles. Higher restraining stress is detrimental for these specimens.
- *Due to the poor fracture toughness values and the significant scatter in their measured values, we recommend no more than three damage-repair cycles for A36 steel. Lower restraining stresses are recommended for repairing the damage. Note that smaller damage may be more detrimental to the A36 steel.*

6.3 DAMAGED-REPAIRED A588 STEEL

Thirty laboratory scale specimens made from A588 steel were tested by subjecting them to multiple damage-repair cycles. The damage and repair parameters for these specimens were summarized in Table 4.2. Standard material tests were conducted on samples taken from the test area of the damaged-repaired specimens and an undamaged specimen as outlined in Section 4.9. The results and comparisons of these material tests are presented in Sections 6.3.1 to 6.3.4. Section 6.3.1 summarizes the results form the tension tests. Section 6.3.2 summarizes the fracture toughness results. Section 6.3.3 focuses on the Rockwell hardness and metallographic inspection results. Finally, Section 6.3.4 presents the conclusions and recommendations for damaged-repaired A588 steel.

6.3.1 Uniaxial Tension Test Results

The uniaxial tension test results for coupons from undamaged and damaged-repaired specimens are averaged and summarized in Table 6.8. The values in Table 6.8 include the yield stress (σ_y), the elastic modulus (E), the yield strain (ε_y), the ultimate stress (σ_t), the ultimate strain (ε_u), the strain ductility

($\varepsilon_u/\varepsilon_y$), the percent elongation, and the percent reduction (area). The damaged-repaired steel material properties (E, σ_y, σ_u, and percent elongation) are normalized with respect to the corresponding undamaged steel material properties and plotted in Figures 6.11 to 6.14. Figure 6.11 shows the normalized yield stress for all damaged-repaired specimens. Figure 6.12 shows the normalized elastic modulus for all damaged-repaired specimens. Figure 6.13 shows the normalized ultimate stress, and Figure 6.14 shows the normalized percent elongation for all damaged-repaired specimens.

The yield stress data in Table 6.8 and Figure 6.11 indicate that:

- Damage-heat straightening repair does not have a significant influence on the yield stress of A588 steel. The yield stress of damaged-repaired steel is within 95-110% of undamaged yield stress.
- The change in yield stress does not have any clear or direct trend with the damage or repair parameters, namely, ε_d, σ_r, or N_r.

The elastic modulus data in Table 6.8 and Figure 6.12 indicate that:

- Damage-repair cycles slightly increase the elastic modulus of A588 steel. This is unique for A588 steel and it was not observed for other steel types.
- The elastic modulus of damaged-repaired steel is within 104-110% of the undamaged elastic modulus. The change in elastic modulus also does not have a clear or direct trend with the damage or repair parameters, namely, ε_d, σ_r, or N_r.

The ultimate stress data in Table 6.8 and Figure 6.13 indicate that:

- Damage-repair cycles do not have a significant influence on the ultimate stress of A588 steel. The ultimate stress of damaged-repaired specimens usually varies between 94-104% of the undamaged ultimate stress.
- Increasing the damage strain usually decreases the ultimate stress of damaged-repaired steel slightly; increasing the restraining stress increases the ultimate stress slightly.
- Increasing the number of damage-repair cycles usually decreases the ultimate stress of steel slightly.

The percent elongation data in Table 6.9 and Figure 6.14 indicate that:

- Damage-heat straightening repair reduces the percent elongation (ductility) of A588 steel. This reduction in ductility is reasonable with percent elongation values for damaged-repaired steel ranging from 74 - 92% of the undamaged percent elongation value. Majority of the damaged-repaired percent elongation values lay between 80-90% of the undamaged percent elongation value.
- The reduction in ductility does not have a clear or direct trend with the damage strain (ε_d) or the number of damage-repair cycles (N_r). Increasing the restraining stress (σ_r) reduces the ductility slightly, but even this is not a very clear or established trend.

6.3.2 Fracture Toughness Results

Fracture toughness tests were conducted on charpy v-notch specimens fabricated from undamaged and damaged-repaired specimens. The toughness tests were conducted at 40 ºF according to the ASTM E23 standard. However, due to some problems with machining procedure (presented in Section 5.2.1), the charpy specimens for the ten A588-20 ($\varepsilon_d = 20\varepsilon_y$) specimens were fabricated with a reduced break depth of 0.300 in., and the charpy specimens for twenty A588-40 ($\varepsilon_d = 40\varepsilon_y$) and A588-60 ($\varepsilon_d = 60\varepsilon_y$) specimens were fabricated with a standard break depth of 0.315 in. Therefore, two sets of charpy specimens with break depths of 0.300 and 0.315 in. were fabricated and tested from the undamaged steel. The results were given in Tables 5.22 and 5.23, respectively.

Table 5.34 presented the fracture toughness values (break depth=0.300 in.) for the damaged-repaired A588-20 ($\varepsilon_d = 20\varepsilon_y$) specimens. The averages of the quarter and mid thickness toughness values for each specimen are also included in the table. Similarly, Table 5.35 presented the fracture toughness values (break depth=0.315 in.) for the damaged-repaired A588-40 ($\varepsilon_d = 40\varepsilon_y$) and A588-60 ($\varepsilon_d = 60\varepsilon_y$) specimens. Table 5.35 includes the quarter and mid thickness toughness values, and the averages of the quarter and mid thickness toughness values for each specimen.

Figure 6.15 compares the fracture toughness values for the damaged-repaired A588-20 specimens with the undamaged fracture toughness (break depth = 0.300 in.). Figure 6.15(a) compares the quarter thickness fracture toughness values, and Figure 6.15(b) compares the mid thickness toughness values. Similarly, Figure 6.16 and 6.17 compare the fracture toughness values for the damaged-repaired A588-40 and A588-60 specimens with the undamaged fracture toughness values (break depth=0.315 in.). Figures 6.15 to 6.17 are not very easy to read or interpret because they compare numerical values without normalization.

The average quarter and mid-thickness toughness values for damaged-repaired specimens were normalized with respect to the average quarter and mid thickness toughness values for the corresponding undamaged specimens. Figure 6.18 presents the normalized quarter and mid-thickness toughness values for all damaged-repaired A588 specimens. Figure 6.18 provides excellent numerical and visual comparison of the effects of damage-repair parameters on fracture toughness. It indicates that:

- Damage-repair cycles reduce the fracture toughness of A588 steel in several cases. However, the reduced fracture toughness never decreases below 50% of the undamaged toughness. In several other cases, damage-repair cycles increase the fracture toughness of A588 steel. This unique behavior was found only for A588 steel, which indicates that it is extremely resilient material.
- The normalized mid-thickness fracture toughness is usually lower than the normalized quarter-thickness fracture toughness in both the undamaged and damage-repaired cases.
- For the A588-20 specimens ($\varepsilon_d = 20\ \varepsilon_y$), increasing the restraining stress from 0.25 to 0.50 σ_y results in a significant reduction in the normalized fracture toughness. The fracture toughness of specimens repaired with 0.25 σ_y restraining stress is close to or greater than the undamaged fracture toughness. The fracture toughness of specimens repaired with 0.50 σ_y restraining stress is close to 75% (quarter thick) or 50% (mid thick) of the undamaged toughness.
- For the A588-40 specimens ($\varepsilon_d = 40\ \varepsilon_y$) also, increasing the restraining stress from 0.25 to 0.50 σ_y results in a significant reduction in the normalized fracture toughness. The fracture toughness of specimens repaired with 0.25 σ_y restraining stress is usually greater than the undamaged fracture toughness. The fracture toughness of specimens repaired with 0.50 σ_y restraining stress is lower than the undamaged fracture toughness.
- For the A588-60 specimens ($\varepsilon_d = 60\ \varepsilon_y$) also, increasing the restraining stress from 0.25 to 0.50 σ_y results in a slight reduction in the normalized fracture toughness. The fracture toughness of specimens repaired with 0.25 σ_y restraining stress is usually greater than or close to the undamaged toughness. The fracture toughness of specimens repaired with 0.50 σ_y is usually less than or close to the undamaged toughness.

Thus, the fracture toughness values are lower for specimens subjected to the smaller damage strain of $20\varepsilon_y$. Additionally, higher restraining stresses result in greater reduction in the fracture toughness. The number of damage-repair cycles does not have a clear trend with the change in fracture toughness.

6.3.3 Rockwell Hardness and Microstructure Investigation Results

Table 5.36 summarized the averaged results of the Rockwell hardness tests and the microstructure investigations. Table 5.36 includes the average Rockwell hardness number and standard deviation, the average grain size, and the average percent of pearlite in the microstructure of damaged-repaired specimens and the undamaged steel. The average hardness of damaged-repaired specimens is normalized with the average hardness of undamaged specimens. Figure 6.19 shows the normalized hardness of the damaged-repaired specimens. This figure indicates:

- Heat straightening generally increases the hardness of A588 steel. The increase in hardness is greater for the specimens subjected to the larger damage strains.
- The hardness of damaged-repaired specimens is within a range of 98-107% of the undamaged steel.
- Increasing the ε_d or σ_r increases the hardness slightly, but the N_r does not have a significant influence on the hardness.

The average grain size of the damaged-repaired specimens is normalized with respect to the undamaged steel grain size. Figure 6.20 shows the normalized grain size of the damaged-repaired specimens. This figure indicates:

- Damage-repair cycles increase the grain size of A588 steel.
- There appears to be no direct relationship between ε_d, σ_r, or N_r and the resulting grain size of A588 steel.

6.3.4 Conclusions and Recommendations for A588 steel

- Damage-heat straightening repair cycles do not have a significant influence on the yield stress, elastic modulus, ultimate stress, surface hardness, or grain size of A588 steel. Most of the damaged-repaired values are within ±15% of the undamaged values, and are acceptable according to AASHTO requirements.
- The percent elongation (ductility) of damaged-repaired A588 steel is approximately 80-90% of the undamaged elongation, which is quite reasonable and usually acceptable according to AASHTO requirements.
- The fracture toughness of damaged-repaired A588 steel is very good. In several cases, the fracture toughness of damaged-repaired specimens is greater than or close to the undamaged toughness.
    - The fracture toughness of damaged-repaired A588 specimens never decreases below 50% of the undamaged toughness (even after five damage-repair cycles).
    - Increasing the restraining stress reduces the fracture toughness of damaged-repaired A588 specimens significantly.
    - The fracture toughness of specimens repaired with 0.25 σ_y restraining stress is greater than or close of the undamaged toughness. Specimens repaired with 0.50 σ_y restraining stress have toughness close to or less than the undamaged toughness, but never less than 50% of the undamaged toughness.
- *A588 steel is extremely resilient material. It has excellent material properties after several damage-repair cycles. Due to the excellent fracture toughness values, we recommend that A588 steel can undergo up to five damage-repair cycles. It can perhaps undergo even more damage-repair cycles, but that will have to be established with additional research. Lower restraining stresses are highly recommended for heat straightening A588 steel.*

6.4 DAMAGED - REPAIRED A7 STEEL

Seventeen laboratory scale specimens made from A7 steel were tested by subjecting them to multiple damage-repair cycles. The A7 specimens were made from the webs of a decommissioned W24x76 steel bridge girder. Their thickness was equal to 0.45 in., which is less than the thickness of A36 and A588 specimens and makes them more susceptible to buckling during heat straightening. Table 4.3 summarized the damage and repair parameters for the A7 specimens. Specimen A7-60-40-5 and all the A7-90 ($\varepsilon_d = 90\varepsilon_y$) specimens developed significant curvature after completing the damage-repair cycles.

Standard material tests were conducted on samples taken from the test area of the damaged-repaired specimens and an undamaged specimen. The results and comparisons of these material tests are presented in Sections 6.4.1 to 6.4.4. Section 6.4.1 summarizes the results form the tension tests. Section 6.4.2 summarizes the fracture toughness results. Section 6.4.3 presents the Rockwell hardness and metallographic inspection results. Finally, Section 6.4.4 presents the conclusions and recommendations for damaged-repaired A7 steel.

6.4.1 Uniaxial Tension Test Results

The uniaxial tension test results for coupons from undamaged and damaged-repaired specimens are averaged and summarized in Table 6.9. The values in Table 6.9 include the yield stress (σ_y), the elastic modulus (E), the yield strain (ε_y), the ultimate stress (σ_u), the ultimate strain (ε_u), the strain ductility ($\varepsilon_u/\varepsilon_y$), the percent elongation, and the percent reduction (area). The values of σ_y, E and ε_y for specimens A7-60-40-5, A7-90-25-1, A7-90-25-3, A7-90-40-1, and A7-90-40-3 could not be determined accurately because the tension coupons had initial curvature.

The steel material properties (E, σ_y, σ_u, and percent elongation) for damaged-repaired specimens are normalized with respect to the corresponding undamaged steel material properties and plotted in Figures 6.21 to 6.24. Figure 6.21 shows the normalized yield stress for all damaged-repaired specimens. Figure 6.22 shows the normalized elastic modulus for all damaged-repaired specimens. Figure 6.23 shows the normalized ultimate stress, and Figure 6.24 shows the normalized percent elongation for all damaged-repaired specimens.

The yield stress data in Table 6.9 and Figure 6.21 indicate that:

- The change in yield stress does not have any clear or direct trend with the damage or repair parameters, namely, ε_d, σ_r, or N_r.
- The yield stress of damaged-repaired steel is within 85-120% of undamaged yield stress.
- The yield stress could not be measured accurately for some damaged-repaired specimens because the tension coupons had initial curvature.

The elastic modulus data in Table 6.9 and Figure 6.22 indicate that:

- Damage-heat straightening repair usually reduces the elastic modulus of A7 steel. The elastic modulus of damaged-repaired steel is within 85-101% of the undamaged elastic modulus.
- The elastic modulus could not be measured accurately for some damaged-repaired specimens because the tension coupons had initial curvature. These specimens are not included in Figure 4.2. This initial curvature may also be an issue for other specimens that are included in Figure 4.2.
- The reduction in elastic modulus does not have any clear or direct trend with the damage or repair parameters, namely, ε_d, σ_r, or N_r.

The ultimate stress data in Table 6.9 and Figure 6.23 indicate that:

- Damage-repair cycles do not have a significant influence on the ultimate stress of A7 steel. The ultimate stress of damaged-repaired specimens usually varies between 95-103% of the undamaged ultimate stress.
- The change in ultimate stress does not have any clear or direct trend with the damage or repair parameters, namely, ε_d, σ_r, or N_r.

The percent elongation data in Table 6.9 and Figure 6.24 indicate that:

- Damage-repair cycles significantly reduce the percent elongation (ductility) of A7 steel. The percent elongation values for most specimens after repair are within 75-80% of the undamaged steel. However, some specimens (A7-30-25-5, A7-60-25-5, and A7-60-40-5) with five damage-repair cycles) have percent elongation values as low as 55-60% of the undamaged steel.
- Increasing the number of damage-repair cycles reduces the percent elongation significantly. Increasing the restraining stress or the damage strain also reduces the percent elongation of damage-repaired specimens.
- The number of damage-repair cycles is perhaps the most important parameter effecting the percent elongation (ductility).

6.4.2 Fracture Toughness Results

Fracture toughness tests were conducted on charpy specimens fabricated from the undamaged and damage-repaired specimens. Six mid-thickness charpy specimens were fabricated from the test area of each damaged-repaired specimen. Additionally, several mid-thickness charpy specimens were fabricated from an undamaged specimen. All these charpy specimens were tested at 40 ºF according to the ASTM E23 standard. Only mid-thickness charpy specimens were fabricated and tested because quarter-thickness charpy specimens cannot be fabricated from the 0.45 in. thick A7 steel specimen.

The fracture toughness values for undamaged A7 steel were given in Table 5.38. This table also includes the results of statistical analysis of the fracture toughness data, namely, the statistical mean (average), the 95% confidence interval (CI) for the actual mean, the standard deviation, the median, and the average absolute deviation from the median. Similarly, Tables 6.10, 6.11, and 6.12 present the fracture toughness values for the damaged-repaired A7-30 ($\varepsilon_d = 30\varepsilon_y$), A7-60 ($\varepsilon_d = 60\varepsilon_y$), and A7-90 ($\varepsilon_d = 90\varepsilon_y$) specimens, respectively. These tables also include the statistical analyses of the fracture toughness data, namely, the above-mentioned statistical mean, 95% CI, etc.

Comparison of toughness results

Figures 6.25 to 6.27 compare (numerically) the fracture toughness values for the damaged-repaired specimens with the toughness values for the undamaged specimens. These figures provide a visual comparison of the effects of damage-repair parameters on the range of fracture toughness values, and indicate that:

- The fracture toughness of several damaged-repaired specimens is lower than the toughness of the undamaged steel. The fracture toughness of several other damaged-repaired specimens is greater than the toughness of undamaged steel.
- The specimens subjected to the smaller damage strain of 30 ε_y, i.e., the A7-30 specimens usually have lower fracture toughness than the specimens subjected to larger damage strains, i.e., the A7-60 ($\varepsilon_d = 90\varepsilon_y$) and A7-90 ($\varepsilon_d = 90\varepsilon_y$) specimens.

- Increasing the restraining stress reduces the fracture toughness of A7-60 specimens significantly. However, it does not have a significant influence on the fracture toughness of A7-30 and A7-90 specimens.
- The number of damage-repair cycles usually reduces the fracture toughness, but this trend is not valid for some specimens.
- The fracture toughness of damaged-repaired specimens falls below the AASHTO limit of 21 ft-lbs for several cases.

Figures 6.25 to 6.27 are not very easy to read or interpret because they present numerical values without normalization. Therefore, the 95% confidence interval (high), mean, and 95% CI low fracture toughness values for each damaged-repaired specimen were normalized with respect to the corresponding values for undamaged A7 steel, respectively. The normalized mean fracture toughness and the 95% confidence interval (CI) bounds are shown in Figure 6.28. The normalized relationships are all to the mean value of the undamaged results. Figure 6.28 provides excellent visual and numerical comparisons of the effects of damage and repair parameters on the fracture toughness. In Figure 6.28, when the 95% CI high and low bounds have a large range about the mean, it implies large variation in the measured toughness values for the corresponding specimen.

Evaluation of toughness results

The results in Tables 6.10, 6.11, 6.12, and 6.13 and Figure 6.28 indicate that:

- The mean fracture toughness of A7-30-25 specimens decreases continuously with the number of damage-repair cycles. After three damage-repair cycles, the fracture toughness is approximately 50% of the undamaged toughness, and it is close to 40% of the undamaged toughness after five damage-repair cycles.
- Increasing the restraining stress for A7-30 specimens seems to benefit the mean fracture toughness. The mean fracture toughness of A7-30-40 specimens first decreases and then increases with the number of damage-repair cycles. However, this trend is not reflected by the lower bound of the 95% confidence interval for the fracture toughness. The lower bound 95% CI toughness decreases continuously with the number of damage-repair cycles. It decreases to approximately 50, 25, and 0% of the undamaged toughness after one, three, and five damage-repair cycles, respectively. The significant variation in the measured toughness values for specimens A7-30-40-3 and A7-30-40-5 is clear from Figure 6.28.
- The mean fracture toughness of A7-60-25 specimens decreases after the first damage-repair cycle to approximately 65% of the undamaged toughness. However, the mean fracture toughness increases significantly beyond the undamaged fracture toughness with further damage-repair cycles. The lower bound 95% CI fracture toughness decreases to 50% of the undamaged toughness after three damage-repair cycles. It increases significantly beyond the undamaged toughness after five damage-repair cycles.
- Increasing the restraining stress has an adverse effect on the fracture toughness of A7-60 specimens. The fracture toughness of A7-60-40 specimens decreases significantly with the number of damage-repair cycles. It decreases to approximately 50% of the undamaged toughness after three cycles, and to 25% of the undamaged toughness after five cycles.
- The mean fracture toughness of A7-90 specimens is close to the undamaged toughness irrespective of the restraining stress and the number of damage-repair cycles (up to three cycles). The lower bound of the 95% confidence interval also follows this same trend with the lower bound damaged-repaired toughness values close to 75% of the undamaged toughness. The lower bound falls below 50% of the undamaged toughness only for A7-90-40-3.

6.4.3 Rockwell Hardness and Microstructure investigations on Damage-Repaired A7

Table 5.46 summarized the averaged results of the Rockwell hardness tests and the microstructure investigations. Table 5.46 includes the average Rockwell hardness number and standard deviation, the average grain size, and the average percent of pearlite in the microstructure. The average hardness of damaged-repaired specimens is normalized with the average hardness of undamaged specimens. Figure 6.29 shows the normalized hardness of the damaged-repaired specimens. This figure indicates:

- Heat straightening increases the hardness of A7 steel. The damaged-repaired hardness is within 102-114% of the undamaged hardness.
- The number of damage-repair cycles usually increases the hardness. However, this trend is not applicable for some specimens.
- Other damage-repair parameters (σ_r and ε_d) do not have a significant influence on the hardness.

The average grain size of the damaged-repaired specimens is normalized with respect to the undamaged steel grain size. Figure 6.30 shows the normalized grain size of the damaged-repaired specimens. This figure indicates:

- Heat straightening usually decreases the grain size of A7 steel.
- Increasing the damage strain or the restraining stress typically decreases the grain size of damaged-repaired A7 steel.
- The number of damage-repair cycles does not seem to have clear or direct trend with the reduction in grain size.

6.4.4 Discussion and Recommendations from the Results of A7 Steel

- Damage-heat straightening repair cycles do not have a significant influence on the yield stress, elastic modulus, ultimate stress, surface hardness, or grain size of A7 steel. Most of the damaged-repaired results are within ± 15% of the undamaged values.
- The percent elongation (ductility) of damaged-repaired A7 steel is usually within 80-90% of the undamaged percent elongations. However, for specimens subjected to five damage-repair cycles, the percent elongation was approximately 55-60% of the undamaged value. Increasing the damage strain, the restraining stress, or the number of damage-repair cycles reduces the percent elongation significantly.
- The fracture toughness of damaged-repaired A7 steel decreases significantly with increase in the restraining stress or the number of damage-repair cycles.
- The fracture toughness of specimens damaged to 30 ε_y reduces to 50% of the undamaged toughness after three damage-repair cycles. The fracture toughness of specimens repaired with the higher restraining stress of 0.40 σ_y has significant scatter.
- The fracture toughness of specimens damaged to 60 ε_y and repaired with the lower restraining stress of 0.25 σ_y is excellent. It is greater than the undamaged toughness after three or five damage-repair cycles. However, increasing the restraining stress has a significant adverse effect on the fracture toughness, which decreases to 50% of the undamaged toughness after three cycles, and to 25% of the undamaged toughness after five cycles.
- The fracture toughness of specimens damaged to 90 ε_y is close to the undamaged toughness after three damage-repair cycles. Increasing the restraining stress reduces the toughness slightly.

- *A7 steel can undergo up to three damage-repair cycles without a drastic reduction in the material properties. The percent elongation values are small after five damage-repair cycles. Similarly, the fracture toughness values are also significantly reduced after three damage-repair cycles. Smaller damage strains have more detrimental effects on the toughness of damaged-repaired A7 steel. A recommended limit of three damage-repair cycles should be conducted on A7 steel, and the use of lower restraining stresses are recommended.*

6.5 DAMAGED-REPAIRED OVERHEATED A36

Sixteen laboratory scale specimens made from A36 steel were tested by subjecting them to multiple damage-heat straightening repair cycles. These specimens were repaired by heating them to temperatures greater than 1200 ºF, which is the current limit, adopted by MDOT among other DOTs. Table 4.4 summarized the damage and repair parameters for these specimens including the maximum heating temperatures (T_{max}). Standard material tests were conducted on samples taken from the test area of the damaged-repaired specimens and on undamaged steel. The results and comparisons of these material tests are presented in Sections 6.5.1 to 6.5.4. Section 6.5.1 summarizes the results form the tension tests. Section 6.5.2 summarizes the fracture toughness results. Section 6.5.3 focuses on the Rockwell hardness and microstructure results. Finally, Section 6.5.4 presents the conclusions and recommendations for damaged-repaired overheated A36 steel.

6.5.1 Uniaxial Tension Test Results

The uniaxial tension test results for coupons removed from undamaged steel and damaged-repaired specimens are averaged and summarized in Table 6.13. The values in Table 6.13 include the yield stress (σ_y), the elastic modulus (E), the yield strain (ε_y), the ultimate stress (σ_t), the ultimate strain (ε_u), the strain ductility ($\varepsilon_u/\varepsilon_y$), the percent elongation, and the percent reduction (area). The damaged-repaired steel material properties (σ_y, E, σ_u, and percent elongation) are normalized with respect to the corresponding undamaged steel material properties and plotted in Figures 6.31 to 6.34. Figure 6.31 shows the normalized yield stress for all damaged-repaired specimens. Figure 6.32 shows the normalized elastic modulus for all damaged-repaired specimens. Figure 6.33 shows the normalized ultimate stress, and Figure 6.34 shows the normalized percent elongation for all damaged-repaired specimens.

The yield stress data in Table 6.13 and Figure 6.31 indicate that:

- Damage-heat straightening repairs using overheated temperatures increase the yield stress of A36 steel. The yield stress of damaged-repaired steel lies between 112-127% of the undamaged yield stress.
- The yield stress of specimen repaired with 0.25 σ_y restraining stress decreases as the number of damage-repair cycles increases from one to three. Besides this, the change in yield stress does not have a clear or direct trend with other damage or repair parameters, namely, ε_d, σ_r, T_{max}, or N_r.

The elastic modulus data in Table 6.13 and Figure 6.32 indicate that:

- Damage-repair cycles have a negligible affect on the elastic modulus of overheated A36 steel. The resulting elastic modulus is within 95-105% of the undamaged material
- The change in elastic modulus does not have a clear or direct trend with the damage or repair parameters, namely, ε_d, σ_r, T_{max}, or N_r.

The ultimate stress data in Table 6.13 and Figure 6.33 indicate that:

- Damage-repair cycles slightly increase the ultimate stress of overheated A36 steel. The ultimate stress values lie between 102-108% of the undamaged ultimate stress.

- Increasing the damage strain usually increases the ultimate stress of damaged-repaired steel slightly.
- Increasing the restraining stress has no direct impact on the resulting ultimate stress.
- Increasing the number of damage-repair cycles usually decreases the ultimate stress of damaged-repaired steel slightly.

The percent elongation data in Table 6.13 and Figure 6.34 indicate that:

- Damage-repair cycles reduce the percent elongation (ductility) of overheated A36 steel. The percent elongation values reduce to between 72-93% of the undamaged percent elongation.
- Using the higher maximum temperature of 1600 °F results in a wider range of ductility results.
- The change in ductility does not have a clear or direct trend with other damage or repair parameters, namely, ε_d, σ_r, or N_r.
- For specimens repaired with a maximum temperature of 1400 °F, increasing the damage strain increases the ductility of damage-repaired steel slightly.

6.5.2 Fracture Toughness Results

Fracture toughness tests were conducted on the charpy v-notch specimens fabricated from undamaged and damaged-repaired specimens. The toughness tests were conducted at 40 °F according to ASTM E23 standard. Six charpy specimens including three from quarter thickness and three from mid-thickness were fabricated from the test area of each damaged-repaired specimen. Additionally, several quarter and mid-thickness specimens were fabricated from an undamaged A36 steel specimen. All the charpy specimens had the standard break depth of 0.315 in.

Comparisons of undamaged and damaged-repaired fracture toughness

Tables 6.14 to 6.17 present the fracture toughness values for the damaged-repaired overheated A36 specimens. Six fracture toughness values are reported for each damaged-repaired specimen. The toughness values for each specimen are arranged in ascending order, and the statistical mean, 95% confidence intervals (high and low), standard deviation, median, and average absolute deviation from median for each specimen are reported.

Figures 6.35 and 6.36 compare (numerically) the fracture toughness values for the damaged-repaired specimen with the toughness values for the undamaged specimens. These figures provide a visual comparison of the effects of damage-repair parameters on the range of fracture toughness values. These figures clearly indicate that the fracture toughness of overheated damaged-repaired specimens is much higher than the fracture toughness of undamaged specimens. Only one value was lower and few toughness values were within the range of the undamaged material.

Figures 6.35 and 6.36 are not very easy to read or interpret because they present numerical values without normalization. Therefore, the 95% confidence interval (high), mean, and 95% CI (low) fracture toughness values for each damaged-repaired specimen were normalized with respect the corresponding mean value for the undamaged A36 steel. The normalized mean fracture toughness and 95% confidence interval (CI) bounds are shown in Figures 6.37 and 6.38. The normalized relationships are all to the mean value of the undamaged results. Figures 6.37 and 6.38 provide excellent visual and numerical comparisons of the effects of damage and repair parameters on the fracture toughness. When the 95% CI high and low bounds have a large range about the mean, it implies large variation in the measured toughness values for the corresponding specimen.

Evaluation of toughness results

As shown in Figures 6.37 and 6.38, the normalized fracture toughness of damage-repaired steel using overheated temperatures is much higher than the toughness of undamaged specimens.

The fracture toughness of specimens repaired with a maximum heating temperature of 1400 °F is much greater than the undamaged toughness. The mean fracture toughness of damaged-repaired specimens is approximately 330-415% of the undamaged specimens. However, the fracture toughness values for damaged-repaired steel have significant variability (scatter), as evident from the wide range of the low and high bound 95% CI values. The lower bound of the 95% CI is typically close to the 100% of the undamaged fracture toughness. The increase in the fracture toughness does not have a clear or direct trend with other damage-repair parameters, namely, ε_d, σ_r, or N_r.

The fracture toughness of specimens repaired with a maximum heating temperature of 1600 °F is again much greater than the undamaged toughness. The mean fracture toughness of damaged-repaired specimens is approximately 250-390% of the undamaged specimens. The toughness values for damaged-repaired steel have significant scatter, which is evident from the wide range of low and high bound 95% CI values. The increase in fracture toughness does not have a clear or direct trend with other damage or repair parameters, namely, ε_d, σ_r, or N_r.

The fracture toughness of damaged-repaired specimens heated to 1400 °F or 1600 °F is quite comparable. Specimens heated to 1600 °F usually had slightly lower fracture toughness and more scatter (variability) than the specimens heated to 1400 °F.

6.5.3 Rockwell Hardness and Microstructure investigation Results

Table 5.54 summarized the averaged results of the Rockwell hardness tests and the microstructure investigations for overheated A36 steel. Table 5.54 includes the average Rockwell hardness number and standard deviation, the average grain size, and the average percent of pearlite in the microstructure of damaged-repaired specimens and the undamaged steel. The average hardness of damaged-repaired specimens is normalized with the average hardness of undamaged specimens. Figure 6.39 shows the normalized hardness of the damaged-repaired specimens. This figure indicates:

- Damage-repair cycles slightly decrease the Rockwell hardness of overheated A36 steel. This behavioral aspect is unique, and applicable only for overheated A36 steel.
- The hardness of damaged-repaired specimens is within a range of 94-102% of the undamaged steel.
- There appears to be no direct relationship between ε_d, σ_r, T_{max}, or N_r and the resulting surface hardness of overheated A36 steel.

The average grain size of the damaged-repaired specimens is normalized with respect to the undamaged steel grain size. Figure 6.40 shows the normalized grain size of the damaged-repaired specimens. This figure indicates:

- Damage-repair cycles decrease the grain size of overheated A36 steel to approximately 62-85% of the undamaged material.
- There appears to be no direct relationship between ε_d, σ_r, T_{max}, or N_r and the resulting grain size of overheated A36 steel.

6.5.4 Conclusions and Recommendations for Overheated A36 Steel

- The results from the material tests indicate excellent material properties for damaged-repaired overheated A36 steel. The strength and fracture toughness of the material increase significantly. The percent elongation (ductility) decreased by approximately the same magnitude as A36 steel repaired with a maximum temperature of 1200 °F.
- These results for overheated A36 steel may be disputed by other researchers and engineers since an upper limit of 1200 °F has been enforced historically for heat straightening.
- We recommend that additional research should be conducted on different types of steel subjected to multiple damage-repair cycles with heating temperatures greater than 1200 °F.
- If the above-mentioned conclusions for overheated steel are validated with further investigations, then we recommend that A36 steel should be heat straightened with maximum heating temperatures close to 1400 °F.
- Temperatures reaching 1600 °F are not recommended because the heat flux from the torch will cause surface damage and produce unwanted distortions.

Table 6.1
Average structural properties of A36 steel

Specimen	σ_y *(ksi)*	*E (ksi)*	ε_y	σ_t *(ksi)*	ε_u	ε_u / ε_y	*% Elongation*	*% Reduction*
Undamaged	38.4	30524	0.00130	64.5	0.19	153.0	39.16	73.34
***A36-30-40-1*	43.6	31559	0.00135	68.2	0.14	101.1	29.41	66.62
A36-30-40-2	45.9	32294	0.00140	68.7	0.15	106.8	30.88	67.32
A36-30-40-3	47.5	32834	0.00145	71.1	0.13	87.5	29.20	67.94
A36-30-40-4	44.9	31841	0.00141	68.1	0.14	96.2	30.40	69.03
A36-30-40-5	43.7	32747	0.00131	64.9	0.14	110.2	32.12	63.27
A36-30-70-1	43.1	31781	0.00132	67.5	0.16	122.2	33.69	70.90
A36-30-70-2	44.0	30575	0.00142	69.1	0.15	109.4	27.60	64.39
***A36-30-70-3*	46.3	30686	0.00150	69.5	0.14	96.4	30.32	64.89
***A36-30-70-4*	46.3	30249	0.00151	68.9	0.15	98.1	31.34	67.91
***A36-30-70-5*	46.1	30053	0.00153	70.2	0.10	68.3	26.10	67.91
A36-60-25-1	40.6	32184	0.00124	63.6	0.17	136.8	34.40	69.57
A36-60-25-2	42.6	30663	0.00136	65.4	0.16	117.4	32.35	69.78
A36-60-25-3	42.5	30044	0.00143	65.6	0.16	108.4	32.04	70.64
A36-60-25-4	42.8	30768	0.00136	63.7	0.18	129.1	34.41	70.55
A36-60-25-5	41.3	31272	0.00129	63.0	0.18	140.4	35.53	71.11
A36-60-50-1	41.3	31991	0.00129	65.4	0.19	143.9	34.69	70.16
A36-60-50-2	42.8	29795	0.00144	67.6	0.15	104.2	32.94	69.77
A36-60-50-3	41.1	31598	0.00130	65.0	0.17	129.7	33.50	70.95
A36-60-50-4	40.6	31021	0.00131	64.5	0.18	138.7	33.48	64.01
***A36-60-50-5*	43.3	30600	0.00142	64.9	0.15	107.5	32.40	71.35
A36-90-25-1	40.0	30016	0.00131	64.5	0.17	131.7	31.63	70.99
A36-90-25-3	39.7	30649	0.00128	61.7	0.19	146.1	36.54	75.08
***A36-90-25-5*	40.9	29448	0.00139	61.2	0.19	134.6	37.58	75.30
A36-90-50-1	40.8	29669	0.00137	63.5	0.19	137.8	32.63	65.24
A36-90-50-2	42.1	29665	0.00137	64.0	0.17	122.5	32.55	72.97
A36-90-50-3	41.4	30806	0.00132	63.1	0.18	137.9	36.90	74.99
A36-90-50-4	42.1	30300	0.00137	63.2	0.18	128.5	36.04	74.59
A36-90-50-5	42.4	30970	0.00137	63.3	0.18	133.1	35.88	74.45

*Refers to speci mens with significant curvature after heat straightening. Data is not entirely reliable.

Table 6.2
Fracture toughness results of A36-30-40 specimens

A36 Specimen ID →	**30-40-1	30-40-2	30-40-3	30-40-4	30-40-5
Charpy Spec. #1	27.5	17.5	40	66	27
Charpy Spec. #2	43	22.5	54	77	28.5
Charpy Spec. #3	70	32	55	87	35
Charpy Spec. #4	72.5	68	66	93	36
Charpy Spec. #5	81	72	81	95	43
Charpy Spec. #6	95	-	93	96	46
Mean	64.8	42.4	64.8	85.7	35.9
95% confidence interval for actual mean	38.58 – 91.08	10.41 – 74.39	44.44 – 85.22	73.15 – 98.19	27.96 – 43.87
Std. Deviation	25.0	25.8	19.4	11.9	7.58
Median	71.3	32	60.5	90.0	35.5
Average absolute deviation from median	18.0	20	15.2	9.00	5.75
Probability of null hypothesis (data is statistically similar to undamaged data from t-test)	0.0007	0.0001	0.0005	0.0060	<0.000 1

Table 6.3
Fracture toughness results of A36-30-70 specimens

A36 Specimen ID →	30-70-1	30-70-2	**30-70-3	**30-70-4	**30-70-5
Charpy Spec. #1	69	24	17	63	8.5
Charpy Spec. # 2	77	24	25	66	40
Charpy Spec. #3	89	26	46	72	49
Charpy Spec. # 4	99	27	61	79	50
Charpy Spec. #5	107	28	64	82	57
Charpy Spec. # 6	115	43	70	91	62
Mean	92.7	28.7	47.2	75.5	44.4
95% confidence interval for actual mean	74.11 – 111.2	21.11 – 36.23	24.18 – 70.16	64.46 – 86.54	24.34 – 64.49
Std. Deviation	17.7	7.20	21.9	10.5	19.1
Median	94.0	26.5	53.5	75.5	49.5
Average absolute deviation from median	14.3	4.00	17.8	8.50	11.9
Probability of null hypothesis (data is statistically similar to undamaged data from t-test)	0.017	<0.000 1	<0.000 1	0.0015	<0.000 1

Table 6.4
Fracture toughness results of A36-60-25 specimens

A36 Specimen ID →	60-25-1	60-25-2	60-25-3	60-25-4	60-25-5
Charpy Spec. # 1	48	16	20	16	10
Charpy Spec. # 2	88	51	31	21	14
Charpy Spec. #3	98	64	36	22.5	15
Charpy Spec. #4	175	110	70	32	19.5
Charpy Spec. #5	213	120	75	63	19.5
Charpy Spec. #6	214	173	97	-	20
Mean	139	89.0	54.8	30.9	16.3
95% confidence interval for actual mean	65.18 - 213.5	29.89 - 148.1	23.17 - 86.50	7.5 – 54.31	12.11 – 20.55
Std. Deviation	70.7	56.3	30.2	18.9	4.02
Median	137	87.0	53.0	22.5	17.3
Average absolute deviation from median	61.3	45.3	25.8	11.6	3.33
Probability of null hypothesis (data is statistically similar to undamaged data from t-test)	0.89	0.050	0.0003	<0001	<0001

Table 6.5
Fracture toughness results of A36-60-50 specimens

A36 Specimen ID →	60-50-1	60-50-2	60-50-3	60-50-4	**60-50-5
Charpy Spec. #1	23.5	26	18	18	17
Charpy Spec. #2	39	28	37	28	19
Charpy Spec. #3	50	95	67	30	61
Charpy Spec. #4	143	157	78	32	77
Charpy Spec. #5	148	200	95	33	78
Charpy Spec. #6	157	219	110	45	89
Mean	93.4	121	67.5	31.0	56.8
95% confidence interval for actual mean	28.35 - 158.5	32.40 – 209.3	30.98 – 104.0	21.85 – 40.15	23.89 – 89.77
Std. Deviation	62.0	84.3	34.8	8.72	31.4
Median	96.5	126	72.5	31.0	69.0
Average absolute deviation from median	55.9	71.2	26.8	5.67	24.5
Probability of null hypothesis (data is statistically similar to undamaged data from t-test)	0.087	0.61	0.0018	<0.000 1	0.0004

*Refers to specimens with significant curvature after heat straightening. Data is not entirely reliable.

Table 6.6
Fracture toughness results of A36-90-25 specimens

A36 Specimen ID →	90-25-1	90-25-3	**90-25-5
Charpy Spec. #1	78	15	13.5
Charpy Spec. #2	112	68	20.5
Charpy Spec. #3	115	169	21.5
Charpy Spec. #4	143	242	220
Charpy Spec. #5	236	242	238
Charpy Spec. #6	239	-	242
Mean	154	147	126
95% confidence interval for actual mean	82.44 – 225.2	19.69 – 274.7	2.13 – 249.7
Std. Deviation	68.0	103.0	118.0
Median	129	169	121
Average absolute deviation from median	52.2	80.2	107
Probability of null hypothesis (data is statistically similar to undamaged data from t-test)	0.47	0.73	0.79

Table 6.7
Fracture toughness results of A36-90-50 specimens

A36 Specimen ID →	90-50-1	90-50-2	90-50-3	90-50-4	90-50-5
Charpy Spec. #1	12	21.5	17	92	67
Charpy Spec. # 2	23	24	19	95	74
Charpy Spec. #3	28	89	21.5	109	94
Charpy Spec. #4	28	97	25	230	95
Charpy Spec. #5	29.5	105	30	232	110
Charpy Spec. # 6	32	240	88	240	232
Mean	25.4	96.1	33.4	166	112
95% confidence interval for actual mean	17.86 – 32.97	12.64 – 179.5	4.94 – 61.90	88.22 – 244.4	48.18 – 175.8
Std. Deviation	7.20	79.5	27.1	74.4	60.8
Median	28.0	93.0	23.3	170	94.5
Average absolute deviation from median	4.42	51.3	14.3	67.7	33.7
Probability of null hypothesis (data is statistically similar to undamaged data from t-test)	<0.000 1	0.16	<0.000 1	0.25	0.32

*Refers to specimens with significant curvature after heat straightening. Data is not entirely reliable.

Table 6.8
Average structural properties of A588 steel

Specimen	σ_y *(ksi)*	*E (ksi)*	ε_y	σ_t	ε_u	ε_u / ε_y	*% Elongation*	*% Reduction*
Undamaged	57.4	28285	0.00203	83.1	0.16	77.7	33.60	71.44
A588-20-25-1	59.7	29580	0.00202	84.1	0.15	76.3	29.71	69.13
A588-20-25-2	58.2	30434	0.00191	83.0	0.15	75.8	30.24	67.65
A588-20-25-3	58.7	30140	0.00195	82.7	0.14	69.7	28.23	68.19
A588-20-25-4	57.3	29852	0.00192	80.8	0.14	72.3	28.29	71.20
A588-20-25-5	59.0	29848	0.00198	81.2	0.13	64.4	27.93	69.35
A588-20-50-1	61.6	30544	0.00202	86.6	0.14	66.9	27.96	68.70
A588-20-50-2	62.2	29245	0.00213	85.7	0.12	54.1	26.45	68.02
A588-20-50-3	61.3	30215	0.00203	84.2	0.12	58.9	26.50	68.52
A588-20-50-4	59.5	29772	0.00200	83.8	0.14	69.5	29.10	70.08
A588-20-50-5	63.5	30132	0.00211	84.9	0.11	53.5	27.12	66.94
A588-40-25-1	56.7	30668	0.00185	81.8	0.13	68.6	27.54	71.52
A588-40-25-2	58.0	30702	0.00189	81.1	0.14	74.7	28.01	69.51
A588-40-25-3	57.4	30832	0.00186	80.6	0.15	82.6	30.87	70.58
A588-40-25-4	59.7	30610	0.00195	81.9	0.14	73.4	28.45	69.19
***A588-40-25-5*	60.4	30615	0.00197	80.5	0.14	71.9	28.11	67.55
A588-40-50-1	61.8	30159	0.00205	84.2	0.11	52.0	25.00	68.06
A588-40-50-2	60.7	29792	0.00204	84.6	0.14	69.2	28.34	67.34
A588-40-50-3	57.3	30834	0.00191	81.3	0.14	71.9	28.19	72.15
A588-40-50-4	57.1	30499	0.00187	81.5	0.13	67.9	26.85	71.12
A588-40-50-5	58.6	30081	0.00195	80.9	0.15	74.9	30.17	70.39
***A588-60-25-1*	57.6	30535	0.00189	82.1	0.14	76.6	28.43	70.72
A588-60-25-2	57.5	29984	0.00192	79.6	0.15	79.9	30.46	71.33
A588-60-25-3	54.9	30252	0.00185	77.7	0.16	88.0	30.66	72.88
***A588-60-25-4*	59.9	30519	0.00193	80.2	0.14	70.9	28.08	66.56
A588-60-25-5	57.6	30643	0.00192	77.8	0.15	79.1	29.77	72.13
A588-60-50-1	60.2	30483	0.00197	85.0	0.14	70.9	28.33	69.18
A588-60-50-2	58.2	30442	0.00191	82.7	0.15	79.4	29.95	70.44
A588-60-50-3	59.2	29977	0.00197	80.6	0.14	72.4	28.56	69.12
A588-60-50-4	62.5	31046	0.00201	82.4	0.12	57.7	25.61	68.55
A588-60-50-5	61.8	30781	0.00201	81.7	0.14	72.0	28.70	69.15

*Refers to speci mens with significant curvature after heat straightening. Data is not entirely reliable.

Table 6.9
Average structural properties of A7 steel

Specimen	σ_y *(ksi)*	*E (ksi)*	ε_y	σ_t	ε_u	ε_u / ε_y	*% Elongation*	*% Reduction*
Undamaged	38.7	31228	0.00124	62.1	0.22	180.53	44.14	61.63
A7-30-25-1	37.6	28972	0.00130	61.2	0.23	173.61	39.36	62.23
A7-30-25-3	36.5	31456	0.00116	60.3	0.18	155.59	35.79	65.07
A7-30-25-5	41.3	26655	0.00155	60.3	0.14	90.13	28.07	58.61
A7-30-40-1	38.7	29125	0.00134	62.2	0.21	155.80	34.95	61.41
A7-30-40-3	41.1	28093	0.00146	62.2	0.22	149.49	35.15	63.33
A7-30-40-5	41.6	26556	0.00156	64.1	0.18	112.50	33.08	59.02
A7-60-25-1	38.4	26869	0.00144	60.5	0.20	142.73	34.12	63.18
A7-60-25-3-1	37.7	31510	0.00120	61.4	0.20	191.73	33.10	58.44
A7-60-25-3-2	35.5	27201	0.00130	58.9	0.20	153.70	33.36	61.50
A7-60-25-5	38.6	27127	0.00142	61.3	0.19	135.57	27.30	59.68
A7-60-40-1	39.8	27440	0.00145	61.3	0.19	132.93	33.82	62.51
A7-60-40-3	37.4	-	-	59.2	0.21	-	35.78	64.88
***A7-60-40-5*	46.7	-	-	62.7	0.12	56.97	25.30	60.46
***A7-90-25-1*	42.7	-	-	60.7	0.20	140.70	38.01	64.76
***A7-90-25-3*	37.2	-	-	60.3	0.20	132.92	32.35	61.36
***A7-90-40-1*	33.3	-	-	59.6	0.24	-	33.86	66.03
***A7-90-40-3*	38.5	-	-	59.7	0.21	-	33.42	63.35

*Refers to specimens with significant curvature after heat straightening. Data is not entirely reliable.

Table 6.10
Fracture toughness results of A7-30 specimens

A7 Specimen ID →	**30-25-1**	**30-25-3**	**30-25-5**	**30-40-1**	**30-40-3**	**30-40-5**
Charpy Spec. # 1	26.5	15	10.5	13	13	5.5
Charpy Spec. #2	30	16	14.5	25.5	13.5	6.5
Charpy Spec. #3	34	17.5	15	26	23	8
Charpy Spec. # 4	38	24	18	26.5	24	53
Charpy Spec. # 5	39	30	18	32	36	92
Charpy Spec. # 6	40	30	19	33	38	97
Mean	34.6	22.1	15.8	26.0	24.6	43.7
95% confidence interval for actual mean	28.89 – 40.28	14.85 – 29.31	12.50 – 19.16	18.51 – 33.49	13.37 – 35.79	-1.789 – 89.12
Std. Deviation	5.43	6.89	3.17	7.13	10.7	43.3
Median	36	20.8	16.5	26.3	23.5	30.5
Average absolute deviation from median	4.42	5.92	2.50	4.50	8.08	37.0
Probability of null hypothesis (data is statistically similar to undamaged data from t-test)	0.24	0.0001	0.0001	0.002	0.0023	0.65

Table 6.11
Fracture toughness results of A7-60 specimens

A7 Specimen ID →	60-25-1	60-25-3	60-25-3 -r	60-25-5	60-40-1	60-40-3	**60-40-5
Charpy Spec. #1	21.5	13.5	13	62	12	8.5	7.5
Charpy Spec. #2	23	15.5	32	67	22	9.5	8.5
Charpy Spec. #3	24.5	31	60	74	23	11.5	9
Charpy Spec. #4	25	90	79	76	29	27	10
Charpy Spec. #5	26	97	90	78	30	30	13
Charpy Spec. #6	28.5	102	92	96	32	33	21.5
Mean	24.8	58.2	61.0	75.5	24.7	19.9	11.6
95% confidence interval for actual mean	22.1-27.29	13.64 - 102.7	26.92 - 95.08	63.23 - 87.77	16.93 - 32.40	8.11-31.72	6.11 - 17.05
Std. Deviation	2.42	42.4	32.5	11.7	7.37	11.2	5.21
Median	24.8	60.5	69.5	75.0	26.0	19.3	9.50
Average absolute deviation from median	1.75	38.2	26.0	7.83	5.67	10.1	3.25
Probability of null hypothesis (data is statistically similar to undamaged data from t-test)	0.0003	0.082	0.015	0.0001	0.0009	0.0002	0.0001

Table 6.12
Fracture toughness results of A7-90 specimens

A7 Specimen ID →	**90-25-1	**90-25-3	**90-40-1	**90-40-3
Charpy Spec. #1	29	23.5	25	10
Charpy Spec. #2	32	24	32	30
Charpy Spec. #3	33	41	46	32
Charpy Spec. #4	38	50	51	34
Charpy Spec. #5	50.5	51	53	44
Charpy Spec. #6	59	62	54	56
Mean	40.3	41.9	43.5	34.3
95% confidence interval for actual mean	27.75 - 52.75	25.57 - 58.26	30.75 - 56.25	18.21 - 50.45
Std. Deviation	11.9	15.6	12.1	15.4
Median	35.5	45.5	48.5	33.0
Average absolute deviation from median	8.92	12.4	9.17	10.3
Probability of null hypothesis (data is statistically similar to undamaged data from t-test)	0.72	0.52	0.28	0.38

*Refers to specimens with significant curvature after heat straightening. Data is not entirely reliable.

Table 6.13
Average structural properties of overheated A36 steel

Specimen	σ_y *(ksi)*	*E (ksi)*	ε_y	σ_t	ε_u	ε_u / ε_y	*% Elongation*	*% Reduction*
Undamaged	39.1	30295	0.00129	66.7	0.20	153.8	38.92	67.29
A36-60-25-1-1400	48	29821	0.00161	71.3	0.18	113.2	32.99	70.57
A36-60-25-3-1400	46.5	29143	0.0016	67.3	0.16	100.9	32.33	72.88
A36-60-50-1-1400	47.1	31570	0.00149	69.8	0.19	124.7	32.74	72.7
A36-60-50-3-1400	47.6	30669	0.00155	69.9	0.16	103.1	32.25	73.49
A36-90-25-1-1400	48.7	30463	0.0016	72.2	0.18	111.4	33.54	67.64
A36-90-25-3-1400	45.7	30421	0.0015	69.8	0.19	127.1	35.1	73.62
A36-90-50-1-1400	49.5	31122	0.00159	71.9	0.19	119.1	36.32	73.29
A36-90-50-3-1400	48.7	29871	0.00163	71.8	0.17	106.4	34.42	72.63
A36-60-25-1-1600	48.6	30543	0.00159	71.5	0.19	121.4	35.8	71.96
A36-60-25-3-1600	48.4	29924	0.00162	70.7	0.14	89.2	28.38	71.74
A36-60-50-1-1600	47.9	29408	0.00163	72.3	0.19	119.1	35.64	71.27
A36-60-50-3-1600	44.5	30766	0.00145	69.8	0.18	125.7	29.5	73.09
A36-90-25-1-1600	47.6	30680	0.00156	71.2	0.16	104.4	29.75	72.85
A36-90-25-3-1600	46.9	31507	0.00149	70.8	0.19	124.8	37.8	70.68
A36-90-50-1-1600	47.1	30305	0.00155	70.9	0.2	127.1	35.75	73.1
A36-90-50-3-1600	47.8	30244	0.00158	70.6	0.13	82.3	28.06	73.13

Table 6.14
Fracture toughness of damaged-repaired overheated A36 steel subjected to damage strains of 60 ε_y and maximum temperatures of 1400 °F

A36 Specimen ID →	A36-60-25-1-1400	A36-60-25-3-1400	A36-60-50-1-1400	A36-60-50-3-1400
Charpy Spec. #1	185	111	131	180
Charpy Spec. #2	189	133	145	185
Charpy Spec. #3	208	175	175	204
Charpy Spec. #4	222	225	179	216
Charpy Spec. #5	241	237	187	216
Charpy Spec. #6	252	250	216	234
Mean	216	189	172	206
95% confidence interval for actual mean	187.6 - 244.8	127.8 - 249.2	140.2-204.1	184.3 - 227.4
Std. Deviation	27.2	57.9	30.4	20.5
Median	225	200	177	210
Average absolute deviation from median	22.2	48.8	21.8	16.2
Probability of null hypothesis (data is statistically similar to undamaged data from t-test)	<0.000 1	<0.000 1	<0.000 1	<0.000 1

Table 6.15
Fracture toughness of damaged-repaired overheated A36 steel subjected to damage strains of 90 ε_y and maximum temperatures of 1400 °F

A36 Specimen ID →	A36-90-25-1-1400	A36-90-25-3-1400	A36-90-50-1-1400	A36-90-50-3-1400
Charpy Spec. #1	75	211	175	109
Charpy Spec. #2	77	216	183	126
Charpy Spec. #3	126	239	206	228
Charpy Spec. #4	159	244	216	243
Charpy Spec. #5	185	263	223	251
Charpy Spec. #6	203	-	238	-
Mean	138	235	207	191
95% confidence interval for actual mean	80.57 - 194.4	208.1 - 261.1	181.6 - 232.1	106.7 - 276.1
Std. Deviation	54.2	21.3	24.1	68.2
Median	44.8	239	211	228
Average absolute deviation from median	143	16	18.8	51.8
Probability of null hypothesis (data is statistically similar to undamaged data from t-test)	<0.000 1	<0.000 1	<0.000 1	<0.000 1

Table 6.16
Fracture toughness of damaged-repaired overheated A36 steel subjected to damage strains of 60 ε_y and maximum temperatures of 1600 °F

A36 Specimen ID →	A36-60-25-1-1600	A36-60-25-3-1600	A36-60-50-1-1600	A36-60-50-3-1600
Charpy Spec. #1	122	170	75	66
Charpy Spec. #2	125	209	125	124
Charpy Spec. #3	128	210	128	170
Charpy Spec. #4	221	248	162	185
Charpy Spec. #5	223	251	198	199
Charpy Spec. #6	230	254	216	228
Mean	175	224	151	162
95% confidence interval for actual mean	117.4 - 232.3	188.7 - 258.6	96.06 - 205.3	100.8 - 223.2
Std. Deviation	54.7	33.3	52	58.3
Median	175	229	145	178
Average absolute deviation from median	49.8	27.3	41.3	42
Probability of null hypothesis (data is statistically similar to undamaged data from t-test)	<0.000 1	<.0001	<.0001	<.0001

Table 6.17
Fracture toughness of damaged-repaired overheated A36 steel subjected to damage strains of 60 ε_y and maximum temperatures of 1600 °F

A36 Specimen ID →	A36-90-25-1-1600	A36-90-25-3-1600	A36-90-50-1-1600	A36-90-50-3-1600
Charpy Spec. #1	90	135	113	30
Charpy Spec. #2	102	177	125	58
Charpy Spec. #3	112	185	126	92
Charpy Spec. #4	217	200	215	200
Charpy Spec. #5	223	212	228	231
Charpy Spec. #6	240	219	251	234
Mean	164	188	176	141
95% confidence interval for actual mean	91.14 - 236.9	156.1 - 219.9	111.8 - 240.9	44.82 - 236.8
Std. Deviation	69.4	30.4	61.5	91.5
Median	165	193	171	146
Average absolute deviation from median	62.7	22.3	55	80.8
Probability of null hypothesis (data is statistically similar to undamaged data from t-test)	<0.000 1	<0.000 1	<0.000 1	0.0003

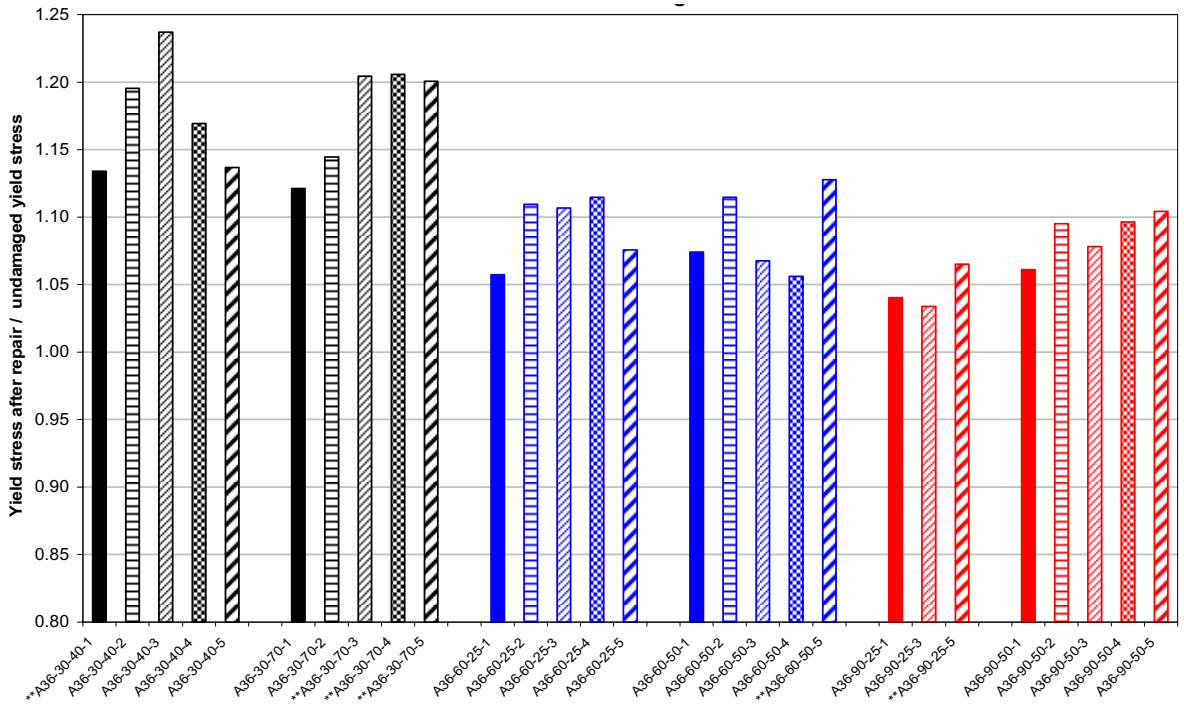

Figure 6.1
Normalized yield stress of damaged-repaired A36 steel

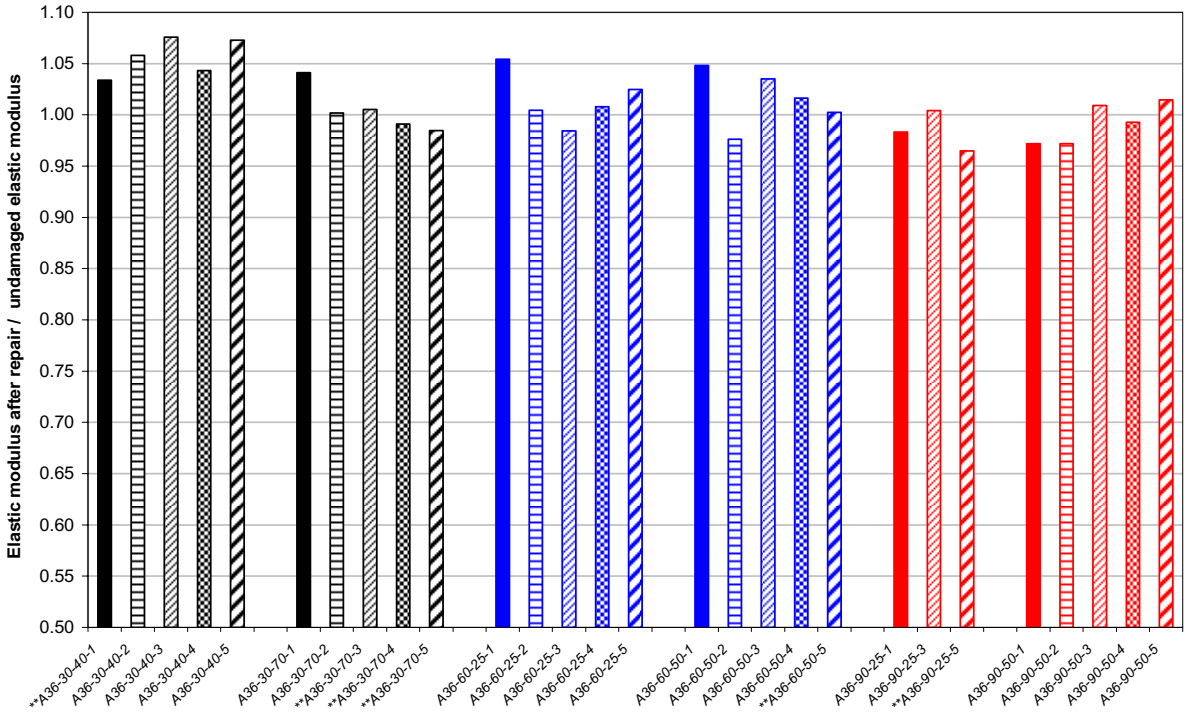

Figure 6.2
Normalized elastic modulus of damaged-repaired A36 steel

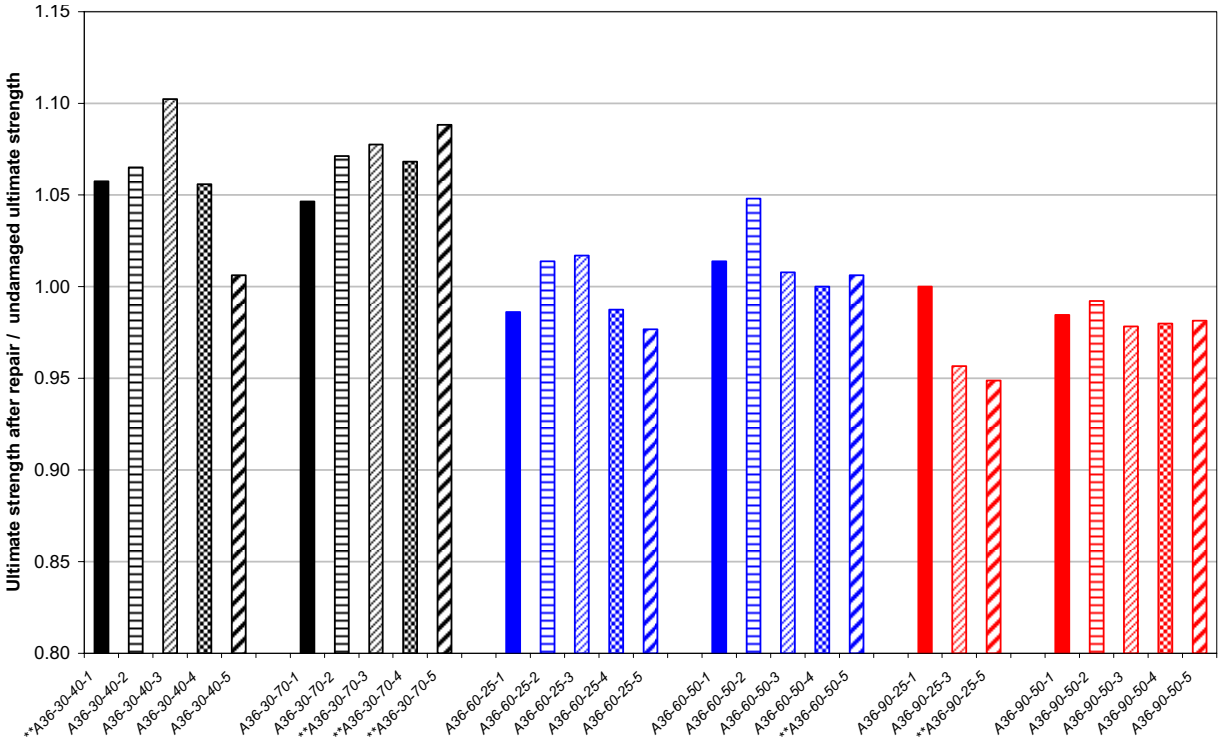

Figure 6.3
Normalized ultimate stress of damaged-repaired A36 steel

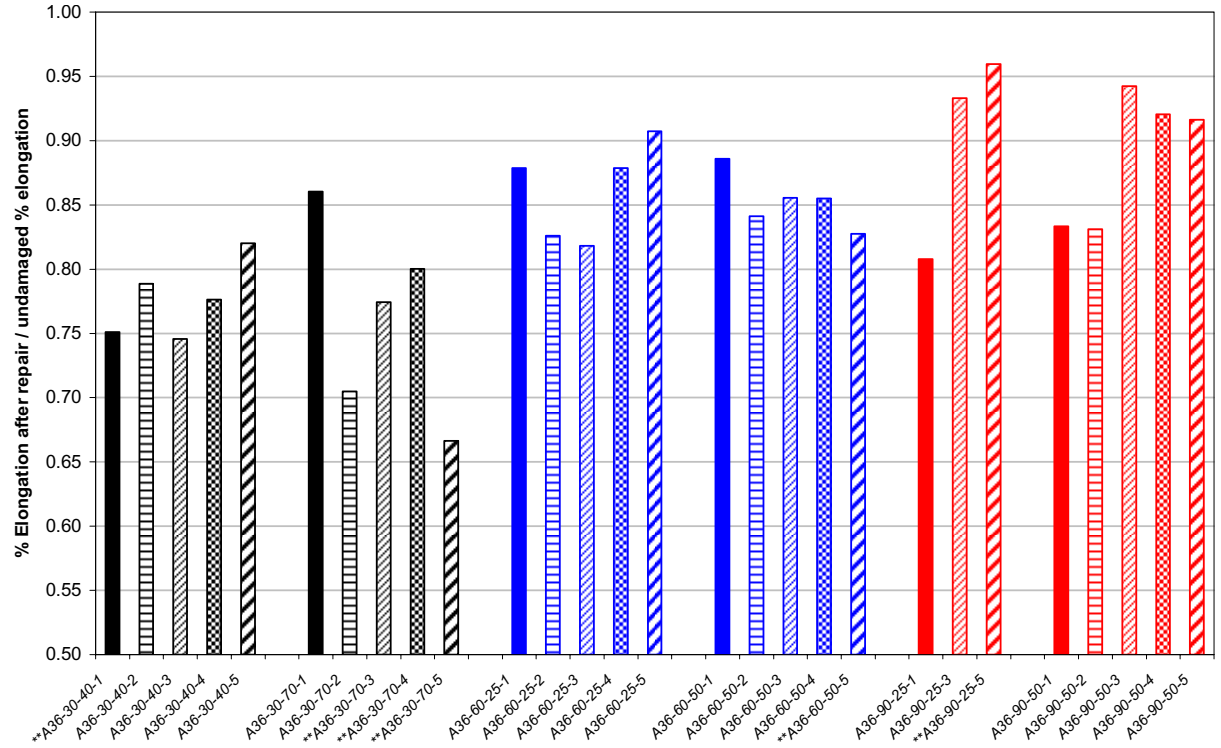

Figure 6.4
Normalized percent elongation of damaged-repaired A36 steel

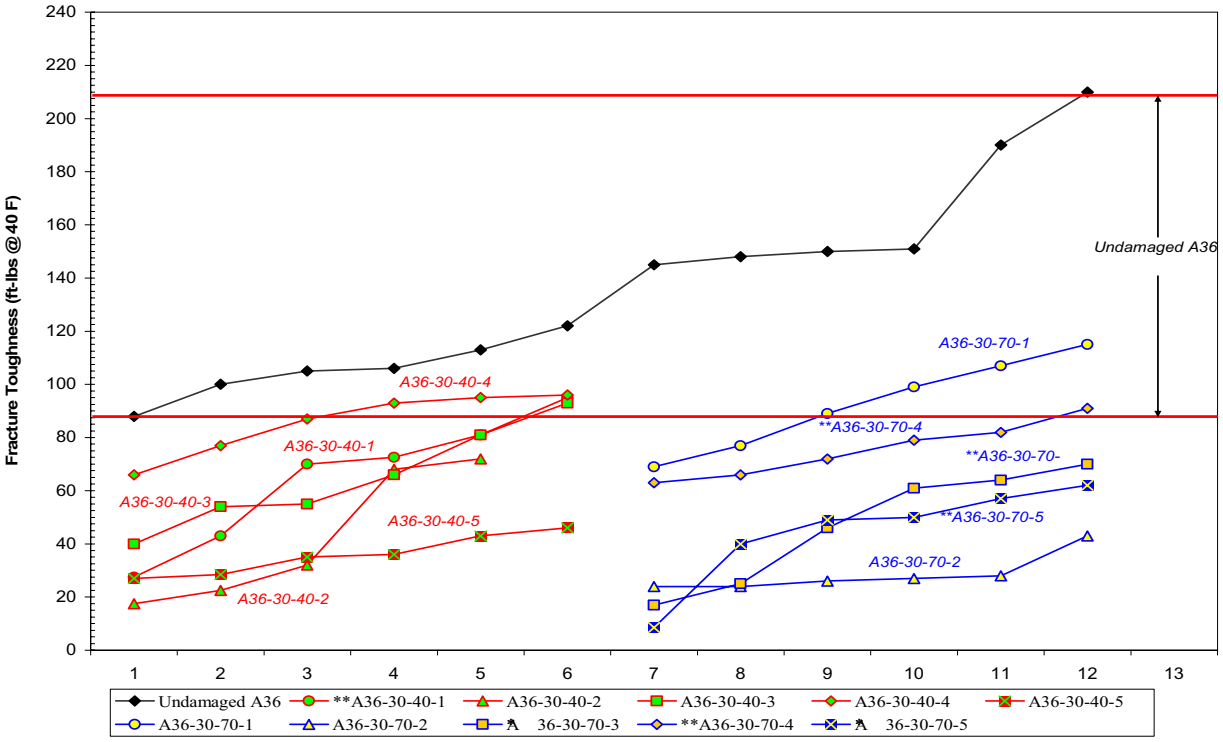

Figure 6.5
Fracture toughness comparisons of A36-30 (ε_d=30 ε_y) specimens

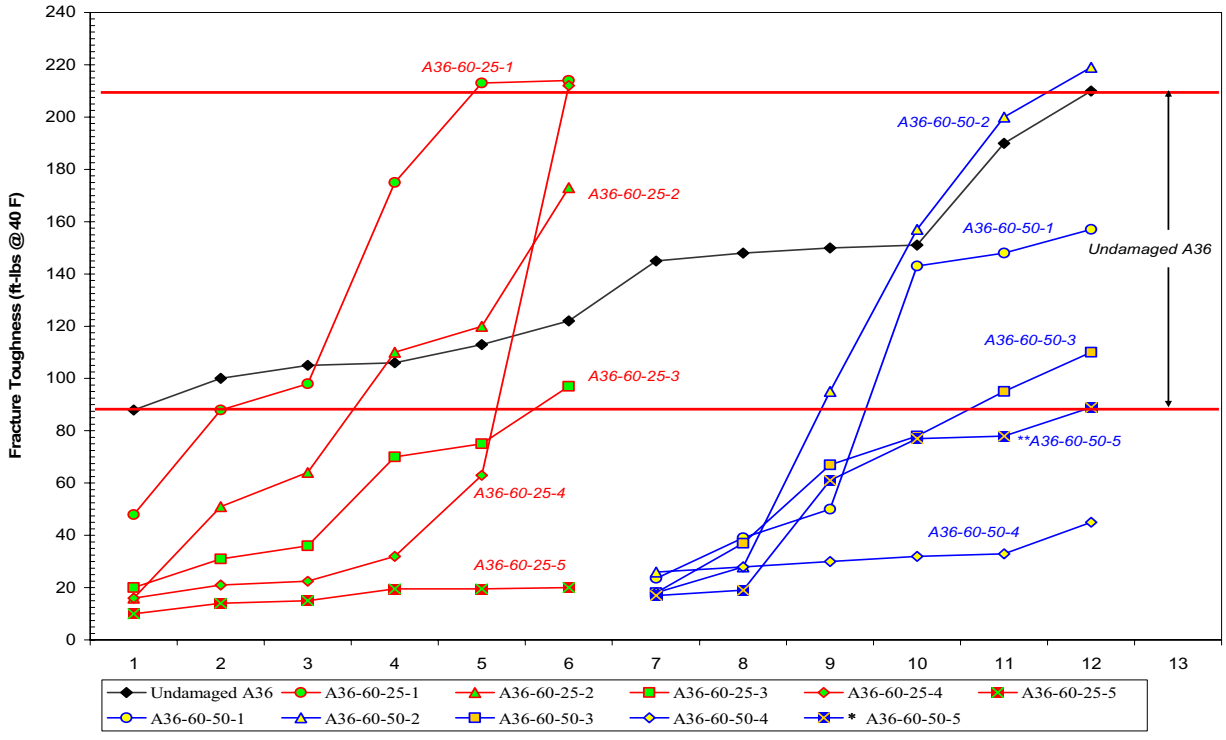

Figure 6.6
Fracture toughness comparisons of A36-60 (ε_d=60 ε_y) specimens

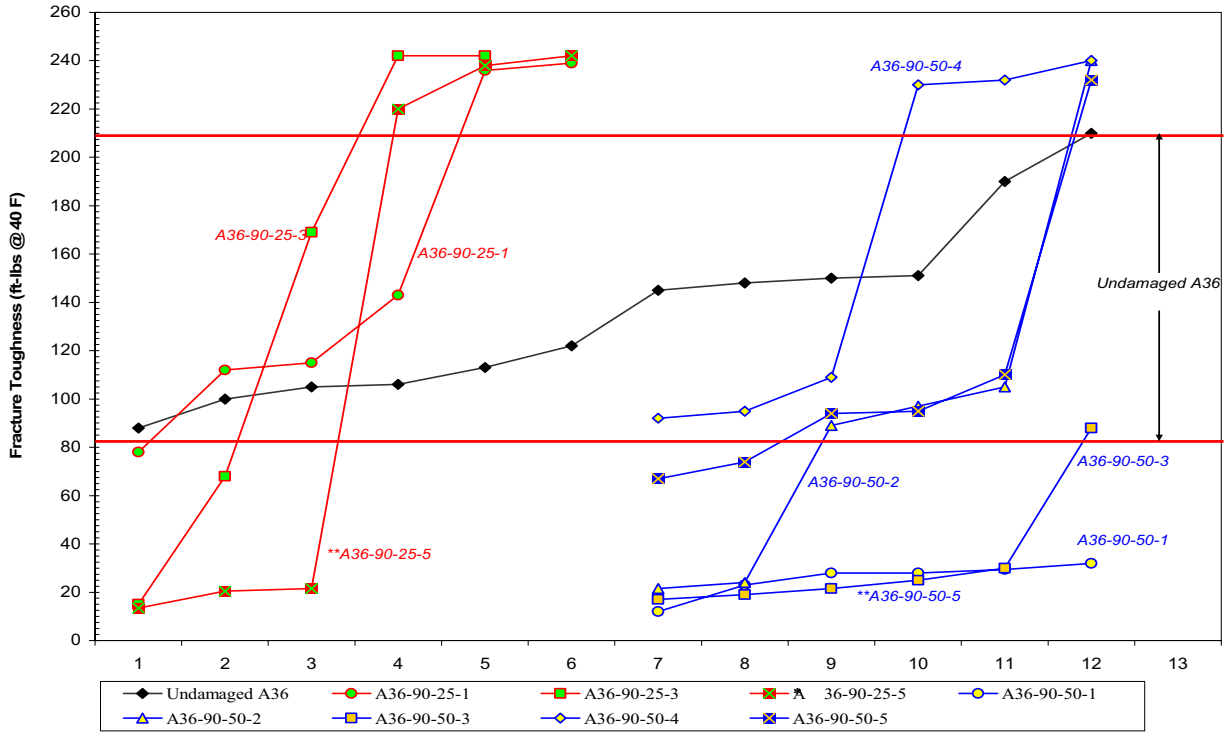

Figure 6.7
Fracture toughness comparisons of A36-90 (ε_d=90 ε_y) specimens

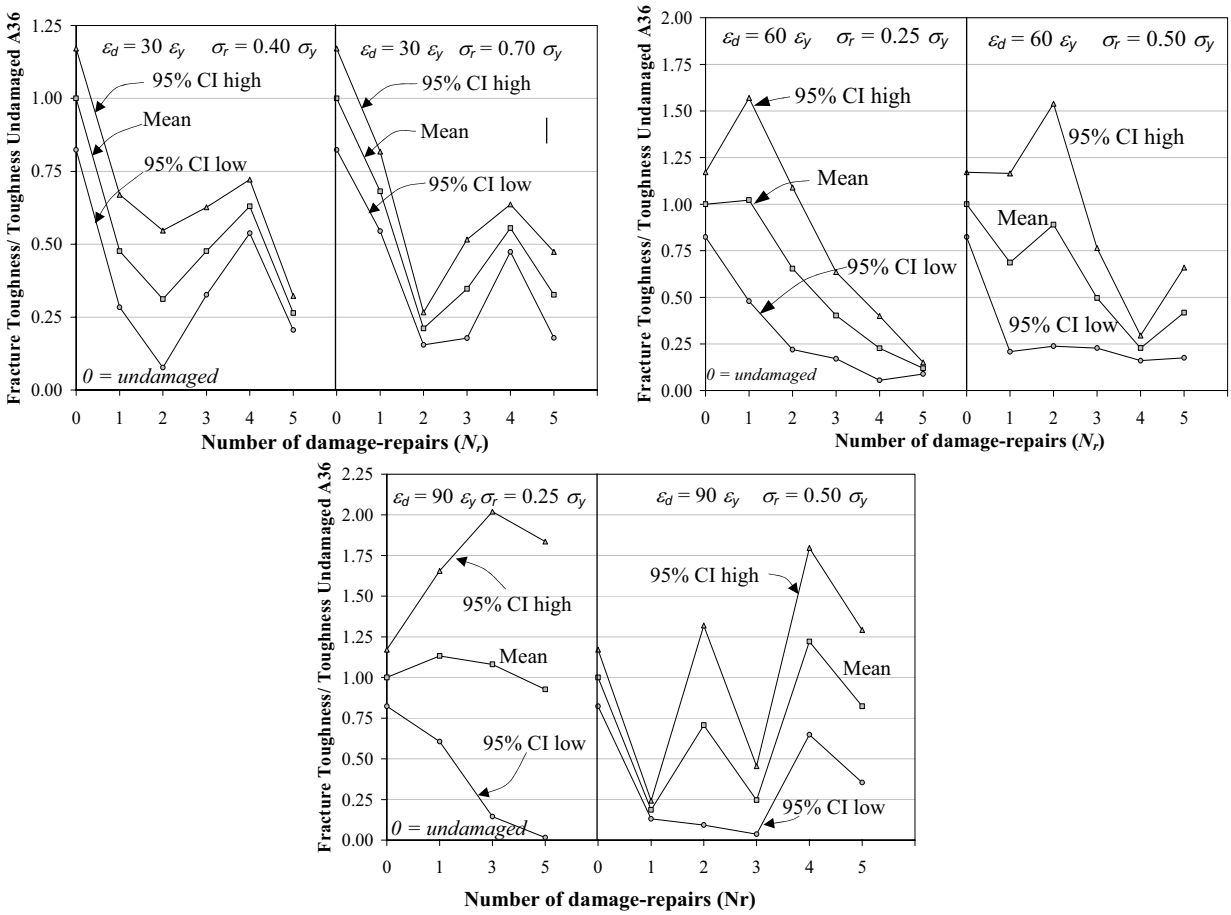

Figure 6.8
Normalized fracture toughness (mean and 95% CI) for damaged-repaired A36 steel

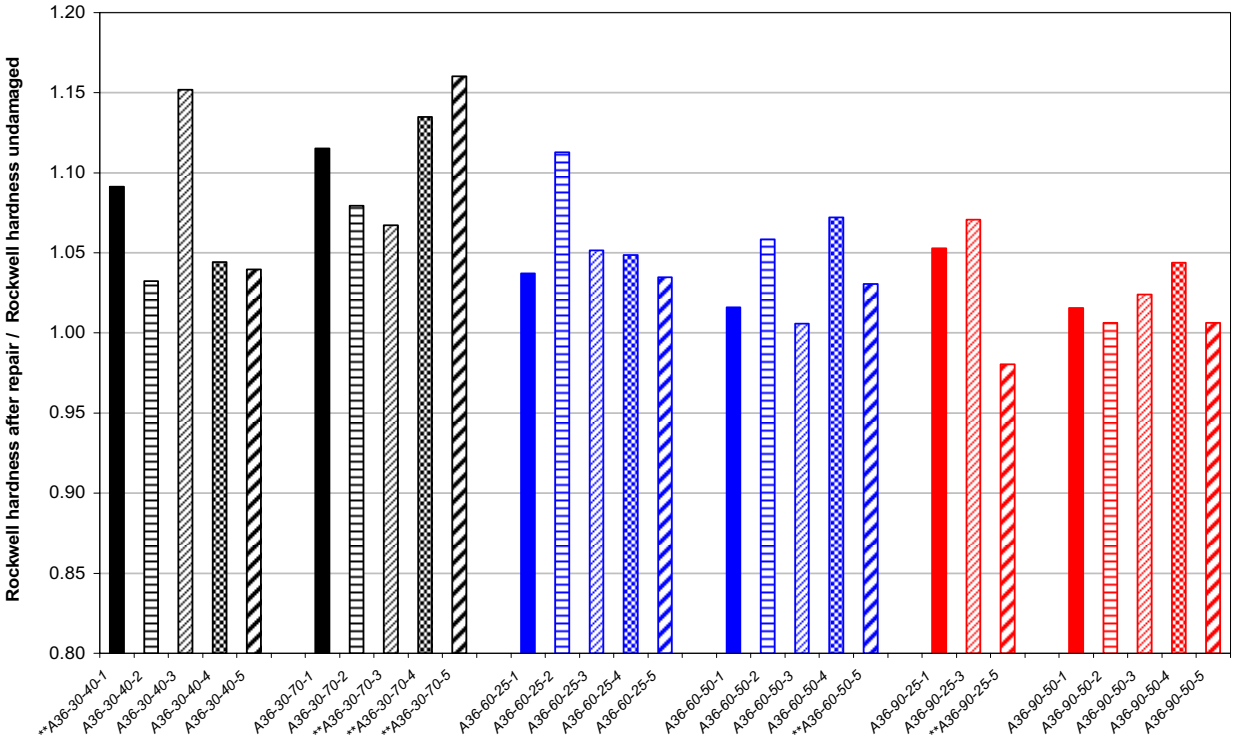

Figure 6.9
Normalized Rockwell hardness of damaged-repaired A36 steel

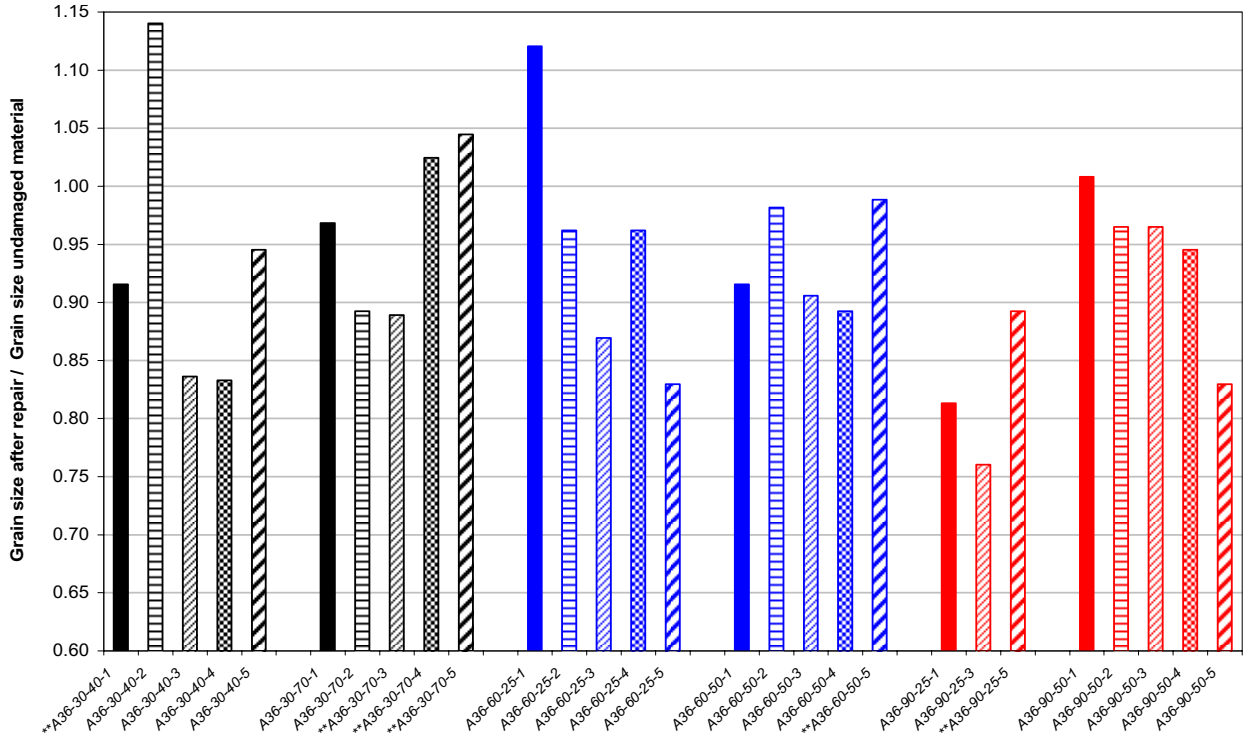

Figure 6.10
Normalized grain size of damaged-repaired A36 steel

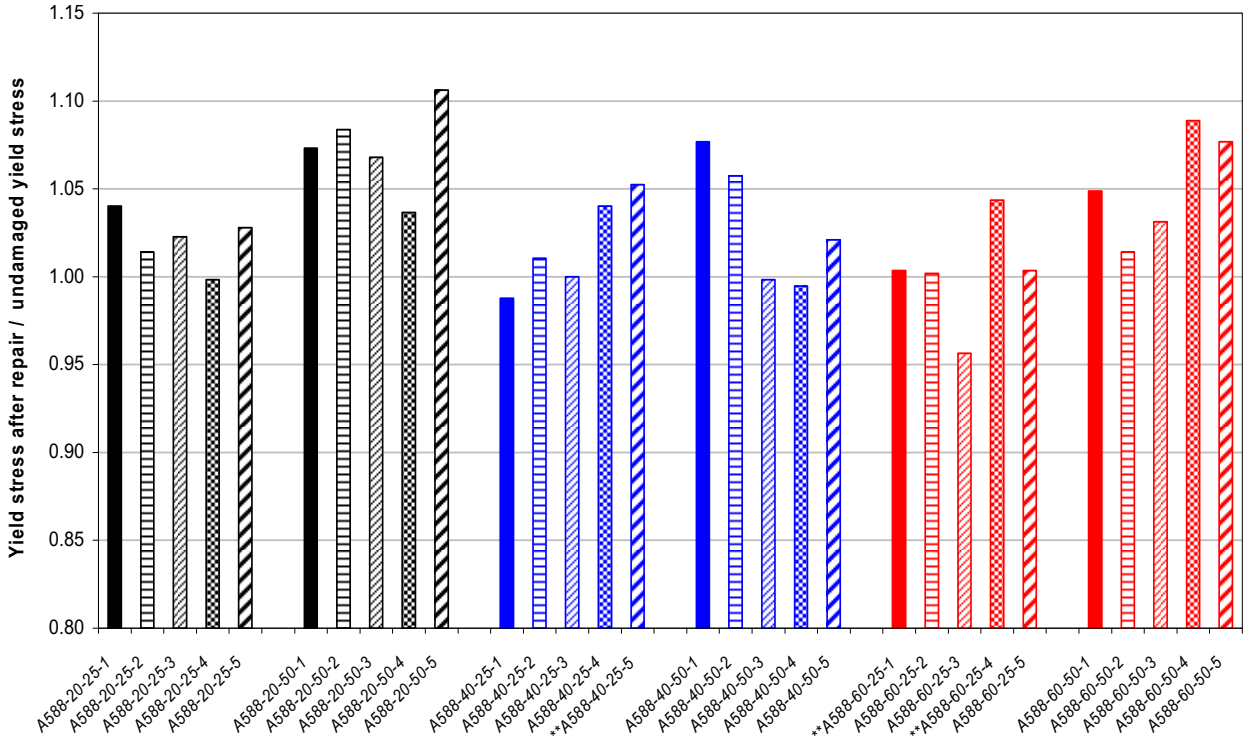

Figure 6.11
Normalized yield stress of damaged-repaired A588 steel

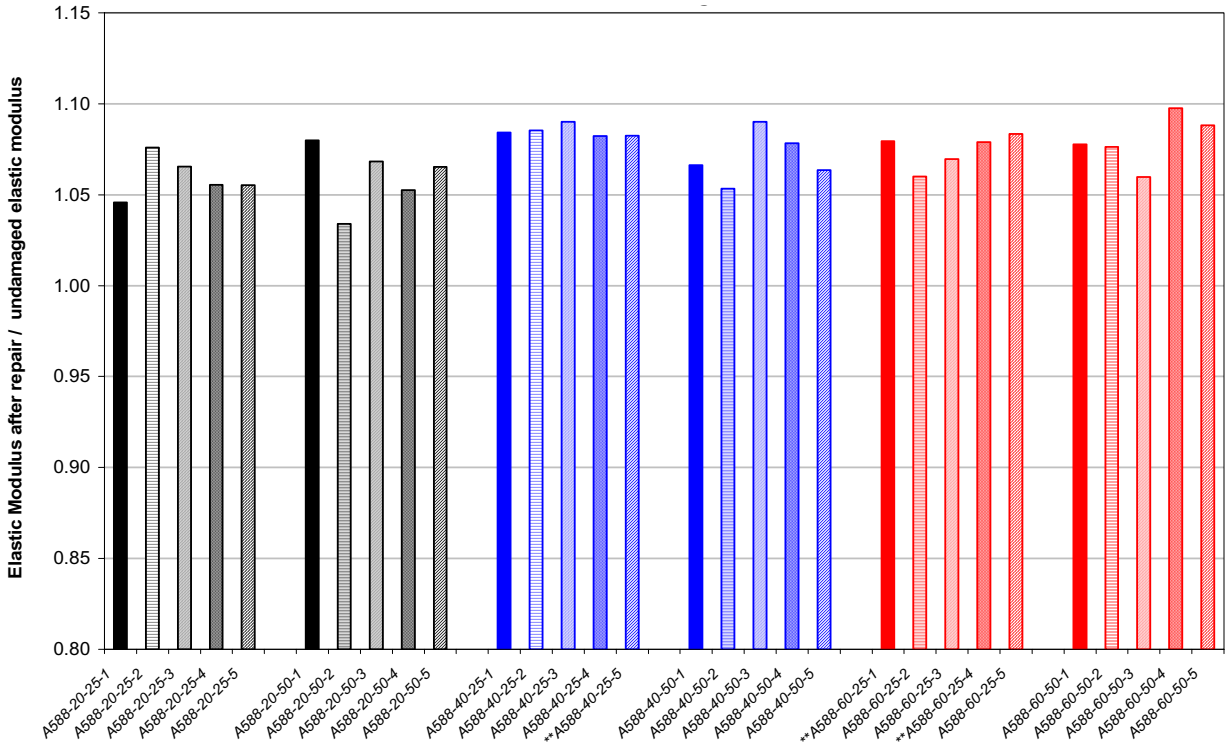

Figure 6.12
Normalized elastic modulus of damaged-repaired A588 steel

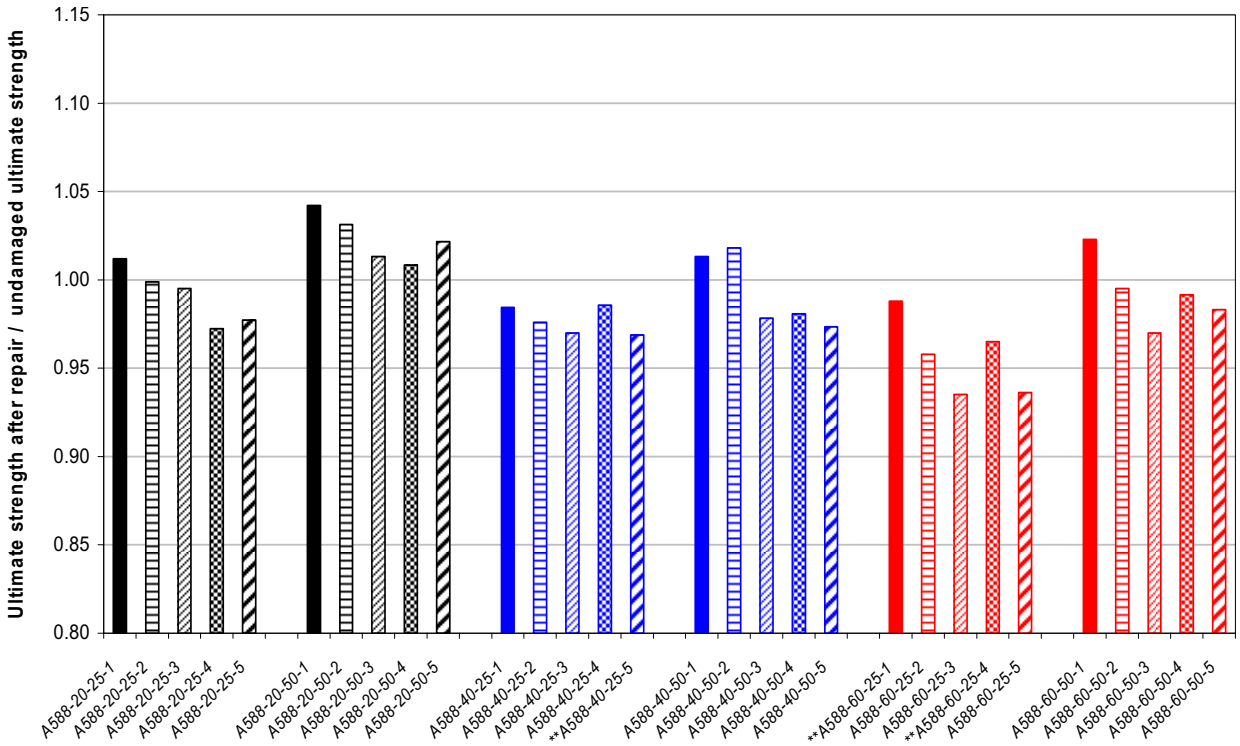

Figure 6.13
Normalized ultimate stress of damaged-repaired A588 steel

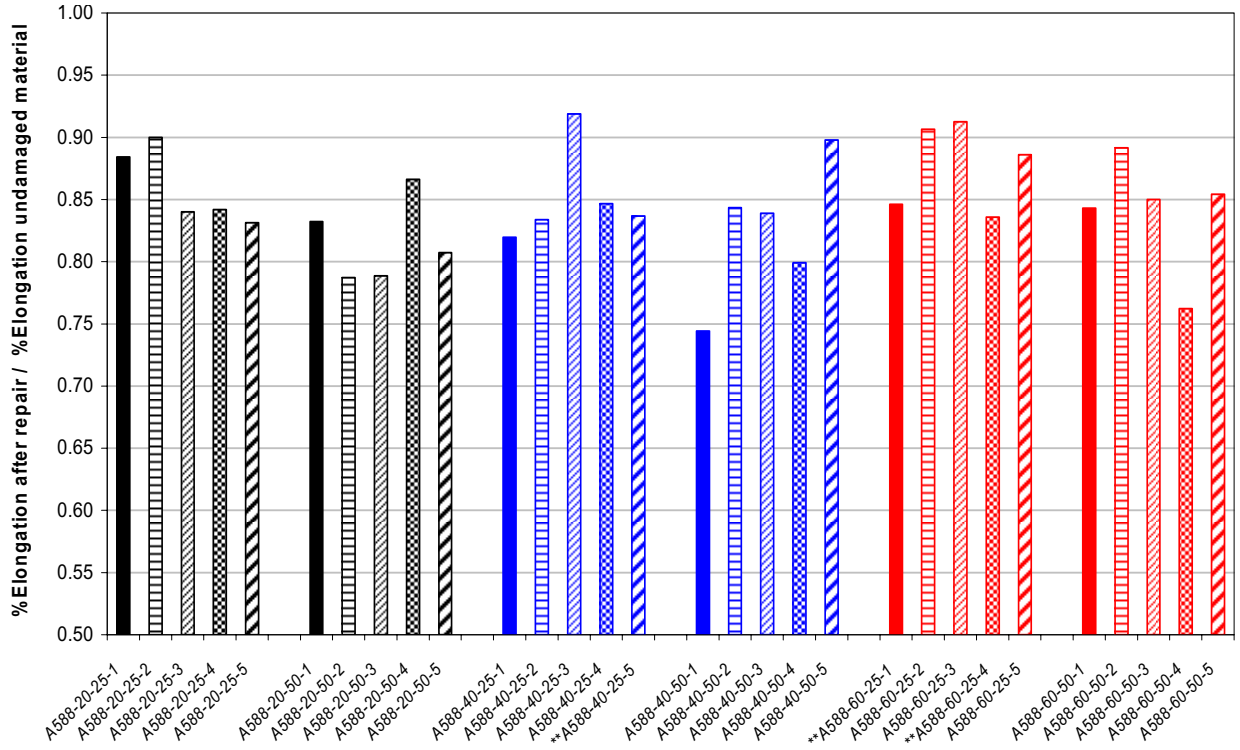

Figure 6.14
Normalized percent elongation of damaged-repaired A588 steel

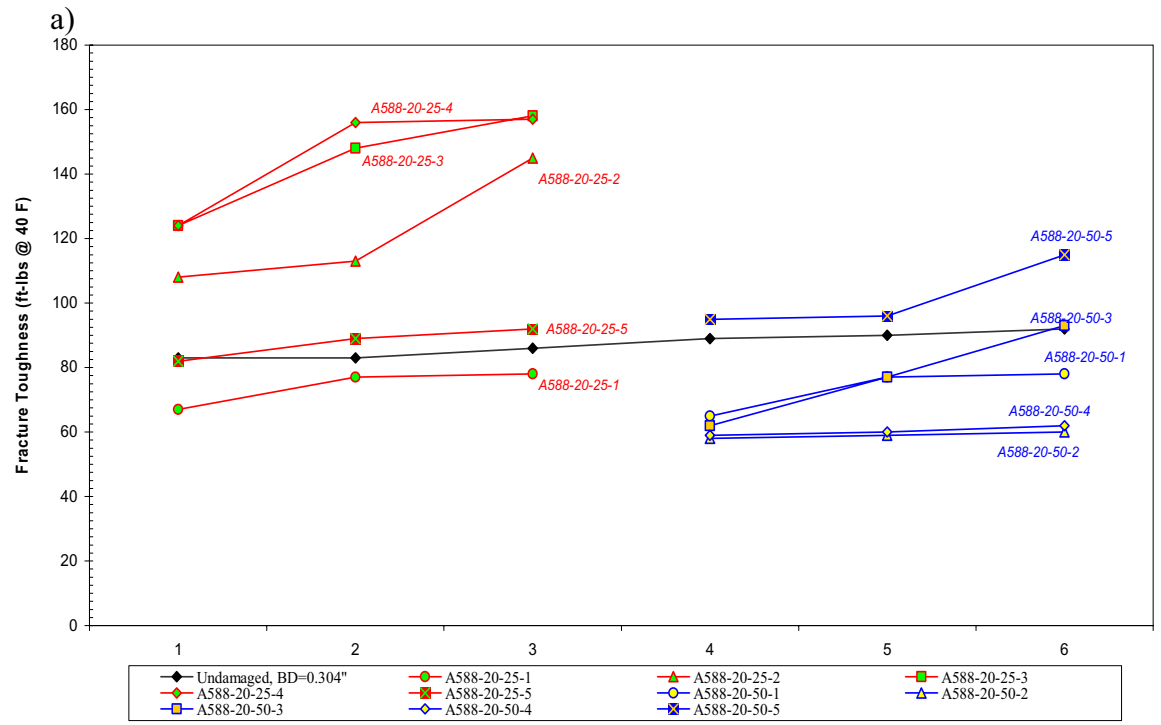

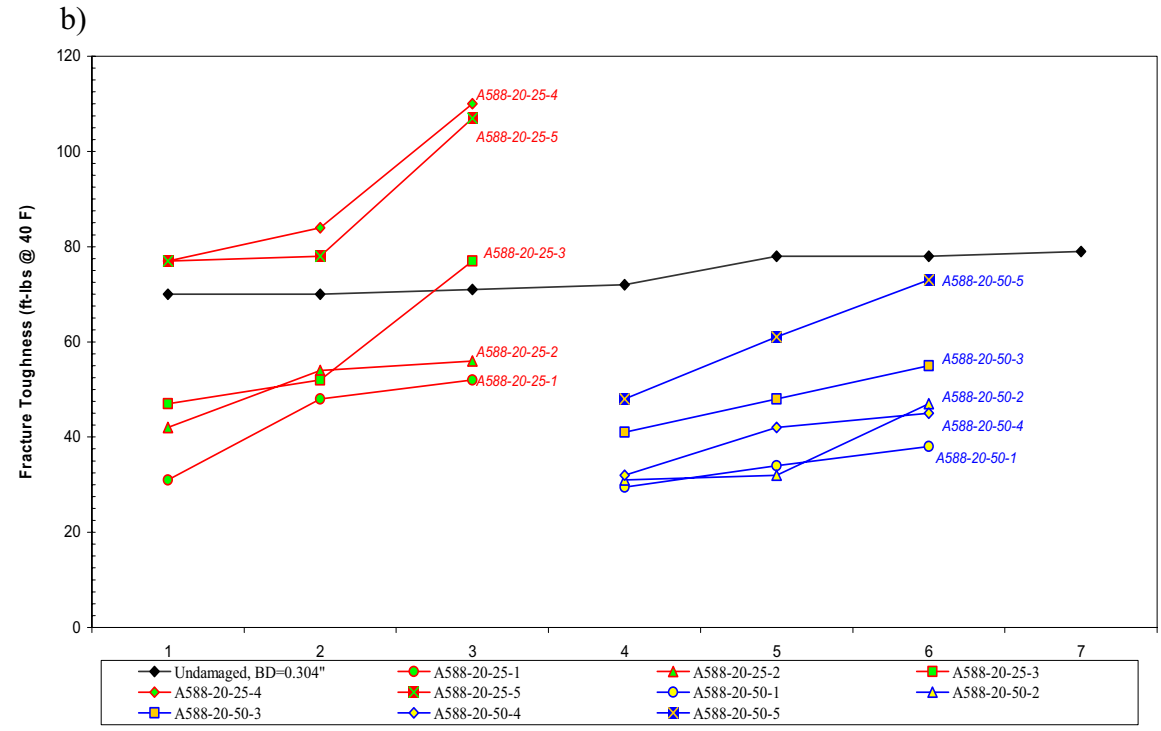

Figure 6.15
Fracture toughness values for A588-20 (ε_d=20 ε_y) specimens: (a) quarter, and (b) mid thickness

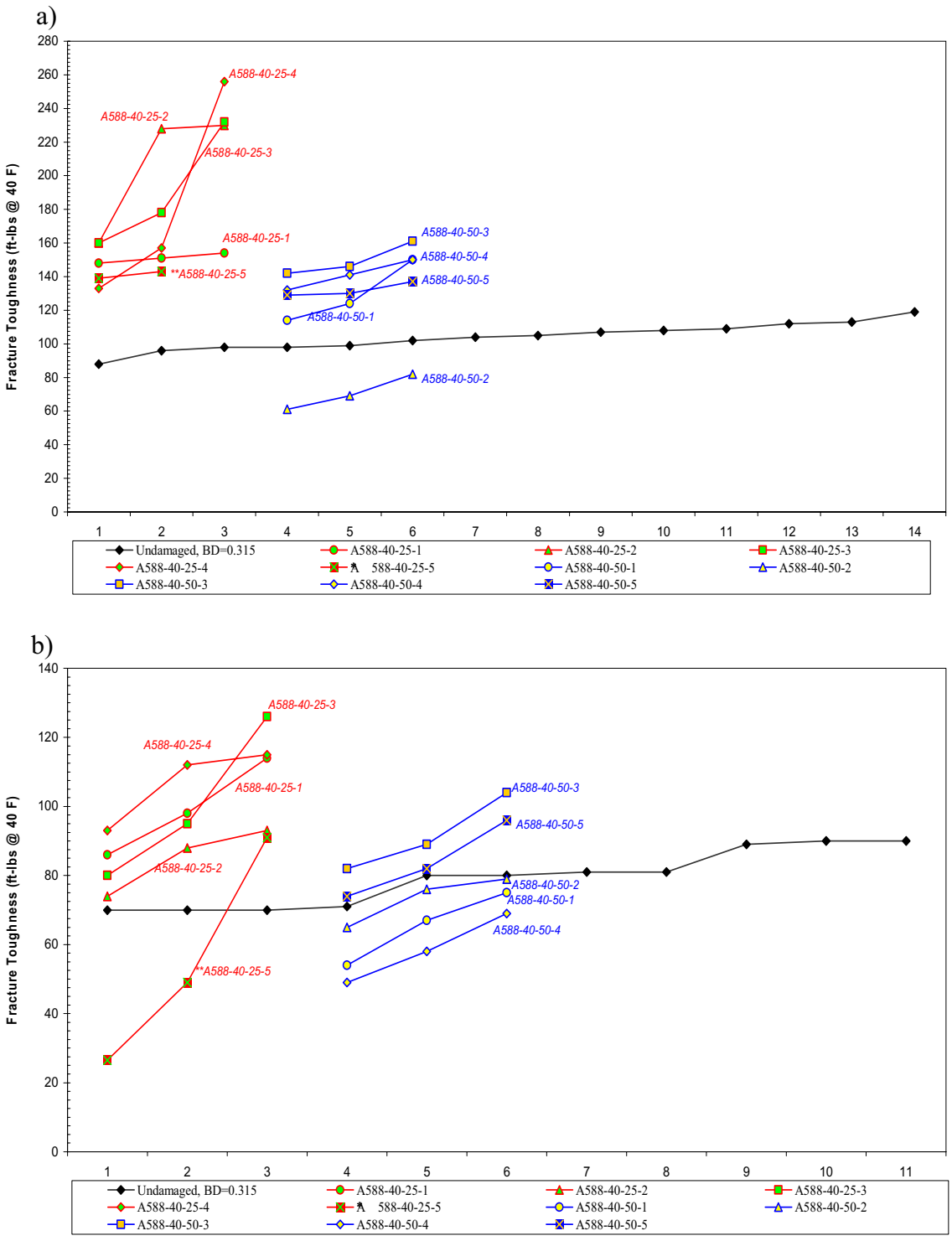

Figure 6.16
Fracture toughness values for A588-40 (ε_{il}=40 ε_y) specimens: (a) quarter, and (b) mid thickness

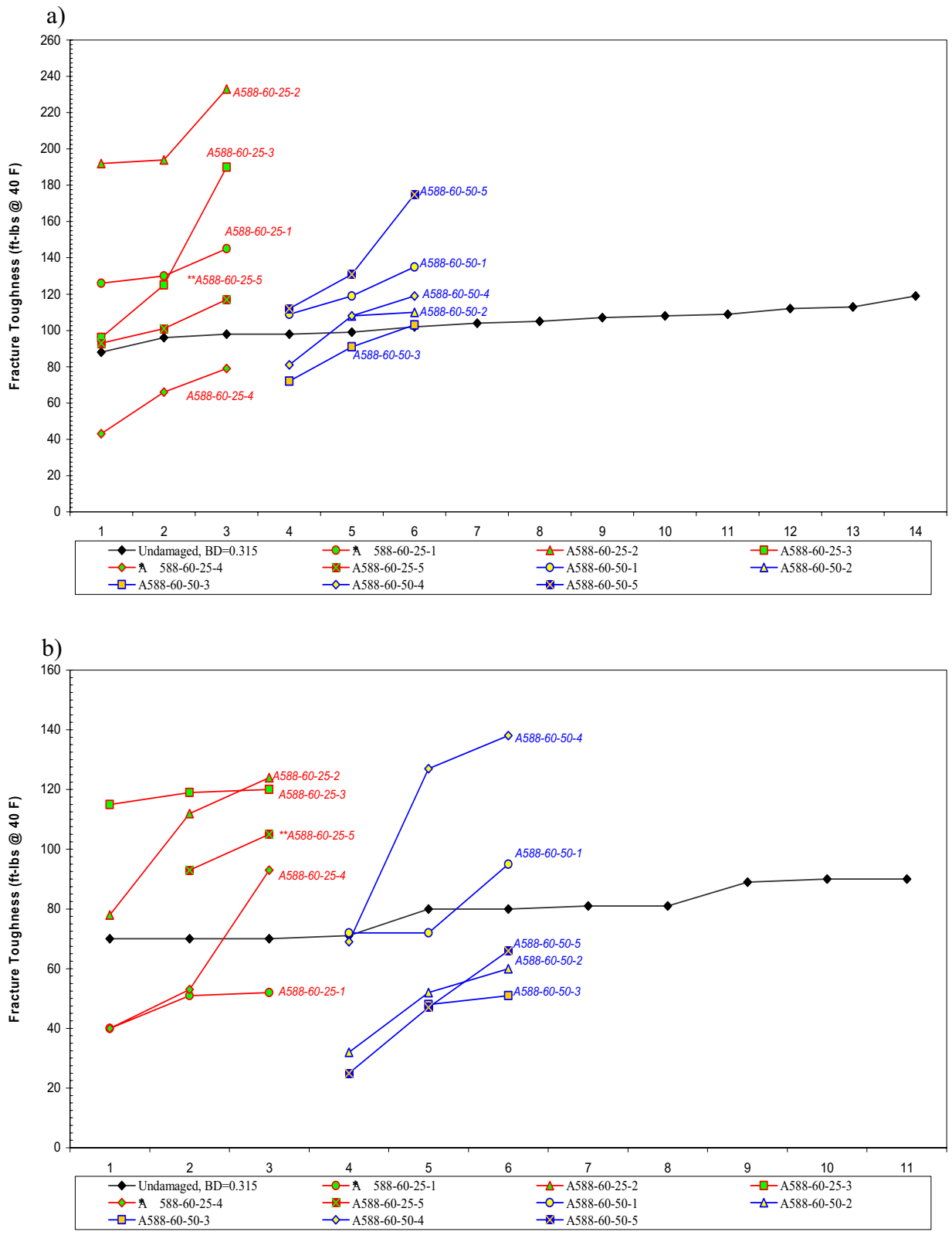

Figure 6.17
Fracture toughness values for A588-60 (ε_d=60 ε_y) specimens: (a) quarter, and (b) mid thickness

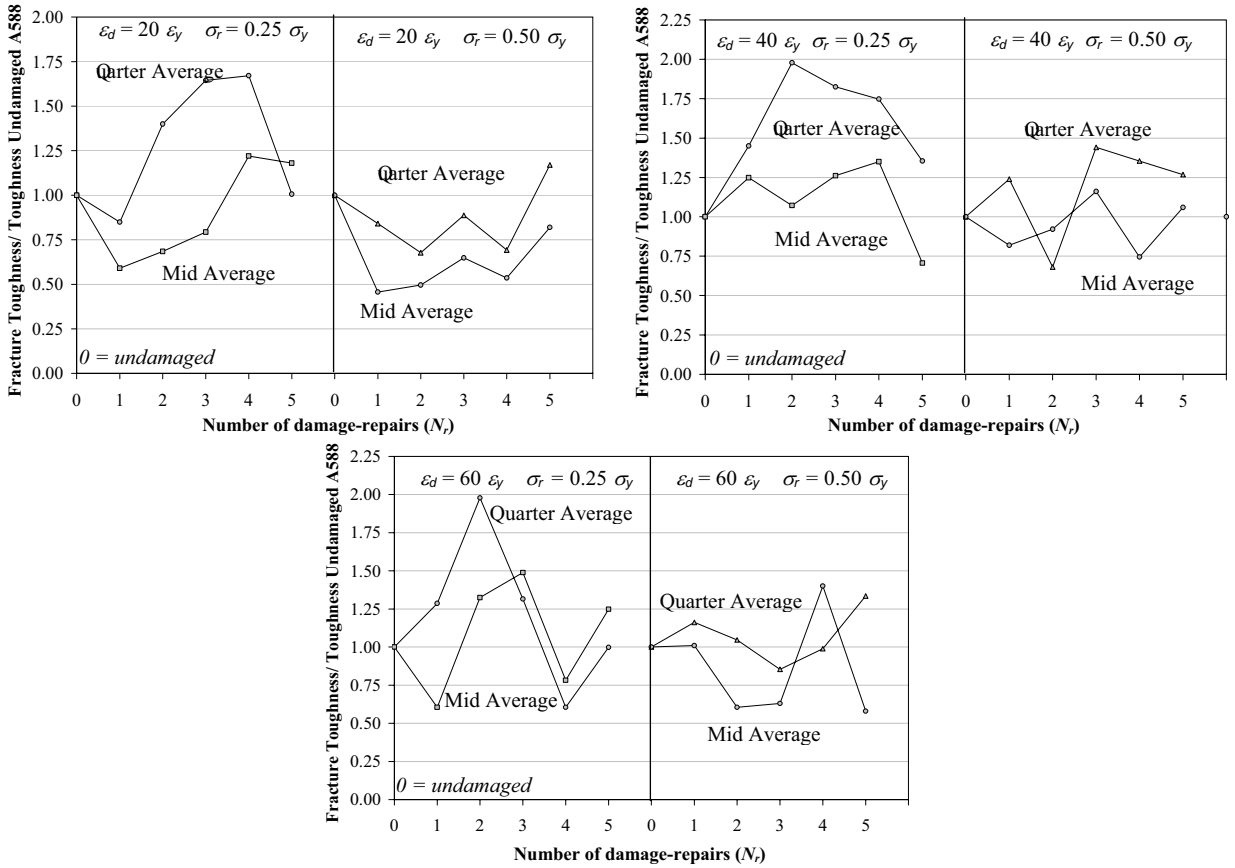

Figure 6.18
Normalized fracture toughness values for damaged-repaired A588 specimens

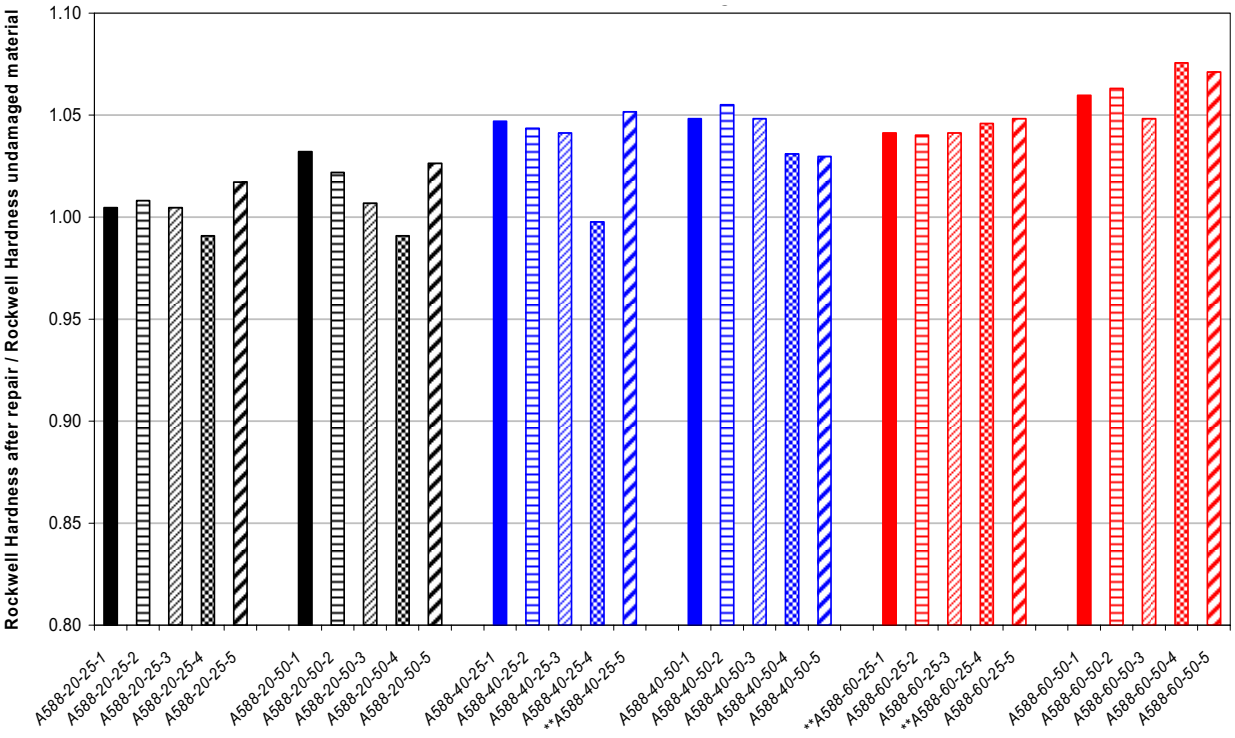

Figure 6.19
Normalized Rockwell hardness of damaged-repaired A588 steel

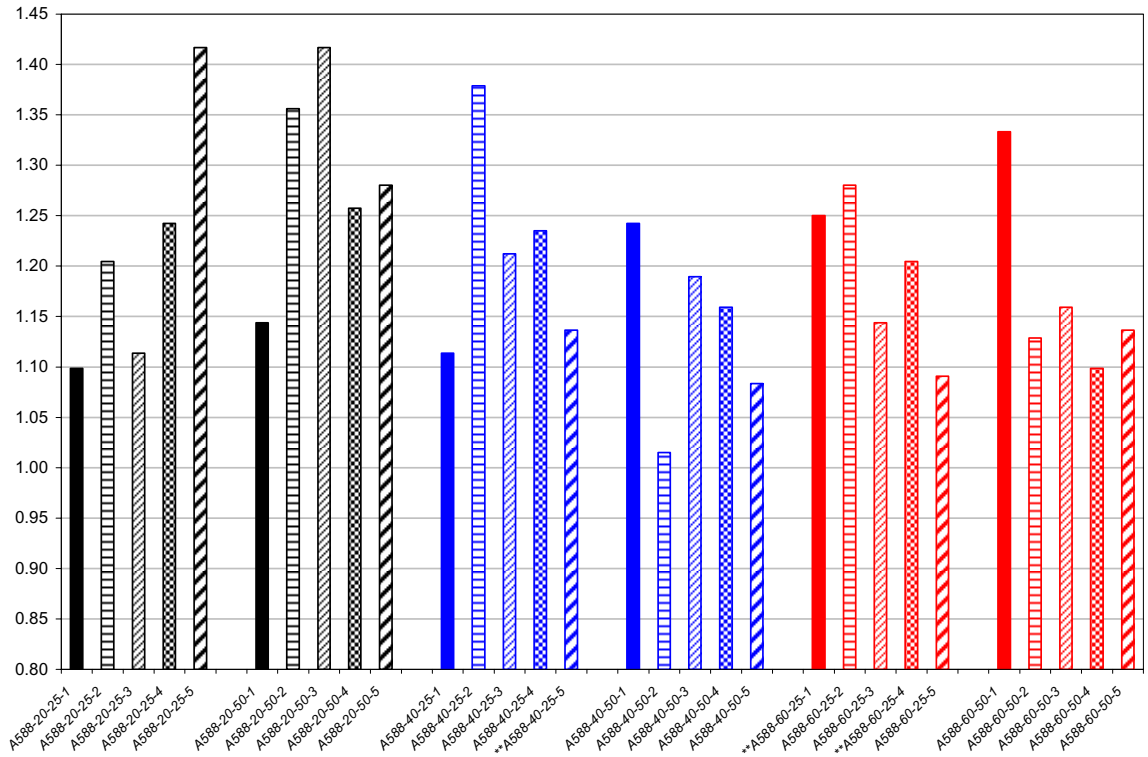

Figure 6.20
Normalized grain size of damaged-repaired A588 specimens

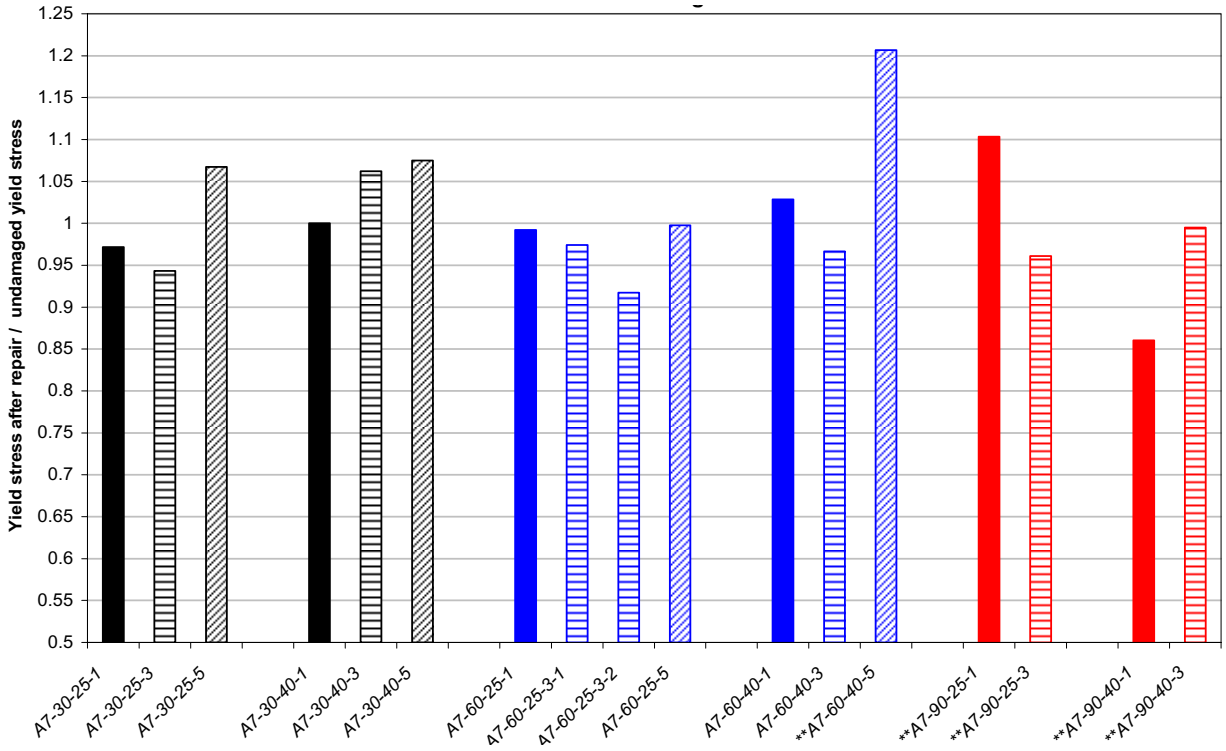

Figure 6.21
Normalized yield stress of damaged-repaired A7 steel

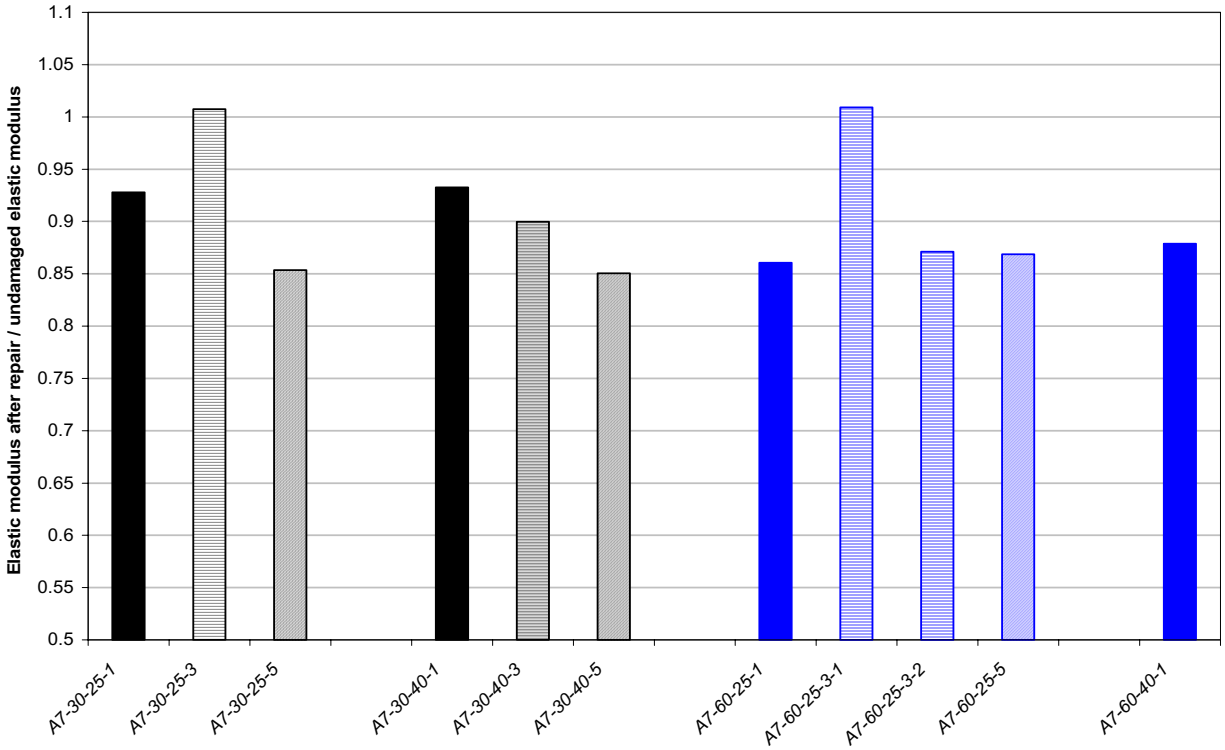

Figure 6.22
Normalized elastic modulus of damaged-repaired A7 steel

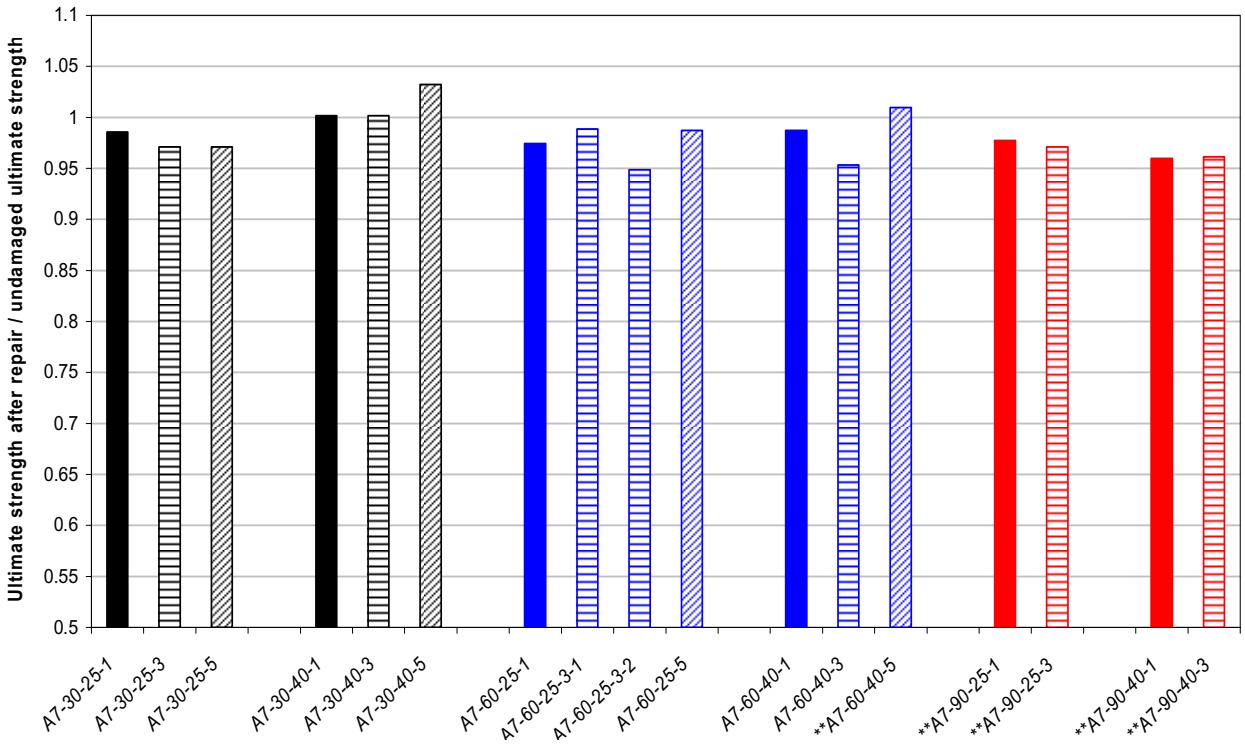

Figure 6.23
Normalized ultimate stress of damaged-repaired A7 steel

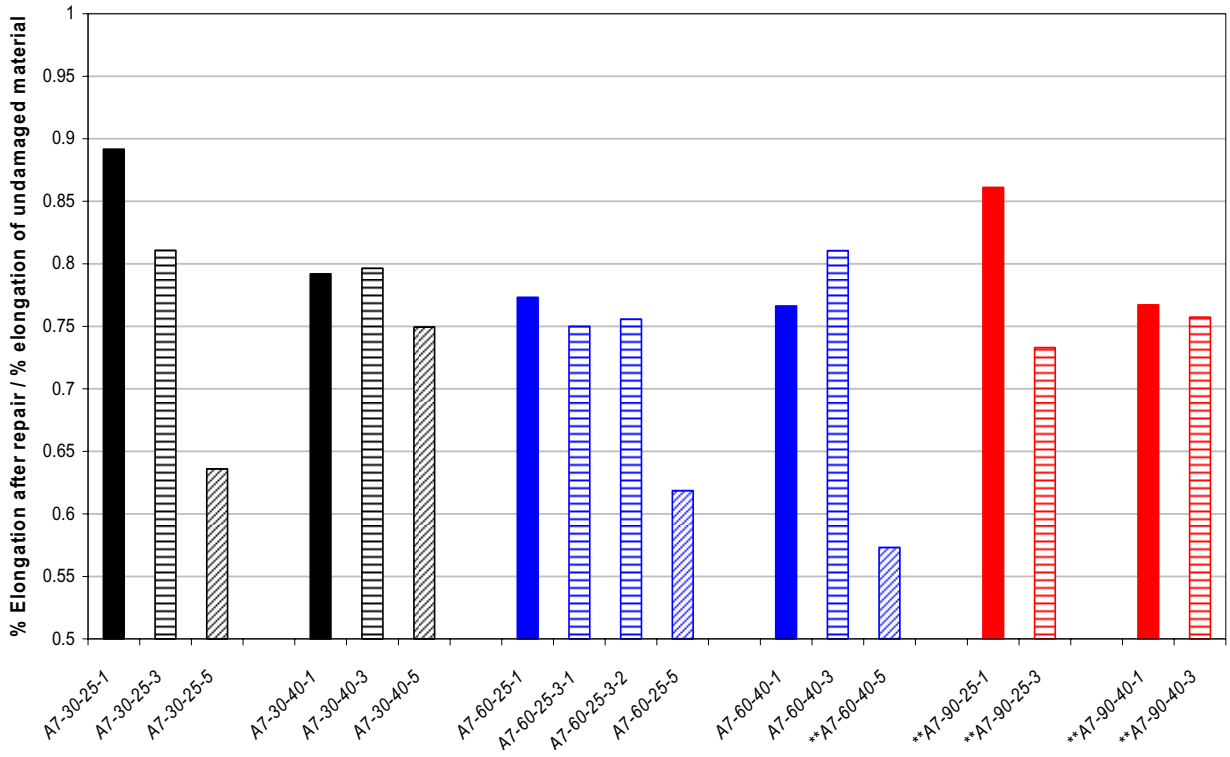

Figure 6.24
Normalized percent elongation of damaged-repaired A7 steel

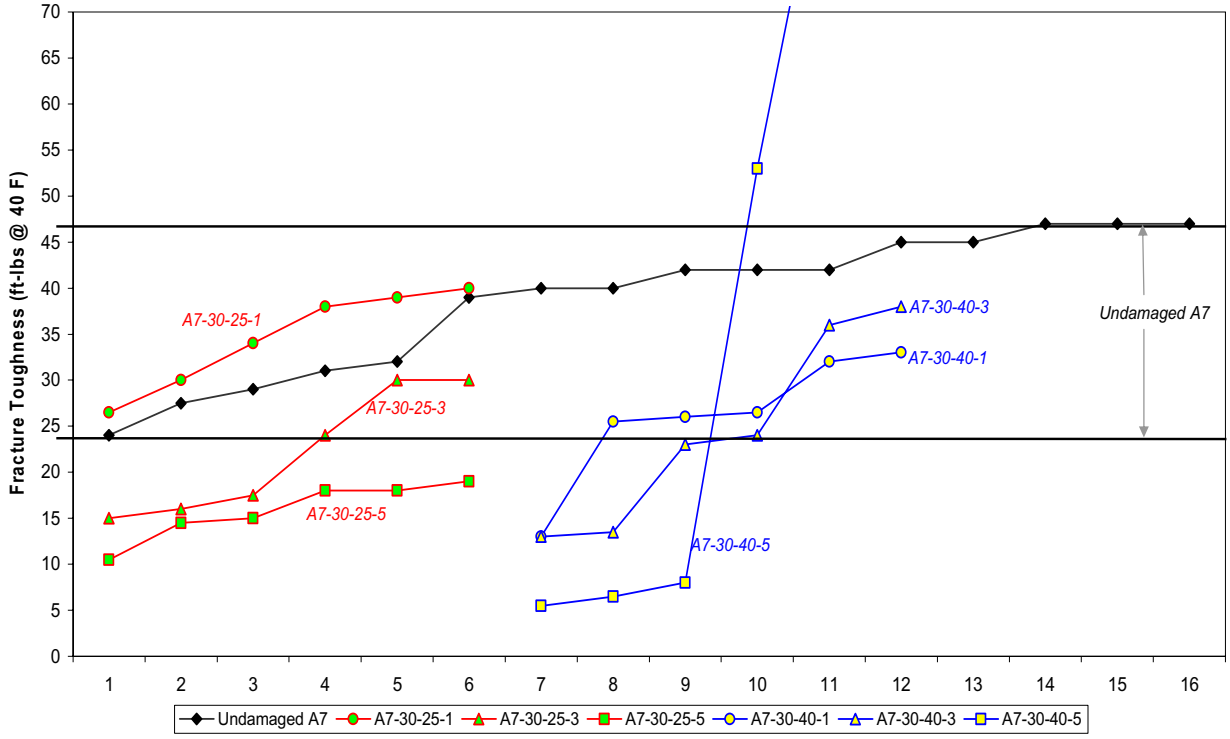

Figure 6.25
Fracture toughness comparisons of damaged-repaired A7-30 (ε_d=30 ε_y) specimens

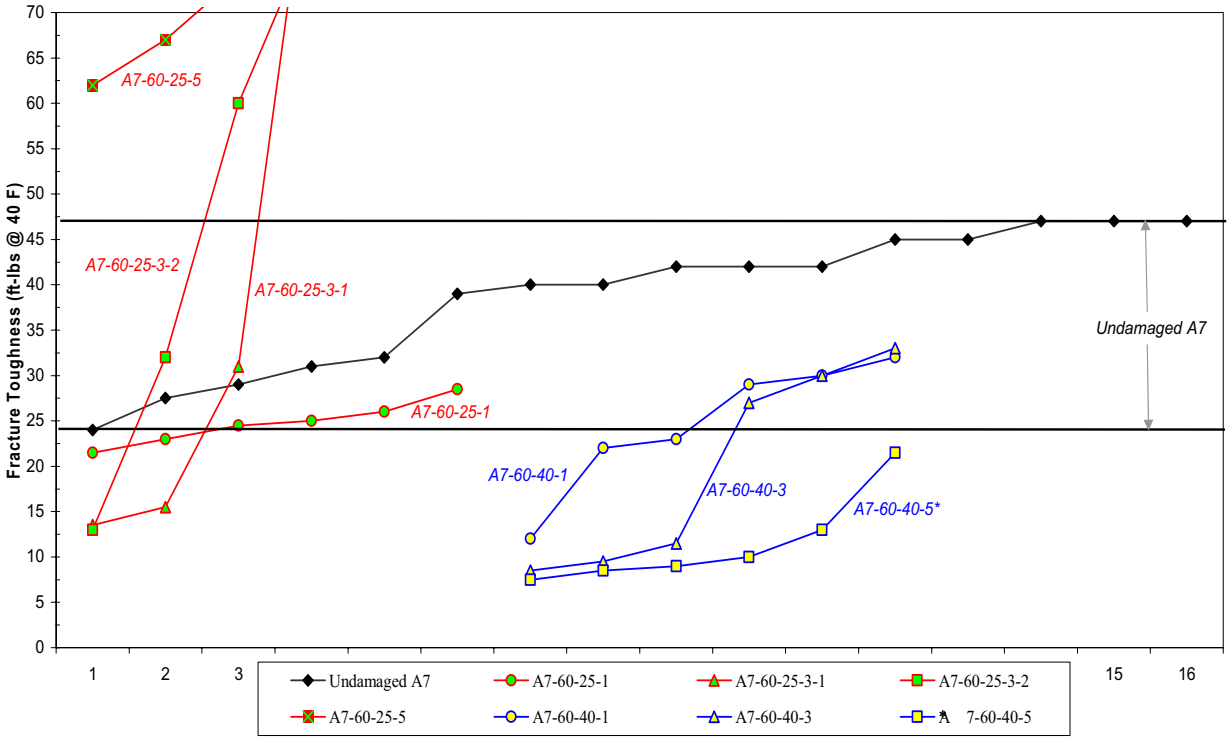

Figure 6.26
Fracture toughness comparisons of damaged-repaired A7-60 (ε_d=60 ε_y) specimens

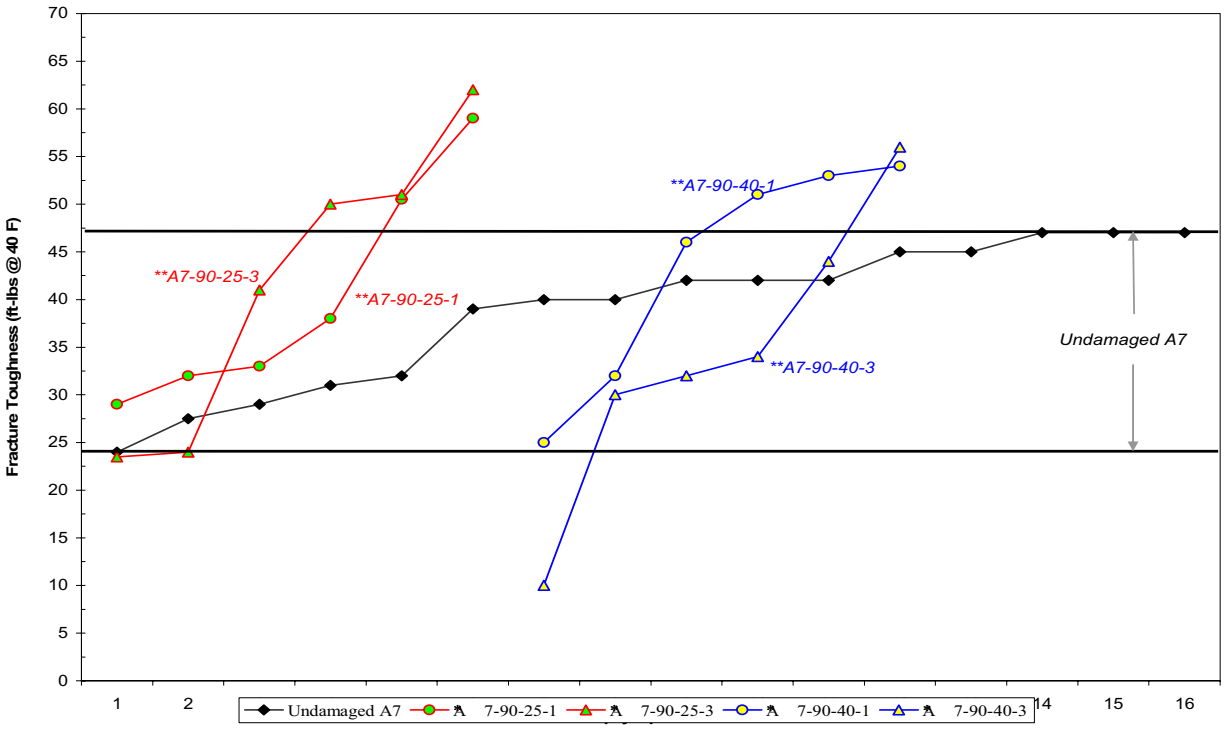

Figure 6.27
Fracture toughness comparisons of damaged-repaired A7-90 (ε_d=90 ε_y) specimens

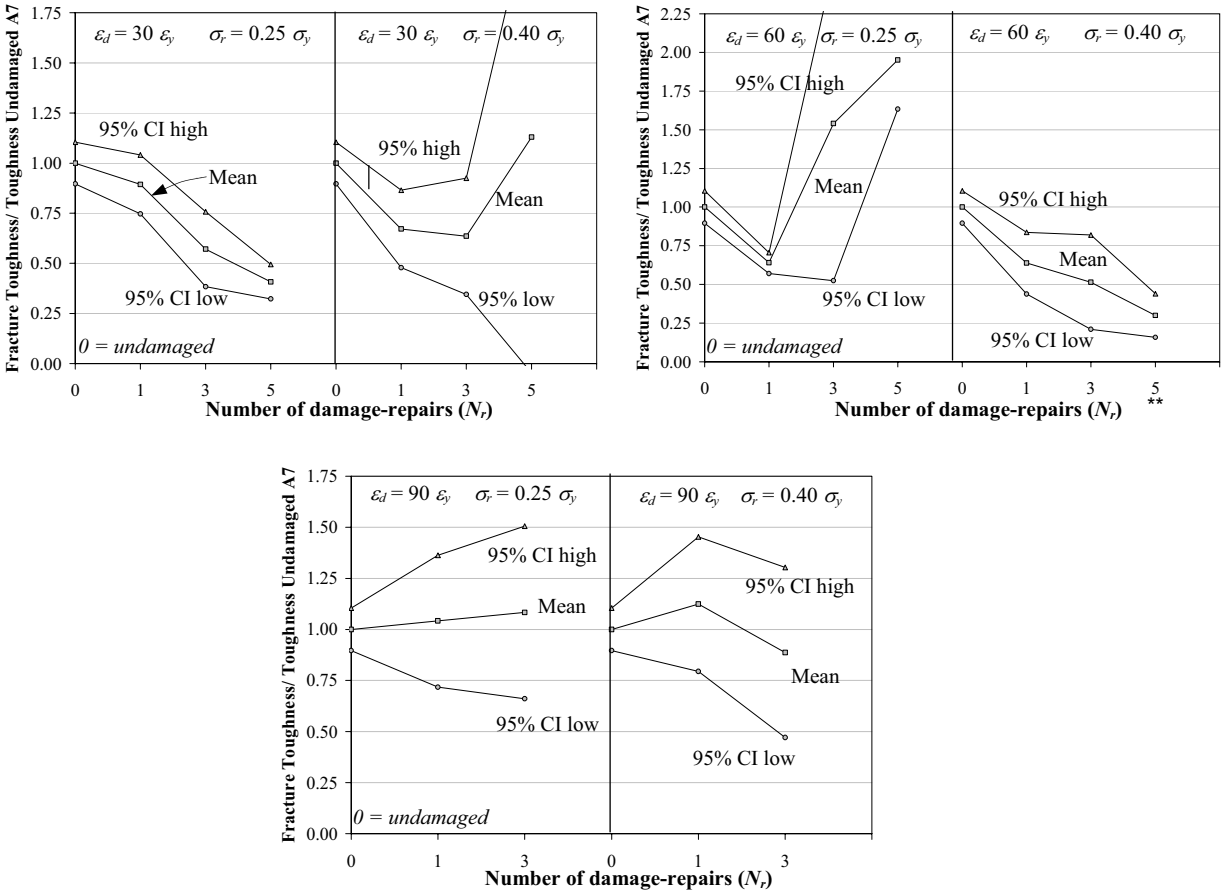

Figure 6.28
Normalized fracture toughness (mean and 95% CI) for damaged-repaired A7 specimens

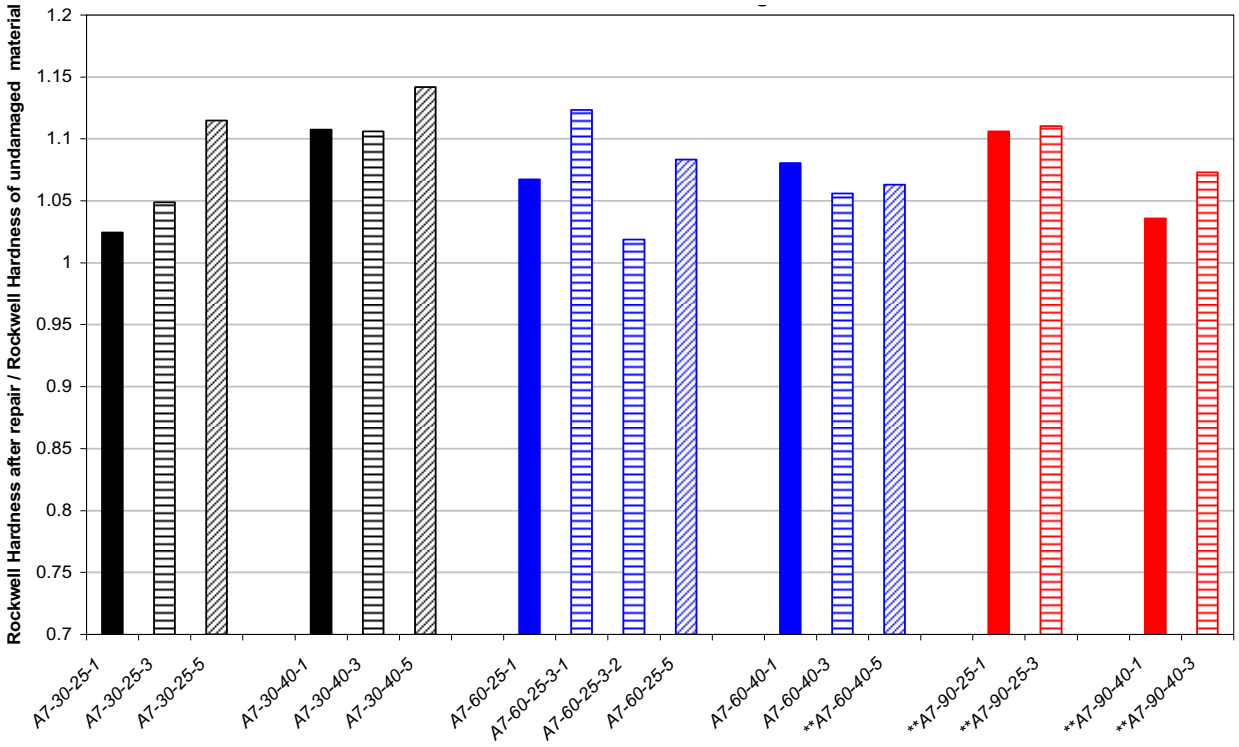

Figure 6.29
Normalized Rockwell hardness of damaged-repaired A7 steel

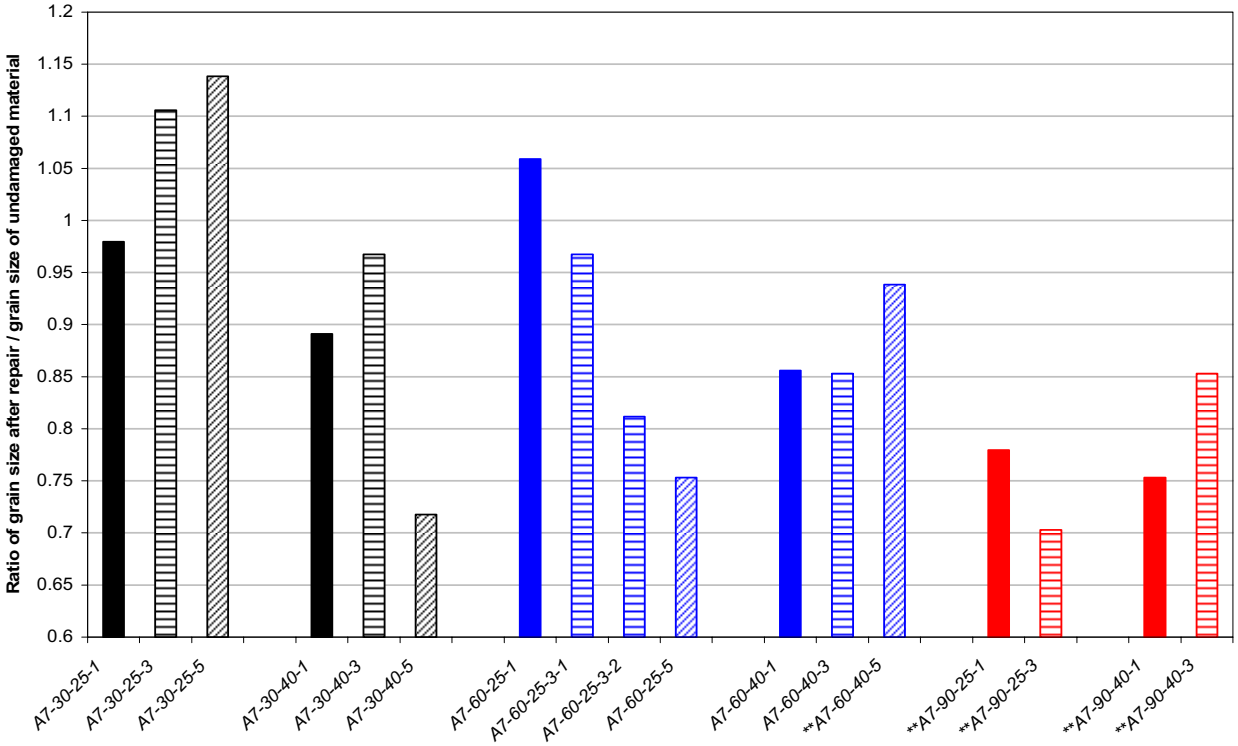

Figure 6.30
Normalized grain size of damaged-repaired A7 steel

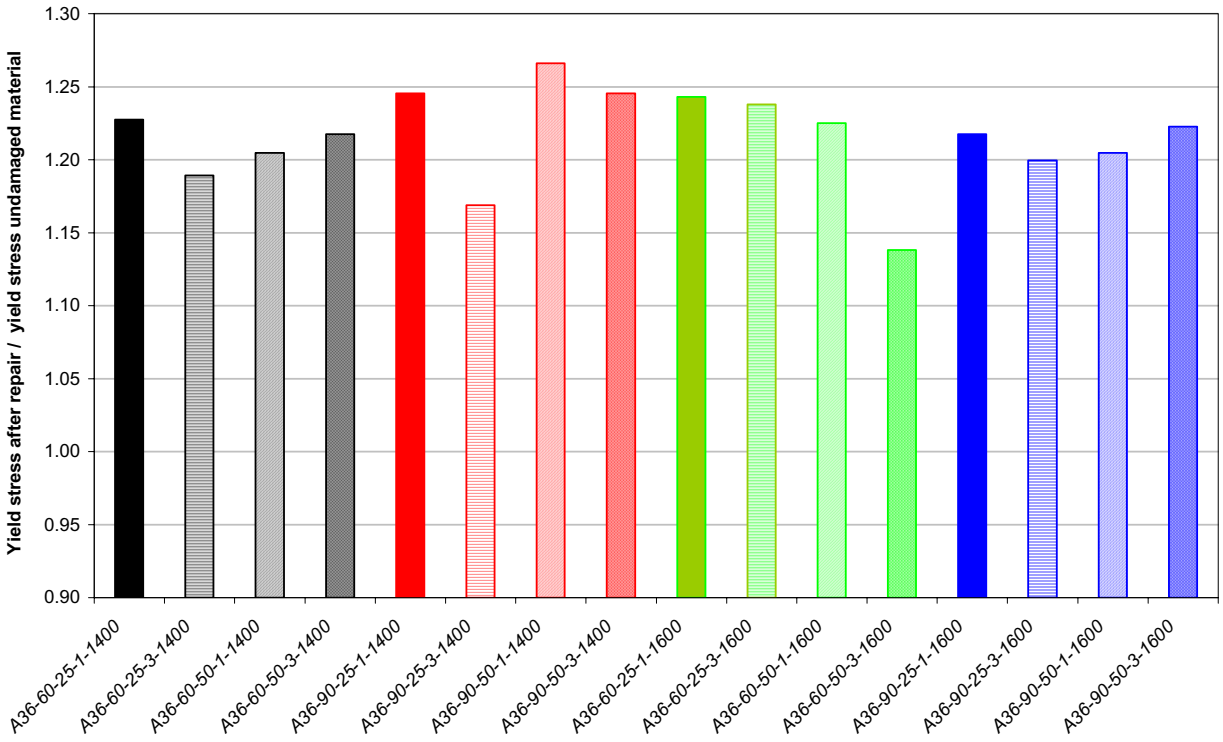

Figure 6.31
Normalized yield stress of damaged-repaired overheated A36 steel

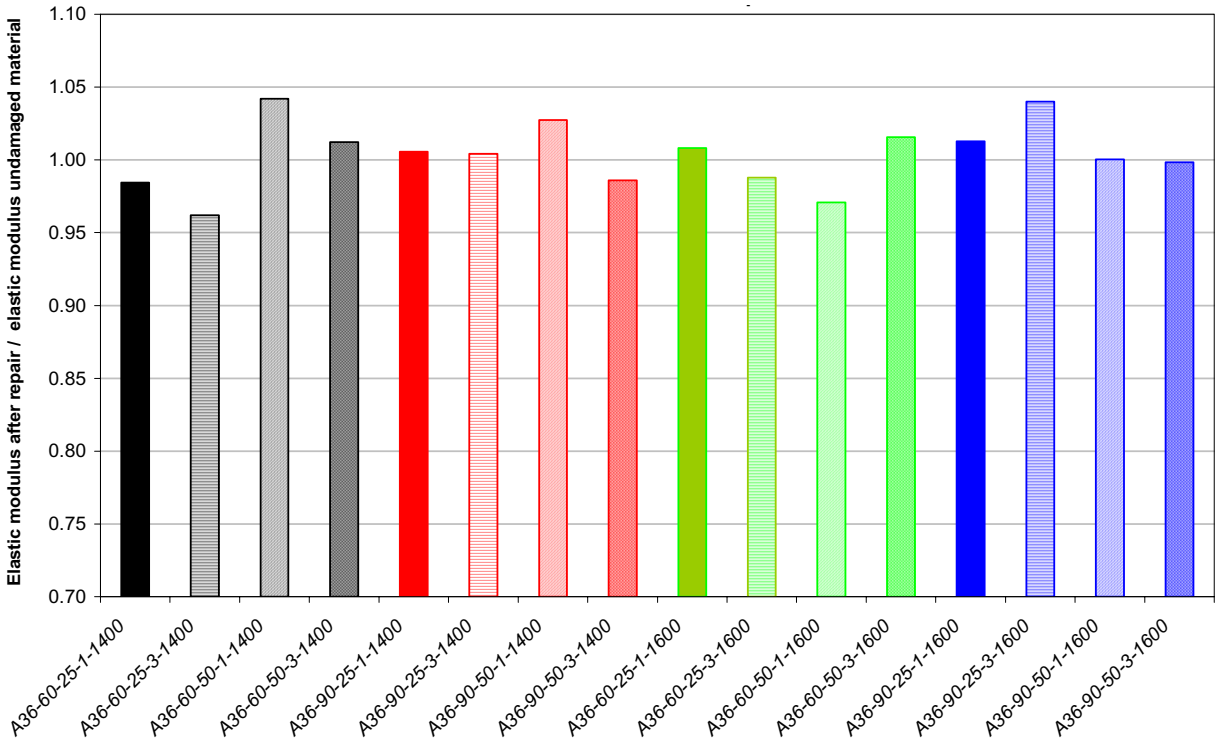

Figure 6.32
Normalized elastic modulus of damaged-repaired overheated A36 steel

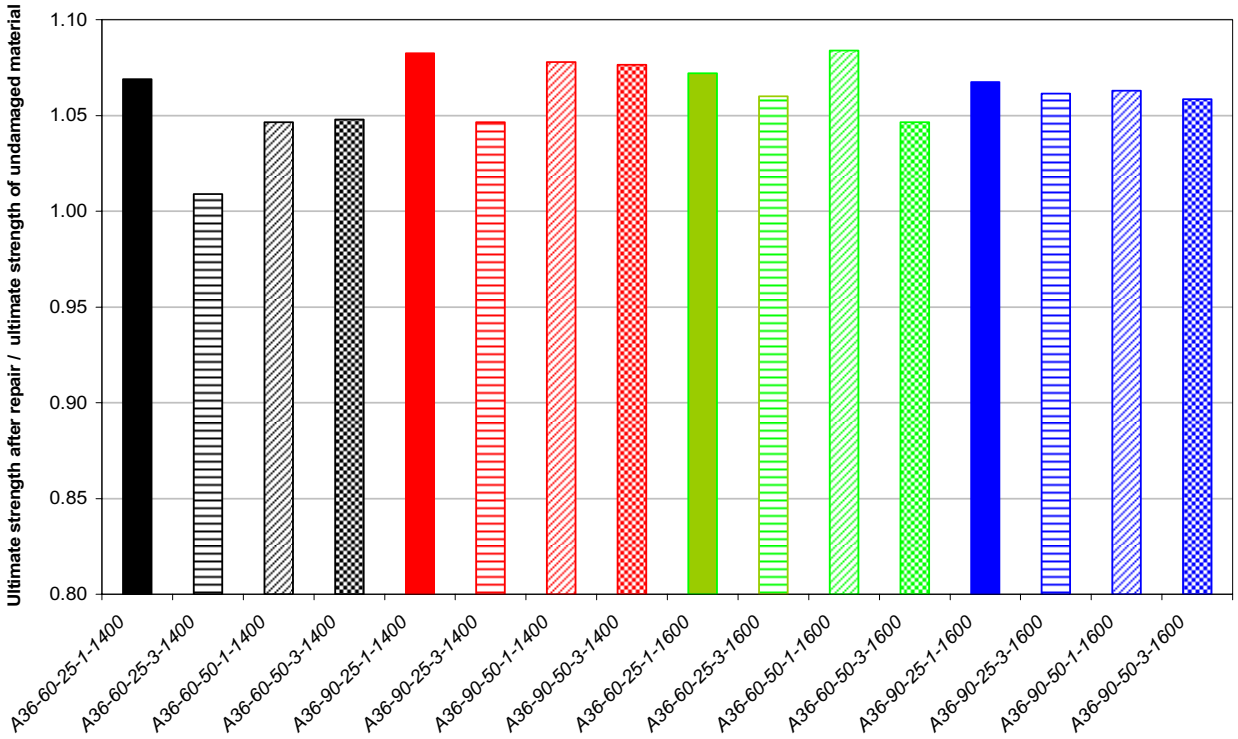

Figure 6.33
Normalized ultimate stress of damaged-repaired overheated A36 steel

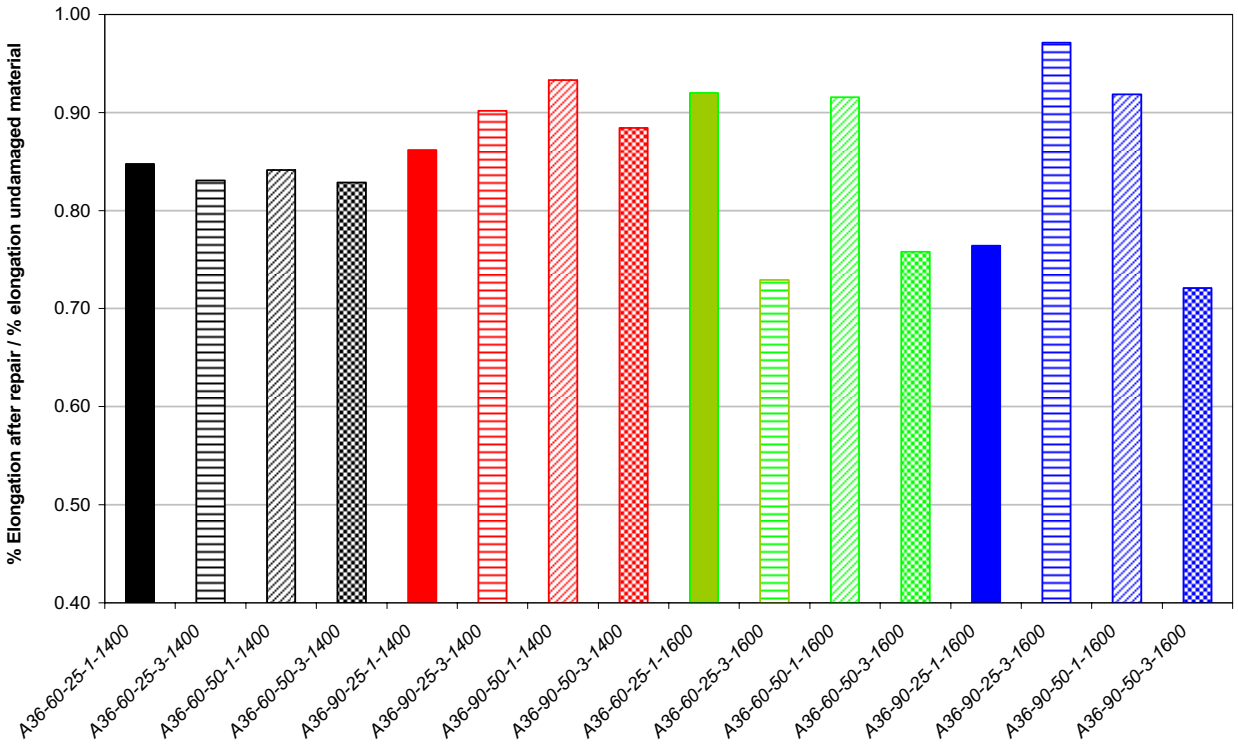

Figure 6.34
Normalized percent elongation of damaged-repaired overheated A36 steel

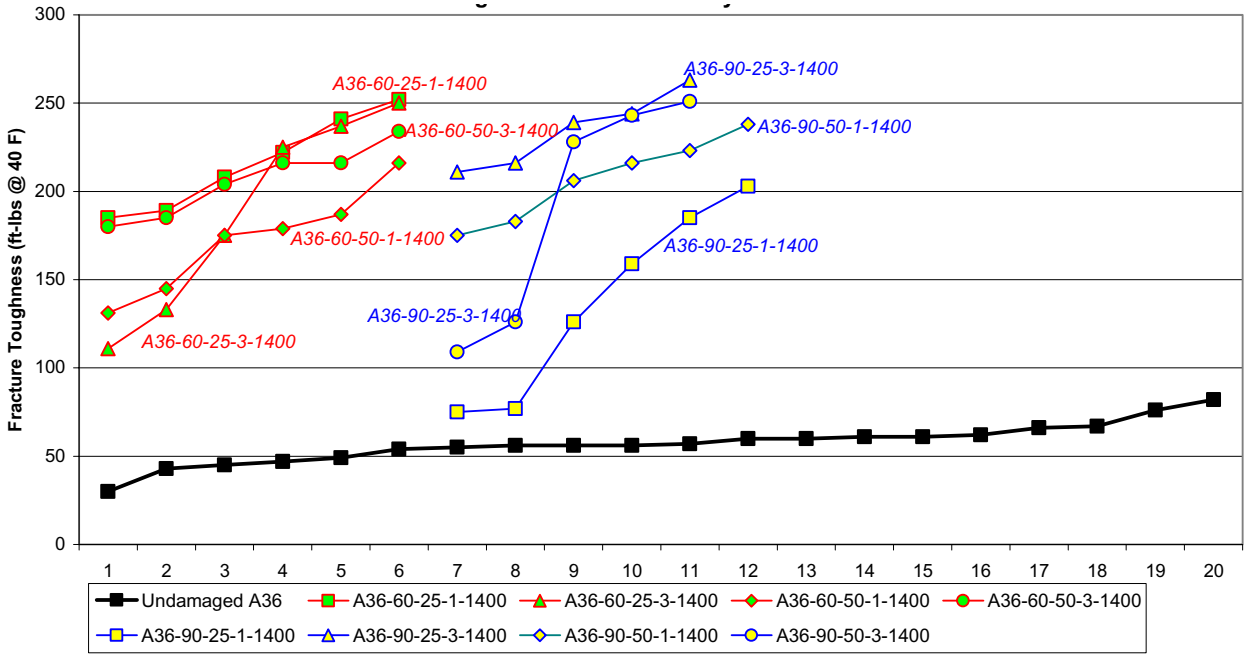

Figure 6.35
Fracture toughness comparisons of damaged-repaired A36 steel overheated to 1400 ºF

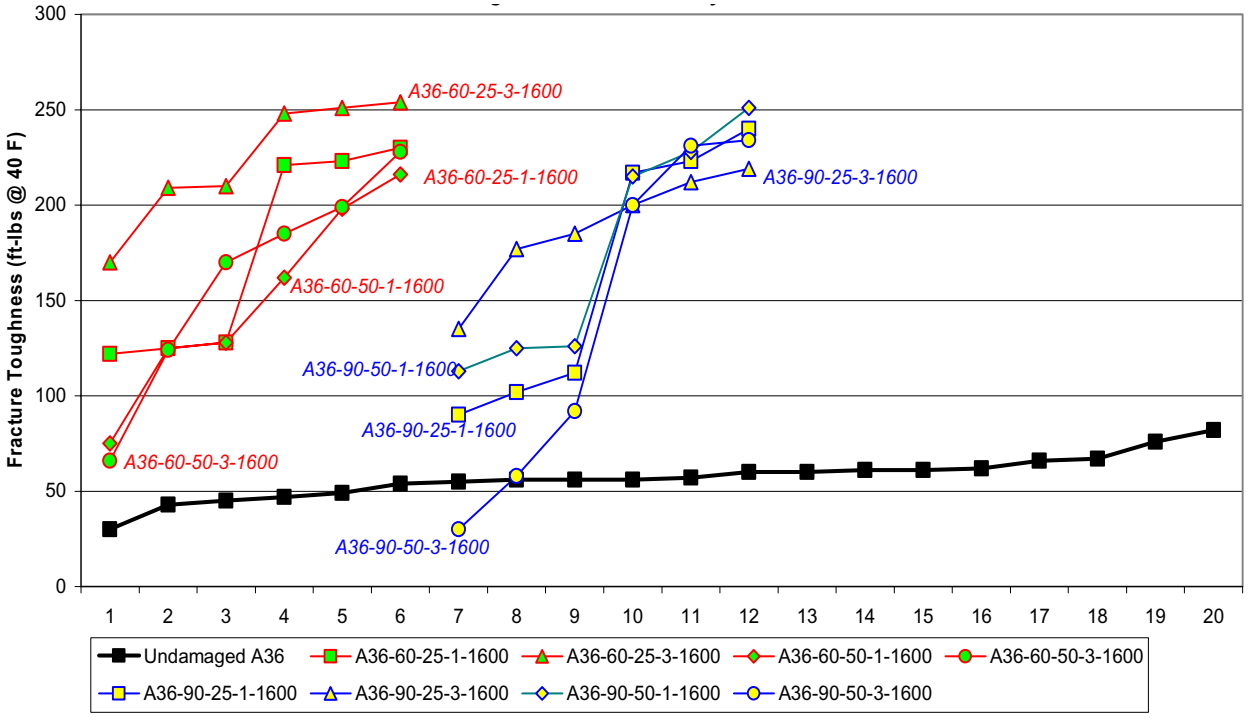

Figure 6.36
Fracture toughness values comparisons of damaged-repaired A36 steel overheated to 1600 ºF

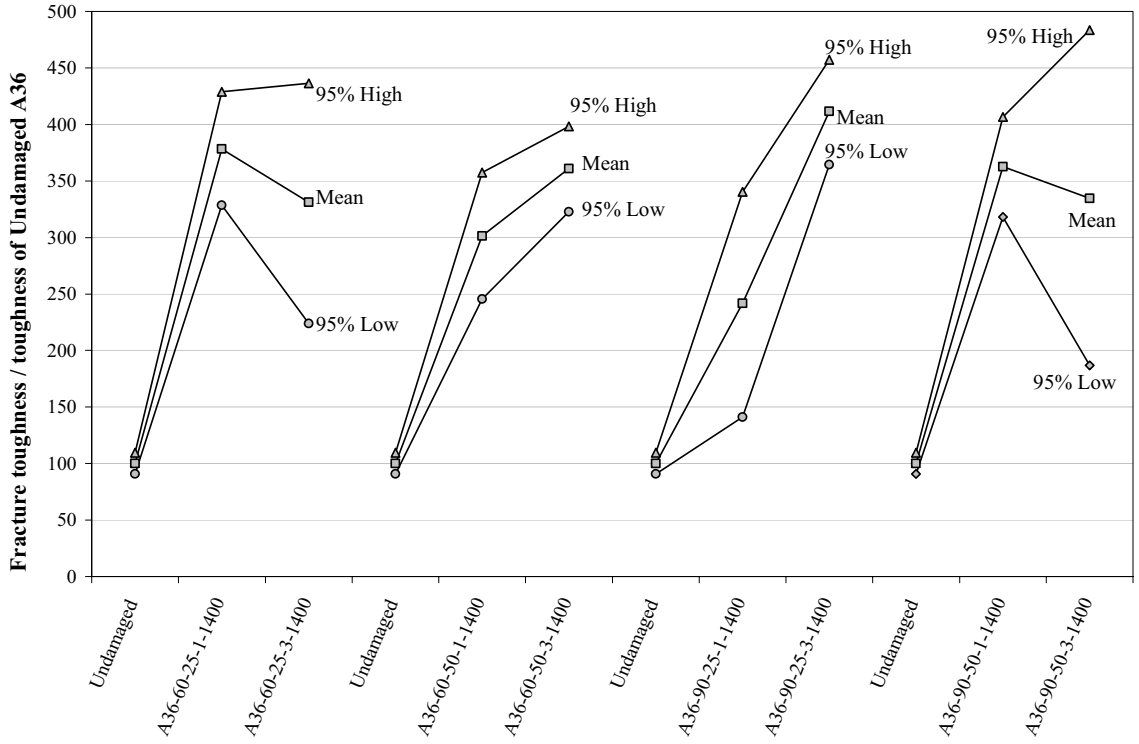

Figure 6.37
Normalized FT (mean and 95% CI) of damaged-repaired A36 steel overheated to 1400 °F

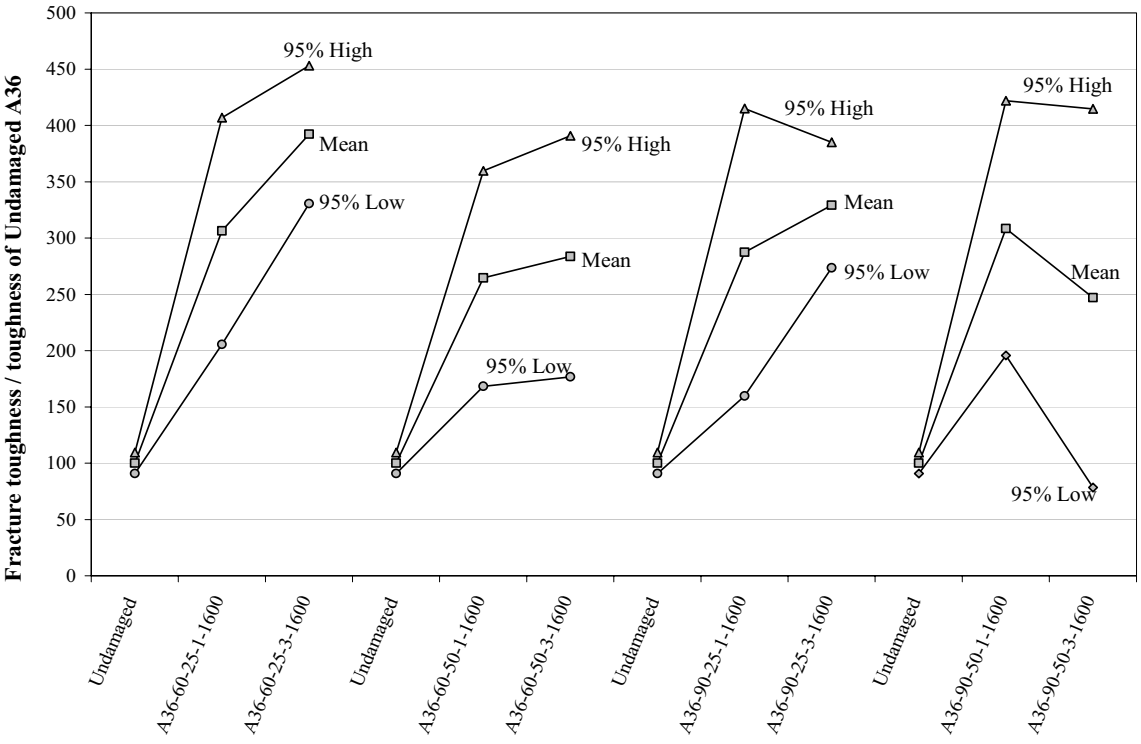

Figure 6.38
Normalized FT (mean and 95% CI) of damaged-repaired A36 steel overheated to 1600 °F

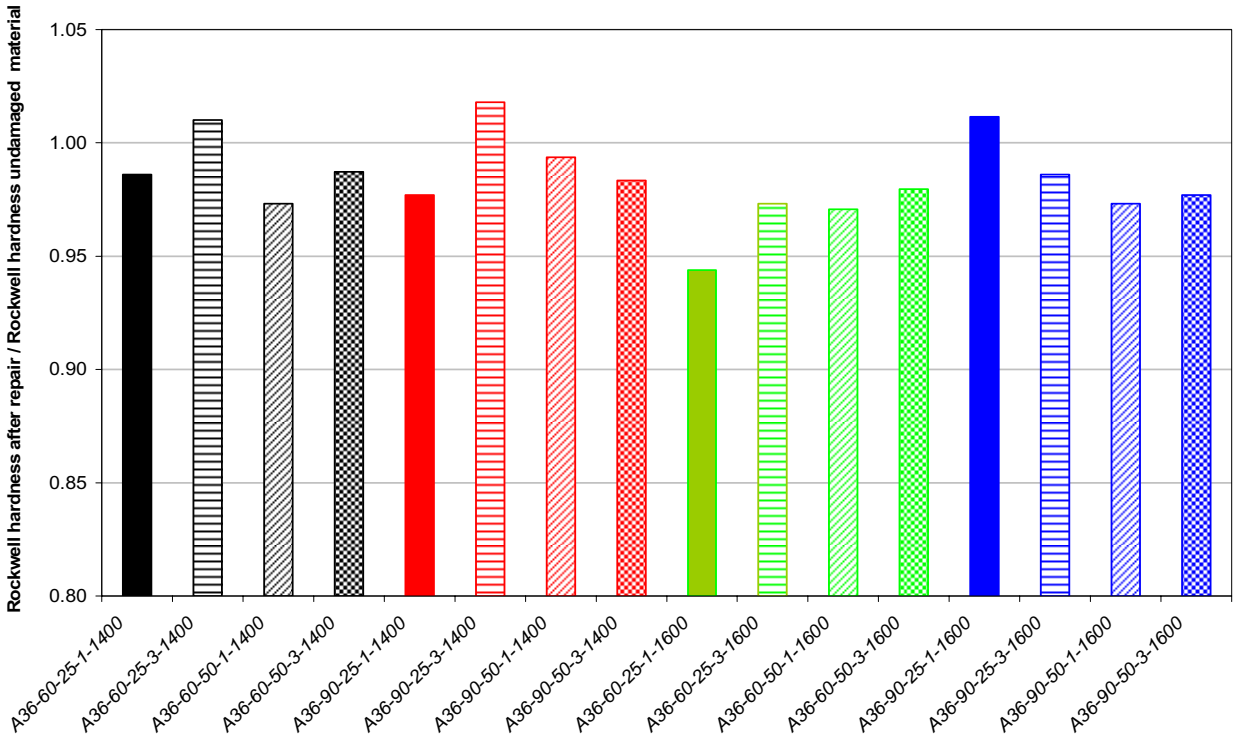

Figure 6.39
Normalized Rockwell hardness of damaged-repaired overheated A36 steel

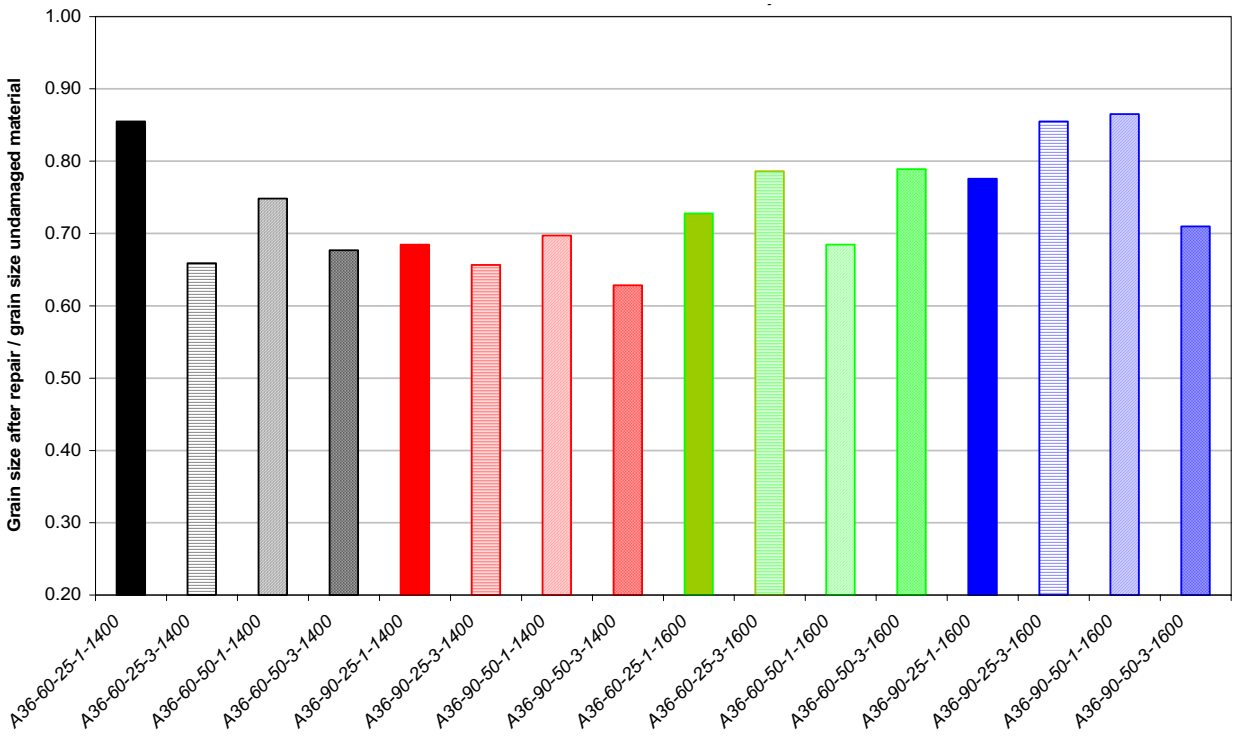

Figure 6.40
Normalized grain size for damaged-repaired overheated A36 steel

[Intentionally Blank Page]

7 EXPERIMENTAL INVESTIGATIONS OF LARGE-SCALE STEEL BEAMS

7.1 INTRODUCTION AND TASK IV OBJECTIVES

The results of Task III offered significant insight into the effects of multiple damage-heat straightening repair cycles on the structural properties of bridge steels. The results were used to develop recommendations for replacing steel beams subjected to multiple damage-repair cycles. These recommendations were evaluated by subjecting large-scale steel beams to multiple damage-repair cycles and determining the structural properties.

Multiple damage-heat straightening repair cycles were conducted on *six* large scale steel beam specimens made from each of the bridge steels studied in Task III. Two beams were made from A36 steel, two from A588 steel, and two from A7 steel. The A7 steel beam specimens were fabricated from one of the two decommissioned W24 x76 steel beams (see Section 4.5.2). The A36 and A588 steel beams were built-up (fabricated) from steel plates similar to the plates used to fabricate the Task III laboratory-scale specimens.

The analysis of the Michigan high-load hits database, presented in Section 2.3, indicated that composite wide-flange steel beams and composite steel plate girders are the most frequently damaged and repaired bridge structure types in Michigan. These structure types are damaged by an overheight truck colliding with the bottom flange of the steel fascia beam. The damage consists of out-of-plane or weak axis bending of the bottom flange combined with twisting of the overall cross-section. This damage is repaired by heat-straightening where several Vee heats are applied to the bottom flange and strip heats are applied to the web. The heat-straightening repair primarily consists of Vee heats applied along the length of the bottom flange. As presented in Sections 3.1.1, 3.1.2, and 3.1.3, all the steel bridges visited in Task II were damaged and heat straightened similarly.

The six steel beam specimens were damaged in weak axis bending (Category W damage) and repaired using several partial-depth Vee-heats along the lengths of both flanges. This damage-repair approach was used for the steel beam specimens for the following three reasons: (1) the damage and repair are similar to that of the bottom flange of a composite beam. (2) The weak axis bending or Category W damage is easier to conduct, control, and repeat in a laboratory type setting as compared to the composite beam damage. (3) Both flanges of the beam are subjected to identical damage-heat straightening repair, which provides twice the material for obtaining consistent material samples.

The steel beam specimens were roller supported at the ends and subjected to concentrated load at midspan to produce weak axis bending (Category W damage). The test setup simulated symmetric loading and boundary conditions, thus allowing the beam to deform freely.

The experimental test matrix for Task IV is summarized in Section 7.2 of this chapter. Section 7.3 describes the fabrication of the experimental beam specimens. Section 7.4 summarizes the experimental test setup. Section 7.5 describes the experimental damage-repair procedures and the instrumentation used to aid the procedures. Section 7.6 describes the material testing procedures on both undamaged and damaged-repaired beam specimens. The undamaged material testing results are provided in Section 7.6. Section 7.7 discusses an analytical fiber analysis procedure used to predict the stress and strain history induced within the experimental beam specimens. Section 7.7 also provides the damage strain-restraining stress history of each material sample removed from the damaged-repaired beam specimens.

7.2 LARGE-SCALE EXPERIMENTAL TEST MATRIX

The test matrix for the large scale investigations of Task IV is summarized in Table 7.1. Table 7.1 identifies each beam specimen by its name and presents the damage-repair histories. The specimens are arranged in the order of testing. Each beam specimen was subjected to three damage-repair cycles, where the damage and repair parameters are: the damage strain (ε_d), the restraining moment (M_r), and the maximum heating temperature (T_{max}). ε_d is defined as the longitudinal strain in the extreme tension fiber of the midspan cross-section. M_r is provided as a ratio of the minor-axis plastic moment capacity (M_p).

The experimental investigations of large-scale A7 steel beams focused specifically on the impact of damage strain and limited to three damage-repair cycles based on the conclusions and recommendations of Task III. The first A7 beam (A7-Beam 1) was subjected to a damage strain of 30 ε_y at the extreme tension fiber of the midspan cross-section for all three damage cycles. Restraining moments of 0.25 M_p, 0.50 M_p, and 0.25 M_p were used for repair cycles 1, 2, and 3, respectively. The second A7 beam (A7-Beam 2) was subjected to higher damage strains of 90 ε_y, 60 ε_y, and 60 ε_y for damage cycles 1, 2, and 3 respectively. The restraining stress of 0.50 M_p was held constant for all three repair cycles. A maximum temperature of 1200 °F was enforced for both A7 beams.

The first A36 beam (A36-Beam 1) was subjected to a damage strain (ε_d) of 30 ε_y for all three damage cycles. Varying restraining moments of 0.25 M_p, 0.50 M_p, and 0.25 M_p were applied for repair cycles 1, 2, and 3, respectively. The maximum heating temperature applied while repairing was strictly enforced to be 1200 °F. The experimental results of Task III indicated that subjecting the A36 steel to overheated temperatures benefited its fracture toughness results substantially. The mean fracture toughness of the damaged-repaired specimens heated to 1400 °F was approximately 330-415% of the undamaged toughness. The mean fracture toughness of the damaged-repaired specimens heated to 1600 °F was approximately 250-390% of the undamaged toughness. However, the recommendations limited the overheating temperature to 1400 °F to prevent surface pitting and excessive distortions. Therefore, the second A36 beam (A36-Beam 2) was subjected to three damage-heat straightening repair cycles with maximum heating temperatures of 1400 °F. The damage strains and restraining moments for each cycle of A36-Beam 2 were identical to those for A36-Beam 1. Thus, the only difference between the two beams is the heating temperature.

The experimental results of Task III indicated that A588 steel is an extremely resilient material with good fracture toughness after even five cycles of damage-heat straightening repairs. The restraining stress (σ_r) was found to have the most significant impact on the resulting fracture toughness of damage-repaired A588 steel. Lower fracture toughness values resulted from specimens repaired with a higher restraining stress of 0.50 σ_y. This comparison was consistent for specimens subjected to all three damage strains of 20 ε_y, 40 ε_y, and 60 ε_y. Other damage-repair parameters, namely the damage strain (ε_d), and the number of damage-repairs (N_r) did not have a direct or clear impact on the fracture toughness results. Hence, both A588 beams (A588-Beam 1 and A588-Beam 2) were subjected to damage strains of 40 ε_y, 20 ε_y, and 20 ε_y, for cycles 1, 2, and 3, respectively. A588-Beam 1 was subjected to a restraining moment of 0.25 M_p for all three repair cycles and A588-Beam 2 was subjected to a restraining moment of 0.50 M_p for all three repair cycles. A maximum heating temperature of 1200 °F was enforced for both A588 beams.

7.3 BEAM SPECIMEN DESIGN

7.3.1 A7 Experimental Beam Specimens

The A7 beam specimens were fabricated from one of the two decommissioned W24x76 A7 steel beams provided by the Michigan Department of Transportation (MDOT). The condition of the beam as received by the researchers was shown in Figure 4.14. The W24x76 steel beam has a depth of 23.9 in., a

base width of 8.99 in., and flange and width thicknesses of 0.68 in. and 0.44 in., respectively. The cross-section of the W24x76 steel beam is shown in Figure 7.1(a). The length of the A7 steel beam after removal of the end conditions was 23 ft. 3 in. A strip of 18 in. was removed from one end of the beam due to a significant denting of one of the flanges. A 3 ft. strip was removed from the center of the beam to obtain material coupons for testing to determine the undamaged A7 steel material properties. The two beams specimens were fabricated from either side of the undamaged material testing area as shown in Figure 7.2. The length of each beam specimen is 113.5 in and the center-to-center length between the end supports is 97 in. (8 ft. 1 in.).

Some fabrication of the beam specimens were required to develop the support and loading condition discussed later in Section 7.4. As explained later, the beam specimens were supported by 3 in. diameter steel shafts, passing through them (at the ends) and the support columns to simulate the roller support conditions. Hence, the webs of each beam specimen were coped (14.5 in. close to each end), and 3.0625 in. diameter holes are made in the flanges to allow the steel shafts to pass through the section at each support end. The last 2.25 in. of web from the ends of each beam was not removed to increase the stiffness between the two flanges. A 4 in. diameter hole was fabricated in the center of the web to allow the threaded rod from the loading frame to pass through. Figure 7.1 (b-c) provides the fabrication details for the A7 beam specimens to be tested.

7.3.2 A36 and A588 Experimental Beam Specimens

The experimental test setup (discussed in more detail in Section 7.4) was designed to be capable of damaging and repairing the W24x76 steel beam for all steel grades. Therefore, the dimensions of the built-up A36 and A588 steel sections related similar to that of the W24x76 section. The A36 and A588 steel beams were fabricated from 20 ft. (240 in.) steel plates. The plates used for the flanges were 9 in. wide and 0.75 in. thick. The plates used for the webs were 21 in. wide and 0.50 in. thick. The total depth of the built-up section is 22.5 in. The 3/8 in. fillet welds which connect the beam flanges and web were made using E70XX electrodes. The built-up cross-section is shown in Figure 7.3(a). The webs used for all beams were fabricated from A36 due to the lack of availability and expense of a 21.0 in. wide and 0.5 in. thick A588 plate.

Additionally, two-ft. were removed from each flange and web plates and welded together to form shorter built-up sections. Material samples for determining the undamaged material properties were obtained from these shorter sections. The lengths of the beam specimens are 108 in. The center-to-center length of the beams between the end supports is 97 in. (8ft. 1 in.). Some fabrication of the beam specimens were required to develop the support and loading condition discussed later in Section 7.4. As explained later, the beam specimens were supported by 3 in. diameter steel shafts, passing through them (at the ends) and the support columns to simulate the roller support conditions. The webs of the beam specimens are coped (14 in. at each end), and 3.0625 in. diameter holes are fabricated in the flanges to allow the steel shafts to pass through the section at each end. A 4 in. diameter hole was fabricated in the center of the webs to allow the threaded rod from the loading frame to pass through. Figure 7.3 (b-c) provides the fabrication details for the beam specimens to be tested.

7.4 TEST SETUP DESIGN AND FABRICATION

Two specially designed built-up steel columns provided support reactions to the beam specimens. Each column was fabricated from two C10x20 channel sections, which were welded together using ¼ in. batten plates to form a rectangular section. The built-up columns were welded to each ½ in. thick base plate, which was post-tensioned to the laboratory strong floor with a force of 140 kips. Figure 7.4 shows the details of the column supports. A photograph of the fabricated column is shown in Figure 7.5.

The beam specimens are supported by 3 in. diameter steel shafts, which pass through the flanges of the beam and the webs of the built-up steel column. These shafts pass through slotted holes fabricated in

the webs of the built-up steel column. The dimensions of the slotted hole are 3.0625 x 4.5625 in [see Figure 7.4(b)]. The additional 1.5 in. width of the slotted hole allows the shaft to translate laterally and act as a roller support. The center-to-center distance from the slots of the two columns is 96 in. (8 ft.). Therefore, the 97 in. beam specimens are free to translate 1.25 in. at each support. The ends of the 3 in. steel shafts were threaded so that structural nuts could be used to secure the shafts to the setup as a safety precaution. The column supports and steel shafts were fabricated from A36 steel.

A specially designed loading frame was used to apply the concentrated force at the beam midspan during the damage and heat straightening repair cycles. The loading frame was designed to apply forces in both the upward and downward directions, i.e., the damaging force in the upward direction (pushing up) and the restraining force in the downward direction (pulling down). The forces were applied using a double-acting hydraulic actuator, which was bolted to a bottom beam post-tensioned to the laboratory strong floor with a force of 100 kips. One end of a 2.5 in. high strength threaded rod was threaded into the plunger of the hydraulic actuator. The other end is fixed to a small built-up loading beam using structural plates and nuts. Figures 7.6(a) shows a schematic of the loading frame. Figure 7.6(b) shows a photograph of this part of the setup. The loading beam is a built-up section with two webs designed for a total section modulus of 21.7 in^3. It is used to apply the concentrated damaging and restraining forces to the beam midspan. The damaging (upward) force is applied by the hydraulic actuator pushing the loading beam against the flanges of the W24x76 (or equivalent) beam specimen being tested. Two semi-circular shafts provide bearing contact between the loading beam and the flanges of the specimen being tested. The shafts allow the specimen to rotate freely with respect to the loading beam at the point of contact. Figure 7.7 shows a drawing of the loading condition from the side view. Additional details of the loading beam including elevation and plan views are shown in Figure 7.8(a – b).

The restraining (pulling downward) force during heat straightening is applied using the loading beam and additional attachments. The additional attachments consist of two 4 x 29 x 1 in. steel plates. Each steel plate is connected to the loading beam using two 0.75 in. threaded rods. The steel plates bear against the top of the flanges of the W24x76 (or similar) beam specimen as shown in Figures 7.6 and 7.7. Two semi-circular shafts are used with each steel plate to provide the bearing between the plates and the two flanges of the specimen being tested. The restraining force is applied by the hydraulic jack pulling the loading beam downwards. Thus, the restraining force is applied as two equal concentrated forces acting at a distance of 4.8 in. on either side of the beam midspan. This was the closest the setup could acquire to applying one concentrated force at the midspan. The midspan Vee-heat was applied in between the threaded rods applying the concentrated forces at midspan during repair.

Figures 7.9 and 7.10 show photographs of the completed test setup with the first W24x76 A7 steel beam (A7-Beam 1) in place, ready to be tested. These photographs identify the supporting columns, loading beam, hydraulic actuator, and the beam specimen.

7.5 INSTRUMENTATION AND EXPERIMENTAL PROCEDURE

7.5.1 Instrumentation

This section describes the instrumentation layout used while damaging and heat straightening the beam specimens. Several instruments that are being used include: (a) pressure transducers for measuring loads, (b) displacement transducers for measuring deflections, (c) rotation meters for measuring end rotations, (d) infrared thermometer for measuring surface temperatures, and (e) strain gages to measure longitudinal strains. Additionally, punch mark sets are made on the specimen flanges and the distances between them are measured to further determine the longitudinal strains. All these are described below after defining the terminology used to address the orientations and locations on the beam specimens.

The following terminology (i.e. front and back, left and right, top and bottom) addresses the orientation of the beam specimen. The front of the beam is considered to be the side where the graduate

researcher applies the Vee-heat. Figure 7.9 shows the front of the beam and Figure 7.10 shows the back of the beam. The front of the beam corresponds to Flange B and the back of the beam corresponds to Flange A as shown in Figures 7.9 and 7.10. The left and right sides are distinguished by looking at the setup from the front of the beam. The bottom of the beam is defined where the semi-circular shafts bear against the flanges while damaging. The top of the beam is referred to as the tension side. It is also the region where the Vee-heats are applied.

Pressure Transducers:

Two pressure transducers were used within the hydraulic network. One transducer measured the pressure when the hydraulic actuator pushes upwards (advance mode) and the specimen is being damaged. The force acting on the beam was computed as the measured pressure multiplied by the cylinder area in advance mode specified by the manufacturer (21.63 in^2) and verified (calibrated) by the MSU researcher. The second transducer measured the pressure when the hydraulic actuator pulls downwards (retract mode) and the specimen is being heat straightened. The restraining force acting on the beam was computed as the measured pressure multiplied by the cylinder area in retract mode specified by the manufacturer (13.54 in^2) and verified (calibrated) by the MSU researcher.

Longitudinal Strain Gages

Six strain gages are used to measure the longitudinal strains in the beam specimens during the damage cycles. These strain gages are located at the midspan cross-section of the beam specimen, which also coincides with the location of the damaging force. Three strain gages are bonded to each flange of the steel beam at the midspan section. On each flange, one strain gage is bonded at the top, one strain gage is bonded 3.0 in. ($b_f / 3$) from the top, and one strain gage is bonded 1.5 in. ($b_f / 6$) from the bottom. The strain gage orientation is shown in Figure 7.11. The strain gages at the top of the flanges are used to monitor the magnitude of the damage strain (ε_d) during the first damage cycle of each beam specimen. The bottom strain gages are located 1.5 in. from the bottom of the flange to avoid distortion effects due to stress concentrations at the point of loading. The intermediate strain gage (3.0 in. from the top) along with the top and bottom gages establishes a linear strain distribution over the cross-section. These strain gages help to estimate longitudinal strains over the cross-section.

Rotation meters

The end rotations of the beam specimen are measured using four rotation meters, where two rotation meters are placed on either flange and at each end of the beam specimen. These rotation meters are located approximately 6 in. from the support (rotation) points. For example, Figure 7.12 shows the location of a rotation meter with respect to the rotationally free end support for the specimen. These four rotation meters are used to monitor the magnitude and symmetry of the beam end rotations during the damage and heat straightening repair cycles. Since curvatures within the end 6 in. is very small, the difference in actual end rotation and the measured values are almost negligible. The MSU researchers initially intended to use two additional rotation meters to measure the relative rotation of the midspan plastic hinge during the damage and heat straightening repair cycles (refer to Figure 7.9). This would provide a better estimate of the magnitude of repair during each heating cycle. However, problems occurred with the rotation meters becoming too hot during the repair cycles regardless of various insulation techniques attempted.

Displacement transducers

Displacement transducers were used to measure the deflections of the beam specimen during damage and repair cycles. Deflections were measured at the beam midspan and at the quarter points along the length of the beam, which are located 2 ft. from the end supports.

- The midspan deflection was measured using two 12 in. stroke displacement transducers that were placed on either side (front and back) of the beam at midspan. The jig used to connect the

displacement transducers to the beam midspan of the beam is shown in Figure 7.13. The transducers were tied to small steel brackets clamped to the loading beam while damaging [Figure 7.13(a)] and to the bottom of flanges while repairing [Figure 7.13(b)].

- The quarter point deflections were measured using two 6 in. stroke displacement transducers that were placed on either side (right and left) of the beam midspan. The location of these displacement transducers in respect to the test setup are shown in Figures 7.14 and 7.15.
- Thus, a total of four displacement transducers were used. They provided deflection measurements at midspan and quarter points during the various damage and repair cycles.
- The displacement transducers also serve as guides for establishing the completion of heat straightening repair. For multiple damage cycles, they determine the magnitude of damage (explained in Section 7.5.2).

Infrared Temperature Thermometer:

An infrared thermometer was used to measure the time-temperature response of the heated steel beam specimen. This non-contact thermometer was placed perpendicular and away from the heating surface. Figure 7.16 shows a picture of the infrared thermometer away from the heating surface.

Digital caliper and punch marks

The digital caliper was used to measure average longitudinal strains at various locations along the length of the beam. The method is performed for each point by: (1) making punch marks in the beam specimen, (2) measure the original length between punch marks, (3) measure the length between punch marks after damage or repair, and (4) calculate the approximate strain as change in length divided by original length. A total of 20 punch mark sets were made on the flanges of the beam specimens. Ten punch mark sets were made on each of the two flanges of the beam specimens. These included punch mark sets at the midspan (both at the top and bottom of each flange), and at the top of Vee heats R1, R3, R5, L1, L3, and L5, which are explained further in Section 7.5.3.

7.5.2 Experimental Damage Procedure

To subject the beam specimen to the damage magnitude, the hydraulic actuators are set to advance mode. This lifts the loading frame and subjects the beam specimen to bending stresses. Hydraulic oil is pumped out of a 20-series electric pump into the bottom of the hydraulic core actuators. The area of the bottom piston within the hydraulic jack as specified by the manufacturer is 20.63 in^2. With the pressure known, the force acting on the beam is computed using Equation 7.1. This equation was verified (calibrated) earlier by the MSU research team.

$$P_i \text{ (kips)} = \text{pressure (psi)} * 20.63 \text{ (in}^2\text{)} / 1000 \qquad (7.1)$$

The damage of the beam specimen during the first damage cycle was monitored using longitudinal strain gages attached to the top of each flange as shown in Figure 7.11. The load was increased slowly until the strain readings from the top of each flange averaged the required damage strain. The required magnitude of damage strain ε_d was determined from using the measured yield strain ε_y of the undamaged steel as summarized later in Section 7.6.7.1. The researchers planned on using similar longitudinal strain gages for subsequent damage cycles. However, the repaired beam flanges developed small out-of-plane distortions, which resulted in poor strain gage readings. Hence, the subsequent damage cycles after the first one were controlled using the midspan displacement and verified using the quarter displacements and end rotations. The midspan deflections, quarter-span deflections, and the end rotations during the first damage cycle were noted carefully. Subsequent damage cycles were completed when the instruments changed in magnitude with respect to the required amount as interpreted using the measurements from the first damage cycle.

7.5.3 Experimental Repair Procedure

Application of an external restraining stress

Heat straightening repair cycles were conducted by applying an external restraining moment (M_r) of 0. 25 M_p or 0.50 M_p. M_p is the plastic moment capacity of the section about the minor axis of bending. M_p is calculated using Equations 7.2, 7.3, and 7.4 for A7, A36, and A588, respectively, where Z_y is the minor-axis plastic section modulus and σ_y is the measured yield strength of the material. The values of in Equations 7.2, 7.3, and 7.4 for σ_y were determined from uniaxial tension tests conducted on the undamaged material summarized in Section 7.6.1.1.

$$M_p = Z_y \text{ x } \sigma_y = 28.6 \text{ x } 36.6 = 1058.2 \text{ kip-in} \quad \text{(A7)} \tag{7.2}$$

$$M_p = Z_y \text{ x } \sigma_y = 31.7 \text{ x } 46.0 = 1458.2 \text{ kip-in} \quad \text{(A36)} \tag{7.3}$$

$$M_p = Z_y \text{ x } \sigma_y = 31.7 \text{ x } 58.5 = 1854.5 \text{ kip-in} \quad \text{(A588)} \tag{7.4}$$

In applying an external restraining force, hydraulic oil was pumped out of a 20-series electric pump into the top of the hydraulic core actuators. The actuator pulls down on the loading frame. The half-circular shafts contact the flange at points approximately 4.8 in. from the beam center (refer to Figures 7.6 and 7.7). The area of the bottom piston within the hydraulic jack is 13.54 in^2. With the pressure known, the force in the actuator was computed in Equation 7.5. This equation was verified (calibrated) by the MSU research team.

$$\text{P (kips)} = \text{pressure (psi)} * 13.54 \text{ (in}^2\text{)} / 1000 \tag{7.5}$$

The maximum moment applied to the beam was computed assuming that one concentrated force was applied at midspan. The moment at midspan was computed as:

$$M = \frac{PL}{4} \tag{7.6}$$

As presented later, Vee heats were also applied at locations away from midspan. The moment at each of the Vee heat locations was computed using the load *P*. The load required to subject the beam to the level of restraining moment at the center of the Vee heat being heated was applied.

Application of Vee heats along length of the beam

Heating cycles were performed using 5/8 in. diameter oxy-acetylene heating torches. Two researchers used two oxy-acetylene torches and applied Vee heats to both flanges of the beam test specimens. The temperature at the surface of the steel was monitored using an ST80 infrared temperature gun as introduced in Section 4.7.2. Heat-straightening was practiced while maintaining the surface temperature between 1100 ºF and 1200 ºF with the exception of A36-Beam 2 which was practiced to overheating of approximately 1400 ºF. Initially, a spot heat is applied to the apex of the Vee until the desired temperature is reached. The torch is moved in a serpentine path from the apex to the edge of the flange to apply the Vee heat.

Figure 7.17 shows the locations of multiple, overlapping Vee heats used to straighten the damaged beam specimens. These Vee heats are within the center 40 in. length of the beam specimen subjected to plastic strains. The nomenclature used to identify the individual Vee heats is also shown in the figure: the Vee heat located at midspan is identified as C; the Vee heats left of the midspan are L1, L2, L3, L4, and L5, respectively; and the Vee heats right of the midspan are R1, R2, R3, R4, and R5, respectively. In some cases, the researcher also applied Vee heats outside to L6, R6, L7, and R7 if needed. This nomenclature is the same for Vee heats located on either flange (front or back) of the beam specimen, i.e., L1 on the front flange is directly opposite to L1 on the back flange. The Vee heat locations and emphasis (repetitions) of each was aided using a plastic damage region analysis which is described later in Section 7.7.2. Some important details of the Vee heating are indicated below:

- Heat straightening was conducted by heating the same Vee on both flanges simultaneously. Therefore, two persons are heating directly across from each other, and are required to conduct a heating cycle on the damaged specimen.
- The depth and width of each Vee are equal to 4.5 in, which corresponds to a Vee angle of about 53^o. These Vee heats are geometrically similar to those used by the Statewide Bridge Crew (SBC). The observations and discussions in Task II (Chapter 3) indicated that the SBC uses half-depth Vees with a width of 5.0 in, which typically results in a Vee angle of about 50^o.
- As indicated in Figure 7.17, Vee heats could not be applied close to the restraining load application points, i.e., the points of contact between the steel plates and flanges while heat straightening.

Significant Data Collection during Experimental Investigations

The researchers kept a well organized table of the instrument history for each beam specimen. An example is provided in Table 7.2, which shows the history of the four rotation meters and the four displacement transducers. For the rotation meters, F_L represents Rotation_Front_Left, etc. In Table 7.2, "Contact" represents the point when the setup begins to load the beam. Due to gaps in the test setup, the "Contact" was recorded when the load reached 1 kip, for consistency. The "full damage" represents the amount of movement at the maximum damage load which was recorded such that multiple damage cycles could be completed when the amount of displacements and rotations are equivalent to the first damage cycle. The "plastic damage" represents the amount the researchers have to repair. This table represents the complete damage-repair history of A7-Beam 1.

7.6 MATERIAL TESTING PROCEDURES

7.6.1 Undamaged Material Testing Procedures and Results

This section summarizes the material testing conducted on undamaged steels. These results are compared to the results obtained from the damaged-repaired experimental beam specimens. The material tests included: (a) uniaxial tension tests, (b) fracture toughness tests, (c) hardness tests, and (d) microstructure inspection. As mentioned previously, the A7 steel beam was a W24 x76 and the A588 and A36 steel beam were built up-sections. Samples were taken out of the flanges of the A7 beam and from the plates used for the flanges of the built-up sections.

The original length of the W24x76 A7 steel beam was 23 ft. 3 in. A 3 ft. strip was removed from the beam at the center. Undamaged material testing was conducted by taking samples from this strip. The two beam specimens were fabricated from either side of the undamaged material testing area as shown in Figure 7.2. The plates used for the built-up A36 and A588 steel sections were 20 ft. long. 2 ft. strips were removed from the center of the plates. Undamaged material testing was conducted by taking samples from these strips. The two experiment beams specimens were fabricated from either sides of the undamaged material testing area.

Due to possible variations in the material properties, each side of each flange segment was specified as 1A, 2A, 1B, or 2B. The nomenclature was later altered to TA, BA, TB, and BB where "TA" would represent the top of Flange A (Vee heated side of the back flange). As mentioned previously, when placed in the test setup, the back of the beam refers to Flange A and the front of the beam refers to Flange B. Variability in material properties was evaluated by comparing the results of the uniaxial tension tests and charpy v-notch fracture toughness conducted on samples taken from flange segments TA, BA, TB, and BB.

7.6.1.1 Uniaxial Tension Tests on Undamaged Steel Plates

Four uniaxial tension test coupons were fabricated from the flange segments TA, BA, TB, and BB (one per segment for each steel type). The material coupons were removed within 1 in. of the edge of the flanges as shown in Figure 7.18. The tension coupons were flat bar-type specimens with standard ASTM dimensions as shown in Figure 7.19. These coupons were tested according to ASTM E8 standard.

The resulting uniaxial tension stress-strain (σ–ε) curves for the undamaged A7 steel are shown in Figure 7.20. The corresponding material properties as described in Section 4.9.1(yield stress, elastic modulus, etc.) are summarized in Table 7.3. Table 7.3 and Figure 7.20 indicate that the variability in flange segment (TA, BA, TB, and BB) material properties is insignificant. Table 7.3 also provides the average material properties of all four coupons which will be used for comparisons to the results from damage-repaired steel.

The resulting uniaxial tension σ–ε curves for undamaged A36 steel are shown in Figure 7.21. The corresponding material properties are summarized in Table 7.4. Table 7.4 also provides the average structural properties from each plate (A or B) and also the overall average structural properties. The results of the two material coupons fabricated from each plate (i.e., 1A and 2A or 1B and 2B) related extremely well to each other. Therefore, each test was considered to be validated and further tests were not required. Flange A has a higher yield strength and tensile strength as compared to Flange B. Flange B exhibited a slight increase in ductility. These discrepancies between the two flange plates were considered for the comparisons to experimental results of damage-repaired A36 steel. As explained later, tension coupons were fabricated only from Flange A of the damaged-repaired steel beam specimens. Hence, only the undamaged tension test results of Flange A are required for further comparisons. The overall average structural properties were only used for determining the required damage strain (ε_d) and for applying the external restraining moment (M_r).

The resulting uniaxial tension σ–ε curves for the undamaged A588 steel are shown in Figure 7.22. The corresponding material properties are summarized in Table 7.5. Table 7.5 also provides the average structural properties from each plate (A or B) and also the overall average structural properties. The ultimate stress of flange segment BA was slightly higher (1 ksi) than the ultimate stress of other flange segments. Other than this slight discrepancy, Table 7.5 and Figure 7.22 indicate that the variability in flange segment (TA, BA, TB, and BB) material properties is insignificant. Therefore, the average values of all structural properties will be used for comparisons to damaged-repaired specimens.

7.6.1.2 Charpy Impact Fracture Toughness Tests on Undamaged Steel

Charpy specimens were fabricated from the four flange segments of each undamaged steel type. Five (A36 and A588) or six (A7) mid-thickness charpy specimens were fabricated from each of the flange segments 1A, 2A, 1B, or 2B with the grain orientation shown in Figure 7.22. As shown in Figure 7.22, all specimens were originally located within 3.00 in. from the flange edges. The results of the fracture toughness tests on undamaged A7 steel are summarized in Table 7.6.

Student's t-test analysis was conducted to evaluate the statistical difference between the A7 fracture toughness results from: (a) flange segments BA and TA; (b) flange segments TB and BB; (c) Flange A and Flange B. As mentioned previously in Section 4.9.2, the t-test evaluates the statistical difference between two data sets using their respective means, standard deviations, and sample set sizes. The results from the t-test include the t-value and the corresponding probability of null hypothesis, where the null hypothesis implies that the data sets are statistically similar. Tables 7.7 to 7.9 provide Student's t-tests which compare the results of fracture toughness data sets. Table 7.7 compares the results from segments BA and TA. Table 7.8 compares the results from segments TB and BB. Table 7.9 compares the results from Flange A and Flange B. Statistical similarity exists within each flange (probability that data sets are

statistically similar = 72%) for Flange A and 0.54 for Flange B). Significant statistical difference exists between the results obtained from Flange A and Flange B (probability that data sets are statistically similar = 2%). Higher values with less variation, as evident from the 95% high and low confidence intervals, is found in the results of Flange B. Table 7.10 provides the mean values, standard deviations, values for the high and low limits of the 95% confidence intervals, median values, and absolute average variation from the median for each flange (A or B). As explained later, charpy specimens were fabricated only from Flange B of the damaged-repaired specimens. Hence, only the undamaged results of Flange B will further be used for comparisons.

For the A36 and A588 undamaged fracture toughness results, Student's t-tests were only conducted to evaluate the statistical difference between the two flanges (A and B) and not between the individual results within each flange (i.e. T and B). Discrepancies within the same flange were further assumed to be insignificant.

The results of the fracture toughness tests on undamaged A36 are provided in Table 7.11. Overall, the fracture toughness results of both A36 steel plates are quite low. Statistical difference again exists between the results obtained from Flange A and Flange B. Higher values with more variation, as evident from the 95% confidence intervals, are found in the results of Flange B. Table 7.12 provides the statistical properties computed for each flange (A or B). Table 7.13 provides the results of a Student's t-test that compares the fracture toughness values obtained from Flange A and Flange B. The results of Student's t-test indicate that the statistical difference between the flanges is not as significant (probability that data sets are statistically similar = 17%) as for the A7 specimens. The statistical difference is significant enough such that the charpy impact results from each flange will still be treated separately for comparing to damage-repaired specimens.

The results of the fracture toughness tests on undamaged A588 are provided in Table 7.14. Statistical difference again exists between the results obtained from Flange A and Flange B. This result was surprising since the rest of the material properties related extremely well. Higher values with more variation, as evident from the 95% confidence intervals, are found in the results of Flange A. Table 7.15 provides the statistical properties computed for each flange (A or B). Table 7.16 provides the results of a Student's t-test that compares the fracture toughness values obtained from Flange A and Flange B. The result of Student's t-test for the A588 charpy data is very similar to the A36 result (probability that data sets are statistically similar = 10%). The statistical difference is significant enough such that the charpy impact results from each flange will still be treated separately for comparing to damage-repaired specimens.

7.6.1.3 Rockwell Hardness and Microstructure Investigations

The procedures for conducting Rockwell Hardness tests and also investigating the microstructure of steel were introduced in Sections 4.9.3 and 4.9.4, respectively. The procedures did not alter in between Task III and Task IV. One specimen from each flange for each steel type was prepared as specified by ASTM E3 standard. The charpy specimens used were taken from flange segments 2A and 2B and are labeled 2 in Figure 7.19. This specimen is the second outermost specimen with respect to the end of the plate. Rockwell hardness tests were conducted according to ASTM E18. Four hardness tests were conducted on each charpy specimen and the average value was considered to represent the overall hardness of the undamaged flange plates. The results of the Rockwell Hardness tests are shown later in Chapter 8 with the corresponding damaged-repaired A7, A36, and A588 specimens in Table 8.8. Table 8.8 also provides comparisons between the approximate ultimate strengths as estimated by ASTM A370 to the actual ultimate strengths. The results from Flange B will be used for normalized comparisons to the results from the damaged-repaired specimens.

In comparing the two A7 flange plates, the hardness of Flange B is higher than the hardness of Flange A. In comparing the two A36 flange plates, the hardness of Flange B is slightly lower with less statistical

variation than Flange A. The two A588 plates compare considerably well to each other. The ASTM approximate tensile strengths are somewhat low for A7 and A36 and compare favorably well with the actual tensile strengths for A588.

The grain sizes were determined using the general line intercept procedure in ASTM E112 standard. Most microstructure pictures were taken at 480X for each steel type. An exception was for Flange A of A7 which was taken at 240X. The resulting microstructures on undamaged A7, A36, and A588 steel specimens are shown in Figure 7.23. The resulting grain sizes and percentages of pearlite grains are shown with the experimental results of damage-repaired specimens in Table 8.9. As discussed in Section 4.9.4, a more fine-grained microstructure is generally stronger and tougher than a more coarse-grained microstructure. There is a slight increase on the surface hardness and a slight decrease on the ductility. A microstructure that is more pearlitic is harder, stronger, and more brittle. However, only significant and consistent changes in the percent pearlite would be further analyzed as the amount is related to the location taken for the picture as discussed in Section 2.4.3. The results are provided in Table 8.8 for completeness.

In comparing the two A7 flanges, the grain size of Flange B was smaller than the grain size of Flange A. A higher percentage of pearlite was also noticed for Flange B in Figure 7.23(b) and Table 8.8. In comparing the two A36 flange plates, a higher amount of pearlite was found in Flange A which is likely related to the higher strength and less ductility of Flange A. The two A588 plates have very similar microstructures. This relates well to the similarities of other material properties.

7.6.2 Damage-Repaired Material Testing Procedure

This section describes the material specimens and testing for damaged-repaired beam specimens. Charpy v-notch specimens were removed from the front flange (Flange B) and uniaxial tension coupons were removed from the back flange (Flange A) for each damaged-repaired beam specimen.

Three uniaxial tension specimens were removed from Flange A of each beam specimen. The dimensions of the uniaxial tension coupons were given in Figure 7.19. All three were removed from Vee heated region (*C*) at midspan. The MSU machinist was instructed to remove all three specimens as close to the edge of the flange as possible within a maximum distance of 2.5 in. The location of the uniaxial tension coupons in the top half of the flange is shown in Figure 7.24. The nomenclature used for each uniaxial tension coupon is also shown in Figure 7.24, where X represents the outermost coupon, Y represents the center coupon, and Z represents the innermost coupon. The reduced sections of all three uniaxial tension coupons lie within the center Vee heat.

The tests conducted on the charpy specimens included fracture toughness tests, Rockwell hardness tests, and microstructure investigations. The charpy specimens were removed from the three Vee heats (i.e. *C*, *L1*, and *R1*) located at the midspan of each beam. The charpy specimens were removed in three columns of four specimens with the notches located along the centerline of each of the three Vee heat locations (i.e. *C*, *L1*, and *R1*). The charpy specimens were removed within a distance of 2.25 in. (b_f/ 4) of the flange edge. The location of the fracture toughness specimens with respect to the top half of the flanges where the Vee heats are applied are shown in Figure 7.25. Figure 7.25 shows that the v-notches open towards to top of the flange similar to the undamaged specimens. The nomenclature used for each specimen is indicated in Figure 7.25. Rockwell hardness tests and microstructure investigations were conducted on charpy Specimen C-2. This specimen is the second outermost specimen in respect to the end of the plate and is located directly at midspan. The undamaged charpy specimen used was also the second outermost specimen in respect to the edge of the flange.

7.7 ANALYTTICAL FIBER-BASED MODEL OF BEAM SPECIMENS

The beam specimen is damaged by a concentrated force acting at midspan. This causes a linear moment gradient along the length of the beam and maximum moment at midspan. As the concentrated force increases, yielding occurs at the midspan and then spreads along the length of the beam. As the material undergoes strain hardening, yielding or plasticity spreads further along the length of the beam. A significant portion of the beam length undergoes plasticity before the target damage strain (ε_d) is achieved at the midspan section. The damaged beam will be repaired by heat straightening, where Vee heats must be applied in the regions of the beam subjected to plastic strains during damage. The region of the beam subjected to plastic strains during damage can be calculated as follows:

- The maximum force (P) required to achieve the damage strain (ε_d) at the midspan section is obtained experimentally from the damage cycle.
- The moment at any location along the length of the beam is equal to $P\ x\ /2$, where x is the distance from the support. Maximum moment at midspan is equal to $P\ L/4$
- Inelastic strains or yielding will occur when the moment $P\ x\ /2$ exceeds the yield moment for the section M_y, which can be calculated as $S_x\ \sigma_y$.
- Therefore, plastic strains will occur in the beam after a distance x from the supports, Where, $x = S_x\ \sigma_y\ 2\ /\ P$

This method provides an estimate of the beam region subjected to yielding (or plastic strains), but it does not provide any information regarding the magnitude and distribution of plastic strains with the damage region. Therefore, a more advanced analysis tool (section fiber analysis) was used to determine the magnitude and distribution of plastic strains within the damage region.

7.7.1 Fiber Models of the Beam Specimens

Fiber models of the beams specimens subjected to weak axis damage were developed using MATLAB version 6.5. In the fiber model, the steel cross-section is discretized into a number of steel web and flange fibers as illustrated in Figure 7.26. Each fiber has an area (A_f), distance from the neutral axis (y_f) measured from the centroid of the section, and an implemented uniaxial stress-strain (σ - ε) curve. The fiber σ-ε responses are integrated over the cross section to obtain the section force-deformation (moment-curvature) response. The amount of fibers used to discretize the cross-section and the accuracy of the σ-ε relationship govern the accuracy of the fiber based model. In the fiber based model, 100 fibers were used to discretize each flange and 20 fibers were used to discretize the web.

The fiber model is initiated assuming a range of varying curvature (ϕ) at midspan and a linear strain distribution as shown in Figure 7.27(a). The average strain in each fiber (ε_f) is computed as the curvature multiplied by the distance from the neutral axis y_f [see Figure 7.27(b)]. The average stress in each fiber (σ_f) is computed using the σ-ε relationship derived from uniaxial tension tests conducted on the undamaged material as in Figure 7.27(c). The material σ-ε curve is idealized into three separate regions; elastic, yield plateau, and strain hardening as shown in Figure 7.28 for the undamaged A7 material. If the strain in the fiber was computed to be less than the yield strain (ε_y), the averaged stress in the fiber was computed using Equation 7.7. If the strain was computed to be greater than εy but less than the strain at the offset of strain hardening ε_{sh}, then the stress in the fiber was identified as σ_y.

$$\sigma_f = \varepsilon_f \text{ x E} \tag{7.7}$$

Fifth-order trend line equations were determined using Microsoft Excel 2003 to predict the stress as a function of the strain in the strain-hardening region, which is shown for undamaged A7 in Figure 7.29. If the strain in the fiber was computed to be higher than ε_{sh}, then the average stress in the fiber is computed

using this fifth order equation or similar for the strain hardening of the A36 and A588 uniaxial σ-ε relationships.

The force contribution of each fiber (F_f) is computed by multiplying the average stress (σ_f) and the area of each fiber (A_f). The moment induced to the cross-section is computed as a sum of the each force multiplied by the distance from the centroidal axis (y_f) as in Equations 7.8 and 7.9. Varying the curvature develops a moment-curvature response of the section which is shown for the W24x76 A7 beam specimen in Figure 7.30. Figure 7.30 also shows the moment curvature relationship assuming an elastic-perfectly plastic σ-ε relationship as usually assumed by AISC for comparisons.

$$F_f = \sigma_f \text{ x } A_f \tag{7.8}$$

$$M = \sum F_f \, x \, y_f \tag{7.9}$$

7.7.2 Plastic Damage Region and Magnitudes

The maximum moment required to achieve the damage strains (ε_d) for each beam was determined using the fiber models. A linear moment distribution is assumed to each support, where the moment at the support is zero. Using an interpolation scheme of the moment-curvature response of the section, the curvature along the length of the beam is calculated. In the fiber analysis using MATLAB, the curvature was computed using interpolation at 1001 points from the support to midspan. The strain in each fiber along the length of the beam is computed as a multiplication of the curvature obtained from interpolation and the distance from the centroidal axis (y_f). The stress in each fiber along the length of the beam is computed using the uniaxial σ-ε relationship as described in Section 7.7.1. The plastic strain is computed in each fiber using Equation 7.10.

$$\varepsilon_{plastic} = \varepsilon - \frac{\sigma}{E} \tag{7.10}$$

Figure 7.31 shows the magnitude and distribution of maximum plastic strains at the top of the flanges of the A7 steel W24x76 beam specimen. The plastic strain distributions are shown for three levels of damage, i.e., when the midspan damage strain ε_d reaches: (a) 30 ε_y, (b) 60 ε_y , and (c) 90 ε_y.

Figure 7.32 shows the magnitude and distribution of maximum plastic strains at the top of the flanges of the A36 steel built-up beam specimen. The plastic strain distribution is shown only for a midspan maximum strain of 30 ε_y since it was the only ε_d for A36 beam specimens. For the A36 beam, the σ-ε relationships of both flanges were taken into consideration. However, the discrepancies in the resulting plastic strain distributions were negligible. The web was assumed to have the σ-ε relationship of Flange B. Figure 7.33 shows the magnitude and distribution of maximum plastic strains at the top of the flanges of the A588 built-up beam specimen. The plastic strain distributions are shown for both damage strain levels, i.e., when the midspan damage strain (ε_d) reaches: (a) 20 ε_y and (b) 40 ε_y. The web was assumed to have the σ-ε relationship as Flange B of the A36 material. As shown in Figures 7.31 and 7.33, larger damage strains results in greater magnitudes and distribution of plastic strains along the length of the beam. Figures 7.31 and 7.33 clearly indicate the need for several Vee heats within the region of the beam subjected to plastic strains.

Figures 7.34, 7.35, and 7.36 show the magnitudes of plastic strains along half the width (tension strains) of the flange at the center of each Vee-heat location for the A7 beams for maximum damage strains of 30 ε_y, 60 ε_y, and 90 ε_y, respectively. The plastic strains for a symmetric Vee-heat location on the opposite side of centerline (i.e. L1 in relation to R1) would be the equivalent. Figure 7.37 show the magnitudes of plastic strains along half the width (tension strains) of the flange at the center of each Vee-heat location for the A36 beams with a maximum damage strain of 30 ε_y. Figures 7.38 and 7.39 show the

plastic strains induced along half the width (tension strains) of the flange at the center of each Vee-heat location for the A588 beams for damage strain of 20 ε_y and 40 ε_y, respectively.

7.7.3 Residual and Restraining Stress Computations

The fiber-based model was further used to compute the induced residual stresses along the length of the beam after damage. The induced residual stresses are significant for determining the actual restraining stress induced to the locations of the removal of each charpy and tensile specimen. In the fiber-based model, the stress in each fiber of the cross-section along the length of beam at the maximum damage strain was computed. The beam unloads elastically assuming Hooke's Law. The unloading stress in each fiber is computed using Equation 7.11; where M is the moment at a point along the length of the beam, c is the distance from the neutral axis of the cross section, and I_y represents the moment of inertia of the cross section about the weak axis.

$$\sigma_{unload} = \frac{Mc}{I_y} \tag{7.11}$$

The induced residual stresses are computed as the damage stress minus the unloading stresses. An example is shown in Figure 7.40 [*1*]. Figure 7.40(a) gives the stress-strain profile of a steel plate subjected to pure bending as shown in Figure 7.40(b). As the plate is bent so that the stresses in the section exceed the elastic capacity, then the curves *AO* and *OA'* would represent the compressive and tensile stresses along the height of the member. Assuming the material follows Hooke's law, it will follow the unloading stress distribution represented by the lines *BO* and *OB'* given by Equation 7.11. Note that the moment required to bend the beam as represented by the stress-distribution *AOA'* is equal to the moment represented by *BOB'* when assuming linear-elastic bending behavior. The resulting residual stresses are found by subtracting the unloading stress-distribution from the bending stress. The final residual stress distribution is shown in Figure 7.40(b) represented by the curve *COC'*.

Residual stresses were computed along the cross-section at every fiber along the length of each experimental beam specimen. This includes 100 fibers along the 9 in. width of the flange at 1001 points from the support to midspan. The residual stresses along the center of the Vee heat locations (i.e., C, R1, L1, L2, R2, etc) were arranged and plotted. The fiber analysis was further verified at a distance of 2 ft. from the support end, which did not undergo plasticity. The residual stresses in the cross section were computed to be zero.

Prior to repairing the beam specimens, they are subjected to an external restraining moment (M_r) of either 0.25 M_p or 0.50 M_p. The actual restraining stress at each fiber along the cross-section is computed as the addition of the elastic reloading stress and the induced residual stresses after damage and unloading. The elastic reloading stress is computed using Equation 7.11 with compressive stresses at the top and tensile stresses at the bottom.

For beam specimens subjected to restraining moments of 0.50 M_p, the restraining stresses in some fibers were computed higher than the yield stress (σ_y). For restraining stresses computed higher than σ_y, the restraining strains were required in order to use the implemented σ-ε relationship of the material. The residual strains were assumed to be equal to the residual stresses divided by the elastic modulus. The additional reloading strains were assumed to be equal to the elastic reloading stresses divided by the elastic modulus. The restraining strains in the fibers were computed as the addition of the residual strains and the reloading strains. All strain values computed higher than the yield strain (ε_y) were found to be less than ε_{sh}. Therefore, no restraining stresses were computed higher than σ_y.

A few examples of the damage-repair stress history are provided in Figures 7.41 to 7.43. The results along the center Vee heat (*C*) of the A36 beam subjected to a damage strain of 30 ε_y at the extreme tension fiber and an external restraining moment of 0.25 M_p are shown in Figure 7.41. The damage

stresses, unloading stresses, residual stresses, reloading stresses, and final restraining stresses are all shown in Figure 7.41. The restraining stresses at the ends of the beam specimen are as high as 40.8 ksi, which corresponds to approximately 88.7 % of the yield stress. The results along the cross-section of the furthest Vee heat (*R5*) for the same beam specimen are shown in Figure 7.42. The stress results away from the center of the beam are not as significant. The results along the center Vee heat (*C*) of the A7 beam subjected to a damage strain of 90 ε_y at the extreme tension fiber and an external restraining moment of 0.50 M_p (first damage-repair cycle of A7-Beam 2) is shown in Figure 7.43. The restraining stresses at the ends of the specimen are equal to the yield stress (36.25 ksi).

The restraining moment of 0.50 M_p subjects the beam specimens to significantly high restraining stresses. The results of the fiber analysis indicate that the steel is being cold worked at the edges before applying heat.

7.7.4 Damage Strain-Restraining Stress History of Each Material Coupon

This section provides a summary of the analytical damage strain (ε_d) and restraining stress (σ_r) subjected to each charpy and tensile coupon. The ε_d and σ_r were computed at the center of each coupon using analytical fiber analysis as described in Sections 7.7.2 and 7.7.3, respectively. For multiple damage-repair cycles, the values are nominal, since residual stresses after repair were not taken into consideration.

Charpy specimens 1, 2, 3, and 4 (for L1, C, and R1) were assumed to be at a distance from the edge of the flange of 0.322 in., 0.841 in., 1.360 in., and 1.879 in., respectively. These distances assume 1/8 in. gaps from the flange end and between each charpy specimen. The results of fiber analysis for the ε_d and σ_r history of each charpy specimen are provided for each damage-repair cycle of all beam specimens in Table 7.17.

Uniaxial tensile coupons X, Y, and Z were assumed to be at a distance of 0.4375 in., 1.2500 in., and 2.0625 in. from the flange end, respectively. These distances assume 1/16 in. gaps from the flange end and in between each coupon. The results of fiber analysis are provided for each damage-repair cycle of all beam specimens in Table 7.18.

In Tables 7.17 and 7.18, the damage strains (ε_d) are given as a ratio to the yield strain (ε_y). The damage strains include the elastic strains before unloading. The restraining stresses (σ_r) are provided as a percentage of the yield stress (σ_y).

7.7.5 Validation of Fiber Based Model with Experimental Data

Figures 7.31-7.39 of Section 7.7.2 were used as guidance to the researchers in how much emphasis (repetition) should be applied to each Vee heat location within the plastic damage region. The curvature and plastic strain distributions along the length could not be experimentally measured. In order to validate the plastic strain distributions, the fiber model was enhanced using MATLAB version 6.3 to compute the load-strain (P-ε), the load-rotation (P-θ), and the load-displacement (P-Δ) behavior of the beam specimens. The load, strain at the extreme tension fiber, end rotations, quarter displacements, and the center displacement were all measured during the experiments using instruments described in Section 7.5.1.

In the fiber analyses, the range of curvature was specified and the moment at every curvature increment was computed as described in Section 7.7.1. The strain at the extreme tension fiber was computed using Equation 7.12:

$$\varepsilon = \phi \; x \; \frac{b_f}{2} \qquad (7.12)$$

As mentioned in Section 7.7.2, the load is applied at midspan and a linear moment distribution is assumed to the end support. The load required to cause this moment distribution was computed using Equation 7.13:

$$P = \frac{4M}{L} \tag{7.13}$$

Figure 7.44 shows a comparison between the *P-ε* behaviors of the first damage cycle of A7-Beam 1 to the results of the fiber analysis. The experimental P-ε behavior compares favorable well with the analytical results.

The curvature along the length of the beam can be expressed by some function of the beam length $\phi(x)$. In the fiber analysis, the curvature at 1001 points was found from the beam midspan to the support. A numerical integration of the curvature-length $\phi(x)$ function can be used to find the rotation at any point along the length of the beam. The change in rotation within any length along the length of the beam is computed using Equation 7.14 where the variable C is a constant:

$$\theta(x) = \int \phi(x)dx + C \tag{7.14}$$

Within a finite length, the change in rotation is represented by the area along that strip underneath the $\phi(x)$ function. In the fiber analysis, the change in rotation within a finite length was found using a trapezoidal rule using two points of curvature at both ends of the finite length; taking the average of the two points and multiplying the average by the finite length. An illustration of the trapezoidal rule is shown in Figure 7.45 where *h* represents the finite length. The change in rotation within length *h* can be computed using Equation 7.15.

$$\Delta\theta_h = \frac{\phi_1 + \phi_2}{2} x\ h \tag{7.15}$$

The change in rotation along the length of the beam was added to the previous to find the full change rotation at every length increment. With the given loading and boundary conditions, it is known that the rotation is decreasing and is zero at midspan. The constant C is therefore computed as the value for the full change in rotation computed at midspan. The vector which forms for each point for the full change in rotation along the length is subtracted from this value. This process is repeated for each value of implemented curvature at midspan to develop the *P-θ* response at any point along the beam length.

The vertical displacement of each point is found by numerically integrating the rotation function in a similar fashion. The displacement at any point along the length of the beam is computed using Equation 7.16 where the variable C is a constant:

$$\Delta(x) = \int \theta(x)dx + C \tag{7.16}$$

With the given loading and boundary conditions, it is known that the constant C is equal to the end displacement which is zero. In the fiber analysis, the change in displacement within each length increment was found using Riemann's integration rule; taking each point of rotation and multiplying it by the finite length. An illustration of implementing Riemann's rule is shown in Figure 7.46 where *h* represents the finite length. Figure 7.45 in comparison to Figure 7.46 indicates that Riemann's rule is not as accurate as the trapezoidal rule. However, Riemann's rule was determined to work as sufficiently as the trapezoidal rule because enough increments along the beam length were used (each finite area under the curve was computed within a length of 0.0485 in). The changes in displacements are added to the previous to compute the full change in displacement at each point. This process is repeated for each value of implemented curvature at midspan to develop the *P-Δ* response at any point along the beam.

Figure 7.47 provides comparisons between the P-Δ relationships derived from fiber analysis and the experimental behavior of A7-Beam 1 (damage cycle 1). The comparisons include the displacement at the center of the beam as well as the displacement at the quarter point (at L/4 from the support). The analytical and experimental results compare well to each other. The right quarter point displacement indicates a better comparison than the center displacement. The experimental stiffness of the center displacement is not as steep as the stiffness of the fiber analysis. This behavior is due to the small indentions which occur in the steel at the point of contact. The analytical elastic P-Δ compares well with equations from beam theory. Figure 7.48 provides a comparison of the P-θ relationships derived from fiber analysis and from the experimental behavior of A7-Beam 1. The P-θ relationships compare extremely well to each other.

Figure 7.49 provides comparisons between the P-Δ relationships derived from the fiber analysis and the experimental behavior of A7-Beam 2 (damage cycle 1). The results include the displacements at the center of the beam as well as at the quarter point (at L/4 from the support). The analytical and experimental results compare extremely well at low values of displacement and favorably well as the displacements increase. The discrepancies at higher displacements are likely due to the implemented σ–ε for the web. The web was assumed to have the same σ–ε behavior as the flange since undamaged material coupons were not removed from the web. The web fibers yielded in the fiber analysis at higher displacements. Figure 7.50 shows a comparison of the P-θ derived from the fiber analysis and the experimental behavior of A7-Beam 2. The P-θ relationships compare better than the P-Δ relationships but discrepancies still exist at higher values of rotation. Since the known A7 experimental behavior compares well with analytical predictions, it is assumed that the analytical plastic strain distribution along the length of the beam is a good approximation of the actual being induced to the beam specimens.

Figure 7.51 provides comparisons between the P-Δ relationships derived from the fiber analysis and the experimental behavior of A36-Beam 1 (damage cycle 1). For the A36 beam, the σ–ε relationships of both flanges were considered. The web was assumed to have the σ–ε relationship of Flange B. The results include the displacement found at the center of the beam as well as the displacement at the quarter point (at L/4 from the support). The analytical and experimental results compare favorably well to each other. Again, the experimental elastic stiffness is likely found to be lower due to indentions that form at the contact points. Figure 7.52 provides a comparison of the P-θ behaviors derived from fiber analysis and that of A36-Beam 1. The P-θ relationship once again compares better than the P-Δ relationships.

Since the known A36 experimental behavior compares well with analytical approximations, it can be assumed that the analytical plastic strain distribution along the length of the beam is a good approximation of the actual being induced in the beam specimens.

Figure 7.53 provides comparisons between the P-Δ relationships derived from the fiber analysis and the experimental behavior of A588-Beam 1 (damage cycle 1). The web was assumed to have a stress-strain relationship as A36-Flange B. The analytical and experimental results compare favorably well to each other but not as well as in the A36 and A7 cases. The analytical stiffness was matched against equations from beam theory in the elastic region and was determined to be accurate. Again, the experimental stiffness at the center is likely found to be lower due to indentions that form at the contact points. The reason for discrepancies of the elastic stiffness at the quarter point is unknown. Figure 7.54 provides a comparison of the P-θ behaviors of the fiber analysis and that from the experimental behavior of A588-Beam 1. The P-θ relationships once again compare better than the P-Δ relationships.

Although the experimental and analytical results do not compare as well for A588, the analytical plastic strain distribution along the length of the beam is likely a good approximation of the actual values being induced to the beam specimens.

7.8 REFERENCE

1. Almen, J. O., and Black , P. H., *Residual Stresses and Fatigue in Metals*, McGraw Hill Book Company, Inc., New York, 1964.

Table 7.1
Experimental test matrix for large-scale beam specimens

Specimen Name	*Cycle Number*	*Damage Strain (ε_d)*	*Approx. Plastic Displacement (in)*	*Restraining Moment (M_r)*	*Maximum Temperature (T_{max})*
A7-Beam 1	1	30 ε_y	2.2	0.25 M_p	1200 ºF
	2	30 ε_y	2.2	0.50 M_p	
	3	30 ε_y	2.2	0.25 M_p	
A7-Beam 2	1	90 ε_y	8.5	0.50 M_p	1200 ºF
	2	60 ε_y	5.5	0.50 M_p	
	3	60 ε_y	5.5	0.50 M_p	
A36-Beam 1	1	30 ε_y	3.1	0.25 M_p	1200 ºF
	2	30 ε_y	3.1	0.50 M_p	
	3	30 ε_y	3.1	0.25 M_p	
A36-Beam 2	1	30 ε_y	3.1	0.25 M_p	1400 ºF
	2	30 ε_y	3.1	0.50 M_p	
	3	30 ε_y	3.1	0.25 M_p	
A588-Beam 1	1	40 ε_y	4.9	0.25 M_p	1200 ºF
	2	20 ε_y	2.1	0.25 M_p	
	3	20 ε_y	2.1	0.25 M_p	
A588-Beam 2	1	40 ε_y	4.9	0.50 M_p	1200 ºF
	2	20 ε_y	2.1	0.50 M_p	
	3	20 ε_y	2.1	0.50 M_p	

Table 7.2
Instrument history during the experimental investigations of A7-Beam 1

	Rot. 1	Rot. 2	Rot. 3	Rot. 4	LVDT	LVDT	LVDT	LVDT
	F_L	B_L	B_R	F_R	6 Left	6 Right	12 Fron	12 Back
Damage 1								
Contact of Damage 1	1.4111	1.3029	-0.6336	1.9574	1.8330	0.5560	0.3114	0.6452
Peak of Damage 1	-2.8070	-1.4818	2.3953	6.2668	3.8055	2.5260	3.7714	4.1006
End of Damage 1	-2.0342	-1.2545	2.1355	5.4771	3.3314	2.0933	2.6215	2.7836
Full Damage	-4.2180	-2.7847	3.0289	4.3094	1.9725	1.9700	3.4600	3.4554
Plastic Damage	-3.4452	-2.5574	2.7691	3.5197	1.4984	1.5373	2.3101	2.1384
Repair 1								
Start of Repair 1	-2.0342	-1.2545	2.1355	5.4771	3.3314	2.0933	5.2978	3.3525
End of Repair 1	1.4080	-	-	2.0085	1.8847	0.5086	2.5876	0.6331
Repair	3.4422	-	-	-3.4686	-1.4467	-1.5847	-2.7103	-2.7194
Damage 2								
Contact of Damage 2	1.3961	-2.0708	4.4942	1.9940	2.0037	0.6282	0.8398	3.1811
Peak of Damage 2	-2.3583	1.6206	0.7016	5.8066	3.6440	2.2952	3.5324	5.8786
End of Damage 2	-1.4688	0.7402	1.6088	4.9086	3.1120	1.7888	2.8325	5.1426
Full Damage	-3.7544	3.6915	-3.7926	3.8126	1.6404	1.6671	2.6926	2.6974
Plastic Damage	-2.8649	2.8110	-2.8854	2.9146	1.1083	1.1607	1.9926	1.9614
Repair 2								
Start of Repair 2	-1.4688	0.7402	1.6088	4.9086	3.1069	1.7786	4.4850	6.7212
End of Repair 2	1.3971	-2.0605	4.4790	1.9650	1.8220	0.4975	2.3587	4.4152
Repair	2.8659	-2.8006	2.8702	-2.9436	-1.2849	-1.2811	-2.1263	-2.3060
Damage 3								
Contact of Damage3	1.3971	-2.0605	4.4790	1.9650	1.8220	0.4975	0.8430	2.8560
Peak of Damage 3	-2.3981	1.4269	0.8782	5.7333	3.2496	2.2763	3.5277	5.5915
End of Damage 3	-1.5007	0.4814	1.7874	4.7710	2.7363	1.7632	2.8323	4.8749
Full Damage	-3.7952	3.4874	-3.6008	3.7683	1.4276	1.7787	2.6847	2.7356
Plastic Damage	-2.8978	2.5419	-2.6916	2.8060	0.9143	1.2657	1.9893	2.0189
Repair 3								
Start of Repair 3	-1.4290	0.5232	1.8685	4.7831	2.6910	1.7261	4.2971	6.3577
End of Repair 3	1.3482	-2.0446	4.4350	1.8649	1.6761	0.4739	2.1602	4.5338
Repair	2.7771	-2.5677	2.5665	-2.9183	-1.0149	-1.2522	-2.1368	-1.8239

Table 7.3
Structural properties of undamaged A7 steel

Specimen	BA	TA	BB	TB	Average
Upper σ_y (ksi)	37.8	36.7	37	37.2	37.2
Lower σ_y (ksi)	35.4	36	36.3	35.5	35.8
Plateau σ_y (ksi)	36.7	36.5	36.5	36.6	36.6
E (ksi)	30220	31086	30520	30193	30505
ε_y	0.00121	0.00117	0.00120	0.00121	0.00120
σ_t (ksi)	61	61.7	61.3	61.6	61.4
ε_u	0.233	0.216	0.234	0.211	0.224
ε_u / ε_y	191.9	184	195.7	174.1	186.4
% Elongation	41.97	42.84	41.67	41.38	41.96
% Reduction	62.69	62.56	62.5	62.27	62.51
$30\ \varepsilon_y$	0.036	0.035	0.036	0.036	0.036
$60\ \varepsilon_y$	0.073	0.07	0.072	0.073	0.072
$90\ \varepsilon_y$	0.109	0.106	0.108	0.109	0.108

Table 7.4
Structural properties of undamaged A36 steel

	BA	TA	Avg A	BB	TB	Avg B	Average
Upper σ_y (ksi)	48.7	48.6	48.7	46.7	46.5	46.6	47.6
Lower σ_y (ksi)	45.5	46.7	46.1	44.3	44.1	44.2	45.2
Plateau σ_y (ksi)	46.6	46.9	46.8	45.1	45.3	45.2	46.0
E (ksi)	29554	31541	30547	31499	30886	31193	30870
ε_y	0.00158	0.00149	0.00153	0.00143	0.00147	0.00145	0.00149
σ_u (ksi)	75.1	75.1	75.1	71.6	71.6	71.6	73.4
ε_u	0.191	0.191	0.191	0.197	0.193	0.195	0.193
ε_u / ε_y	121.13	128.45	124.79	137.59	131.59	134.59	129.69
% Elongation	36.94	36.77	36.85	38.85	39.26	39.06	37.95
% Reduction	60.72	58.56	59.64	62.02	61.72	61.87	60.75
$30\ \varepsilon y$	0.0473	0.0446	0.0460	0.0430	0.0440	0.0435	0.0447

Table 7.5
Structural properties of undamaged A588 steel

	BA	TA	Avg A	BB	TB	Avg B	Average
Upper σ_y (ksi)	59.4	60.0	59.7	60.2	60.5	60.4	60.0
Lower σ_y (ksi)	58.1	58.2	58.2	57.1	57.7	57.4	57.8
Plateau σ_y (ksi)	59.0	58.5	58.8	58.3	58.0	58.2	58.5
E (ksi)	30208	29837	30022	29280	30453	29867	29945
ε_y	0.00195	0.00196	0.00196	0.00199	0.00190	0.00195	0.00195
σ_u (ksi)	85.4	84.3	84.9	84.3	84.1	84.2	84.5
ε_u	0.144	0.144	0.144	0.143	0.143	0.143	0.144
ε_u / ε_y	73.73	73.44	73.59	71.82	75.08	73.45	73.52
% Elongation	36.17	35.16	35.66	34.74	35.62	35.18	35.42
% Reduction	69.96	68.79	69.37	69.41	69.09	69.25	69.31
20 εy	0.0391	0.0392	0.0391	0.0398	0.0381	0.0390	0.0390
40 εy	0.0781	0.0784	0.0783	0.0796	0.0762	0.0779	0.0781

Table 7.6
Fracture toughness results of undamaged A7 steel

Specimen	BA	TA	BB	TB
1	73	61	73	67
2	78	82	86	72
3	58	55	75	60
4	52	28	50	90
5	27	40	66	67
6	44	42	84	48
Mean	55.3	51.33	72.33	67.33
Std. Dev.	18.8	19.01	13.19	13.88

Table 7.7
Student's t-test results comparing the means of data sets in Table 7.6 (BA and TA)

t-test to establish the statistical difference between the fracture toughness of A7 charpy specimens from BA and TA
Results of unpaired t-test (see Section 4.9.2):
t=0.366
Std. deviation=18.9
Degrees of freedom=10
Probability of null hypothesis (the data sets are statistically similar) = 0.72

Table 7.8
Student's t-test results comparing the means of data sets in Table 7.6 (BB and TB)

t-test to establish the statistical difference between the fracture toughness of A7 charpy specimens from BB and TB
Results of unpaired t-test (see Section 4.9.2):
t=0.64
Std. deviation=13.5
Degrees of freedom=10
Probability of null hypothesis (the data sets are statistically similar) = 0.54

Table 7.9
Student's t-test results comparing the means of data sets in Table 7.6 (Flange A and Flange B)

t-test to establish the statistical difference between the fracture toughness of A7 charpy specimens from Flange A and Flange B
Results of unpaired t-test (see Section 4.9.2):
t=2.55
Std. deviation=15.9
Degrees of freedom=22
Probability of null hypothesis (the data sets are statistically similar) = 0.018

Table 7.10
Statistical values of undamaged A7 fracture toughness of both flanges

Statistical Property	Flange A	Flange B
Mean	53.3	69.8
Std. Dev.	18.2	13.2
95% High	64.88	78.2
95% Low	41.79	61.47
Median	53.5	69.5
Average Absolute From Median	14.5	10.2

Table 7.11
Fracture toughness results of undamaged A36 steel

Specimen	BA	TA	BB	TB
1	41	51	75	62
2	46	47	60	44
3	38	35	36	38
4	41	40	48	39
5	44	35	35	45
Mean	42	41.6	50.8	45.6
Std. Dev.	2.76	6.44	15.14	8.64

Table 7.12
Statistical values of undamaged A36 fracture toughness of both flanges

Statistical Property	Flange A	Flange B
Mean	41.8	48.2
Std. Dev.	5.22	13.3
95% High	45.54	57.7
95% Low	38.06	38.7
Median	41.0	44.5
Average Absolute From Median	4.0	13.3

Table 7.13
Student's t-test results comparing the means of data sets in Table 7.12 (Flange A and Flange B)

t-test to establish the statistical difference between the fracture toughness of A36 charpy specimens from Plate A and Plate B
Results of unpaired t-test (see Section 4.9.2):
t=1.42
Std. deviation= 10.1
Degrees of freedom=18
Probability of null hypothesis (the data sets are statistically similar) = 0.17

Table 7.14
Fracture toughness results of undamaged A588 steel

Specimen	1A	2A	1B	2B
1	96	99	85	99
2	125	99	94	96
3	100	100	95	87
4	110	107	84	106
5	101	90	110	101
Mean	106.4	99.0	93.6	97.8
Std. Dev	11.59	6.04	10.45	7.05

Table 7.15
Statistical values of undamaged A588 fracture toughness of both flanges

Statistical Property	Flange A	Flange B
Mean	103	95.7
Std. Dev.	9.55	101.9
95% High	109.5	89.48
95% Low	95.87	8.69
Median	100.0	95.5
Average Absolute From Median	5.9	6.7

Table 7.16
Student's t-test results comparing the means of data sets in Table 7.15 (Flange A and Flange B)

t-test to establish the statistical difference between the fracture toughness of A588 charpy specimens from Plate A and Plate B
Results of unpaired t-test (see Section 4.9.2):
t=1.71
Std. deviation= 9.13
Degrees of freedom=18
Probability of null hypothesis (the data sets are statistically similar) = 0.10

Table 7.17
Nominal damage strain-restraining stress of each uniaxial tension coupon using fiber analysis

	Damage-Repair 1		*Damage-Repair 2*		*Damage-Repair 3*	
Specimen	$\varepsilon_d / \varepsilon_y$	σ_r / σ_y	$\varepsilon_d / \varepsilon_y$	σ_r / σ_y	$\varepsilon_d / \varepsilon_y$	σ_r / σ_y
A7-Beam 1						
X	26.9	77.9	26.9	100.0	26.9	77.9
Y	21.6	46.4	21.6	78.6	21.6	46.4
Z	15.7	16.6	15.7	41.1	15.7	16.6
A7-Beam 2						
X	80.8	100.0	53.9	100.0	53.9	100.0
Y	64.9	73.8	43.2	82.0	43.2	82.0
Z	48.9	20.5	32.6	33.0	32.6	33.0
A36-Beam 1 and A36-Beam 2						
X	26.9	77.3	26.9	100.0	26.9	77.3
Y	21.6	44.1	21.6	74.8	21.6	44.1
Z	16.3	12.8	16.3	35.4	16.3	12.8
A588-Beam 1						
X	36.3	80.2	18.2	74.2	18.2	74.2
Y	29.1	40.2	14.6	39.3	14.6	39.3
Z	21.9	2.0	11.0	5.8	11.0	5.8
A588-Beam 2						
X	36.3	100.0	18.2	100.0	18.2	100.0
Y	29.1	67.9	14.6	67.8	14.6	67.8
Z	21.9	22.9	11.0	27.3	11.0	27.3

Table 7.18
Nominal damage strain-restraining stress of each charpy specimen using fiber analysis

	Damage-Repair 1				*Damage-Repair 2*				*Damage-Repair 3*			
	C		*L1 or R1*		*C*		*L1 or R1*		*C*		*L1 or R1*	
Specimen	$\varepsilon_d / \varepsilon_y$	σ_r / σ_y	$\varepsilon_d / \varepsilon_y$	σ_r / σ_y	$\varepsilon_d / \varepsilon_y$	σ_r / σ_y	$\varepsilon_d / \varepsilon_y$	σ_r / σ_y	$\varepsilon_d / \varepsilon_y$	σ_r / σ_y	$\varepsilon_d / \varepsilon_y$	σ_r / σ_y
A7-Beam1												
1	27.5	81.4	22.7	80.8	27.5	100.0	22.7	100.0	27.5	81.4	22.7	80.8
2	24.0	60.2	19.8	60.4	24.0	95.8	19.8	96.0	24.0	60.2	19.8	60.4
3	20.4	39.7	16.8	40.5	20.4	70.1	16.8	71.0	20.4	39.7	16.8	40.5
4	17.5	23.1	14.4	24.4	17.5	49.3	14.4	50.6	17.5	23.1	14.4	24.4
A7-Beam2												
1	82.6	100.0	64.1	100.0	55.1	100.0	44.9	100.0	55.1	100.0	44.9	100.0
2	72.0	96.3	55.8	94.1	48.0	100.0	39.1	100.0	48.0	100.0	39.1	100.0
3	61.3	62.8	47.5	62.7	40.9	71.8	33.3	72.0	40.9	71.8	33.3	72.0
4	52.4	35.9	40.6	37.8	34.9	47.2	28.5	48.7	34.9	47.2	28.5	48.7
A36-Beam1 and A36-Beam 2												
1	27.5	81.1	22.7	79.6	27.5	100.0	22.4	100.0	27.5	81.1	22.7	79.6
2	24.0	58.6	19.8	58.2	24.0	93.1	19.5	92.7	24.0	58.6	19.8	58.2
3	20.4	36.9	16.8	37.5	20.4	65.9	16.6	66.5	20.4	36.9	16.8	37.5
4	17.5	19.5	14.4	20.8	17.5	43.9	14.2	45.2	17.5	19.5	14.4	20.8
A588-Beam1												
1	37.1	84.7	26.4	81.2	18.6	78.1	14.2	76.1	18.6	78.1	14.2	76.1
2	32.3	57.8	23.0	56.1	16.2	54.6	12.4	53.7	16.2	54.6	12.4	53.7
3	27.5	31.5	19.6	31.5	13.8	31.7	10.5	31.8	13.8	31.7	10.5	31.8
4	23.5	10.3	16.7	11.8	11.8	13.1	9.0	13.8	11.8	13.1	9.0	13.8
A588-Beam2												
1	37.1	100.0	26.4	100.0	18.6	100.0	14.2	100.0	18.6	100.0	14.2	100.0
2	32.3	88.6	23.0	86.8	16.2	86.3	12.4	85.4	16.2	86.3	12.4	85.4
3	27.5	57.7	19.6	57.7	13.8	58.6	10.5	58.7	13.8	58.6	10.5	58.7
4	23.5	32.7	16.7	34.1	11.8	36.1	9.0	36.8	11.8	36.1	9.0	36.8

a) Cross-Section

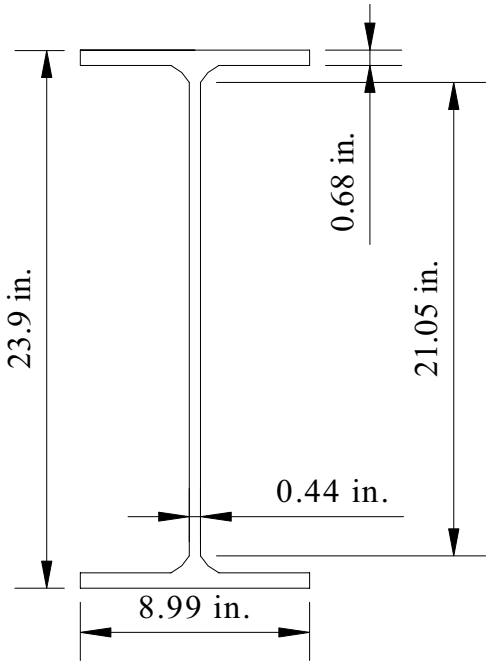

b) Plan View

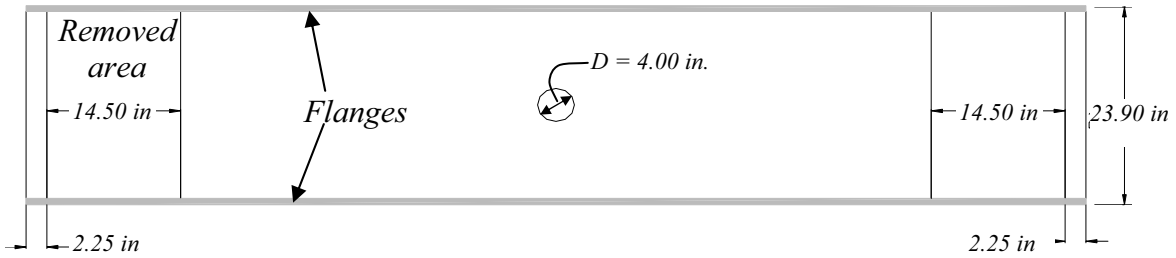

c) Elevation View

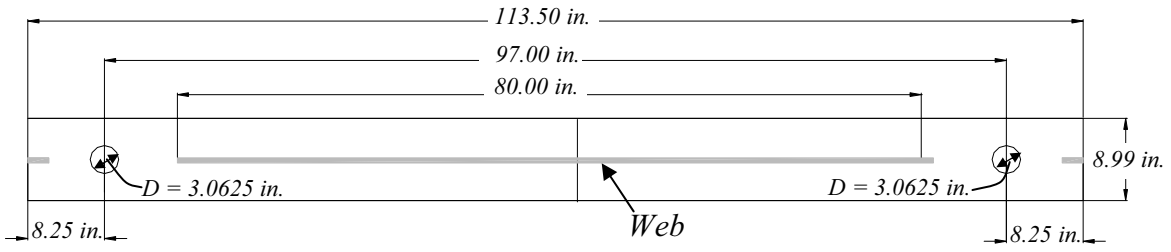

Figure 7.1
Details of the A7 experimental beam specimens

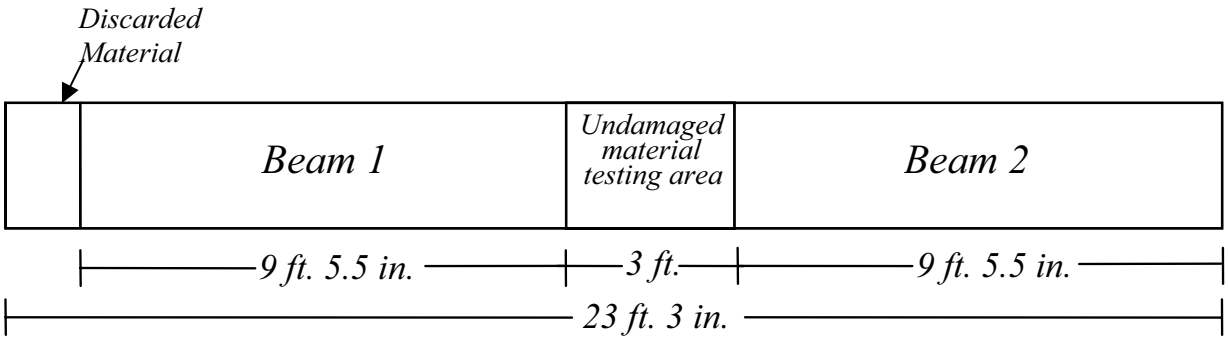

Figure 7.2
Fabrication of A7 beam used for large scale testing

a) Cross-Section

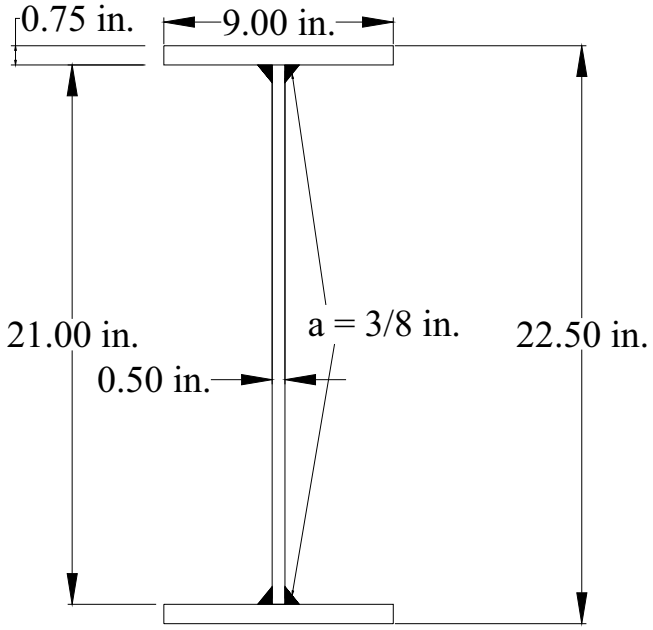

b) Plan View

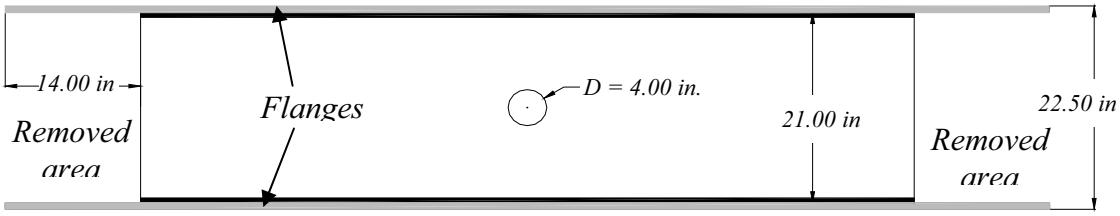

c) Elevation View

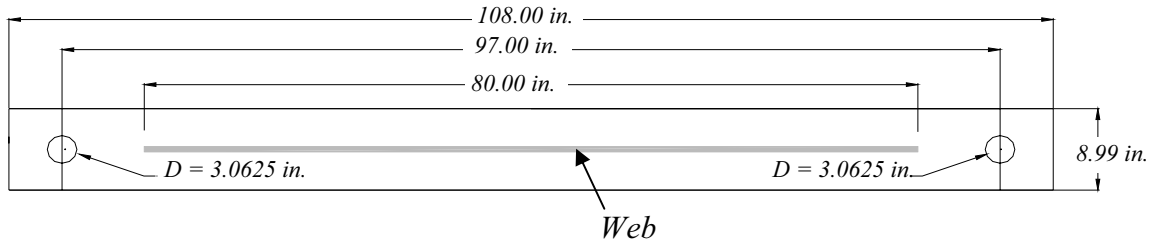

Figure 7.3
Details of the A36 and A588 experimental beam specimen

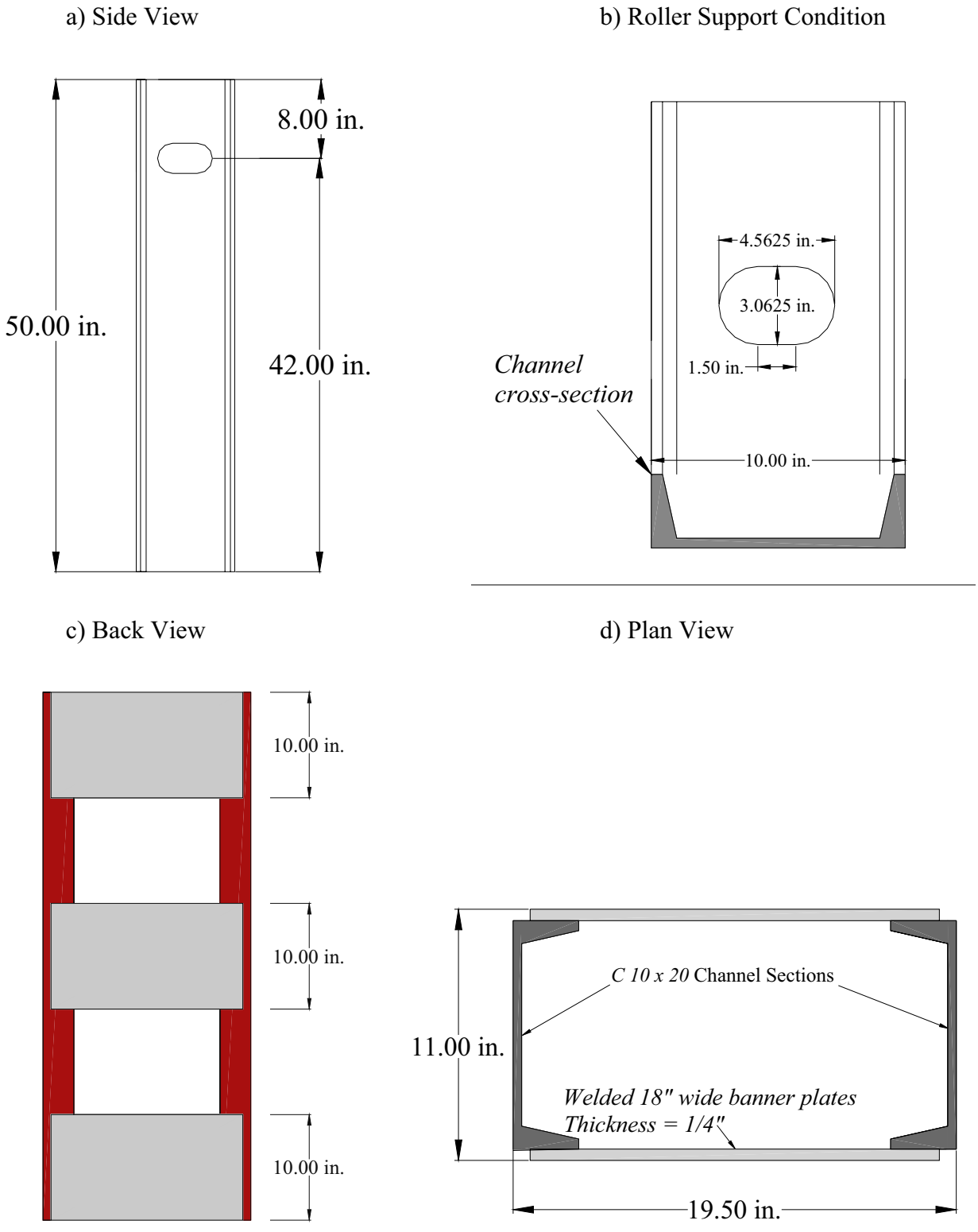

Figure 7.4
Details of the roller support columns

Figure 7.5
Photograph of the roller support column

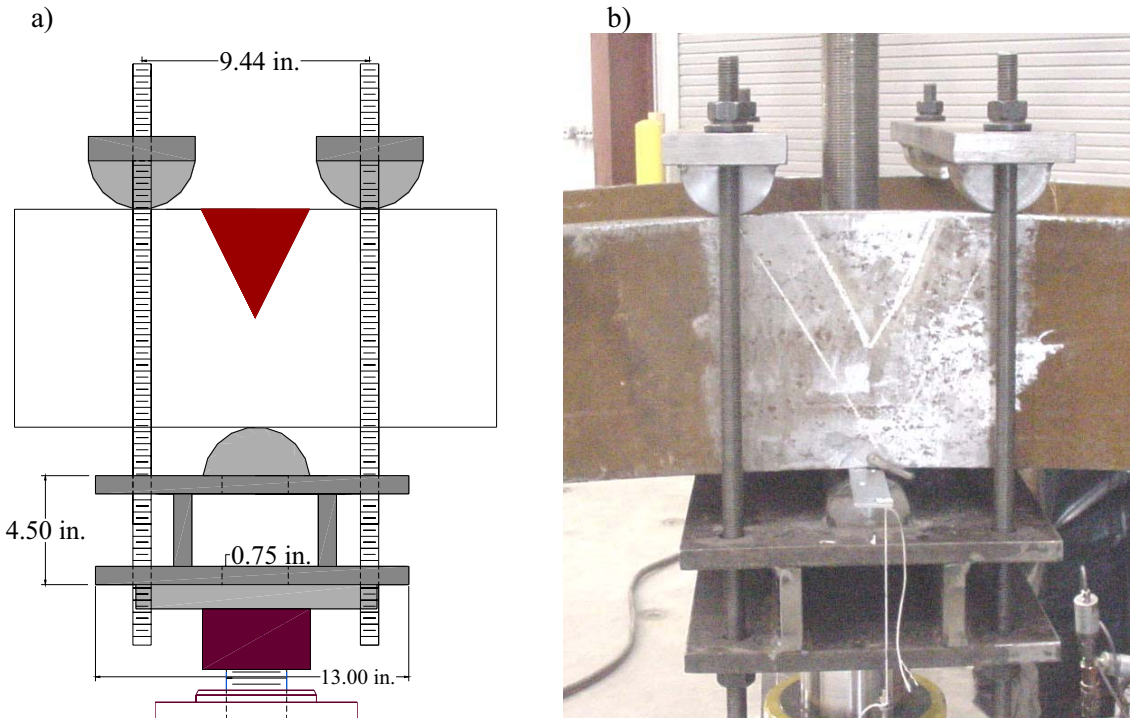

Figure 7.6
Schematic (a) and photograph (b) of the loading frame at beam midspan

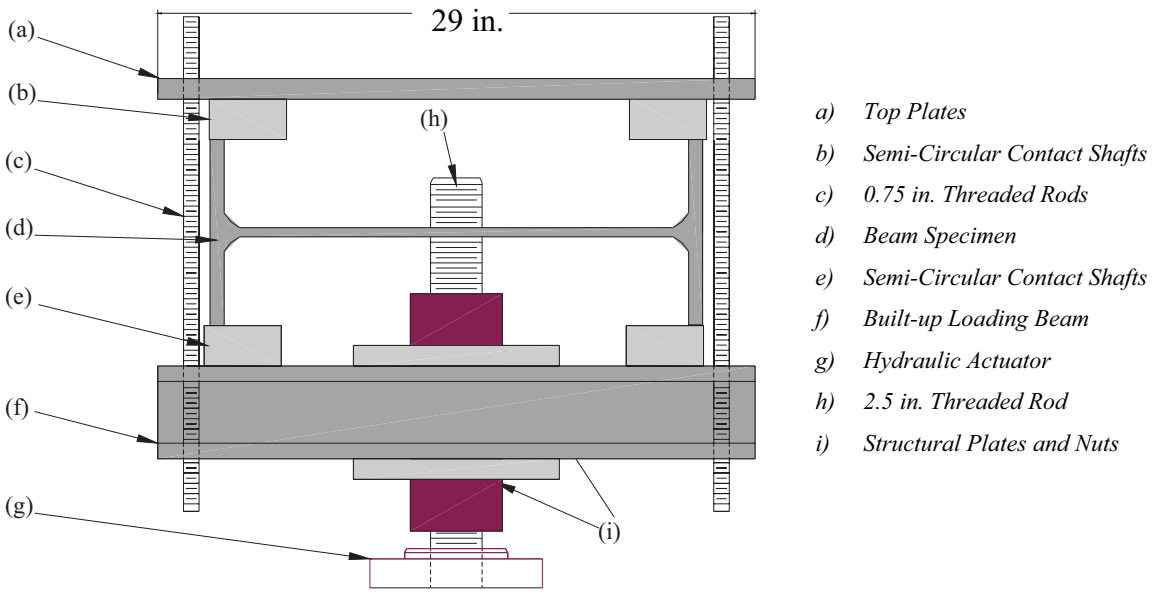

Figure 7.7
Schematic side view of the loading setup

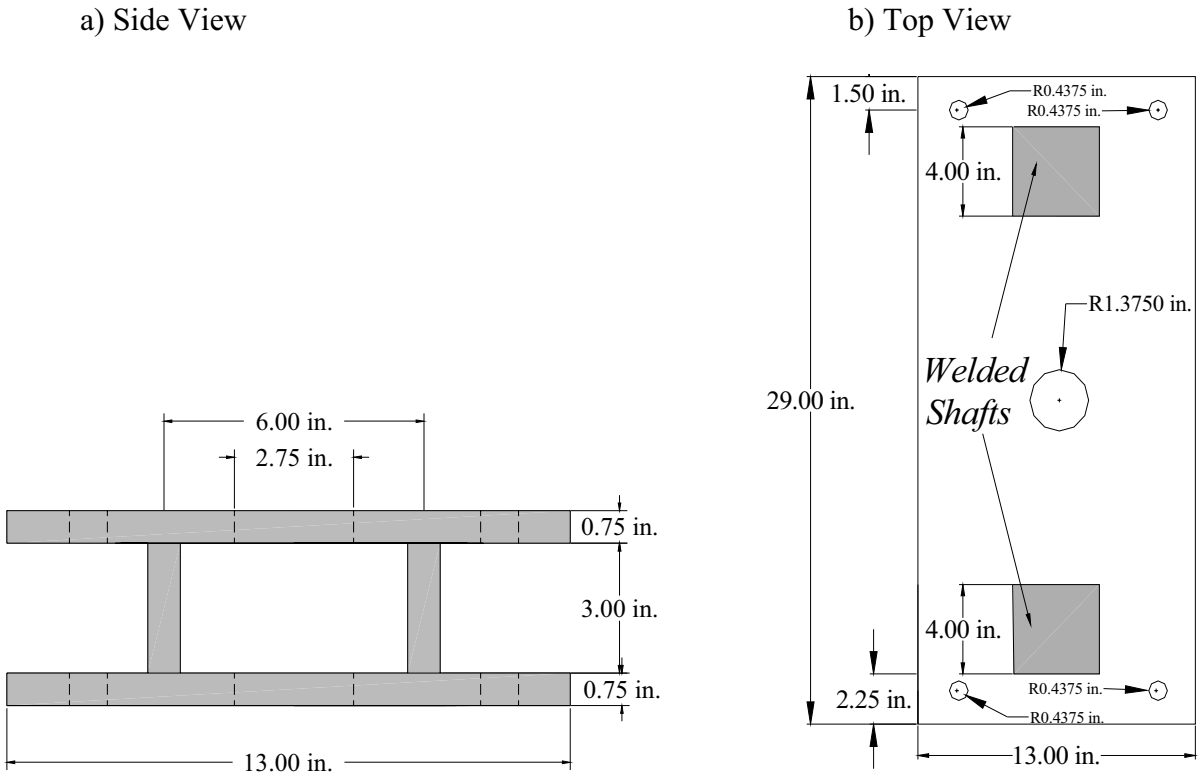

Figure 7.8
Details of the built-up loading beam

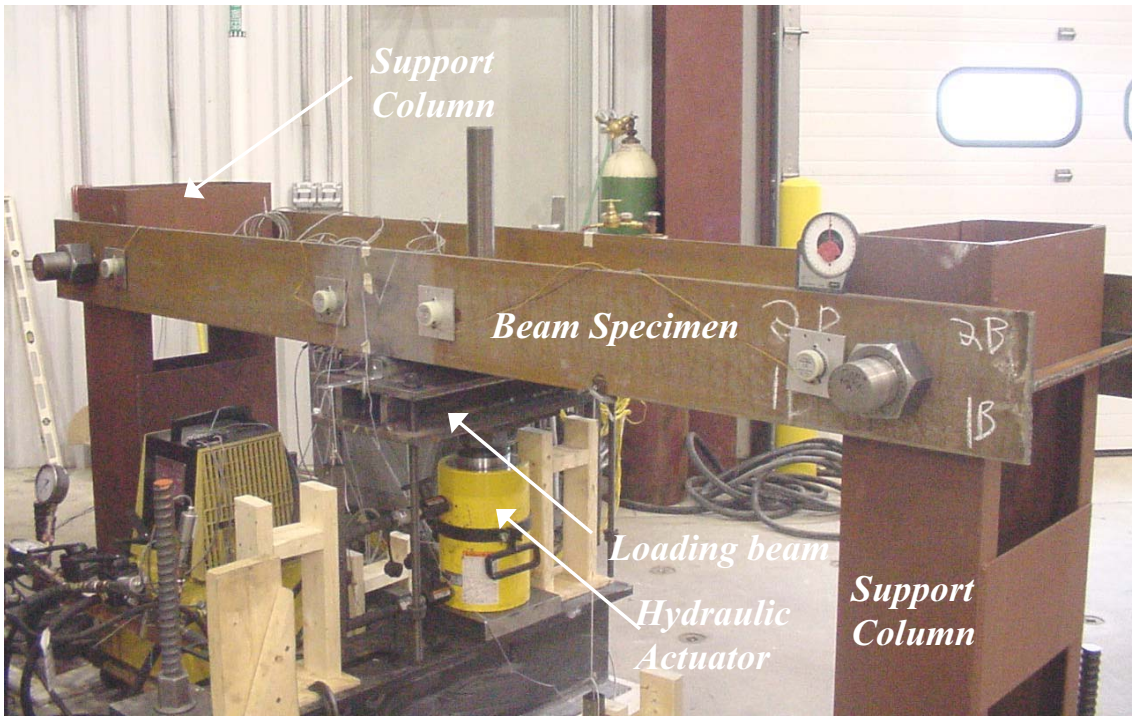

Figure 7.9
Photograph of the front side of the test setup

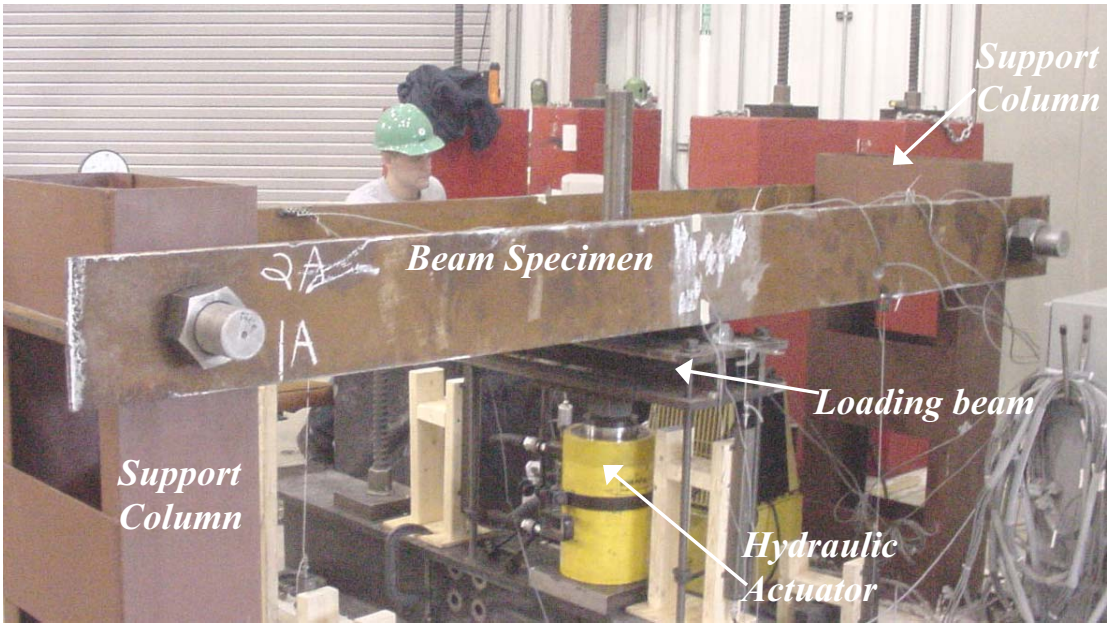

Figure 7.10
Photograph of the back side of the test setup

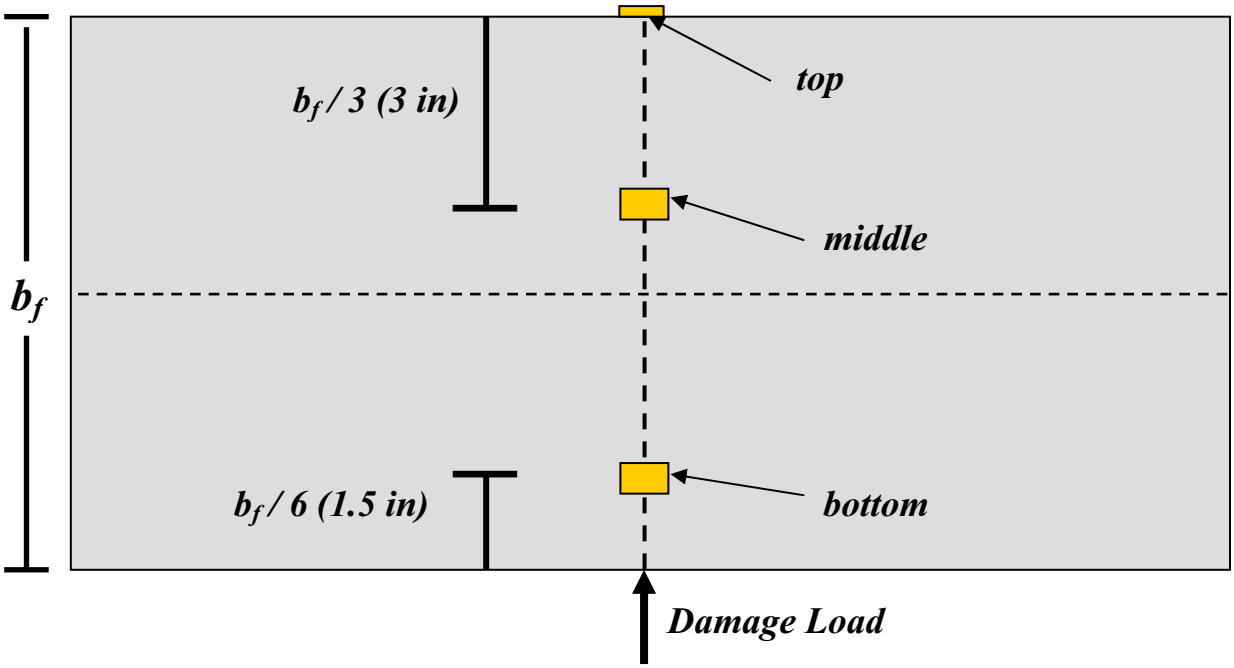

Figure 7.11
Location of longitudinal strain gages attached to both flanges at midspan

Figure 7.12
Location of rotation meter in respect to roller support

a) During Damage

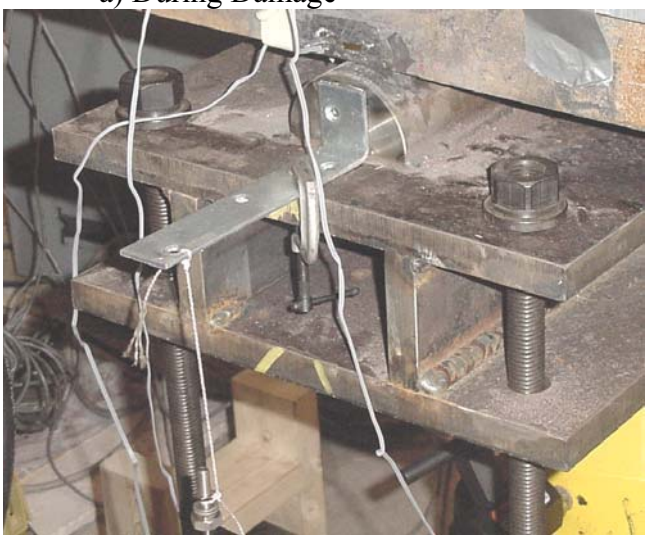

b) During Repair

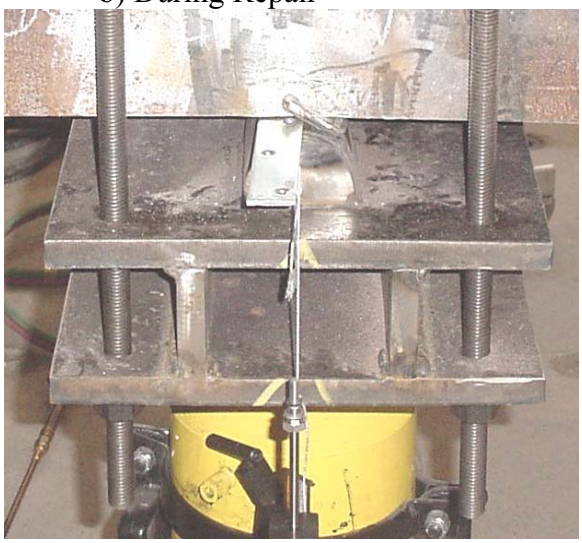

Figure 7.13
Location of displacement transducers (12 in. stroke) located at beam midspan

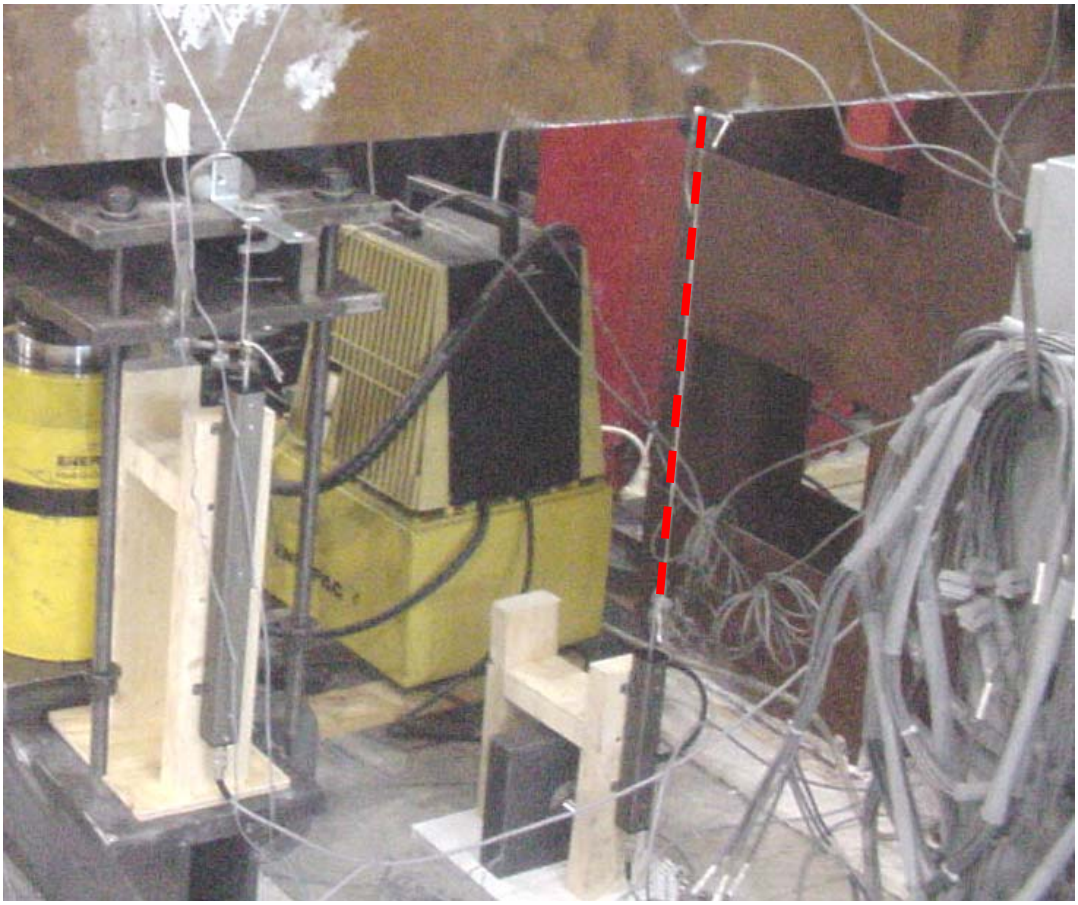

Figure 7.14
Location of displacement transducer (6 in. stroke) at left quarter point

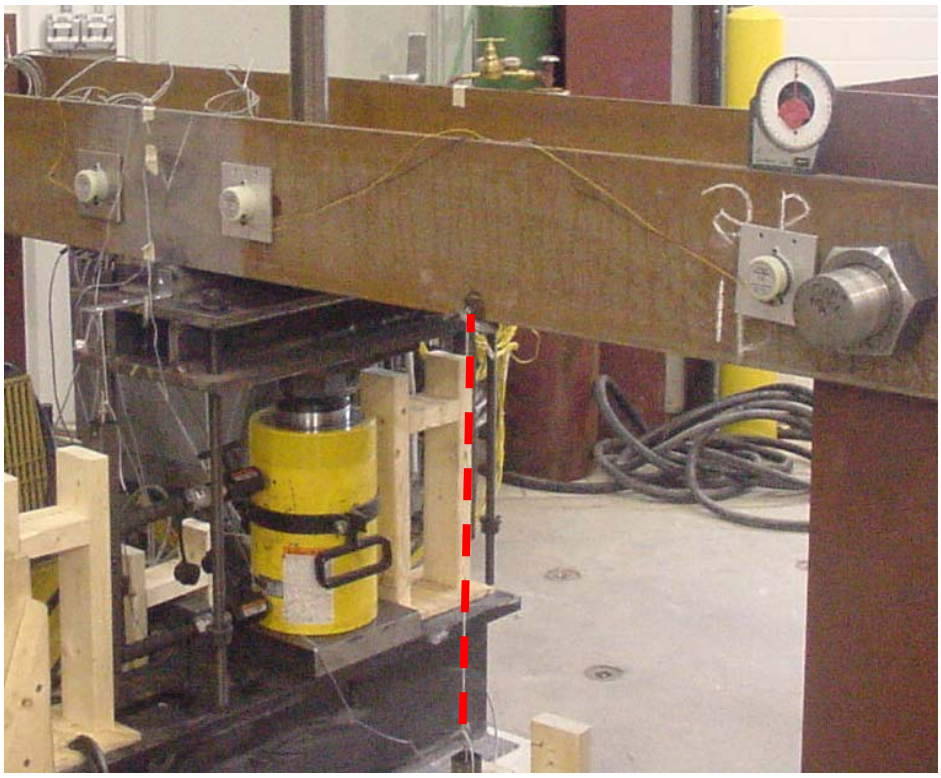

Figure 7.15
Location of displacement transducer (6 in. stroke) at right quarter point

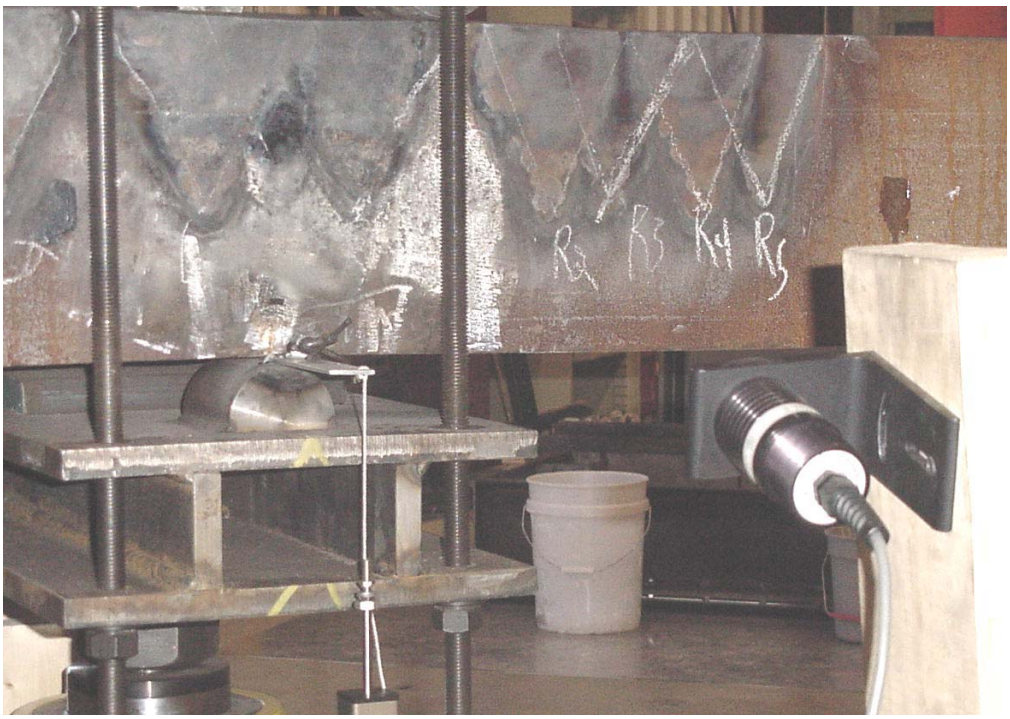

Figure 7.16
Location of infrared thermometer in respect to test setup

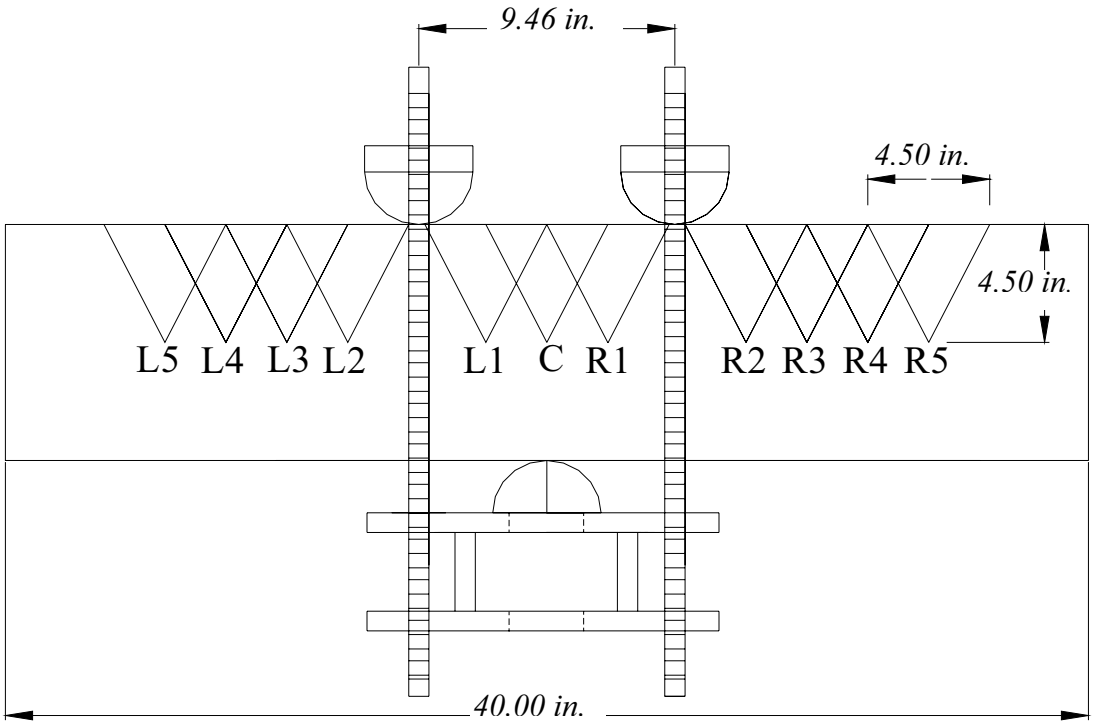

Figure 7.17
Front side view of Vee heat locations and nomenclature

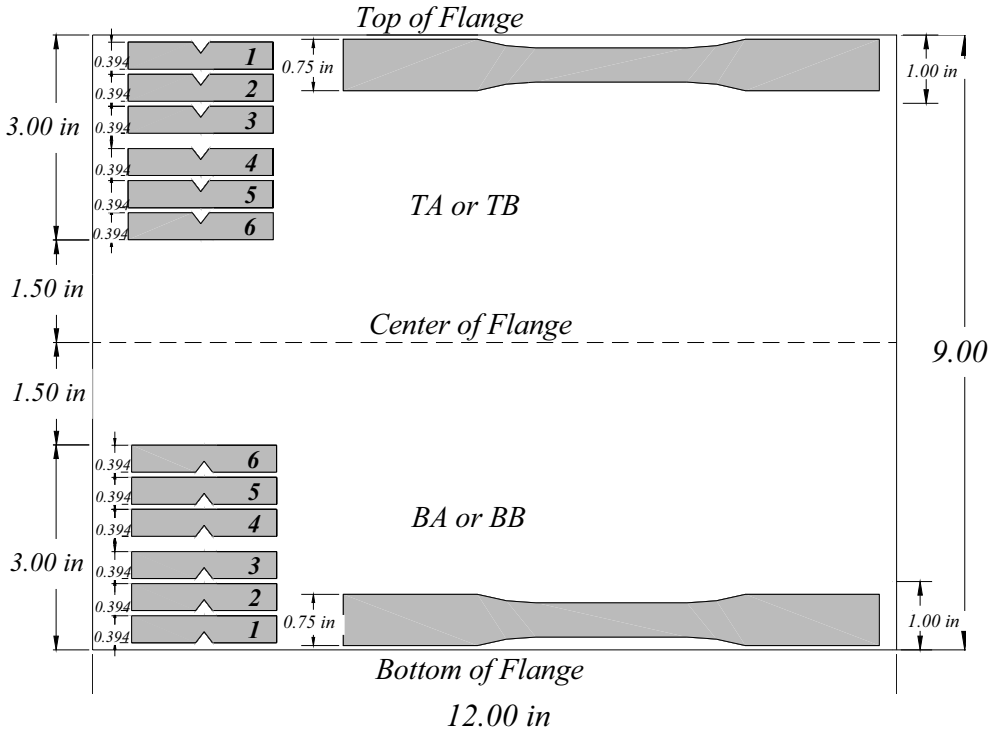

Figure 7.18
Location and nomenclature of undamaged material testing coupons

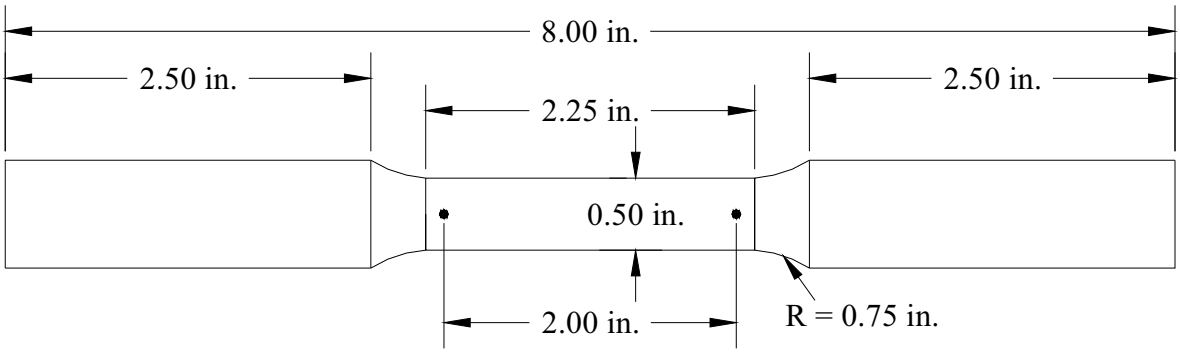

Thickness = 0.50 in

Figure 7.19
Uniaxial tension coupon fabricated from the flanges of beam specimens

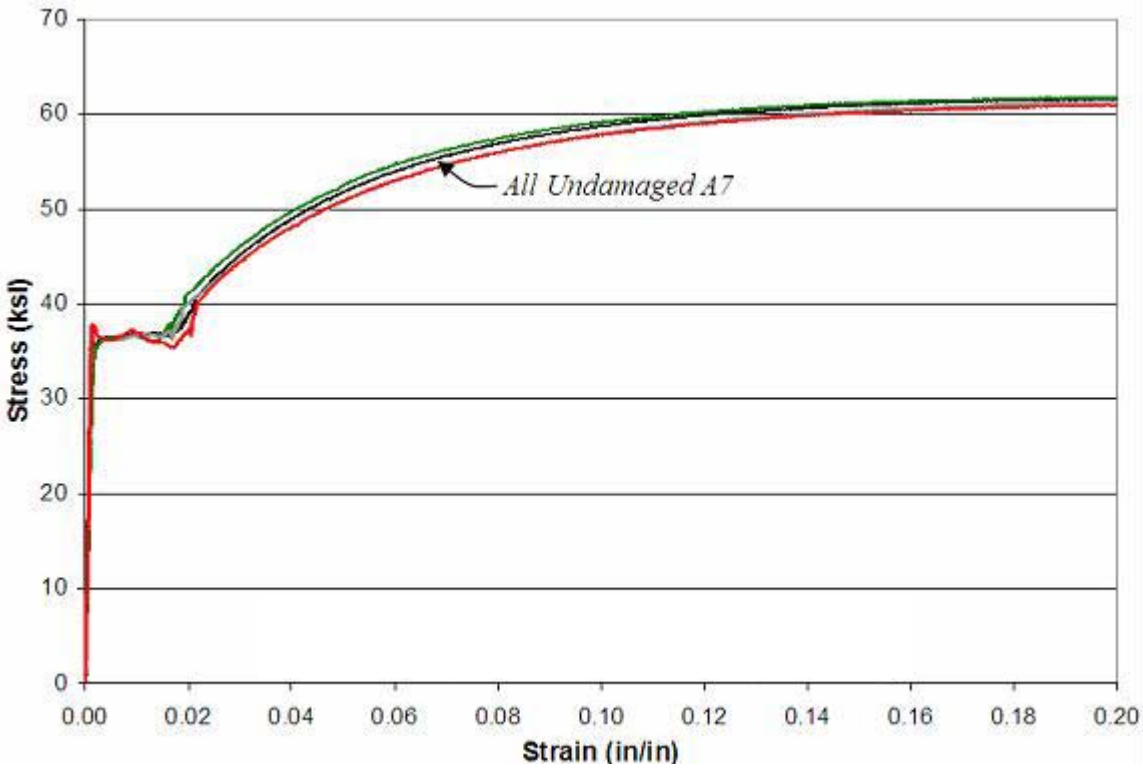

Figure 7.20
Stress-strain relationships of undamaged A7 steel

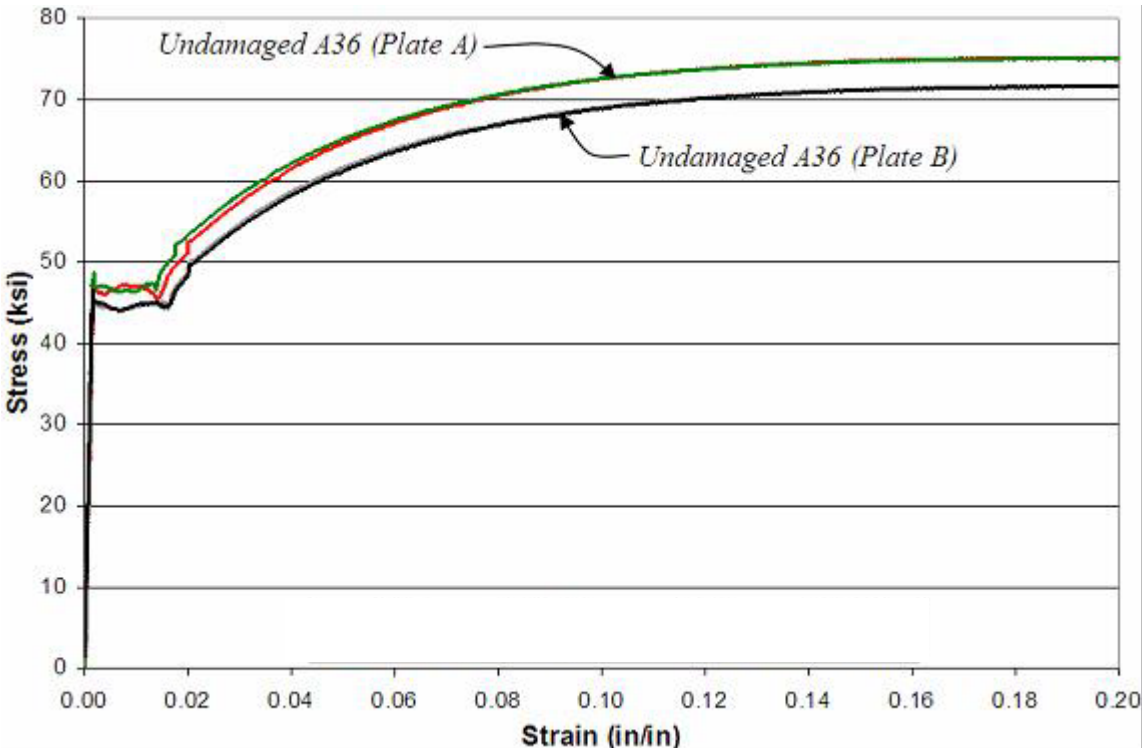

Figure 7.21
Stress-strain relationships of undamaged A36 steel

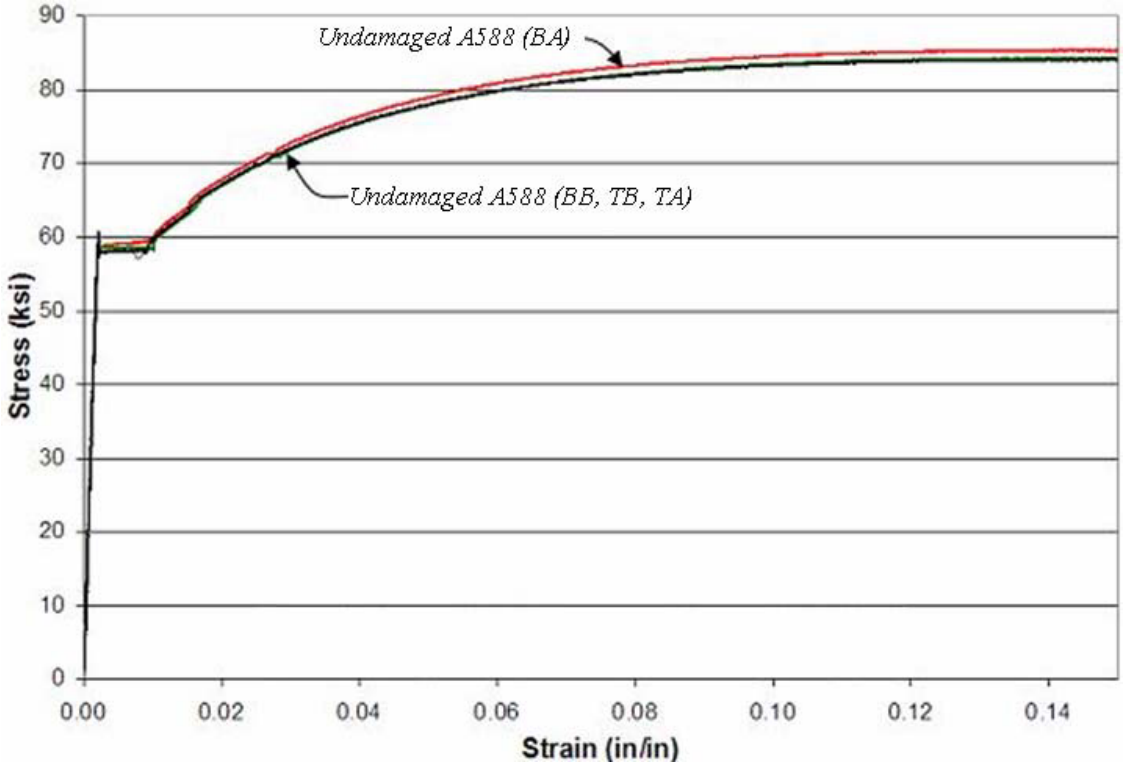

Figure 7.22
Stress-strain relationships of undamaged A588 steel

a) Undamaged A7-Flange A

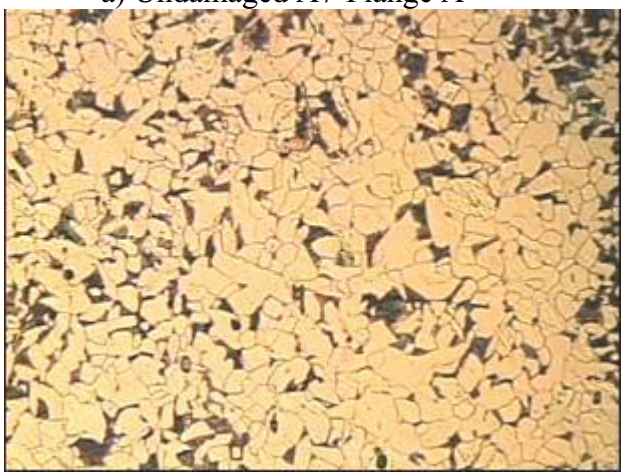

b) Undamaged A7-Flange B

c) Undamaged A36-Flange A

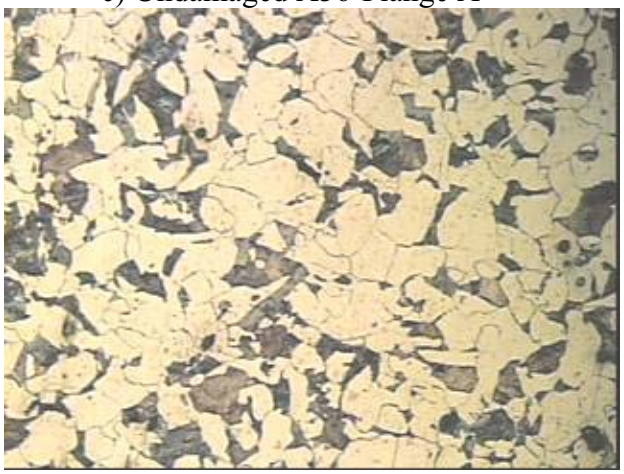

d) Undamaged A36-Flange B

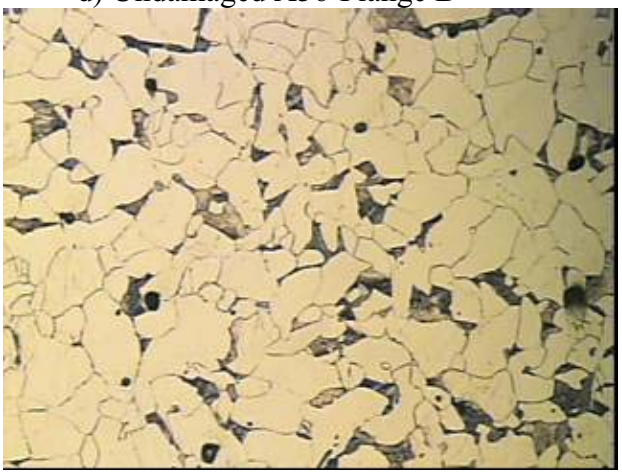

e) Undamaged A588-Flange A

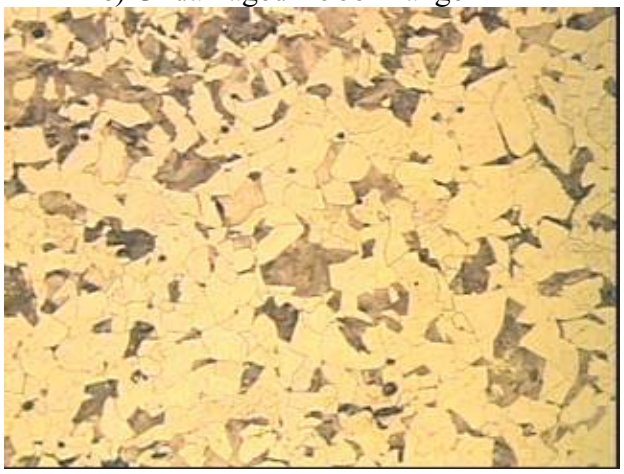

f) Undamaged A588-Flange B

Figure 7.23
Microstructure of undamaged A7, A36, and A588 steel

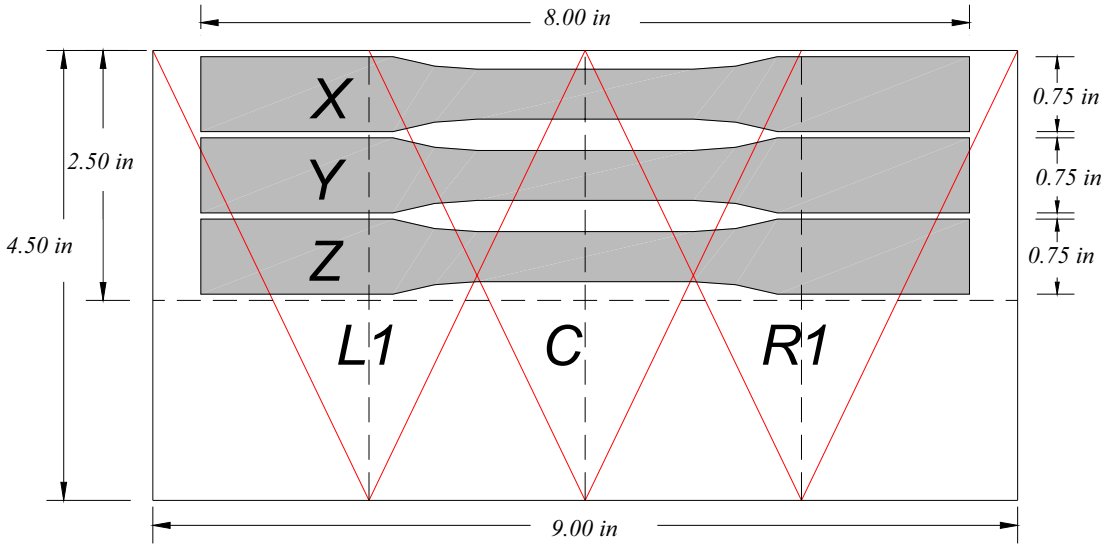

Figure 7.24
Nomenclature and location of damaged-repaired uniaxial tension coupons

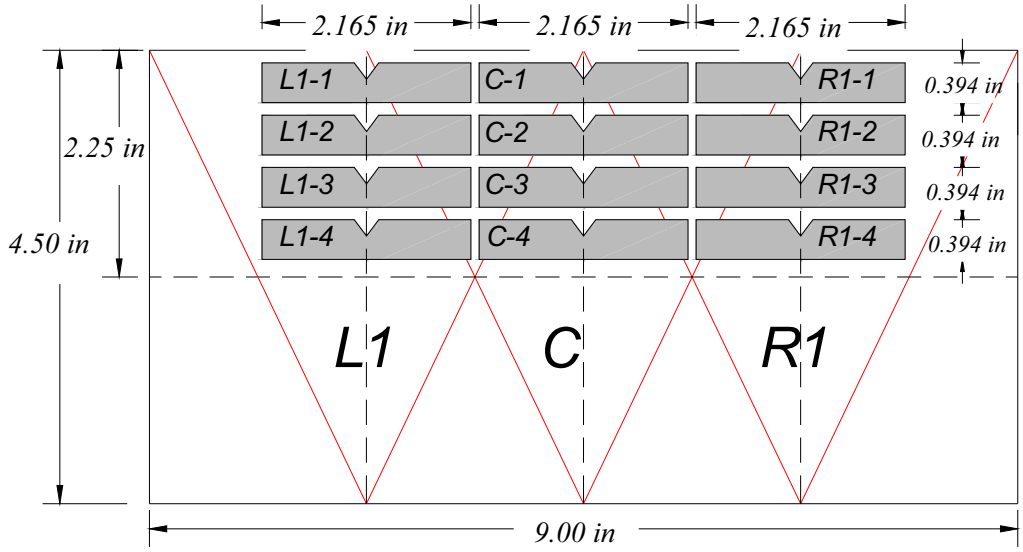

Figure 7.25
Nomenclature and location of damaged-repaired fracture toughness specimens

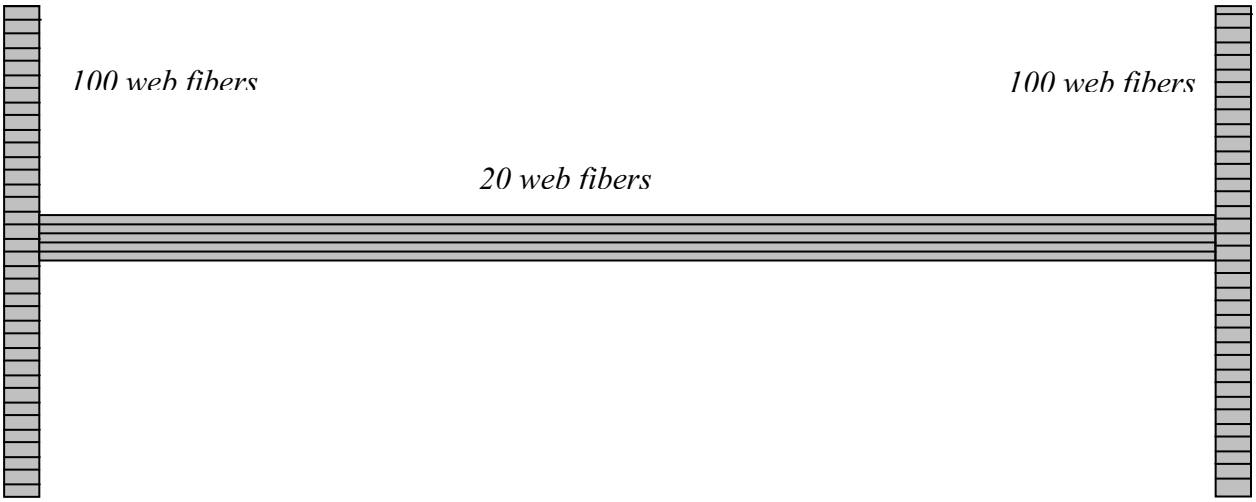

Figure 7.26
Discretization of steel flange and web fibers

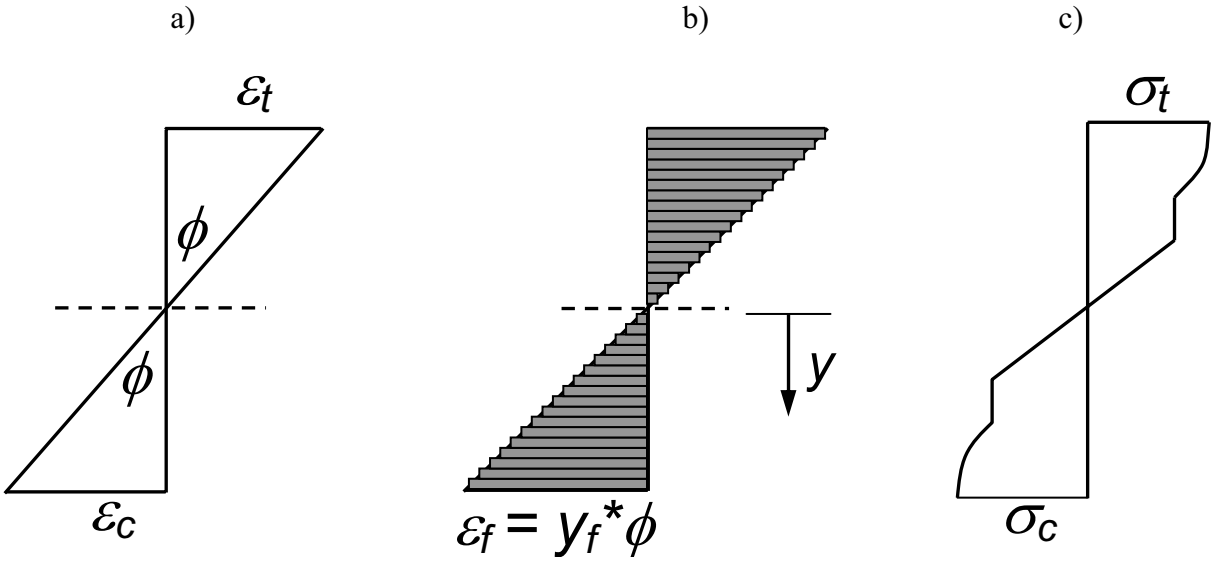

Figure 7.27
Illustration of computing the stress in each fiber

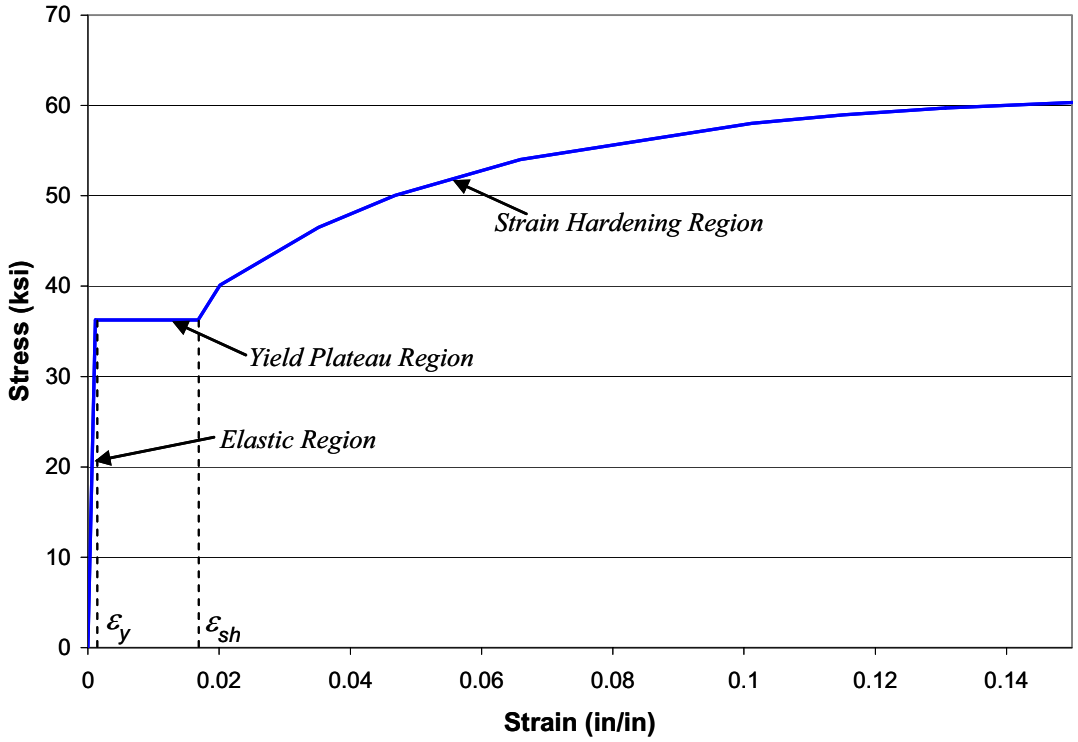

Figure 7.28
Idealized stress-strain relationship of undamaged A7 steel

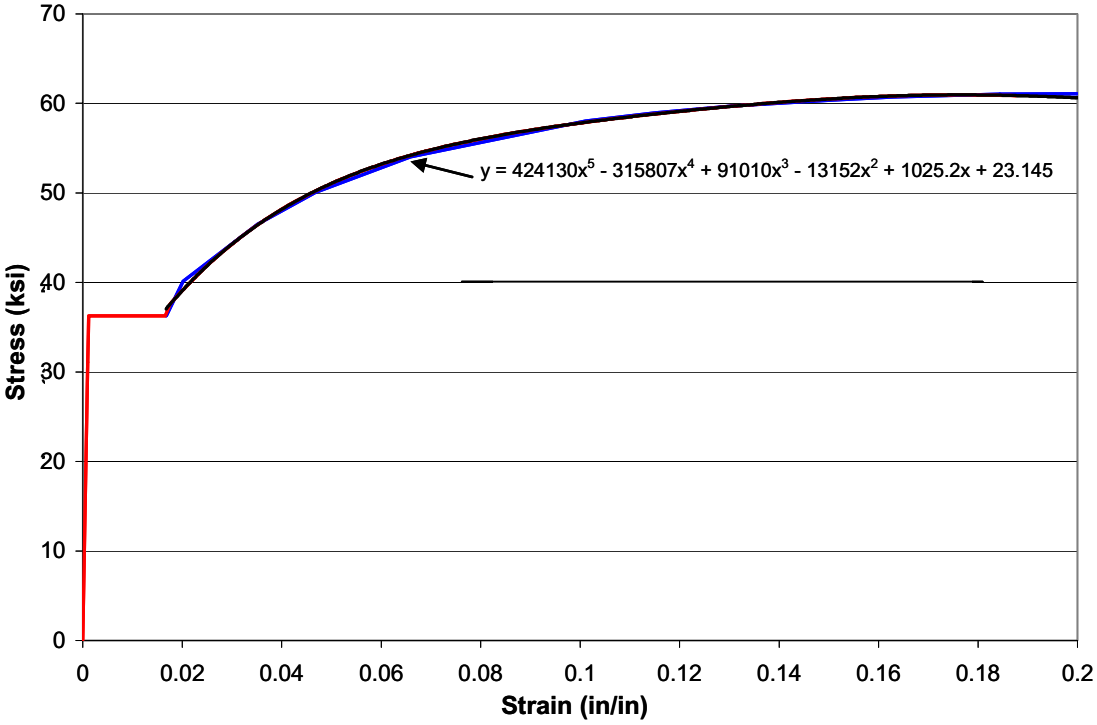

Figure 7.29
Fifth order equation computed by Excel for the strain hardening of A7 steel

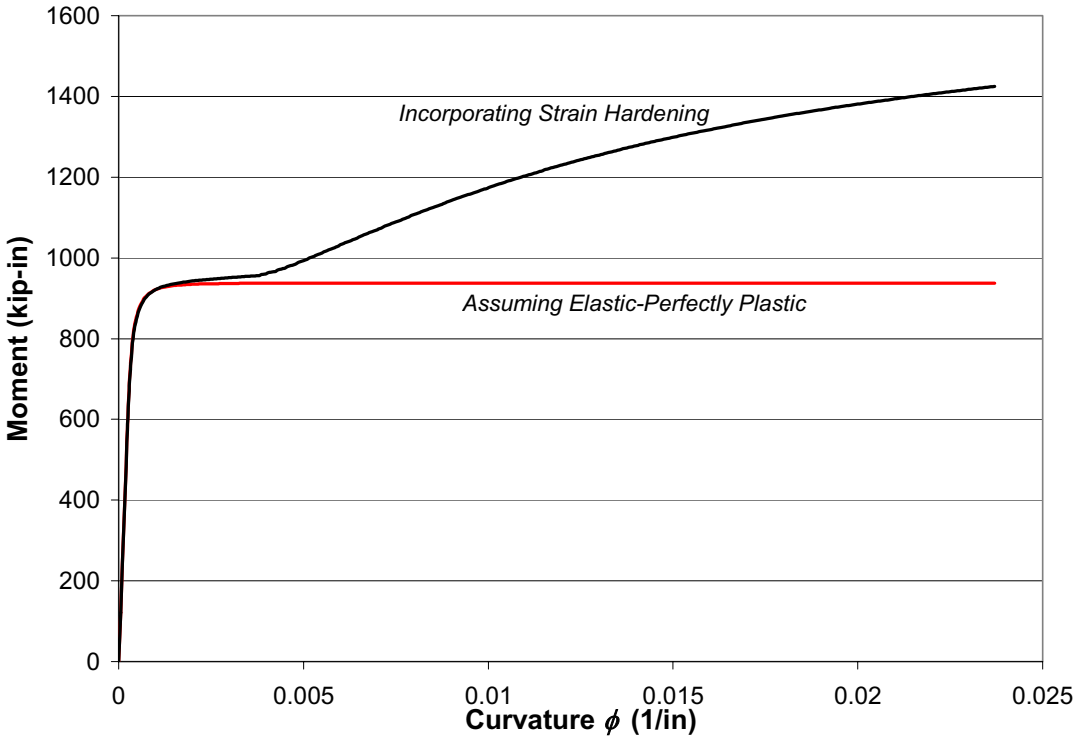

Figure 7.30
Moment-curvature relationship for W24 x76 A7 beam subjected to weak axis bending

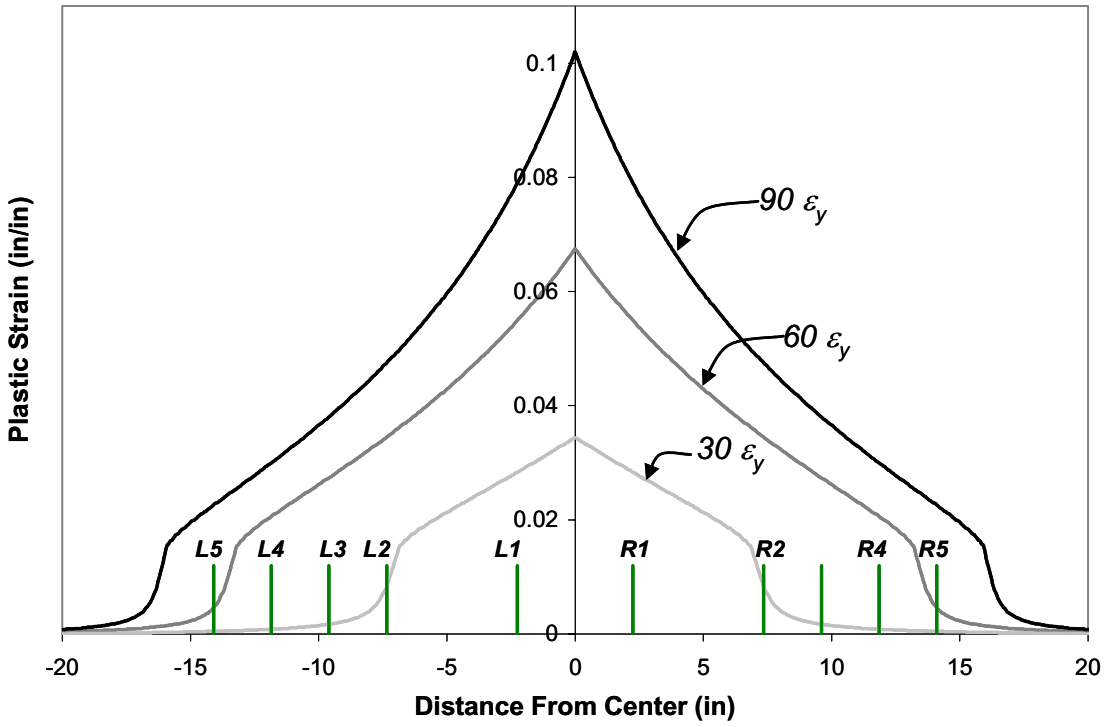

Figure 7.31
Plastic strain distribution along the top of A7 beam specimens

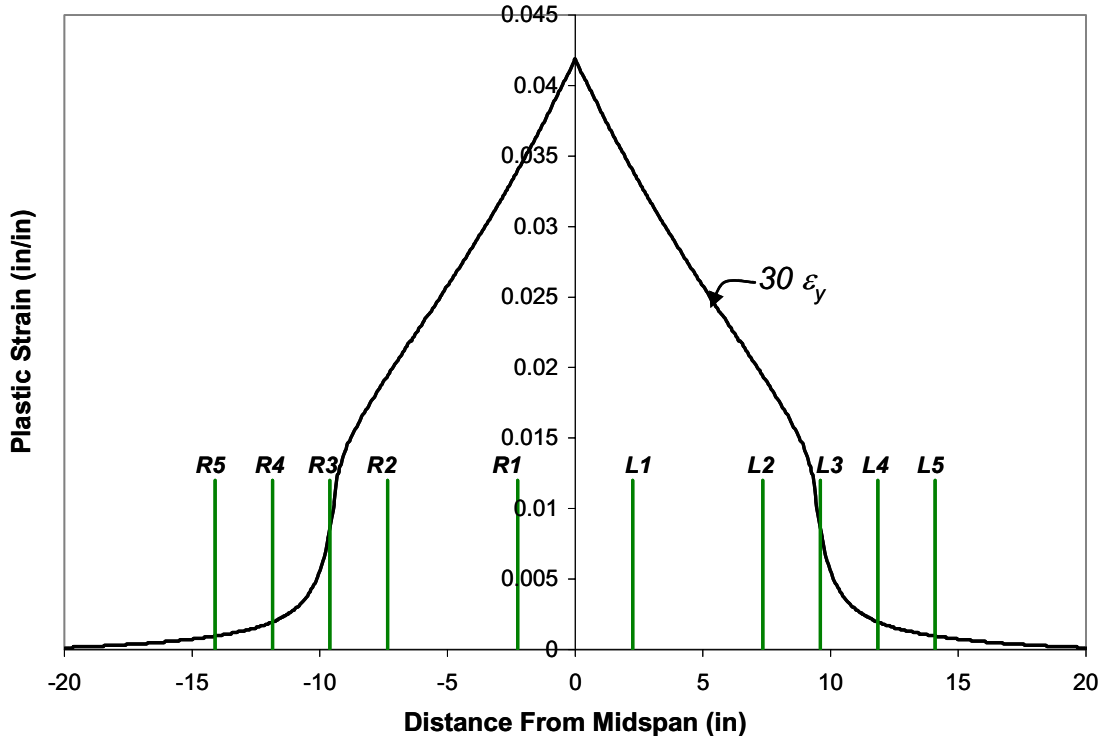

Figure 7.32
Plastic strain distribution along the top of A36 beam specimens

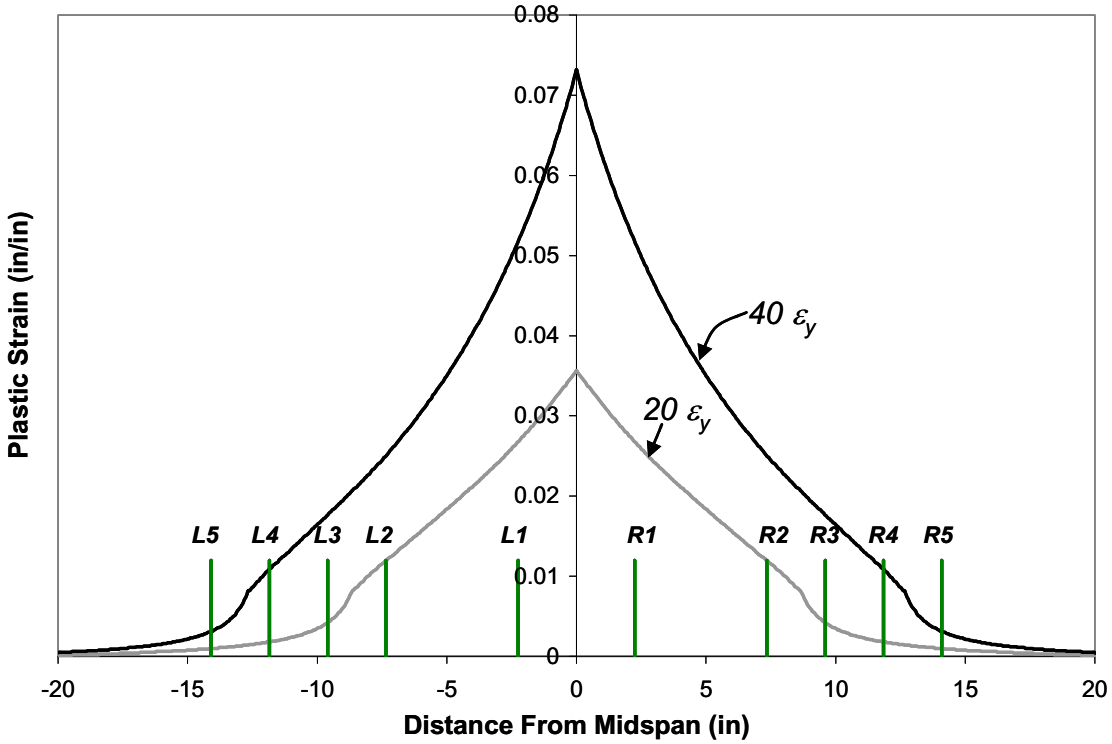

Figure 7.33
Plastic strain distribution along the top of A588 beam specimens

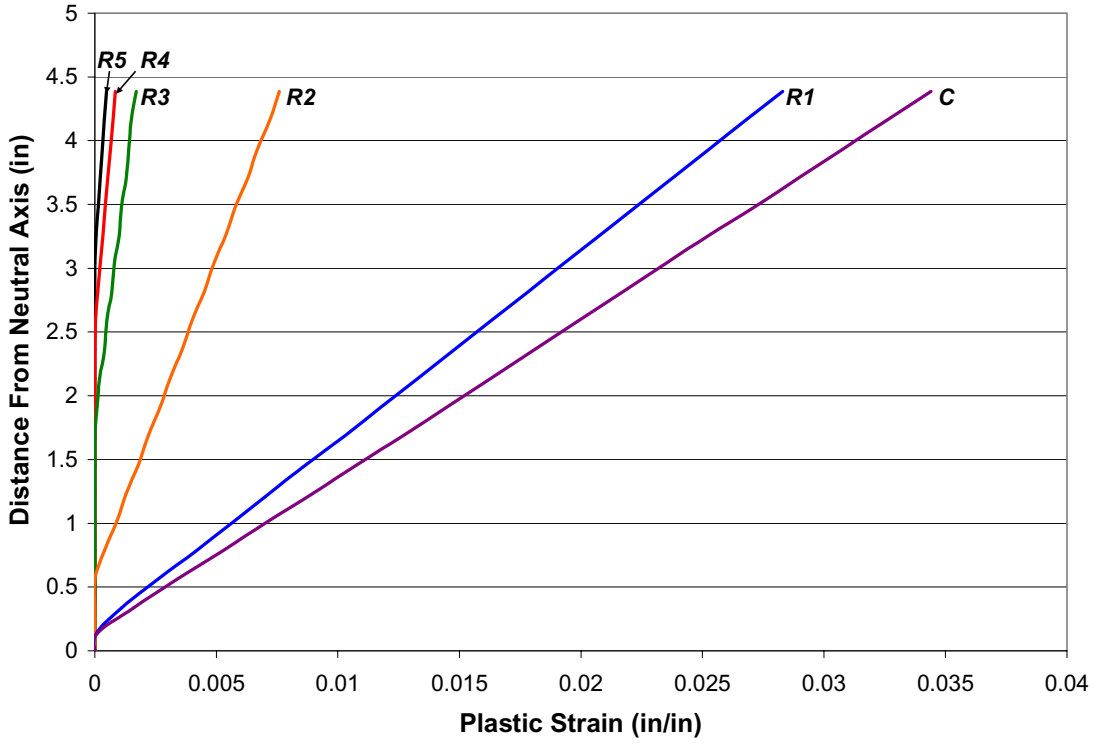

Figure 7.34
Plastic strain distribution along half the depth of A7 beams damaged to 30 ε_y

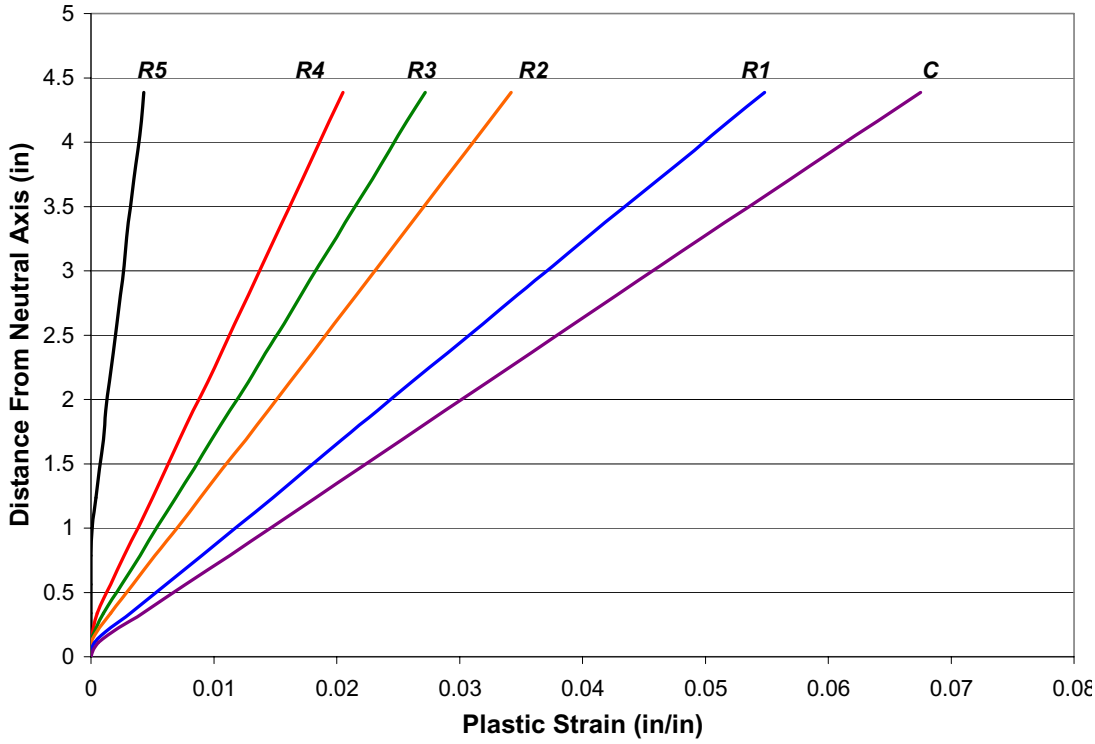

Figure 7.35
Plastic strain distribution along half the depth of A7 beams damaged to 60 ε_y

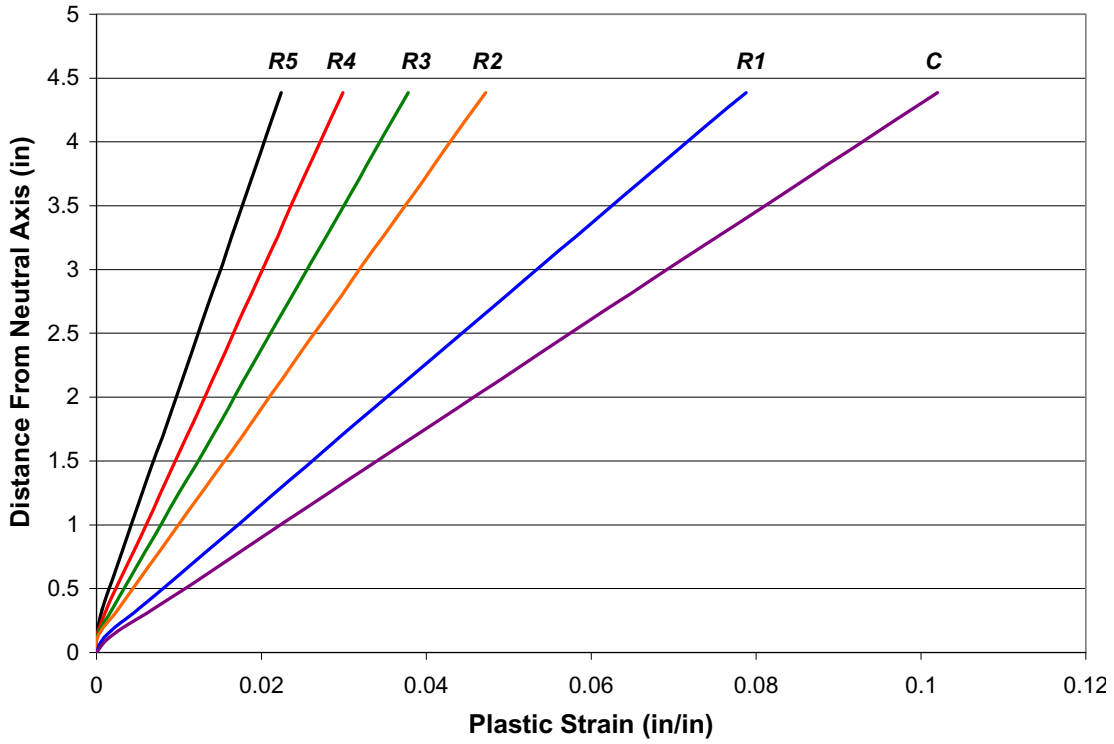

Figure 7.36
Plastic strain distribution along half the depth of A7 beams damaged to 90 ε_y

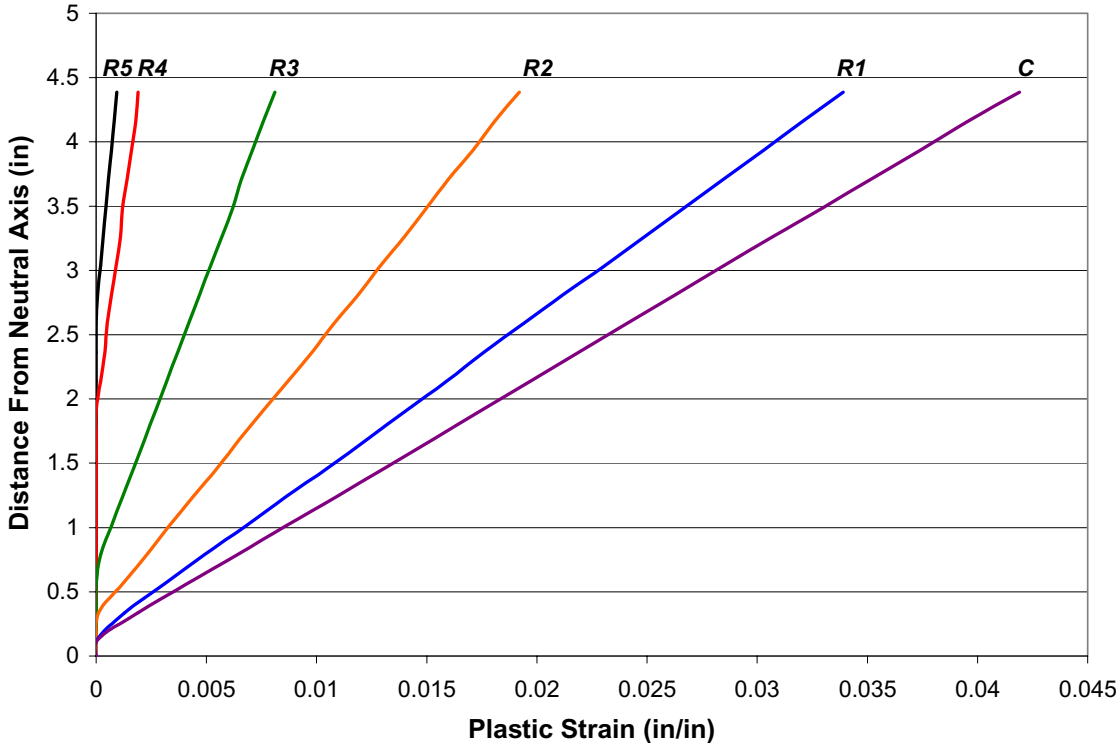

Figure 7.37
Plastic strain distribution along half the depth of A36 beams damaged to 30 ε_y

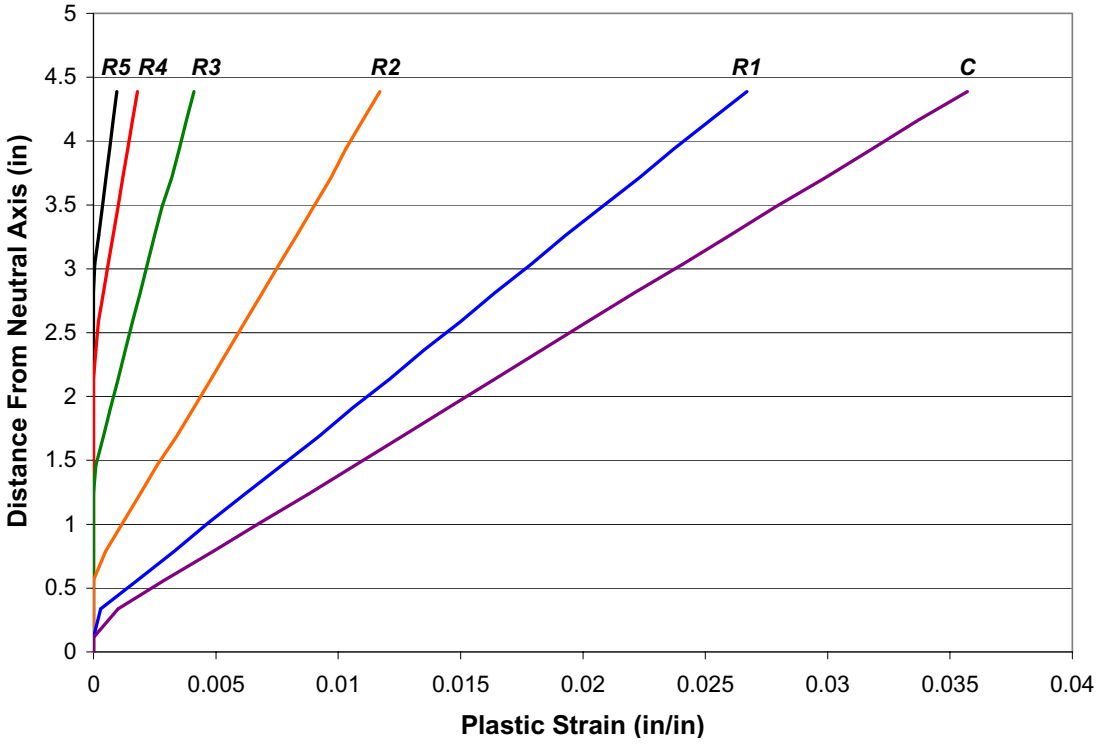

Figure 7.38
Plastic strain distribution along half the depth of A588 beams damaged to 20 ε_y

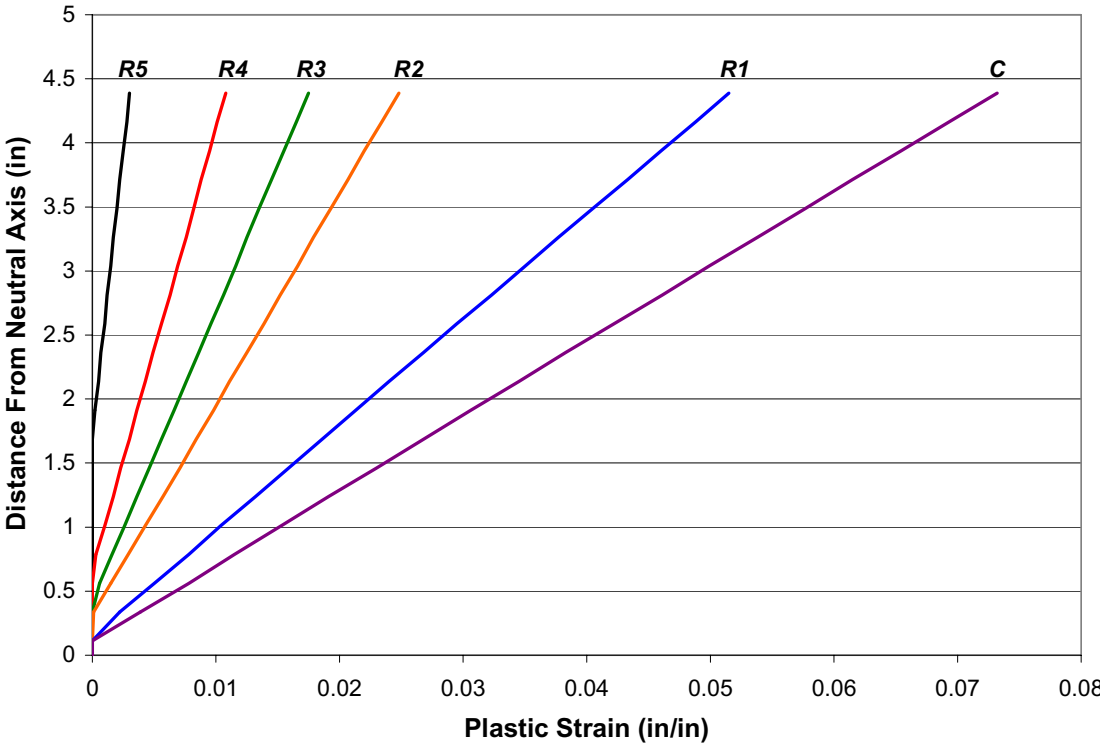

Figure 7.39
Plastic strain distribution along half the depth of A588 beams damaged to 40 ε_y

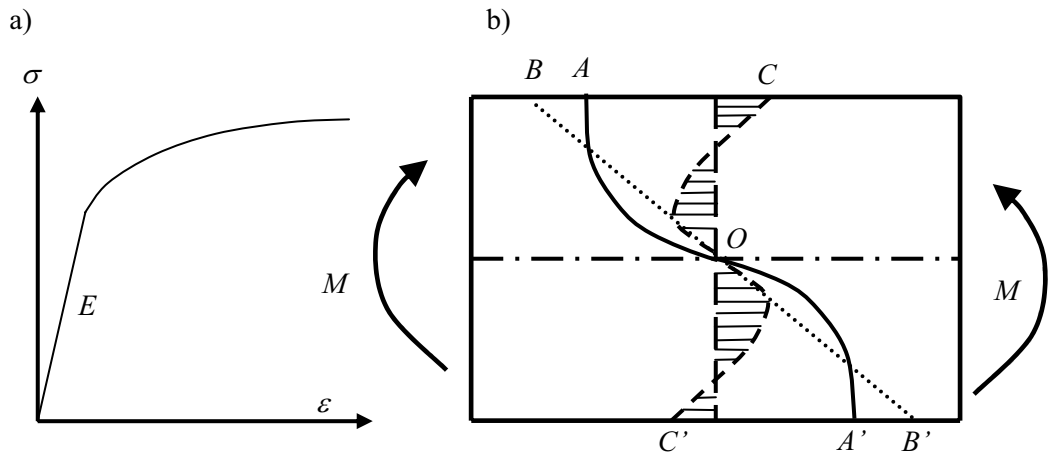

Figure 7.40
Induced residual stresses in a steel beam subjected to bending [*I*]

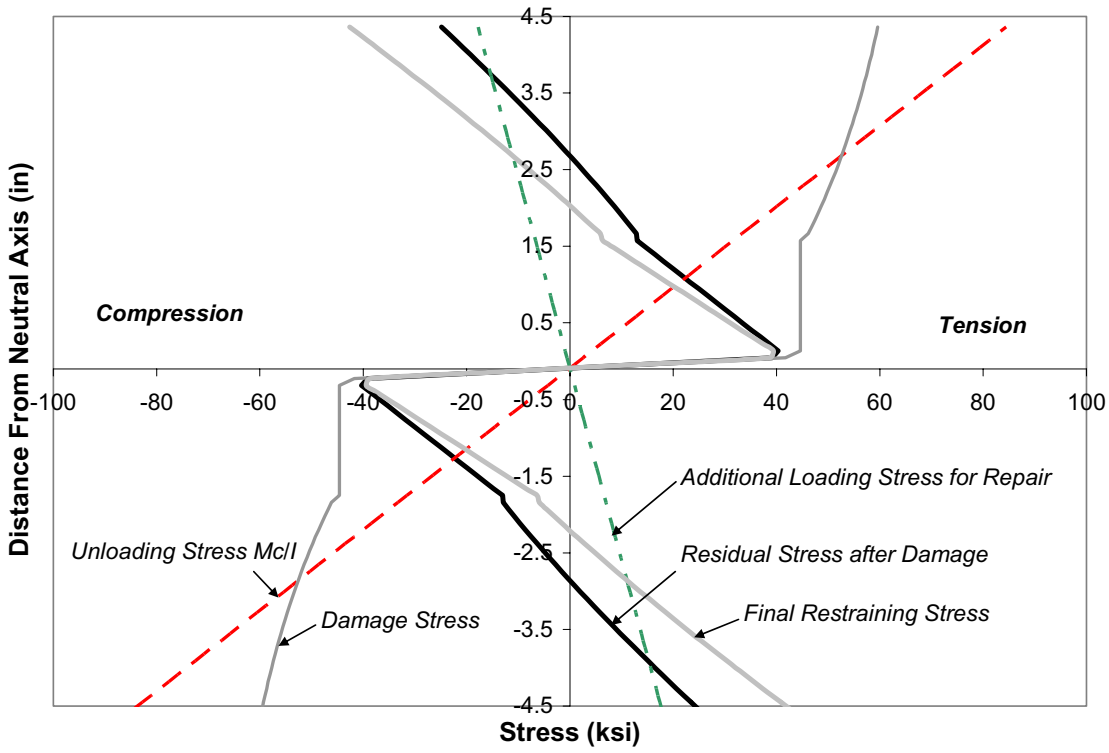

Figure 7.41
Damage-repair stress history of A36-Beam 1 (30 ε_y max) along the center Vee heat (*C*)

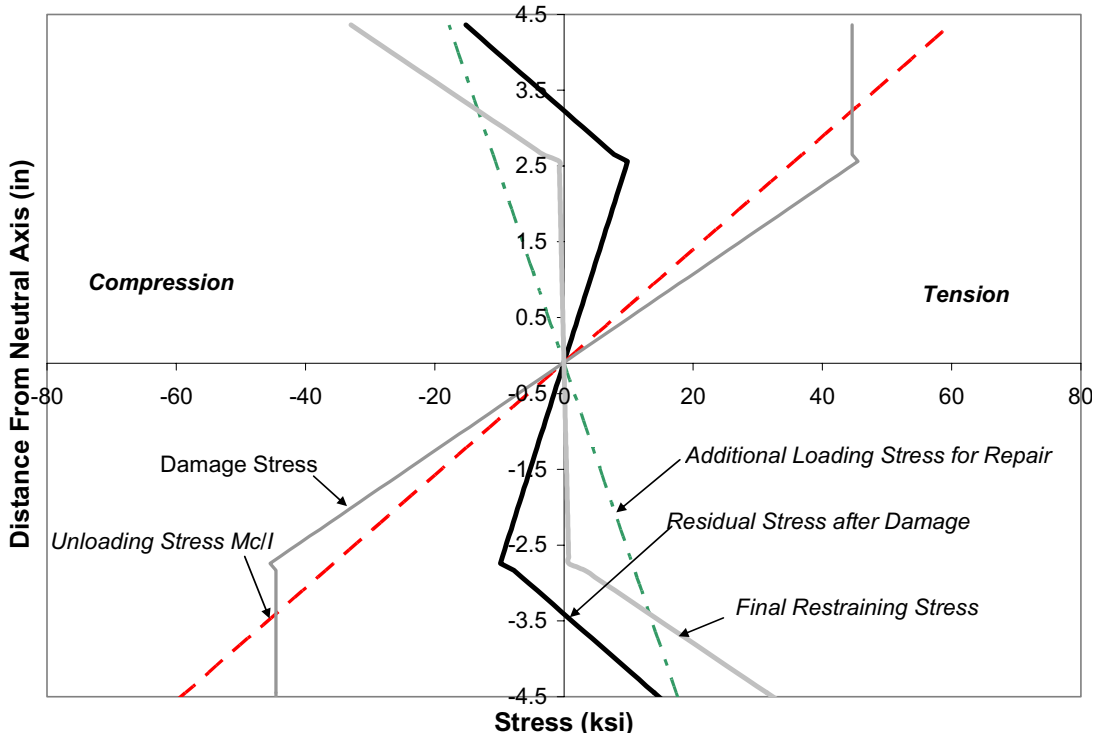

Figure 7.42
Damage-repair stress history of A36-Beam 1 along the furthest Vee heat from center (*R5*)

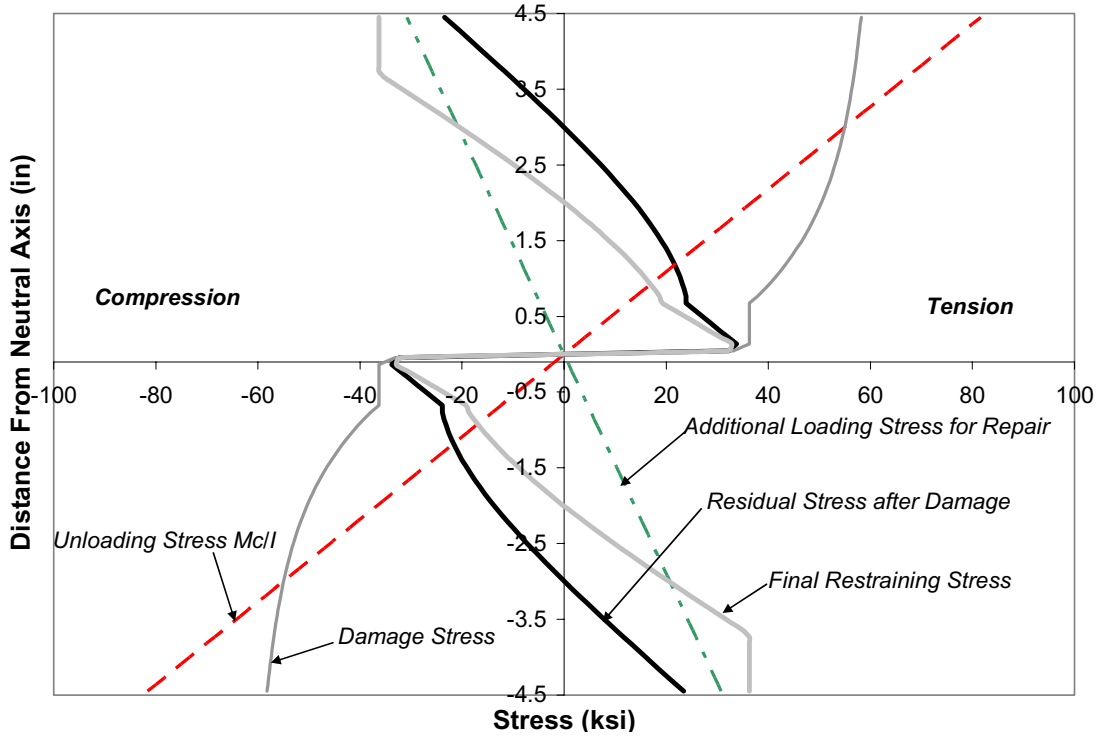

Figure 7.43
Damage-repair stress history of A7-Beam 2 (90 ε_y max) along the center Vee heat (*C*)

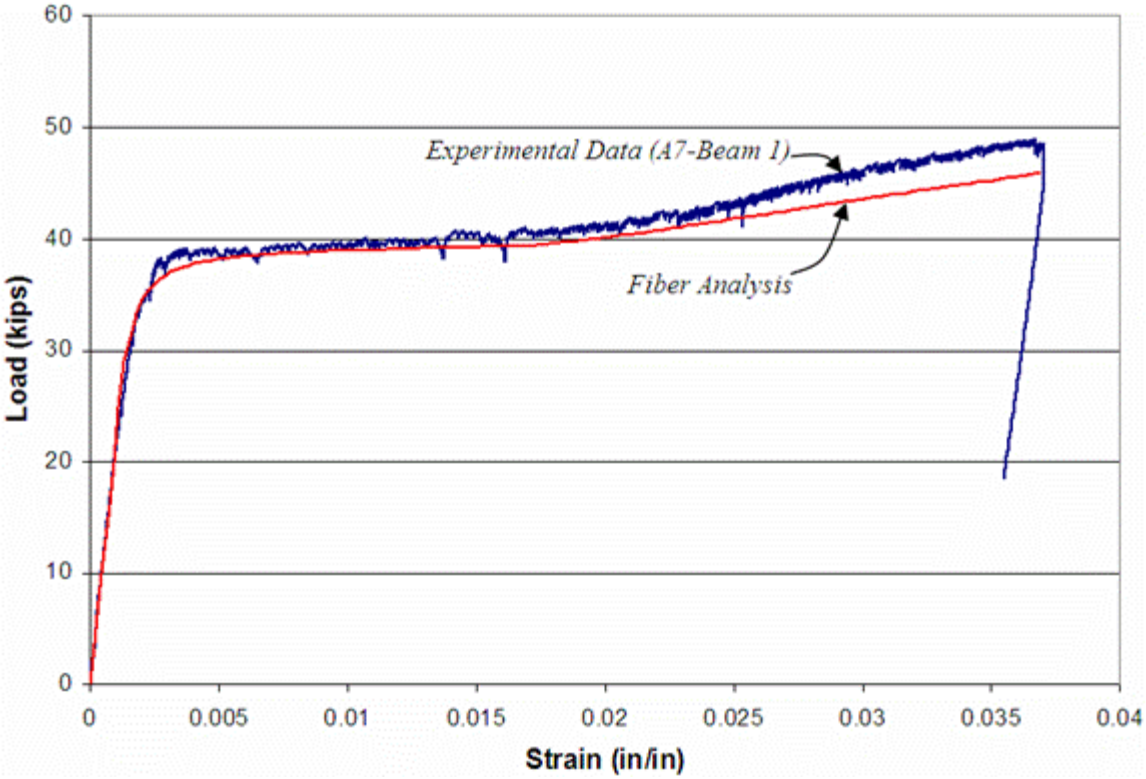

Figure 7.44
Load-strain comparisons between fiber analysis and experimental results (A7-Beam 1)

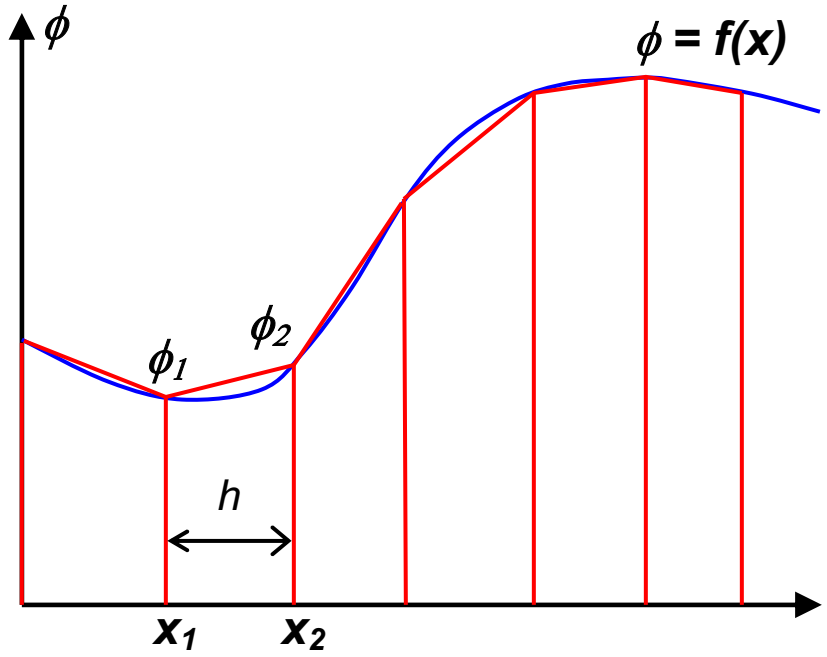

Figure 7.45
Illustration of trapezoidal rule of integration used to compute rotations

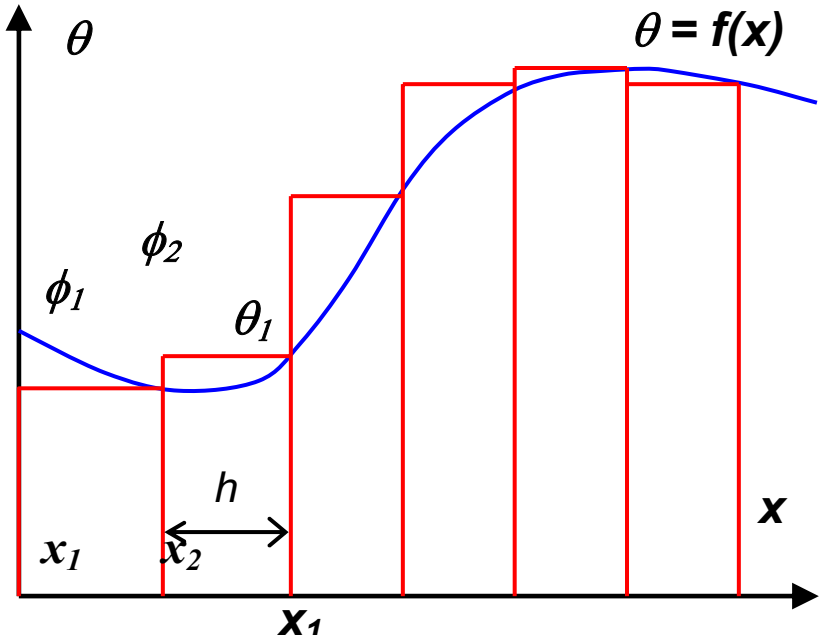

Figure 7.46
Illustration of Rieman's rule of integration used to compute displacements

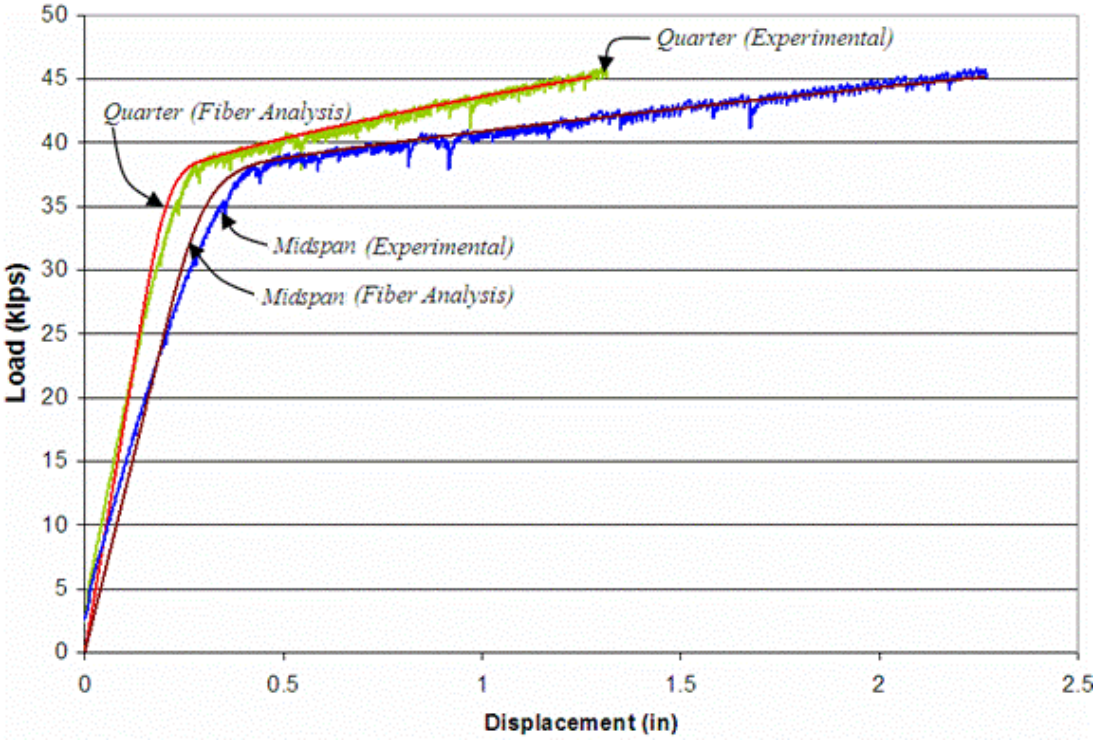

Figure 7.47
Load-displacement comparisons between fiber analysis and experimental data (A7-Beam 1)

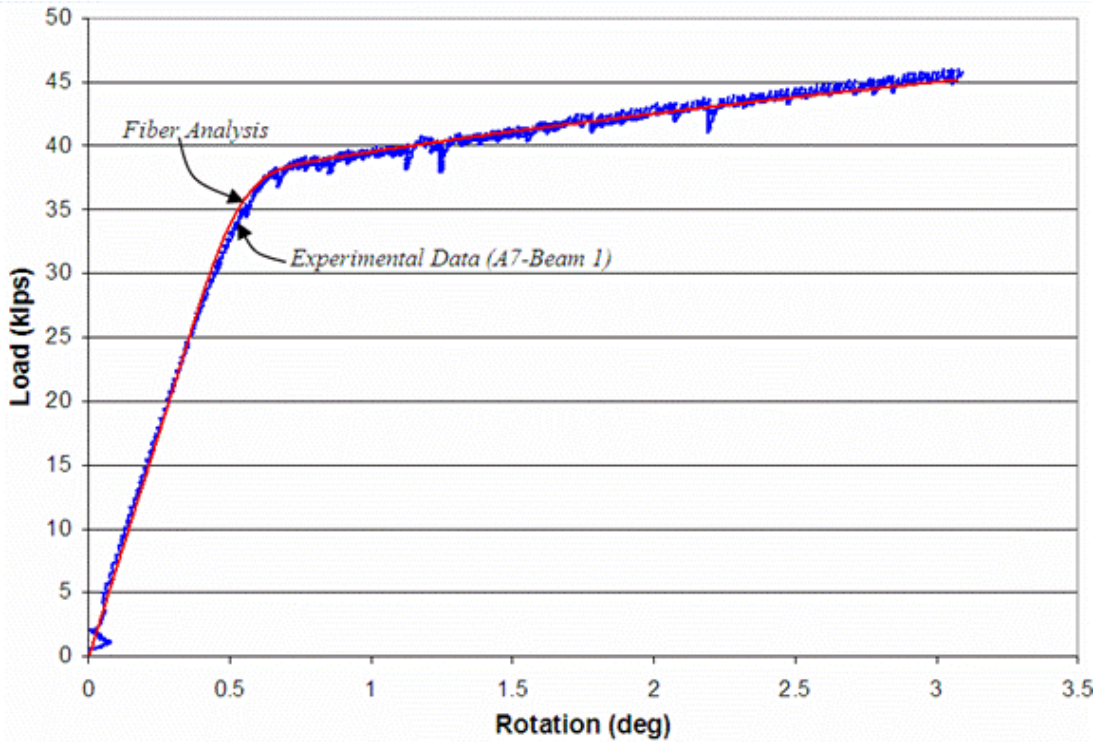

Figure 7.48
Load-rotation comparisons between fiber analysis and experimental data (A7-Beam 1)

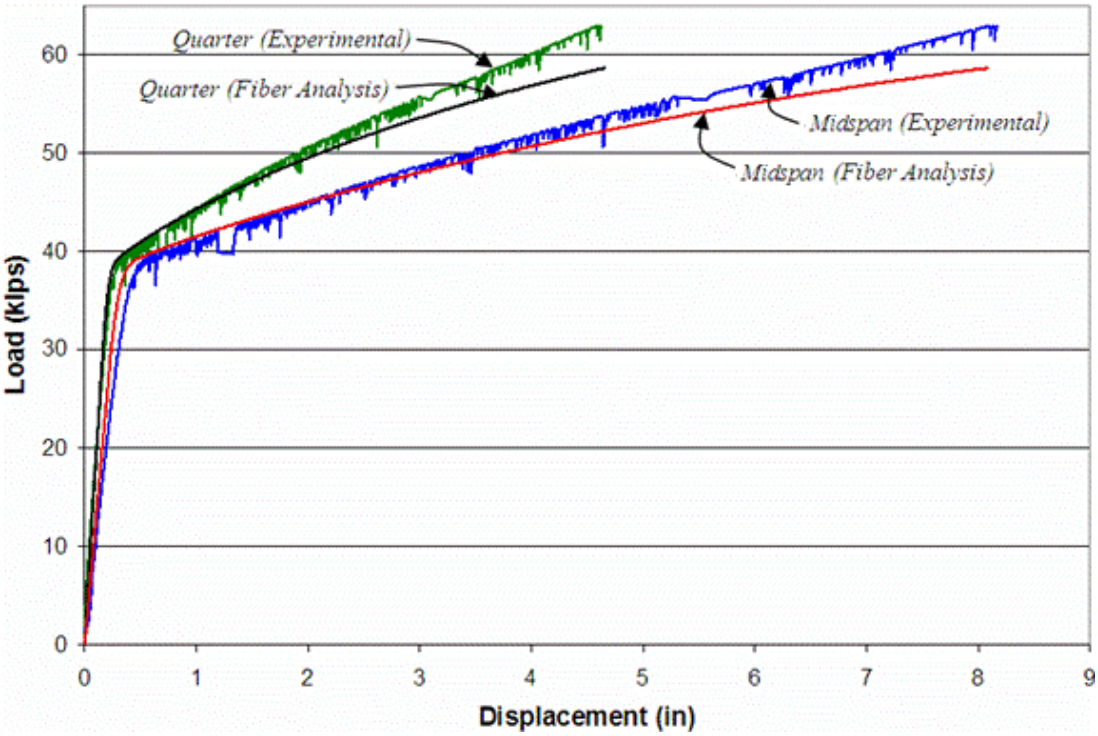

Figure 7.49
Load-displacement comparisons between fiber analysis and experimental data (A7-Beam 2)

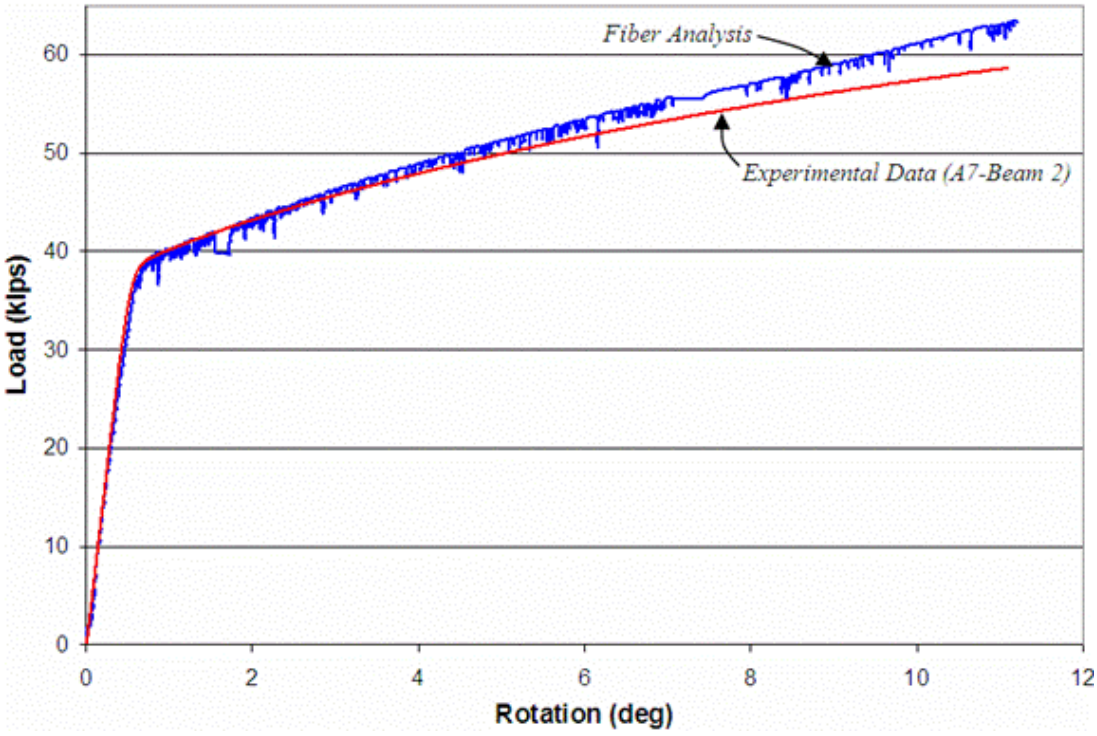

Figure 7.50
Load-rotation comparisons between fiber analysis and experimental data (A7-Beam 2)

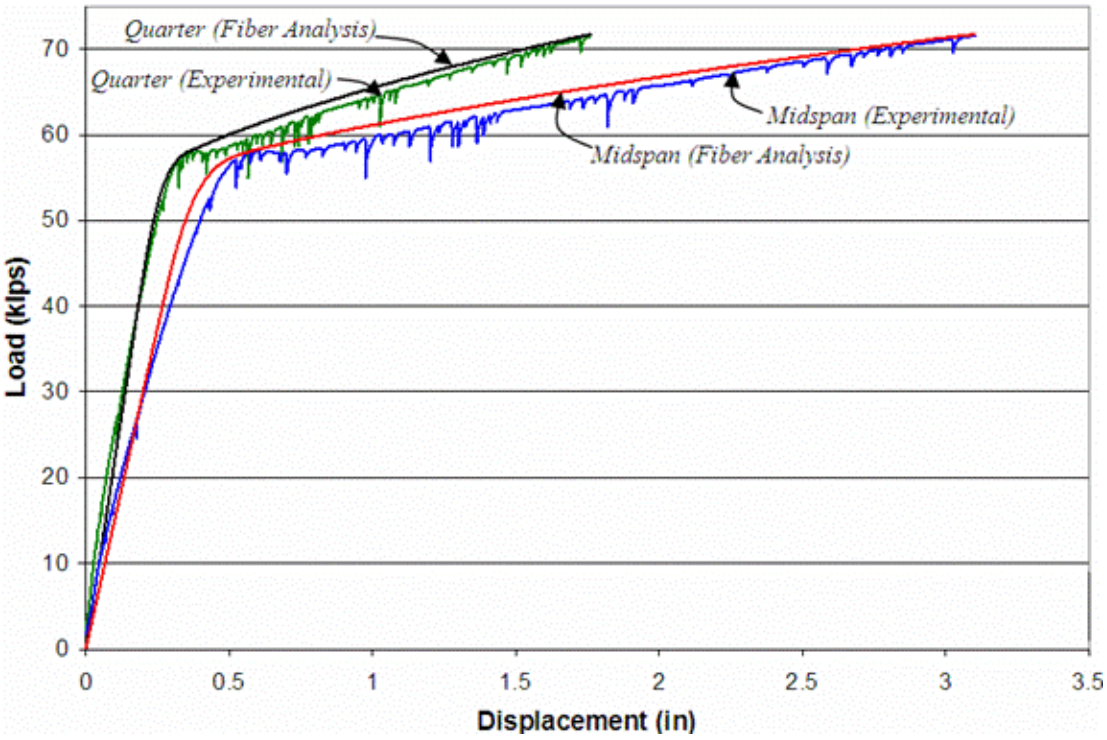

Figure 7.51
Load-displacement comparisons between fiber analysis and experimental data (A36-Beam 1)

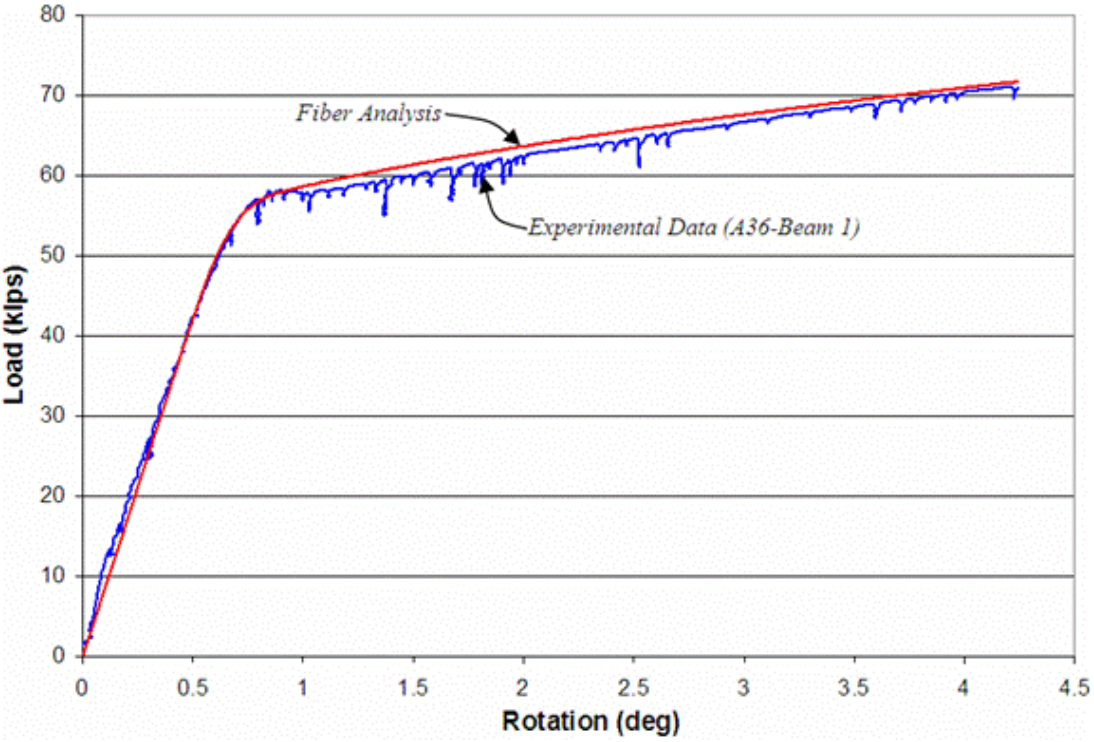

Figure 7.52
Load-rotation comparisons between fiber analysis and experimental data (A36-Beam 1)

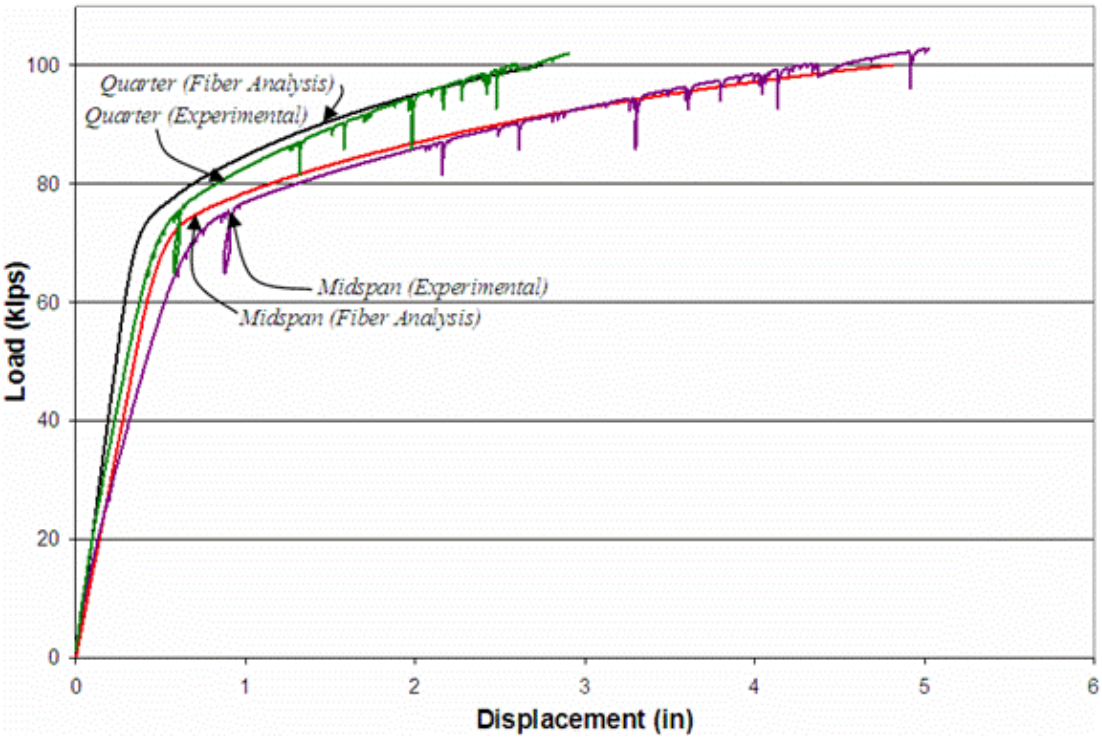

Figure 7.53
Load-displacement comparisons between fiber analysis and experimental data (A588-Beam 1)

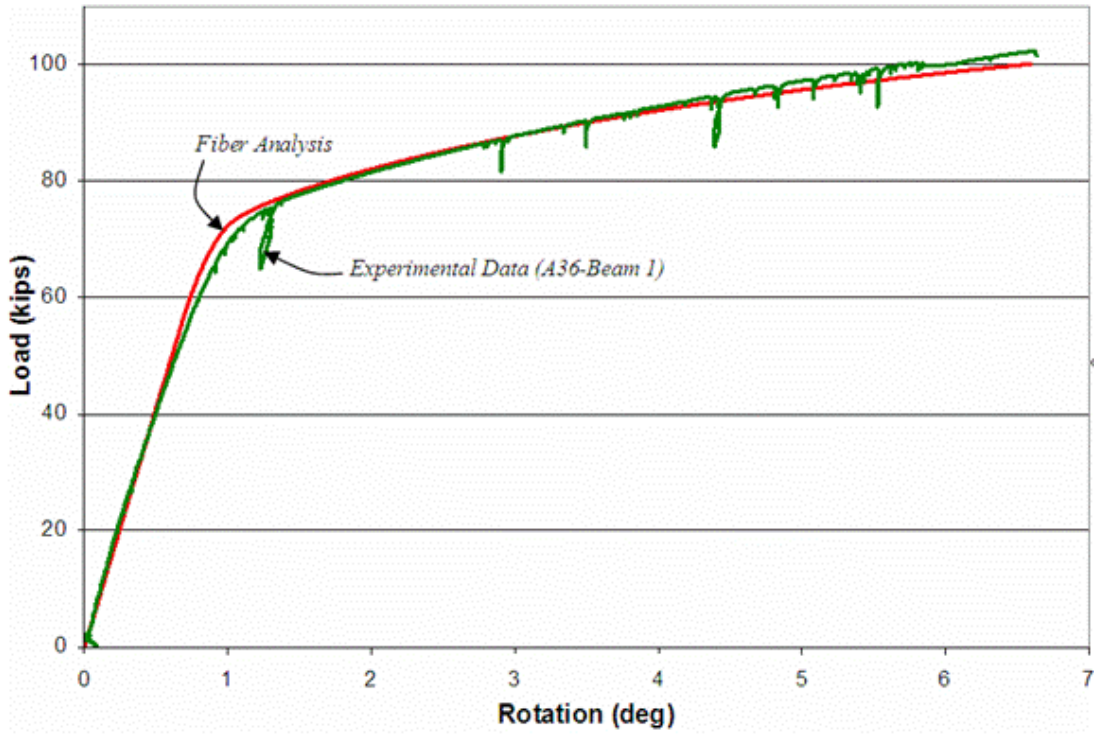

Figure 7.54
Load-rotation comparisons between fiber analysis and experimental data (A588-Beam 1)

[Intentionally Blank Page]

8 EXPERIMENTAL BEHAVIOR AND RESULTS FROM LARGE-SCALE BEAMS

8.1 EXPERIMENTAL DAMAGE-REPAIR HISTORY

Six large-scale beam specimens were tested by subjecting them to multiple damage-heat straightening repair cycles. These beams specimens and the damage and heat straightening repair parameters were presented in Table 7.1. The following sections, 8.1.1, 8.1.2, 8.1.3, 8.1.4, 8.1.5, and 8.1.6, summarize the damage and heat straightening repairs conducted on A7-Beam 1, A7-Beam 2, A36-Beam 1, A36-Beam 2, A588-Beam 1, and A588-Beam 2, respectively. Each sub-section summarizes the three damage cycles and the three repair cycles of the corresponding beam. For example, Section 8.1.1.1 summarizes all three damage cycles conducted on A7-Beam 1 and Section 8.1.1.2 summarizes all three repair cycles conducted on A7-Beam 1

The experimental behavior of the beam specimens during the damage cycles is presented and discussed using the data provided by the instrumentation (see Section 7.5.1). As mentioned previously, the longitudinal strain gages worked well during the first damage cycle only. Hence, the load-strain P-ε behavior during the first damage cycle and the load-midspan deflection P-Δ and the load-end rotation P-θ during all three damage cycles are shown. These comparisons indicate the change in strength and stiffness of the beam after the previous damage-repair event. Photographs of the beam specimens before and after the first damage cycle are provided. Other significant information noted during the experimental damage cycles is provided.

The behavior of the beam specimens during the repair cycles is presented using some of the data provided by the instrumentation (see Section 7.5.2). At least one figure which shows the pressure in the hydraulic jack, the temperature at the surface of the Vee heated steel, and the deflections measured by the displacement transducers is provided for each steel type. The final condition of the damaged-repaired beam specimens are also shown and discussed. Finally, the number of Vee heats required to repair each damage cycle is also reported. A frequency chart showing the total number of times each Vee was heated is also shown for the beam specimens. All three repair cycles are combined in the development of these frequency charts.

8.1.1 A7-Beam 1

8.1.1.1 Damage cycles

Longitudinal strain gages were used to monitor the longitudinal strains during the first damage cycle of A7-Beam 1. These strain gages were located slightly differently than the layout mentioned in Section 7.5.1:

- Two strain gages were bonded to the top of the front and back flanges as in Figure 7.11 (one each).
- Two strain gages were bonded close to the bottom of the front and back flanges (one each). These gages were too close to the bearing contact with the concentrated force, which causes localized multiaxial strains. These strain gages did not provide useful data, and were moved further away from the contact point for future beam specimens.
- One strain gage was bonded 3 in. from the top of the front flange as in Figure 7.11. This is referred to as the “Front_Middle” strain gage.
- One strain gage was bonded 1 in. below the top of the front flange. This strain gage provided redundant measurements for the first damage cycle and is referred to as the “Front Top_2” strain gage.

The beam specimen was damaged by monotonically increasing the concentrated force. The damage was monitored using the longitudinal strain gages. The test was considered complete when the average value of front top and back top strain gages reached 30 ε_y (0.036 in/in). The complete strain gage data for the first damage cycle is shown in Figure 8.1. Figure 8.2 shows the initial loading slopes of the strain gage readings during the first damage cycle. This figure clearly indicates that the placing strain gages directly at the bottom results in unreliable readings. Figure 8.3 shows photographs of the beam specimen before (a) and after (a) the first damage cycle.

For the second and third damage cycles, four strain gages were attached to the beam. Two gages were bonded to the top of the front and back flanges (see Figure 7.11), and two strain gages were bonded 1.5 in. from the bottom of the front and back flanges (see Figure 7.11). The initial intent was to use the front and back top strain gages to control the level of damage during the second damage cycle. However, the flanges had undergone out-of-plane distortions after the first damage-repair cycle. As a result, the front and back top strain gage data were unreliable as shown in Figure 8.4.

The researchers reviewed the results of the first damage cycle and conducted subsequent damage cycles in displacement control. The plastic displacement after the first cycle of damage was found to be 2.7 in. Therefore, the beam was damaged to a displacement of 2.7 in. in the second damage cycle. The amount of elastic recovery had been underestimated, and the final damage displacement for the second damage cycle was slightly lower than the damage displacement for the first damage cycle. The beam specimen was also subjected to a midspan displacement of 2.7 in. during the third damage cycle. The front and back top strain gages were moved 2 in. below the top to avoid poor measurements due to flange curvature. This approach also did not work well.

Figure 8.5 shows the P-Δ relationships for all three damage cycles. As shown in Figure 8.5, the load required for a higher beam displacement is significantly higher for subsequent damage cycles. However, the load required to cause a low displacement is reduced. Figure 8.6 shows the P-θ relationships for all three damage cycles.

8.1.1.2 Repair Cycles

Repair cycles 1, 2, and 3 were conducted by applying external forces causing restraining moments (M_r) of 0.25 M_p, 0.50 M_p, and 0.25 M_p at the midspan, respectively. The first repair cycle was initially conducted using simultaneous Vee heats applied at the center (C) Vee of the front and back beam flanges. This process progressed well until the heated area began distorting out-of-plane. The researchers conducted the plastic strain distribution analysis presented in Section 7.7.2, and applied further heats strategically to other Vees (R1, L1, R2, and L2, etc.) besides the center (C) one.

The second and third repair cycles for A7-Beam 1 progressed smoothly. The resistance of the beam to heat straightening increased after several heats probably due to the build up of residual stresses in the cross-section. However, the displacements and rotations required to straighten the beam were achieved successfully. Twenty-six Vee heats were required to complete the first repair cycle, i.e., repair the damage caused by the first damage cycle. Fourteen Vee heats were required to repair the second damage cycle, and thirty-eight Vee heats were required to repair the third damage cycle. The frequency chart indicating the amount of Vee heats applied to each location is shown in Figure 8.7.

- Figure 8.8 shows the data from second repair cycle. This figure includes: (a) the displacements from the four displacement transducers in inches, (b) the pressure in the hydraulic jacks in ksi, and (c) the temperature of the steel in F, which is divided by 1000 (i.e. 1.0 on the graph corresponds to 1000 °F) for clarity.
- Figure 8.9 shows the same data for the first four heats of the third repair cycle. This figure indicates that approximately 0.1 in. midspan deflection was achieved for each Vee heat at a restraining moment of 0.25 M_p. It also shows that as the temperature of the steel increases, the load slightly increases and

as the material expands. As more heating cycles were applied during repair cycle 3, the load increased more considerably and less movement was achieved during each heating cycle. The beam resisted the repair more as the repair progressed.

- Figures 8.10 and 8.11 show the condition of the beam specimen after three damage-repair cycles. Figure 8.10 shows the full beam and Figure 8.11 shows the out-of-plane distortion that remained in the front and back flanges.

For the first repair of A7-Beam 1, the first six Vee heats were all applied directly to the center Vee heat (*C*). For the majority of repair cycles on all beam specimens, the location of the Vee heat was altered immediately after the first or second Vee heat was applied to the center (*C*). An additional analysis was conducted using the first six heats of the first repair cycle to study the load and displacement behavior of the beam for multiple Vee heats applied to the same location. Previous research investigations have indicated that the amount of displacement achieved reduces for multiple Vee heats applied to the same location. This behavior was also noticed during the experimental investigations of this research project.

Also observed during the experimental investigations was a significant increase in the load while subjecting the beam to several heating cycles to the same location. The chart used to conduct this analysis is shown in Figure 8.12. The center displacement is shown in inches and the load is given in kips and is divided by 20 to be seen on the same plot. The target load was approximately 11 kips. The dashed line in Figure 8.12 shows that approximately equal loads were applied to the beam before heating each cycle. The dashed line indicates that higher loads occurred for additional heating cycles due to the beam resisting the downward movement. The increase in loads while heating the beam was not caused by the researcher applying an initial higher load.

In this analysis, the increase in load was measured from the point when the Vee heat started to the maximum load achieved as the material expanded. The load increase is illustrated using an example in Figure 8.13. The amount of displacement achieved during each heating cycle was measured between the points where loads were applied as illustrated in Figure 8.13. This was the most logical place to estimate the amount of movement achieved during each heating cycle as the beam was subjected to equivalent loads. Since the beam was not reloaded after the sixth heating cycle, the amount of displacement achieved during the sixth heating cycle was unknown using this procedure. The results of this displacement analysis are provided in Table 8.1. Table 8.1 indicates that the load increases for subsequent Vee heats to the same location. The amount of displacement achieved during each heating cycle decreased for subsequent heating cycles with the exception of Heat 3 as opposed to Heat 4. After reviewing the results in Table 8.1, it appears as if a higher amount of movement was achieved during Heat 4 than expected. This analysis was also conducted during the first repair cycle of A588-Beam 2, which is discussed in Section 8.1.6.2.

8.1.2 A7-Beam 2

8.1.2.1 Damage Cycles

For the first damage cycle of A7-Beam 2, the strain gage layout as described in Section 7.5.1 was used (see Figure 7.11). Two strain gages were attached to the top of either flange, two were attached 3.0 in. ($b_f/3$) from the top, and two were attached 1.5 in. ($b_f/6$) from the bottom. The beam specimen was loaded to achieve an average strain of 90 ε_y (0.108 in/in) in the extreme tension fiber as indicated by the front and back top strain gages. This required a total midspan deflection of approximately 8.5 in. However, the hydraulic jack pushing the beam upwards had a stroke of only 6 in. Therefore, the beam had to be unloaded, the loading setup readjusted, and the beam re-loaded to achieve the required damage strain and deflection level.

Towards the end of the first damage cycle, the bottom of front flange (close to the contact point with the applied force) buckled inwards towards the web of the section. This local buckling progressed very slowly and was not observed visually until close to the end of the damage cycle. Figure 8.14 shows the P-ε data for the first damage cycle. Due to buckling, the strain gage at the bottom of the front flange began to debond. Figure 8.15 shows the beam specimen before and after the first damage cycle.

Damage cycles 2 and 3 were conducted even more cautiously than the first damage cycle due to the condition of the bottom of the front flange. Both these damage cycles were conducted in displacement control, because the front and back top strain gage data had become unreliable due to the flange curvature from heating. The target displacement for the 60 ε_y damage strain cycles had been noted in the previous 90 ε_y damage cycle. These target displacements were used carefully by the researchers to control the damage during the second and third cycles.

- During the second damage cycle, all the displacements and end rotations compared favorably with the corresponding values noted from the first damage cycle when ε_d=60 ε_y. Therefore, the midspan displacement transducers (12 in. stroke) were used to control the damage cycle.
- During the third damage cycle, the midspan displacement transducers did not compare favorably with noted values or with each other. However, the quarter length (6 in. stroke) displacement transducers and the end rotations compared favorably with each other and the noted values. Therefore, the third damage cycle was controlled using the end rotation and quarter length displacement measurements.

Figure 8.16 compares the load-displacement relationships for the three damage cycles. The figure includes data from one 6 in. stroke displacement transducer at quarter length and one 12 in. stroke displacement transducer at midspan. Figure 8.17 shows and compares the front flange end rotations for all three damage cycles. Figures 8.16 and 8.17 indicate that the bending strength of the beam increases after one damage-repair cycle and then increases slightly after the second damage-repair cycle.

While conducting the second and third damage cycles, the bottom of the front flange continued buckling inwards. However, all three damage-repair cycles were completed successfully. The condition of the bottom of the front flange after all three damage cycles is shown in Figure 8.18.

8.1.2.2 Repair Cycles

All three repair cycles of A7-Beam 2 were conducted by applying an external restraining moment (M_r) of $0.50\ M_p$. The first repair cycle took 4 days and a total of seventy-five Vee heats on both sides in order to complete. The second and third repair cycles took 3 days and approximately sixty Vee heats each to complete. The frequency distribution of the total number of Vee heats with respect to location is shown in Figure 8.19.

The Vee heats were strategically applied along the length of the beam. Strip heats were also applied to the bottom of the front flange in order to straighten out the buckled flange. This was crucial to aid in re-damaging the beam during the second and third damage cycles. Strip heats were also applied to the web of the beam since the plastic strain analysis of Section 7.7.2 indicated plastic strains were being induced in the web. This did not benefit the researchers as much as expected. Since the researchers intended on taking material coupons from the flanges, the web was left with slight curvature after experimental investigations. Figure 8.20 shows the locations of the web strip heats.

During the third repair cycle, the torch used to apply Vee heats to the back flange of the beam was replaced since it was behaving poorly. The new torch provided more heat flux to the specimen and it seemed that the researcher might have overheated the back flange occasionally. The overheating temperatures were less than 1350 °F. However, once this was noticed, future heats were applied more carefully to restrict the maximum temperature to 1200 °F.

- Figures 8.21 to 8.23 show the final condition of the beam specimen (A7-Beam 2) after three damage-repair cycles.
- Figure 8.21 shows the full beam span from the front side.
- Figure 8.22 shows the final condition of the center of the front (a) and back (b) flanges. The red spots seen in Figure 8.21(b) are induced from a lack of acetylene supply from the torch and not from overheating.
- Figure 8.23 shows the lateral displacement of the front (a) and back (b) flanges.

After completing the third damage-repair cycle, the researcher attempted more strip heats to repair the local buckling at the bottom of the front flange. However, during the first strip heat itself; the flange fractured (tore) slightly at the crest of the local buckling. This can be seen clearly in Figure 8.24. The researcher halted and left the flange bottom as it was.

Heat straightening the beam specimen caused the flanges to curve slightly outwards. While the exact reason for this curving is not known, it is speculated that slight unavoidable eccentricities of loading and heating with respect to the mid thickness of the flange caused it. The beam specimen was removed from the test setup and line heats were applied along 5 in. lines of the top k-region in order to straighten the flanges longitudinally. An illustration of line heats applied to the inside of the flanges at the k-region is shown in Figure 8.25. The next heating cycle involved applying 5 in. line heats to the k-regions in between the line heats from the previous cycle.

An external restraining force was provided by using a large clamp with a nominal pressure of 4.88 kips and pulling the two flanges together as shown in Figure 8.25. The level of restraining force was limited to the researcher's ability to twist the clamp, which could not be measured. After applying several line heats, the flanges moved approximately 0.75 in. towards each other at midspan. This procedure was also used as an aid for other beam specimens (i.e. A7-Beam 1, A588-Beam 1, and A588-Beam 2) but not as much as for A7-Beam 2.

The damage-repair of A7-Beam 2 did not proceed efficiently. A number of problems had to be addressed and the repair focused only on the vertical displacement of the beam specimen. The restraining force caused unintentional out-of-plane distortions of the flanges. It would seem that the amount of damage subjected to this test specimen was too high for the researchers to control with the test setup capabilities. The researchers therefore decided it beneficial to limit the magnitude of damage induced to further A36 and A588 beam specimens.

8.1.3 A36-Beam1

8.1.3.1 Damage Cycles

In all three damage cycles, A36-Beam 1 was loaded to achieve the required displacement to cause an average strain of 30 ε_y (0.045 in/in) in the extreme tension fiber as indicated by the front and back top strain gages. The strain gage layout as described in Section 7.5.1 (see Figure 7.11) was used for the first damage cycle. Two strain gages were attached to the top of either flange, two were attached 3.0 in. ($b_f / 3$) from the top, and two were attached 1.5 in. ($b_f / 6$) from the bottom. The strain gage data from the first damage cycle is provided in Figure 8.26. The condition of A36-Beam 1 before (a) and after (b) the first damage cycle is provided in Figure 8.27.

Damage cycles 2 and 3 were conducted much more smoothly than the multiple damage cycles conducted on the A7 beam specimens. In general, all rotation meters and displacement transducers related well to each other when comparing what was observed during the first damage cycle. Figure 8.28

compares the P-Δ behavior of all three damage cycles of A36-Beam 1. The quarter displacements are not shown for clarity. Figure 8.29 compares the P-θ behavior of all three damage cycles of A36-Beam 1.

As shown in Figures 8.28 and 8.29, the initial bending stiffness of the beam was affected after the first damage-repair event. Also distinguished in Figures 8.28 and 8.29 is that the bending strength of the beam increases for higher displacements after each damage-repair event. These behaviors are likely due to built-up residual stresses along the flange plates and not as substantially due to significant material property changes (i.e. σ-ε relationships). However, the A36 material is becoming a little stronger after damage-repairs, which was verified after the material testing results of Section 8.2.2.1. Since the onset of nonlinearity happens at a substantially lower load, the induced residual stresses must be quite significant.

8.1.3.2 Repair Cycles

Repair cycles 1, 2, and 3 of A36-Beam 1 were conducted by applying external forces corresponding to restraining moments (M_r) of 0.25 M_p, 0.50 M_p, and 0.25 M_p, respectively. The first repair cycle took 2 days and thirty-nine Vee heats on both sides in order to complete. The second repair cycle took less than 1 day and sixteen Vee heats to complete. The third repair cycle took 2.5 days and fifty Vee heats to complete. The frequency distribution of the total number of Vee heats with respect to location is shown in Figure 8.30. All three repair cycles progressed well. Some out-of-plane distortions were noticed in the flanges. The final condition of the beam specimen was much better than the final condition of the A7 beam specimens.

- Figures 8.31 and 8.32 show the final condition of the beam specimen (A36-Beam 1) after three damage-repair cycles.
- Figure 8.31 shows the full beam span from the front side.
- Figure 8.32 shows the out-of-plane curvature of the flanges.

8.1.4 A36-Beam2

8.1.4.1 Damage Cycles

A36-Beam 2 was subjected to three damage-repair cycles, where each damage cycle corresponded to an average damage strain of 30 ε_y (0.045 in/in). The damage strain in the first cycle was measured using the strain gage layout described in Section 7.5.1 (see Figure 7.11). Two strain gages were attached to the top of either flange, two were attached 3.0 in. ($b_f / 3$) from the top, and two were attached 1.5 in. ($b_f / 6$) from the bottom. One of the bottom strain gages debonded while testing. The strain gage data from the first damage cycle is provided in Figure 8.33. The condition of A36-Beam 2 after the first damage cycle was very similar to that of A36-Beam 1 (refer to Figure 8.27).

Damage cycles 2 and 3 were conducted under displacement control, where the displacement at midspan reached the required magnitude. Figure 8.34 compares the P-Δ behavior of all three damage cycles of A36-Beam 2. The quarter displacements are not shown for clarity. Figure 8.35 compares the P-θ behavior of all three damage cycles of A36-Beam 2. In all three damage cycles of A36-Beam 2, the back flange appeared to displace and rotate slightly more than the front.

As shown in Figures 8.34 and 8.35, the initial stiffness of the beam has been affected after the first damage-repair event similar to that found for A36-Beam 1. This behavior is likely due to built-up residual stresses in the cross section. Figures 8.34 and 8.35 also indicate that the bending strength of the beam increases for higher displacements after each damage-repair event. The increase is very similar to A36-Beam 1 but the load increase in not as significant. The material becomes stronger after damage-repairs, which was verified after the material testing results of Section 8.2.2.1.

8.1.4.2 Repair Cycles

Repair cycles 1, 2, and 3 of A36-Beam 2 were conducted by applying external forces corresponding to restraining moments (M_r) of 0.25 M_p, 0.50 M_p, and 0.25 M_p, respectively. These restraining forces were equal to those used for A36-Beam 1. The difference was that each Vee heat was subjected to a maximum temperature of 1400 °F as opposed to 1200 °F. The color of the Vee at a maximum temperature of 1400 °F is shown in Figure 8.36 (a). Figure 8.36(b) shows the color of a Vee heat on A36-Beam 1 at a maximum temperature of 1200 °F for comparison. Figure 8.37 shows the color of the backside of the front flange at slightly lower temperatures than 1400 °F.

Twenty Vee heats on both flanges were required to complete the first repair cycle. The second repair cycle took nineteen Vee heats to complete. The third repair cycle took twenty-nine Vee heats to complete. Repair cycles on A36-Beam 1 took thirty-nine, sixteen, and fifty Vee heats to complete. The frequency distribution of the total number of Vee heats with respect to location is shown in Figure 8.38.

Figure 8.39 shows the behavior of A36-Beam 2 during the second repair cycle. In Figure 8.39, the center displacement (back side) and quarter displacement (right side) are shown positive as the beam descends in inches. The pressure in the hydraulic jack is shown in ksi. The temperature of the steel is given in degrees Fahrenheit and is divided by 1000 to be seen on the same graph. The temperature in Figure 8.39 was measured at the center Vee (C), and it is lower than 1400 ºF for cases where the heat was applied to other Vees.

The displacement behavior of this specimen was found to be quite unique. For the first few heating cycles, the steel material expands and the beam moves up. The beam descends slowly as it cools. For later Vee heats, the beam expanded but continued to ascend as the material cooled. The only downward movement occurred when the load was applied.

Some out-of-plane distortion was noticed in the flanges after the experimental investigations. The condition of the final beam specimen was in better condition than the previous beams specimens and flange straightening was not required for the removal of material coupons from the flanges.

- Figures 8.40 and 8.41 show the final condition of the beam specimen (A36-Beam2) after three damage-repair cycles.
- Figure 8.40 shows the full beam span from the front side.
- Figure 8.41 shows the out-of-plane curvature of the flanges.

8.1.5 A588-Beam1

8.1.5.1 Damage Cycles

In the first damage cycle of A588-Beam 1, the beam specimen was loaded to achieve an average strain of 40 ε_y (0.078 in/in) in the extreme tension fiber as indicated by the front and back top strain gages. For the first damage cycle, the strain gage layout as described in Section 7.5.1 was used (see Figure 7.17). Two strain gages were attached to the top of either flange, two were attached 3.0 in. ($b_f / 3$) from the top, and two were attached 1.5 in. ($b_f / 6$) from the bottom. One of the bottom strain gages debonded while testing. The strain gage data from the first damage cycle is provided in Figure 8.42.

During the first damage cycle, the spread of yielding was seen with the peeling of mill scale at the surface. Figure 8.43 shows a close up of the yielded area. The surface began to look as in Figure 8.43 at locations with a damage strain of approximately 10-15 ε_y or higher. It appears that more yielding is occurring at the bottom of the beam specimen as opposed to the top of the beam specimen. This theory may be contradicted as the bottom of the beam is in compression instead of tension, which may peal the

mill scale at smaller damage strains. The conditions of A588-Beam 1 around 4 ε_y and after the first damage cycle are shown in Figures 8.44(a) and (b), respectively.

Damage cycles 2 and 3 were conducted until the displacement transducers at midspan (front and back) reached the required magnitude of displacement to cause a damage strain of 20 ε_y at the extreme tension fiber. The required magnitude of displacement was found by relating to the first damage cycle of 40 ε_y. The condition of the beam after the third damage cycle corresponding to 20 ε_y is shown in Figure 8.45.

Figure 8.46 compares the P-Δ behavior of all three damage cycles of A588-Beam 1. The quarter displacements are not shown for clarity. Figure 8.47 compares the P-θ behavior of all three damage cycles of A588-Beam 1. As shown in Figures 8.46 and 8.47, the P-Δ and P-θ behaviors of the beam specimen during the second and third damage cycles appear very similar. The stiffness of the beam has been affected after the first damage-repair event. It also appears as if the bending strength of the beam increases slightly for higher displacements after the first damage-repair event. The material testing results on small-scale test specimens (see Section 6.2) have indicated that the strength of A588 steel does not increase significantly after damage-repair cycles. Therefore, both the strength and stiffness changes are likely due to built-up residual stresses along the cross-section and not due to significant material changes (i.e. σ-ε relationships).

8.1.5.2 Repair Cycles

All three repair cycles of A588-Beam 1 were conducted using an external restraining moment (M_r) of 0.25 M_p. The Vee heats were subjected to a maximum temperature of 1200 °F and applied strategically along the length of the plastic damage region, which was determined as described in Section 7.7.2. Since the specimen was subjected to so many heating cycles during the first repair cycle, the out-of-plane curvature of the top flanges became significant. The researcher added Vee heats in between L1 and L2, as well as R1 and R2. These Vee heats were identified as RC and LC, where the nomenclature identified the right and left contact points. The center of these Vee heats was directly at the contact points. The Vee heats were 4.5 in. wide and along half the depth. These are the same dimensions as all other Vee heats applied to the beam specimens. These locations was not heated on the first four beam specimens as the researchers were concerned about the threaded rods becoming too hot as well as localized indentions which may occur significantly at the contact points. However, the researcher sensed that applying these heats might benefit the repair substantially. Applying Vee heats to RC and LC aided the displacement of the beam and did not cause damage to the threaded rods or significant indentions to the top of the flanges. Therefore, these Vee heats were applied during all repairs on both A588 beam specimens.

The first repair cycle took 89 Vee heats on each side to complete. The second repair cycle took 33 Vee heats to complete. The third repair cycle took 40 Vee heats to complete. The frequency distribution of the total number of Vee heats with respect to location is shown in Figure 8.48.

The condition of A588-Beam 1 after three damage-repairs was found to be better than A7-Beam 2 but more out-of-plane curvature was found in the flanges than other A7 or A36 beam specimens. Therefore, the beam flanges were clamped together as shown in Figure 8.25 and strategic line and strip heats were applied within the bent region as shown in Figure 8.49. The researcher applied enough heating cycles to the flanges in order to remove straight material coupons. In order to ensure that the flanges were straight enough, the researcher laid a 0.5 in. wide steel tape, 8 in. long at the center of the flanges. This is the size, along the thickness, of the uniaxial tension coupon.

- Figures 8.50 and 8.51 show the final condition of the beam specimen (A588-Beam 1) after three damage-repair cycles.
- Figure 8.50 shows the full beam span from the front side.

- Figure 8.51 shows the out-of-plane curvature of the flanges before (a-b) and after (c-d) straightening.

8.1.6 A588-Beam 2

8.1.6.1 Damage Cycles

In the first damage cycle of A588-Beam 2, the beam specimen was loaded to achieve an average strain of 40 ε_y (0.078 in/in) in the extreme tension fiber as indicated by the front and back top strain gages. The strain gage layout as described in Section 7.5.1 was used (see Figure 7.11) with additional strain gages. Two strain gages were attached to the top of either flange, two were attached 3.0 in. ($b_f / 3$) from the top, and two were attached 1.5 in. ($b_f / 6$) from the bottom. One of the bottom strain gages debonded while testing. Strain gage data from the first damage cycle is provided in Figure 8.52. The condition of A588-Beam 2 after the first damage cycle was very similar to that of A588-Beam 1 (Refer to Figures 8.43 and 8.44). Mill scale peeled off in the plastic damage region similar to A588-Beam 1 as shown in Figure 8.43.

Four additional strain gages were attached along the top of the front flange. These strain gages were placed along the center lines of Vee heat locations L4, L2, R2, and R4. These measurements were used and compared to validate the analytical plastic strain analysis presented in Section 7.7.2. The load-strain behavior as indicated by all strain gages attached to the top of the front flange is shown in Figure 8.44. As shown in Figure 8.44, plastic strains are clearly being induced at locations away from the beam center. The results of this analysis indicated that more strain was being measured by the strain gages away from midspan than that interpreted from fiber analysis. The maximum average elastic strain from the tops of R2 and L2 was found to be approximately 0.0336 in/in as opposed to the analytical result of 0.0278 in/in. The maximum average elastic strain from the tops of R4 and L4 was found to be approximately 0.0184 in/in as apposed to the analytical results of 0.0131 in/in. Reasons for the discrepancies are unknown.

Damage cycles 2 and 3 were conducted until the displacement transducers at midspan (front and back) reached the required amount of displacement to cause a damage strain of 20 ε_y at the extreme tension fiber. The condition of the beam after the second and third damage cycles was similar to A588-Beam 1 as shown in Figure 8.45.

Figure 8.54 compares the load-midspan deflection behavior of all three damage cycles of A588-Beam 2. Figure 8.55 compares the load-end rotation behavior of all three damage cycles of A588-Beam 2. As shown in Figures 8.54 and 8.55, the P-Δ and P-θ behaviors of the beam specimen during the second and third damage cycles appear very similar. The stiffness of the beam has been affected after the first damage-repair event. It also appears as if the bending strength of the beam increases slightly for higher displacements after the first damage-repair event. The P-Δ and P-θ behaviors of the beam specimen during the second and third damage cycles appear very similar as they did with A588-Beam 1. A comparison between the midspan P-Δ behaviors of A588-Beam 1 and A588-Beam 2 during their respected second and third damage cycles is shown in Figure 8.56. The P-Δ results for multiple damage cycles conducted to both beams are indeed very similar. It appears from this experimental data that applying a higher external restraining stress is having a negligible effect on the strength and stiffness of the A588 beam specimen.

8.1.6.2 Repair Cycles

All three repair cycles of A588-Beam 2 were conducted using an external restraining moment (M_r) of 0.50 M_p. The Vee heats were subjected to a maximum temperature of 1200 °F and applied strategically along the length of the plastic damage region. Additional Vee heats were applied to locations RC and LC as with A588-Beam 1.

The first repair cycle took 47 Vee heats on each side to complete. The second repair cycle took 20 Vee heats to complete. The third repair cycle also took 20 Vee heats to complete (repair cycles 1, 2, and 3 on A588-Beam 1 took 83, 33, and 40 Vee heats to complete, respectively). The frequency distribution of the total number of Vee heats with respect to location is shown in Figure 8.57.

Figure 8.58 shows the behavior of A588-Beam 2 during the second repair cycle. In Figure 8.58, the center displacement (back side) and quarter displacement (right side) are shown positive as the beam descends in inches. The pressure in the hydraulic jack is shown in ksi. The temperature of the steel is given in degrees Fahrenheit and is divided by 1000 to be seen on the same graph. The temperature in Figure 8.58 was measured at the center Vee (*C*), and it is lower than 1200 ºF for cases where the heat was applied to other Vees.

The condition of the final beam specimen was found to be very similar to A588-Beam 1. Therefore, the beam flanges were pulled together using the clamp shown in Figure 8.25. Similar line and strip heating patterns were applied to the bent flanges of A588-Beam 2 as illustrated in Figure 8.49.

- Figures 8.59 and 8.60 show the final condition of the beam specimen (A588-Beam 1) after three damage-repair cycles.
- Figure 8.59 shows the full beam span from the front side.
- Figure 8.60 shows the out-of-plane curvature of the flanges before (a-b) and after (c-d) straightening.

Additional load-displacement analyses were conducted using experimental data of the first repair cycle of A588-Beam 2. This analysis investigated the load increase and displacements achieved for subsequent heating cycles to the same location and was conducted similar to the load-displacement analysis conducted on A7-Beam 1 as discussed in Section 8.1.1.2. For the first repair of A588-Beam 2, the first six Vee heats were all applied directly to the center Vee heat (*C*). The seventh Vee heat was conducted on R1 which required the same amount of load for 0.50 M_p. Figure 8.61 presents the experimental data for the seven heating cycles used to conduct this analysis. Both the front and back center displacements were used and are shown in inches. The load is in kips and divided by 20 to plot on the same chart. The dashed line in Figure 8.61 shows that the researcher applied the same load at the beginning of each heating cycle. The load increased with each heating cycle as the steel expanded. The increase in load was determined as illustrated in Figure 8.13. The displacement achieved during each heating cycle was also determined as illustrated in Figure 8.13. The results of the load increases and displacements achieved during each heating cycle are summarized in Table 8.2. Table 8.2 indicates that the load increases more during subsequent Vee heating of the same location. The amount of displacement achieved decreased for subsequent heating cycles with the exception of the sixth heating cycle which increased with respect to the fifth heating cycle. From the experimental data in Figure 8.61, it appears that this discrepancy probably relates to the amount of time the steel was allowed to cool during the fifth heating cycle.

8.2 DAMAGE-REPAIRED MATERIAL TESTING RESULTS

This section summarizes the standard material tests conducted on material specimens removed from the flanges of the damaged-repaired beam specimens. The procedure for obtaining material specimens from the flanges of the damaged-repaired beam specimens was outlined in Section 7.6.2. Uniaxial tension coupons were removed from the back flange (Flange A) as shown in Figure 7.24. Charpy specimens were removed from the front flange (Flange B) as shown in Figure 7.25. Rockwell Hardness tests and microstructure investigations were conducted on charpy Specimen C-2 that is shown in Figure 7.25. The effects of multiple damage-heat straightening repair cycles were evaluated by developing similar comparison charts shown in Chapter 6 for Task III. The following sections present the results of the material testing and the comparisons with the corresponding undamaged material properties to evaluate the effects of multiple damage-repair cycles.

8.2.1 A7 Beam Specimens

8.2.1.1 Uniaxial Tension Tests

Uniaxial tension tests were conducted according to ASTM E8 on tension coupons from the damaged-repaired A7 steel beams. The flanges of the W24x76 steel beams had a total thickness of 0.64 in. The initial intent was to remove 0.50 in. thick and 8 in. long tensile specimens from the flanges as shown in Figure 7.18. However, due to significant curvature in the repaired flanges, the removal of such coupons was not possible. Only specimens from the position labeled Z in Figure 7.25 could be removed with the full dimensions. This was the case for both A7 beam specimens. Specimens X and Y had reduced grip lengths of 1 in. as opposed to 2 in. The resulting specimens were only 6 in. long instead of 8 in. as shown in Figure 8.62. Additionally, to make all specimens straight, Specimen X from A7-Beam 1 had to be fabricated with a reduced thickness of 0.450 in. and Specimen X from A7-Beam 2 had to be fabricated with a reduced thickness of 0.383 in. These specimens are shown in Figure 8.62.

In order to investigate the impact of the reduced size, one specimen 6 in. long with a thickness of 0.383 in. was fabricated from the undamaged A7 material. The coupon was fabricated from flange segment TA. The results of the structural properties are compared to the average results of the four full size tensile specimens in Table 8.3. The values in Table 8.3 include the yield stress (σ_y), the elastic modulus (E), the yield strain (ε_y), the ultimate stress (σ_t), the strain at ultimate stress (ε_u), the strain ductility ($\varepsilon_u/\varepsilon_y$), the percent elongation, and the percent reduction (area) (refer to Section 4.9). The results in Table 8.3 indicate that there is a slight reduction of only 1% in the elongation of the reduced size specimen. The elastic modulus also differs slightly. The rest of the structural properties compare favorably well to the full size uniaxial tension specimen.

The uniaxial tension stress-strain (σ–ε) relationships from the coupons removed from A7-Beam 1 are shown in Figure 8.63. The σ–ε relationships from the coupons removed from A7-Beam 2 are shown in Figure 8.64. Figures 8.63 and 8.64 also include the σ–ε relationships of the undamaged specimen removed from flange Segment TA with full dimensions for comparisons. The results of the structural properties of both A7 beams are summarized in Table 8.4, which includes the individual results of X, Y, and Z as well as an average of the three of each beam. The damage-repaired steel material properties (σ_y, E, σ_t, and percent elongation) were normalized with respect to the undamaged steel material properties and plotted in Figures 8.65 (a-d).

Figure 8.65(a) shows the normalized yield stress for all damaged-repaired specimens. Figure 8.65(b) shows the normalized elastic modulus for all damaged-repaired specimens. Figure 8.65(c) shows the normalized ultimate stress, and Figure 8.65(d) shows the normalized percent elongation for all damaged-repaired specimens.

The yield stress data in Table 8.4 and Figure 8.65(a) indicate that:

- Damage-repair cycles increase the yield stress of A7 steel to approximately 108-123% of the undamaged steel.
- The yield stress increases more for specimens subjected to lower ε_d. This result is valid when comparing the trends of Specimens X, Y, and Z, as well as those from A7-Beam 1 and A7-Beam 2.

The elastic modulus data in Table 8.4 and Figure 8.65(b) indicate that:

- Damage-repair cycles do not have a significant influence on the elastic modulus of A7 steel. The elastic modulus slightly decreases in most cases but is not less than 93% of the undamaged steel.
- The change in elastic modulus does not have a clear or direct trend with the damage strain (ε_d).

The ultimate stress data in Table 8.4 and Figure 8.65(c) indicate that:

- Damage-repair cycles do not have a significant influence on the ultimate stress of A7 steel. The ultimate strength increases in all cases, but is never greater than 106% of the undamaged steel.
- The magnitude of damage strain (ε_d) appears to have a negligible effect on the ultimate stress. However, the tensile specimen subjected to the lowest ε_d (A7-Beam1-Z) did result with the highest ultimate strength and yield strength.

The percent elongation (ductility) data in Table 8.4 and Figure 8.65(d) indicate that:

- Damage-heat straightening repair reduces the percent elongation (ductility) of A7 steel. This reduction in ductility ranges from approximately 80%-95% of the undamaged material. This margin appears to be within an acceptable range.
- The change in ductility does not have a clear or direct trend with the damage strain (ε_d). It still appears that higher damage strains result in a higher ductility level as Specimens Z in both cases resulted in the lowest values.

8.2.1.2 Charpy Impact Fracture Toughness Tests

The results of the fracture toughness tests on damaged-repaired A7 steel are provided in Table 8.5. Averages were taken both across the width of the flanges (i.e. averages of 1, 2, 3, and 4) and along the flange length (i.e. averages of 1, 2, 3, or 4 for L1, C, and R1). The overall average and standard deviations of all twelve charpy specimens are also provided in Table 8.5. These fracture toughness values were normalized with respect to the average (mean) undamaged fracture toughness of undamaged A7 steel from Plate B only. The results from undamaged Plate B were only used for normalized ratios as Table 7.9 indicated a significant statistical difference between the fracture toughness of Plate A and Plate B (probability that the data sets are statistically similar=2%). The normalized fracture toughness values are also shown in Table 8.5. Figure 8.66 shows the normalized fracture toughness of the charpy specimens from the damaged-repaired beams. Table 8.6 provides the means, standard deviations, 95% confidence intervals for the actual mean, medians, and absolute average deviations from the median for the twelve charpy specimens removed from each beam specimen.

Student's t-test analysis was conducted to evaluate the statistical difference between the undamaged fracture toughness values and the fracture toughness of A7-Beam 1 and A7-Beam 2. As mentioned previously in Section 4.9.2, the t-test evaluates the statistical difference between two data sets using their respective means, standard deviations, and sample set sizes. The results from the t-test include the t-value and the corresponding probability of null hypothesis, where the null hypothesis implies that the data sets are statistically similar. Tables 8.7 and 8.8 compare the fracture toughness of A7-Beam 1 and A7-Beam 2 with the undamaged fracture toughness, respectively. Table 8.7 indicates less than 0.01% probability that

the data sets are statistically similar and Table 8.8 indicates an 86% probability that the data sets are statistically similar.

The results in Tables 8.5 to 8.8 and Figure 8.66 indicate that:

- The fracture toughness of A7-Beam 1 is much lower than the undamaged toughness. The beam has become unusable after three damage-repair cycles.
- The fracture toughness of A7-Beam 2 compares favorably with the undamaged toughness. However, some variability is seen in the results and the toughness of material closer to the flange-web junction (k-region) is lower.
- For both beams, the fracture toughness of the specimens from the center Vee heat (*C*) is lowest. The fracture toughness of specimens closer to the flange-web junction (k-region) is low.
- The results indicate that A7-Beam 2 has comparable fracture toughness with the undamaged material, but significant variation with much lower toughness values are also observed.

8.2.1.3 Rockwell Hardness and Microstructure Investigations

Rockwell hardness tests were conducted on damage-repaired A7 steel according to ASTM E18. Four points were taken on Specimens C-2, identified in Figure 7.24. Table 8.9 summarizes the averaged results of the Rockwell hardness tests and the microstructure investigations. Table 8.9 also provides comparisons between the approximate ultimate strengths as estimated by ASTM A370 to the actual results from Section 8.2.1.1.

Microscopic preparation was conducted using the procedures outlined in Section 7.6.1.3. The resulting microstructures of the two A7 steel beam specimens at 480X are shown in Figure 8.67 (Refer to Figure 7.23 for comparisons to undamaged steel). A clear reduction in the grain size is seen for A7-Beam 2. As discussed in Section 4.9.4, a more fine-grained microstructure is generally stronger and tougher than a more coarse-grained microstructure. There is a slight increase on the surface hardness and a slight decrease on the ductility. A microstructure that is more pearlitic is harder, stronger, and more brittle. However, only significant and consistent changes in the percent pearlite would be further analyzed as the amount is related to the location taken for the picture as discussed in Section 2.4.3. The results are provided in Table 8.9 for completeness.

The average hardness and grain sizes of damaged-repaired steel were normalized with respect to the undamaged steel. Figure 8.68 shows the normalized hardness and grain size results of the damaged-repaired steel.

The results in Table 8.9 and Figure 8.68 indicate that:

- Heat straightening increases the hardness of A7 steel. The increase in hardness was more substantial for A7-Beam 2 as apposed to A7-Beam 1.
- Good correlations do not exist between the trends in the hardness data and the ultimate stress of damaged-repaired A7 steel.
- Damage-repair cycles decrease the grain size of A7 steel. The grain size of A7-Beam 2 was as low as 51% of the undamaged steel grain size.

8.2.2 A36 Beam Specimens

8.2.2.1 Uniaxial Tension Tests

Uniaxial tension tests were conducted according to ASTM E8 on tension coupons from the damaged-repaired A36 steel beams. All the A36 tension coupons were fabricated with the dimensions shown in Figure 7.18. Figures 8.68 and 8.69 show the uniaxial stress-strain (σ–ε) relationships of tension coupons from A36-Beam 1 and A36-Beam 2, respectively. Figures 8.69 and 8.70 also include the σ–ε relationships of the undamaged specimen removed from flange Segment TA for comparisons. The structural properties of the damaged-repaired A36 beam specimens are summarized in Table 8.10, which includes the individual results of X, Y, and Z coupons and their average. The damage-repaired steel material properties (σ_y, E, σ_t, and percent elongation) were normalized with respect to the corresponding undamaged steel material properties and plotted in Figures 8.71 (a-d). Figure 8.71(a) shows the normalized yield stress for all damaged-repaired specimens. Figure 8.71(b) shows the normalized elastic modulus for all damaged-repaired specimens. Figure 8.71(c) shows the normalized ultimate stress, and Figure 8.71(d) shows the normalized percent elongation for all damaged-repaired specimens.

The yield stress data in Table 8.10 and Figure 8.71(a) indicate that:

- Damage-repair cycles increased the yield stress of A36-Beam 1 (heated to 1200 °F). The increased yield stress is within 109% of the undamaged yield stress. The results were very consistent for X, Y, and Z.
- Damage-repair cycles significantly yield stress of A36-Beam 2 (heated to 1400 °F). There is move variation and the results range from 111-124% of the undamaged material.

The elastic modulus data in Table 8.10 and Figure 8.71(b) indicate that:

- Damage-repair cycles do not significantly affect the elastic modulus of A36 steel. All results were within 92-103% of the undamaged material.

The ultimate stress data in Table 8.10 and Figure 8.71(c) indicate that:

- Damage-repair cycles do not significantly affect the ultimate stress of A36 steel heated 1200 °F. The values are within 98-100% of the undamaged material.
- The ultimate strength of specimens repaired with overheated temperatures increased slightly (101-107%). The increase was most significant for Specimen X.

The percent elongation (ductility) data in Table 8.10 and Figure 8.71(d) indicate that:

- Damage-heat straightening repairs reduce the percent elongation (ductility) of A36 steel. For specimens subjected to 1200 °F, the reduction in ductility ranges from approximately 86%-94% of the undamaged material. This appears to be within an acceptable range.
- The reductions in the percent elongation from the overheated steel were much more substantial. The reduction was found from 86% to as low as 67% of the undamaged material. The reasons for this reduction are not known.

8.2.2.2 Charpy Impact Fracture Toughness Tests

The results of the fracture toughness tests on damaged-repaired A36 steel are provided in Table 8.11. Averages were taken both across the width of the flanges (i.e. averages of 1, 2, 3, and 4) and along the flange length (i.e. averages of 1, 2, 3, or 4 for L1, C, and R1). The overall average and standard deviations of all twelve charpy specimens are also provided in Table 8.11. These fracture toughness values were normalized with respect to the average (mean) undamaged fracture toughness of undamaged A36 steel

from Plate B only. These fracture toughness values were normalized with respect to the average (mean) undamaged fracture toughness of undamaged A36 steel from Plate B only. The results from undamaged Plate B were used only for normalized ratios as Table 7.13 indicated a slight statistical difference between the fracture toughness of Plate A and Plate B (probability that data sets are statistically similar=17%). The normalized fracture toughness values are also shown in Table 8.11. Figure 8.72 shows the normalized fracture toughness of the charpy specimens from the damaged-repaired beams. Table 8.12 provides the means, standard deviations, 95% confidence intervals for the actual mean, medians, and absolute average deviations from the median for the twelve charpy specimens removed from each beam specimen.

Student's t-test analysis was conducted to evaluate the statistical difference between the undamaged fracture toughness values and the fracture toughness of A36-Beam 1 and A36-Beam 2. As mentioned previously in Section 4.9.2, the t-test evaluates the statistical difference between two data sets using their respective means, standard deviations, and sample set sizes. The results from the t-test include the t-value and the corresponding probability of null hypothesis, where the null hypothesis implies that the data sets are statistically similar. Tables 8.13 and 8.14 compare the fracture toughness of A36-Beam 1 and A36-Beam 2, respectively. Table 8.13 indicates a 47% probability that the data sets are statistically similar and Table 8.14 indicates a 0.5% probability that the data sets are statistically similar.

The data in Tables 8.11 to 8.14 and Figure 8.72 indicates that:

- The overall fracture toughness of A36-Beam 1 is comparable to the undamaged toughness. However, significant variability exists in the toughness of A36-Beam 1. In fact, the toughness of specimens from the center Vee heat (*C*) is much lower than the undamaged toughness.
- With the exception of one value, the fracture toughness of damage-repaired overheated A36 increased. The increase ranges from 101-460% of the undamaged material.
- The fracture toughness results of specimens removed from the center Vee heat (*C*) results in the lowest values. A general trend was noticed that the fracture toughness decreased as the specimens are removed closer to the web (away from the edge of the flange).

8.2.2.3 Rockwell Hardness and Microstructure Investigations

Rockwell hardness tests were conducted on damage-repaired A36 steel according to ASTM E18. Four points were taken on Specimens C-2 identified in Figure 7.24. Table 8.9 summarizes the averaged results of the Rockwell hardness tests and the microstructure investigations. Table 8.9 also provides comparisons between the approximate ultimate strengths as estimated by ASTM A370 to the actual ultimate strengths given in Section 8.2.2.1.

Microscopic preparation was conducted using the procedures outlined in Section 7.6.1.3. The resulting microstructures of the two A36 steel beam specimens at 480X are shown in Figure 8.73 (Refer to Figure 7.23 for comparisons to undamaged steel). The average hardness and grain sizes of damaged-repaired steel were normalized with respect to the undamaged steel from Flange B. Figure 8.74 shows the normalized hardness and grain size results of the damaged-repaired specimens. As discussed in Section 4.9.4, a more fine-grained microstructure is generally stronger and tougher than a more coarse-grained microstructure. There is a slight increase on the surface hardness and a slight decrease on the ductility. A microstructure that is more pearlitic is harder, stronger, and more brittle. However, only significant and consistent changes in the percent pearlite would be further analyzed as the amount is related to the location taken for the picture as discussed in Section 2.4.3. The results are provided in Table 8.9 for completeness.

The results in Table 8.9 and Figure 8.74 indicate that:

- Damage-repair cycles increase the Rockwell hardness of A36 steel heated to a maximum temperature of 1200 °F. The resulting hardness was approximately 110% of the undamaged hardness.

- Damage-repair cycles slightly decrease the Rockwell hardness of overheated A36 steel.
- Poor correlations exist between the hardness data and the ultimate stress of damaged-repaired A36 steel.
- Damage-repair cycles decrease the grain size of A36 steel to either 60% or 73% of the undamaged material. The grain size decreased less when using the overheated temperatures.

8.2.3 A588 Beam Specimens

8.2.3.1 Uniaxial Tension Tests

Uniaxial tension tests were conducted according to ASTM E8 on tension coupons from the damaged-repaired A588 steel beams. All A588 tensile coupons were fabricated with the dimensions shown in Figure 7.18. Figures 8.75 and 8.76 show the uniaxial stress-strain (σ–ε) relationships of tension coupons from A588-Beam 1 and A588-Beam 2, respectively. Figures 8.75 and 8.76 also include the σ–ε relationships of the undamaged specimen removed from flange Segment TA for comparisons. The structural properties of the damaged-repaired A588 beam specimens are summarized in Table 8.15, which includes the individual results of X, Y, and Z coupons and their average. The damage-repaired steel material properties (σ_y, E, σ_t, and percent elongation) were normalized with respect to the corresponding undamaged steel material properties and plotted in Figures 8.77 (a-d). Figure 8.77(a) shows the normalized yield stress for all damaged-repaired specimens. Figure 8.77(b) shows the normalized elastic modulus for all damaged-repaired specimens. Figure 8.77(c) shows the normalized ultimate stress, and Figure 8.77(d) shows the normalized percent elongation for all damaged-repaired specimens.

The yield stress data in Table 8.15 and Figure 8.77(a) indicate that:

- Damage-repair cycles decreased the yield stress of Specimens X and Y from both beam specimens to 89-96% of the undamaged material.
- Damage-repair cycles increased the yield stress of Specimens Z from both beam specimens to approximately 107-108% of the undamaged material.
- Applying a higher external restraining force slightly decreased the yield stress of Specimens X and Y and very slightly increased the yield stress of Specimen Z.

The elastic modulus data in Table 8.15 and Figure 8.71(b) indicate that:

- Damage-repair cycles do not affect the elastic modulus of A588 steel. All results were within a range of 97-102% of the undamaged material.

The ultimate stress data in Table 8.15 and Figure 8.71(c) indicate that:

- Damage-repair cycles decreased the ultimate stress of A588 steel. The results were found within 89-98% of the undamaged material.
- The ultimate stress increased as the specimens were removed closer to the web.
- Applying a higher external restraining force slightly decreased the ultimate stress of Specimens X and Y and very slightly increased the ultimate stress of Specimen Z.

The percent elongation (ductility) data in Table 8.15 and Figure 8.71(d) indicate that:

- Damage-repair cycles increased the percent elongation of the outmost (X) specimen and decreased the percent elongation of the middle (Y) and innermost (Z) specimens.
- The percent elongation decreased as the specimens were removed closer to the web.

- Applying a higher external restraining moment had an insignificant effect on the resulting ductility. A higher restraining stress decreased the ductility of the outermost (X) specimen slightly and increased the ductility of the middle (Y) and innermost (Z) specimens.

8.2.3.2 Charpy V-notch Fracture Toughness Tests

The results of the fracture toughness tests on damaged-repaired A588 steel are provided in Table 8.16. Averages were taken both across the width of the flanges (i.e. averages of 1, 2, 3, and 4) and along the flange length (i.e. averages of 1, 2, 3, or 4 for L1, C, and R1). The overall average and standard deviations of all twelve charpy specimens are also provided in Table 8.16. These fracture toughness values were normalized with respect to the average (mean) undamaged fracture toughness of undamaged A588 steel from Plate B only. The results from undamaged Plate B were only used for normalized ratios as Table 7.16 indicated a slight statistical difference between the fracture toughness of Plate A and Plate B (probability that data sets are statistically similar=10%). The normalized fracture toughness values are also shown in Table 8.16. Figure 8.78 shows the normalized fracture toughness of the charpy specimens from the damaged-repaired beams. Table 8.17 provides the means, standard deviations, 95% confidence intervals for the actual mean, medians, and absolute average deviations from the median for the twelve charpy specimens removed from each beam specimen.

Student's t-test analysis was conducted to evaluate the statistical difference between the undamaged fracture toughness values and the fracture toughness of A588-Beam 1 and A588-Beam 2. As mentioned previously in Section 4.9.2, the t-test evaluates the statistical difference between two data sets using their respective means, standard deviations, and sample set sizes. The results from the t-test include the t-value and the corresponding probability of null hypothesis, where the null hypothesis implies that the data sets are statistically similar. Tables 8.18 and 8.19 compare the fracture toughness of A588-Beam 1 and A588-Beam 2, respectively. Table 8.18 indicates less than 0.01% probability that the data sets are statistically similar) and Table 8.19 indicates a 0.35% probability that the data sets are statistically similar.

The data in Tables 8.16 to 8.19 and Figure 8.78 indicates that:

- Damage-repair cycles increased the fracture toughness of A588 steel significantly.
- Charpy Specimen C-4 from A588-Beam 2 was the only one found to have lower fracture toughness than the mean undamaged value.
- Fracture toughness decreased as the charpy specimens were closer to the flange-web junction (k-area region). In each row, Specimen 1 had higher fracture toughness than Specimen 2, Specimen 2 had higher fracture toughness than Specimen 3, and Specimen 3 had higher fracture toughness than Specimen 4. All three charpy specimens removed across the beam specimens (i.e. 1's, 2's, 3's, and 4's) related very well to each other.
- From A588-Beam 1, Specimens 1, 2, and 3 (including L, C, and R) were found to be exceptionally high with values ranging from 263-308% of the undamaged mean. Specimen 4 was found to be moderately high with values ranging from 126-147% of the undamaged material.
- From A588-Beam 2, Specimens 1 and 2 (including L, C, and R) were found to be exceptionally high with values ranging from 272-308% of the undamaged mean. Specimens 3 and 4 ranged from 77-136% of the undamaged material.
- Therefore, applying a higher external restraining stress reduces the fracture toughness.

8.2.3.3 Rockwell Hardness and Microstructure Investigations

Rockwell hardness tests were conducted on damage-repaired A588 steel according to ASTM E18. Four points were taken on Specimens C-2, identified in Figure 7.24. Table 8.9 summarizes the averaged

results of the Rockwell hardness tests and the microstructure investigations. Table 8.9 also provides comparisons between the approximate ultimate strengths as estimated by ASTM A370 to the actual ultimate strengths given in Section 8.2.3.1.

Microstructure preparations were conducted using the procedures outlined in Section 7.6.1.3. The resulting microstructures of the two A588 steel beam specimens are shown in Figure 8.79 (Refer to Figure 7.23 for comparisons to undamaged steel). The average hardness and grain sizes of damaged-repaired steel were normalized with respect to the undamaged steel from Flange B. Figure 8.80 shows the normalized hardness and grain size results of the damaged-repaired steel. As discussed in Section 4.9.4, a more fine-grained microstructure is generally stronger and tougher than a more coarse-grained microstructure. There is a slight increase on the surface hardness and a slight decrease on the ductility. A microstructure that is more pearlitic is harder, stronger, and more brittle. However, only significant and consistent changes in the percent pearlite would be further analyzed as the amount is related to the location taken for the picture as discussed in Section 2.4.3. The results are provided in Table 8.9 for completeness.

The results in Table 8.9 and Figure 8.80 indicate that:

- Damage-repair cycles decrease the surface hardness of A588 steel to approximately 95% of the undamaged material.
- For A588, the approximate tensile strengths as estimated by ASTM A370 relate well to the actual tensile strengths for both undamaged and damage-repaired steel. The reduction in hardness is likely linked to the sufficient decrease in tensile strength.
- Applying a higher external restraining force had a negligible effect on the resulting hardness.
- Damage-repair cycles decreased the grain size of A588 steel to either 65% or 70% of the undamaged material.
- Applying a higher external restraining force appears to increase the resulting grain size slightly and decrease the amount of pearlite. However, both of these results may simply be a function of the spot chosen for taking the photographs.

8.2.4 Indirect Verification of Fracture Toughness Results

The MSU researchers further verified the fracture toughness testing procedure and Charpy testing machine by examining the broken charpy specimens. A recommended practice guide has been published by the National Institute of Standards and Technology (*NIST*) entitled “Installing, Maintaining, and Verifying your Charpy Impact Machine” [*3*]. Examining the broken charpy specimens is an indirect verification procedure and there are seven possible defects listed in the *NIST* practice guide for performing an indirect verification:

1. Worn Anvils
2. Off center specimen
3. Off center strike
4. Uneven anvil marks
5. Chipped anvil marks
6. Bent Pendulum
7. Damaged anvils

Case 2 is the only defect caused by mishandling of the charpy specimen prior to impact and examines the placement of the specimen and its contact with the anvils. An off-center specimen is misaligned as the striker does not contact the center (directly opposite of the v-notch) at the time of impact. An off-center specimen can be detected by placing the specimens together as shown schematically in Figure 8.81 [*3*].

Off-center specimens can be the resultant of worn centering tongs, careless testing procedures, or the use of cooling fluid too viscous at the test temperature.

Other defects (Case 1, Cases 3-7) are caused by imperfections in the Charpy impact testing machine. It is likely that if imperfections existed in the Charpy testing machine, they would be present towards the end of testing. The damage-repaired charpy specimens from beam specimens were tested after all tests on damaged-repaired small scale specimens as well as undamaged specimens. Therefore, all broken charpy specimens from damaged-repaired beam specimens were further analyzed for the possibilities of imperfections in the testing machine. Each possible imperfection was considered when evaluating each Charpy specimen and was recorded as shown for A36-Beam 2 in Table 8.20. The broken charpy specimens and fracture toughness values from A36-Beam 2 are provided in Figure 8.82.

Table 8.20 and Figure 8.82 indicate that Charpy specimen R-3 has slight misalignment. However, the fracture toughness does not appear to be an outlier as it is between the fracture toughness of Specimens R-2 and R-4. This relationship is expected from other fracture toughness testing of beam specimens. The description of specimens tested with worn anvils is seen in Specimens R-1, R-2, and C-1. However, this defect is unlikely, as it would be noticed in for other specimens as well.

Similar tables were developed for the other beam specimens. The MSU researchers concluded that specimen C-2 from A36-Beam 1 might be a possible outlier since it value was 68 ft-lb and C-1, C-3, and C-4 had fracture toughness values of 16 ft-lb, 16 ft-lb, and 11 ft-lb, respectively. However, after investigating the broken specimen, the test appeared to be conducted accordingly. Some charpy specimens were not broken into two pieces due to high ductility and fracture toughness. An example is shown for A588-Beam 2 in Figure 8.83. For specimens that did not fracture into two pieces, the researchers used their best judgment in estimating possible off-centered specimens.

The researchers found no defects from the broken charpy specimens from A36-Beam 1, A588-Beam 1, and A7-Beam 1. For A588-Beam 2, Specimen C-1 appeared to have slight misalignment, and Specimen R-3 showed signs of chipped anvils (see Figure 8.83). From A7-Beam 2, Specimens L-1 and L-2 indicated slight misalignment. None of these charpy specimens appears to be outliers in the data.

Since the broken Charpy specimens from beam specimens indicated that the Charpy impact machine was functioning adequately, further examinations were not required on charpy specimens from all small-scale specimens. However, some were chosen after examining the data and identifying outliers. Outlier specimens were chosen from significant variation of the three specimens in series (i.e. 1, 2, 3 or 4, 5, 6). The specimens chosen were from A36-30-70-3, A36-30-70-5, A36-60-50-3, A36-60-50-5, A36-90-25-3, A588-60-25-3, A588-60-50-2, A7-60-25-3-2, and A36-90-50-3-1600. All six broken Charpy specimens from each of these damaged-repaired specimens were examined and verified.

Most of the specimens questioned as outliers from the small-scale results had lower fracture toughness values than others. A slight and insignificant amount of defects could be identified in the examination of these specimens. In general, a specimen with lower fracture toughness will have less visible gouge marks and a shinier and flatter fracture surface as shown in Figure 8.84(a-c). Figure 8.84(a-c) shows Specimens 4, 5, and 6, from A36-30-70-3. The fracture toughness results were 17 ft-lb, 61 ft-lb, and 64 ft-lb respectively.

Of all specimens examined, only the results from Specimens 1, 2, and 3 of A36-30-70-5 appear questionable. The fracture toughness results were 8.5 ft-lb, 49 ft-lb, and 56 ft-lb respectively. The gouge marks on Specimen 1 were really light but appeared to be aligned in respect to each broken side. The gouge marks on Specimens 2 and 3 appeared to be slightly misaligned which could persuade a higher fracture toughness result. Overall, the examination of broken Charpy specimens indicates that good practice was performed in conducting the tests and a valid Charpy impact machine was used.

8.3 COMPARISONS OF RESULTS FROM TASKS III AND IV

As mentioned earlier, the large-scale beams tests of Task IV were designed and conducted to validate some of the major conclusions and recommendations from Task III. This section compares the relevant results from Tasks III and IV for each steel type.

8.3.1 A7 Steel

The results from Task III indicated that smaller damage strains have more detrimental effects on the structural properties of damaged-repaired A7 steel and the total number of damage-repairs must be limited to three (see Section 6.4.4). Therefore, the large-scale A7-Beam 1 was tested to evaluate the effects of smaller damage strain (ε_d=30 ε_y) and three damage-repair cycles on the structural properties. Large-scale A7-Beam 2 was tested to compare the effects of larger damage strains (60 ε_y, 90 ε_y) and three damage-repair cycles on the structural properties. The results for A7 steel from Tasks III and IV compare as follows:

- The basic structural properties (yield stress, elastic modulus, and ultimate stress) of damaged-repaired A7 steel are usually comparable to the corresponding undamaged material properties. The Task III results for elastic modulus and yield stress were not completely reliable due to the curvature of some tension coupons, which developed during the damage-repair process. The Task IV results indicate that the yield stress increased for both A7-Beam 1 and A7-Beam 2, but the increase was greater for the A7-Beam-1 subjected to the smaller damage strain.
- The percent elongation (ductility) of A7 steel decreases after three damage-repair cycles. Task III results indicate percent elongation values within 75-80% of the undamaged percent elongation after three damage-repair cycles. However, the Task IV results indicate higher elongation values within 80-95% of the undamaged percent elongation after three damage-repair cycles.
- The fracture toughness of A7 steel subjected to the smaller damage strain of 30 ε_y decreases after three damage-repair cycles. Task III results indicate that the fracture toughness reduces to approximately 50% of the undamaged fracture toughness. However, Task IV results indicate an even more drastic reduction in the fracture toughness to approximately 25% of the undamaged toughness.
- Task III results indicate that the fracture toughness of A7 steel subjected to the higher damage strains of 60 or 90 ε_y is dependent on the restraining stress σ_r; higher σ_r (0.40 σ_y) results in lower fracture toughness (approx. 50-75% of the undamaged toughness) and lower σ_r (0.25 σ_y) results in fracture toughness comparable to the undamaged toughness. The Task IV results for A7-Beam 2 indicate that the mean fracture toughness of A7 steel after three damage-repair cycles (ε_d = 90ε_y or 60ε_y and M_r=0.50 M_p or 0.25 M_p) is approximately equal to the undamaged toughness. However, there is significant variability in the fracture toughness with material location. The average fracture toughness in the center Vee heat (*C*) was 56% of the undamaged toughness with some values as low as 10-20% of the undamaged toughness.

The results for A7 steel from Tasks III and IV compare favorably. Based on the fracture toughness results of Tasks III and IV, it is recommended that A7 steel beams should not be subjected to more than three damage-heat straightening repair cycles. Smaller damage strains are more detrimental to A7 steel as compared to larger damage strains.

8.3.2 A36 Steel

The results from Task III indicate that smaller damage strains have more detrimental effects on the structural properties of damaged-repaired A36 steel and the total number of damage-repairs must be limited to three (see Section 6.2.4). The Task III results also indicate that overheating the steel to 1400 ºF during repair results in improved structural properties and fracture toughness after three damage-repair cycles. Hence, the large-scale A36-Beam 1 was tested to evaluate the effects of smaller damage strain (ε_d=30 ε_y) and three damage-repair cycles on the structural properties. A36-Beam 2 was tested to evaluate the effects of overheating to 1400 ºF on the structural properties, while maintaining the other damage and repair parameters (ε_d, σ_r, and N_r) the same as A36-Beam 1. The results for A36 steel from Tasks III and IV compare as follows:

- The basic material properties (yield stress, elastic modulus, and ultimate stress) of damaged-repaired A36 steel are comparable to the corresponding undamaged material properties. Damage-repair cycles increase the yield stress of A36 steel. Overheating the steel to 1400 ºF increases the yield stress more significantly. Damage-repair cycles at 1200 ºF or 1400 ºF have a small influence on the elastic modulus and ultimate stress of A36 steel.
- The percent elongation (ductility) of A36 steel decreases after three damage-repair cycles. Task III results indicate percent elongation values within 75-80% of the undamaged percent elongation after three damage-repair cycles at 30 ε_y. However, the A36-Beam 1 results from Task IV indicate higher percent elongation values within 85-95% of the undamaged percent elongation after three damage-repair cycles at 30 ε_y and heating up to 1200 ºF. The results from A36-Beam 2 indicate that overheating the steel during repair reduces the percent elongation values significantly to 67-87% of the undamaged percent elongation.
- The fracture toughness of A36 steel subjected to the smaller damage strain of 30 ε_y decreases after three damage-repair cycles. Task III results indicate that the mean fracture toughness reduces to approximately 25-50% of the undamaged fracture toughness. The A36-Beam 1 results from Task IV indicate that the overall mean fracture toughness is 90% of the undamaged fracture toughness. However, the fracture toughness varies significantly with the location of the charpy specimens and the values range from 25-150% of the undamaged toughness. For example, the mean fracture toughness in the center Vee is only 62% of the undamaged toughness with three out of four values close to 30% of the undamaged toughness.
- Task III results indicate that the mean fracture toughness of A36 steel overheated to 1400 ºF during repair is approximately 330-415% of the undamaged fracture toughness. The Task III studies were performed for higher damage strains of 60 or 90 ε_y; there were no studies involving overheating and damage strains of 30 ε_y. The A36-Beam 2 results indicate that the overall mean fracture toughness is 245% of the undamaged toughness. The fracture toughness varies with the location of the charpy specimens and the values range from 101-460% of the undamaged toughness with one outlier at 40%.

The results for A36 steel from Tasks III and IV compare favorably. Based on the fracture toughness results of Tasks III and IV, it is recommended that A36 steel beams should not be subjected to more than three damage-heat straightening repair cycles. Overheating the A36 steel during damage-repair improves its material properties and fracture toughness significantly.

8.3.3 A588 Steel

The results from Task III indicate that A588 steel is extremely resilient. It can undergo several damage-repair cycles without impacting the structural properties and fracture toughness adversely. Task III results also indicate that restraining stress during repair is an important parameter. Higher restraining stresses reduce the fracture toughness of the damaged-repaired A588 steel but never below 50% of the undamaged fracture toughness. The large-scale A588 steel beams in Task IV were subjected to three damage-repair cycles with damage strains of 40 and 20 ε_y combined. A588-Beam 1 was repaired using a lower restraining moment of 0.25 M_p. A588-Beam 2 was repaired using the higher restraining moment of 0.50 M_p to evaluate the effects of restraining stresses. The results for A588 steel from Tasks III and IV compare as follows:

- The basic structural properties (yield stress, elastic modulus, and ultimate stress) of damaged-repaired A588 steel are comparable to the corresponding undamaged material properties. Results from Task III indicate yield stresses within 95-110% and ultimate stresses within 94-104% of the undamaged A588 material. However, results from Task IV indicate smaller yield stresses (approximately 89-96%) and ultimate stresses (approx. 89-98%) than the undamaged A588 material. The reason for this discrepancy is not known. The A588 steels for both Tasks III and IV had similar chemical composition and were ferrite-pearlite steels made without using the quenching and tempering process.
- Task III results indicate that the percent elongation (ductility) of A588 steel decreases after three damage-repair cycles. This reduction in ductility is reasonable with percent elongation values ranging from 74-92% of the undamaged steel. The results from Task IV indicate smaller changes in the percent elongation values (ductility) with damage-repair cycles.
- Task III results indicate that after three damage-repair cycles, the fracture toughness of A588 steel is equal to or greater than the undamaged toughness with values ranging from 75-250% of the undamaged toughness. Increasing the restraining stress reduces the fracture toughness after three damage-repair cycles slightly to values close to 75-100% of the undamaged toughness.
- The results from Task IV indicate that the fracture toughness of A588-Beam 1 repaired with the lower restraining moment is approximately 250% of the undamaged toughness. The toughness varies with the location of the charpy specimens but never reduces below the undamaged toughness. The mean fracture toughness of A588-Beam 2 repaired with the higher restraining moment is approximately 204% of the undamaged fracture toughness (slightly lower than the toughness values for A588-Beam 1). The toughness varies significantly with the location of the charpy specimens with several values close to the undamaged toughness and one value below (approximately 77% of the undamaged toughness).

The results from Tasks III and IV for A588 steel compare favorably. A588 steel is an extremely resilient material that can undergo several (up to five) damage-repair cycles without significant adverse effects on the structural properties including fracture toughness. It is recommended that A588 steel beams can be subjected to several (up to five) damage-heat straightening repair cycles. Lower restraining stresses should be used preferably. However, higher restraining stresses can also be used without impacting the material properties adversely.

8.4 REFERENCE

1. NIST, “Installing, Maintaining, and Verifying your Charpy Impact Machine”, National Institute of Standards and Technology, Special Publication 960-4, Washington, 2000.

Table 8.1
Load increases and displacements during subsequent Vee heats to Location *C* (A7-Beam 1)

Number	Displacement (in)	Load Increase (kips)
Heat 1	0.1674	0.30
Heat 2	0.1560	2.30
Heat 3	0.1459	2.93
Heat 4	0.1531	4.14
Heat 5	0.0756	4.49
Heat 6	-	5.13

Table 8.2
Load increases and displacements during subsequent Vee heats to Location *C* (A588-Beam 2)

	Displacements (in)			
Number	Front	Back	Average	Load Increase (kips)
Heat 1	0.1984	0.2509	0.2247	0.16
Heat 2	0.1843	0.1437	0.164	2.24
Heat 3	0.1408	0.1276	0.1342	2.31
Heat 4	0.1022	0.1327	0.1174	2.85
Heat 5	0.0814	0.0891	0.0853	3.57
Heat 6	0.0906	0.1028	0.0967	4.06

Table 8.3
Comparison of uniaxial tension tests of undamaged A7 with full and reduced dimensions

Property	t=0.500	t=0.383
Upper σ_y *(ksi)*	37.2	37.9
Lower σ_y *(ksi)*	35.8	36.2
Plateau σ_y *(ksi)*	36.6	36.9
E (ksi)	30505	28590
ε_y	0.00120	0.00129
σ_t *(ksi)*	61.4	61.0
ε_u	0.224	0.234
ε_u / ε_y	186.39	181.30
% Elongation	41.96	40.80
% Reduction	62.51	62.00

Table 8.4
Structural properties of damaged-repaired A7 beam specimens

	A7-Beam 1					A7-Beam 2			
	X	**Y**	**Z**	**Avg.**		**X**	**Y**	**Z**	**Avg.**
Upper σ_y *(ksi)*	42.3	43.9	47.5	44.6		39.9	42.9	45.3	42.7
Lower σ_y *(ksi)*	40.8	40.9	45.4	42.4		39.0	41.9	42.9	41.3
Plateau σ_y *(ksi)*	42.3	42.5	45.7	43.5		39.2	42.0	44.0	41.7
E (ksi)	30670	28630	28437	29246		29132	29272	28782	29062
ε_y	0.00138	0.00148	0.00161	0.00149		0.00135	0.00143	0.00153	0.00144
σ_t *(ksi)*	62.3	62.6	65.1	63.3		63.0	62.8	63.2	63.0
ε_u	0.189	0.190	0.168	0.182		0.180	0.217	0.179	0.192
ε_u / ε_y	137.04	127.99	104.54	123.19		133.77	151.24	117.09	134.03
% Elongation	40.20	40.09	33.90	38.07		33.57	39.64	33.55	35.58
% Reduction	60.42	69.08	62.68	64.06		64.62	65.15	63.35	64.37

Table 8.5
Fracture toughness results of damaged-repaired A7 beam specimens

	A7-Beam 1					A7-Beam 2			
	L	**C**	**R**	**Avg**		**L**	**C**	**R**	**Avg**
1	51	9	17.5	25.8		141	74	198	137.7
2	16	5	10	10.3		168	58	62	96.0
3	13	10	9	10.7		72	8	61	47.0
4	8	6.5	8	7.5		9	15	12.5	12.2
Average	22.0	7.6	11.1	**13.6**		97.5	38.8	83.4	**73.2**
Normalized Results									
	A7-Beam 1					**A7-Beam 2**			
	L	**C**	**R**	**Avg**		**L**	**C**	**R**	**Avg**
1	0.734	0.129	0.252	0.372		2.029	1.065	2.849	1.981
2	0.230	0.072	0.144	0.149		2.417	0.835	0.892	1.381
3	0.187	0.144	0.129	0.153		1.036	0.115	0.878	0.676
4	0.115	0.094	0.115	0.108		0.129	0.216	0.180	0.175
Average	0.32	0.11	0.16	**0.20**		1.40	0.56	1.20	**1.05**

Table 8.6
Statistical values of 12 charpy specimens from A7 beam specimens

Statistical Property	A7-Beam 1	A7-Beam 2
Mean	13.6	73.2
Std. Dev.	12.3	64.0
95% High	21.4	113.9
95% Low	5.7	32.5
Median	9.5	61.5
Average Absolute From Median	6.0	46.0

Table 8.7
Student's t-test comparing toughness results of A7-Beam 1 to undamaged A7 (Flange B)

Results of unpaired t-tests:
t=10.8
Std. deviation=12.8
Degrees of freedom=22
Probability of null hypothesis < 0.0001

Table 8.8
Student's t-test comparing toughness results of A7-Beam 2 to undamaged A7 (Flange B)

Results of unpaired t-tests:
t=0.179
Std. deviation=46.2
Degrees of freedom=22
Probability of null hypothesis 0.86

Table 8.9
Rockwell hardness and microstructure results from undamaged and damage-repaired A7steel

Specimen	Hardness		ASTM Approx Tensile σ_t (ksi)	Measured Avg. Tensile σ_t (ksi)	Grain Size (mm)	% Pearlite
	Avg.	Std. Dev.				
Undamaged A7-A	64.1	0.83	55	61.2	0.0293	26.54
Undamaged A7-B	68.9	0.80	59	61.6	0.0249	33.01
A7-Beam 1	73.9	1.12	65	63.3	0.0200	38.74
A7-Beam 2	77.2	0.51	68	63.0	0.0127	25.08
Undamaged A36-A	80.7	0.89	73	75.1	0.0203	35.64
Undamaged A36-B	78.2	0.54	69	73.4	0.0223	23.98
A36-Beam 1	86.3	2.42	83	73.0	0.0134	23.86
A36-Beam 2	83.6	1.81	81	75.5	0.0163	25.21
Undamaged A588-A	87.0	0.39	84	84.9	0.0267	30.07
Undamaged A588-B	86.6	0.38	84	84.5	0.0252	29.70
A588-Beam 1	82.5	0.40	80	79.3	0.0164	24.88
A588-Beam 2	81.6	0.69	77	78.3	0.0176	14.29

Table 8.10
Structural properties of damaged-repaired A36 beam specimens

	A36-Beam 1					A36-Beam 2			
	X	**Y**	**Z**	**Avg.**		**X**	**Y**	**Z**	**Avg.**
Upper σ_y (ksi)	50.1	53.9	52.5	52.2		59.4	54.0	56.1	56.5
Lower σ_y (ksi)	49.5	48.6	49.7	49.3		56.2	49.9	50.8	52.3
Plateau σ_y (ksi)	50.1	50.0	50.2	50.1		56.8	54.0	51.2	54.0
E (ksi)	30435	28495	31669	30200		31711	29610	30037	30453
ε_y	0.00165	0.00175	0.00159	0.00166		0.00179	0.00182	0.00170	0.00177
σ_u *(ksi)*	73.4	72.2	73.4	73.0		78.5	74.2	73.8	75.5
ε_u	0.164	0.189	0.169	0.174		0.149	0.103	0.160	0.137
ε_u / ε_y	99.63	107.71	106.61	104.65		83.19	56.48	93.86	77.84
% Elongation	35.70	34.55	32.60	34.28		32.63	25.36	28.96	28.99
% Reduction	66.01	65.65	63.97	65.21		62.76	62.50	62.15	62.47

Table 8.11
Fracture toughness results of damaged-repaired A36 beam specimens

	A36-Beam 1					A36-Beam 2			
	L	**C**	**R**	**Avg.**		**L**	**C**	**R**	**Avg.**
1	68	16	97	60.3		92	205	180	159.0
2	66	68	37	57.0		112	142	188	147.3
3	17	16	64	32.3		92	55	108	85.0
4	10.5	11	16	12.5		45	18	73	45.3
Average	40.4	27.8	53.5	**40.5**		85.3	105.0	137.3	**109.2**
Normalized Results									
	A36-Beam 1					**A36-Beam 2**			
	L	**C**	**R**	**Avg.**		**L**	**C**	**R**	**Avg.**
1	1.528	0.360	2.180	1.356		2.067	4.607	4.045	3.573
2	1.483	1.528	0.831	1.281		2.517	3.191	4.225	3.311
3	0.382	0.360	1.438	0.727		2.067	1.236	2.427	1.910
4	0.236	0.247	0.360	0.281		1.011	0.404	1.640	1.019
Average	0.91	0.62	1.20	**0.91**		1.92	2.36	3.08	**2.45**

Table 8.12
Statistical values of 12 charpy specimens from A36 beam specimens

Statistical Property	A36-Beam 1	A36-Beam 2
Mean	40.5	109.2
Std. Dev.	30.2	59.4
95% High	59.7	146.9
95% Low	21.3	71.5
Median	27.0	100.0
Average Absolute From Median	26.1	46.7

Table 8.13
Student's t-test comparing toughness results of A36-Beam 1 to undamaged A36 (Flange B)

Results of unpaired t-tests:
t=0.742
Std. deviation=24.1
Degrees of freedom=20
Probability of null hypothesis 0.47

Table 8.14
Student's t-test comparing toughness results of A36-Beam 2 to undamaged A36 (Flange B)

Results of unpaired t-tests:
t=3.17
Std. deviation=44.9
Degrees of freedom=20
Probability of null hypothesis 0.0048

Table 8.15
Structural properties of damaged-repaired A588 beam specimens

	A588-Beam 1					A588-Beam 2			
	X	**Y**	**Z**	**Avg.**		**X**	**Y**	**Z**	**Avg.**
Upper σ_y (ksi)	55.8	57.9	63.6	59.1		52.3	58.7	63.6	58.2
Lower σ_y (ksi)	54.8	55.5	61.8	57.4		51.6	53.4	62.5	55.8
Plateau σ_y (ksi)	55.4	56.4	62.9	58.2		52.1	55.1	63.3	56.8
E (ksi)	29928	29809	30287	30008		29262	30527	29571	29787
ε_y	0.00185	0.00189	0.00208	0.00194		0.00178	0.00180	0.00214	0.00191
σ_u (ksi)	76.2	78.3	83.3	79.3		75.3	76.0	83.6	78.3
ε_u	0.175	0.149	0.120	0.148		0.187	0.157	0.119	0.154
ε_u / ε_y	94.54	78.75	57.78	77.02		105.03	86.98	55.59	82.53
% Elongation	36.74	30.04	28.12	31.63		36.28	33.17	28.84	32.77
% Reduction	72.34	69.42	65.81	69.19		73.05	69.36	67.88	70.10

Table 8.16
Fracture toughness results of damaged-repaired A588 beam specimens

	A588-Beam 1					A588-Beam 2			
	L	**C**	**R**	**Avg.**		**L**	**C**	**R**	**Avg.**
1	295	295	295	295.0		295	293	288	292.0
2	294	292	294	293.3		293	275	260	276.0
3	265	252	292	269.7		130	120	106	118.7
4	141	121	130	130.7		104	74	102	93.3
Average	248.8	240.0	252.8	**247.2**		205.5	190.5	189.0	**195.0**
Normalized Results									
	A588-Beam 1					**A588-Beam 2**			
	L	**C**	**R**	**Avg.**		**L**	**C**	**R**	**Avg.**
1	3.083	3.083	3.083	3.083		3.083	3.062	3.009	3.051
2	3.072	3.051	3.072	3.065		3.062	2.874	2.717	2.884
3	2.769	2.633	3.051	2.818		1.358	1.254	1.108	1.240
4	1.473	1.264	1.358	1.365		1.087	0.773	1.066	0.975
Average	2.60	2.51	2.64	**2.58**		2.15	1.99	1.97	**2.04**

Table 8.17
Statistical values of 12 charpy specimens from A588 beam specimens

Statistical Property	A588-Beam 1	A588-Beam 2
Mean	247.0	195.0
Std. Dev.	71.7	94.3
95% High	292.7	245.9
95% Low	201.6	135.1
Median	292.0	195.0
Average Absolute From Median	47.0	89.0

Table 8.18
Student's t-test comparing toughness results of A588-Beam 1 to undamaged A588 (Flange B)

Results of unpaired t-tests:
t=6.61
Std. deviation=53.5
Degrees of freedom=20
Probability of null hypothesis < .0001

Table 8.19
Student's t-test comparing toughness results of A588-Beam 2 to undamaged A588 (Flange B)

Results of unpaired t-tests:
t=3.30
Std. deviation=70.2
Degrees of freedom=20
Probability of null hypothesis 0.0035

Table 8.20
Possible defects indicated in broken Charpy specimens from A36-Beam 2

Specimen	Worn Anvil	Off Center Specimen	Off Center Anvil	Uneven Anvil Marks	Chipped Anvils	Damaged Anvils	Bent Pendulum
R1	possible	ok	ok	ok	ok	ok	ok
R2	possible	ok	ok	ok	ok	ok	ok
R3	ok	slightly	ok	ok	ok	ok	ok
R4	ok	ok	ok	ok	ok	ok	ok
C1	possible	ok	ok	ok	ok	ok	ok
C2	ok	ok	ok	ok	ok	ok	ok
C3	ok	ok	ok	ok	ok	ok	ok
C4	ok	ok	ok	ok	ok	ok	ok
L1	ok	ok	ok	ok	ok	ok	ok
L2	ok	ok	ok	ok	ok	ok	ok
L3	ok	ok	ok	ok	ok	ok	ok
L4	ok	ok	ok	ok	ok	ok	ok

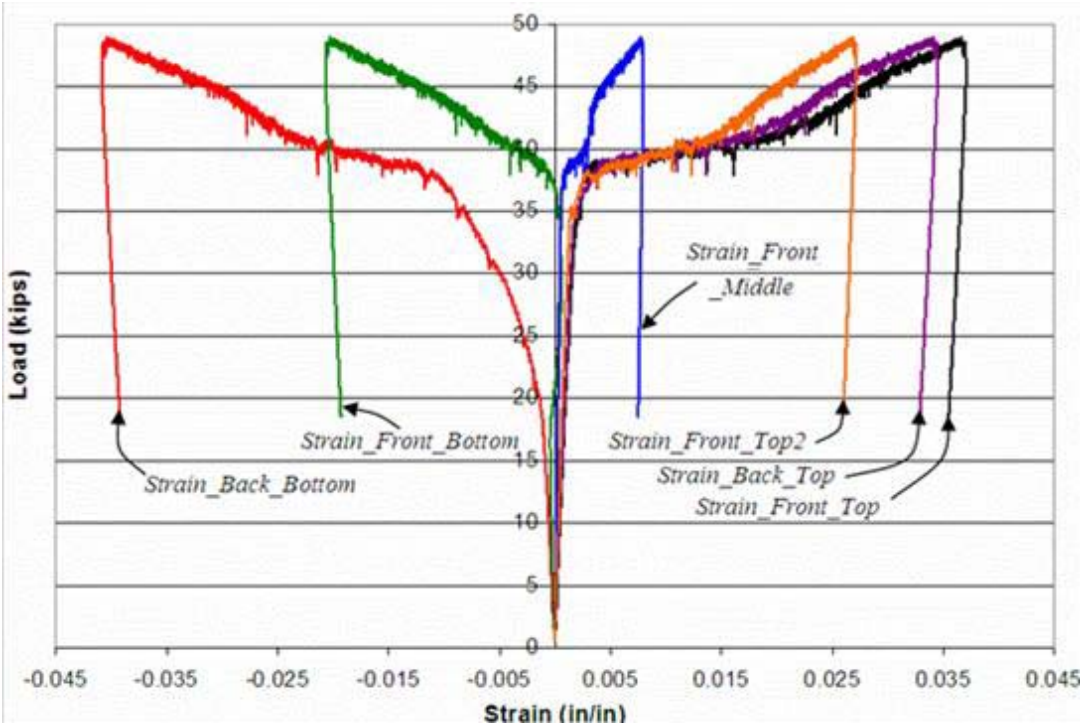

Figure 8.1
Strain gage data during the first damage cycle of A7-Beam 1

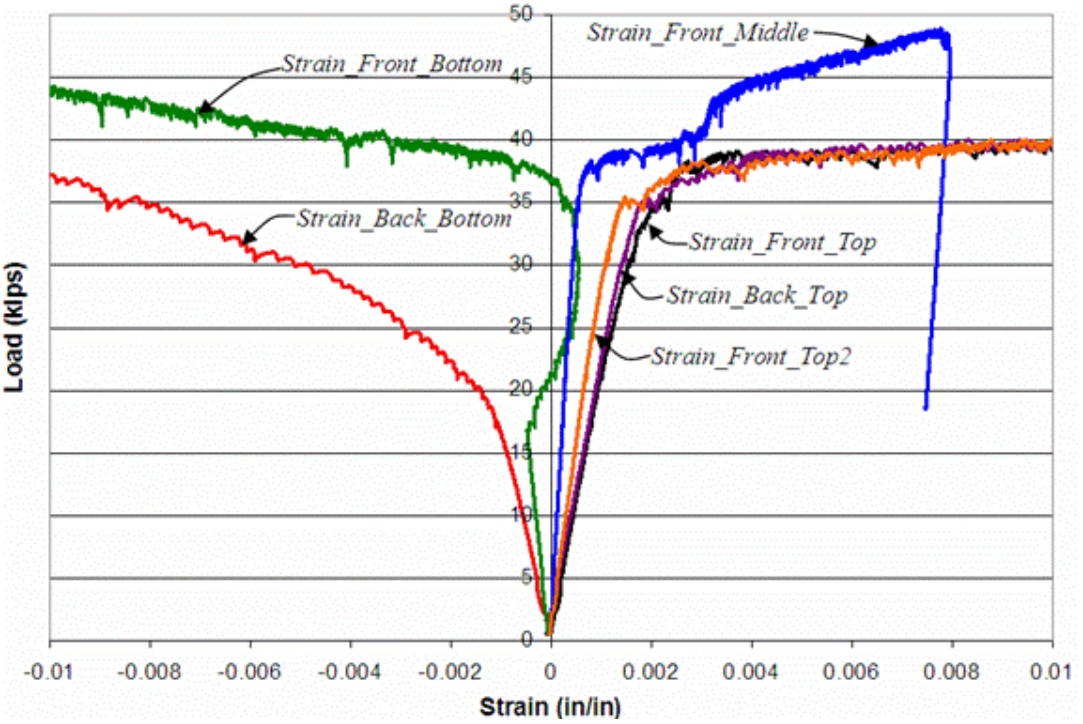

Figure 8.2
Initial strain gage data during the first damage cycle of A7-Beam 1

(a)

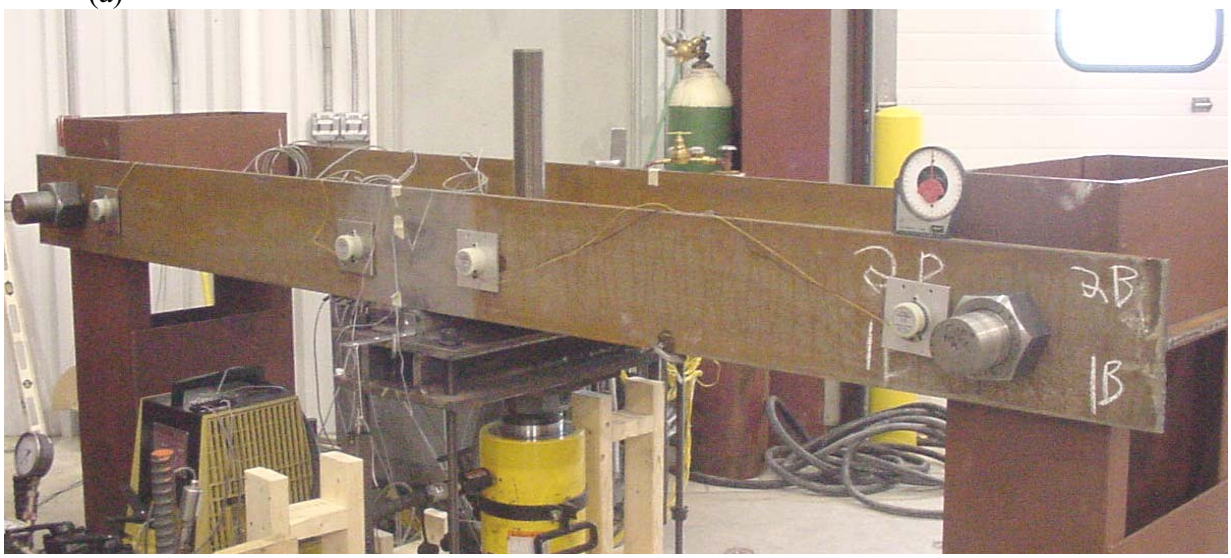

(b)

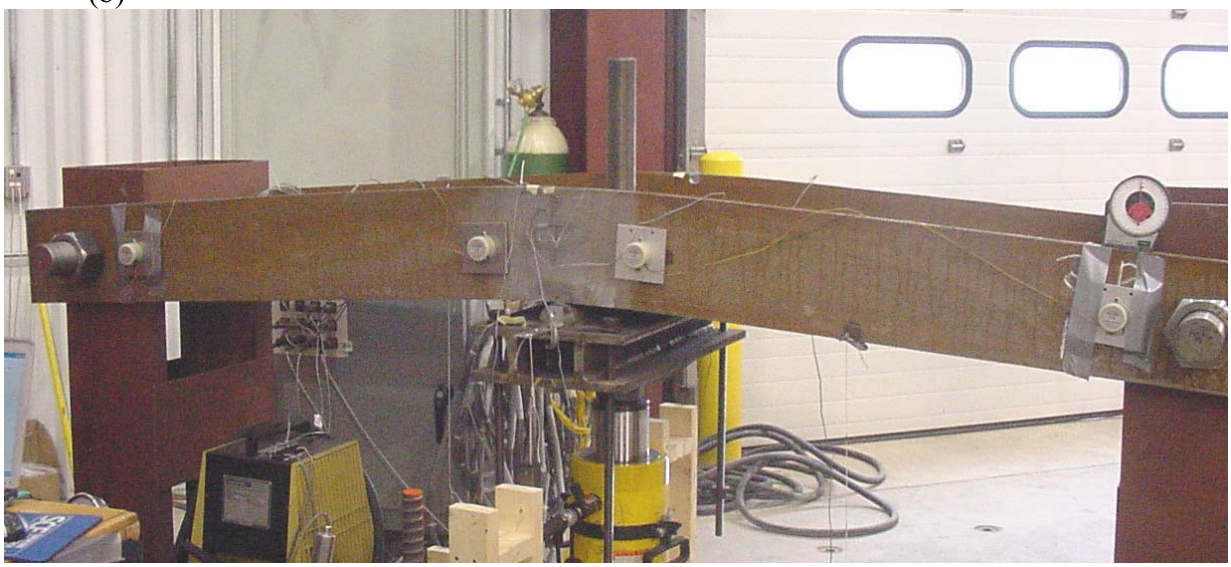

Figure 8.3
Before (a) and after (b) photographs of the first damage cycle of A7-Beam 1

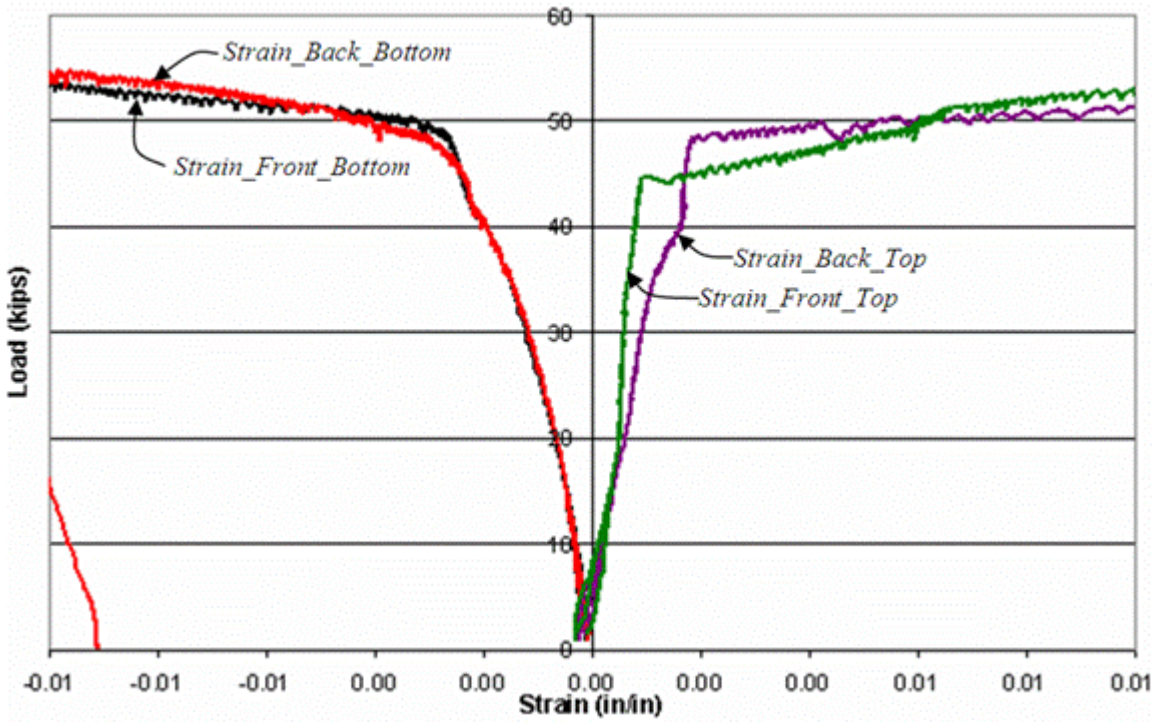

Figure 8.4
Strain gage data during the second damage cycle of A7-Beam 1

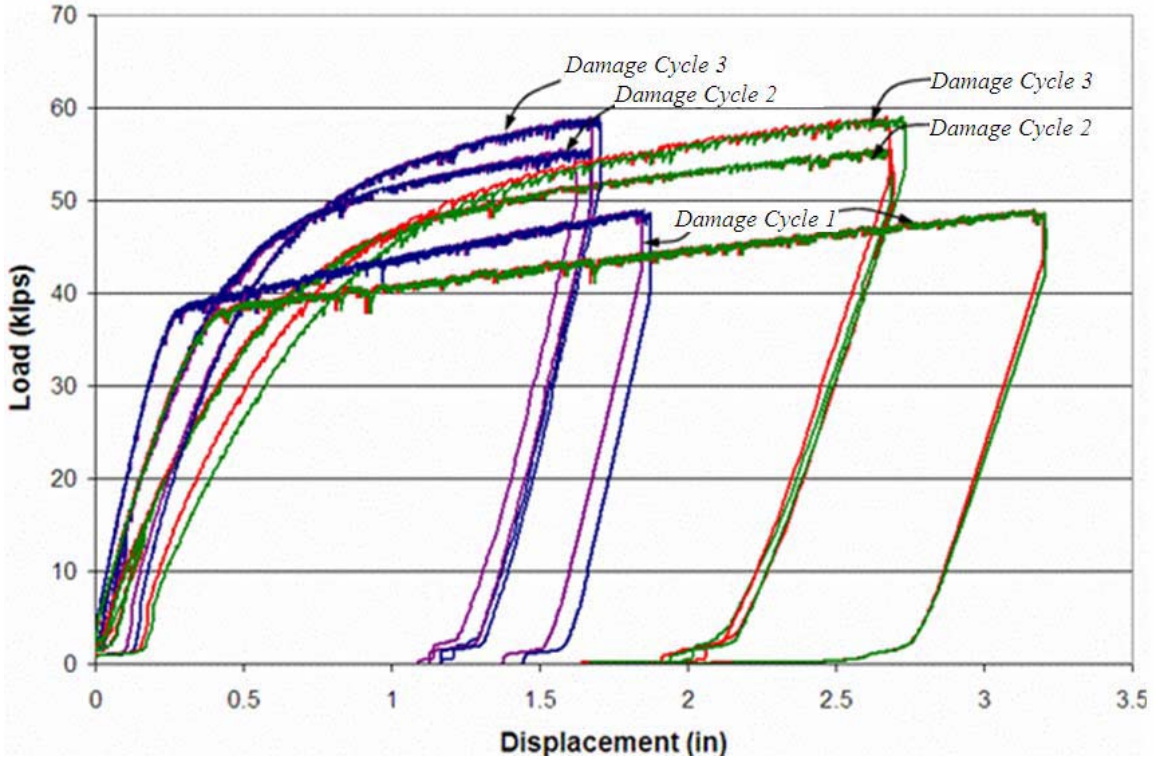

Figure 8.5
Load-displacement behaviors of all three damage cycles of A7-Beam 1

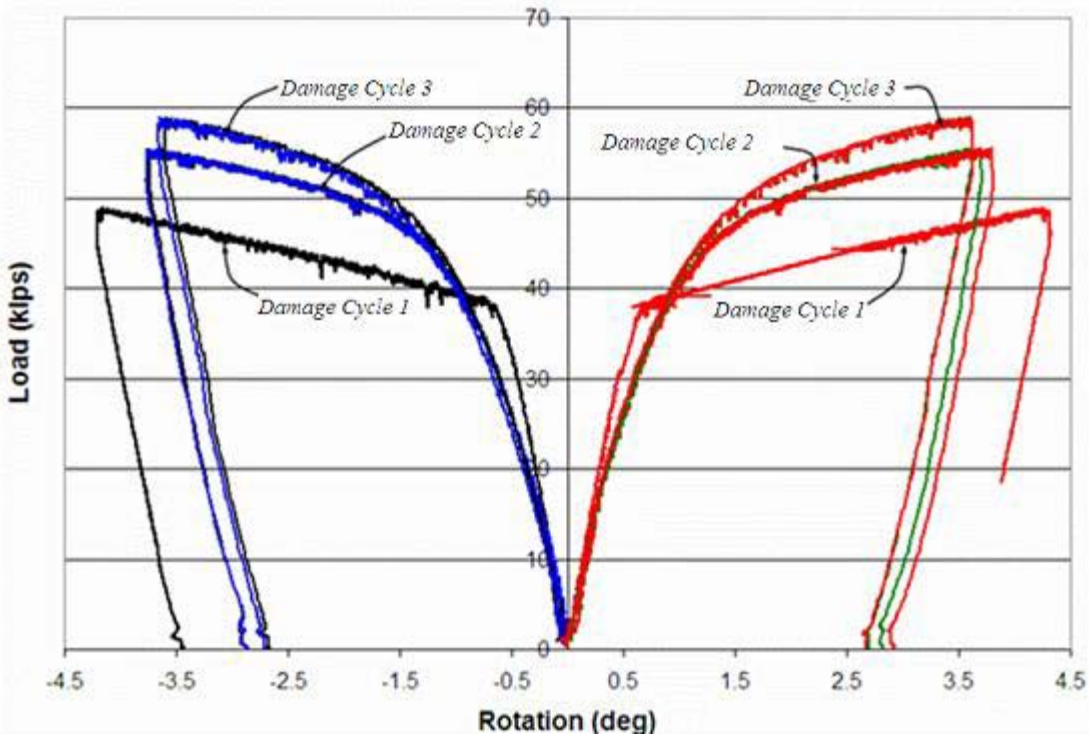

Figure 8.6
Load-rotation behaviors of all three damage cycles of A7-Beam 1

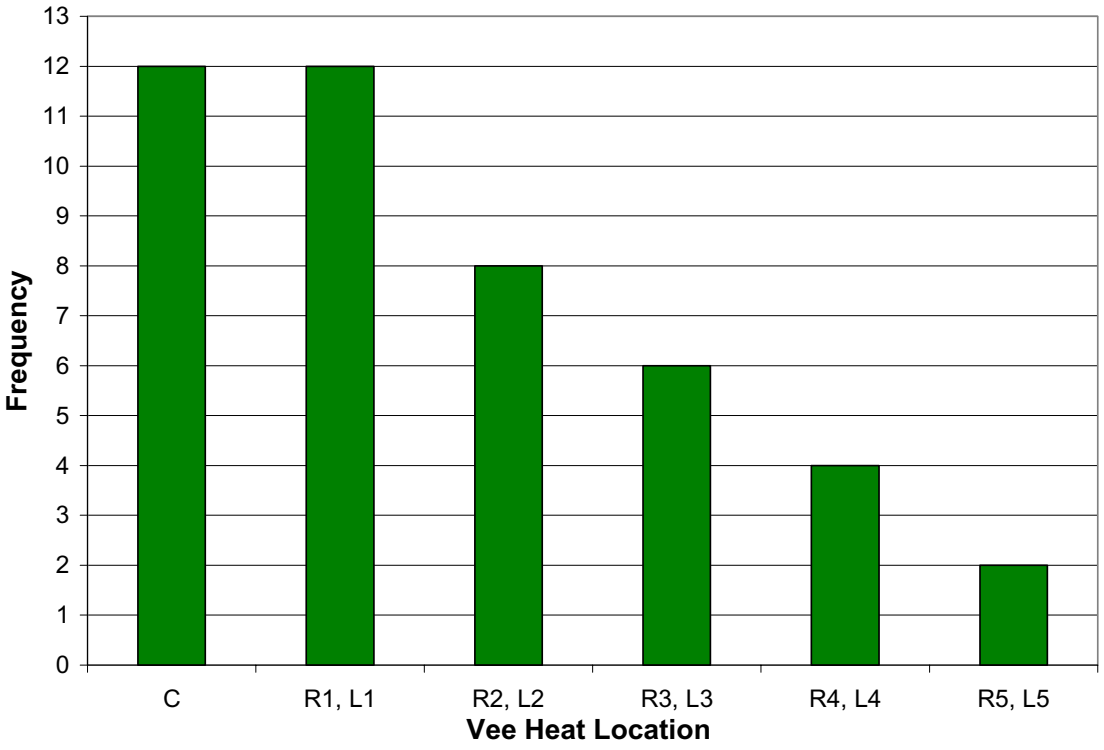

Figure 8.7
Frequency chart of each Vee heat location during three repairs of A7-Beam 1

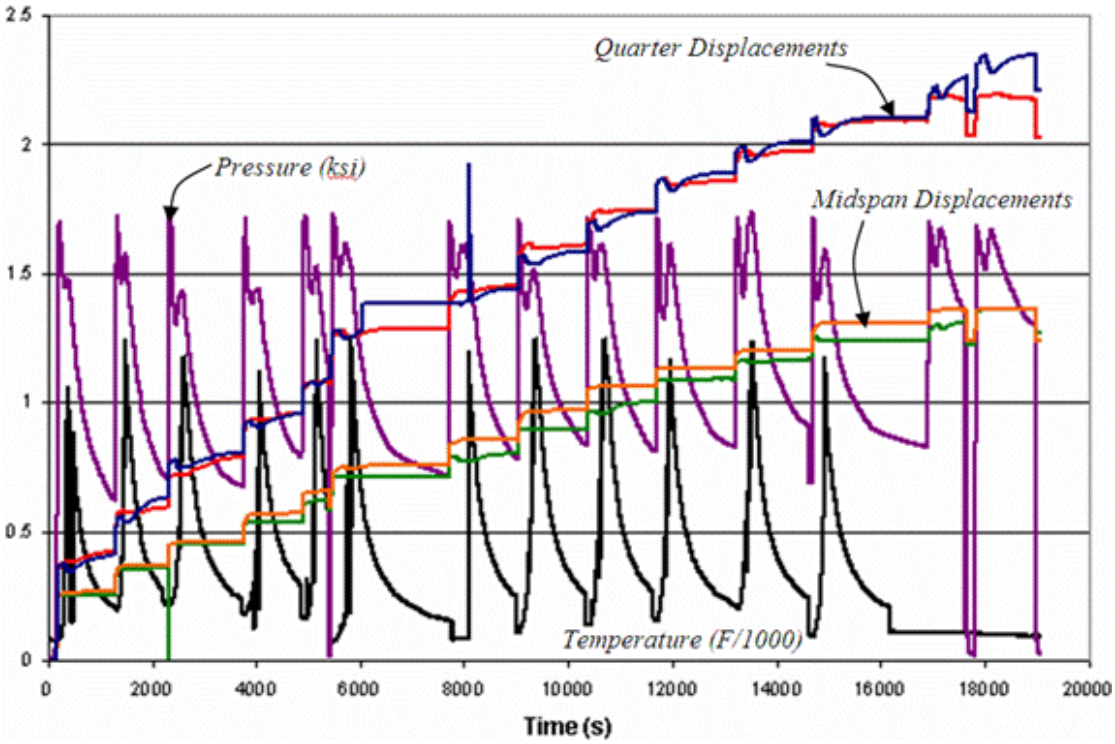

Figure 8.8
Instrument data during the second repair cycle of A7-Beam 1

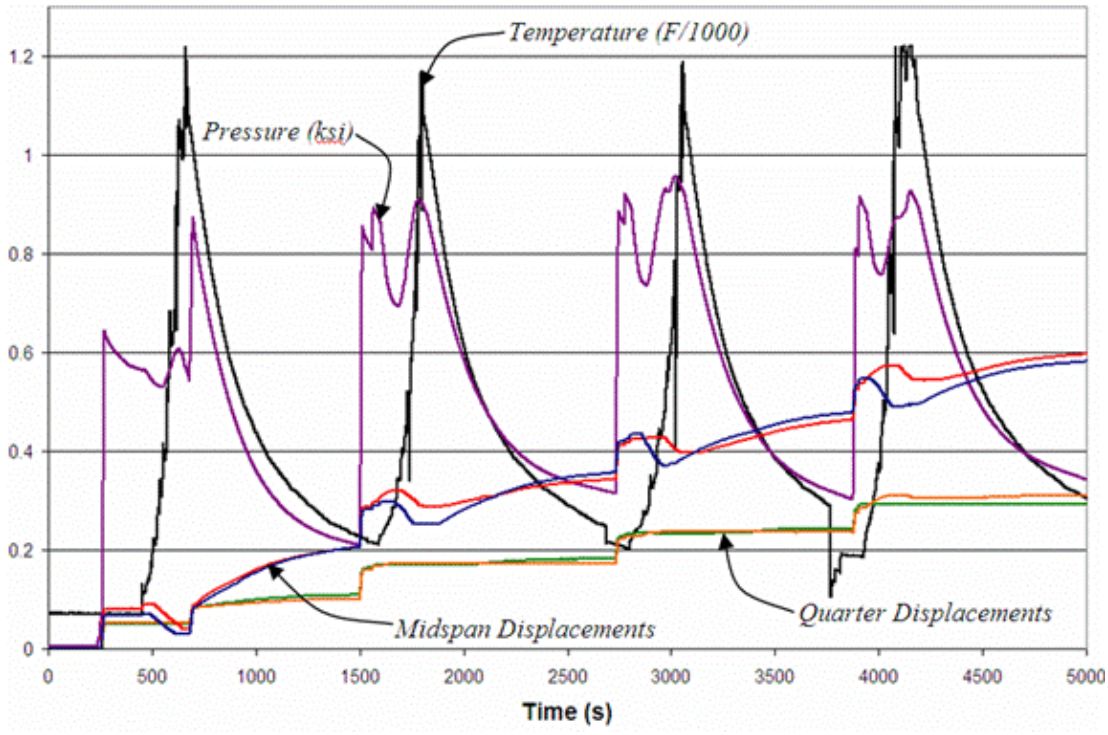

Figure 8.9
Instrument data during the third repair cycle of Beam 1

Figure 8.10
Front view of A7-Beam 1 after experimental investigations

(a) (b)

Figure 8.11
Lateral displacement of front (a) and back (b) flanges after repair cycle 3 of A7-Beam 1

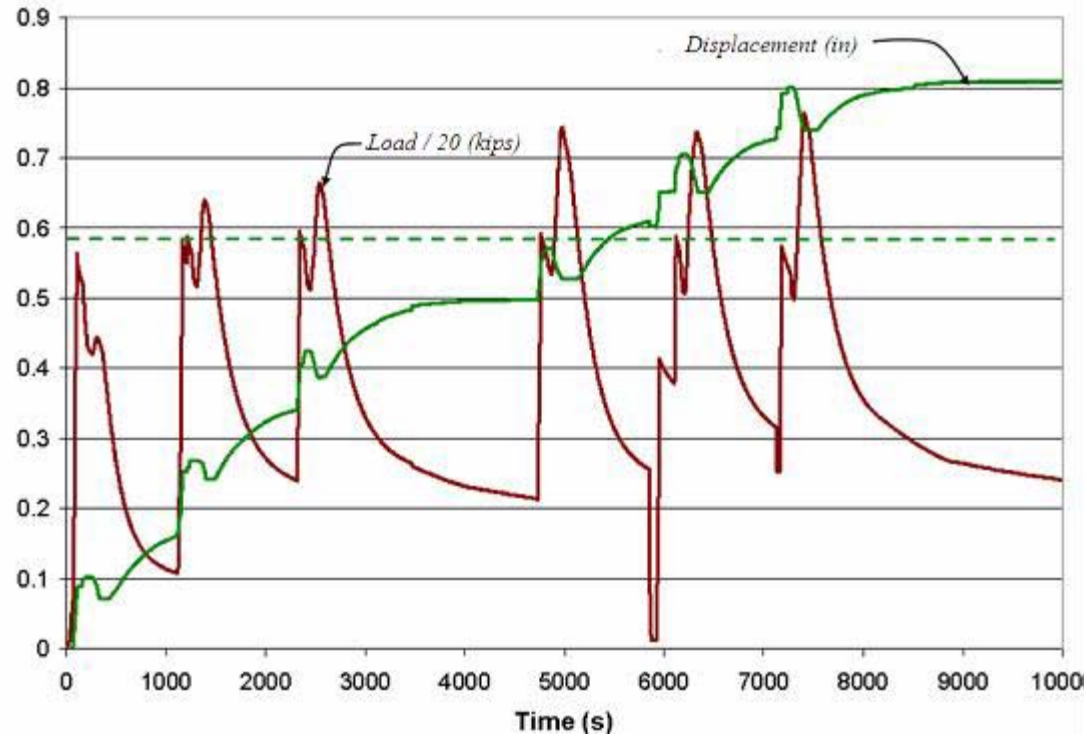

Figure 8.12
Load and displacement data during the first six heating cycles of A7-Beam 1

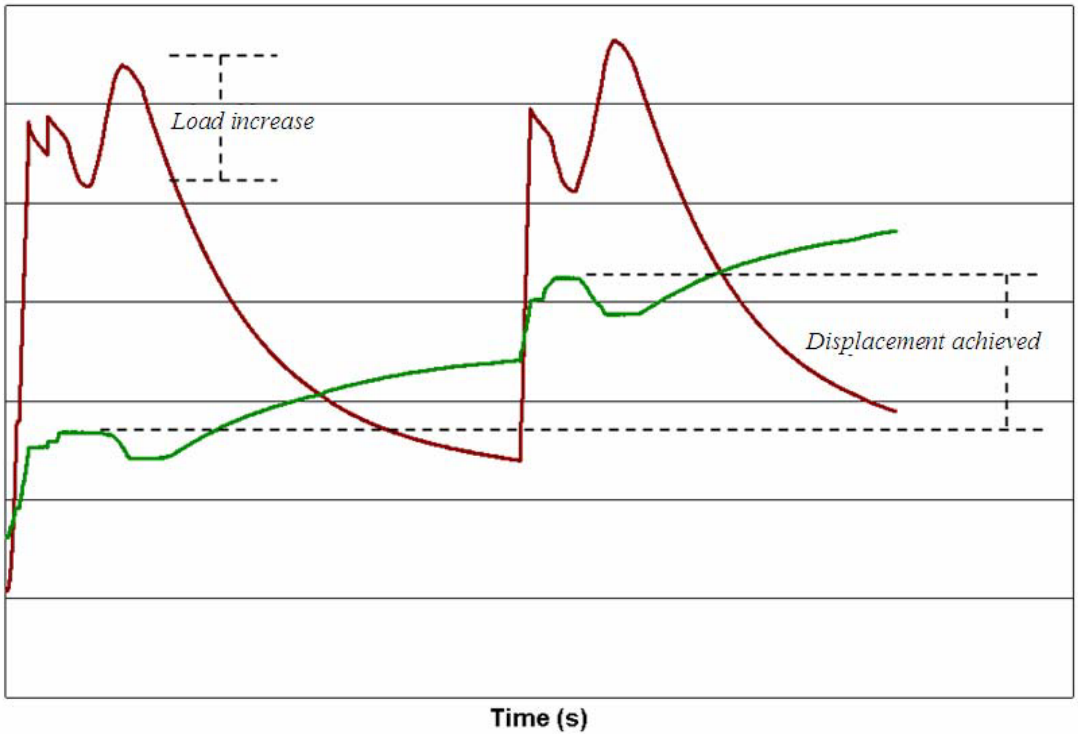

Figure 8.13
Illustration of the load increase and displacements achieved during each heating cycle

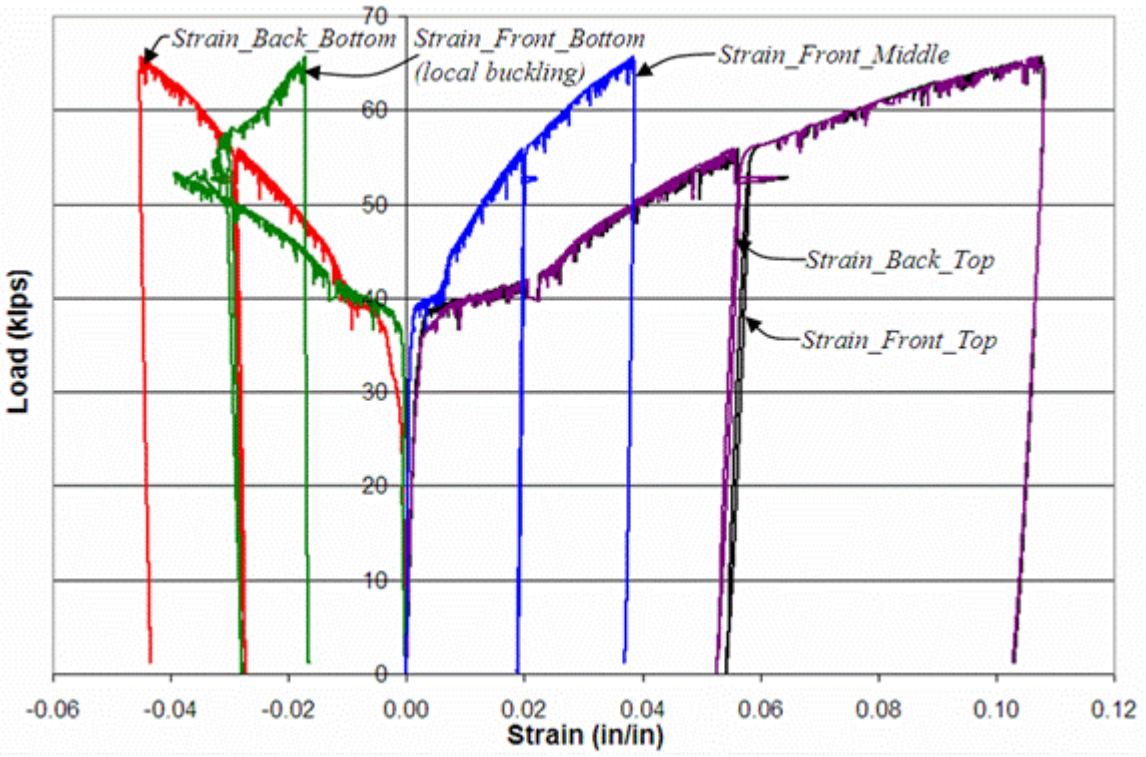

Figure 8.14
Strain gage data during the first damage cycle of A7-Beam 2

(a)

(b)

Figure 8.15
Before (a) and after (b) photographs of the first damage cycle of A7-Beam 2

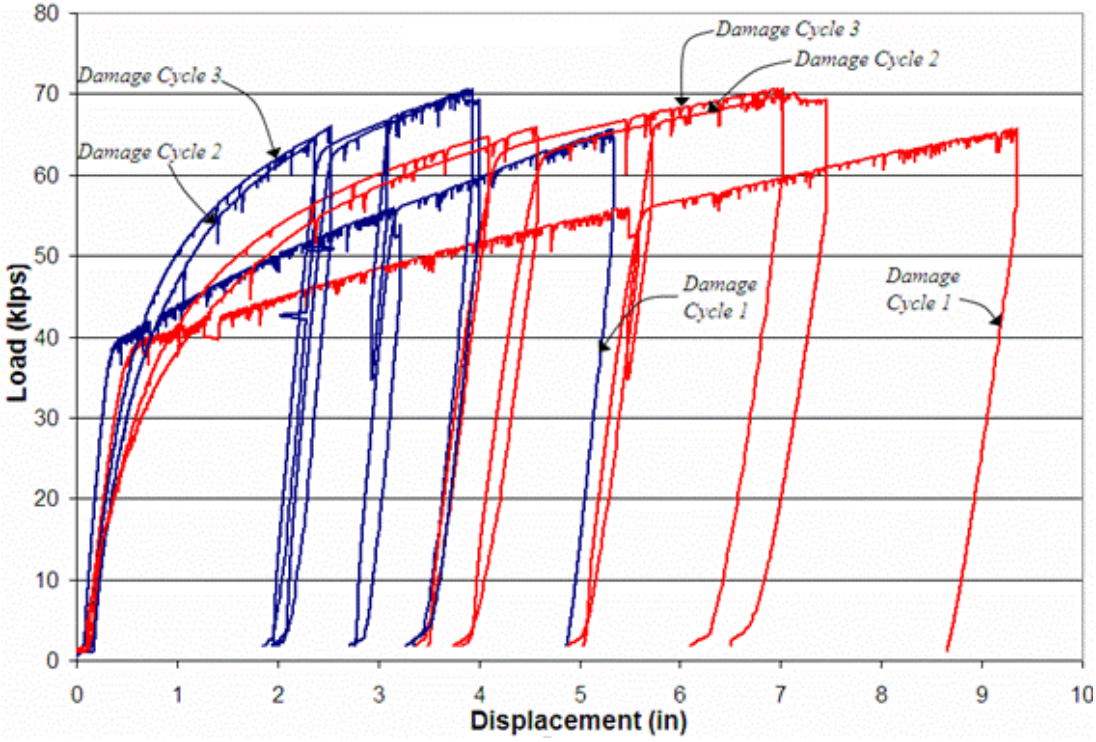

Figure 8.16
Load-displacement behaviors of all three damage cycles of A7-Beam 2

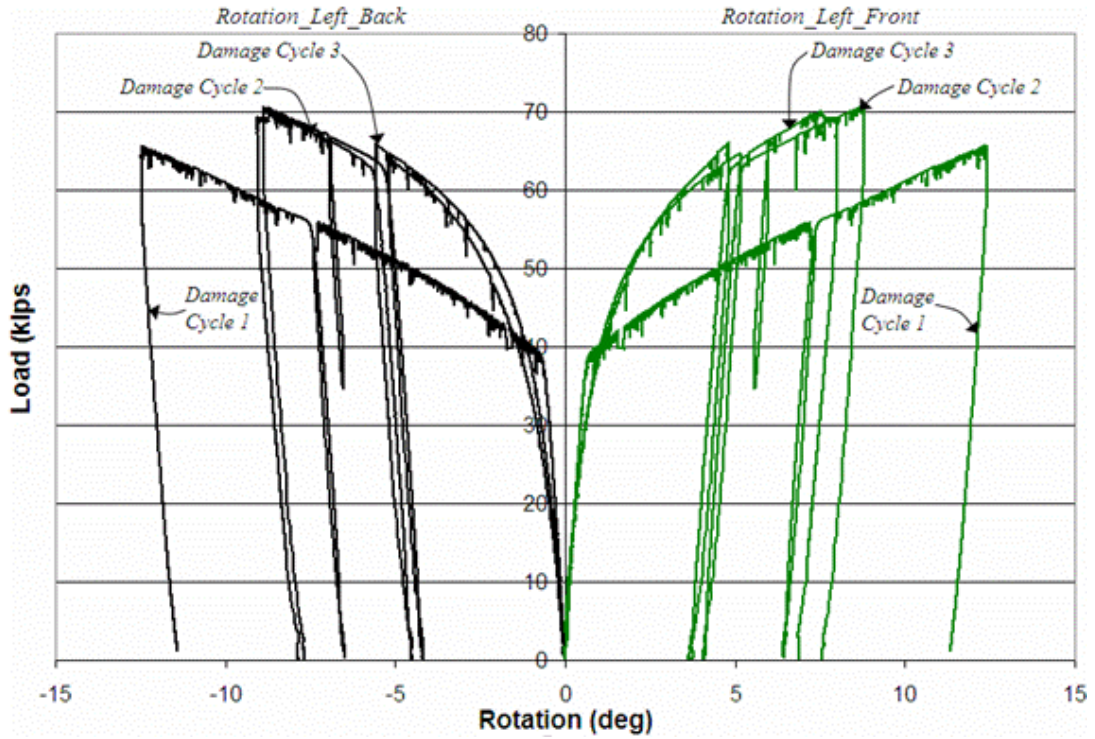

Figure 8.17
Load-rotation behaviors of all three damage cycles of A7-Beam 2

a) Damage Cycle 1 b) Damage Cycle 2 c) Damage Cycle 3

Figure 8.18
Condition of front flange at mid-length after each damage cycle of A7-Beam 2

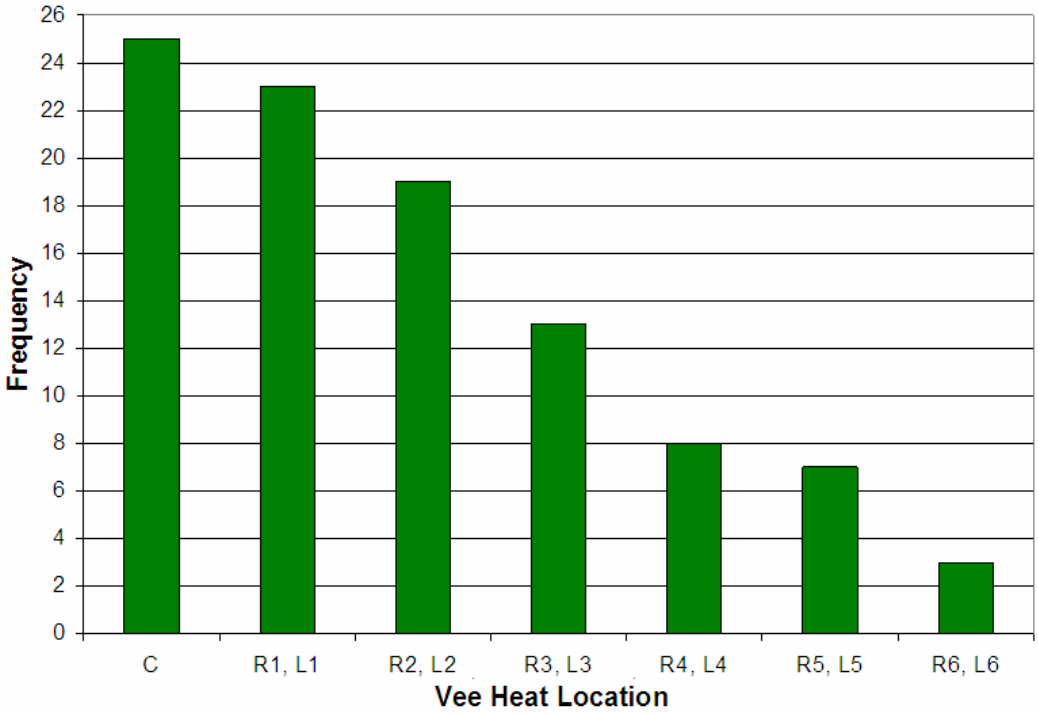

Figure 8.19
Frequency chart of each Vee heat location during three repairs of A7-Beam 2

a) Front side

b) Back side

Figure 8.20
Location of strip heats applied to the web of A7-Beam 2

Figure 8.21
Front view of A7-Beam 2 after experimental investigations

(a) (b)

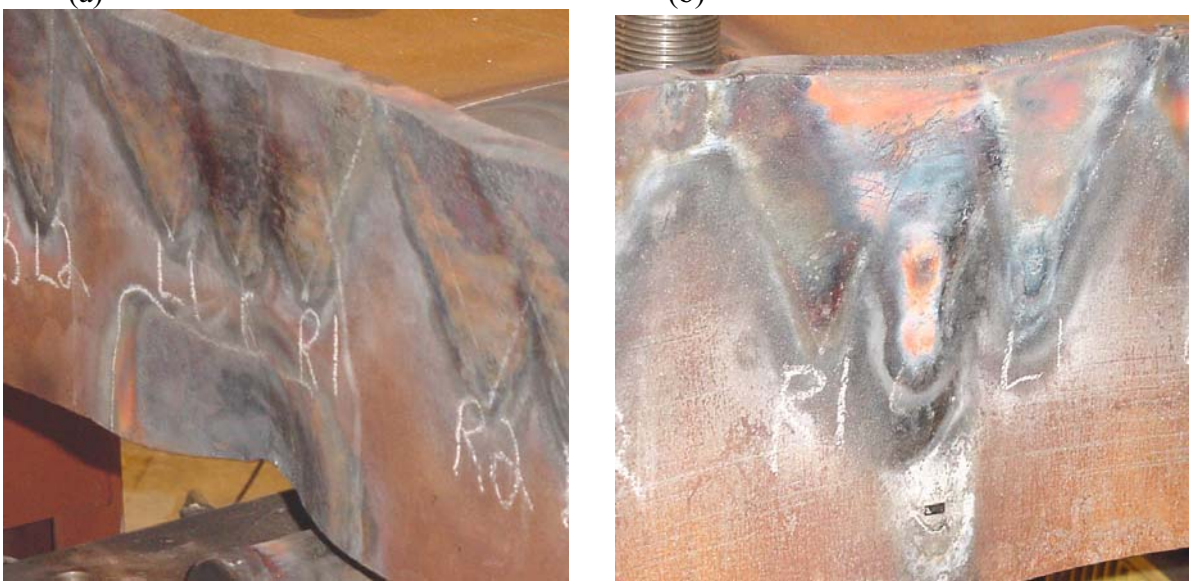

Figure 8.22
Condition of front (a) and back (b) flanges of A7-Beam 2 after repair cycle 3

(a) (b)

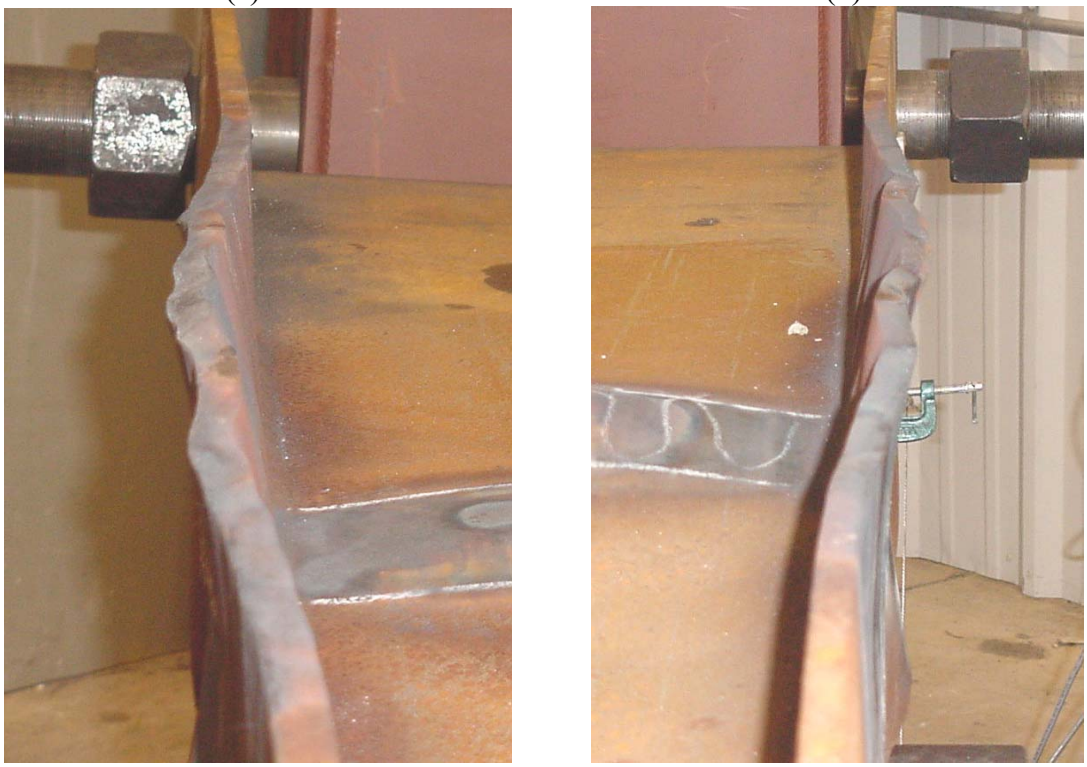

Figure 8.23
Lateral displacement of front (a) and back (b) flanges after repair cycle 3 of A7-Beam 2

Figure 8.24
Fracture of the material at the buckled location of the front flange of A7-Beam 2

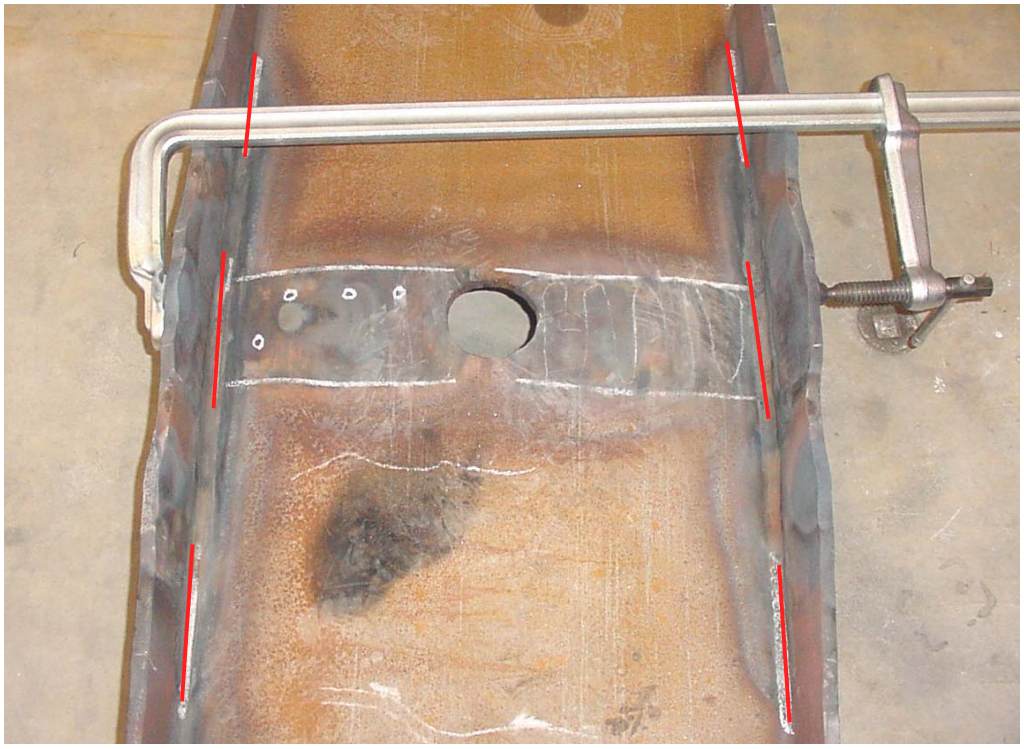

Figure 8.25
Location of line heats applied to straighten flanges (A7-Beam 2)

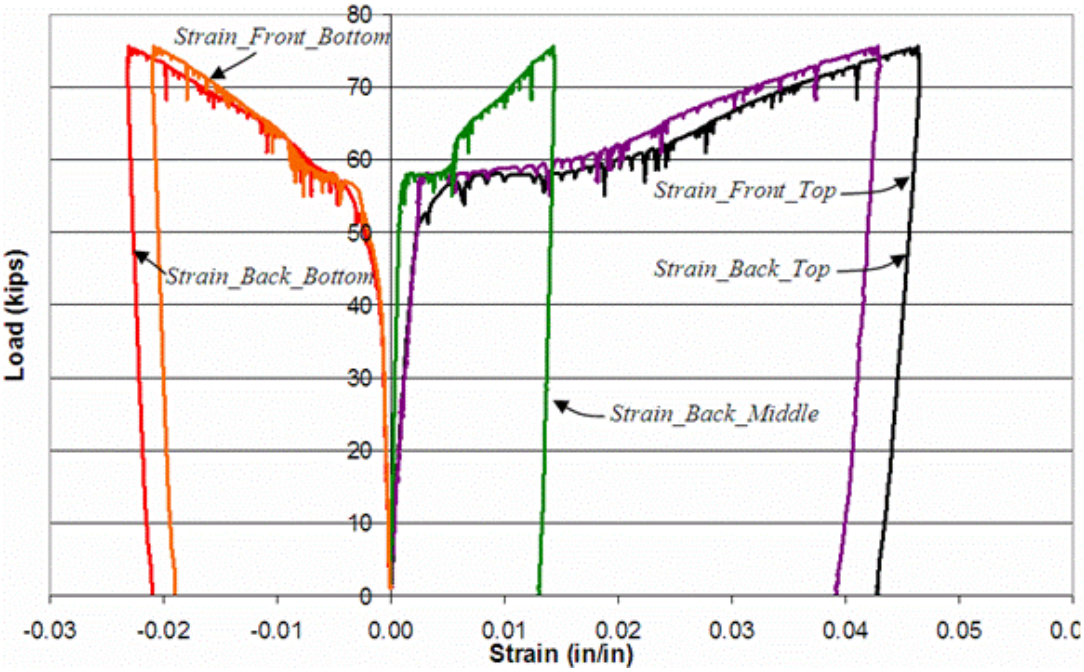

Figure 8.26
Strain gage data during the first damage cycle of A36-Beam 1

(a)

(b)

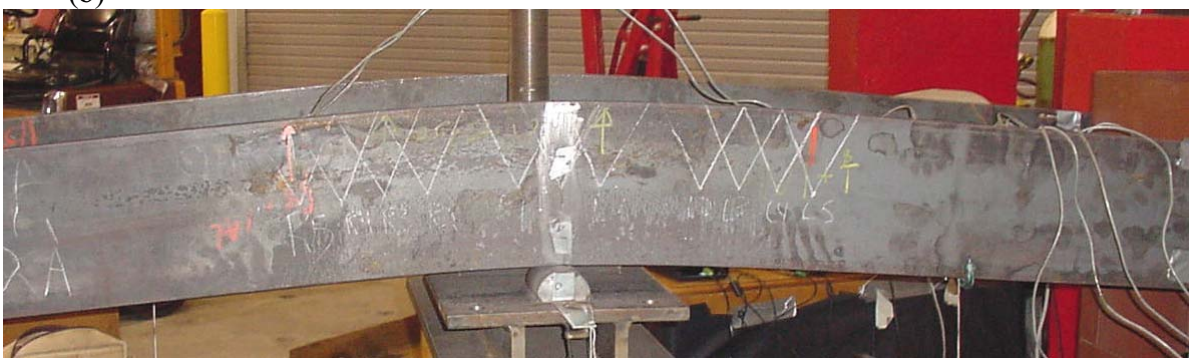

Figure 8.27
Before (a) and after (b) photographs of the first damage cycle of A36-Beam 1

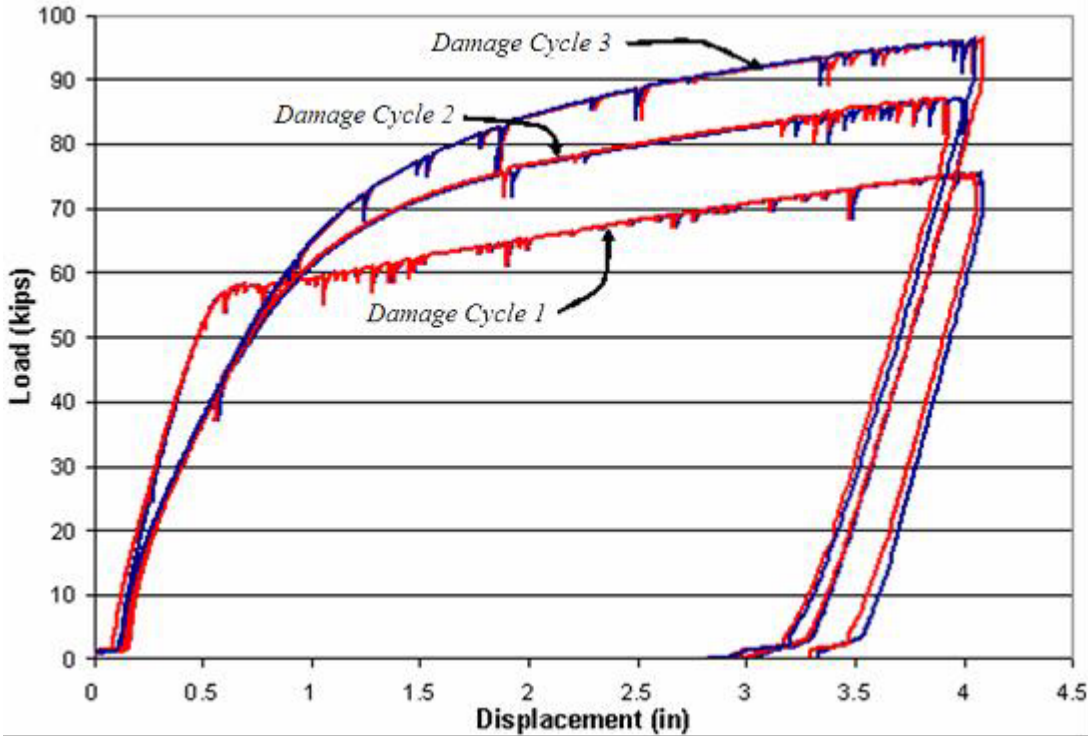

Figure 8.28
Load-displacement behaviors of all three damage cycles of A36-Beam 1

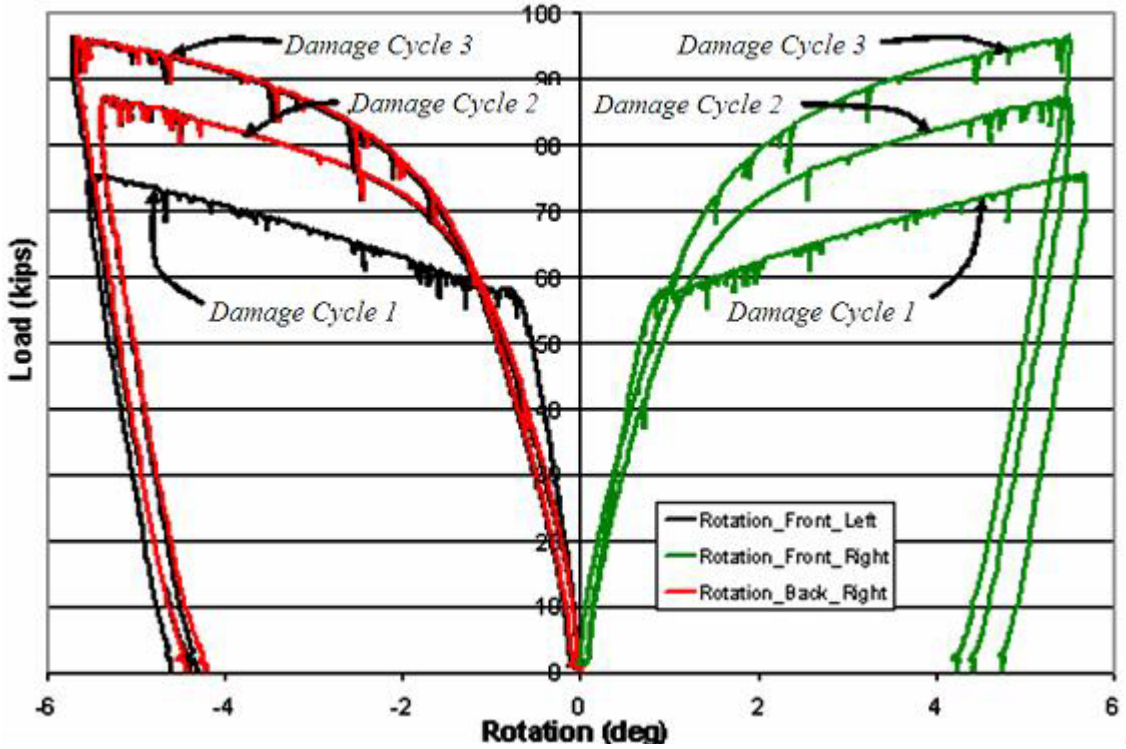

Figure 8.29
Load-rotation behaviors of all three damage cycles of A36-Beam 1

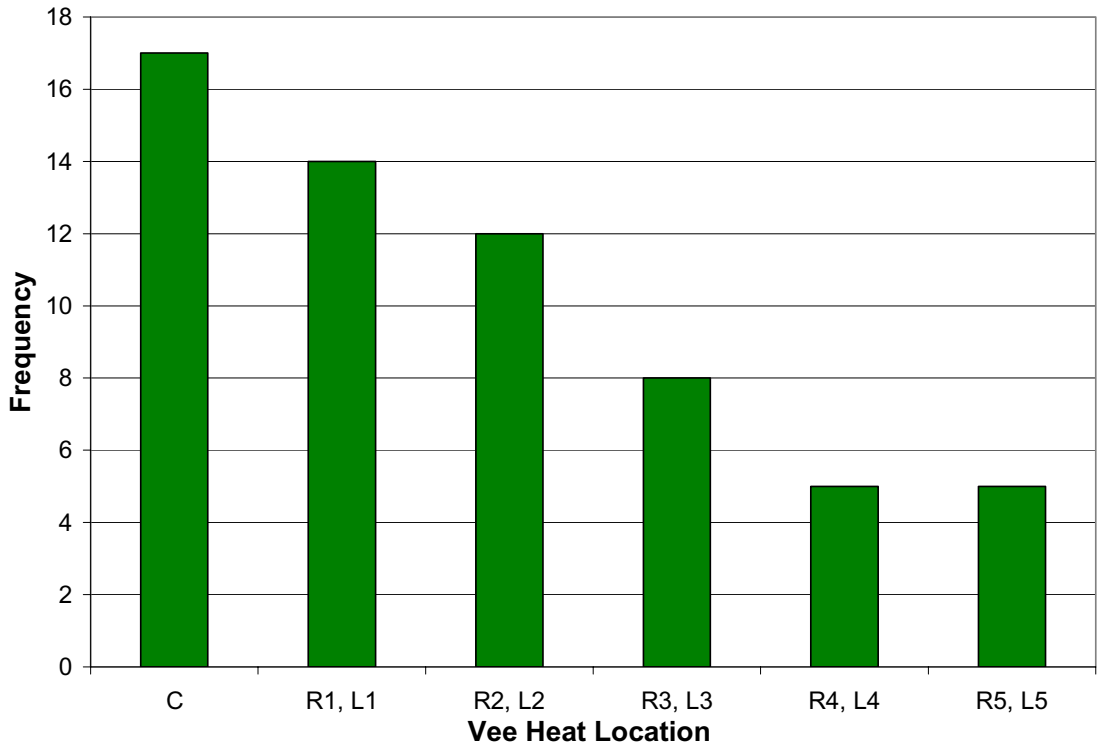

Figure 8.30
Frequency chart of each Vee heat location during three repairs of A36-Beam 1

Figure 8.31
Frontal view of A36-Beam 1 after experimental investigations

Figure 8.32
Lateral displacement of A36-Beam 1 after experimental investigations

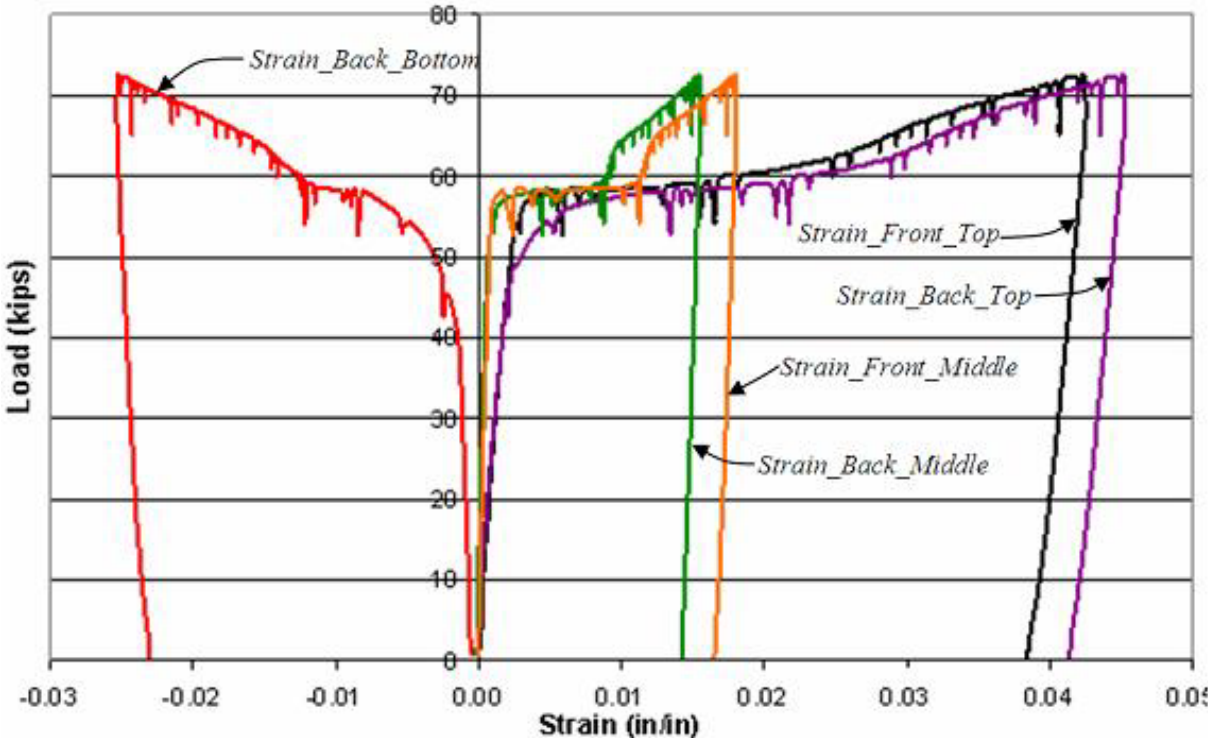

Figure 8.33
Strain gage data during the first damage cycle of A36-Beam 2

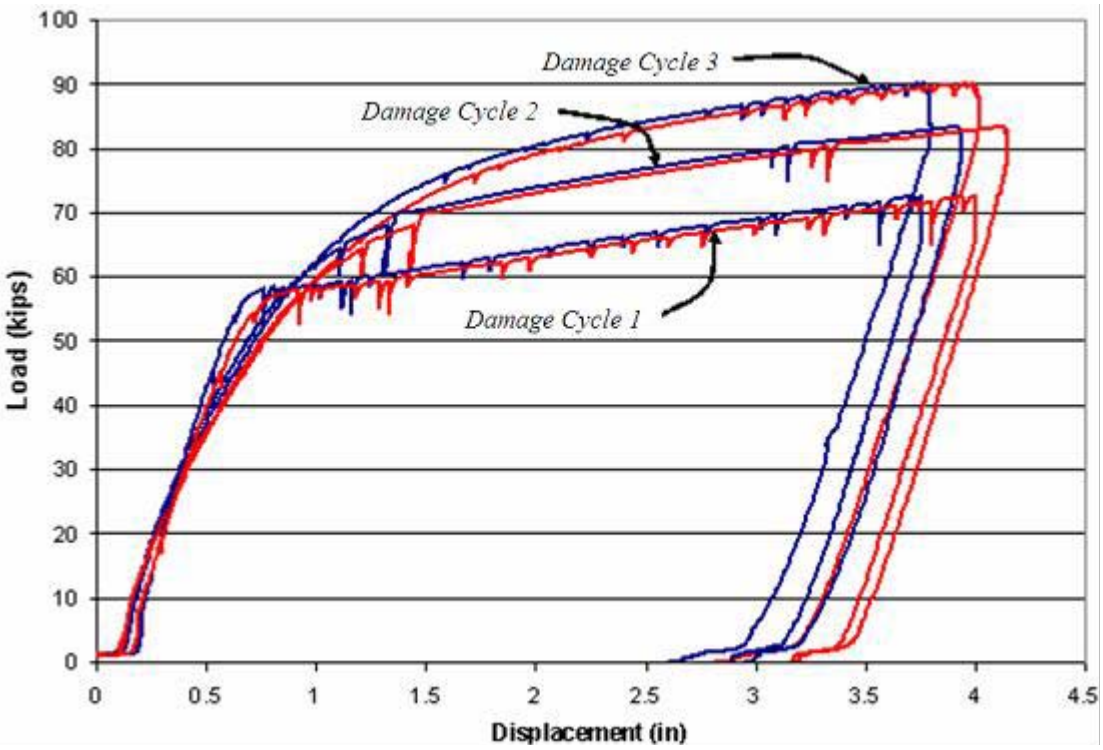

Figure 8.34
Load-displacement behaviors of all three damage cycles of A36-Beam 2

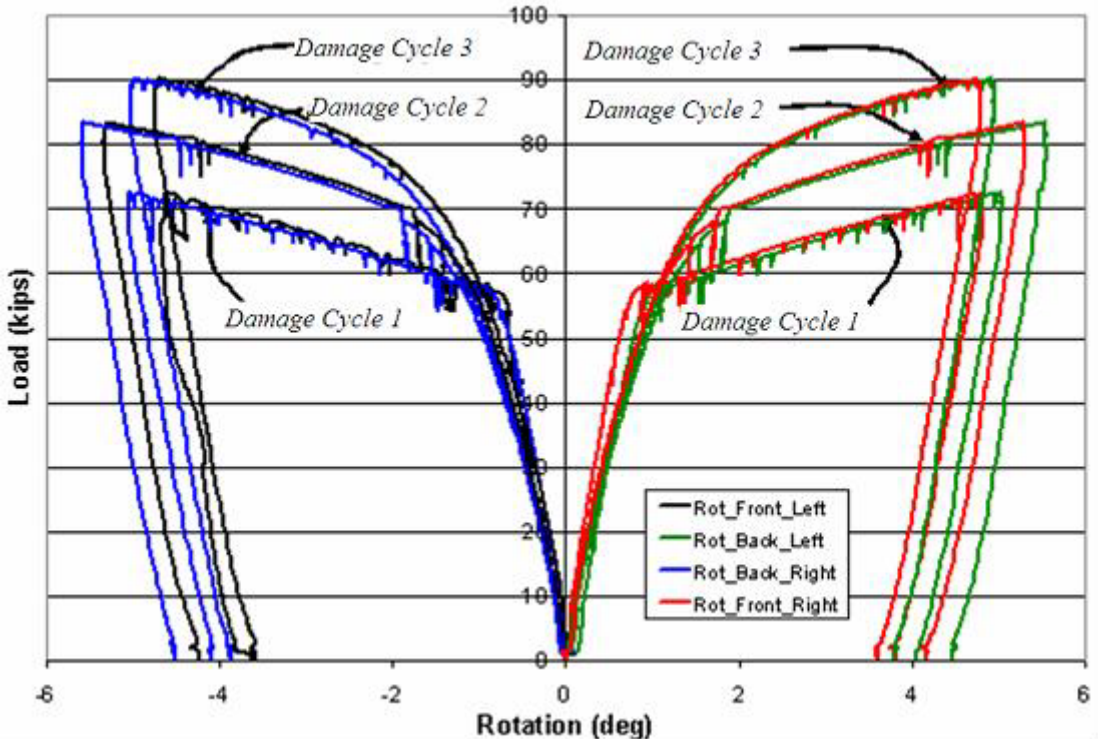

Figure 8.35
Load-rotation behaviors of all three damage cycles on A36-Beam 2

a) 1400 °F (A36-Beam 2)

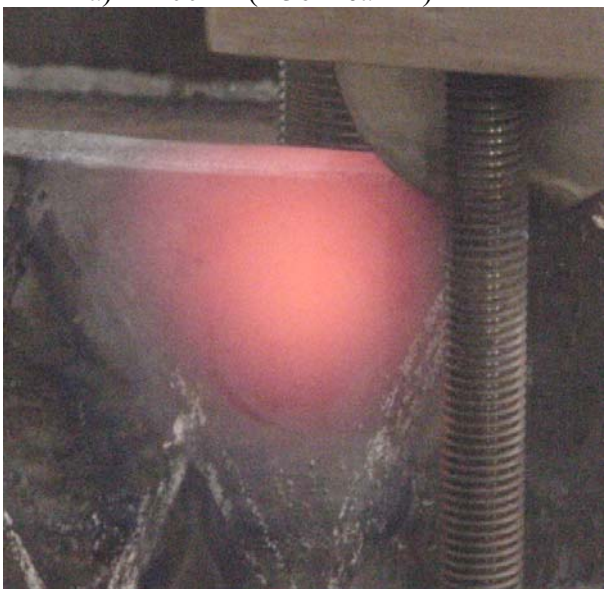

b) 1200 °F (A36-Beam 1)

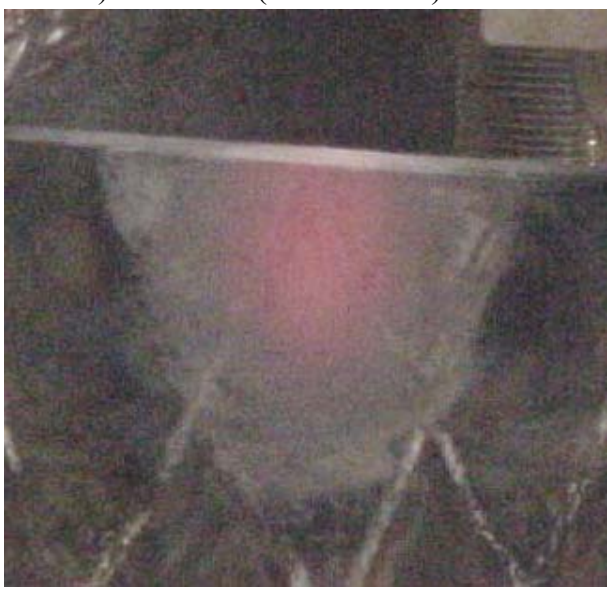

Figure 8.36
Color of A36 steel at maximum heating temperatures

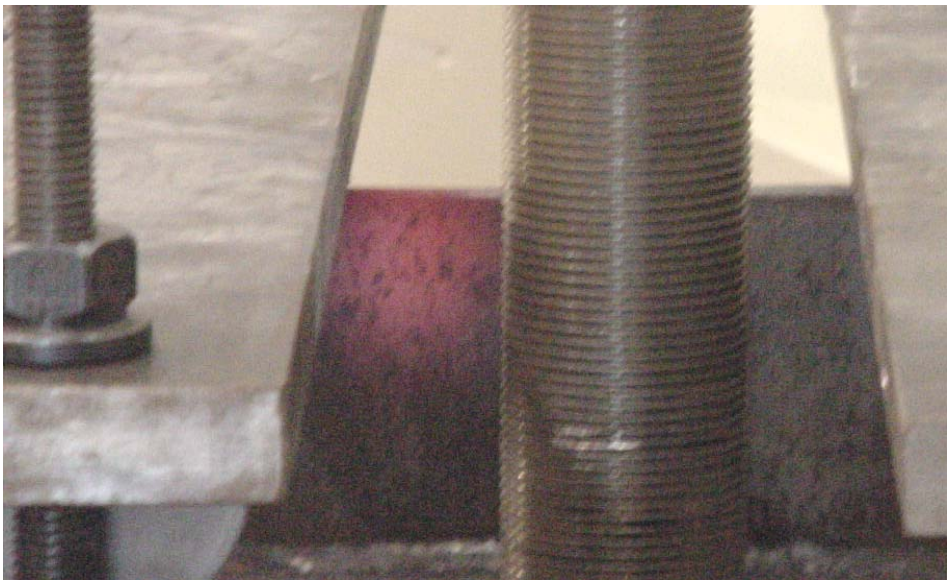

Figure 8.37
Opposite side of Vee heated to a maximum temperature of 1400 °F

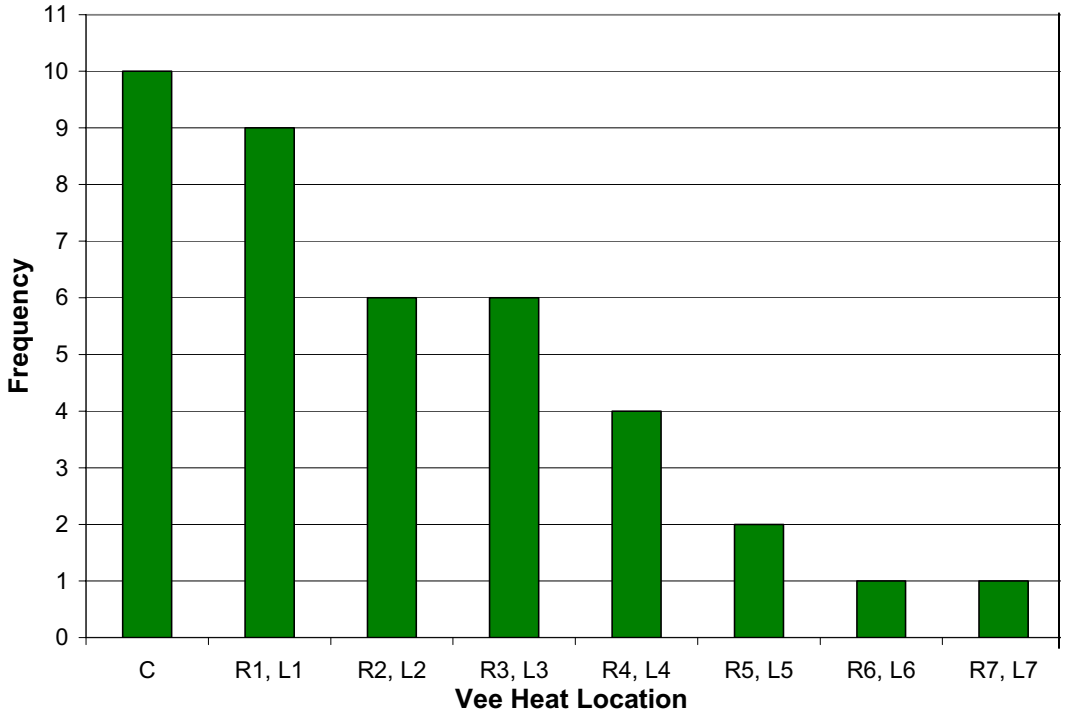

Figure 8.38
Frequency chart of each Vee heat location during three repairs of A36-Beam 2

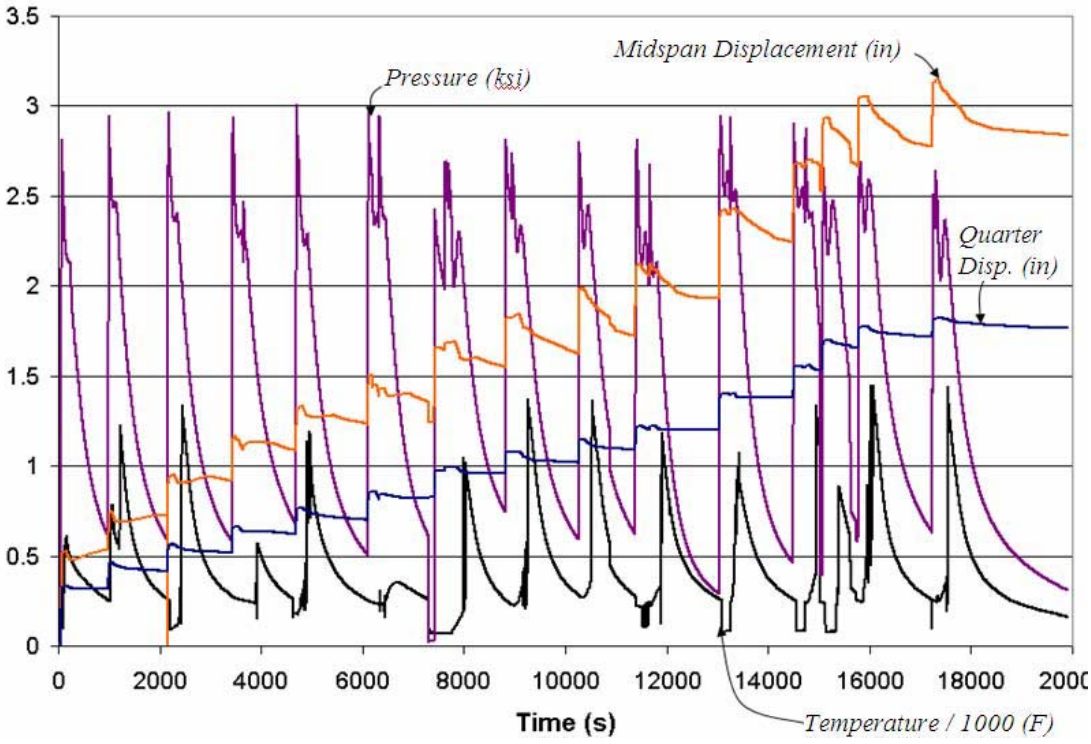

Figure 8.39
Instrument data during the second repair cycle of A36-Beam 2

Figure 8.40
Front view of A36-Beam 2 after experimental investigations

Figure 8.41
Lateral displacement of A36-Beam 2 after experimental investigations

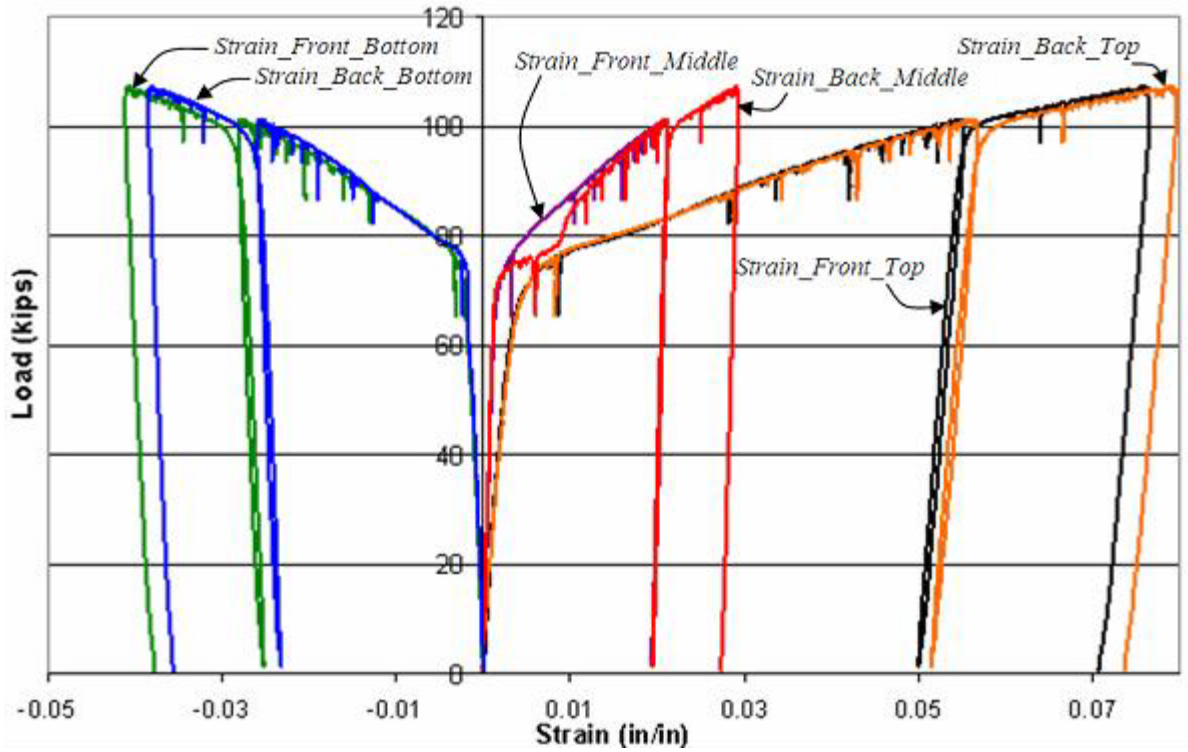

Figure 8.42
Strain gage data during the first damage cycle of A588-Beam 1

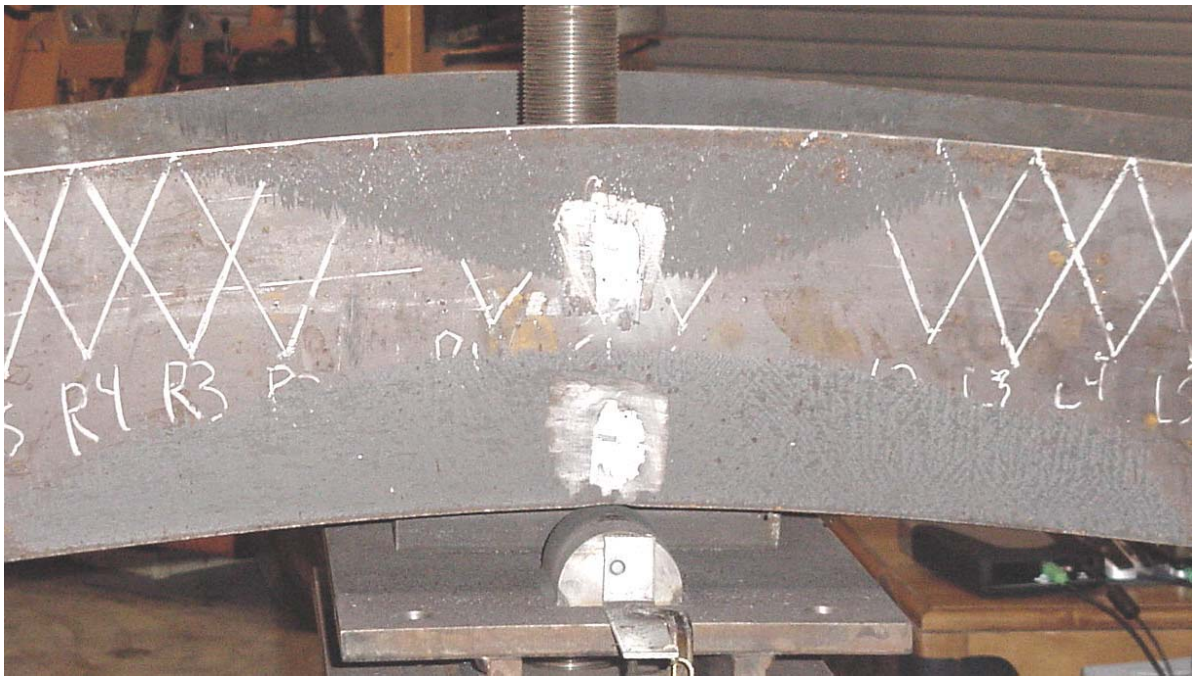

Figure 8.43
Spread of yielding after the first damage cycle of A588-Beam 1

(a)

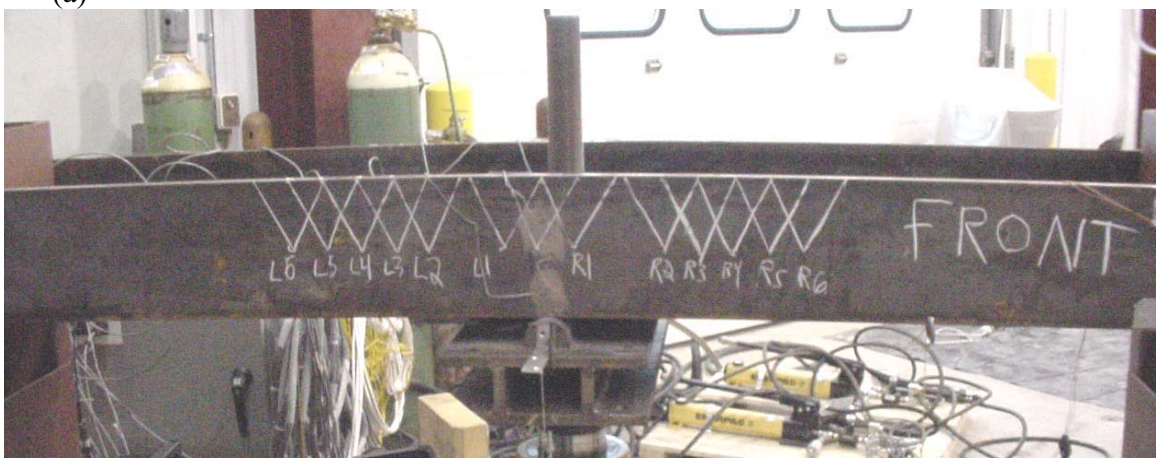

(b)

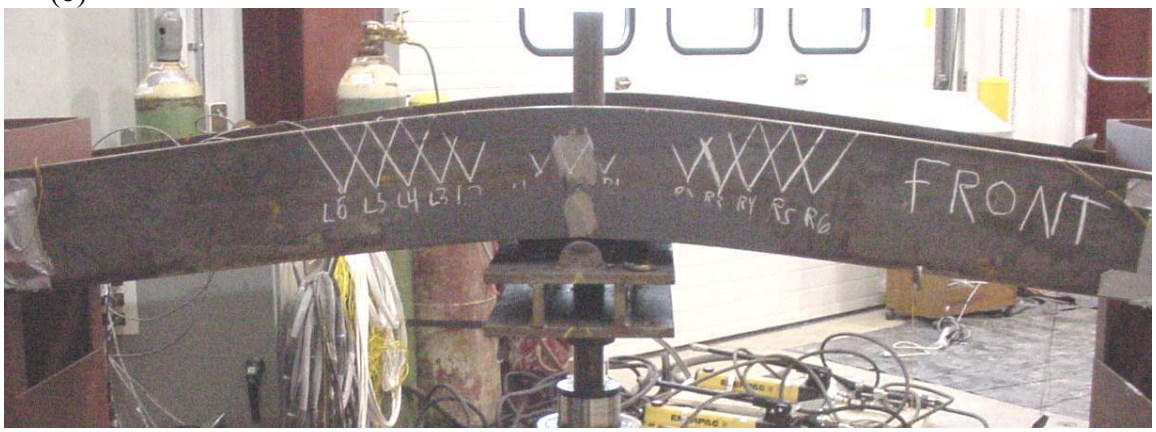

Figure 8.44
Before (a) and after (b) photographs of the first damage cycle of A588-Beam 1

Figure 8.45
Photograph of A588-Beam1 after the third damage cycle

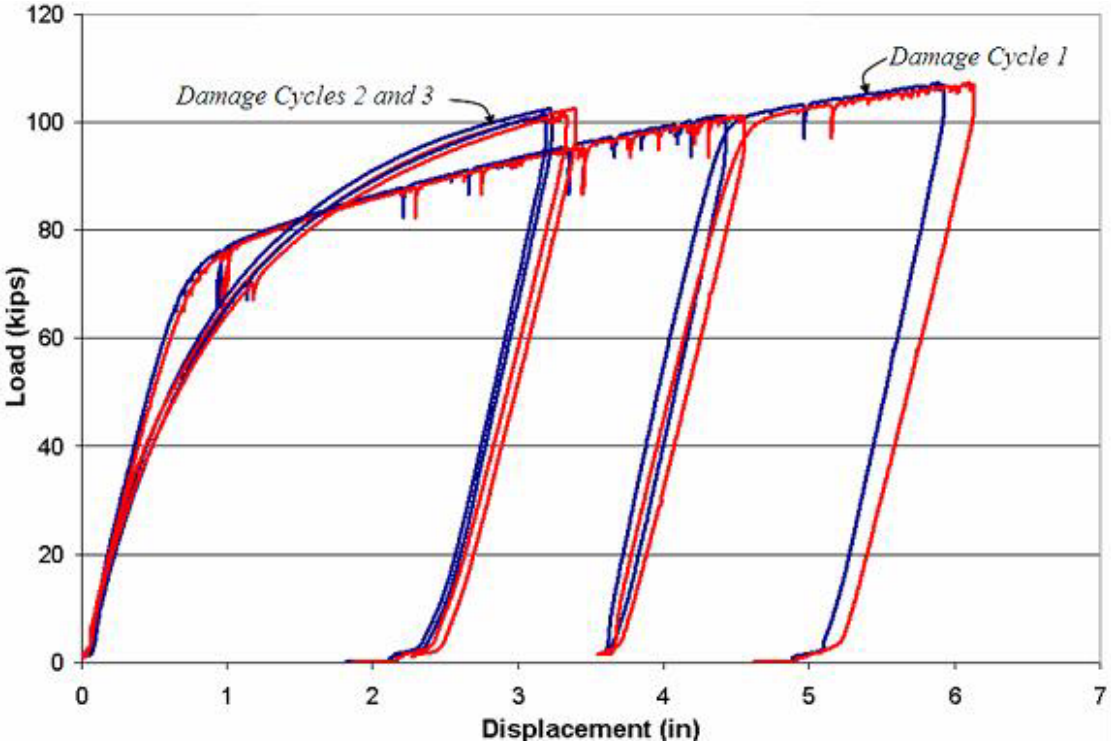

Figure 8.46
Load-displacement behaviors of all three damage cycles of A588-Beam 1

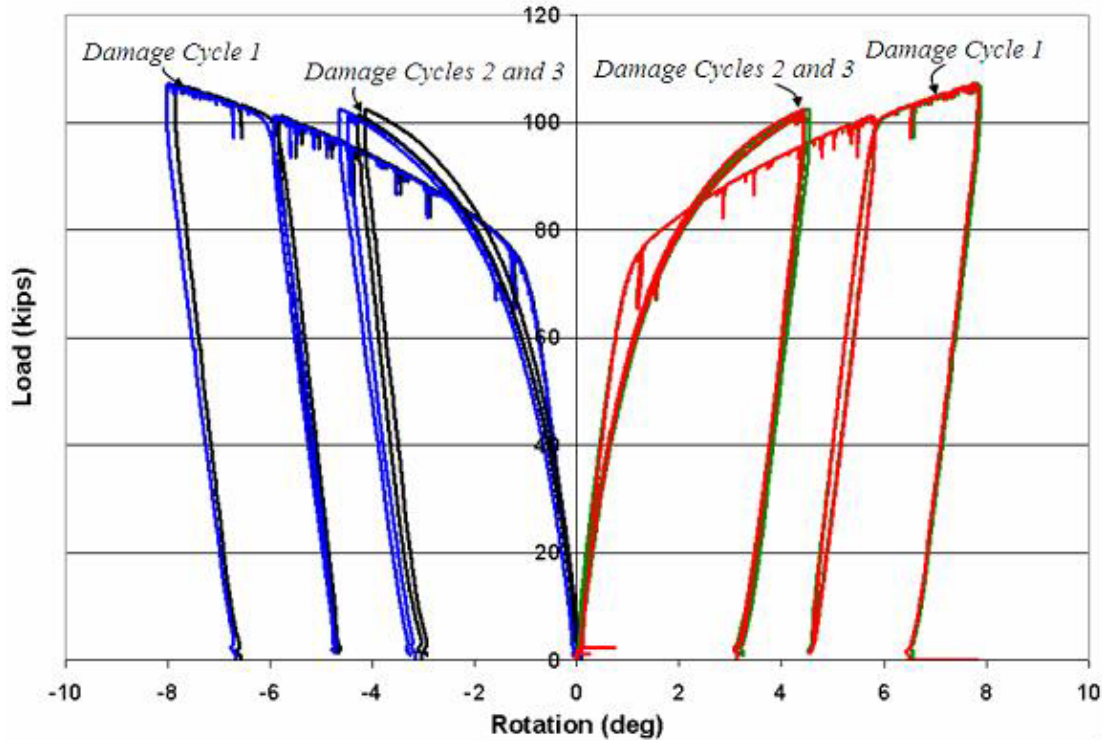

Figure 8.47
Load-rotation behaviors of all three damage cycles of A588-Beam 1

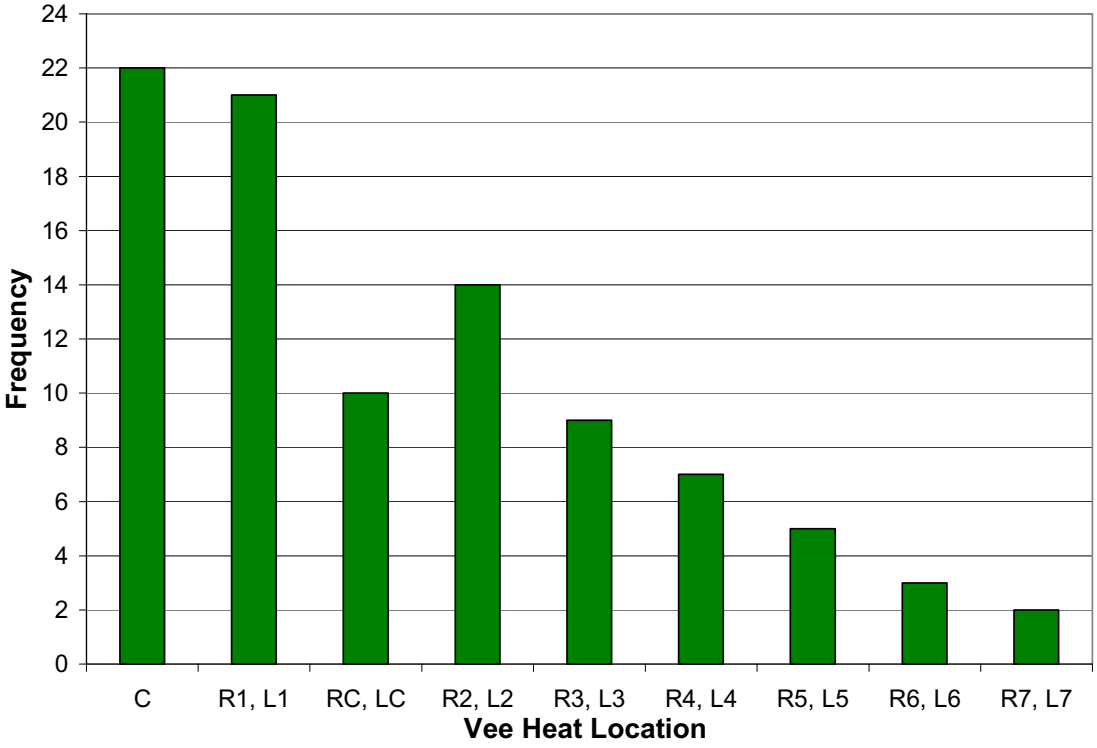

Figure 8.48
Frequency chart of each Vee heat location during three repairs of A588-Beam 1

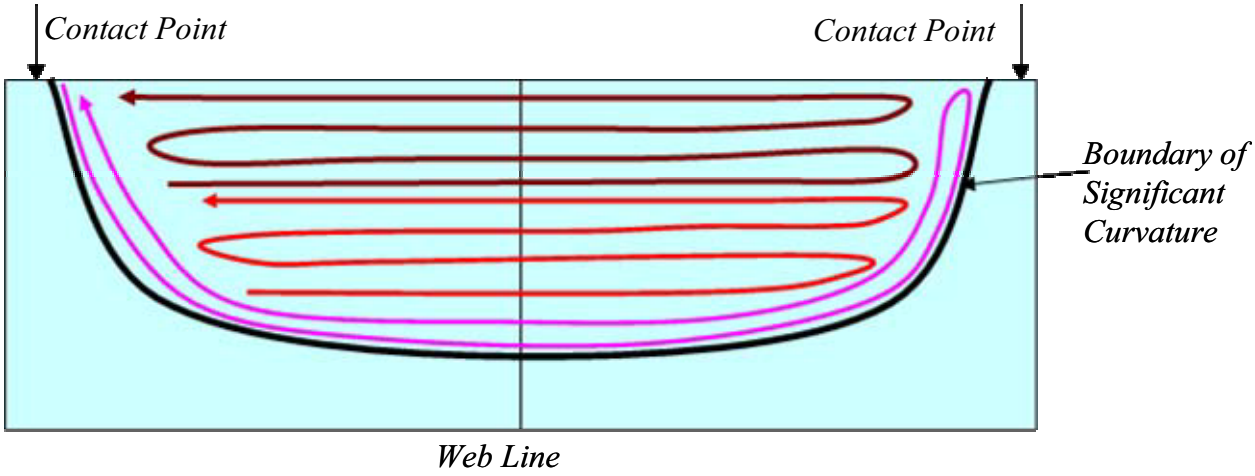

Figure 8.49
Heating patterns used on the inside of flanges to reduce curvature of A588 beams

Figure 8.50
Front view of A588-Beam 1 after experimental investigations

a)

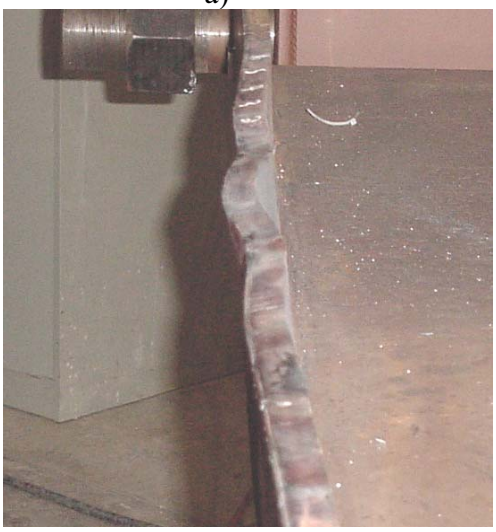

b)

c)

d)

Figure 8.51
Lateral displacement of A588-Beam 1 before (a and b) and after (c and d) straightening

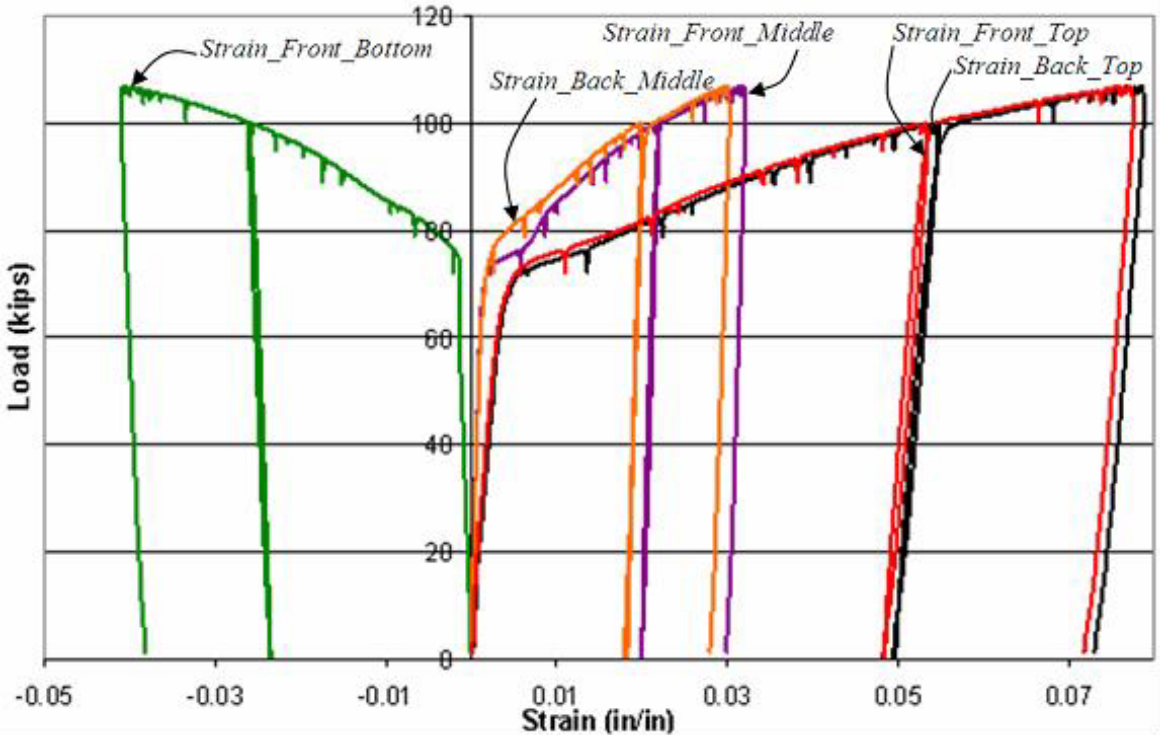

Figure 8.52
Strain gage data during the first damage cycle of A588-Beam 2

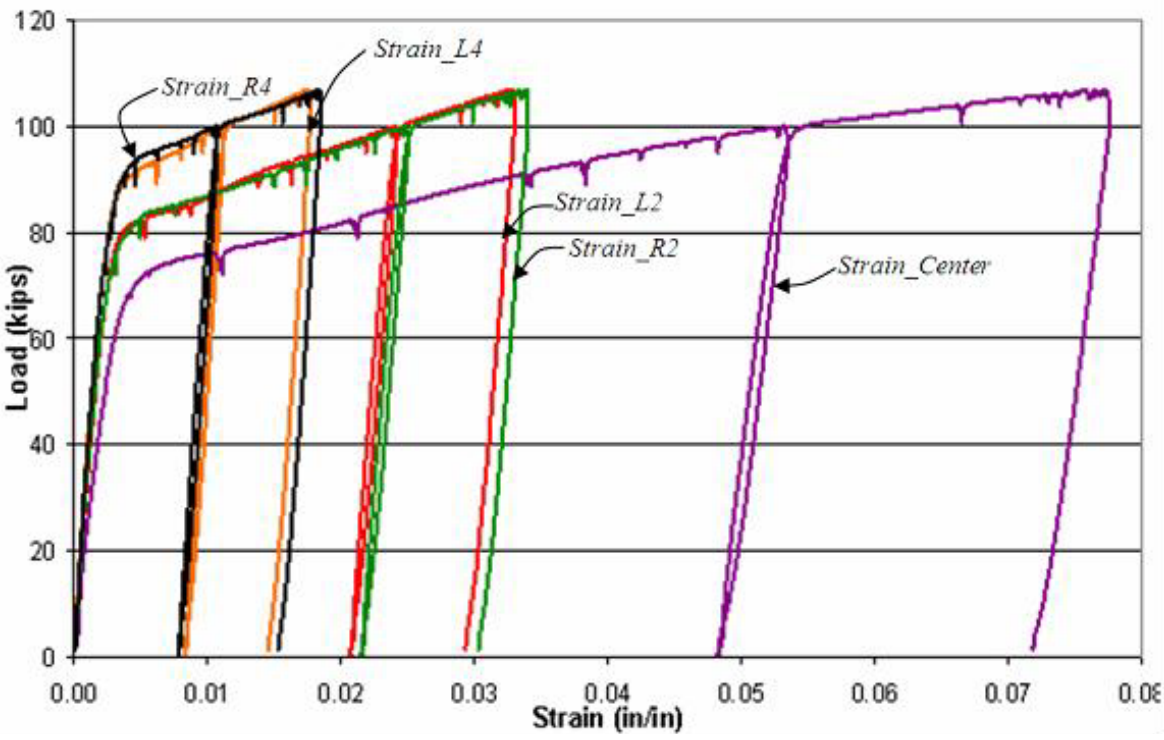

Figure 8.53
Strain gage data at various Vee heat locations during the first damage cycle of A588-Beam 2

Figure 8.54
Load-displacement behaviors of all three damage cycles of A588-Beam 1

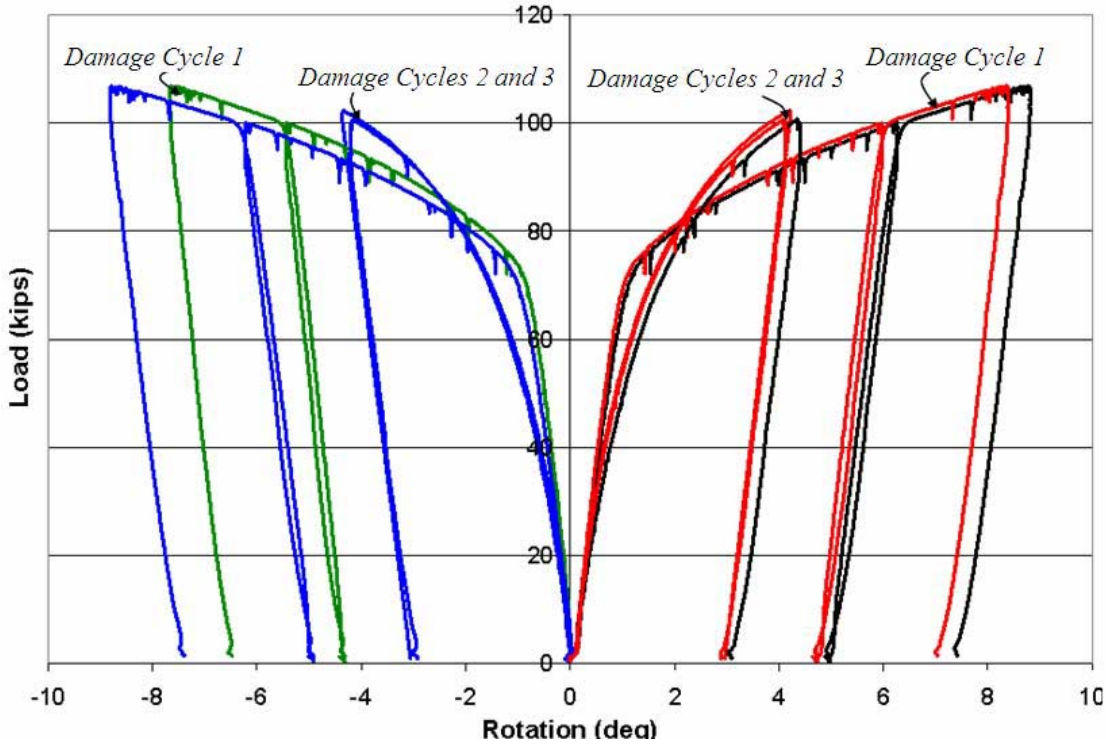

Figure 8.55
Load-displacement behaviors of all three damage cycles of A588-Beam 1

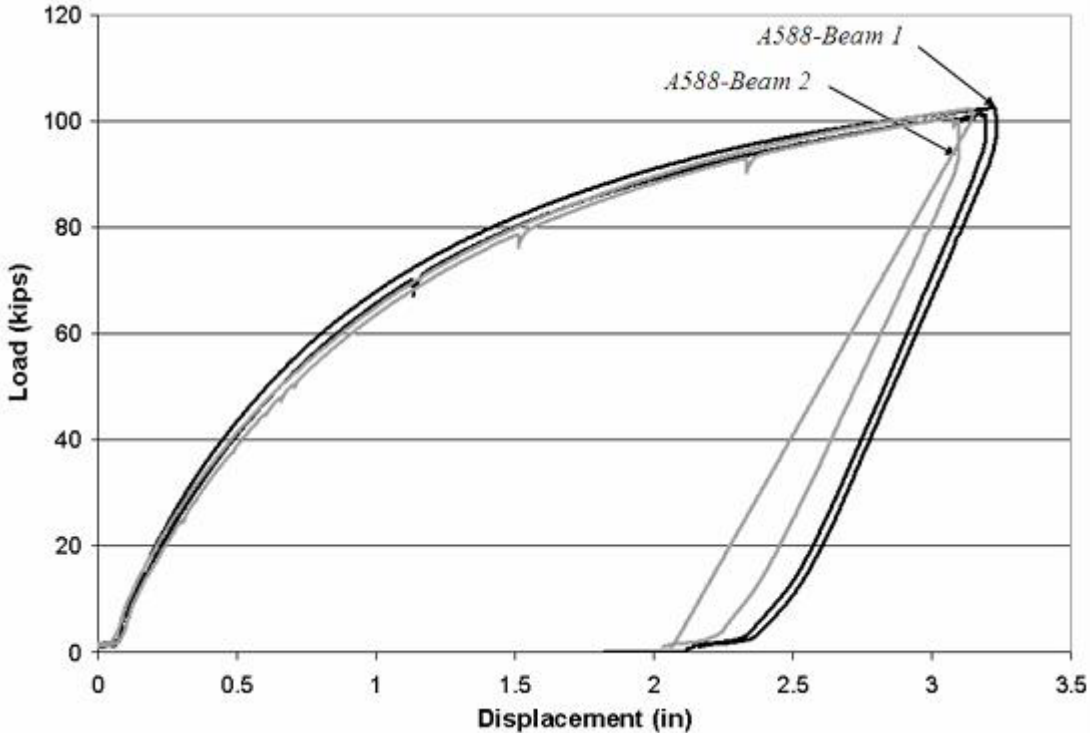

Figure 8.56
Comparison of midspan load-displacement behaviors of A588-Beam 1 and A588-Beam 2 during their respected second and third damage cycles

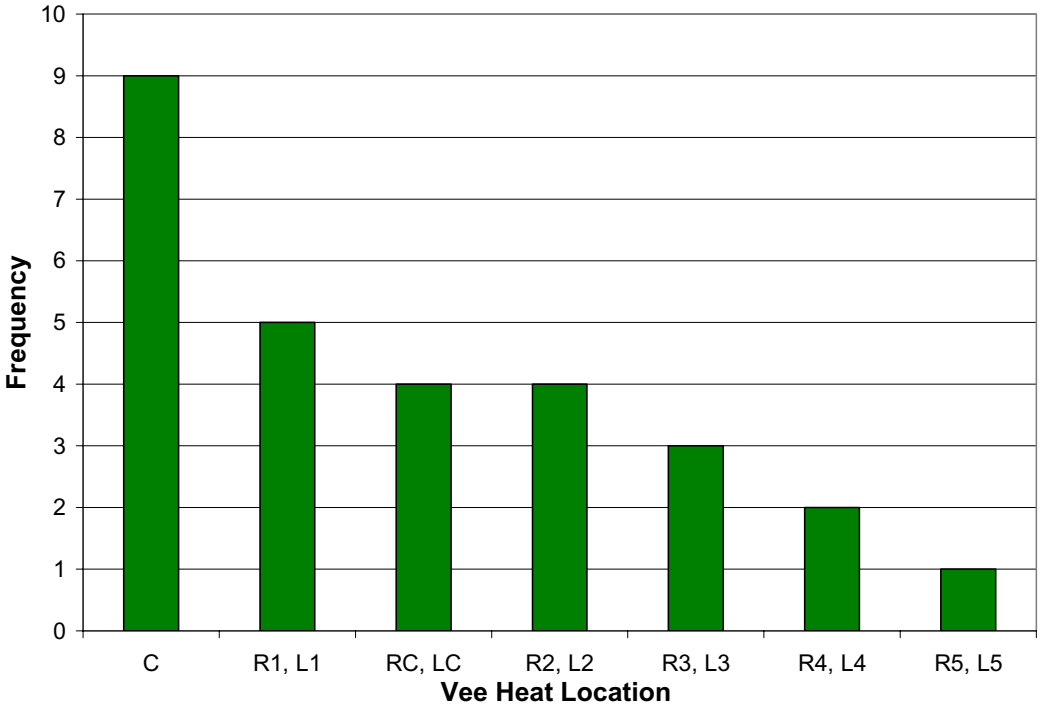

Figure 8.57
Frequency chart of each Vee heat location during three repairs of A588-Beam 2

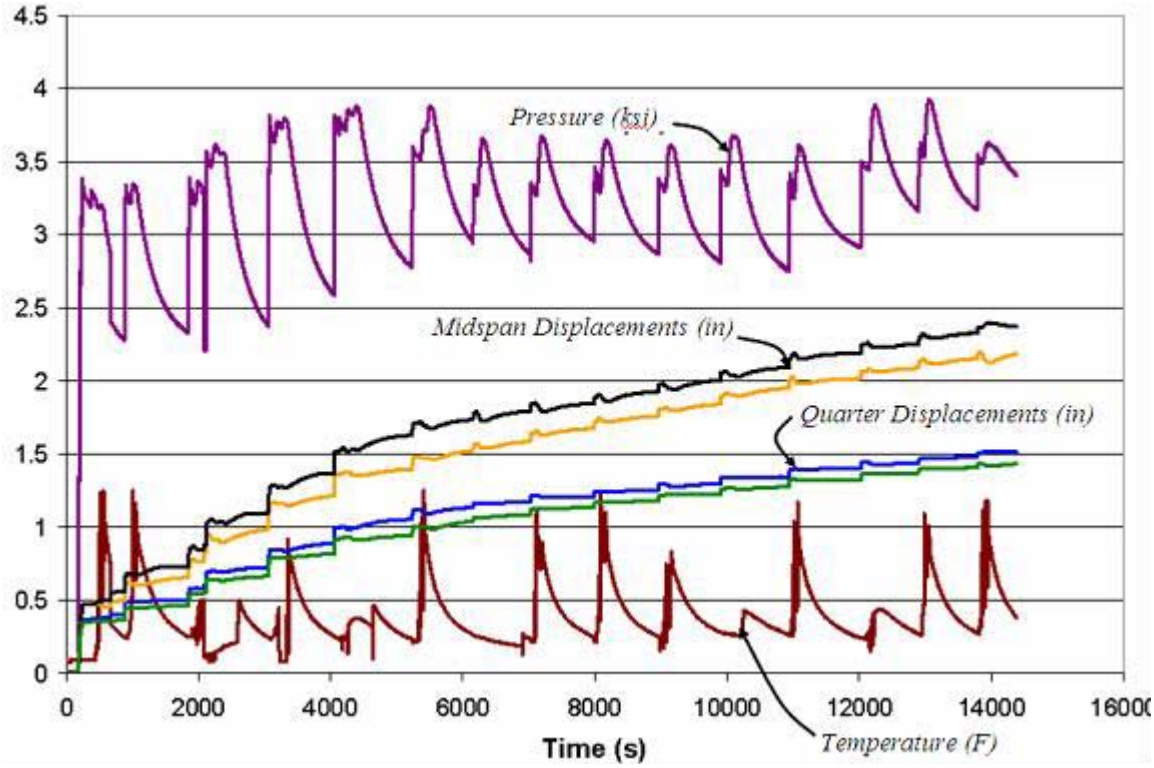

Figure 8.58
Instrument data during the second repair cycle of A588-Beam 2

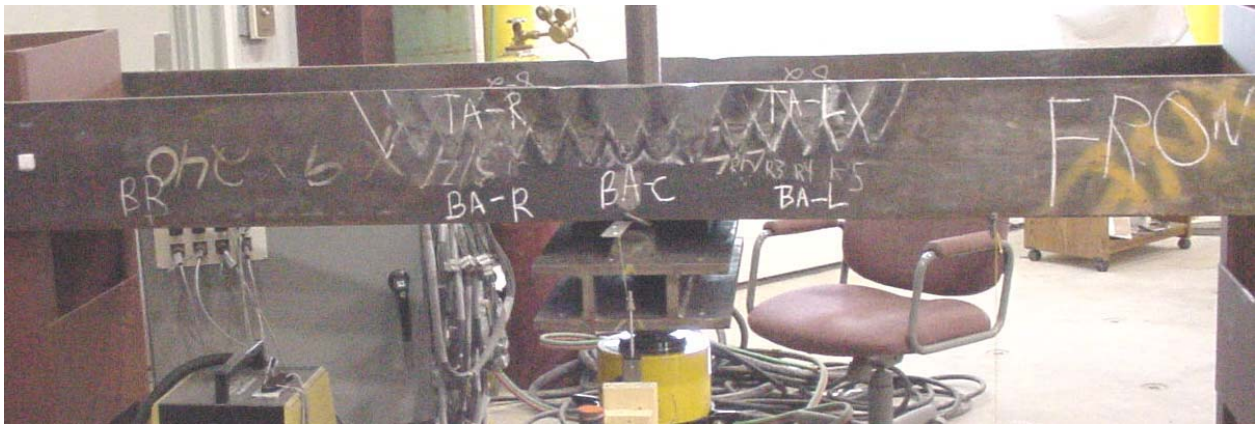

Figure 8.59
Front view of A588-Beam 2 after three damage-repair cycles

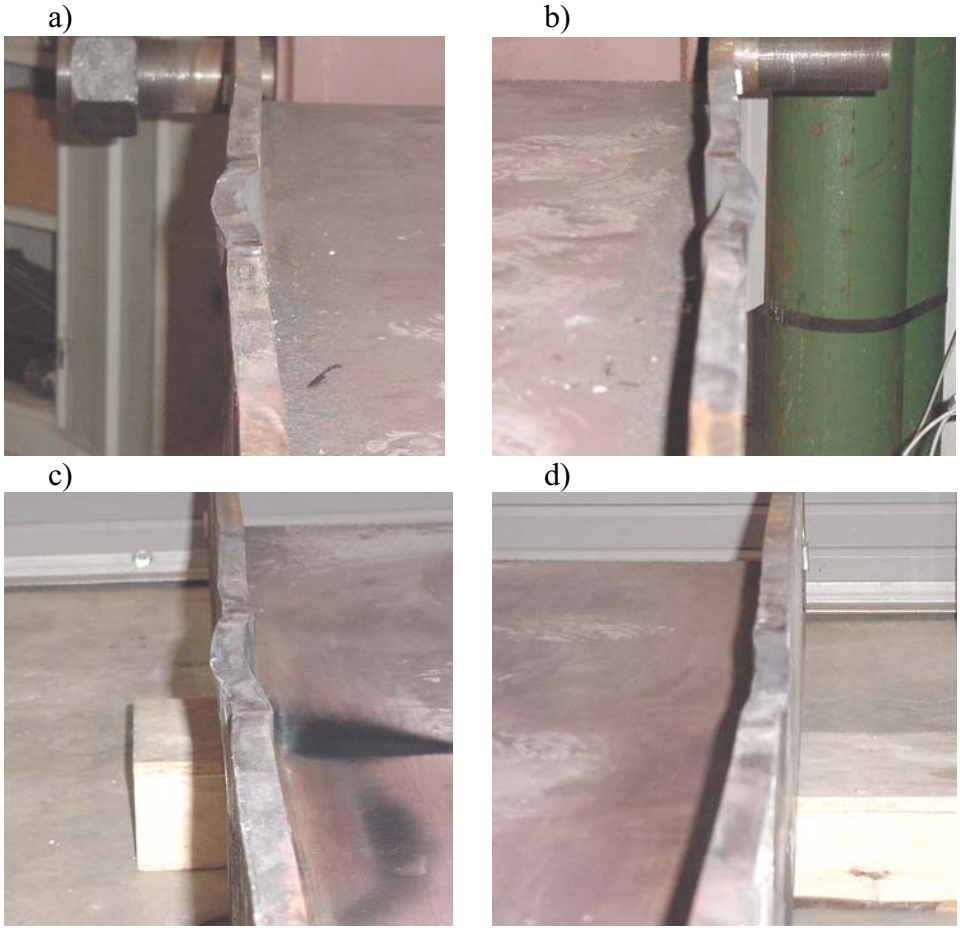

Figure 8.60
Lateral displacement of A588-Beam 2 before (a and b) and after (c and d) straightening

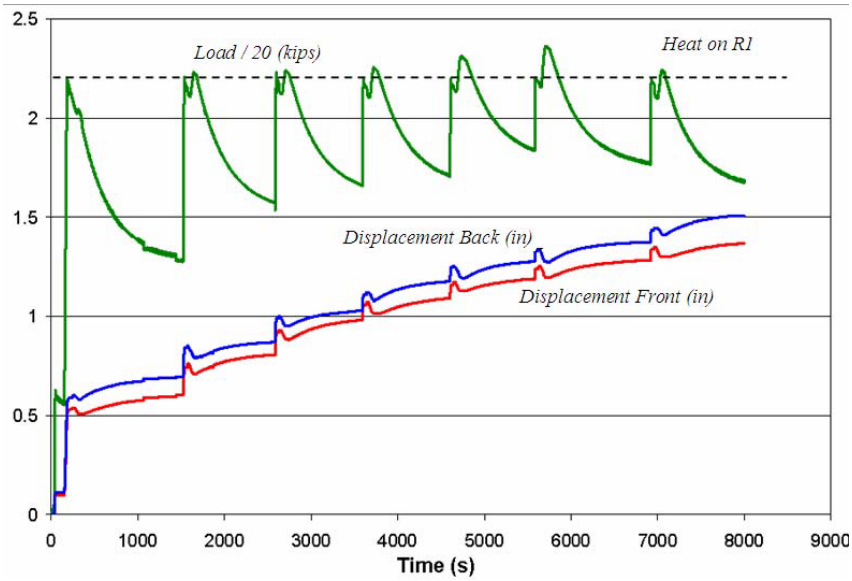

Figure 8.61
Load and displacement data during the first six heating cycles of A7-Beam 1

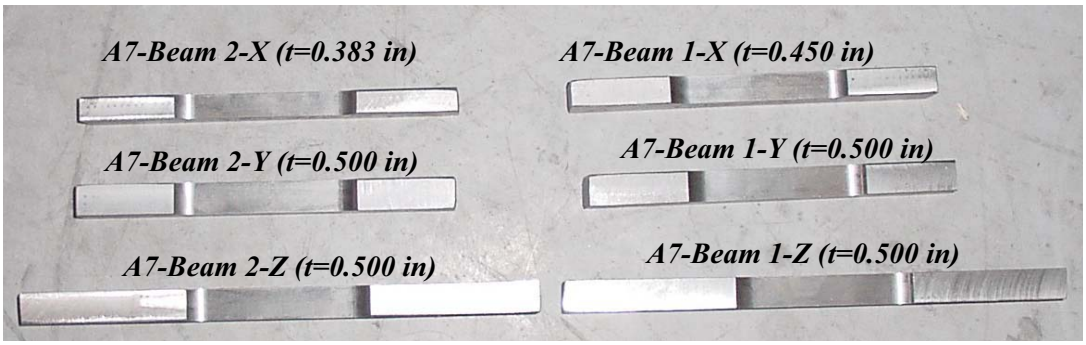

Figure 8.62
Uniaxial tension coupons fabricated from A7 beam specimens

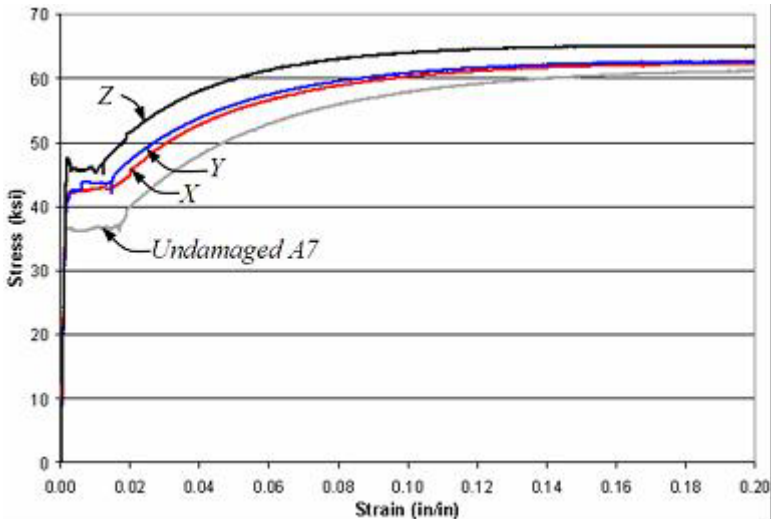

Figure 8.63
Stress-strain behavior of uniaxial tension coupons removed from A7-Beam 1

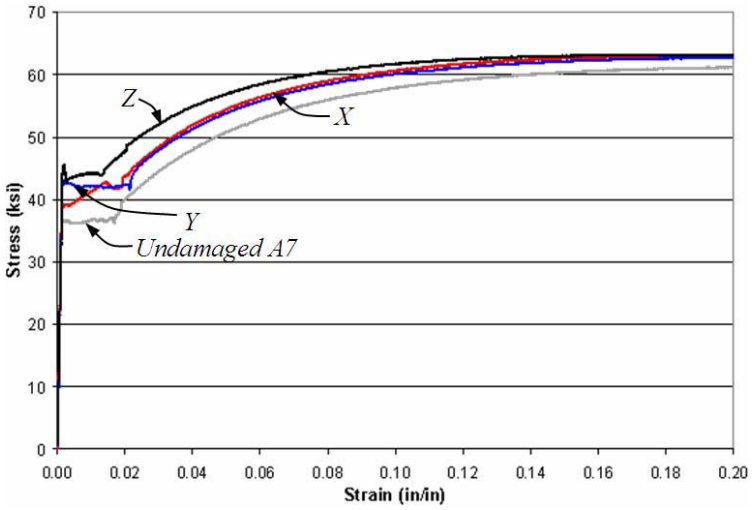

Figure 8.64
Stress-strain behavior of uniaxial tension coupons removed from A7-Beam 2

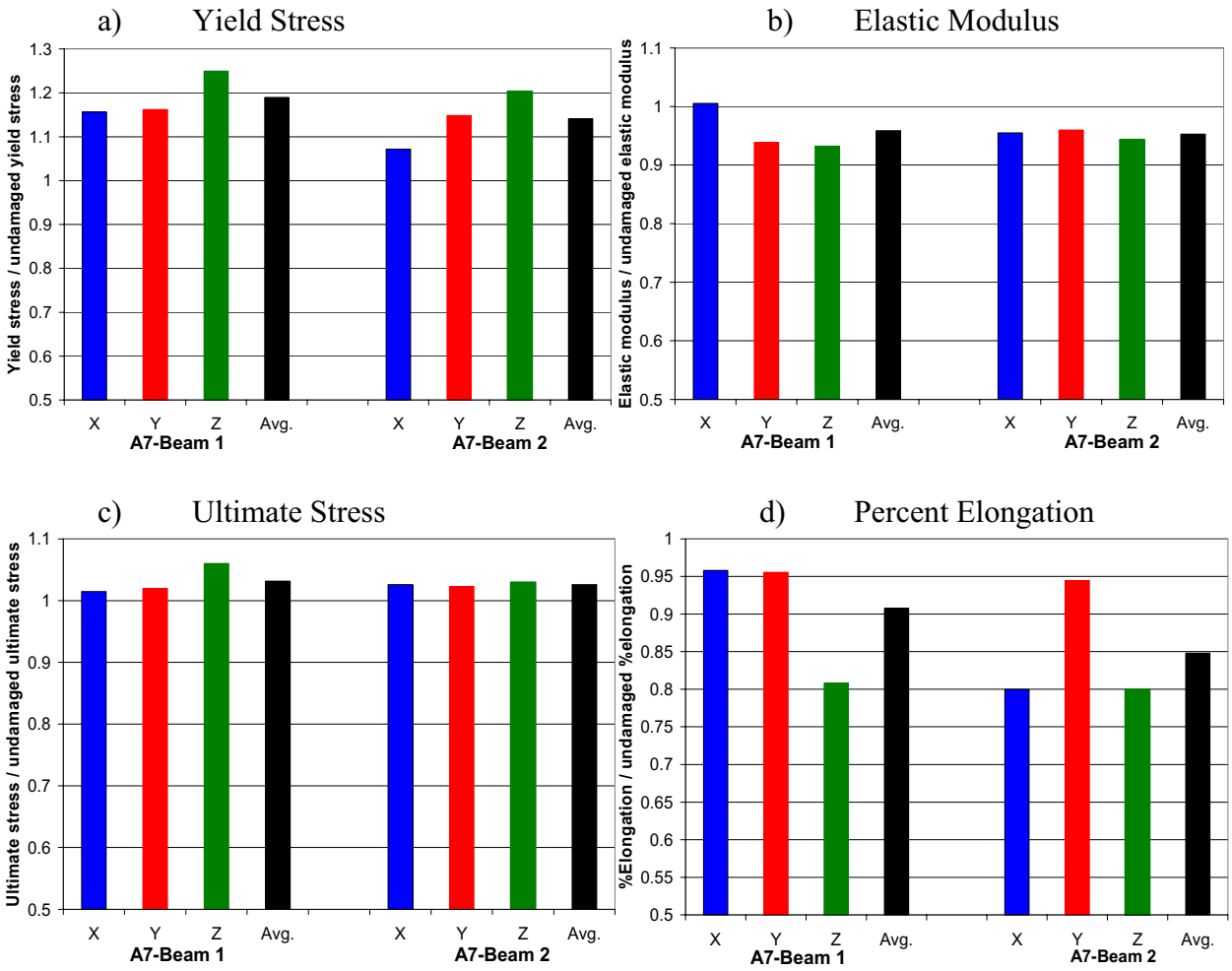

Figure 8.65
Normalized structural properties of damaged-repaired A7 steel

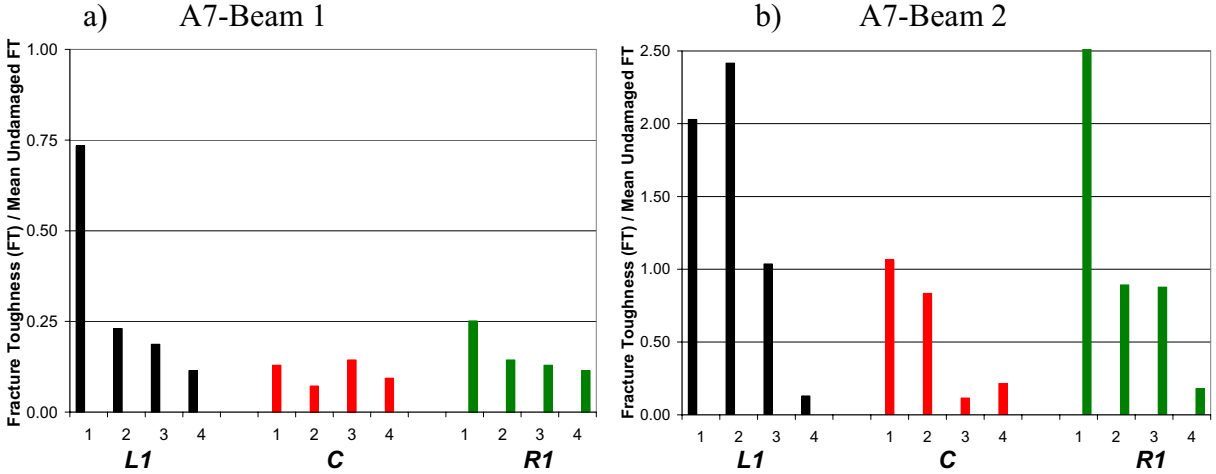

Figure 8.66
Normalized fracture toughness of damaged-repaired A7 steel

a) A7-Beam 1 b) A7-Beam 2

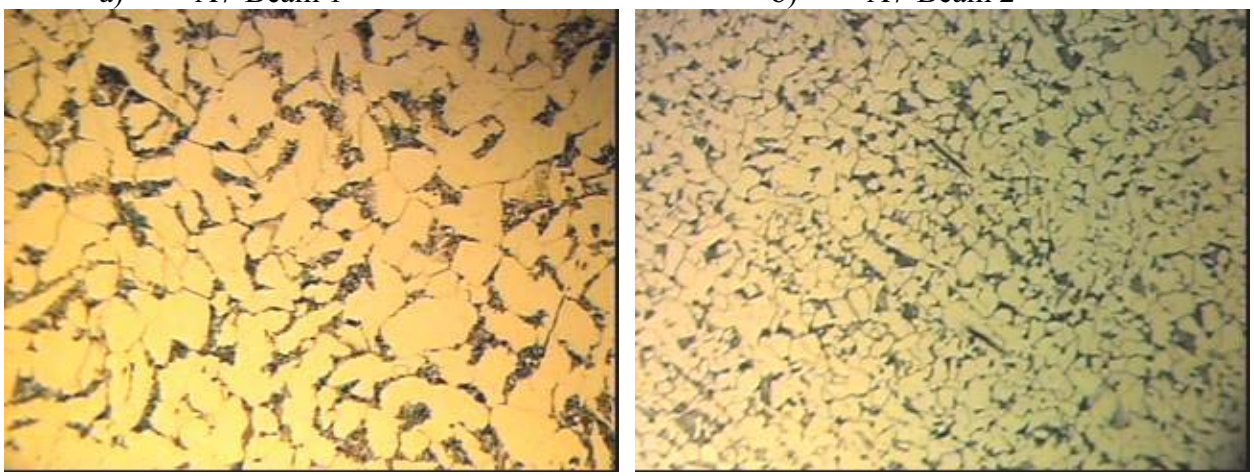

Figure 8.67
Microstructures of the damaged-repaired A7 experimental beam specimens (480X)

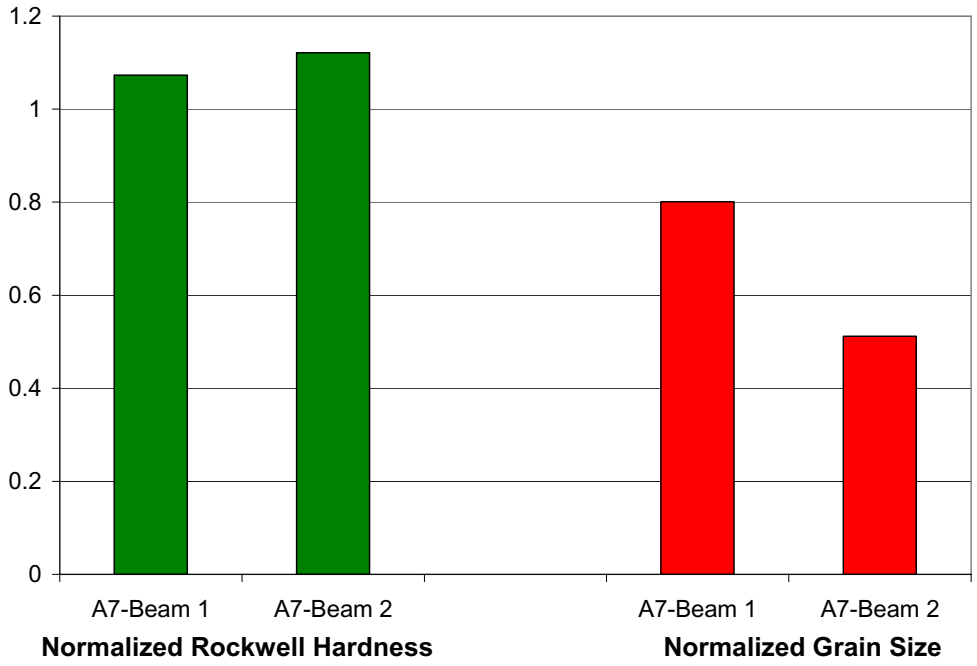

Figure 8.68
Normalized hardness and grain size of damaged-repaired A7 steel

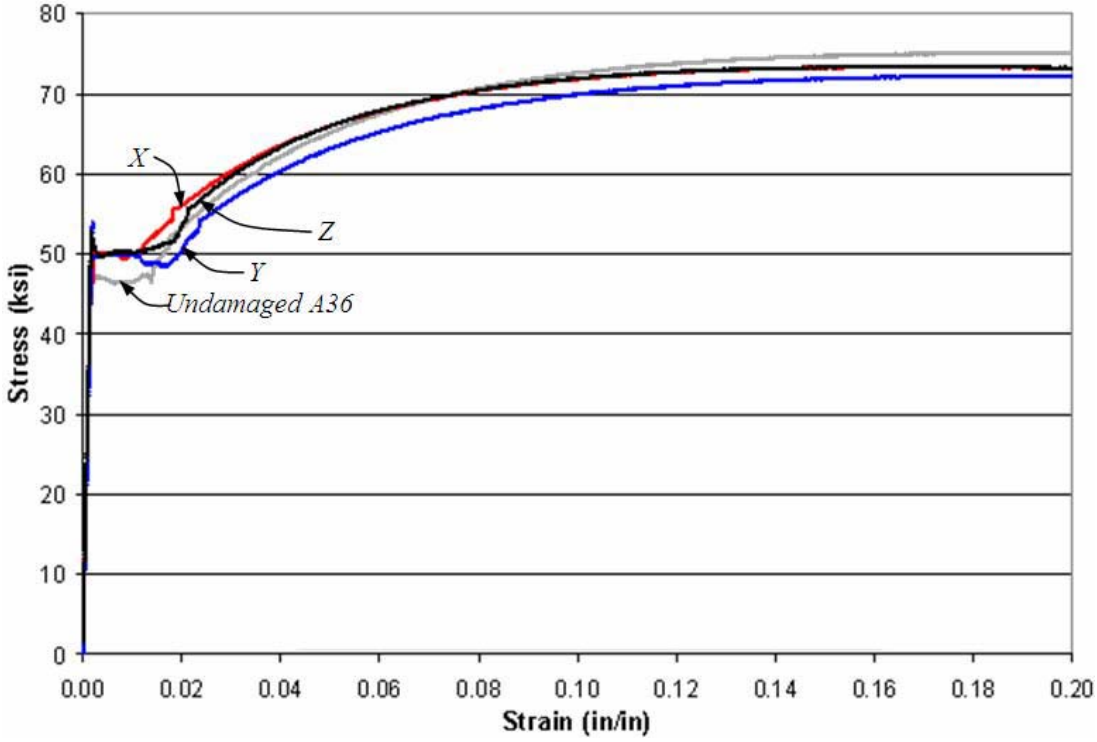

Figure 8.69
Stress-strain behavior of uniaxial tension coupons removed from A36-Beam 1

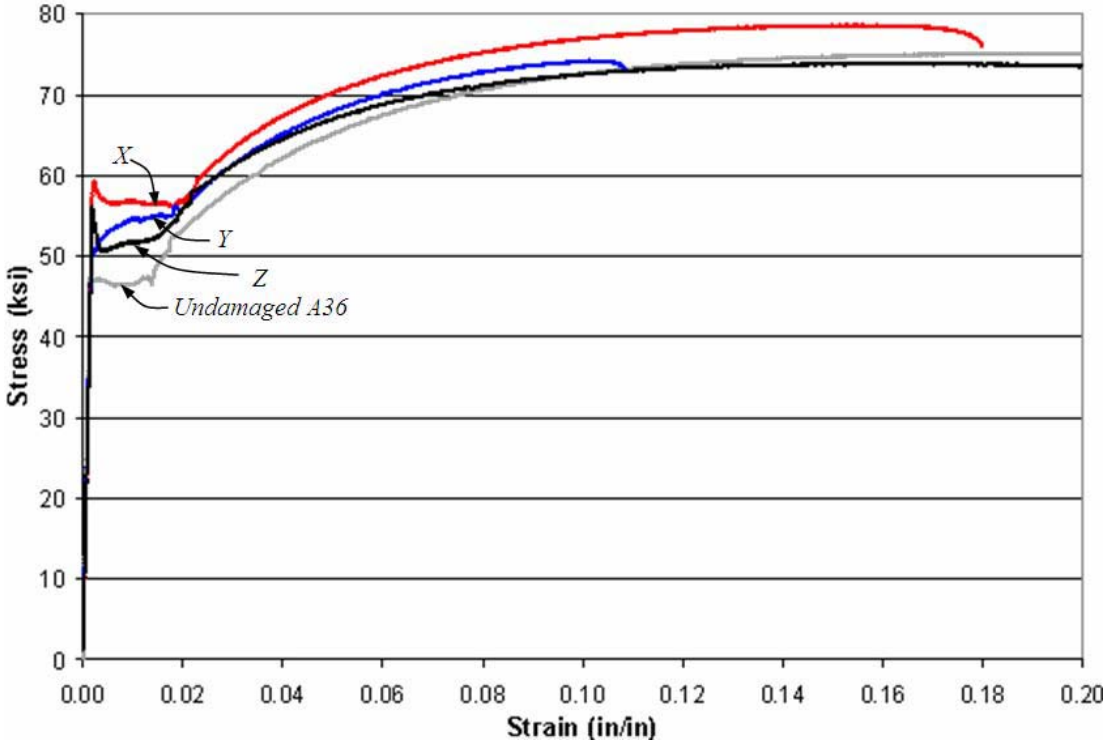

Figure 8.70
Stress-strain behavior of uniaxial tension coupons removed from A36-Beam 2

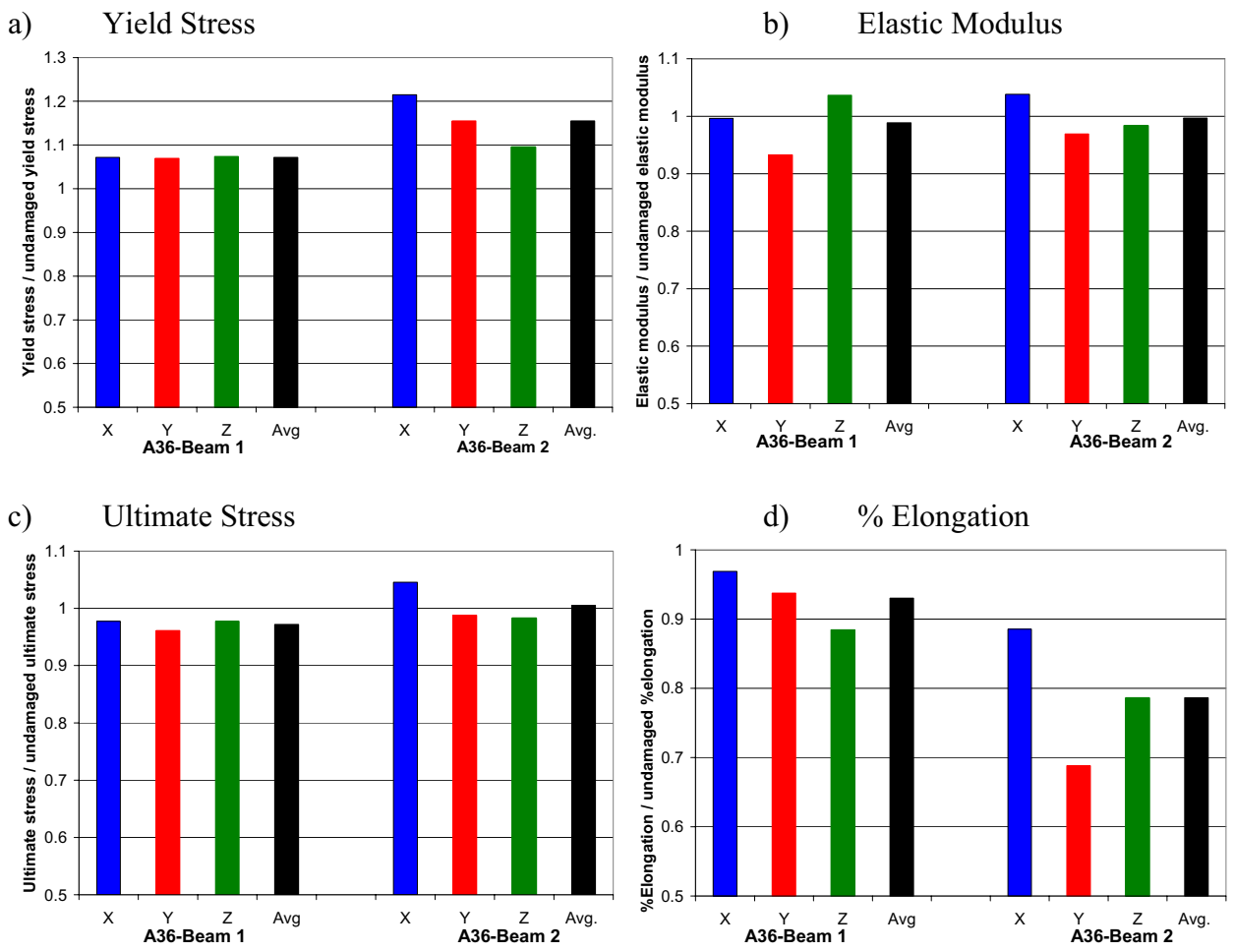

Figure 8.71
Normalized structural properties of damaged-repaired A36 steel

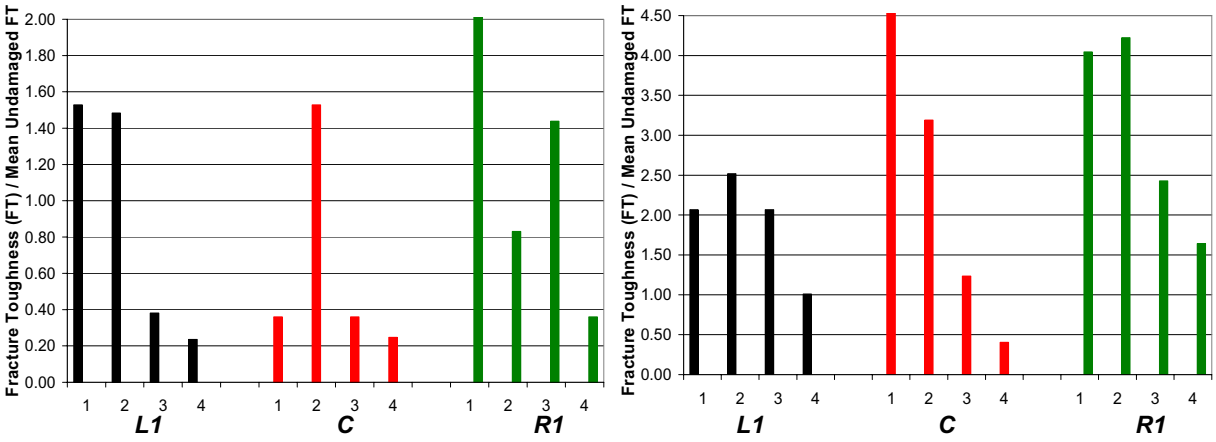

Figure 8.72
Normalized fracture toughness of damaged-repaired A36 steel

a) A36-Beam 1 b) A36-Beam 2

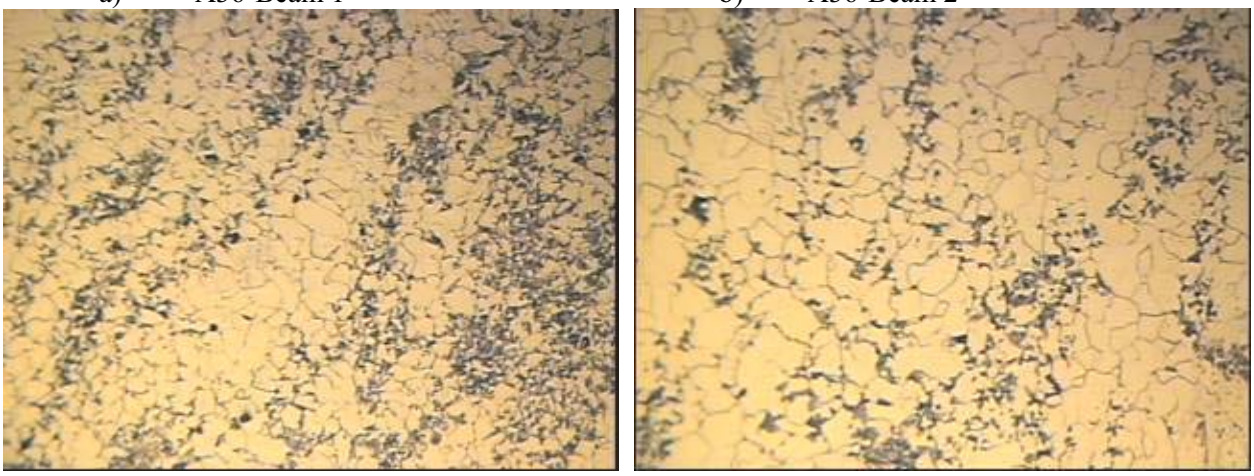

Figure 8.73
Microstructures of the damaged-repaired A36 experimental beam specimens (480X)

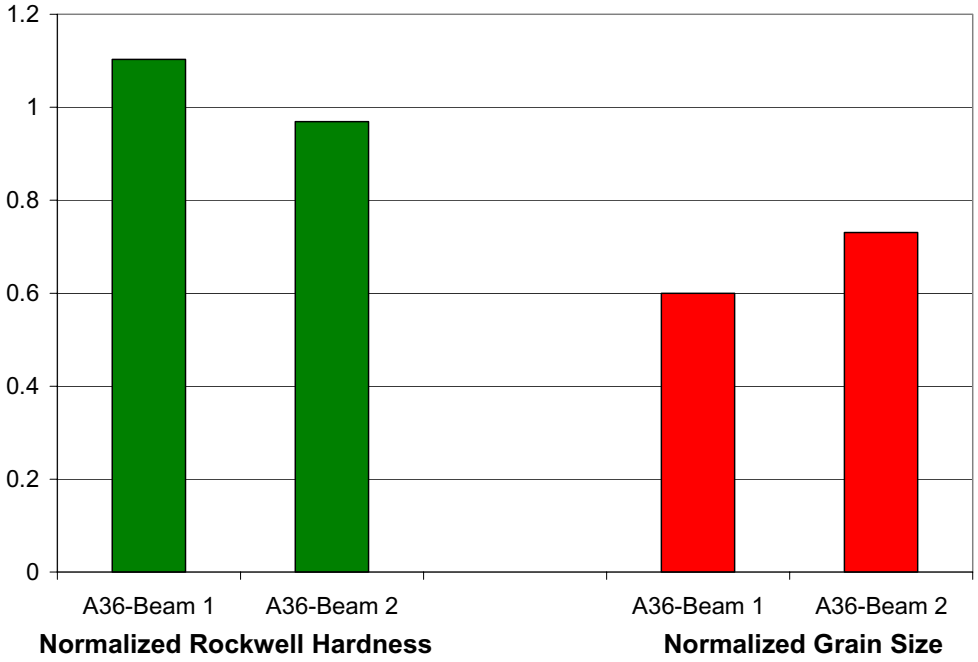

Figure 8.74
Normalized hardness and grain size of damaged-repaired A36 steel

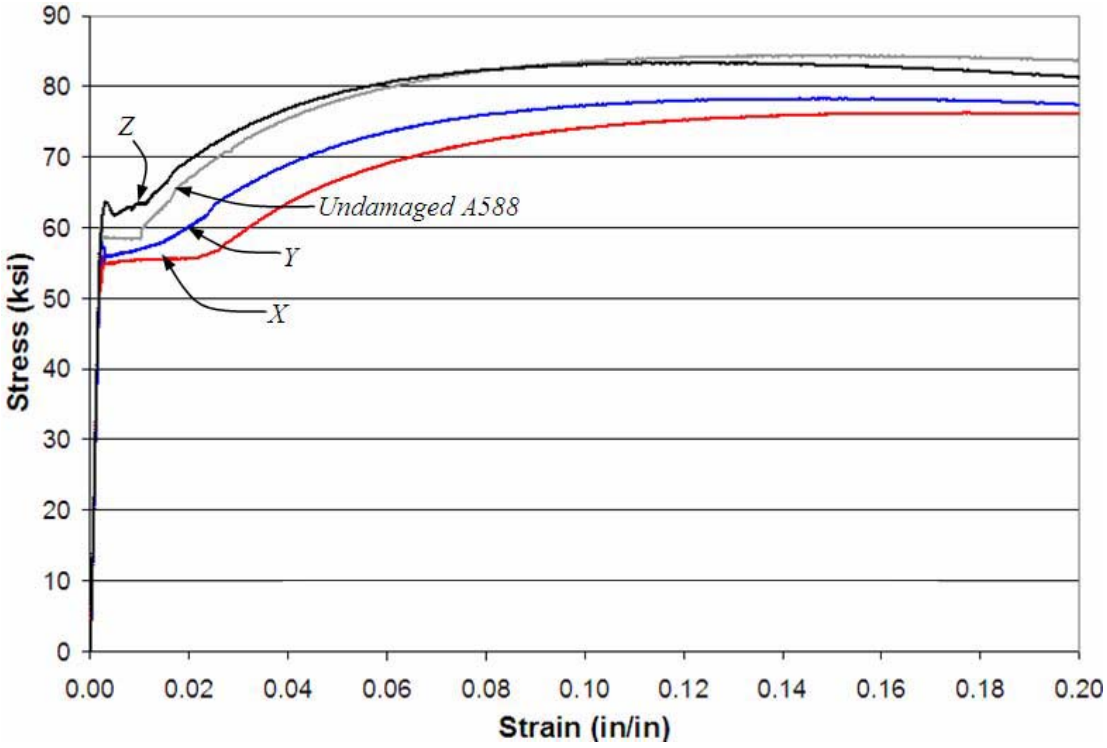

Figure 8.75
Stress-strain behavior of uniaxial tension coupons removed from A588-Beam 1

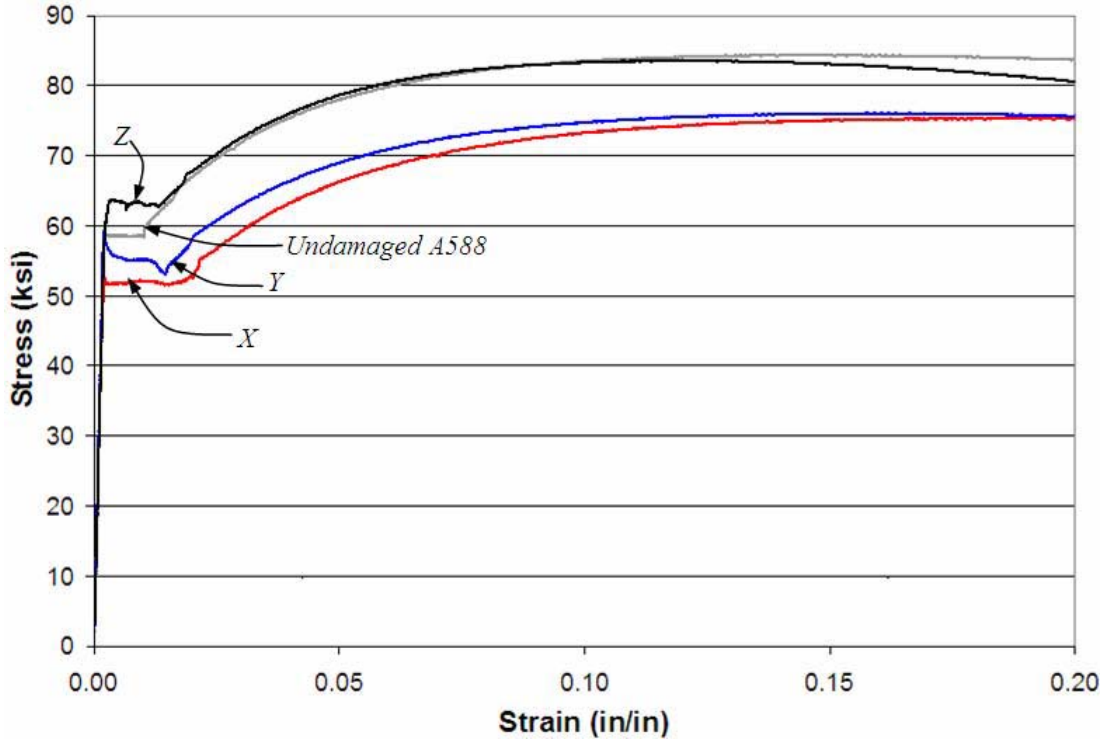

Figure 8.76
Stress-strain behavior of uniaxial tension coupons removed from A588-Beam 2

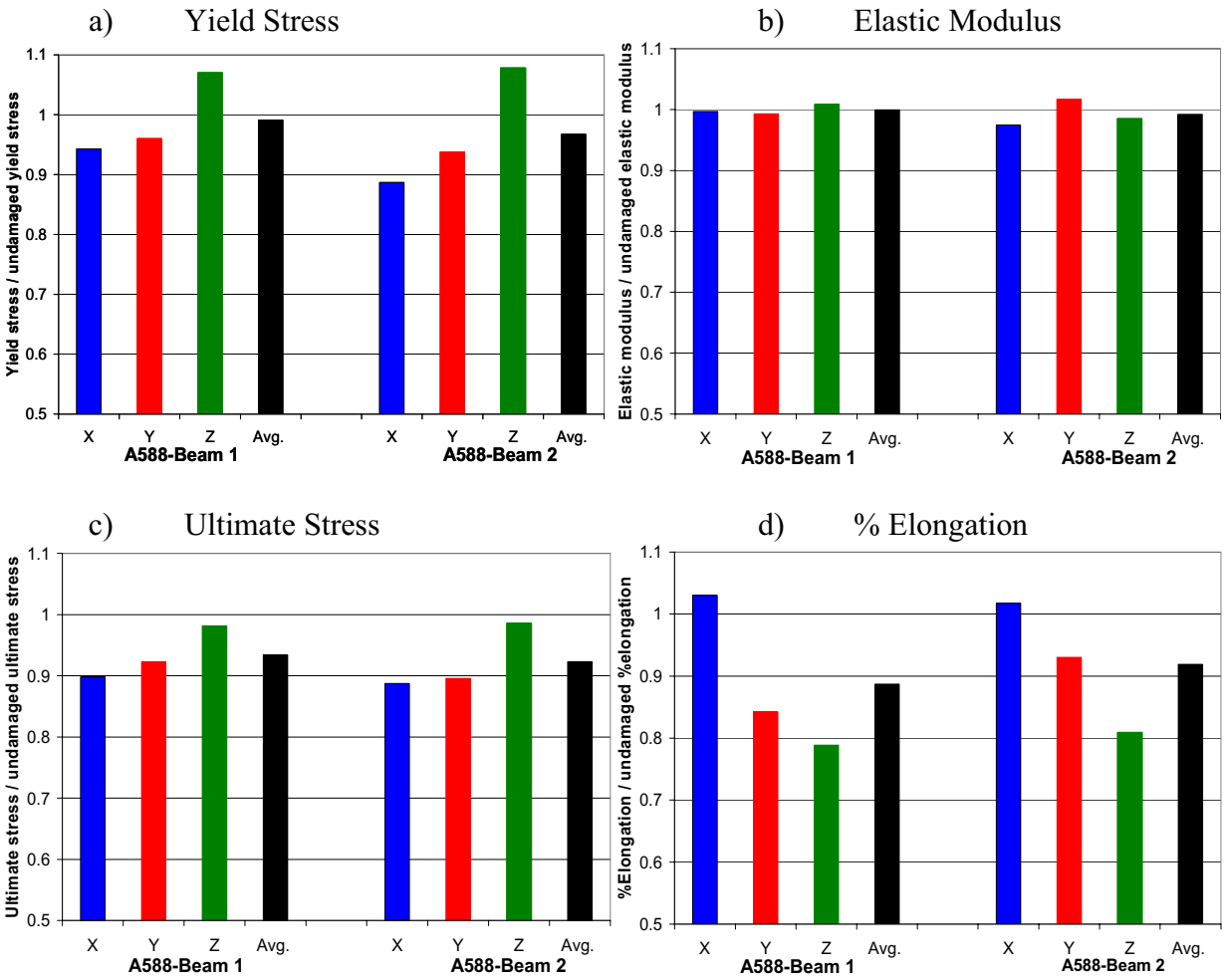

Figure 8.77
Normalized structural properties of damaged-repaired A588 steel

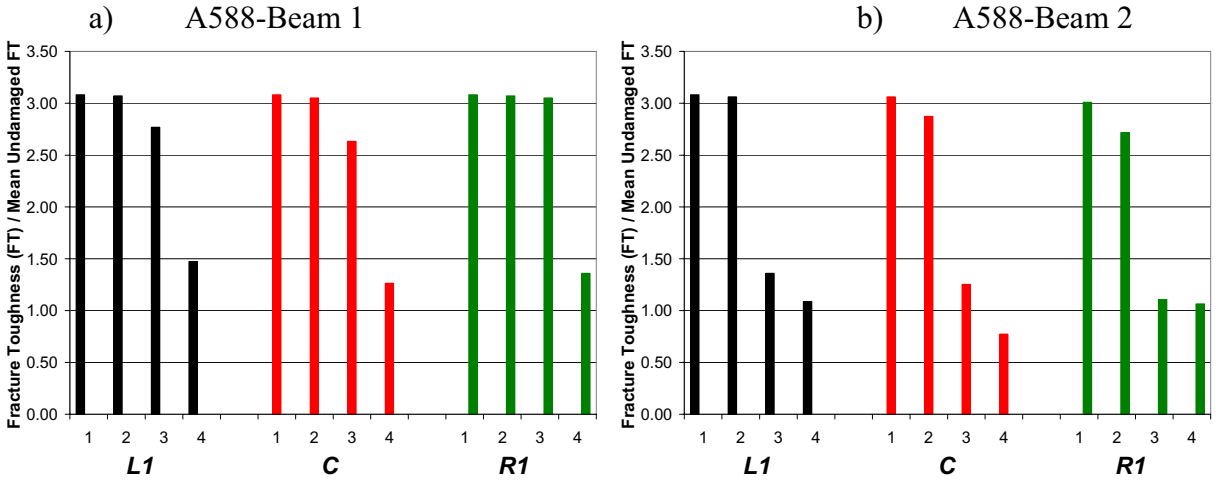

Figure 8.78
Normalized fracture toughness of damaged-repaired A588 steel

a) A588-Beam 1 b) A588-Beam 2

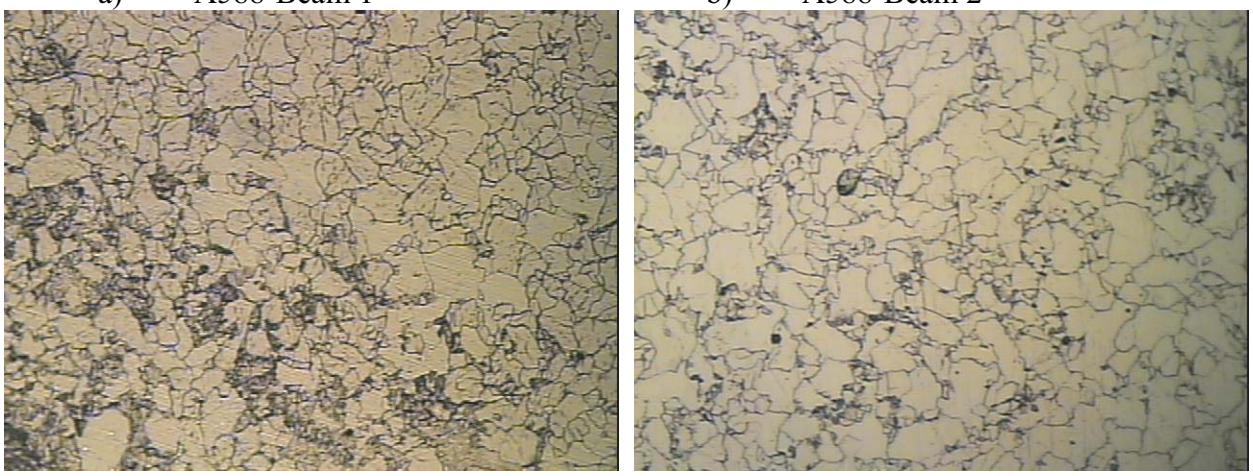

Figure 8.79
Microstructures of the damaged-repaired A588 experimental beam specimens (480X)

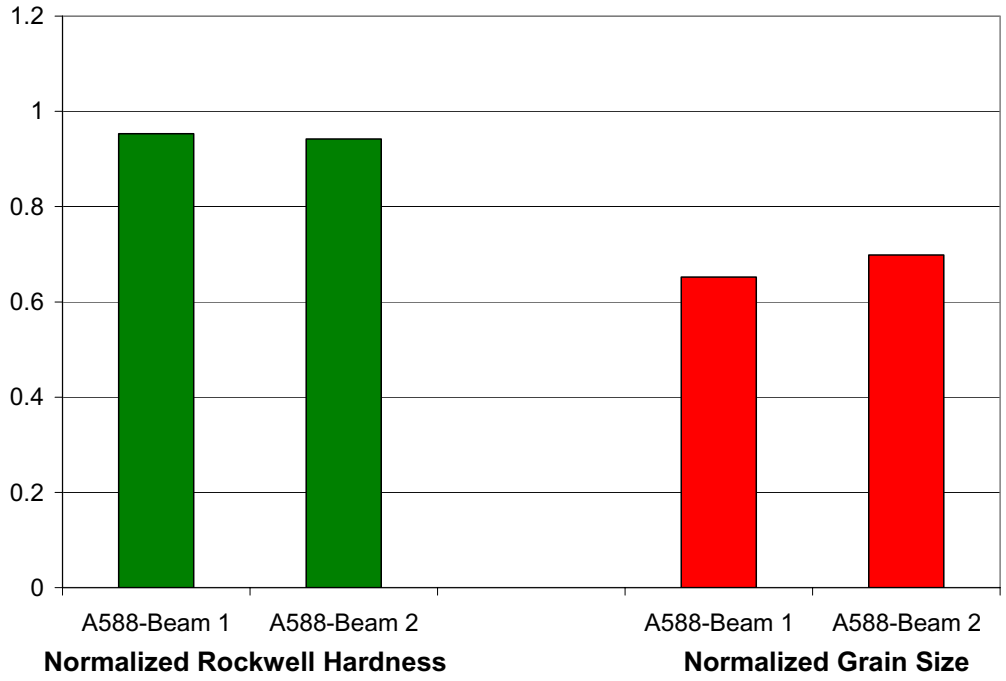

Figure 8.80
Normalized hardness and grain size of damaged-repaired A588 steel

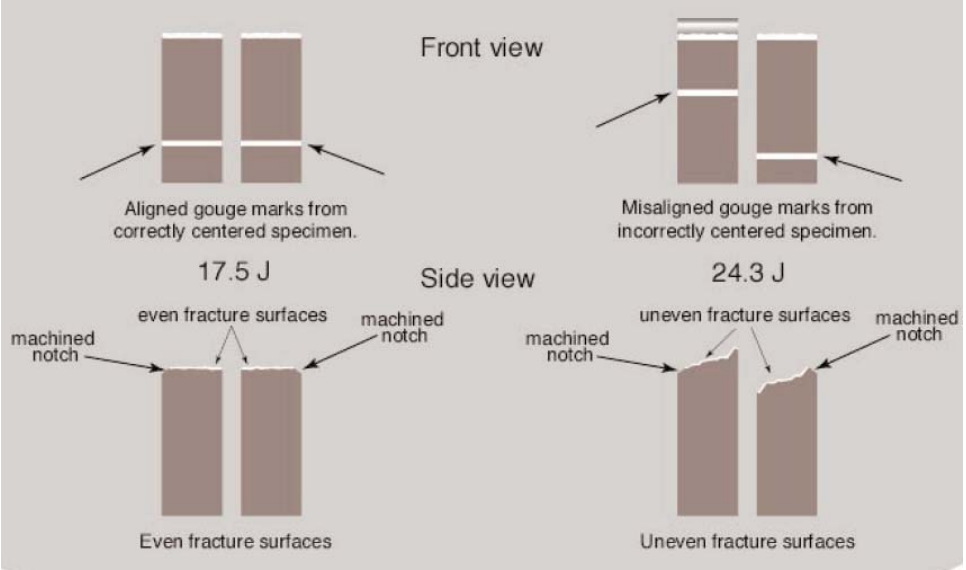

Figure 8.81
Broken orientation of off centered charpy specimens [*1*]

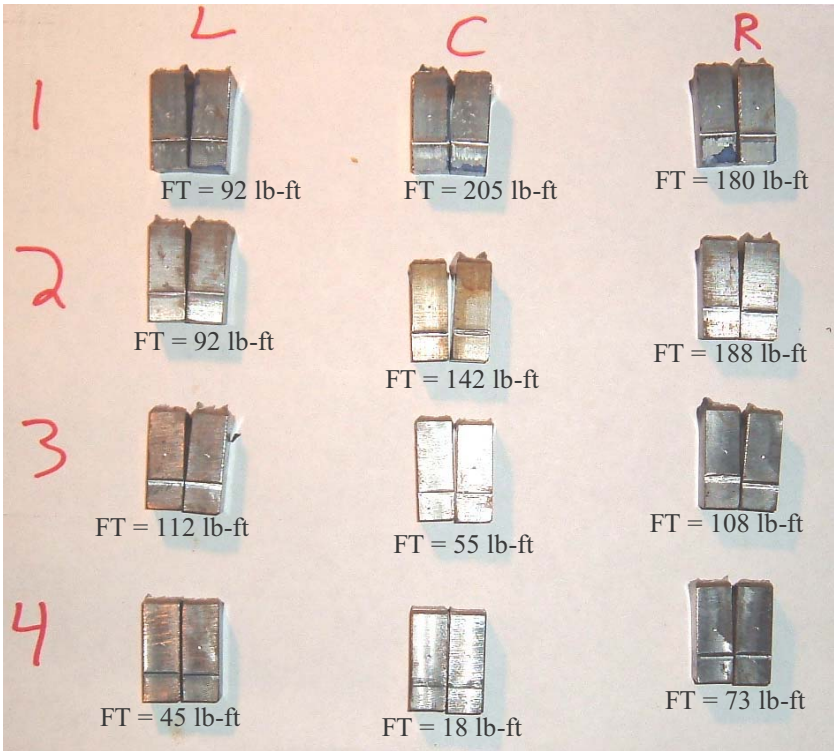

Figure 8.82
Charpy specimens from A36-Beam 2

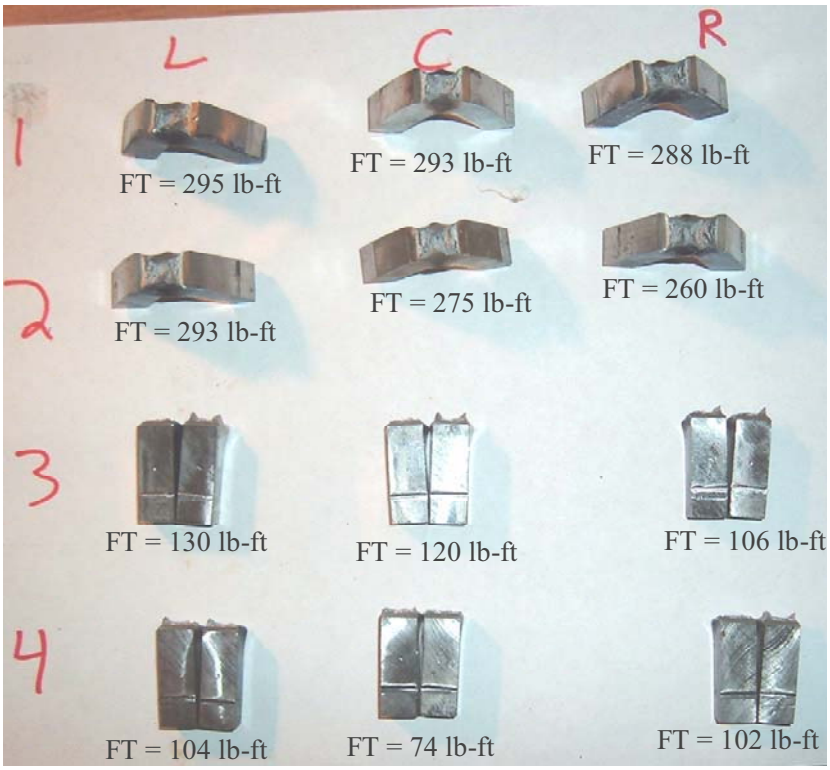

Figure 8.83
Charpy specimens from A588-Beam 2

(a) (b) (c)

Figure 8.84
Illustration of broken specimens with lower fracture toughness (A36-30-70-3)

9 SUMMARY, CONCLUSIONS, RECOMMENDATIONS, AND FUTURE WORK

9.1 SUMMARY AND CONCLSIONS FROM TASK I

Task I, Literature Review and Survey, was summarized in Chapter 2. This task included three sub-tasks: (1) literature review; (2) Survey of various DOTs; and (3) analysis of the MI high load hits database.

A comprehensive review of existing literature on heat straightening and its effects on the structural properties of steel was provided as part of this report (see Section 2.1). The results indicate that significant research has been conducted on the heat straightening repair of damaged steel members. Most of this research has focused on: (a) the development of heat straightening repair techniques for damaged steel members, (b) the development of guidelines and recommendations for heat straightening repair, and (c) the effects of heat straightening on the structural properties of steel. Currently, there is a lack of lack of knowledge of the fundamental effects of multiple damage events followed by heat straightening repairs on the structural properties including the fracture toughness and microstructure of steel. This research project focused on developing fundamental knowledge to address this shortcoming.

State DOTs across the U.S. were surveyed to determine their current heat straightening procedures and guidelines. Twenty-two state DOTs responded to the survey. The results from this survey indicate that: (a) a majority (68%) of the surveyed DOTs do not have special provisions or guidelines for heat straightening; (b) there is significant variation in the heat straightening guidelines adopted by the state DOTs across the U.S.; (c) none of the surveyed state DOTs have provisions for multiple heat straightening; (d) a majority (54%) of the surveyed state DOTs believe that the combination of the damage magnitude and the number of repairs governs the maximum number of multiple heat straightening repairs; and (e) 100% of the surveyed state DOTs are interested in the results of this research project. More specific heat straightening guidelines were provided by six of the DOTs surveyed. The different guidelines were considered very similar.

The 1976-2001 Michigan high load hits database was analyzed to determine the steel and structure types that are damaged and repaired by heat straightening most frequently. The results from this database indicate that in Michigan, A7 and A373 are the steel types most frequently damage and repaired by heat straightening followed by A588, A36, and A572. The simply supported composite wide-flange steel beam is the type of structure most frequently damaged and repaired by heat straightening in Michigan. Eighty-two percent of damage-repair cases were either composite wide-flange steel beams or composite plate girders. The steel and structure types identified by the high-load hits database were considered for the decisions made in the experimental investigations conducted in this research project.

9.2 SUMMARY AND CONCLSIONS FROM TASK II

Task II, Review MDOT Heat Straightening Procedures, was discussed in Chapter 3. This task included: (a) three site visits to Michigan steel bridges being repaired by heat-straightening, and (b) review of MDOT's documented provisions for conducting heat-straightening in the field.

In all three site visits, the repairs were conducted on composite steel beams damaged by collisions with overheight trucks. This damage caused large out-of-plane displacements of the bottom flanges. In order to repair each beam, the Statewide Bridge Crew (SBC) first applied strip heats high on the web in 5 in. bands using a low restraining force of 6 kips and temperatures significantly below 1200 °F. According to the SBC, this process is used to straighten the web and soften the beam-to-concrete slab interface. However, since the heating temperatures were significantly below 1200 °F (close to 600-800 °F), we

believe that this step did not produce any beneficial movement. This step can be removed from the overall repair procedure, or the heating temperatures must be closer to 1200 °F to repair the web effectively.

After applying the web strip heats, the SBC increased the restraining force to 15 kips, and applied partial (half) depth Vee-heats to the bottom flange on the tension (elongated) side within the damage region. The Vee angles were computed to be approximately 50-55°. The Vee-heat temperatures were typically close to 1200 °F, but sometimes increased to values as high as 1400 °F. Towards the end of the repair procedure significant overheating of the steel (red-hot color of the steel) was observed at some locations. The temperatures were too high to be measured with the temperature device, which was limited to 1450 °F. In some cases, the SBC used a sledge hammer while the steel was hot to get additional movements. These improper practices were usually limited towards the end of the repair procedure.

The current MDOT heat-straightening provisions were reviewed. The comparisons relate well with what is suggested by the Federal Highway Admission (FWHA). Besides some of the improper practices mentioned above, the SBC usually followed the MDOT guidelines. The SBC did not use Vee angles of 10° and had a tendency to heat beyond 1200 °F. The MDOT provisions should be improved to provide specific guidelines for the magnitude of restraining force or stress used while heating to repair. The engineer should design and have more control over the heat straightening repair procedure.

9.3 SUMMARY AND CONCLSIONS FROM TASK III

Task III, Effects of Multiple Heat Straightening on the Structural Properties of Steel, was discussed in Chapters 4, 5, and 6. Ninety-one small scale specimens were subjected to multiple cycles of damage followed by heat straightening repair. The damage-repair parameters included in the study were the steel type, the initial damage strain (ε_d), the restraining stress (σ_r), the maximum heating temperature (T_{max}), and the number of damage-repairs (N_r). Structural properties included in the study were the elastic modulus (E), yield stress (σ_y), ultimate stress (σ_u), strain ductility, fracture toughness, hardness, and microstructure of steel. A summary of the specimen behavior during the damage and repair cycles was included in this report (see Chapter 5). The key findings from the material tests conducted on specimens fabricated from the damaged-repaired steel specimens are as follows:

9.3.1 A7 Steel

- Damage-heat straightening repair cycles do not have a significant influence on the yield stress, elastic modulus, ultimate stress, or surface hardness of A7 steel. Most of the damaged-repaired results are within ± 15% of the undamaged values.
- The percent elongation (ductility) of damaged-repaired A7 steel is usually within 80-90% of the undamaged percent elongations. However, for specimens subjected to five cycles, the percent elongation was approximately 55-60% of the undamaged value. Increasing the damage strain, the restraining stress, or the number of damage-repair cycles reduces the percent elongation significantly.
- The fracture toughness of damaged-repaired A7 steel decreases significantly with increase in the restraining stress or the number of damage-repair cycles.
    - The fracture toughness of specimens damaged to 30 ε_y reduces to 50% of the undamaged toughness after three damage-repair cycles.
    - The fracture toughness of specimens damaged to 60 ε_y and repaired with the lower restraining stress of 0.25 σ_y is greater than the undamaged toughness after three or five cycles. Increasing the restraining stress has an adverse effect on the fracture toughness, which decreases to 50% and 25% of the undamaged toughness after three and five cycles, respectively.

- The fracture toughness of specimens damaged to 90 ε_y is close to the undamaged toughness after three damage-repair cycles. Increasing the restraining stress reduces the toughness slightly.

A7 steel can undergo up to three damage-repair cycles without a drastic reduction in the material properties. The percent elongation values are small after five damage-repair cycles. The fracture toughness values are also reduced significantly after three damage-repair cycles. Hence, a limit of three damage-repair cycles is recommended for A7 steel. The use of lower restraining stresses is also recommended.

9.3.2 A588 steel

- Damage-heat straightening repair cycles do not have a significant influence on the yield stress, elastic modulus, ultimate stress, or surface hardness of A588 steel. Most of the damaged-repaired values are within ± 15% of the undamaged values.
- The percent elongation (ductility) of damaged-repaired A588 steel is approximately 80-90% of the undamaged elongation, which is quite reasonable and usually.
- The fracture toughness of damaged-repaired A588 steel is very good. In several cases, the fracture toughness of damaged-repaired specimens is greater than or close to the undamaged toughness.
  - The fracture toughness of damaged-repaired A588 specimens never decreases below 50% of the undamaged toughness (even after five damage-repair cycles).
  - Increasing the restraining stress reduces the fracture toughness of damaged-repaired A588 specimens significantly.
  - The fracture toughness of specimens repaired with 0.25 σ_y restraining stress is greater than or close of the undamaged toughness. Specimens repaired with 0.50 σ_y restraining stress have toughness close to or less than the undamaged toughness, but never less than 50% of the undamaged toughness.

A588 steel is extremely resilient material. It has excellent material properties after several damage-repair cycles. Hence, we recommend that A588 steel can undergo up to five damage-repair cycles, which was the limit of the experimental program. Lower restraining stresses are also recommended for repair.

9.3.3 A36 Steel

- Damage-heat straightening repair cycles do not have a significant influence on the yield stress, elastic modulus, ultimate stress, or surface hardness of A36 steel. Most of the damaged-repaired are within ± 15% of the undamaged values, and are acceptable according to AASHTO requirements.
- However, the percent elongation (ductility) of damaged-repaired A36 steel is quite low, approximately 66-95% of the undamaged percent elongation. The reduction in percent elongation is greater for specimens subjected to smaller damage strains. Overall, it seems that the smaller damage strain of ε_d=30ε_y had more adverse effects on the strength and ductility of A36 steel.
- The fracture toughness of damaged-repaired A36 steel is quite poor with respect to the undamaged toughness.
  - The mean fracture toughness of specimens damaged to 30 ε_y becomes less than 50% of the undamaged toughness after two damage-repair cycles.
  - The fracture toughness of specimens damaged to 60 ε_y becomes less than 50% of the undamaged toughness after three damage-repair cycles.

- The mean fracture toughness of specimens damaged to 90ε_y was found to have significant scatter. The lower bound of the 95% confidence interval reduces below 25% generally after three damage-repair cycles. Higher restraining stress is detrimental for these specimens.

Due to the poor fracture toughness values and the significant scatter in their measured values, we recommend no more than three damage-repair cycles for A36 steel. Lower restraining stresses are recommended for repairing the damage.

9.3.4 Overheated A36 Steel

- The results from the material tests indicate excellent material properties for damaged-repaired overheated A36 steel. The strength and fracture toughness of the material increased significantly. The percent elongation (ductility) decreased by approximately the same magnitude as A36 steel repaired with a maximum temperature of 1200 °F.
- Temperatures reaching 1600 °F are not recommended because the heat flux from the torch will cause surface damage and produce unwanted distortions.

We recommend that additional research should be conducted on different types of steel subjected to multiple damage-repair cycles with heating temperatures greater than 1200 °F. If the conclusions for overheated steel are validated with further investigations, then we recommend that A36 steel should be heat straightened with maximum heating temperatures close to 1400 °F. This will also allow several damage-repair cycles to the same beam without significant reduction in the material properties.

9.4 SUMMARY AND CONCLSIONS FROM TASK IV

Task IV, Effects of Multiple Heat Straightening on Large-Scale Steel Beams, was discussed in Chapters 7 and 8. Six beam specimens were subjected to three cycles of damage followed by heat straightening repair each. Two beams were fabricated from A7 steel, two were fabricated from A36 steel, and two were fabricated from A588 steel. The behavior of the beam specimens during the damage and repair cycles was discussed in detail in Section 8.1. The results of the material tests conducted on specimens from the damage-repaired beam specimens were presented and discussed in detail in Section 8.2. The major findings from the material tests were as follows:

9.4.1 A7 Beam Specimens

- Damage-heat straightening repair cycles do not have a significant influence on the yield stress, elastic modulus, ultimate stress, or surface hardness of A7 steel. Most of the damaged-repaired are within ± 15% of the undamaged values, and are acceptable according to AASHTO requirements.
- Damage-repair cycles reduce the percent elongation (ductility) of A7 steel. This reduction in ductility ranges from approximately 80%-95% of the undamaged material.
- The fracture toughness of A7-Beam 1 subjected to three damage-repair cycles at the smaller damage strain of 30 ε_y is much lower than the undamaged toughness. The beam has become unusable after three damage-repair cycles.
- The fracture toughness of A7-Beam 2 compares favorably with the undamaged toughness. However, some variability is seen in the results and the toughness of material closer to the flange-web junction (k-region) is much lower.

9.4.2 A36 Beam Specimens

- Damage-heat straightening repair cycles do not have a significant influence on the yield stress, elastic modulus, ultimate stress, or surface hardness of A36 steel heated to 1200 ^{o}F or 1400 ^{o}F. Most of the damaged-repaired are within ± 15% of the undamaged values, and are acceptable according to AASHTO requirements.
- Damage-repair cycles reduce the percent elongation (ductility) of A36 steel. For specimens subjected to 1200 °F, the reduction in ductility ranges from approximately 86%-94% of the undamaged material. The reductions in the percent elongation from the overheated steel were much more substantial. The reduction was found from 86% to as low as 67% of the undamaged material. The reasons for this reduction are not known.
- The overall fracture toughness of A36-Beam 1 is comparable to the undamaged toughness. However, significant variability exists in the toughness of A36-Beam 1. In fact, the toughness of specimens from the center Vee heat (*C*) is much lower (average 62%) than the undamaged toughness.
- The fracture toughness of damage-repaired overheated A36 steel increased. The increase ranges from 101-460% of the undamaged toughness. There was one low value (77% of undamaged toughness).
- The fracture toughness results of specimens removed from the center Vee heat (*C*) results in the lowest values. A general trend was noticed that the fracture toughness decreased as the specimens are removed closer to the web (away from the edge of the flange).

9.4.3 A588 Beam Specimens

- Damage-heat straightening repair cycles do not have a significant influence on the yield stress, elastic modulus, ultimate stress, or surface hardness of A588 steel. Most of the damaged-repaired are within ± 15% of the undamaged values, and are acceptable according to AASHTO requirements
- Damage-repair cycles increased slightly the percent elongation of the outmost (X) specimen and decreased the percent elongation of the middle (Y) and innermost (Z) specimens. Applying a higher external restraining moment had an insignificant effect on the resulting ductility.
- Damage-repair cycles increased the fracture toughness of A588 steel significantly. However, the fracture toughness values were smaller for charpy specimens loser to the flange-web junction (k-area region)
- From A588-Beam 1, Specimens 1, 2, and 3 (including L, C, and R) were found to be exceptionally high with values ranging from 263-308% of the undamaged mean. Specimen 4 was found to be moderately high with values ranging from 126-147% of the undamaged material.
- From A588-Beam 2, Specimens 1 and 2 (including L, C, and R) were found to be exceptionally high with values ranging from 272-308% of the undamaged mean. Specimens 3 and 4 ranged from 77-136% of the undamaged material. Thus, applying a higher external restraining stress reduces the fracture toughness.

9.5 FINAL CONCLUSIONS COMBINING TASKS III AND IV

The comparisons of the major findings from Tasks III and IV were presented in Section 8.3. The major findings from the comparisons of Tasks III and IV were as follows:

- *The results for A7 steel from Tasks III and IV compare favorably. Based on the fracture toughness results of Tasks III and IV, it is recommended that A7 steel beams should not be subjected to more than three damage-heat straightening repair cycles. Smaller damage strains are more detrimental to A7 steel as compared to larger damage strains.*
- *The results for A36 steel from Tasks III and IV compare favorably. Based on the fracture toughness results of Tasks III and IV, it is recommended that A36 steel beams should not be subjected to more than three damage-heat straightening repair cycles. Overheating the A36 steel during damage-repair improves its material properties and fracture toughness significantly.*
- *The results from Tasks III and IV for A588 steel compare favorably. A588 steel is an extremely resilient material that can undergo several (up to five) damage-repair cycles without significant adverse effects on the structural properties including fracture toughness. It is recommended that A588 steel beams can be subjected to several (up to five) damage-heat straightening repair cycles. Lower restraining stresses should be used preferably. However, higher restraining stresses can also be used without impacting the material properties adversely.*

9.6 FUTURE RESEARCH

This research project developed significant knowledge of the effects of multiple damage-heat straightening repair cycles on the structural properties of bridge steels. However, some observations were interesting and additional research is needed to further validate the conclusions as follows:

- Due to a limited source of available material, the lab-scale A7 specimens of Task III had a relatively low thickness causing significant curvature in the test area of specimens subjected to higher damage strains. The researchers suggest additional investigations should be conducted on A7 steel if thicker plates become available.
- The researchers highly strongly recommend additional research and experimental investigations of the effects of overheating on the structural properties and fracture toughness of bridge steels. Due to its relevance to MDOT and poor fracture toughness results when heated to 1200 °F, perhaps A7 should be the focus for future overheating investigations. Since the fracture toughness of A588 steel never decreased substantially after multiple damage-repair events, overheating steel grade may not be necessary.